Yu Zhou
A.D. Lucey
Yang Liu
Lixi Huang *Editors*

Fluid-Structure-Sound Interactions and Control

Proceedings of the 3rd Symposium on Fluid-Structure-Sound Interactions and Control

Springer

Lecture Notes in Mechanical Engineering

About this Series

Lecture Notes in Mechanical Engineering (LNME) publishes the latest developments in Mechanical Engineering—quickly, informally and with high quality. Original research reported in proceedings and post-proceedings represents the core of LNME. Also considered for publication are monographs, contributed volumes and lecture notes of exceptionally high quality and interest. Volumes published in LNME embrace all aspects, subfields and new challenges of mechanical engineering. Topics in the series include:

- Engineering Design
- Machinery and Machine Elements
- Mechanical Structures and Stress Analysis
- Automotive Engineering
- Engine Technology
- Aerospace Technology and Astronautics
- Nanotechnology and Microengineering
- Control, Robotics, Mechatronics
- MEMS
- Theoretical and Applied Mechanics
- Dynamical Systems, Control
- Fluid Mechanics
- Engineering Thermodynamics, Heat and Mass Transfer
- Manufacturing
- Precision Engineering, Instrumentation, Measurement
- Materials Engineering
- Tribology and Surface Technology

More information about this series at http://www.springer.com/series/11236

Yu Zhou · A.D. Lucey · Yang Liu
Lixi Huang

Editors

Fluid-Structure-Sound Interactions and Control

Proceedings of the 3rd Symposium
on Fluid-Structure-Sound Interactions
and Control

Editors
Yu Zhou
Shenzhen Graduate School
Harbin Institute of Technology
Shenzhen
China

A.D. Lucey
Curtin University
Bentley
Australia

Yang Liu
The Hong Kong Polytechnic University
Hong Kong
China

Lixi Huang
The University of Hong Kong
Hong Kong
China

Printed on acid-free paper

Preface

Fluid-related structural vibration and noise are phenomena frequently encountered in many engineering applications, causing increasingly severe concerns. Turbulence clearly has a significant impact on these problems. However, there is cause for optimism as new capabilities emerge with the advent of various new techniques such as signal processing, flow visualization and diagnostics, functional materials, sensors and actuators, and control methods that are revitalizing research activities in an interdisciplinary area and constantly generating interesting new experimental and numerical findings. Within this context, the Fluid-Structure-Sound Interactions and Control (FSSIC) conference series was launched, jointly hosted by the China Aerodynamics Research and Development Center and The Hong Kong Polytechnic University, and held in Yinchuan City, China, in 2011. The series was internationalized in its second meeting held at The Hong Kong Polytechnic University in Hong Kong and Macau in 2013. This conference series aims to provide a forum for academics, scientists, and engineers working in the interconnected branches of research within FSSIC to exchange and share the latest progress, ideas and advances in these branches, bringing them together to chart and push forward the frontiers of FSSIC.

The meeting held during 5–9 July 2015 in Perth was the third of this conference series, attracting participants from all over the world and featuring prominent keynote speakers such as Profs. John Kim, Nigel Peake, Colin Hansen and Song Fu. A broad range of talks was presented covering topics such as turbulence, unsteady fluid dynamics, fluid-structure interaction, fluid-related noise and the control/management aspects of these research areas. This book contains a selection of the papers presented. We trust that it will be of interest to a broad spectrum of the engineering community.

Yu Zhou
A.D. Lucey
Yang Liu
Lixi Huang

Acknowledgements

Contents

Part I
Acoustics and Sound–Flow–Structure Interaction

Infrasound and Low-Frequency Noise from Wind Turbines

Colin Hansen, Branko Zajamšek and Kristy Hansen

Abstract Infrasound, low-frequency noise (ILFN) and amplitude modulation of the noise are known to disturb some residents living near wind farms. However, the mechanisms responsible for ILFN and amplitude modulation are not well understood. In an attempt to shed some light on these mechanisms, acoustic measurements were taken close to a wind farm, at residences located two or more kilometres from the nearest turbine in a wind farm and in an anechoic chamber using a scale-model, electrically-driven, wind turbine. The measured spectra reveal distinct peaks at the frequencies corresponding to the blade-pass frequency and its harmonics, and the characteristics of these peaks are remarkably similar for field and laboratory measurements, indicating that the zero mean flow simulation is a good representation of an actual wind turbine. Near field acoustic holography measurements on the scale-model turbine confirm that tonal components at the frequencies corresponding to the blade-pass frequency and its harmonics are generated as a result of blade-tower interaction, suggesting that it is likely to be an important mechanism of infrasound generation for industrial wind turbines. Inaccuracies in the assumed location of sources of noise generated by a wind turbine affect the accuracy of community noise predictions. This is because the source height affects the distance from the turbine beyond which sound rays arrive at the receiver having been reflected from the ground more than once, thus reducing the attenuation with distance from the turbine.

C. Hansen (✉)
The University of Adelaide, Adelaide, North Terrace, SA 5000, Australia
e-mail: colin.hansen@adelaide.edu.au

B. Zajamšek
University of New South Wales, Sydney, Kensington, NSW 2052, Australia
e-mail: b.zajamsek@student.unsw.edu.au

K. Hansen
Flinders University, Adelaide, Bedford Park, SA 5042, Australia
e-mail: kristy.hansen@flinders.edu.au

1   Introduction

One of the drawbacks of wind energy is that turbines generate sufficient noise to result in adverse reactions from some nearby residents. The noise that causes problems is infrasound and low-frequency noise (ILFN) and the associated noise levels are highly variable as a function of time, due to meteorological factors, blade loading variations, directivity variations as the turbine blades rotate, and interaction between the sound from two or more turbines. These characteristics make wind turbine noise more annoying at comparable levels than industrial and transportation noise. Also, low frequency noise and infrasound are less attenuated over large propagation distances and can penetrate buildings more readily than mid- to high-frequency noise.

In the future, the size of wind turbines is expected to increase since larger turbines are more efficient energy generators. Unfortunately, this will lead to an increase in the thrust force acting on the blades as well as an increase in the infrasound and low-frequency noise due to higher hub heights, which introduce larger variations in blade loading during a revolution. Larger wind turbines also rotate more slowly due to limitations in the allowable blade-tip velocity and therefore mechanical noise is expected to decrease in frequency. A shift of the noise spectrum to lower frequencies by approximately 1/3 of an octave has already been observed in the transition from small to large wind turbines (Møller and Pedersen 2011). If infrasound and low frequency noise are to be reduced, it is important that the corresponding noise generation and propagation mechanisms are well understood.

2   Effect of Wind Turbine Noise on People

Annoyance and sleep disturbance are reported by many residents near wind farms, even when the measured noise levels are relatively low. One reason for this is that wind farms are often found in rural areas that are characterised by low background noise levels, particularly at night time. The contrast between ambient noise and noise due to wind farm operation is also exacerbated during the evening and night-time due to stable atmospheric conditions (Van den Berg 2004). During these conditions, the wind turbines continue to operate, while the wind speed at residences is negligible, so corresponding background noise levels are often well below 20 dBA.

Stable atmospheric conditions are also characterised by high wind shear, which has been suggested as a major factor responsible for the amplitude modulation of wind turbine noise (RenewableUK 2013). Residents living near wind farms describe the associated noise as "thumping" (Van den Berg 2004) or "rumbling" (Hansen et al. 2014) in character, indicating the presence of low frequency, time varying noise. The difference between the audibility threshold and perceived loudness is small when the noise is dominated by low-frequencies (Møller and Pedersen 2004) and thus if a low-frequency noise is amplitude modulated as well as being above the normal hearing threshold, it is likely to be annoying to many people.

Some people living near wind farms also report symptoms of motion sickness, including nausea, vertigo, dizziness, and headaches. It is possible that these symptoms are related to exposure to infrasound, which is primarily generated as a result of blade-tower interaction. The amplitude of vertical motion in the 2–4 Hz range required to produce seasickness in sensitive individuals corresponds to an atmospheric pressure variation that is similar to the levels of acoustic pressure variation experienced by people living in the vicinity of wind farms (Dooley 2013). The regular, periodic nature of these variations, or the symmetry of the maximum and minimum values compared to the mean, may explain why similar levels of random environmental infrasound do not result in motion sickness symptoms in sensitive individuals. Another explanation for adverse health symptoms reported by people living near wind farms is that infrasound can be detected by the outer hair cells of the human ear at levels below the audibility threshold (Salt and Lichtenhan 2014), which may result in feelings of fullness, pressure or tinnitus. Salt's work is by no means generally accepted and the subject of infrasound is still surrounded by controversy and ongoing debate about its significance. One or more of the above mentioned symptoms can also be attributed to excessive exposure to low frequency noise.

3 Infrasound and Low-Frequency Noise Generating Mechanisms

Wind turbines generate infrasound and low-frequency sound, as well as mid-and high-frequency sound. However, as low-frequency sound and infrasound are not attenuated by atmospheric absorption nor by reflection from the ground, they dominate the noise spectrum at residences more than one or two kilometres from the wind farm. These sounds are either aeroacoustic or mechanical in origin and can be either tonal or broadband in nature, depending on the generation mechanism. Aerodynamic infrasound and low-frequency noise originate as a result of changes in the aerodynamic force acting on the blades as they rotate. This can be caused by wind shear, atmospheric turbulence, cross-wind conditions, or interaction with the disturbed flow between the blade and tower as the blade passes the tower. The disturbed flow is a result of the flow streamlines having to deviate to negotiate the tower obstacle. It has been shown analytically that this phenomenon, illustrated in Fig. 1, is responsible for variations in the blade loading and hence generation of tonal components at the blade-pass frequency and harmonics (Doolan et al. 2012). In Fig. 1, it can be seen that the potential flow over the support tower creates a region of reduced velocity in front of the support tower. When the blade passes through that region, the angle of attack varies which changes the lift force and subsequently produces sound.

Interaction between the in-flow turbulence and the turbine blades as they rotate also leads to aerodynamic loading fluctuations, which are responsible for the generation of low frequency, broadband noise. The level of in-flow turbulence, and hence noise generation, varies with the extent to which turbines are located in the wake
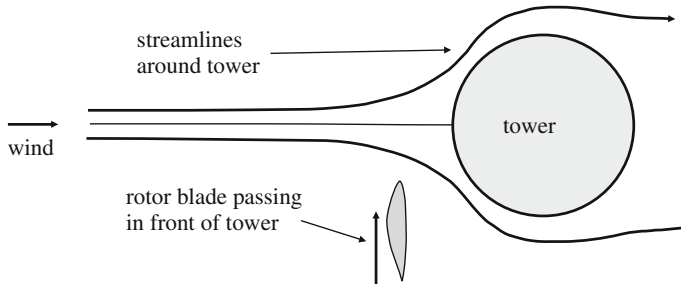
Fig. 1 Blade-tower interaction

of others as well as wind gradients, temperature gradients and atmospheric stability. The resulting far field noise from this interaction is strongly dependent on the in-flow turbulence spectrum. Large eddies in the in-flow cause a change in the aerodynamic force over the whole blade surface and consequently noise radiation has a dipole directivity pattern and the peak radiating frequency is low, typically below 20 Hz for a modern turbine (Doolan et al. 2012).

A general theory, explaining sound radiation due to unsteady blade loading was first proposed by Tyler and Sofrin (1962) for the case of turbo-machinery and was later expanded to an open rotor via the concept of pressure modes (Wright 1976). More recently, this theory has been applied to wind turbines by (Dooley and Metelka 2014). According to the theory, any rotor can be thought of as a system of rotating forces whose magnitude varies with rotor azimuthal position. These rotating forces can be simulated by a point source on the blade at a location, r_e, which is usually 0.8 times the blade span from the centre of the rotor plane. At any instant in time, these pressure variations are in-phase at each blade location, but they are not sinusoidal and thus can be described in terms of harmonics of the blade pass frequency, which rotate with the blade—hence their name, "spinning modes". The mode order indicates the number of 2π changes during one complete blade revolution.

Each pressure harmonic radiates noise in all directions, but the radiation to the side of the rotor is slightly greater. The tonal peaks in the radiated noise spectrum are broadened a little by the Doppler shift as a result of the motion of the blades. The broadening is dependent on the observer location and increases as the observer moves from on-axis to the side of the rotor plane.

When a rotating wind turbine blade passes the tower, the blade experiences a loading excursion that adds to the other pressure variations and increases the sound radiation in the directions normal to the rotor plane (see Fig. 2). Although the blade experiences the change in loading across the whole span, it can be simulated by an equivalent point loading at an effective radius, r_e. The sinusoidal signal at the top of the figure represents both the sound pressure variation as a function of time for a specified location as well as the sound pressure distribution around the circle containing the equivalent point sources at any instant in time. The sound field at

Fig. 2 Principle of spinning modes. The *dashed line* represents the effective radius of the equivalent point source and the *solid line* indicates the blade loading, showing a step excursion as a result of blade tower interaction
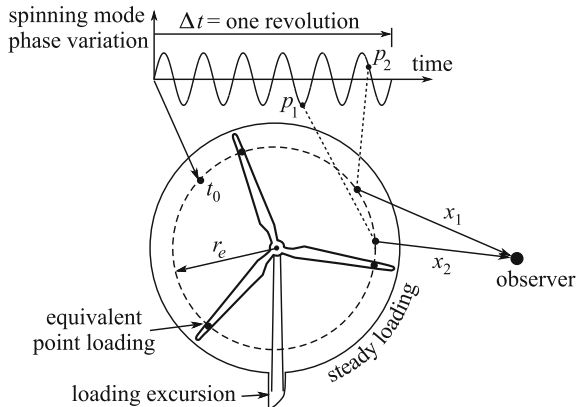
an arbitrary observer is a function of the path difference x_1 and x_2 (see Fig. 2), and also linear phase variations around the spinning mode at p_1 and p_2. It is thus the modal phase and path difference that define the frequencies at which constructive and destructive interference occur at any particular location. This process produces characteristic interference lobes that radiate in specific directions, and which appear at higher blade-pass frequency harmonics.

Loading unsteadiness caused by turbulent in-flow is random in nature and is highly influenced by meteorological conditions, which affect the level of atmospheric turbulence as well as the characteristics of the wake generated by upstream turbines. Time-varying noise characteristics at the receiver can also be caused by constructive/destructive reinforcement of sound waves arriving at a residence from two or more wind turbines. The regions in which constructive/destructive interference occur are defined by the relative phase of the incoming sound waves, which varies with wind direction and blade rotation rate, leading to a time dependent amplitude variation of sound at any given location. This phenomenon is accentuated in stable atmospheric conditions which have low associated atmospheric turbulence, resulting in different turbines rotating at more similar speeds with reduced fluctuations (Van den Berg 2005).

In addition to the random amplitude variations discussed above, periodic variations in the loudness (or amplitude modulation) of wind turbine noise also occur, with the frequency of variation generally equal to the rate at which blades pass the tower. In cases where local stall occurs, the trailing edge noise spectra shifts to lower frequencies and the resulting time-varying noise has been described as "thumping" (RenewableUK 2013). In contrast to attached flow trailing edge noise, which shows most significant amplitude modulation in the crosswind direction at large distances (Oerlemans and Schepers 2009), amplitude modulation associated with stall noise is highest in the upstream and downstream directions (RenewableUK 2013).

Another noise source that is subject to amplitude modulation is gearbox noise. This can occur when the planetary gear mesh noise is amplitude modulated by the

blade/planet-pass frequency and this phenomenon appears to be responsible for the "rumbling" noise that has been measured near the South Australian Waterloo wind farm (Hansen et al. 2014).

4 Infrasound and Low Frequency Noise Propagation

In general, sound spreads spherically from a given source, resulting in an attenuation rate of 6 dB/doubling of distance. However, in the downwind direction, the wind speed gradient causes the sound waves to bend towards the ground, reducing the attenuation of noise in the downwind direction. Vertical temperature gradients also give rise to sound speed gradients, but the effect of the wind speed gradient is generally dominant in the propagation of sound from wind turbines. The effect of a downward refracting atmosphere is that beyond a certain distance, more than one ground reflected ray will arrive at the receiver. The first ground reflected ray will have been reflected from the ground once, the second ground reflected ray will have been reflected from the ground twice, etc.

The distance from the sound source at which sound will begin to attenuate at a rate less than 6 dB/doubling of distance is a function of the source height as well as the strength of the atmospheric sonic velocity gradient (and the consequent strength of the downward refraction), as this determines the distance from the source at which the receiver will experience the arrival of more than one ground reflected wave. The effect only occurs at low-frequencies for which losses due to ground reflection and atmospheric absorption are negligible. The path length of reflected sound rays increases as the number of reflections increase and so the amplitude of the sound pressure (relative to the direct, non-reflected ray) arriving at the receiver from each reflected ray decreases as the number of reflections increases, until after a certain number of reflections, a particular ray is no longer an important contributor to the sound pressure level at the receiver. It has been shown that the sum of all reflected rays results in a decay of the sound field of approximately 3 dB/doubling of distance (Willshire Jr and Zorumski 1987), which is why it is often referred to as "cylindrical spreading". Of course there is a gradual transition over both decreasing frequency and increasing distance from the source, during which the decay rate changes from 6 to 3 dB/doubling of distance.

5 Experimental Measurements of Blade-Tower Interaction

To develop an understanding of how blade-tower interaction contributes to wind turbine infrasound and low-frequency noise generation, experimental work was undertaken in the anechoic chamber at the University of Adelaide using the scale-model wind turbine shown in Fig. 3a. The anechoic chamber has dimensions of $4.79 \times 3.9 \times 3.94$ m. The blades on the wind turbine model had a symmetrical airfoil

(a)

(b)
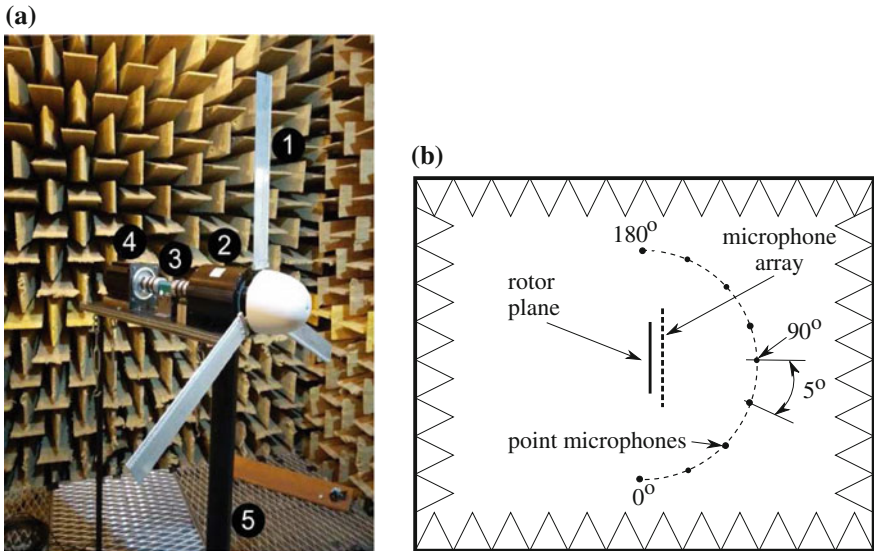
Fig. 3 Scale-model wind turbine. Parts are: (*1*) NACA 0012 airfoil (tripped at 10 % chord length, 70 mm chord, 450 mm span), (*2*) Slip ring (24 channels), (*3*) Torque sensor, (*4*) AC driver and (*5*) Support tower (70 mm outer diameter)

shape, they were mounted at 0° angle of attack and they were driven by an electric motor in conditions of zero net flow. Although this experimental configuration does not replicate the effect of the reduced velocity field in-front of a turbine tower, which is the major source of unsteady aerodynamic loading, the blade-tower interaction is still adequately re-created via the interaction of the support tower with the potential velocity field surrounding the blade. The 0° angle of attack is ideal for studying BTI as the resulting noise spectrum is not affected by noise generated by thrust and torque loading. However, for zero angle of attack symmetrical blades, the pressure resulting from the displacement of fluid caused by the advancing blades, results in pressure variations in the air that it passes through, generating "thickness noise" that adds to the BTI noise as the blades pass the tower.

The rotor model was driven at 900 RPM, giving a blade tip speed of ~47 m/s and a blade-pass frequency of 45 Hz. The rotor plane was located 70 mm away from the closest point on the tower. This distance is comparable to one blade chord length and is found to be a good scaled representation of the blade-to-tower distance on a utility-scale wind turbine. The blade-tower interaction was investigated using point microphone measurements and a 1.5 m diameter circular microphone array containing 64 GRAS 40PH phase and magnitude matched microphones on a plane parallel to the rotor plane and 10 cm from it. The data obtained with the microphone array were processed using statistically optimised near-field acoustic holography (SONAH) (Hald 2009) to obtain low-frequency sound source visualisation in the rotor plane.

Fig. 4 Effect of the distance, d, between the support tower and the blade on the blade-tower interaction noise at 0° angle of attack
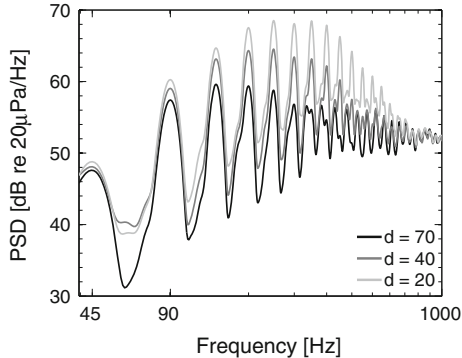
Fig. 5 Blade-tower interaction noise directivity pattern for selected frequencies. *Dashed* circular contours denote sound pressure level in dB and are 5 dB apart
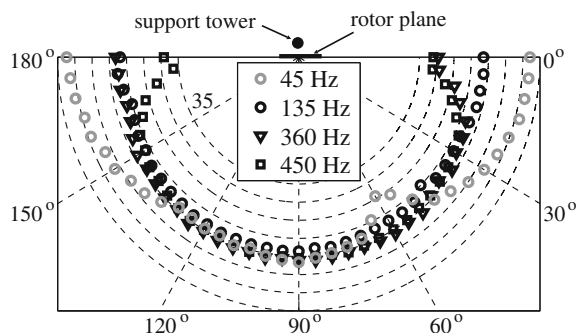
Figure 4 shows the power spectral density of the blade-tower interaction noise measured on an axis perpendicular to the rotor plane centre. As can be seen, the spectrum consists of a series of "peaks" which are harmonically related to the blade-pass frequency of 45 Hz. It is also evident that the noise magnitude is inversely proportional to the distance d between the rotor plane and the support tower, which is in accordance with previous research (Madsen 2010). This indicates that the support tower does have an effect on the blade loading via interaction with the potential field surrounding the blade and the noise production mechanism is identical to the one experienced by full-size wind turbines.

Figure 5 shows the directivity pattern for 45, 135, 360 and 450 Hz. These frequencies correspond to the 1st, 3rd, 8th and 10th harmonics of the blade-pass frequency, respectively. It can be seen that sound radiation at 135 Hz is omnidirectional, assuming symmetry across the rotor plane. For 360 and 450 Hz, a significant reduction in the sound pressure level is observed at angles < 30° and > 150°. For 45 Hz, constructive interference is seen on each side of the rotor plane (between 0° and 30° and between 150° and 180°) and destructive interference is seen at 60°. The constructive and destructive interference at any particular harmonic frequency is a result of the spinning mode acoustic interference in the rotor plane.
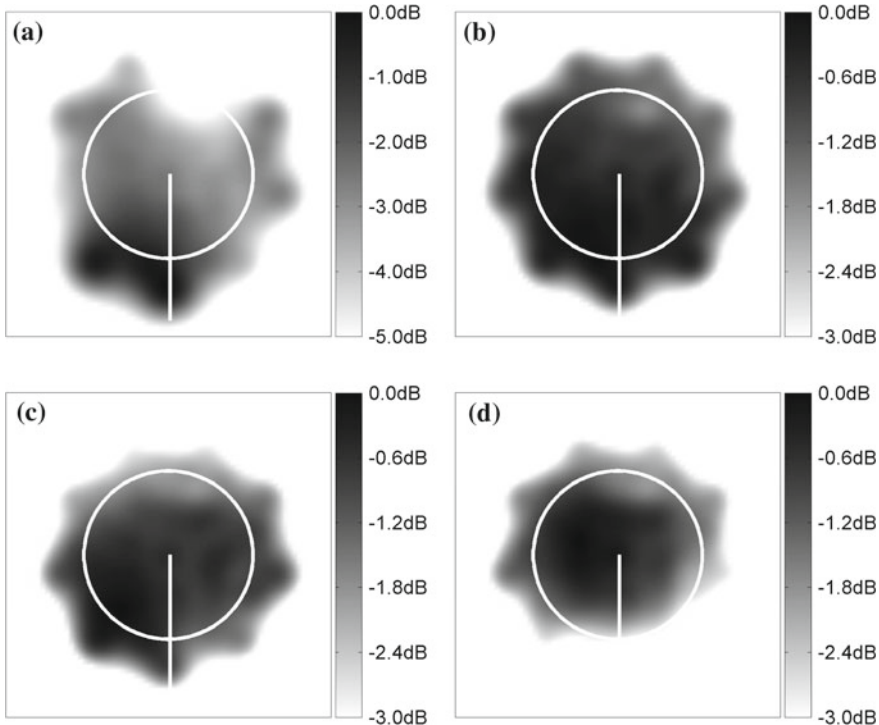
Fig. 6 Near-field acoustic holography. The *white circle* indicates the outer edge of the rotor plane and the thin *white vertical line* represents the support tower. **a** $f = 45\,$Hz, **b** $f = 135\,$Hz, **c** $f = 360\,$Hz, **d** $f = 450\,$Hz

The SONAH sound field visualisation shown in Fig. 6 indicates that the majority of energy at the blade-pass frequency, $f = 45\,$Hz, in Fig. 6a originates at the support tower position. Radiation at higher blade-pass frequencies, $f = 135, 360$ and $450\,$Hz in Fig. 6b–d, respectively, is no longer highly concentrated at the support tower location but is rather spread out in the lower or middle part of the rotor plane. The most likely reason for the peak sound source being located slightly to the left of the tower in Fig. 6a, is that the peak loading occurs close to the leading edge (Wright 1971). Since the blades are rotating in a clockwise direction, the leading edge is thus on the left side of the support tower when the blade is directly in front of the tower. The appearance of two sources in Fig. 6a, separated by the microphone spacing between the nine microphones in the outer circle of the array is an artefact of the SONAH process. This should be interpreted as a single source. Similarly the separate sources shown on the outer circle in Fig. 6b, c should be interpreted as a single source with intensity varying from a maximum at the bottom to a minimum at the top of the rotor plane.

The spread of the apparent source location at higher frequencies is an effect of the spinning modes and the frequency at which it begins to occur is a function of how close the observation plane is to the rotor plane.

6 Field Measurements of Propagation

Indoor and outdoor measurements were made continuously for approximately one-week periods at 3 residences near the Waterloo wind farm, which consists of 37 turbines. Measurements were made outdoors using a G.R.A.S. type 40AZ microphone with an electrical noise floor of 16 dB(A) and with a linear response down to 0.5 Hz. Hemispherical secondary windshields of 450 mm diameter, designed according to the IEC-61400-11 (2012) standard, were used to minimise wind-induced noise. Wind speed and direction were measured at 5-min intervals at heights of 1.5 and 10 m, and the 10-min average was calculated from the 5-min data. Wind speed and direction at hub height were measured using a SODAR unit which was located on the ridge-top in the gap between the Northern and Southern wind turbine group shown in Fig. 7. The wind farm operator also provided hub height wind speed and direction for the period in which data for House 1 and House 2 were collected.

The residence locations relative to the wind farm is shown in Fig. 7. House 1 is 3.5 km from the nearest wind turbine, which is positioned close to the centre of the main turbine group. House 2 is 8.7 km from the nearest wind turbine, which is the furthest north turbine of the main group. House 3 is 3.3 km from the nearest wind turbine, which is the furthest south turbine in the smaller northern group. The downwind directions from the closest wind turbine to residences 1, 2 and 3 are 88°, 268° and 300°, respectively. The wind speeds and directions at 1.5 m, 10 m and hub height are presented in Table 1 along with the overall output power from the wind farm and stability factor for the measurements shown in Fig. 7. For each measurement, the

Fig. 7 Field measurement locations
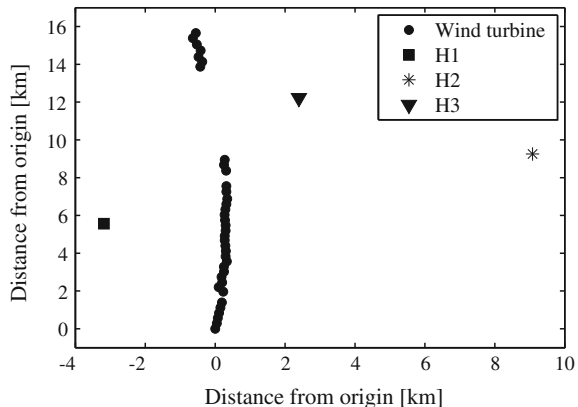
Table 1 Wind and turbine operational conditions for the data shown in Fig. 8

Description	Wind speed (m/s)			Wind direction (°)			Power	Stability
	1.5 m	10 m	Hub height	1.5 m	10 m	Hub height	Output (%)	factor
H1	1.8	3.4	10.5	135	135	133	44	0.4
H2	1.6	2.9	8.7	293	281	305	56	0.4
H3	0	0.4	10.4	–	22.5	287	53	1.1

Wind speed at hub height is for the turbine nearest to the residence

residence was located in a downwind direction (±45°) from the nearest wind turbine. It can be seen that the most stable conditions occurred during the measurements at House 3 according to the definition of stability factor, m.

$$m = \frac{\log_{10}\left(v_h/v_{ref}\right)}{\log_{10}\left(h/h_{ref}\right)} \tag{1}$$

where v_h is the velocity at 80 m hub height, v_{ref} is the velocity at 10 m, h is the height of wind turbine hub above a given residence and h_{ref} is 10 m.

Figure 8 shows the measured infrasound at three different locations near the Waterloo wind farm. The harmonics of the 0.8 Hz blade-pass frequency extend up to at least the 8*th* order at all three residences, including the one located 8.7 km away from the wind farm. The relative amplitude of the peaks is consistent with their distances from the wind farm, and maximum attenuation occurs at H2. Propagation to H2 would also be affected by a ridge which is located between the residence and the wind farm and runs parallel to the line of wind turbines. The fundamental blade-pass frequency is not consistently visible in the outdoor spectra and this is attributed to the presence of wind-induced noise at some locations. The wind-induced noise raises the level of the broadband infrasound, particularly at very low frequencies and this causes masking of the peak at 0.8 Hz at H1 and H2. The blade-pass frequency harmonics can also be observed in the indoor results but the magnitude of the peaks below 6 Hz is not representative of the true signal due to the roll-off characteristic of the B&K 4955 microphones that were used for the measurements made indoors.

Comparison between Figs. 4 and 8 indicates that there are striking similarities between the experimental and measured results. In both cases, the amplitude of the infrasonic peaks is significantly higher than the sound pressure levels at adjacent frequencies and the harmonics extend to similar orders. For the blade-tower spacing in Fig. 4 of $d = 70$ mm, which represents the spacing for an industrial wind turbine based on scaling considerations, it can be seen that the relative amplitudes of the first six harmonics are similar to those in Fig. 8, which were measured on an industrial turbine.

To investigate the effect of source height, receiver position and atmospheric velocity profile on the distance at which multiple reflections first occur, a ray tracing model was used and the results are shown in Fig. 9. Field measurement data
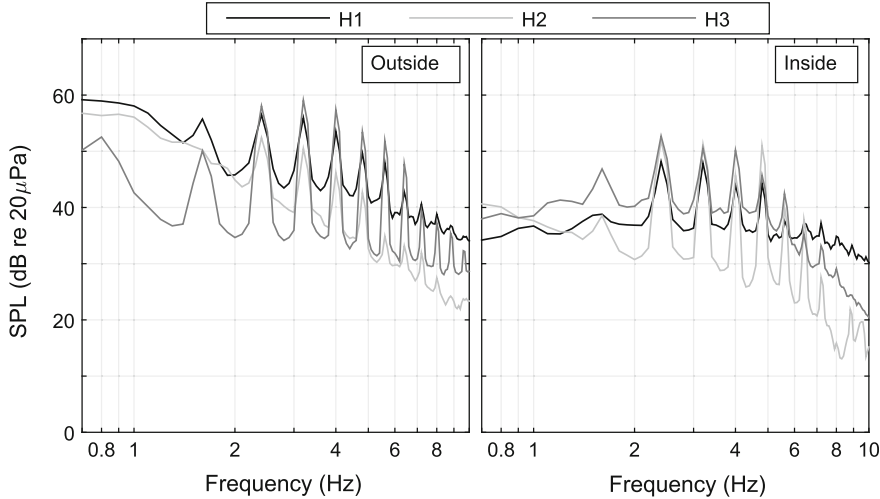
Fig. 8 Measured infrasound

Fig. 9 Comparison between ray tracing results and published data for the distance from the source at which multiple ground reflections begin to occur
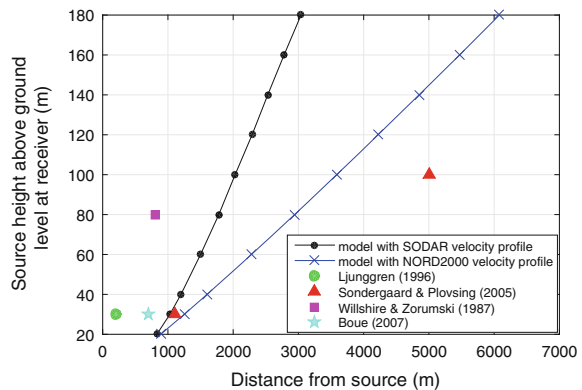
published in a wide range of studies (Ljunggren 1996; Sondergaard and Plovsing 2005; Willshire Jr and Zorumski 1987; Boué 2007) are also plotted for comparison. Differences between the model and measurements by others can be attributed to the vertical atmospheric sonic velocity profile associated with the measurements. Since this information was not available from the literature, the profile used in this study was specified according to SODAR data measured under stable atmospheric conditions (Hansen et al. 2015) and according to the logarithmic velocity profile used in the Nord2000 propagation model (Plovsing and Kragh 2006; Plovsing 2007). It is evident that the assumed vertical sonic velocity profile has a large impact on the model output, particularly at large propagation distances.

As indicated in Fig. 9, it is important to take into account the height of the source when considering propagation of noise from a wind farm. Since noise at infrasonic frequencies is attributed to blade-tower interaction, the source height for these frequencies is the point at which this interaction noise is maximum. In the case of the experiments presented in Sect. 5, the maximum noise occurred close to the blade-tip as the blade passed the tower. It is possible that this point would vary for an industrial wind turbine since the blades have significant twist and taper, which has a large impact on the corresponding aerodynamic forces. Nonetheless, it is anticipated that the source height for blade-tower interaction noise would be appreciably lower than the hub height, which is generally assumed as the relevant source height in propagation analyses. Therefore, the distance from the source at which multiple reflections first occur would be reduced. If the blade-tower interaction noise source is in fact located at the blade-tip for a Vestas V90 3MW wind turbine model (installed at Waterloo), the corresponding source height would be 36 m. According to Fig. 9, this would reduce the distance at which multiple reflections first arrive at the ground by 0.5–1.3 km, depending on the relevant velocity profile. Therefore, due to the contribution of an increased number of ray paths, the attenuation of noise at infrasonic frequencies would be less than would be predicted if the source were assumed to be at hub height.

Determination of the relevant source height is also an important consideration for the other aerodynamic and mechanical noise sources that were discussed in Sect. 3. It is therefore important to determine the blade positions at which blade stall occurs, how mechanical noise is radiated by structural components such as the blades and tower and which blade location the noise due to in-flow turbulence would be maximum. The directivity of these noise sources is also important.

7 Conclusions

Comparison between the field measured noise data near a wind farm and laboratory measurements using a motor-driven model turbine in zero incident flow reveals striking similarities in the infrasonic acoustic spectra. The accurate prediction of the propagation of this noise is dependent on the source height that is used, which is why the relative source height determined from laboratory measurements is a useful input to noise prediction models. The source height together with the vertical wind speed profile determine the distance from the source beyond which sound rays that have experienced more than one ground reflection will arrive at the receiver, thus resulting in increased noise levels over what would be expected due to a sound field decay of 6 dB/doubling of distance.

References

Boué M (2007) Long-range propagation over the sea with application to wind turbine noise. Technical report, KTH

Doolan C, Moreau DJ, Brooks LA (2012) Wind turbine noise mechanisms and some concepts for its control. Acoust Australia 40(1):7–13

Dooley KA (2013) Significant infrasound levels a previously unrecognized contaminant in landmark motion sickness studies. J Acoust Soc Am 134(5):4097

Dooley KA, Metelka A (2014) Acoustic interaction as a primary cause of infrasonic spinning mode generation and propagation from wind turbines, vol 20, p 2272

Hald J (2009) Basic theory and properties of statistically optimized near-field acoustical holography. J Acoust Soc Am 125(4):2105–2120

Hansen K, Hessler G, Hansen C, Zajamsek B (2015) Prediction of infrasound and low frequency noise propagation for modern wind turbines: a proposed supplement to ISO 9613–2. In: Proceedings of WTN15, the sixth international conference on wind turbine noise

Hansen K, Zajamsek B, Hansen C (2014) Comparison of the noise levels measured in the vicinity of a wind farm for shutdown and operational conditions. In: InterNoise 2014

IEC-61400-11 (2012) Wind turbine generator systems—part 11: acoustic noise measurement. Technical report, International Standard IEC 61400–11

Ljunggren S (1996) Ljudutbredning kring havsbaserade vindkraftverk. resultat fren litteraturstudie. Technical report, Department of Civil and Architectural Engineering, KTH

Madsen HA (2010) Low frequency noise from wind turbines mechanisms of generation and its modelling. J Low Freq Noise Vib Active Control 29(4):239–251

Møller H, Pedersen CS (2004) Hearing at low and infrasonic frequencies. Noise Health 6(23):37

Møller H, Pedersen CS (2011) Low-frequency noise from large wind turbines. J Acoust Soc Am 129:3727–3744

Oerlemans S, Schepers J (2009) Prediction of wind turbine noise and validation against experiment. Int J Aeroacoust 8(6):555–584

Plovsing B (2007) Proposal for nordtest method: Nord 2000-prediction of outdoor sound propagation. DELTA Acoustics, Report AV, 1106(07)

Plovsing B, Kragh J (2006) Nord 2000, comprehensive outdoor sound propagation model. part 2: propagation in an atmosphere with refraction. Delta Acoustics for Nordic Noise Group, Report AV 1851/00

RenewableUK (2013) Wind turbine amplitude modulation: research to improve understanding as to its cause and effect. Technical report

Salt AN, Lichtenhan JT (2014) How does wind turbine noise affect people. Acoust Today 10:20–28

Sondergaard B, Plovsing B (1016) (2005) Noise from offshore wind turbines. Environmental Project

Tyler JM, Sofrin TG (1962) Axial flow compressor noise studies. SAE Trans 70:309

Van den Berg G (2004) Effects of the wind profile at night on wind turbine sound. J Sound Vib 277:955–970

Van den Berg G (2005) The beat is getting stronger: the effect of atmospheric stability on low frequency modulated sound of wind turbines. J Low Freq Noise Vib Active Control 24(1):1–24

Willshire Jr WL, Zorumski WE (1987) Low-frequency acoustic propagation in high winds. In: NOISE-CON 87; Proceedings of the National conference on noise control engineering, vol 1, pp 275–280

Wright S (1971) Discrete radiation from rotating periodic sources. J Sound Vib 17(4):437–498

Wright S (1976) The acoustic spectrum of axial flow machines. J Sound Vib 45(2):165–223

The Aeroacoustics of the Owl

Nigel Peake

Abstract The secret of certain owl species enabling them to fly stealthily is investigated and adapted to the suppression of aeroacoustic noise at the trailing edge of a wing or blade. Two features from the owl are mimicked: the poro-elastic trailing edge in the owl's feather, and the fibrous canopy structure above the nominal wing surface. Initial modelling and experimental results demonstrate up to 10 dB noise reduction over a wide frequency range without reducing aerodynamic performance.

Keywords Aeroacoustics · Biomimicry

1 Introduction

Many species of owl can hunt in acoustic stealth. The question of precisely how the owl actually manages to fly so quietly has remained open. However, it has long been appreciated that owls which need to hunt silently possess two unique features, which are not found on any other bird, and indeed are not even found on owls which do not need to hunt silently (e.g. on small owls which feed on insects, or Fish owls). First, the microstructure of the feathers on the upper wing surface is exceedingly complex, with an array of hairs and barbs which form a thick canopy just above the nominal wing surface—see Fig. 1. Second, the wing trailing edge possesses a small flexible and porous fringe—see Fig. 2.

Our research objective is to answer the following two questions: First, how do these two features of the owl actually work to suppress noise? And second, can we learn something form the owl which can be applied in engineering practice? The first question is exceedingly complex, and as I will describe has only been partially

N. Peake (✉)
Department of Applied Mathematics & Theoretical Physics, University
of Cambridge, Wilberforce Road, Cambridge CB3 0WA, UK
e-mail: n.peake@damtp.cam.edu.uk
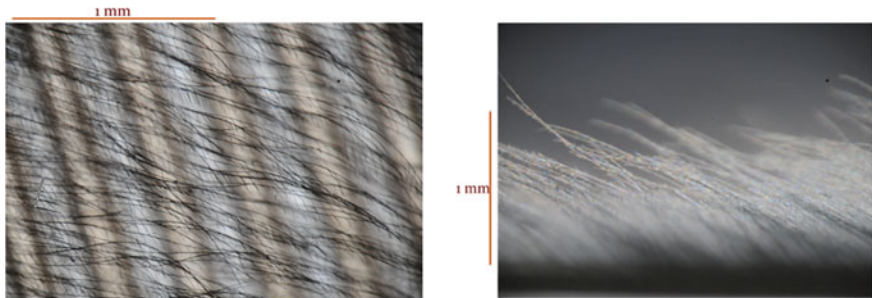
Fig. 1 Top and side view of upper surface of wing feather, Great Grey Owl

Fig. 2 Trailing edge fringe, Siberian Eagle Owl. Scale in 1 mm gradations
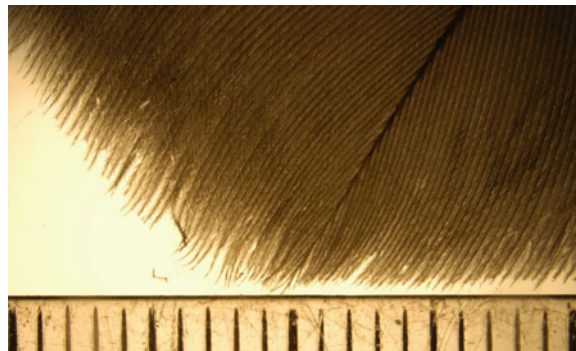
answered to date. However, we have made definite progress with the second question, and I will present very promising test results for an owl-inspired trailing-edge noise reduction device. The research I am going to describe is part of an ongoing theoretical and experimental program between Cambridge, Virginia Tech, Lehigh University and Florida Atlantic University.

2 Modelling and Results

A theoretical model for the trailing-edge fringe has been developed in Jaworski and Peake (2013), where we consider the sound scattering properties of a poro-elastic trailing edge, which crucially is seen to be significantly less noisy than a rigid trailing edge. In Clark et al. (2014) we conduct both experimental and theoretical studies of the feather micro-structure, and demonstrate that the canopy observed in Fig. 1 can have a very significant effect in shielding the surface from the unsteady pressure fluctuations associated with the turbulent boundary layer (inclusion of a canopy composed of a relatively open fine fabric mesh can lead to reductions of up to 30 dB in the surface pressure spectrum). This observation has led us in Clark

et al. (2015) to present a trailing-edge noise reduction device which makes use of this canopy effect. Sample results are given in Fig. 3, where we show sound intensity maps for a tripped DU96 (wind turbine) blade at $Re = 3 \times 10^6$. Without the treatment most of the noise comes, as expected, from the turbulent boundary layer passing over the trailing edge. However, significant noise reduction (in this case up to 10 dB) is seen once the device is included, over a wide range of
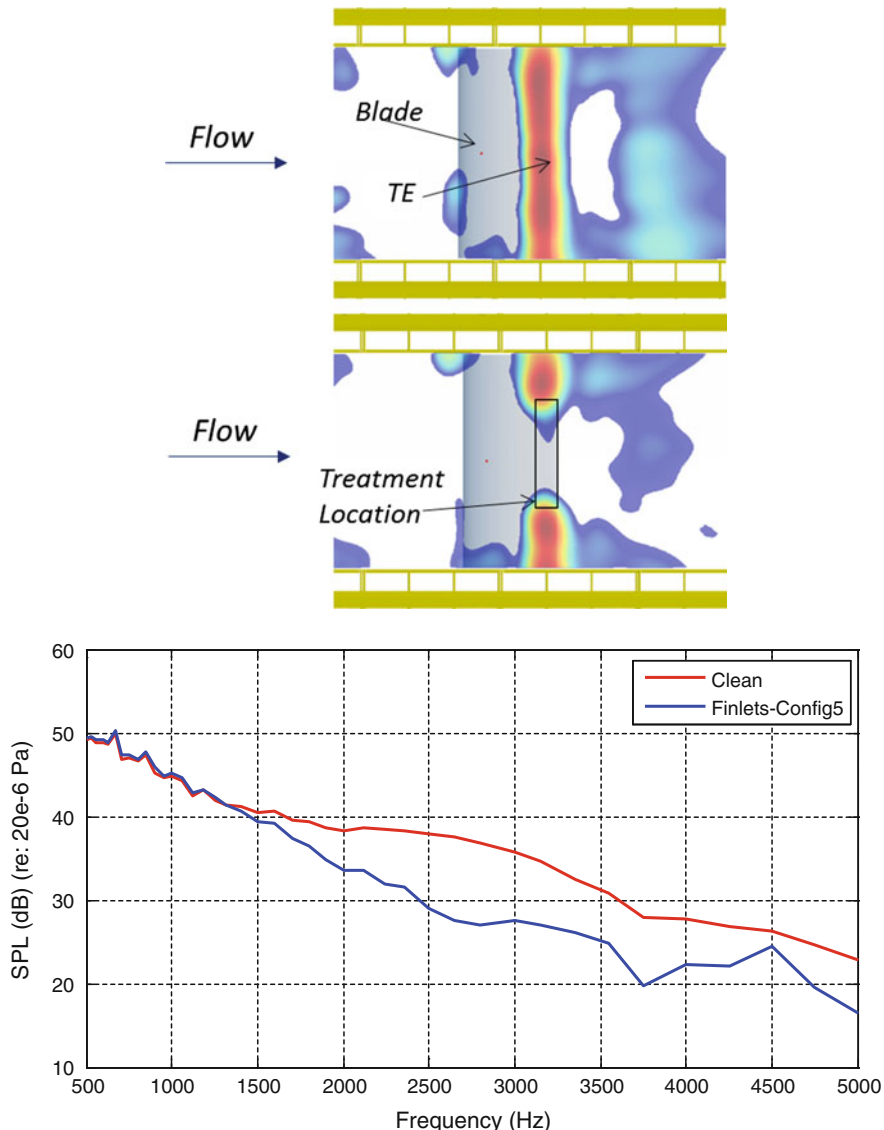
Fig. 3 Sample results; noise map at single frequency, and power-integrated spectrum

frequencies. The device will be described in detail in the presentation, and full details are given in Clark et al. (2015). Interestingly, preliminary results indicate that the device has only a very small effect on the aerodynamic performance of the aerofoil, and that noise suppression is retained over quite a wide range of angles of attack and tunnel speeds.

3   Further Work

A range of further wind-tunnel testing to produce an optimised design is currently being completed. Theoretical investigations into better understanding the canopy mechanism are also continuing; some explanation can be found from shear sheltering, whereby unsteady disturbances in the upper boundary layer are shielded by mixing layer just above the canopy, but further calculations are required. Effects of spanwise flows and angle of attack are also being considered theoretically.

References

Jaworski JW, Peake N (2013) J Fluid Mech 723:456–479
Clark I, Devenport WJ, Jaworski J, Daly C, Peake N, Glegg SA (2014) AIAA Paper 2014-2911
Clark I, Alexander WN, Devenport WJ, Glegg SA, Jaworski J, Daly C, Peake N (2015) AIAA
    Paper

A Comparison of NACA 0012 and NACA 0021 Self-noise at Low Reynolds Number

A. Laratro, M. Arjomandi, B. Cazzolato and R. Kelso

Abstract The self-noise of NACA 0012 and NACA 0021 airfoils are recorded at a Reynolds numbers of 96,000 in an anechoic wind tunnel at an angle-of-attack range of −5°–40°. Results suggest that the low angle-of-attack tonal noise of the airfoils behaves differently, with the NACA 0021 producing tones at much higher angles-of-attack but not near 0°. Noise generated at the onset of stall is subtly different, with signature of the NACA 0012 forming over a larger angular range compared to the NACA 0021 where the stall signature forms suddenly.

Keywords Aeroacoustics · Stall noise · Airfoil noise

1 Introduction

At low angles-of-attack airfoils produce tonal noise as transitional boundary layer instabilities convect past the trailing edge, generating noise which further excites the boundary layer (McAlpine 1997; Arcondoulis et al. 2009). On NACA 0012 airfoils this noise typically occurs over a small range of angles-of-attack, when the separation point is near the trailing edge the tonal frequencies tend to increase or stay constant as the angle increases (McAlpine 1997; Arcondoulis et al. 2009). A study by Hansen et al. (2010) on NACA 0021 airfoils indicates that tonal noise is not present at 0°, persists to higher angles-of-attack and decreases in frequency as the angle-of-attack is increased. These differences were not discussed by Hansen et al. (2010) but suggest that the tonal noise properties of the airfoils differ. This tonal noise is also sensitive to environmental factors hindering comparisons (Hansen et al. 2010).

At high angles-of-attack airfoils act similar to bluff bodies and shed large vortex streets. This generates sound at a frontal-height based Strouhal Number of between 0.15 and 0.2 at moderate Reynolds numbers similar to a flat plate (Fage and Johansen

A. Laratro (✉) · M. Arjomandi · B. Cazzolato · R. Kelso
School of Mechanical Engineering, The University of Adelaide, Adelaide, SA, Australia
e-mail: alex.laratro@adelaide.edu.au

1927; Colonius and Williams 2011). During the transition to fully separated flow airfoil noise is less well understood.

Brooks et al. (1989) conducted extensive testing of the self-noise of NACA 0012 airfoils over a range of angles-of-attack. They found that as angle-of-attack increases and the airfoil stalls the shed vortices become larger and self-noise shifts to lower frequencies. While the data of Brooks et al. uses range of angles and Reynolds numbers its detail is limited by the use of 1/3-octave spectra which makes it difficult to discern peaks due to vortex shedding. More recent work by Moreau et al. (2009) presented much higher resolution spectra and showed that there are peaks in the airfoil noise near stall that are not resolved when the data is presented in third-octave bands. At angles of attack from approximately 14–20° they reported small peaks in the spectra attributed to separation noise that decreased in amplitude as the angle-of-attack was further increased. Beyond this range the larger and sharper peaks attributed due to bluff body vortex shedding formed and moved to lower frequencies with higher angles as expected.

The objective of the current work is two-fold; Firstly to expand upon the experimental findings of Moreau et al. (2009) by recording data in the light-stall regime for both NACA 0012 and NACA 0021 airfoils and identifying if there are differences in their spectra. Secondly to use the data collected to investigate the differences between tonal noise of the NACA 0012 and NACA 0021 airfoils as seen in the data of (Hansen et al. 2010).

2 Method

In order to achieve high angles-of-attack with the available facilities the airfoils had to be mounted vertically. This resulted in a design span of 73 mm, to account for small deflections in the end plates. A servo motor mounted to the rig enabled remote control of the angle-of-attack, and did not significantly affect the background noise at high flow-speeds. The rig placed the airfoil several chord lengths from the exit of the nozzle (as shown in Fig. 1) in order to give a larger arc line-of-sight to the airfoil

Fig. 1 Experimental setup
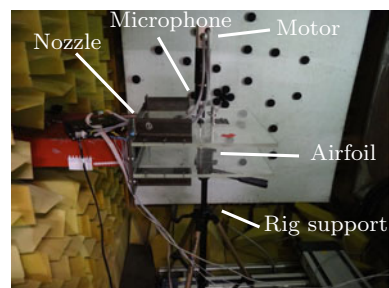
Table 1 Experimental parameters

Nozzle size	75mm × 275mm	
Airfoil profile	NACA 0012	NACA 0021
Chord	50mm	
Span	73mm	
Thickness	6mm	10.5mm
Aspect ratio	1.46	
Relative flow width	5.5	

for future testing, and several chord lengths before the end of the plates to allow wake development.

The microphone used was located 0.61 m from the rotation axis at polar and azimuthal angles of 91.2° and −0.4° respectively. Each spectrum was created with Welch's method with a sampling frequency of 2^{15} Hz and a window length of 2^{13} Hz with 150 averages. The experiment was conducted a speed of 30m/s, corresponding to a Reynolds numbers of 96,000. Spectra were produced for angles-of-attack from −5 to 40° at a resolution of 1° (Table 1).

3 Results

The experimental results, shown in Fig. 2, show two regimes of tonal noise at low and at high angles-of attack, as expected. The NACA 0021 airfoil does not generate tones until 2–3° which then decrease in frequency as the angle-of-attack is increased before fading at 12°. This is in some agreement with the results of Hansen et al. (2012) where tonal noise was detected as low as 1° and corroborates both the trend of tonal noise not being generated at 0° and the frequency decreasing as the angle is increased. This suggests that the tonal noise behaviour observed in the NACA 0021 is intrinsic to the airfoil at this Reynolds number and not a result of environmental
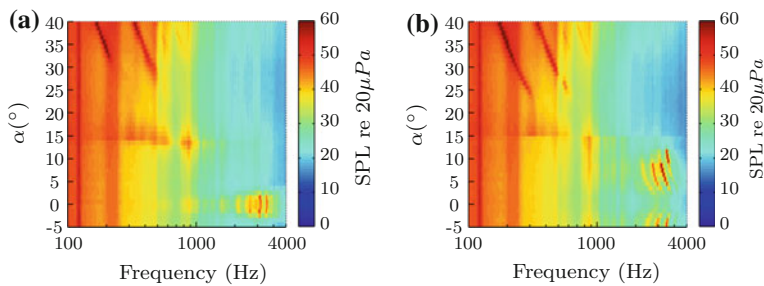
Fig. 2 Spectra of airfoils at U = 30 ms^{-1}, Re = 96,000, $\Delta\alpha = 1°$, $\Delta f = 4$ Hz

conditions. Note that the geometric angles-of-attack is presented here and the true angle-of-attack is given by $\alpha_t = 0.76\alpha$ (Brooks et al. 1989).

At post-stall angles-of-attack the airfoils display similar vortex shedding behaviour. In this regime the airfoils are acting as bluff bodies, and the change in thickness does not significantly affect vortex shedding frequency. A low frequency peak similar to that reported by Moreau et al. (2009) is seen between the tonal and bluff body noise, referred to as light stall in that study. Secondary peaks are also seen at slightly higher frequencies and will be discussed in further detail below. It is important to note that as the airfoil begins to stall there is a noticeable increase in broadband noise level below approximately 900 Hz and a decrease in noise level above. The speed at which this change occurs is noticeably different for each airfoil, with the NACA 0021 experiencing a more rapid change in noise signature. This is believed to be indicative of the NACA 0021 stalling more sharply in these conditions. The behaviour of the NACA 0012 is consistent with both lift data in literature (Marchman et al. 1998) and a direct numerical simulation by Rodríguez et al. (2013) which indicated that the onset of stall occurred over a range of angles for the NACA 0012 in this Reynolds number range. The simulation indicated that the peaks in the noise at stall occur due to instabilities in the separated shear layer near the leading edge as well as vorticity produced near the trailing edge. Similarly lift data for the NACA 0021 near the experimental Reynolds number how a sharp decrease in lift at the onset of stall corresponding to the sharp increase in low-frequency noise observed in this study (Marchman et al. 1998). Comparable simulations could not be found in the literature, however it is reasonable to assume that similar flow phenomenon are responsible for the observed noise for both airfoils.

As mentioned previously, some anomalous peaks appear in the data, with a wide peak near 950 Hz that increases in strength with angle-of-attack and then decreases as the airfoil stalls. What was initially believed to be secondary peaks at around 550 Hz may be due to a related phenomenon. These peaks at are located at frequencies that are prominent in the background noise when the end-plates are installed as shown in Fig. 3, however they rise and fall with the changes in noise at stall. Because of this it is currently believed that these peaks are a result of an aeroacoustic coupling between

Fig. 3 Spectra of airfoils at stall for U = 30 ms⁻¹, Re = 96,000
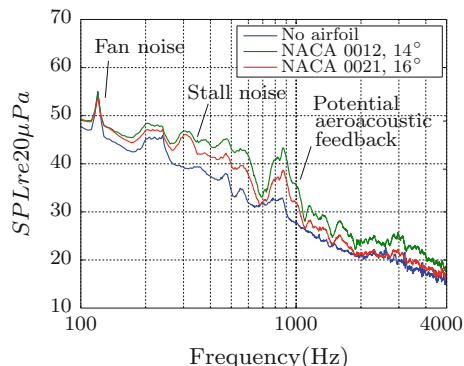
the airfoil and the end-plates, and steps are being taken to attempt to reduce the effect. Regardless, the large difference in the behaviour of this coupling between the NACA 0012 and NACA 0021 airfoils suggests that after the coupling is suppressed that some difference in spectrum will remain.

4 Conclusion

NACA 0012 and NACA 0021 airfoils with 50 mm chord were tested in the anechoic wind tunnel at the University of Adelaide at a Reynolds number of 96,000 at various angles-of-attack. Noticeable differences were found in the characteristics of how their self-noise spectra change as the angle-of-attack is increased, including confirmation of a lack of NACA 0021 tonal noise near 0° as seen in the data of Hansen et al. (2010). The onset of bluff body behaviour occurred later for the NACA 0012 airfoil and the onset of stall took place more gradually compared to the NACA 0021. There is evidence that there are differences in the broadband behaviour of these airfoils as they approach stall, however due to a possible aeroacoustic coupling between the airfoil and the experimental rig this cannot be determined conclusively.

References

Arcondoulis E, Doolan C, Zander A (2009) Airfoil noise measurements at various angles of attack and low Reynolds number. In: Proceedings on Acoustics 2009

Brooks T, Pope D, Marcolini M (1989) Airfoil self-noise and prediction. NASA Reference Publication, Technical report 1218

Colonius T, Williams D (2011) Control of vortex shedding on two- and three-dimensional aerofoils. Phil Trans R Soc A 369(1940):1525–1539

Fage A, Johansen F (1927) On the flow of air behind an inclined flat plate of infinite span. Proc R Soc Lond Ser A 116:170–197

Hansen K, Kelso R, Doolan C (2010) Reduction of flow induced tonal noise through leading edge tubercle modifications. AIAA Paper 2010:3700

Marchman F, Gunther C, Gundlach J (1998) Semi-span testing at low reynolds number. AIAA Paper 608

McAlpine A (1997) Generation of discrete frequency tones by the flow around an aerofoil. PhD thesis, School of Mathematics, University of Bristol

Moreau S, Roger M, Christophe J (2009) Flow features and self-noise of airfoils near stall or in stall. In: 15th AIAA/CEAS Aeroacoustics conference

Rodríguez I, Lehmkuhl O, Borrell R, Oliva A (2013) Direct numerical simulation of a naca0012 in full stall. Int J Heat Fluid Flow 43:194–203

High Order and High Resolution Numerical Schemes for Computational Aeroacoustics and Their Applications

Shuhai Zhang, Xuliang Liu, Hanxin Zhang and Chi-Wang Shu

Abstract A class of high order central compact schemes with spectral-like resolution are designed for the computational aeroacousitcs (CAA). The schemes have the features of high order, high resolution, low dissipation and the ability to capture strong shock wave in flow field, which are perfect methods for computational aeroacoustics. Typical problems are solved through direct numerical simulation, including the merging process of two co-rotating Gaussian vortices, the interaction between an oblique shock wave and a shear layer and cavity flow. The mechanisms of noise generation are studied.

Keywords Compact scheme · High resolution · Sound generation

1 Introduction

Direct numerical simulation (DNS) is an important method to reveal the mechanisms of noise generation of flow fields. However, compared with traditional aerodynamics and turbulence, aeroacoustics has its specific features, such as unsteady, multi-scale and propagating coherently. The requirement of the computational aeroacoustics to numerical scheme is very high. The numerical scheme should be high order, high resolution and low dissipation. For the supersonic problems, such as the shock associated noise, the numerical scheme should have the ability to compute strong shock wave without artificial oscillation. This becomes a great challenge to design a perfect method. To meet this requirement, we developed a new class of central compact schemes with spectral-like resolution.

S. Zhang (✉) · X. Liu · H. Zhang · C.-W. Shu
Division of Applied Mathematics, Brown University, Providence RI 02912, USA
e-mail: shuhai_zhang@163.com

2   High Order Central Compact Scheme with Spectral-like Resolution

Our developed high order central compact scheme contains two parts. The first part is the linear compact scheme. The second part is the nonlinear compact scheme, which can compute strong shock wave in flow field.

The linear compact scheme is developed based on Lele's linear compact scheme (Lele 1992), which has following formula:

$$\beta f'_{j-2} + \alpha f'_{j-1} + f'_j + \alpha f'_{j+1} + \beta f'_{j+2} = a\frac{f_{j+\frac{1}{2}} - f_{j-\frac{1}{2}}}{\Delta x} + b\frac{f_{j+\frac{3}{2}} - f_{j-\frac{3}{2}}}{3\Delta x} + c\frac{f_{j+\frac{5}{2}} - f_{j-\frac{5}{2}}}{5\Delta x} \quad (1)$$

The prominent feature of this compact scheme is its spectral-like resolution for short wave. However, there are two distinguished drawbacks. First, the stencil contains both the grid point and cell centers, but only part information is used. The accuracy of the designed scheme is not optimal. Second, the scheme contains the values on the cell-centers, which are unknown. Lele proposed a compact interpolation to compute the values on cell-centers from those on nodes. However, the compact interpolation can introduce transfer error. As a result, the resolution is significantly reduced for high wave numbers.

In paper (Liu et al. 2013), we proposed a new idea to design a compact scheme to improve the accuracy and resolution. First, instead of using only the values on cell centers, both the values of cell centers and grid nodes are used on the right hand side of compact schemes. Second, the function values on both grid nodes and cell centers are directly computed with the same scheme instead of using interpolation. Hence, the two drawbacks of Lele's compact scheme can be overcome. Our compact scheme is as following:

$$\begin{cases} \beta f'_{j-2} + \alpha f'_{j-1} + f'_j + \alpha f'_{j+1} + \beta f'_{j+2} = a\frac{f_{j+\frac{1}{2}} - f_{j-\frac{1}{2}}}{\Delta x} + b\frac{f_{j+1} - f_{j-1}}{2\Delta x} + c\frac{f_{j+\frac{3}{2}} - f_{j-\frac{3}{2}}}{3\Delta x} + d\frac{f_{j+2} - f_{j-2}}{4\Delta x} + e\frac{f_{j+\frac{5}{2}} - f_{j-\frac{5}{2}}}{5\Delta x} \\ \beta f'_{j-\frac{5}{2}} + \alpha f'_{j-\frac{3}{2}} + f'_{j-\frac{1}{2}} + \alpha f'_{j+\frac{1}{2}} + \beta f'_{j+\frac{3}{2}} = a\frac{f_j - f_{j-1}}{\Delta x} + b\frac{f_{j+\frac{1}{2}} - f_{j-\frac{3}{2}}}{2\Delta x} + c\frac{f_{j+1} - f_{j-2}}{3\Delta x} + d\frac{f_{j+\frac{3}{2}} - f_{j-\frac{5}{2}}}{4\Delta x} + e\frac{f_{j+2} - f_{j-3}}{5\Delta x} \end{cases}$$

$$(2)$$

The coefficients can be found in paper (Liu et al. 2013). The accuracy order is increased from original 8th to 14th, while, the resolution is maintained, which can be seen in Fig. 1.

To capture strong shock waves in flow field, we developed the above linear compact scheme to non-linear one by introducing the WENO interpolation. The implementation is as follow. The values on cell centers of the right hand side of the Eq. (2) are partially interpolated locally from the values on a stencil. In general, we can get a $(2r - 1)$th order approximation based on the flux function in a stencil
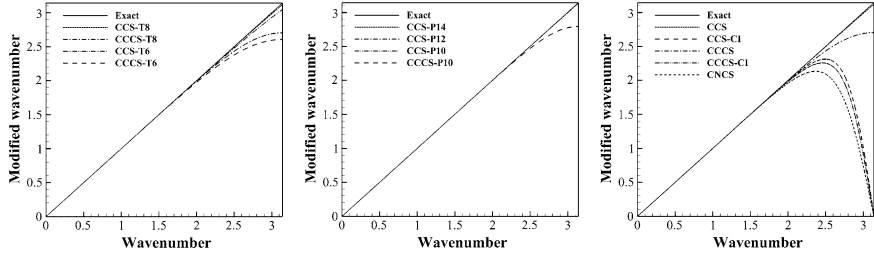
Fig. 1 The modified wavenumber of central compact schemes with spectral—like resolution and their comparison

$S^{2r-1} = (x_{i-r+1},...,x_{i+r-1})$. Using this stencil, the flux at any point can be evaluated as an interpolating polynomial:

$$\hat{f}^{2r-1}(x) = f_i + \sum_{l=1}^{2(r-1)} a_l(x - x_i)^l \tag{3}$$

Evaluating the function at the cell-center $x_{i+1/2}$, the $(2r-1)$th order approximation is given by:

$$\hat{f}^L_{i+\frac{1}{2}} = q^{2r-1}(f_{i-r+1}, \ldots, f_{i+r-1}). \tag{4}$$

Similar to the reconstruction process of WENO scheme, the stencil S^{2r-1} can be divided into r sub-stencils $S_k^{2r-1} = (x_{i+k-r+1}, x_{i+k-r+2}, \ldots, x_{i+k})$, $k = 0, 1,..., r - 1$. In each of these sub-stencils, the rth order approximation can be obtained

$$\hat{f}^{(k)}_{i+\frac{1}{2}} = q_k^r(f_{i+k-r+1}, \ldots, f_{i+k}) \tag{5}$$

The value $\hat{f}^L_{i+\frac{1}{2}}$ can be obtained by a linear combination of $\hat{f}^{(k)}_{i+\frac{1}{2}}$

$$q^{2r-1}(f_{i-r+1}, \ldots, f_{i+r-1}) = \sum_{k=0}^{r-1} C_k^r q_k^r(f_{i+k-r+1}, \ldots, f_{i+k}) \tag{6}$$

where C_k^r is the linear weights. Similar to the process of WENO reconstruction, we use nonlinear weights ω_k^r to replace the linear weights C_k^r and obtain a nonlinear approximation. Substituting the nonlinear approximation to the linear Eq. (2), we can obtain nonlinear compact scheme.

3 Direct Numerical Simulation and Mechanisms of Sound Generation

3.1 Revisit the Interaction of Two Co-rotating Gaussian Vortices

Gaussian vortex is a typical vortex. At some condition, two co-rotating Gaussian vortices can merge together. In the merging process, sound wave is generated. we study the merging of two co-rotating Gaussian vortices to show the superiority of our developed compact scheme.

Two Gaussian vortices are initially separated by distance 2R. The initial value of the physical parameters is the same as that in (Mitchell et al. 1995). They are $M_0 = U_0/c_\infty = 0.56$, $\alpha = 1.2564312086261697$, $\beta = 0.7153318629591616$ and $r_0/R = 0.15$. Reynolds numbers based on the circulation of each vortex is Re = 7500.

Figure 2 contains the evolution of the vorticity field in the vortex merging of two corotating Gaussian vortices. Figure 3 is the time history of the quadrupole acoustic source term, and it clearly shows a peak in amplitude corresponding to the vortex merger. The source terms are the second-order moments of vorticity

$$Q_1 \equiv 2 \iint xy\omega dxdy \quad and \quad Q_2 \equiv \iint (y^2 - x^2)\omega dxdy \tag{7}$$

The connection between the near-field vortex-dynamics and far-field quadrupole acoustic pressure in two-dimensional flow is:

$$P(r, \theta, t) = \frac{\rho_\infty}{8\pi c_\infty^2} \int_0^{\xi_0} \left[\frac{d^3 Q_1}{dt^3}(t^*) \cos(2\theta) + \frac{d^3 Q_2}{dt^3}(t^*) \sin(2\theta) \right] d\xi \tag{8}$$

Figure 4 is the temporal evolution of far-field sound pressure and its comparison. Note that after merger, the frequency approximately doubles and the amplitude diminishes significantly. Our numerical result agrees with that given by Eldredge
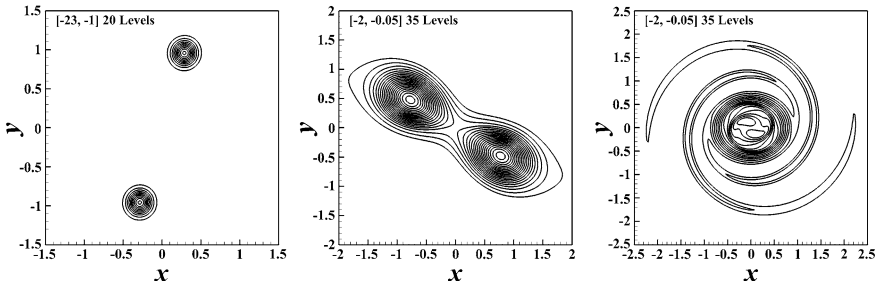
Fig. 2 The evolution of the vorticity field in the vortex merging of two corotating Gaussian vortices. *Left* 4 = 5; *Middle* t = 450; *Right* t = 550
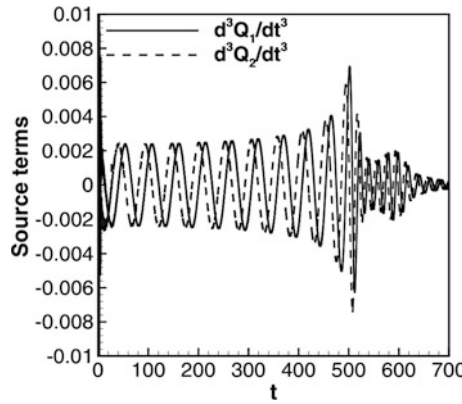
Fig. 3 The time evolution of second-order moments of second-order moments of vorticity
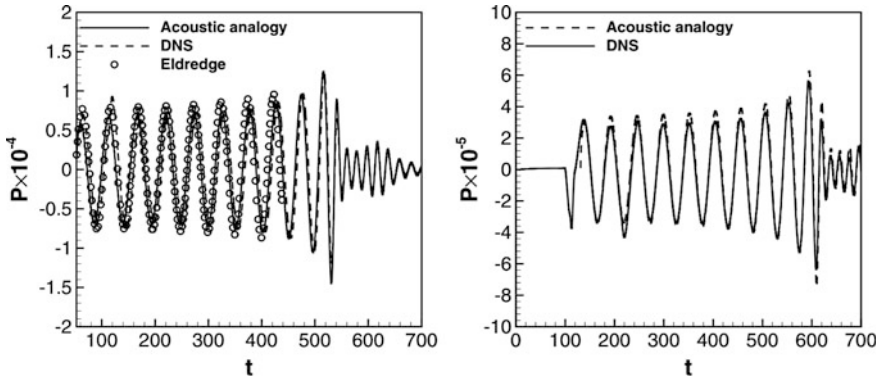
Fig. 4 The temporal evolution of far-field sound pressure. *Left*: The measurement probe is located at $(x, y) = (0, \lambda/2)$. *Right* The measurement probe is located at $(x, y) = (0, 2\lambda)$

et al. (2002). However, because of the difference in the merging instant, it is different from that given by Mitchell et al. (1995).

3.2 The Mechanism of Sound Generation in the Interaction Between Shock Wave and Shear Layer

Our second example is the interaction between an oblique shock wave and a shear layer. An oblique shock with an angle of $\beta = 12°$ is made to impinge on a spatially developing shear layer at an initial convective Mach number of 0.6. The upper boundary condition is fixed using Rankine-Hugoniot relationship. For the left and right boundaries, supersonic inflow/outflow conditions are imposed, whereas
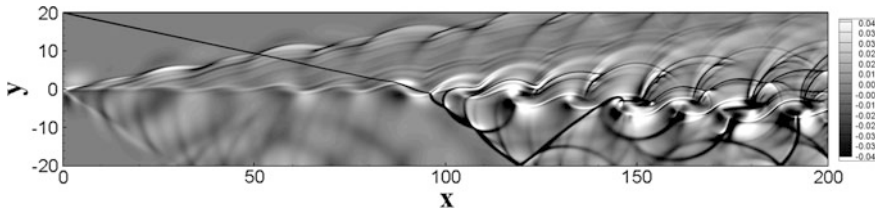
Fig. 5 Two zones of shock wave passing through supersonic shear layer

slip-wall conditions are assumed at the bottom boundary. The inflow is specified with a hyperbolic tangent profile, fluctuations are added to the inflow.

Numerical results show that there are two mechanisms of sound generation. The first is the interactions between the incident shock wave and the vortices, which appears in the location of the incident shock wave imping on the shear layer. The second is the leakage of shock wave, which appears in the location of the reflected shock wave imping on the shear layer. This process can be observed in Fig. 5 for the dilatation at t = 120.

4   Conclusion

To meet the requirement of computation aeroacoustics, we developed a class of central compact scheme with high order, high resolution and low dissipation. Numerical experiments show that it is a good method for CAA.

References

Eldredge JD, Colonius T, Leonard A (2002) A vortex p article method for two-dimensional compressible flow. J Comput Phys 179:371–399

Mitchell BE, Lele SK, Moin P (1995) Direct computation of the sound from a compressible co-rotating vortex pair. J Fluid Mech 285:181–202

Lele SK (1992) Compact finite difference schemes with spectral-like resolution. J Comput Phys 103:16–42

Liu X, Zhang S, Zhang H, Shu C-W (2013) A new class of central compact schemes with spectral-like resolution I: Linear schemes. J Comput Phys 248:235–256

Flow-Induced Noise Prediction Using a RANS-BEM Technique

P. Croaker, H. Peters, L. Chen, C. Doolan and N. Kessissoglou

Abstract A hybrid RANS-BEM technique is applied to calculate the self-noise produced by low Mach number flow past a flat plate. The flow field and turbulence statistics of the flow over the flat plate is predicted using a two-dimensional Reynolds Averaged Navier-Stokes (RANS) simulation. A statistical noise model is used to process the mean velocity, turbulent kinetic energy and turbulent dissipation rate to predict the incident pressure on the flat plate. This incident field is then applied as a load to a three-dimensional boundary element method (BEM) model of the flat plate to predict the far-field sound. Turbulent flow past a flat plate is used to demonstrate the hybrid RANS-BEM technique. The flow has a Reynolds number based on chord $Re_c = 2.0 \times 10^5$ and Mach number $M = 0.044$. The far-field pressure predicted with the hybrid RANS-BEM technique compares favourably with experimental measurements from literature.

P. Croaker (✉) · H. Peters · C. Doolan · N. Kessissoglou
School of Mechanical and Manufacturing Engineering,
UNSW Australia, Sydney, Australia
e-mail: p.croaker@unsw.edu.au

H. Peters
e-mail: herwig.peters@unsw.edu.au

C. Doolan
e-mail: c.doolan@unsw.edu.au

N. Kessissoglou
e-mail: n.kessissoglou@unsw.edu.au

L. Chen
Maritime Division, Defence Science and Technology Organisation,
Melbourne, Australia
e-mail: li.chen@dsto.defence.gov.au

1   Introduction

Numerical prediction of flow induced noise generated by high Reynolds number flows past large complex submerged bodies is computationally demanding. A high fidelity computational fluid dynamics (CFD) mesh is required to accurately resolve the high Reynolds number wall bounded flows. Traditional aeroacoustic techniques which extract flow noise sources from fluctuating hydrodynamic velocity and pressure fields are impractical. In this work, the turbulence statistics and mean flow data from a steady-state RANS simulation are used to derive statistical noise sources (Doolan et al. 2010; Albarracin et al. 2012). These statistical noise sources are then combined for the first time with a near-field formulation for the incident pressure derived by Croaker et al. (2015) and a three-dimensional BEM technique to calculate the interaction and scattering of the incident field with the body. The boundary element method is well suited to calculate the interaction and scattering of flow induced noise by a large complex geometry as described by Khalighi et al. (2010), making it an ideal choice for marine vessels. Also, recent advances in BEM techniques for flow induced noise can include the effect of a non-uniform mean flow on the scattering and propagation of sound (Wolf et al. 2013). The hybrid RANS-BEM technique is applied to predict the flow-induced noise produced by a flat plate immersed in a turbulent flow. The flow has a Reynolds number based on the chord of $Re_c = 2 \times 10^5$ and a Mach number of $M = 0.044$. The far-field sound pressure is compared with experimental results from literature.

2   Numerical Procedure

2.1   Incident Pressure from a Turbulent Flow Noise Source

The incident pressure on the rigid body due to flow noise sources in a single CFD cell, neglecting the effect of viscous stresses, is calculated using the following equation (Croaker et al. 2015)

$$p_{c,\text{inc}}(\mathbf{x}, \omega) = \int_{\Omega_c} \left(\rho_f U_{i,\mathbf{y}_c} U_{j,\mathbf{y}_c} \right) \frac{\partial^2 G_h(\mathbf{x}, \mathbf{y})}{\partial y_i \partial y_j} d\Omega_c \tag{1}$$

where $p_{c,\text{inc}}(\mathbf{x}, \omega)$ is the incident pressure due to the cth CFD cell. $\mathbf{x}$ is the field point on the body and ω is the angular frequency. $\mathbf{y}_c$ is the source point located within the cth CFD cell. ρ_f is the fluid density. $U_{i,c}$ is the ith component of the fluid velocity for CFD cell c. Ω_c denotes the volume occupied by the cth CFD cell. The term $\left(\rho_f U_{i,c} U_{j,c} \right)$ is the Lighthill tensor. $G_h(\mathbf{x}, \mathbf{y}) = \frac{e^{ik_a r}}{4\pi r}$ is the harmonic free-field Green's function. k_a is the acoustic wave number and $i = \sqrt{-1}$. $r = \|\mathbf{x} - \mathbf{y}_c\|$ is the distance from the source of CFD cell c to the field point. Equation (1) is solved using the

near-field formulation for the incident pressure derived by Croaker et al. (2015). The vertical component of the fluctuating velocity $u_{2,\mathbf{y}_c}$ in CFD cell c is used to normalise the incident pressure to produce

$$\hat{p}_{c,\mathrm{inc}}(\mathbf{x}, \omega) = \frac{p_{c,\mathrm{inc}}(\mathbf{x}, \omega)}{u_{2,\mathbf{y}_c}} \tag{2}$$

where $\hat{p}_{c,\mathrm{inc}}(\mathbf{x}, \omega)$ is the velocity normalised incident pressure.

2.2 Scattered Pressure with the Boundary Element Method

The three-dimensional BEM solver predicts the velocity normalised scattered pressure $\hat{p}_c(\mathbf{y}, \omega)$ produced by CFD cell c by solving the following non-homogeneous Helmholtz equation

$$c(\mathbf{y})\hat{p}_c(\mathbf{y}, \omega) = -\int_\Gamma \frac{\partial G_h(\mathbf{x}, \mathbf{y})}{\partial n(\mathbf{x})}\hat{p}_c(\mathbf{x}, \omega)\,d\Gamma(\mathbf{x}) \tag{3}$$
$$+ \mathrm{i}\rho_f c_f k_a \int_\Gamma G_h(\mathbf{x}, \mathbf{y})\,\hat{v}_c(\mathbf{x}, \omega)\,d\Gamma(\mathbf{x}) + \hat{p}_{c,\mathrm{inc}}(\mathbf{y}, \omega)$$

where Γ is the surface of the body. c_f is the sound speed of the fluid at rest. Inside the computational domain, the free-term coefficient $c(\mathbf{y}) = 1$, whereas on a smooth boundary $c(\mathbf{y}) = 0.5$. n is the unit normal to the boundary and $\hat{v}_c$ is the acoustic particle velocity normalised by $u_{2,\mathbf{y}_c}$.

2.3 Far-Field Acoustic Pressure Power Spectral Density

The far-field power spectral density $S(\mathbf{x_f}, \omega)$ is calculated as follows

$$S(\mathbf{x_f}, \omega) = \sum_{b=1}^{C}\sum_{c=1}^{C} \Phi(\mathbf{y}_c, \mathbf{y}_b, \omega)\left[\hat{p}_b(\mathbf{x_f}, \omega)\hat{p}_c^*(\mathbf{x_f}, \omega)\right] \tag{4}$$

where $\mathbf{x_f}$ is the far-field point and C is the total number of CFD cells. $()^*$ and $[\cdot]$ respectively denote the complex conjugate and cross spectrum. $\Phi(\mathbf{y}_c, \mathbf{y}_b, \omega)$ is the cross spectrum of the turbulent velocity and is represented by (Doolan et al. 2010)

$$\Phi(\mathbf{y}_c, \mathbf{y}_b, \omega) = \left[u_{2,\mathbf{y}_b}u_{2,\mathbf{y}_c}^*\right] = \frac{Au_s^2}{\omega_s}\exp\left(-\frac{|\mathbf{y}_c - \mathbf{y}_b|^2}{l_s^2}\right)\exp\left(-\frac{\omega^2}{4\omega_s^2}\right) \tag{5}$$

where u_s, ω_s and l_s are the characteristic velocity, frequency and length scales, respectively, of the turbulence in each CFD cell. The RANS turbulence statistics are used to calculate the model parameters as follows (Albarracin et al. 2012)

$$u_s = \sqrt{2k/3}, \qquad \omega_s = 2\pi/\tau_s, \qquad \tau_s = c_\tau k/\varepsilon, \qquad l_s = c_l k^{3/2}/\varepsilon \qquad (6)$$

where k is the turbulent kinetic energy and ε is the turbulent dissipation rate. c_l and c_τ are semi-empirical parameters and have both been assigned a value of unity. A correlation strength parameter of $A = 1/150$ produced good agreement between the present method and experimental measurements.

3 Results

A flat plate with a circular leading edge and a 12° symmetric wedge tailing edge was modelled. The plate had a thickness of 5 mm, a 200 mm chord and a 275 mm wetted span. Turbulent flow is simulated past the sharp-edged flat plate. The flow has a Reynolds number based on chord of $Re_c = 2.0 \times 10^5$. The flow noise sources and turbulence velocity cross correlations are calculated from the mean velocities, turbulent kinetic energy and dissipation rate. An incident pressure field is computed for each CFD cell at each frequency. Figure 1 shows the magnitude and phase of the velocity normalised incident field on the surface of the flat plate at 4 kHz produced by a flow noise source located near the trailing edge. The trailing edge is at the top in these images and the direction of flow is from the bottom to the top. The region of peak incident pressure is oriented mainly along the streamwise axis with a small contribution due to the spanwise velocity fluctuations shifting it slightly off-axis. The phase plot shows the distorted wavefront propagating away from the source. The distortion of the wavefront and orientation of peak incident pressure is caused by the interaction of the different components of Lighthill's tensor and their associated Green's function.
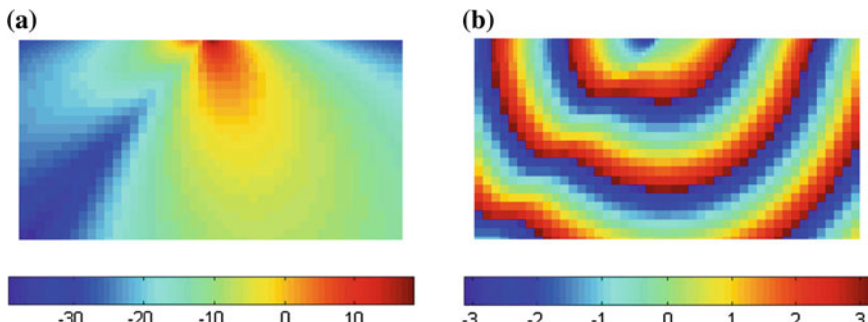
Fig. 1 Incident field produced by noise source at the trailing edge. **a** Magnitude in dB (ref 2×10^5 Pa). **b** Phase ib radians

Fig. 2 Comparison of numerical and experimental far-field sound
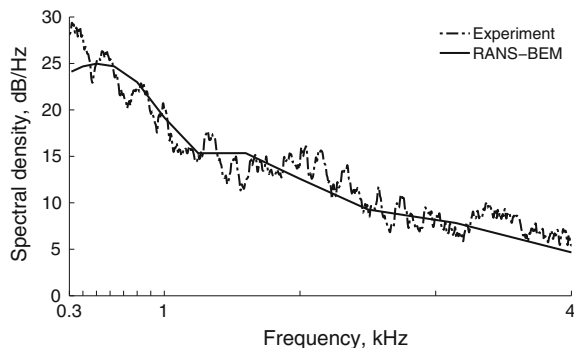
Figure 2 presents the far-field sound predicted with the hybrid RANS-BEM technique. The experimental measurements of Moreau et al. (2012) are also shown. Good agreement is achieved between the present results and the experimental measurements at frequencies above 600 Hz. The difference between the present results and the experimental data increases as the frequency decreases. The low frequency noise produced by the sharp edged plate is dominated by incident turbulence interacting with the leading edge. The present RANS-BEM analysis did not include significant upstream turbulence and hence their impact on the flow induced noise was not captured here.

4 Conclusions

A hybrid RANS-BEM technique has been used to predict the flow induced noise produced by turbulent flow past a flat plate. Turbulence statistics and mean flow data obtained from a two-dimensional CFD simulation were used to define the statistical noise sources. These noise sources produced complicated incident pressure distributions which were combined with a three-dimensional BEM model of the flat plate to predict the scattered field. The power spectral density of the far-field sound pressure agrees well with experimental measurements.

References

Albarracin CA, Doolan CJ, Jones RF, Hansen CH, Brooks LA, Teubner MD (2012) A RANS-based statistical noise model for trailing edge noise. In: Proceedings of the 18th AIAA/CEAS Aeroacoustics Conference (33rd AIAA Aeroacoustics Conference), Colorado, USA

Croaker P, Kessissoglou N, Marburg S (2015) Strongly singular and hypersingular integrals for aeroacoustic incident fields. Int J Numer Methods Fluids 77:274–318

Doolan C, Albarracin CA, Hansen C (2010) Statistical estimation of trailing edge noise. In: Proceedings of the 20th International congress on acoustics, Sydney, Australia

Khalighi Y, Mani A, Ham F, Moin P (2010) Prediction of sound generated by complex flows at low Mach numbers. AIAA J 48(2):306–316

Moreau D, Brooks L, Doolan C (2012) The effect of boundary layer type on trailing edge noise from sharp-edged flat plates at low-to-moderate Reynolds number. J Sound Vib 331:3976–3988

Wolf W, Lele S (2013) Fast acoustic scattering predictions with non-uniform potential flow effects. J Brazilian Soc Mech Sci Eng 35:407–418

Trailing-Edge Noise Prediction Using a Periodic BEM Technique

M. Karimi, P. Croaker and N. Kessissoglou

Abstract The noise generated by a sharp-edged strut under quadrupole excitation is predicted using a periodic boundary element method technique. The strut is considered as a continuous periodic structure so that the matrix equation formulated by periodic boundary element method for this acoustic scattering problem is a block Toeplitz matrix. By exploiting the Toeplitz structure, the computational time and storage requirements for constructing the coefficient matrix are significantly reduced. The original matrix is embedded into a larger and more structured matrix called the block circulant matrix. Discrete Fourier Transform is then employed in an iterative algorithm to solve the block Toeplitz system. Directivity plots obtained using the proposed method are compared with numerical results obtained using a conventional boundary element model.

Keywords Trailing edge noise · Boundary element method · Block Toeplitz matrices

1 Introduction

Scattering of acoustic pressure fluctuations induced by boundary layer turbulent structures over the trailing edge geometry produces trailing edge noise. One of the first systematic studies of trailing edge noise was reported by Ffowcs Williams and Hall (1970) based on the classical Lighthill analogy (Lighthill 1952). Khalighi et al. (2010) developed a boundary integral equation from Lighthill's wave equation which was solved using the boundary element method (BEM).

Exterior acoustic problems are commonly solved using the BEM. For complex structures, the frequency-dependent coefficient matrices are very large and there is very little that can be done to alleviate the computational and storage requirements. However, applying the BEM to periodic structures leads to the formation of a block

M. Karimi(✉) · P. Croaker · N. Kessissoglou
School of Mechanical and Manufacturing Engineering, UNSW, Sydney, Australia
e-mail: m.karimi@unsw.edu.au

Toeplitz system, due to the translational invariance of the free-space Green's function. A block Toeplitz system is a linear system of equations in which the coefficient matrix has constant blocks along each diagonal (Golub and Van Loan 1989). Toeplitz systems arise in various fields such as mathematics, engineering and signal processing. Czuprynski et al. (2012) showed that for acoustic radiation problems with rotationally symmetric boundary surfaces, the coefficient matrix is a block circulant matrix. In this work, a periodic BEM technique is demonstrated by predicting the noise generated by a sharp-edged strut under quadrupole excitation to represent the turbulent flow noise source. The periodic acoustic problem is formulated as a block Toeplitz system. Directivity results obtained by the proposed method are compared with results from a conventional BEM model.

2 Numerical Methodology

Assuming a time harmonic dependence of the form $e^{-i\omega t}$, the Helmholtz equation is given by

$$\Delta p(\mathbf{x}) + k^2 p(\mathbf{x}) = -F \tag{1}$$

where $p(\mathbf{x})$ is the acoustic pressure at field point $\mathbf{x}$, F is the source, Δ is the Laplacian operator, $k = \omega/c$ is the acoustic wave number, ω is the angular frequency and c is the speed of sound. Equation (1) can be written in a weak formulation after integrating by parts twice as follows (Marburg and Nolte 2008)

$$c(\mathbf{x})p(\mathbf{x}) + \int_{\Gamma} \frac{\partial G(\mathbf{x},\mathbf{y})}{\partial n(\mathbf{y})} p(\mathbf{y})\, d\Gamma(\mathbf{y}) = i\omega\rho_0 \int_{\Gamma} G(\mathbf{x},\mathbf{y})v_f(\mathbf{y})\, d\Gamma(\mathbf{y}) + p_{\text{inc}}(\mathbf{x}) \tag{2}$$

where ρ_0 is fluid density and $i = \sqrt{-1}$ is the imaginary unit. The vector $\mathbf{n}(\mathbf{y})$ represents the outward normal vector at the point $\mathbf{y}$, $\partial/\partial n(\mathbf{y})$ is the normal derivative, $v_f(\mathbf{y})$ is the fluid particle velocity and $\mathbf{y}$ is a source point position on the boundary Γ. Solution of the Helmholtz equation can be obtained by calculating the incident acoustic pressure radiated by the source and applying it as a load to the boundary integral equation (2). $p_{\text{inc}}(\mathbf{x})$ is the acoustic pressure incident as a result of the acoustic source. $c(\mathbf{x})$ is a free-term coefficient and equals 1 in the domain interior and 0.5 on a smooth boundary. $G(\mathbf{x},\mathbf{y})$ is the free-space Green's function for the Helmholtz equation given by

$$G(\mathbf{x},\mathbf{y}) = \frac{e^{ikr}}{4\pi r} \qquad \text{where} \qquad r = |\mathbf{x} - \mathbf{y}| \tag{3}$$

The sharp-edged strut examined in this work is considered as a rigid structure. Hence the fluid particle velocity at the strut surface is zero, that is, $v_f(\mathbf{y}) = 0$, $\mathbf{y} \in \Gamma$. The BEM formulation then becomes a linear system of equations which can be expressed as follows

$$\mathbf{T}\,\mathbf{a} = \mathbf{b} \qquad (4)$$

where $\mathbf{T}$ is the coefficient matrix and $\mathbf{a}$, $\mathbf{b}$ represent the sound pressure and incident pressure at nodal points, respectively. For an acoustic scattering problem which includes periodic structures, the matrix equation formulated by BEM is a block Toeplitz matrix. An $mn \times mn$ matrix $\mathbf{T}$ is called a block Toeplitz matrix (BTM) if it has constant blocks along each diagonal. Hence, a BTM has the form:

$$\mathbf{T} = \begin{pmatrix} \mathbf{T}_0 & \mathbf{T}_{-1} & \cdots & \cdots & \mathbf{T}_{1-m} \\ \mathbf{T}_1 & \mathbf{T}_0 & \mathbf{T}_{-1} & \cdots & \mathbf{T}_{2-m} \\ \vdots & \mathbf{T}_1 & \ddots & \ddots & \vdots \\ \vdots & \vdots & \ddots & \ddots & \mathbf{T}_{-1} \\ \mathbf{T}_{m-1} & \mathbf{T}_{m-2} & \cdots & \mathbf{T}_1 & \mathbf{T}_0 \end{pmatrix} \qquad (5)$$

where each $\mathbf{T}_i$ is an $n \times n$ matrix. The number of unique blocks corresponds to the number of periodic sections found on the boundary surface. In the present work, the BTM is not necessarily a symmetric matrix.

Matrix $\mathbf{T}$ is specified by its first block row and its first block column. An $m \times m$ Toeplitz matrix can be embedded into a $2m \times 2m$ circulant matrix (Golub and Van Loan 1989). In the present work, a similar approach is used to embed the $mn \times mn$ BTM into a $2mn \times 2mn$ block circulant matrix $\mathbf{C}$ which can be represented by rightward circular shifts of its first block row: $\mathbf{R} = \{\mathbf{T}_0\ \mathbf{T}_{-1}\ \ldots\ \mathbf{T}_{1-m}\ \mathbf{0}\ \mathbf{T}_{m-1}\ \ldots\ \mathbf{T}_1\}$. Note that an $n \times n$ zero matrix is also incorporated into matrix $\mathbf{R}$. Using this embedding, Eq. (4) can be written in the form of

$$\mathbf{C}\,\mathbf{a}' = \mathbf{b}' \qquad \Leftrightarrow \qquad \begin{bmatrix} \mathbf{T} & \mathbf{S} \\ \mathbf{S} & \mathbf{T} \end{bmatrix} \begin{bmatrix} \mathbf{a} \\ \mathbf{0} \end{bmatrix} = \begin{bmatrix} \mathbf{b} \\ \mathbf{z} \end{bmatrix} \qquad (6)$$

The block circulant system in Eq. (6) is equivalent to a Toeplitz system expressed by Eq. (4). The difference between these two formulations is that the left-hand side vector $\mathbf{a}$ in Eq. (4) contains all the unknown quantities whereas in the block circulant system, there are unknown entries in both the left-hand and right-hand side vectors. That is, $\mathbf{a}'$ and $\mathbf{b}'$ are partially known since $\mathbf{a}$ and $\mathbf{z}$ are unknown. The proposed algorithm for solving Toeplitz equations by Ferreira and Domínguez (2010) is extended to solve the block Toeplitz system. Only the first block row and column of the linear system must be computed and stored. Hence the storage of the linear system is significantly reduced. The computational time to construct the coefficient matrix is also considerably decreased.

3 Numerical Results

Prediction of the scattered acoustic field from a strut submerged in low Mach number flow was recently studied by the authors (Karimi et al. 2014). The same strut is used in this work to determine the scattered field due to a point lateral quadrupole as described by Crocker (2007), which is located near the trailing edge of the strut as a sound source. The directivity of the sound pressure field scattered by the sharp-edged strut under quadrupole excitation at four distinct frequencies is presented in Fig. 1. It can be seen that the directivity of the sound pressure field predicted by the periodic BEM technique is in excellent agreement with results obtained from a conventional BEM model. The conventional BEM results are obtained by computing all the entries of the coefficient matrix and solving the corresponding linear system of equations. More details of the conventional BEM technique can be found in Marburg and Nolte (2008). At low frequencies, the chord of the strut is acoustically compact and the directivity pattern is a dipole. As the frequency increases, the scattering by
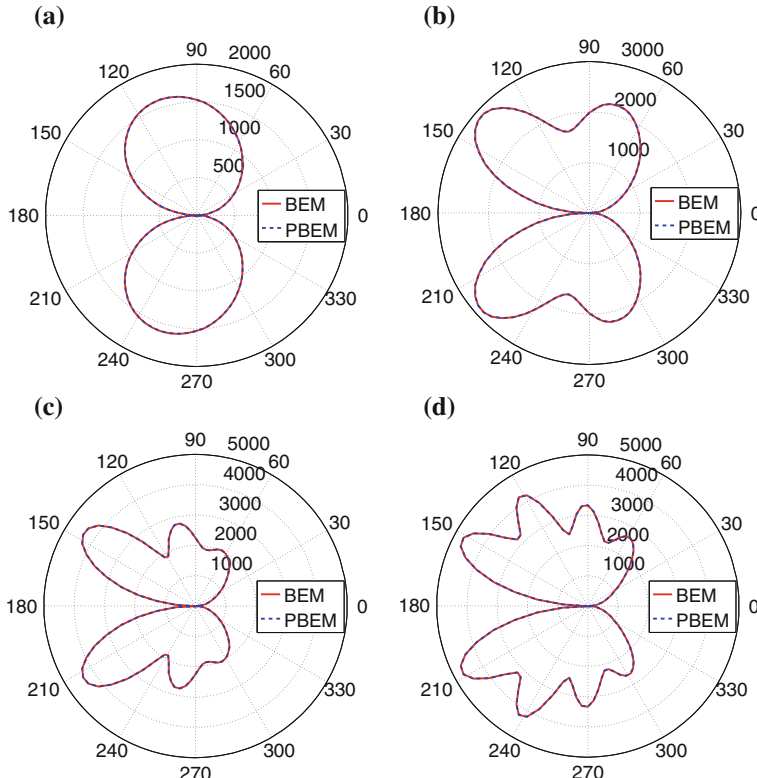
Fig. 1 Directivity of the sound pressure field scattered by the sharp-edged strut under quadrupole excitation predicted by periodic BEM (PBEM) and conventional BEM (CBEM)
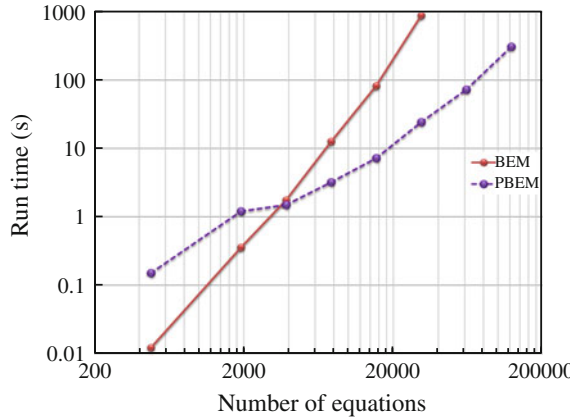
Fig. 2 Comparison of the run time for the solution of the matrix equation

the trailing edge begins to dominate as shown by the upstream focusing of the scattered sound. At high frequencies, the geometry becomes acoustically non-compact and the sound scattered by the trailing edge is back-scattered by the leading edge, resulting in multiple lobes appearing in the directivity plots. Figure 2 presents the run time for solving the matrix equation for both the periodic and conventional BEM. The horizontal axis shows the matrix size which corresponds to the number of collocation points in the BEM formulation. These results reveal that the run time to solve the matrix equations are substantially reduced.

4 Summary

In this work, a block Toeplitz matrix formulation by the BEM for an acoustic scattering problem from a periodic structure was developed. By exploiting the Toeplitz structure, the computational time and storage requirements to solve the linear system of equations were significantly reduced. The noise generated by a sharp-edged strut under a quadrupole excitation was predicted using the periodic BEM technique, showing excellent agreement with results from a full BEM model.

References

Crocker M (2007) Handbook of noise and vibration control. Wiley, Hoboken

Czuprynski KD, Fahnline JB, Shontz SM (2012) Parallel boundary element solutions of block circulant linear systems for acoustic radiation problems with rotationally symmetric boundary surfaces. In: Proceedings of the inter-noise 2012, 19–22 Aug 2012, NY, USA

Ferreira PJ, Domínguez ME (2010) Trading-off matrix size and matrix structure: handling Toeplitz equations by embedding on a larger circulant set. Digital Signal Proc 20(6):1711–1722

Ffowcs Williams JE, Hall LH (1970) Aerodynamic sound generation by turbulent flow in the vicinity of a scattering half plane. J Fluid Mech 40(4):657–670

Golub G, Van Loan C (1989) Matrix computations, 2nd edn. Johns Hopkins University Press, Baltimore

Karimi M, Croaker P, Kessissoglou N, Doolan C, Marburg S (2014) Self-noise prediction of a sharp-edged strut using a quasi-periodic CFD-BEM technique. In: Proceedings of the inter-noise,16–19 Nov 2014, Melbourne, Australia

Khalighi Y, Mani A, Ham F, Moin P (2010) Prediction of sound generated by complex flows at low Mach numbers. AIAA J 48(2):306–316

Lighthill MJ (1952) On sound generated aerodynamically. Proc Soc Roy Soc A 211:564–587

Marburg S, Nolte B (2008) Computational acoustics of noise propagation in fluids—finite and boundary element methods. Springer, Berlin

An Experimental Investigation of Wall-Mounted Finite Airfoil Turbulent Boundary Layer Noise

D.J. Moreau, C.J. Doolan, W.N. Alexander, T.W. Meyers and W.J. Devenport

Abstract Measurements of flow-induced wall-mounted finite airfoil noise have been taken in the Stability Wind Tunnel at Virginia Tech to examine the influence of airfoil three-dimensionality on noise production. The airfoil has an aspect ratio (ratio of airfoil span, L, to chord, C) of $L/C = 3$ and measurements encompass variations in geometric angle of attack of $\alpha = 0$ to $12°$ at a Reynolds number of $Re_c = 1.6 \times 10^6$ (based on chord). The results include far-field acoustic spectra and sound maps taken with a microphone array and reveal contributions of flow at the airfoil tip and wall junction to noise production.

Keywords Airfoil noise · Trailing edge noise · Tip noise · Beamforming

1 Introduction

Many real-world technologies employ an airfoil that is wall-mounted and finite in length with boundary layer impingement at the airfoil-wall junction and flow over the tip. Examples include submarine hydrofoils mounted to a hull, wind turbine blades mounted to a hub or the stators in an aeroengine that are connected to an outer wall. An important aspect of airfoil noise production that has received little attention in literature (Moreau et al. 2014; Brooks and Marcolini 1986) is the influence of airfoil three-dimensionality, boundary layer impingement and flow at the tip on noise generation and this is therefore the focus of the present study. An experimental program to study wall-mounted finite airfoil turbulent boundary layer noise has been performed in the Stability Wind Tunnel at Virginia Tech. Acoustic measurements

D.J. Moreau (✉) · C.J. Doolan
School of Mechanical and Manufacturing Engineering, UNSW,
Sydney, NSW 2052, Australia
e-mail: d.moreau@unsw.edu.au

W.N. Alexander · T.W. Meyers · W.J. Devenport
Aerospace and Ocean Engineering, Virginia Tech, Blacksburg, VA 24061, USA

taken with a microphone array are presented here for a wall-mounted finite airfoil with aspect ratio (ratio of airfoil span, L, to chord, C) of $L/C = 3$ at a Reynolds number of 1.6×10^6 (based on chord) and geometric angles of attack of $\alpha = 0 - 12°$.

2 Experimental Method

Experiments have been performed in the anechoic test section of the Stability Wind Tunnel at Virginia Tech (Devenport et al. 2013). The test section has dimensions of 1.83 m × 1.83 m × 7.3 m and tensioned Kevlar walls that contain the flow while being acoustically transparent. Sound generated in the test section passes through the Kevlar walls into two anechoic chambers located on either side of the test section where acoustic instrumentation is placed (see Fig. 1).

The airfoil model used in this study is a NACA 0012 with flat ended tip, a chord of $C = 0.4$ m, a span of $L = 1.2$ m and an aspect ratio of $L/C = 3$, corresponding to a length to thickness ratio of $L/T = 25$ (Fig. 1a). The incoming boundary layer thickness at a location of 130 mm upstream of the airfoil leading edge location was measured to be $\delta = 68$ mm using hot-wire anemometry and therefore the incoming boundary layer height is 5.7 % of the airfoil span. The airfoil was tripped at 10 % chord with serrated trip tape to ensure turbulent boundary layer formation at the airfoil trailing edge.

Experiments were conducted at a free-stream velocity of $U_\infty = 60$ m/s corresponding to a Reynolds number of $Re_c = 1.6 \times 10^6$. Measurements are presented for an airfoil geometric angle of attack of $\alpha = 0 - 12°$ where the model was rotated about
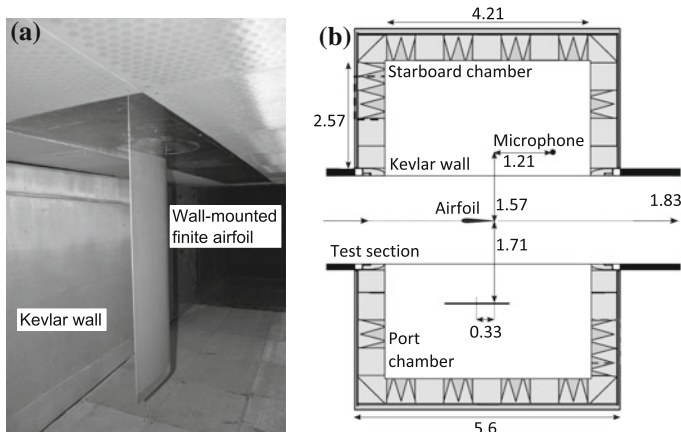
Fig. 1 The wall-mounted finite airfoil model and the stability wind tunnel anechoic test section. **a** The wall-mounted airfoil. **b** Top view of the anechoic test section

its quarter chord location. Far-field noise measurements have been taken with an AVEC microphone array (see Fig. 1b). The microphone array consists of 117 Panasonic model WM-64PNT Electret microphones arranged in a 9-armed spiral with an outer diameter of 1.1 m. The array was positioned with its centre 0.93 m above the test section floor. The 117 microphones were connected to an AVEC designed signal conditioning and filtering box and two 64-channel PCI-based data acquisition cards. Data from the 117 microphones were acquired at a sampling frequency of 51,200 Hz for a sample time of 32 s. Maps of local sound pressure contributions were obtained using AVECs post-processing algorithm and are displayed in 1/12th octave bands. In addition to sound maps, 1/12th octave band acoustic spectra have been estimated by integrating the sound map over the entire airfoil noise source region. This integration process yields the sound pressure level as measured at the microphone array centre due to the sources located in the integration region.

3 Experimental Results

Integrated airfoil spectra for the wall-mounted airfoil with $L/C = 3$ at $\alpha = 0 - 12°$ are shown in Fig. 2. Figure 3 shows sound maps measured at an airfoil geometric angle of attack of $\alpha = 0$ and 12°. In Fig. 3, the airfoil is shown in white, x is the streamwise direction where the flow is from left to right and y is the spanwise direction.

The spectra in Fig. 2 show the airfoil produces broadband noise over the entire frequency range of interest. Noise levels below 1.6 kHz are observed to increase with angle of attack. Conversely, the noise levels in the mid frequency range between 1.6 and 2.5 kHz reduce in amplitude with increasing angle of attack. The spectra also display a high frequency broadband hump centered at 3.55 kHz which increases in amplitude as the angle of attack is increased. The sound maps in Fig. 3 show that

Fig. 2 Integrated spectra for the wall-mounted finite airfoil at $\alpha = 0 - 12°$
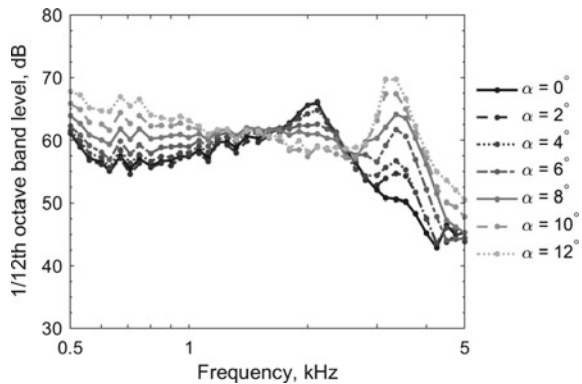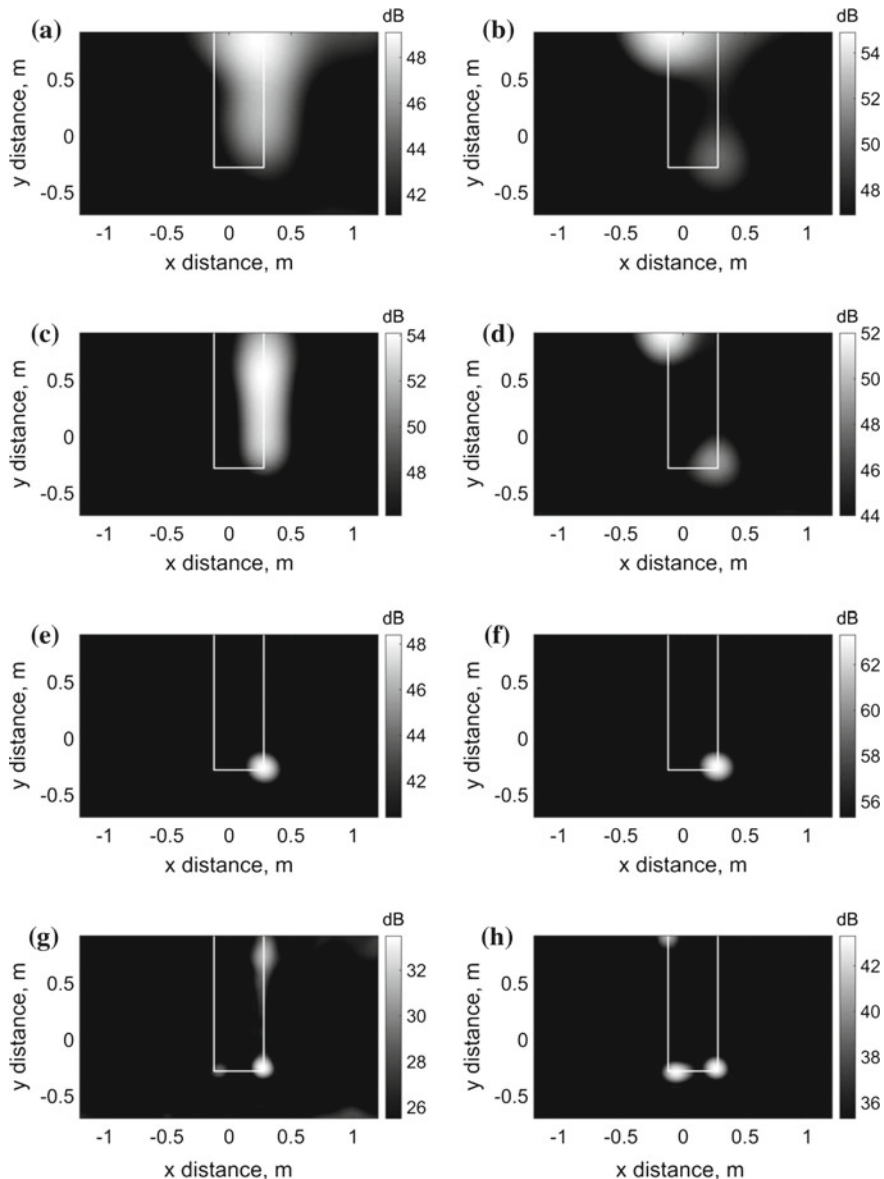
Fig. 3 1/12th octave band sound maps for the wall-mounted finite airfoil at $\alpha = 0$ and 12°. **a** f = 1:32 kHz, $\alpha = 0°$. **b** f = 1:32 kHz, $\alpha = 12°$. **c** f = 2 kHz, $\alpha = 0°$. **d** f = 2 kHz, $\alpha = 12°$. **e** f = 3:35 kHz, $\alpha = 0°$. **f** f = 3:35 kHz, $\alpha = 12°$. **g** f = 4:5 kHz, $\alpha = 0°$. **h** f = 4:5 kHz, $\alpha = 12°$

this broadband hump is due to the production of noise at the airfoil trailing edge-tip.

At $\alpha = 0°$, the sound maps in Fig. 3 show the dominant noise source at a frequency of 1.32 kHz is the trailing edge-wall junction. Turbulent trailing edge noise distributed along the entire airfoil span is then the primary noise generation mechanism at a frequency of 2 kHz. At higher frequencies of 3.55 and 4.5 kHz, the trailing edge-tip is the dominant noise source. Additional noise sources are also detected at the airfoil leading edge-tip and trailing edge-wall junction at a high frequency of 4.5 kHz.

At a higher angle of attack of $\alpha = 12°$, the sound maps in Fig. 3 show that noise due to flow at the airfoil tip and wall junction dominates and no significant trailing edge noise contribution is visible. At lower frequencies of 1.32 and 2 kHz, the dominant noise source location is the airfoil leading edge-wall junction. The airfoil trailing edge-tip then becomes the primary noise mechanism at higher frequencies of 3.35 and 4.5 kHz. As observed in the spectra of Fig. 2, trailing edge-tip noise at $\alpha = 12°$ is higher in amplitude (by more than 15 dB) compared to tip noise generated at zero angle of attack. At a high frequency of 4.5 kHz, secondary noise sources are also observed at the airfoil leading edge-tip and leading edge-wall junction.

4 Conclusion

An experimental investigation of the noise generated by a wall-mounted finite airfoil at high Reynolds number has been presented. The experimental results include acoustic spectra and beamforming sound maps at a variety of angles of attack that show the individual noise contributions from the airfoil leading edge, trailing edge, tip and wall junction.

References

Brooks T, Marcolini M (1986) Airfoil tip vortex formation noise. AIAA J 24(2):246–252

Devenport WJ, Burdisso RA, Borgoltz A, Ravetta PA, Barone MF, Brown KA, Morton MA (2013) The Kevlar-walled anechoic wind tunnel. J Sound Vib 332:3971–3991

Moreau DJ, Prime Z, Porteous R, Doolan CJ, Valeau V (2014) Flow-induced noise of a wall-mounted finite airfoil at low-to-moderate Reynolds number. J Sound Vib 333(25):6924–6941

Experimental Study on Airfoil Noise Reduction with Trailing Edge Serrations Under Various Incoming Flow Conditions

F. Tong, X.N. Wang, L.F. Wang and W.Y. Qiao

Abstract An experimental investigation of airfoil trailing edge noise reduction at Reynolds number of 2.76×10^5–4.31×10^5 was conducted within the attack angle of $-10°$–$10°$ using the trailing edge serrations. An unequally spaced linear microphone array was used to identify the sound source around the airfoil. The results show that trailing edge serrations can effectively reduce airfoil trailing edge noise under various incoming flow conditions. The noise reduction effect varies with incoming flow condition and a maximum noise reduction of about 6 dB is observed. The noise reduction effect is more obvious under negative attack angles. For a specified serration configuration, there is an optimal velocity range for noise reduction.

Keywords Airfoil trailing edge noise · Trailing edge serration · Microphone array

1 Introduction

Trailing edge noise is an important broadband noise source for both aircraft and turbomachinery of turbofan. Therefore, trailing edge noise reduction is of great interest for aviation industry and designers. Howe (1991) firstly proposed the

F. Tong (✉) · L.F. Wang · W.Y. Qiao
School of Power and Energy, Northwestern Polytechnical University,
Xi'an 710129, China
e-mail: nwputongfan@163.com

X.N. Wang
State Key Laboratory of Aerodynamics, China Aerodynamics
Research and Development Center, Mianyang 621000, China

application of trailing edge serrations to reduce trailing edge noise. Following Howe's encouraging work, many researchers have experimentally and numerically investigated the noise reduction effects and the noise reduction mechanism of trailing edge serrations (Gruber et al. 2011; Chong et al. 2011; Moreau et al. 2013; Jones and Sandberg 2012). Even so, the detailed understanding of noise reduction effects of trailing edge serrations is still limited, which may hinder the technique to be applied in the future. This paper presents an experimental study to investigate the effects of trailing edge serrations on airfoil trailing edge noise reduction under various incoming flow conditions (different velocities and attack angles) which will add to our understanding of the basic laws of the noise reduction effects by use of trailing edge serrations.

2 Experimental Details

The experiment was carried out in the low speed open jet wind tunnel of Turbomachinery Aerodynamics & Acoustics Lab (TAAL) in Northwestern Polytechnical University of China. The wind tunnel outlet cross section is 0.3 m × 0.09 m. An unequally spaced linear microphone array with 31 microphones was used to identify the sound source around airfoil and to analysis noise strength (Fig. 1). The array was placed just underneath the airfoil about 0.405 m. The total length of the microphone array is 1.72 m. The microphone array spatial resolution is about 0.1 m around 1250 Hz and about 0.015 m around 8000 Hz. A SD2030 airfoil (chord = 150 mm) with and without trailing edge serrations was used. The trailing edge serrations peak to peak amplitude ($2h$) is 10 % of airfoil chord and the wavelength (λ) is 4 % of airfoil chord ($\lambda/h = 0.8$).
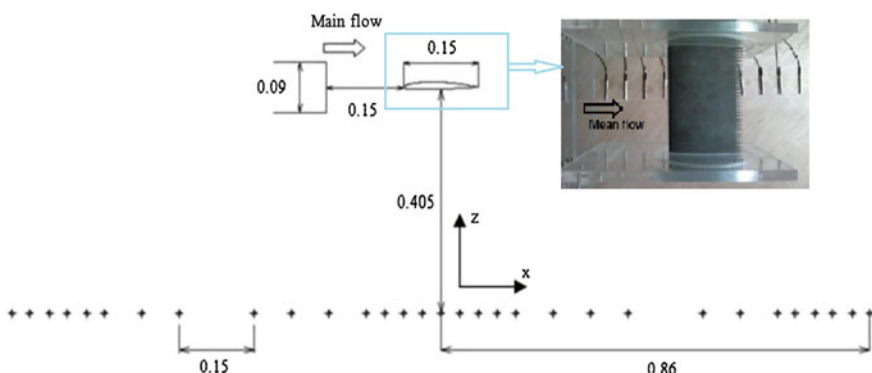
Fig. 1 Experiment setup

3 Results and Discussion

3.1 Noise Source Distribution

Figure 2 shows the result of noise source distributions for main flow velocity of 42 m/s. Figure 2a is the background noise distribution(without airfoil). Figure 2b, c are the noise source distribution for straight/serrated trailing edge airfoil respectively. Three obvious noise sources can be found when the straight trailing edge airfoil is placed downstream of the wind tunnel. The three obvious noise sources are wind tunnel noise (around x = −0.21 m), airfoil leading edge noise (around x = −0.06 m) and airfoil trailing edge noise (around x = 0.07 m). When the straight trailing edge airfoil is replaced by serrated trailing edge airfoil, a reduction of the trailing edge noise is clearly observed by comparing Fig. 2b, c. Over all, the beamforming technique successfully distinguishes the airfoil leading/trailing edge noise from wind tunnel noise and can be used to investigate the noise reduction effects of trailing edge serrations.
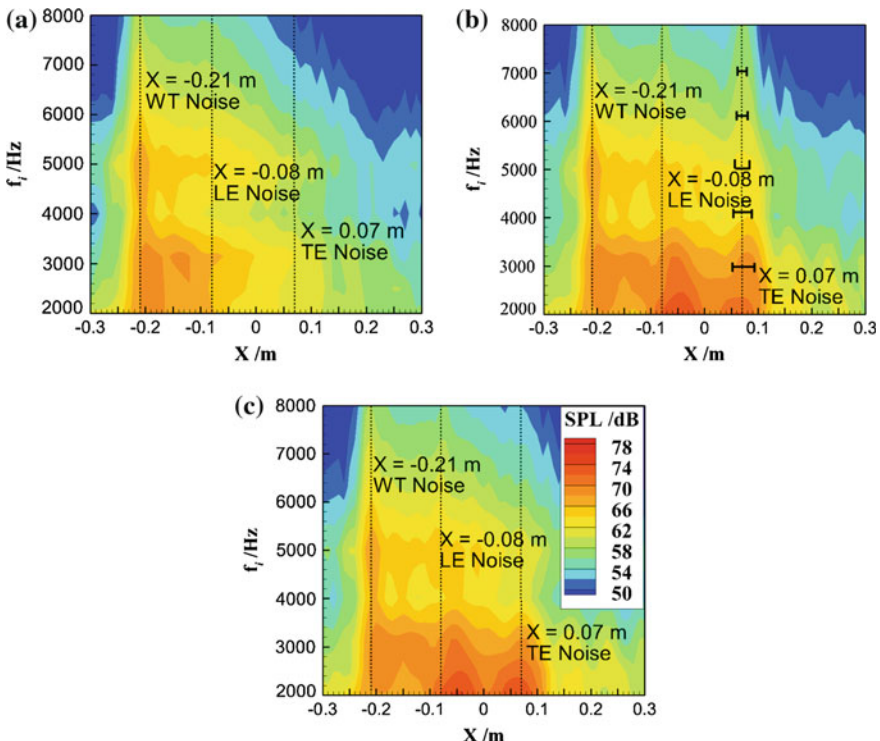
Fig. 2 Noise source distribution **a** background noise **b** airfoil with straight TE, **c** airfoil with serrated TE (the *short black line* in the contour **b** represents spatial resolution, velocity 42 m/s, α = 0°)

3.2 Noise Reduction Under Different Velocities

To investigate the effect of different velocities on the noise reduction effect of trailing edge serrations, Fig. 3 shows the noise reduction effects under different velocities at each attack angle. The noise reduction ΔSPL is defined as follows

$$\Delta SPL = SPL_{Serrated\ TE} - SPL_{Straight\ TE} \qquad (1)$$

It is shown in Fig. 3 that the effective frequency range of noise reduction will move towards high frequency as the velocity is increased. Take $\alpha = 0°$ for example, the noise reduction effect in frequency range of 1–6 kHz for velocity of 27 and 31 m/s is better than that for 38 and 42 m/s and the biggest difference is about 6 dB (at 2.5 kHz). However, the noise reduction effect in frequency range of 6–10 kHz for velocity of 38 and 42 m/s is better than that for 27 and 31 m/s. It should be pointed out that the serrated trailing edge airfoil can lead to a noise increase under low frequency range (1–3 kHz) at velocity of 38 and 42 m/s (Fig. 3c). In addition, the frequency range of this noise increase would increase as the attack angle is increased from −10° to 10°. For a specified trailing edge serration configuration, its noise reduction effect can only be most obvious at some velocity range.
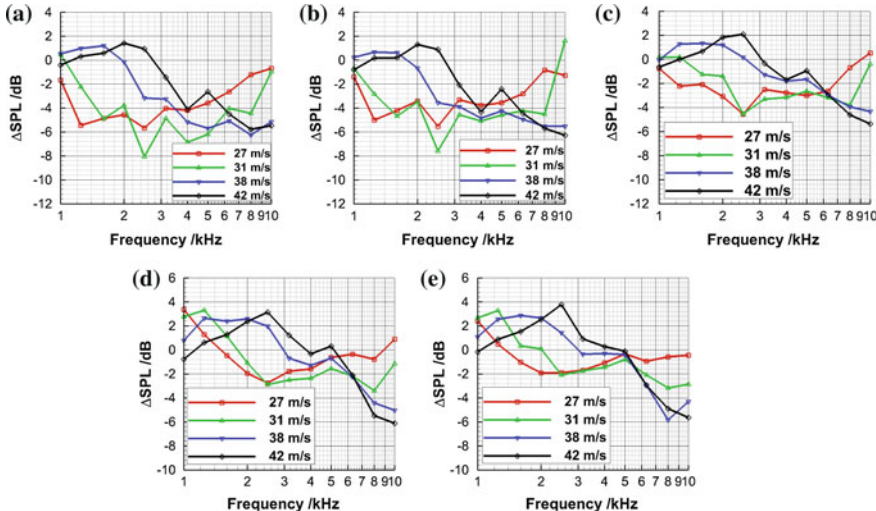
Fig. 3 Effects of main flow velocity on the noise reduction effect of trailing edge serrations **a** $\alpha = -10°$, **b** $\alpha = -5°$, **c** $\alpha = 0°$, **d** $\alpha = 5°$, **e** $\alpha = 10°$
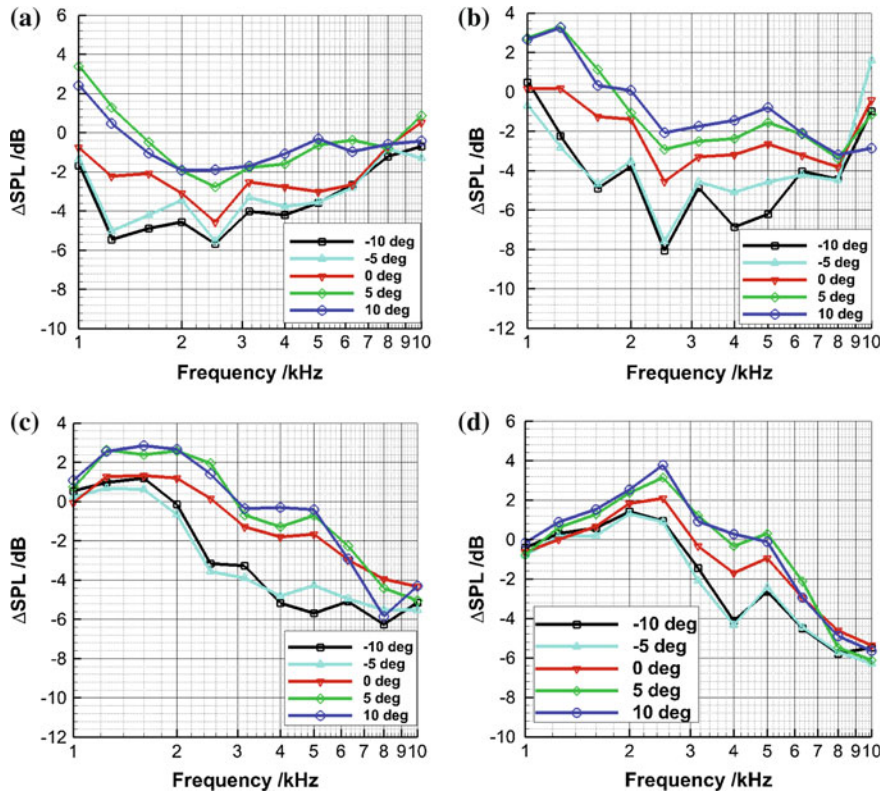
Fig. 4 Effects of attack angle on the noise reduction effect of trailing edge serrations **a** velocity 27 m/s, **b** velocity 31 m/s, **c** velocity 38 m/s, **d** velocity 42 m/s

3.3 Noise Reduction Under Different Attack Angles

The attack angle also has an effect on the noise reduction. To investigate this problem, Fig. 4 shows the attack angle effects on the noise reduction effect of trailing edge serrations.

It can be seen from Fig. 4 that the spectrum shape of noise reduction varies with different velocity. At velocity of 27 and 31 m/s, the noise reduction amplitude first increases and then decreases as the frequency increases. However, at velocity of 38 and 42 m/s, the noise reduction amplitude first decreases and then increases as the frequency increases. In addition, the noise reduction effect is more obvious at negative attack angles than that at positive attack angles. The noise reduction effect is best at $\alpha = -10°$ and worst at $\alpha = +10°$. Take velocity of 31 m/s for example, the noise reduction amplitude is decreased by 2–6 dB in frequency range of 1–6 kHz when the attack angle is changed from $-10°$ to $+10°$.

It is also found that although the spectrum shape of noise reduction changed a lot when the attack angle changes from zero attack angle to negative/positive attack angles, the spectrum shape of noise reduction is similar between $-5°$ attack angle and $-10°$ attack angle (or $+5°$ attack angle and $+10°$ attack angle).This implies that when the attack angle turns to some extent, further increase of attack angle will alter the noise reduction effect only a little.

4 Conclusions

The noise reduction effect of trailing edge serrations on airfoil noise is experimentally investigated under Reynolds number of 2.76×10^5–4.31×10^5 and at different attack angles. The beamforming technique is used to identify airfoil trailing edge noise. The results show that: (1) the effective frequency range of trailing edge noise reduction will gradually move to higher frequency range as the main flow velocity is increased. (2) For a specified trailing edge serration configuration, the best noise reduction effect can only be achieved under some velocity range. (3) The noise reduction effect of trailing edge serrations is decreased as the attack angle turns from negative attack angle to positive attack angle.

References

Chong TP, Vathylakis A, Joseph P et al (2011) On the noise and wake flow of an airfoil with broken and serrated trailing edges. In: 17th AIAA/CEAS aeroacoustics conference, AIAA paper, Portland, Oregon

Gruber M, Joseph PF, Chong TP (2011) On the mechanisms of serrated airfoil trailing edge noise reduction. In: 17th AIAA/CEAS aeroacoustics conference, AIAA paper, Portland, Oregon

Howe MS (1991) Noise produced by a saw tooth trailing edge. J Acoust Soc Am 90(1):482–487

Jones LE, Sandberg RD (2012) Acoustic and hydrodynamic analysis of the flow around an aerofoil with trailing-edge serrations. J Fluid Mech 706:295–322

Moreau DJ, Doolan CJ (2013) Noise-reduction mechanism of a flat-plate serrated trailing edge. AIAA J 51(10):2513–2522

Noise Source Analysis and Control for Two Axial-Flow Cooling Fans in Series

C. Wang, W. Zhang and L. Huang

Abstract The noise signature of two identical small axial-flow cooling fans in series was analyzed and a technique of synchronous averaging with time-base stretching was used to decompose the raw sound signals into various noise source components. Acoustic directivity measurements were conducted for the case of distorted inlet flow caused by a flat plate covering half of the circular inlet flow passage. The effects of the flat plate and the axial distance between the flat plate and the fan inlet were studied as well. It is found that the inlet flow distortion increases the total sound pressure level (SPL), random and rotary noise of the upstream fan a lot but it barely affects the rotary noise of the downstream fan. A flow straightener consisting of many small hexagons is mounted at the inlet of the upstream fan to reduce the adverse effect of the inlet flow distortion. The total SPL is reduced by 1.2 dB on average.

1 Introduction

Fan noise is a serious issue in electronic cooling applications and it has been a frequent subject of study (Huang 2003). For one single typical computer cooling fan operating in free field, the dominant noise source is the aerodynamic interaction between the impeller blades and the downstream struts. Usually one single fan is enough in applications such as computer cooling and building ventilation. However, when the pressure drop is high, two axial-flow fans in series are often used

C. Wang (✉) · W. Zhang · L. Huang
Lab of Aerodynamics and Acoustics, HKU Zhejiang Institute of
Research and Innovation, Shenzhen Institute of Research and Innovation,
and Department of Mechanical Engineering, The University of Hong Kong,
Hong Kong, China
e-mail: chadwong@hku.hk

W. Zhang
School of Energy and Power Engineering, Beihang University, Beijing, China

and the noise created by the two fans is complex. In this study, two identical small axial-flow cooling fans in series, or a two-stage fan, are investigated experimentally. The fan is 120 mm in casing diameter and it has 7 rotor blades and 11 stators behind the rotor to adjust the flow direction and support the motor assembly. Even without the inlet flow blockage by an obstacle plate, noise radiated by a two-stage fan is more complicated and the main noise sources are expected to be the following: (1) unsteady loading on the first rotor blade caused by the inlet flow distortion which has a spatial pattern defined by the square outer casing; (2) interactions between rotor and stator blades, with downstream blade row making more noise than upstream in a pair of interacting blade rows; (3) tip leakage flow.

In an effort to decompose the noise source between upstream and downstream rotors, emphasis is placed on the signal correlation between noise signal and exact rotor positions. The technique of synchronous averaging with time-base stretching (SATS) (Huang and Wang 2005) was used. The part of noise signal that is correlated with the blade rotation is considered to be rotary noise, which can be further attributed to either upstream or downstream rotors by correlation with the rotational signal of corresponding rotor, while the rest is considered as component of random (or broadband) noise.

2   Experimental Set-up and Signal Processing

The measurement is conducted in an anechoic chamber. The sample fan is installed vertically on a rack. A tachometer (ONO SOKKI Digital Tachometer HT-5500) with pulse output is installed at the inlet of the fan, whose signal is used as trigger to correct the variation of instantaneous rotational speed in every cycle. Sound is measured by a ½ in. B&K microphone (Type 4955), powered by B&K Nexus conditioning amplifier (type 2690). In order to construct the noise directivity, measurements are repeated at an angular interval of 30° by manually rotating the microphone along a circle of 0.8 m in radius on the central horizontal plane with the fan at the center. The fan inlet is defined as the angular origin of 0°. The signals from the tachometer and microphone are sampled simultaneously by a 16-bit NI A/D card (NI USB-6251), and then processed in a PC equipped with MATLAB.

The rotating speed of the fan is set at 4200 rpm, or 70 revolutions per second (rps). The signals are sampled at a rate of $f_s = 21$ kHz. Thus, $N = f_s/$rps $= 300$ data points are obtained during one complete rotational cycle. The sampling duration for all positions is $t = 20$ s, which gives rps $\times t = 1400$ cycles for cyclic averaging. The period of one complete rotational cycle is found by their two rising edges of two adjacent tachometer pulses. During the post-processing, the raw signal is digitally resampled to 300 points in every cycle using time-base stretching to correct the effect of rotational speed variation, which gives the time-base stretched signal. Then the resampled cycles are overlapped for averaging; the result is a synchronously averaged signal. For noise mechanisms locked with rotation, no energy is lost

during such averaging, while mechanisms not strictly determined by rotor positions are suppressed through such averaging. The signal that remains through synchronous averaging is defined as the rotary sound, while the difference between the raw noise power and the rotary sound power is defined as the random noise power. Since signals below 420 Hz or 6 rps are contaminated by the microphone self-noise and are filtered out, the attention is focused on the noise at BPF and above.

3   Inlet Flow Distortion and Its Noise Control

In order to obtain noise radiated by the two rotors, slightly different rotational speeds are used for the purpose of noise decomposition. The downstream rotor is set to rotate at 35 rpm higher speed than the upstream. The rotary components of upstream and downstream fan can be obtained successively by two measurements of the two-stage fan, each with the rotational signal of the upstream and downstream fan as the trigger signal respectively. The random noise is studied as a whole instead of separating it into two parts made by the two fans respectively.

The flow into the fan inlet is distorted by an obstacle (a flat plate) covering half of the circular inlet flow passage as shown in Fig. 1. Note that several different thicknesses of spacers can be inserted behind the obstacle to adjust the axial distance between the obstacle and the upstream rotor.

Fig. 1 Structure of inlet distortion by a plate covering half of the circular inlet flow passage
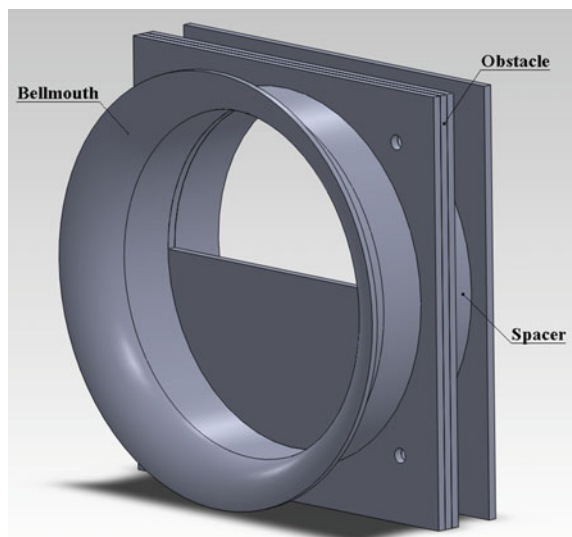
3.1 Noise Source Analysis

In consideration of the symmetry of the fan structure and symmetrical radiated noise directivity indicated in our previous study (Wang et al. 2015), measurement over 180° suffices. The monitoring point at the outlet (180°) was left out since its noise data is contaminated by wind without a wind screen. The total number of measurements is therefore six for one directivity pattern (0°, 30°, 60°, 90°, 120° and 150°). Three different axial distances (20, 30, 40 mm) between the obstacle plate and the fan inlet are conducted, and the directivity of the total, random and rotary noise components for the obstructed and unobstructed flow cases are shown in Fig. 2. It should be noted that the case of unobstructed inlet here is still with bellmouth and spacer. In the legend, "Rotary" and "Random" mean the rotary and random components of the total noise. "1" and "2" represent the upstream and downstream rotor respectively.

First of all, the obstacle plate increases the levels of total SPL, Random and rotary noise from the upstream fan (Rotary 1) compared with the unobstructed inlet flow. When averaged over the six measurement points, the increments are 8.4, 9.6 and 15.7 dB, respectively for the 20 mm plate-fan spacing. The rotary noise from the downstream fan (Rotary 2) is nearly the same level in all directions. Comparison of results for different plate-fan spacings, 20, 30 and 40 mm, shows that spacing has little effect on all noise components except Rotary 1. It may indicate that 40 mm is still well within the zone of strong influence of the low-speed vortex behind the flat plate. For unobstructed inlet, the rotary component from the downstream fan dominates over that from the upstream fan. The former is 9.9 dB larger than the latter. It certainly does not result from the minor contribution of the 35 rpm difference. However, the dominance by the downstream fan is reversed when inlet
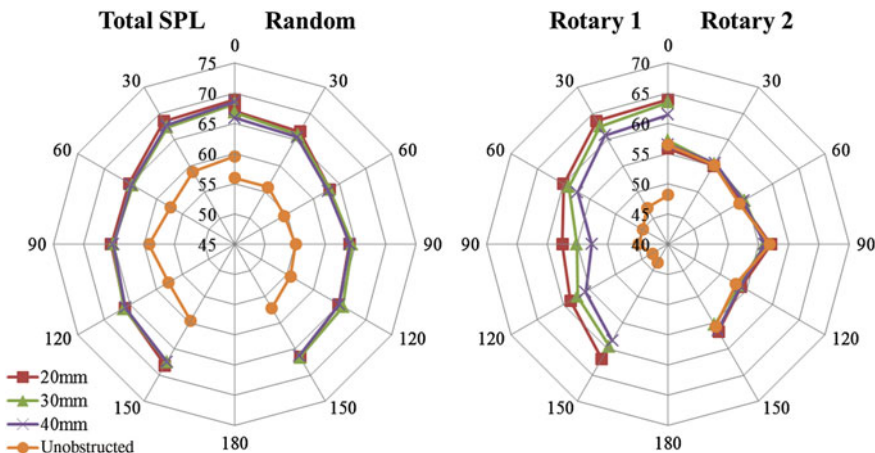
Fig. 2 Noise directivity comparison between the cases of distorted and unobstructed inlet flow

flow is distorted by the flat plate. That is, Rotary 1 surpasses Rotary 2 by 5.6 dB for the 20 mm spacing.

3.2 Noise Control by a Flow Straightener Behind the Obstacle

A flow straightener is used in front of the upstream fan in an attempt to reduce the adverse effect of the inlet flow distortion caused by the flat plate. The flow straightener consists of many small hexagons of 2 mm in side length, 0.1 mm in thickness and 7 mm in depth. Here, the plate-fan spacing is fixed at 20 mm. Figure 3 shows the noise directivity measured for the three cases: unobstructed inlet, obstructed inlet with and without the flow straightener.

First of all, it is observed that flow straightener has little effect on the rotary noise from the upstream (Rotary 1) and downstream rotor (Rotary 2). However, the random noise is reduced by 3.2 dB and the total noise is reduced by 1.2 dB on average over the six positions. It is interesting to note that the flow straightener did reduce Rotary 1 in an earlier study (Wang el al. 2015) in which a big gap exists between the obstacle plate and the fan inlet. Thus, air flows can come to the fan inlet directly from the gap, without passing through the obstacle.

The flow straightener is expected to reduce the inlet flow distortion by homogenizing the nonuniform incoming flow in the same way as a honeycomb device in a wind tunnel. However, it cannot remedy the basic flow distortion of free inlet in the upper half and severe blockage in the lower half of the inlet flow passage.
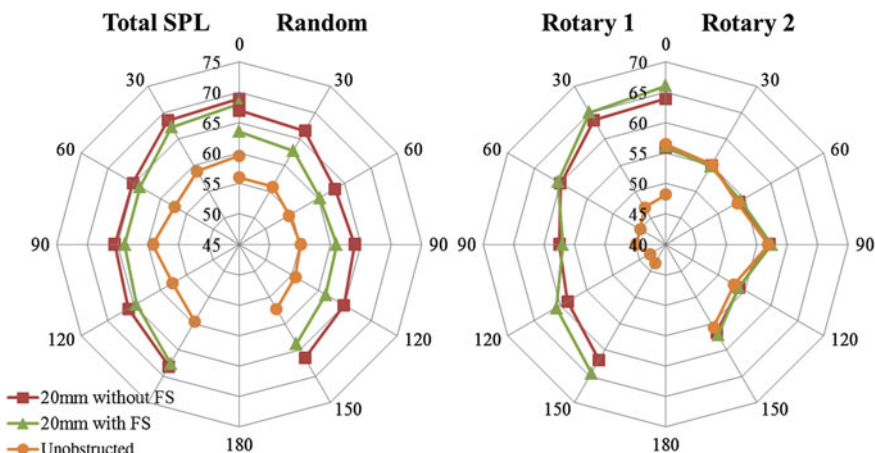
Fig. 3 Noise directivity comparison between the cases with and without a flow straightener (FS) in front of the upstream fan

4   Conclusions

Acoustic directivity measurement and noise source analysis were conducted for two identical small axial-flow cooling fans in series with distorted inlet flow caused by a flat plate covering half of the inlet flow passage. A flow straightener was mounted at the inlet of the upstream fan in an attempt to reduce the adverse effect of the inlet flow distortion. The following conclusions are drawn.

(1) For unobstructed inlet, the rotary component radiated by the downstream fan dominates over that radiated by the upstream fan. After a flat plate is mounted to distort the inlet flow, total SPL, Random and Rotary 1 noise all increase a lot while it barely has any effect on Rotary 2 component.
(2) In the range of 20–40 mm, the axial distance between the flat plate and the fan inlet has almost no influence on the total SPL and the random noise, but it has some influence on the rotary noise of the upstream fan.
(3) When a flow straightener is mounted at the inlet of the upstream fan to reduce the adverse effect of the inlet flow distortion, the random noise and total SPL are reduced by 3.2 and 1.2 dB respectively while Rotary 1 and Rotary 2 are hardly affected.

References

Huang L (2003) Characterizing computer cooling fan noise. J Acoust Soc Am 114(6):3189–3200
Huang L, Wang J (2005) Acoustic analysis of a computer cooling fan. J Acoust Soc Am 118:2190–2200
Wang C, Zhang W, Huang L (2015) Noise source analysis and control for two axial-flow cooling fans in series. Fan Noise 2015, Lyon, France

Fan Noise Control by a Flexible Casing Structure

Z.B. Wang, Y.S. Choy and Q. Xi

Abstract The work presented here examines the performance and effectiveness of fan noise control in a duct by using light panels with backing cavity. The method aims to suppress the low-frequency noise by destructive interference between the acoustic field in the duct and sound radiation from the panel. A three-dimensional numerical model is established to investigate the details of flow-structure interaction and its influence on the fan noise suppression. The aerodynamic characteristics near the fan blades and the vibration of the flexible structure also plays an important role in the noise suppression. The findings of this study will provide an alternative method of fan noise abatement focusing on the source.

Keywords Fan noise · Flexible structure · Flow-structure interaction

1 Introduction

Fan installed in a short duct can often be found in domestic and industrial applications. When the fan operates at low rotational speed, the low frequency noise component is normally dominant and it is very annoying. Noise can be controlled in the propagating path or directly on the noise source itself. In the first category, conventional passive control approach, such as porous materials, is commonly used but its performance is limited by its length for attenuating low frequencies. The use of the multiple expansion chambers with perforated tubes is normally bulky and pressure loss is high. In order to eliminate the pressure loss, Huang introduced the concept of drum silencer, which consists of an expansion chamber with two side-branch cavities covered by light membranes under high tension (Huang 2002; Choy and Huang 2002, 2005). The whole device including fan may be quite

Z.B. Wang · Y.S. Choy (✉) · Q. Xi
Department of Mechanical Engineering, The Hong Kong Polytechnic University,
Hong Kong, China
e-mail: mmyschoy@polyu.edu.hk

lengthy when the drum-like silencer is installed at the propagating path. Recently, Liu, Choy and Huang adopted a new configuration in which the membranes are covered by two side-branch cavities to house the fan, which is essentially a dipole source, in order to control the sound radiation from the fan directly (Liu et al. 2014). This configuration is similar to the drum-like silencer but the physical mechanism behind is totally different. This device aims at directly suppressing the sound radiation from dipole sources through its interaction with the membrane vibration; while drum-silencer, which is installed downstream of the source, relies on reflecting sound back to the source along the propagating path. The proposed noise control device with tensioned membrane can achieve a desirable *IL* with a stopband wider than an octave, but there is a need for a special mechanism to apply the tensile force on the membrane. To solve this problem, the membrane is replaced by a light but relatively stiff plate. Therefore the objective of the current study is to examine the performance of the conceived device with a light panel and its application for fan noise control. In this regard, a three dimensional numerical model is established to investigate the fluid-structure interaction and its influence on the fan noise suppression. Besides, an experiment with a small axial fan is conducted to validate the theoretical predictions.

2 Theoretical Analysis

Figure 1 shows the three-dimensional configuration of the silencing device, which is composed of two flush-mounted panels covering a side-branch rigid-walled cavity in an otherwise rigid-walled duct with a height of *h*. The plate with the length *L* is supported at the leading and trailing edges of the cavity. An axial fan is placed at the middle of the duct. Dipole sound waves from the fan are radiated to both upstream and downstream sides with mean flow speed U^*. The response of the plate is fully coupled with the acoustic waves in the duct and cavity. For convenience, all variables are non-dimensionalized by three basic quantities, air density ρ_0^*, duct height h^* and speed of sound in free space c_0^* as follows:
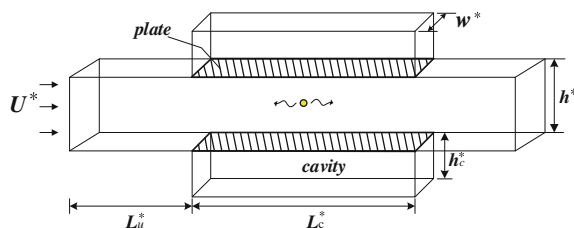
Fig. 1 Three dimensional model of plate housing device

$$h_c = \frac{h_c^*}{h^*}, \ L = \frac{L^*}{h^*}, \ L_c = \frac{L_c^*}{h^*}, \ f = \frac{f^* h^*}{c_0^*}, \ m = \frac{m^*}{\rho_0^* c_0^*}, \ B = \frac{B}{\rho_0^* c_0^{*2} h^{*3}}$$

where m is the plate-to-air mass ratio, B is the dimensionless bending stiffness of the plate.

2.1 Numerical Simulation

Finite element simulation is adopted to solve the structural and acoustic coupling problem in three dimensional configuration in the current study. The commercial software package Comsol Multiphysics was employed because of its strong multiphysics capability. In the numerical simulation, there are two domains. One is a three-dimensional domain for fluid to describe the sound wave propagation in the flow duct and cavity. Another is the two-dimensional domain for the structural vibration of the panel. The unsteady fluid dynamics of the air in the duct is governed by the following equation:

$$\left(1 - M^2\right) \frac{\partial^2 p}{\partial x^2} + \frac{\partial^2 p}{\partial y^2} + \frac{\partial^2 p}{\partial z^2} - \frac{2i\omega M}{c_0} \frac{\partial p}{\partial x} + \frac{\omega^2}{c_0^2} p = \frac{\partial F_x}{\partial x} \delta(x - x') \qquad (1)$$

where p is the acoustic pressure, M is the Mach number of the mean flow.

The panel vibration with the displacement of η_p is driven by air pressure difference across the interface at $y = 0$,

$$B \frac{\partial^4 \eta_p}{\partial x^4} + m \frac{\partial \eta_p}{\partial t} + (p_{duct} - p_{cavity}) = 0 \qquad (2)$$

where B is the bending stiffness of the panel, and p_{duct} and p_{cavity} are the fluid loading on the surface of panel at the duct and cavity, respectively. Equations (1)-(2) are solved in a coupled manner. In the current study, sound insertion loss (IL) is used to assess the performance of the proposed device.

$$IL = 10 \log 10 \left(\frac{\int_{str} |p|^2 ds}{\int_{panel} |p|^2 ds} \right) \qquad (3)$$

where p is the pressure at the duct outlets, the "str" refers to the straight duct without the panel housing device, which is used as a reference, and "panel" refers to the duct with panel and covered backing cavity.

Fig. 2 Mean flow effect on the insertion loss of the duct plate silencer
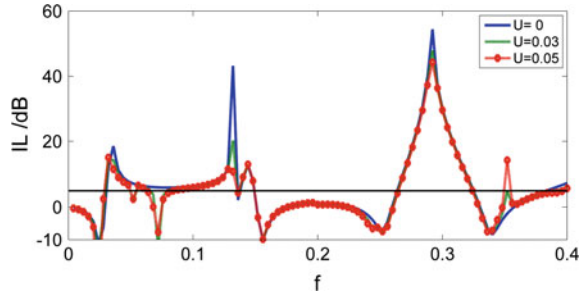
2.2 Numerical Results

The performance of the device is characterized by the widest stopband that can be achieved. For an axial fan with 7 blades running at 4000 rpm speed, the dimensionless first and second blade passing frequencies are 0.14 and 0.28, respectively, when the duct height is 0.1 m. In order to achieve an effective abatement of noise at the first and second blade passage frequency at the same time, two stopbands covering these two frequencies was the designed. Aiming to develop panel housing device with a compact geometry to control the ducted fan noise, the cavity was fixed at length $L_c = 3$ and height $h_c = 0.5$, for which the criterion level of noise control is 5 dB. After optimization for the widest stopbands, the optimal mass ratio $m = 0.2$ and bending stiffness $B_{opt} = 0.0014$ are found. Figure 2 shows the insertion loss of the panel housing device at different mean flow speed under the optimized structural parameters. As the mean flow velocity increases, the insertion loss is shifted to higher frequencies and the performance deteriorates due to the appearance of a trough point between f = 0.05 and f = 0.1. This is because of the cross-modal coupling (Choy and Huang 2005).

3 Experimental Analysis

A small loudspeaker and an axial fan are employed in the experiment as shown in Fig. 3. They are placed at the center of the duct with a cross sectional of 100 mm by 100 mm. The panel has a mass of $m = 0.6$, bending stiffness $B = 0.0011$, thickness 0.04 mm and a length of $L = 300$ mm. It is flushly mounted on the duct. Further details of the experimental setup can be found in (Liu et al. 2012). The dashed and solid lines show the comparison between the experimental and numerical results for insertion loss when the small loudspeaker is used in the duct. Roughly speaking, the agreement is quite good.

Figure 4 shows the experimental results for the axial fan with different operational speed and different mean flow velocity from 3.3 to 5.7 m/s. The current panel housing device effectively controls the noise from 250 to 500 Hz, and from 800 to
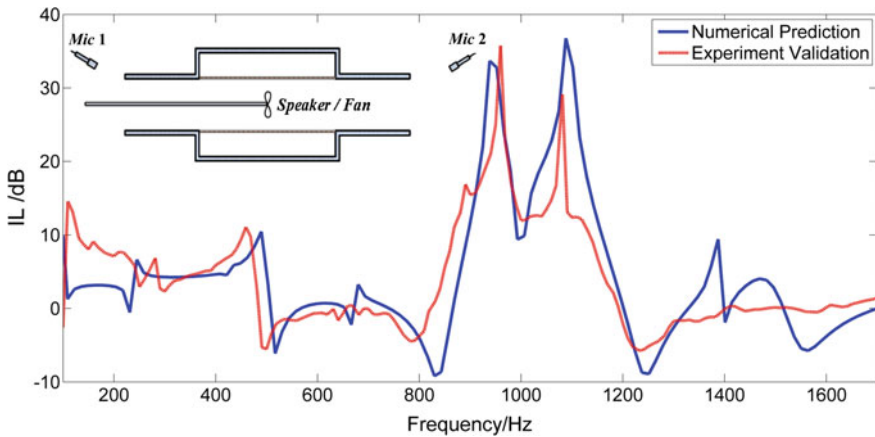
Fig. 3 Insertion loss of the panel housing device when a small speaker is used as dipole source
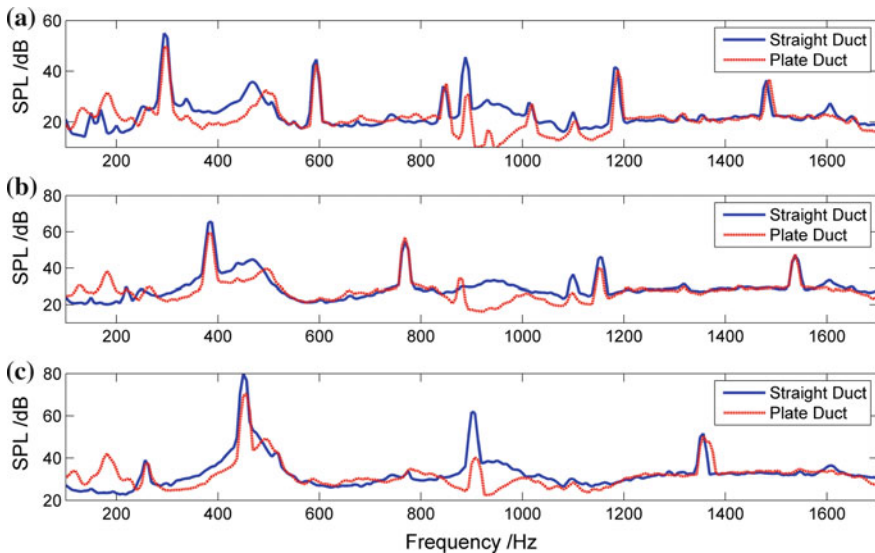
Fig. 4 Comparison of the sound pressure level measured for the axial fan in straight duct and plate duct: **a** $U = 3.3$m/s; **b** $U = 4.4$ m/s; **c** $U = 5.7$ m/s

1200 Hz, so it can reduce the noise by about 5 dB at the first blade passage frequency for different operational speed of the fan. For the second blade passage frequency, the effectiveness of noise reduction depends on whether it is within the frequency range of 800–1200 Hz. Figure 4c shows that the noise at the second blade passage frequency is reduced by about 18 dB when the flow speed is 5.7 m/s. This shows that the proposed device can control the first and second blade passage

frequency of a real axial fan effectively when the structural property of panel is chosen appropriately.

4   Conclusions

A three-dimensional numerical model for vibro-acoustic coupling between the panel covering the backing cavities in a duct and an axial-flow fan has been established. The numerical results have been validated by experiments. With the appropriate choices of the structural property of the panel, such as the mass and bending stiffness, the panel housing device can effectively control the noise at the first and second blade passage frequencies at various fan operation conditions.

References

Choy YS, Huang LX (2002) Experimental studies of a drumlike silencer. J Acoust Soc Am 112:2026–2035
Choy YS, Hung LX (2005) Effect of flow on the drumlike silencer. J Acoust Soc Am 118:3077–3085
Huang LX (2002) Modal analysis of a drumlike silencer. J Acoust Soc Am 112:2014–2025
Liu Y et al (2012) Noise suppression of a dipole source by tensioned membrane with side-branch cavities. J Acoust Soc Am 132:1392–1402
Liu Y et al (2014) Reactive control of subsonic axial fan noise in a duct. J Acoust Soc Am 136:1619–1630

Acoustical Wind Tunnel Studies of Landing Gear Noise

Jian Wang, Wenjiang Wang and Kangle Xu

Abstract Landing gear noise can be significant at aircraft approach. It is difficult to quantify the landing gear noise during a flight test. The motivation of this work is to develop a feasible method with acoustic wind tunnel test to predict the in-flight landing gear noise. The prediction is based on an empirical model (Guo 2006) calibrated by wind tunnel test. The wind tunnel test was conducted on a 1:7.6 scale model of an airframe. The calibration of the empirical model and the wind tunnel test focuses on the installation effects that include interaction with flap and the local flow velocity in the existing empirical model. The installation effect on the far-field directivity factor is investigated by the experimental studies. The mean flow patterns of the wing with deployed slat and flap at approach configuration are calculated by CFD solver ANSYS. After validation of the empirical model, the result of the scale model is transposed to the full scale landing gear noise in the flight condition.

Keywords Acoustic wind tunnel tests · Landing noise and prediction · Acoustic directivity · Installation effects

1 Introduction

Landing gear noise is studied with a acoustic wind tunnel test of a 1:7.6 scaled full aircraft model. A similar set-up for an aircraft model test in DNW-LLF is described by studies of slap noise (Dobrzynski and Pott-Pollenske 2001). During the test, the main landing gear was mounted under fuselage wind with flap deployed, when slat is switched from close to open. These test configurations explored the landing gear noise interaction with high lift device system. The landing gear noise incuding landing gear insallation noise is studied with test results when landing gear mounted

J. Wang (✉) · W. Wang · K. Xu
Shanghai Aircraft Design and Research Institute, COMAC, Shanghai, China
e-mail: jian.wang97@hotmail.com

and removed. A empirical modelling of landing gear noise predciton (Guo 2006) is performed to remodel the landing gear installation effects on far file diectivity.

2   Empirical Modelling

The far field sound associated with the landing gear can be predicted by Ffowcs Williams and Hawkings (1969) Equation. For typical aircraft landing speed, the Mach number is about 0.2, the dominant sound is the dipole noise induced by the surface pressure fluctuations and the sound power scaled by M^6 where M is flight Mach number. The emprical model (Guo 2006) represents that landing gear noise contributed by three groups associated with low, middle and high frequency components according to the length scales. A Matlab code is developed to implement this empirical prediction model. The code can perform three conditions: the first condition is to predict the isolated landing gear noise at laboratory condition. The directivity for isolated landing gear is given as:

$$D_0(\theta) = (1 + h\cos^2\theta)^2 \tag{1}$$

For validating the Matlab code, the prediction of isolated landing gear for B737 was solid line ploted in Fig. 1a, which is very close to the predictions of (Guo 2006). The second condition accounts the installation effects when landing gears are installed on the airframe, which changes the directivity due to reflection of the wing, and also interaction noise induced by landing gear trailing edge interaction with deployed flap. The emprical model (Guo 2006) simulates airframe reflection noise by far-field directivity factor.

$$D(\theta) = 1.2 \times (1 - 0.9\cos^2\theta)^2 \times D_0(\theta) \tag{2}$$

Fig. 1 Directivities of the empirical prediction wind tunnel test result and remodeling result
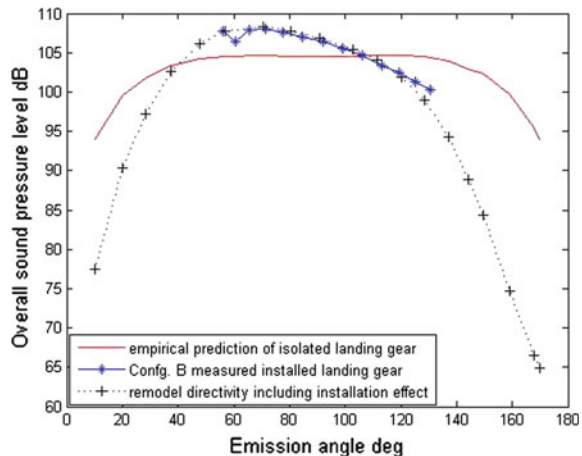
One focus of this paper is to remodel directivity for accounting installation effects by the acoustic wind tunnel results.

As dominant noise source follows the sixth power to the Mach number, the noise level is sensitive to the local Mach number. The empirical model assumes that local speed through main landing gear is reduced about 70–80 % of the flight Mach number, M∞, for producing lift on the wing. The variations of this range flow velocity change noise level up to be $60 \lg(0.8/0.7) = 3.48$ dB, which shows that the landing gear noise is sensitive to the flow speed. The mean flow patterns of wing with slat and flap deployed at approach configuration are calculated by CFD solver ANSYS.

2.1 Acoustic Wind Tunnel Tests

The experimental measurements of a 1:7.6 scaled full airframe model were conducted in DNW-LLF wind tunnel facilities. The test section is anechoic chamber with an open jet and downstream jet collector. Figure 2 shows the location of the landing gear related to the wing when flap was deployed. The two installation effects can be observed to be significant: reflection/diffraction from fuselage and flow interaction between landing gear trailing edge and flap. The power integration spectra resulted from the beamforming technique (Pieter 1999) is most useful to quantify the installation noise. The areas of flap, slat and wing are selected for power integration scan processing, because interaction noise from landing gear noise and flap is clearly observed in these scaning areas. The three test configurations listed in Table 1 are investigated for the installation noise. The power integration spectra plotted through Figs. 3, 4 and 5 show noise difference on slat, flap and wing induced by landing gear. The microphone array is straight position under the wing that means the power integration spectrum is noise level at

Fig. 2 Geometry of landing gear installation
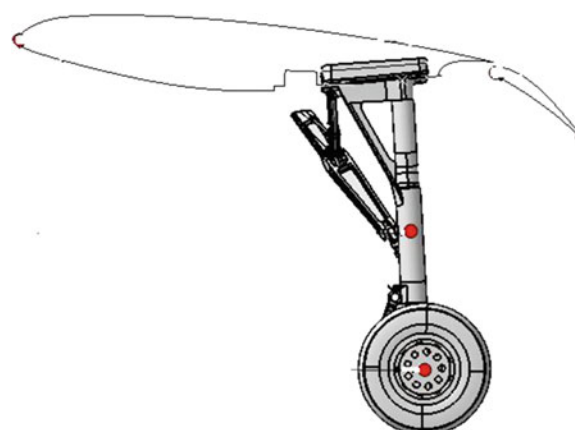
90° angle. The distance of the array from geometrical center of the test model is around 7 m.

Configuration B plotted in Fig. 3, the landing gear installation mainly influence on inner flap, because the landing gear is in front of inner flap that induces 4 dB noise increased. Comparing configuration C and D in Fig. 4 shows that the slap noise changed a little. It can mean that landing gear does not effect on slat noise. Frequency from 1000 Hz separates slat noise to other noise sources, as Figs. 4 and 5

Table 1 Test configurations

Configuration	Slat in\out	Flap	Landing gear
B	Off	On	On
C	On	On	On
D	On	On	Off
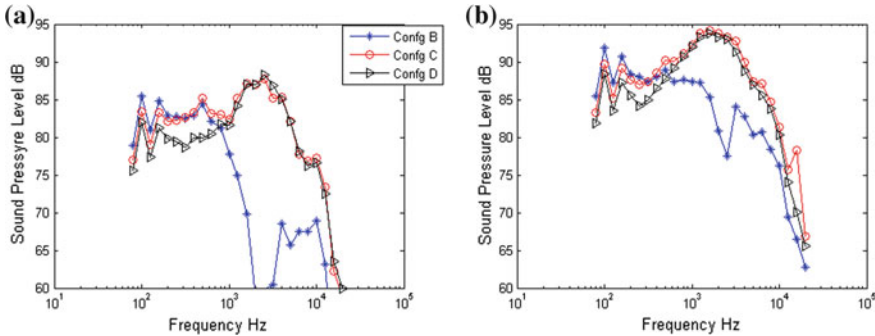
Fig. 3 Installation effects on flap noise: **a** inner flap noise, **b** out flap noise
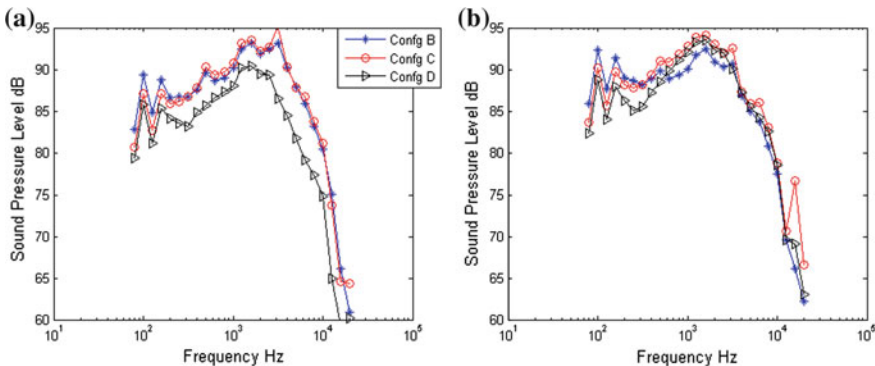
Fig. 4 Installation effects on slat noise: **a** inner slat noise, **b** out slat noise

Fig. 5 Installation effects on integrated wing
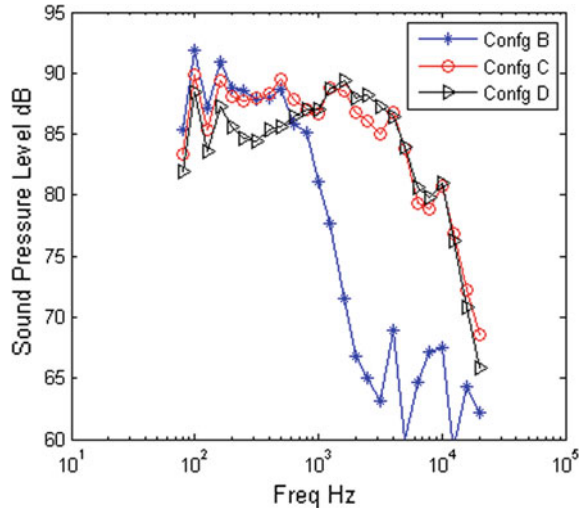
show noise of configuration B dramatically starts dropping down, when slat is off. Figure 5 shows that landing gear installation cannot be significant to change entire wing noise above 1000 Hz, but it increases 3–4 dB noise at frequency below 1000 Hz. As landing gear installation does not effect on slat noise, configuration B is selected to process the landing gear including installation noise. The far field directivity measurement data is used to quantify landing gear noise.

Since the power integration spectrum shows that the installation noise is significant below 1000 Hz, landing gear noise directivity covers frequency range up to 1000 Hz components. Figure 1a shows isolated landing gear noise directivity given by Eq. (1) compared with wind tunnel test directivity of installed landing gear noise. The installation effects caused tilted directivity. Tuning the directivity factor according to in Eq. (2) for the tilted directivity gives:

$$D(\theta) = 1.4 \times (1 - 0.9 \times \cos^2(\theta - \varphi))^2 D_0(\theta) \tag{3}$$

Angle φ is phase delay due to flap reflection, which varies with frequency and flap deployment angle. For isolated landing gear directivity $D_0(\theta)$ given by Eq. (1), where factor h depends on frequency. For middle frequency component, $h = 0.6$. As the landing gear noise and its installation noise is dominant at middle frequency component, when delay angle φ tunes to $10°$, that matches tilting directivity to the test results of landing gear noise as shown in Fig. 1a.

Fig. 6 PNLT prediction for
landing gear noise
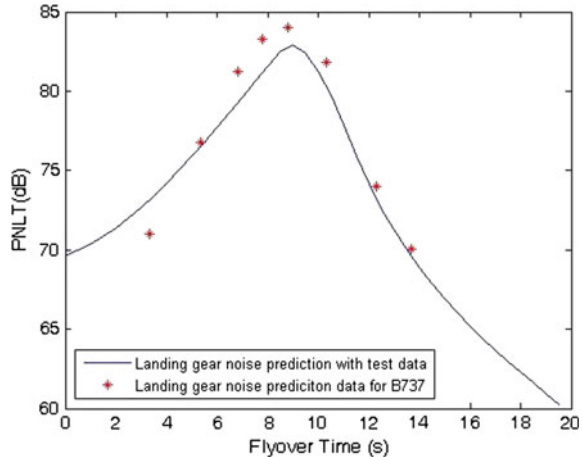
3   In-flight Landing Gear Noise Predcitions

In order to simulate landing gear noise in flight condition from scaled landing gear model test data, two transformations are performed. The first transformation is to convert measured model noise to full scale landing gear's noise. The frequency is accounted by non-dimensional Strouhal number St, while the amplitude is extended with scale factor by 7.6. The second transformation is for flight transposition which is based on presedure according to ICAO ETM[3] specified by' Ground to Flight Equivalence (GTFE)'. The amplitude is correlated by convective amplification meanwhile frequency shifting with moving source is accounted by Doppler effects.

After transposing the test data to flight condition, according to ICAO Annex 16, Effective Perceived Noise Level (EPNL) is calculated to be 86.4 EPNdB from the wind tunnel test results of Conf. B. Noise propagation effects include distance correction, air absorption, and ground effects. The calculated PNLT-t curve is plotted in Fig. 6 comparing with B737 prediction data (2005). EPNL is calculated according to 10 dB-down segment included in PNLT-t curve.

4   Conclusions

Acoustic wind tunnel test of landing gear noise and landing gear installation noise is studied. The wind tunnel test results demonstrated that installation noise is mainly from flow interaction between landing gear and flap, and flap reflection. The directivity of landing gear noise include installation noise denpends on frequency components and flap deployement angle, which is remodeled as Eq. (3). After validation of the empirical model, the noise of the scale model is transposed to the full scale landing gear noise in the flight condition. The final in-flight landing gear noise level is similar to B737 landing gear prediction.

References

Guo Y (2006) A semi-empirical model for aircraft landing gear noise prediction. In: 12th AIAA/CEAS aeroacoustics conference (27th AIAA aeroacoustics conference)

Dobrzynski W, Pott-Pollenske M (2001) Slat noise source studies for farfield noise prediction. AIAA 2001–21:58

Ffowcs William JE, Hawkings DL (1969) Sound generation by turbulence and surfaces in arbatrary montion. Phil Trans Roy Soc Lond A 26:321

Sijtsma P, Holthusen, H (1999) Source location by phased array measurements in a closed wind tunnel test sections. AIAA-99-1814

The Spectrum and Directivity Extrapolation Method of an Acoustic Wind Tunnel Test for a Scaled Airframe Noise

Xu Kangle and Wang Jian

Abstract The wind tunnel test for a scaled airframe model normally can not obtain the high frequency components when transform the scaled model to full scale. Meanwhile, due to the limitation of the acoustic wind tunnel facilities, the measurement can not perform a full acoustic directivity covering from 0 to 180°. In order to extend the frequency and polar angle information acquired by wind tunnel test results, a method for extrapolation of frequency and directivity of a 1:7.6 scaled full airframe wind tunnel test data is developed. The entire sound pressure spectrum is decomposed into two segments: low frequency segment and mid-high frequency segment. Each segment is fitted by a spectrum envelope with different slopes generated from flight test spectrums. An auto regressive model (AR model) is also developed and applied to extrapolate the acoustic directivity in this paper.

Keywords Frequency extrapolation · Directivity extrapolation · Airframe noise

1 Introduction

Due to the limitation of the acoustic wind tunnel facilities,the high frequency component noise and information at two sides of the polar angle can usually not be acquired in tests. Because of Reynold number effects there are differences between wind tunnel and flight test. In order to correct all information from wind tunnel test to fight data, the spectrum and directivity should be extrapolated.

X. Kangle (✉) · W. Jian
Shanghai Aircraft Design and Research Institute, COMAC, Shanghai, China
e-mail: xklaly1011@126.com

2   Frequency Extrapolation

Figure 1 illustrates a spectrum for 1:7.6 scaled airframe model measured in an open jet acoustic wind tunnel at the landing configuration. The highest frequency transformed from the test data to full scaled data is limited to 5 K Hz. The flight test data for the aircrafts that has similar configurations, such as Boeing 737, DC-10, MD-11 and A320 are provided by reference, which are illustrated in Fig. 1. According to the flight data, the spectrum envelope can be decomposed into the following two segments. The low frequency segment ranges from 400 to 3000 Hz that is normally generated from slap. Mid-high frequency segment ranges from 3000 to 10000 Hz which is mostly induced by flap trailing edge and side edges.
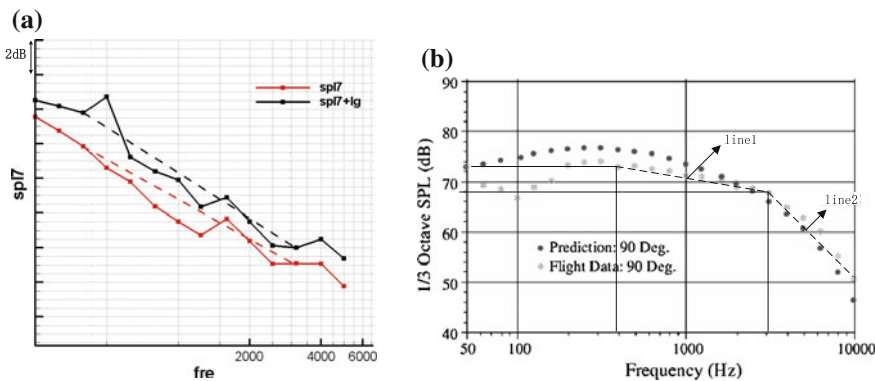
Fig. 1 Spectrum of wind tunnel test or flight data and the straight line envelop of the first segment (overhead position) **a** wind tunnel, **b** Boeing 737 flight test
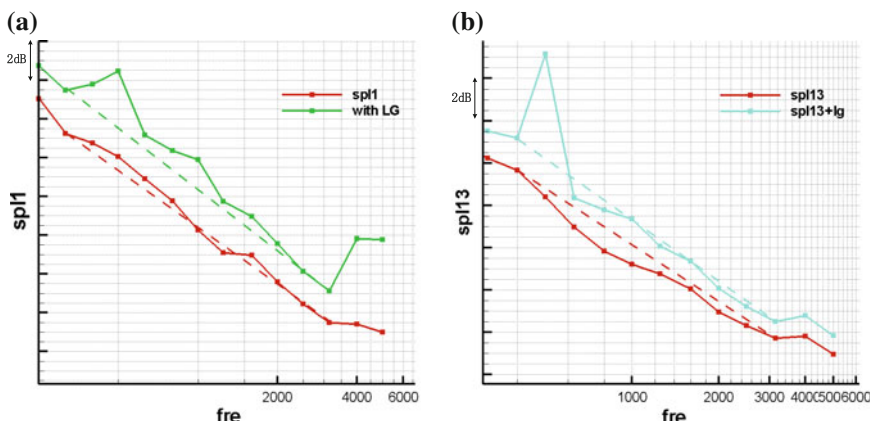
Fig. 2 Spectrum of wind tunnel test WT test and straight line envelop (landing configuration; AOA 9° attack angle; +lg means with landing gear) **a** polar angle 60°, **b** polar angle 120°

Each segment can be enveloped by a straight line. As generally airframe noise feature is broadband noise, any spectrum irregularity can be smoothed by straight line envelop. Figure 2 shows the spectrum envelop at the first segment. The plots demonstrate that the straight line can envelope the spectrum shape quite well both at overhead position and other polar angles. It shows that slopes is important for this linear fitting method. The first and second segment slopes are calculated for B737/DC-10/MD-11/A320. The mean value is taken for the second fitting segment.

3 Extrapolation from Wind Tunnel Data to Flight Data

It has been studied that Reynold number effects induce the difference between wind tunnel test to flight test. In Sect. 2, the entire sound pressure spectrum covering from 400 to 10000 Hz are acquired by linear fitting and are compared with the wind tunnel test data. As A320 is very close to configuration of the airframe model, the flight test data of A320 is used for current plane flight data corrections, which is given by Fig. 3. In order to acquire the slope of flight data at the other emission positions, the second hypothesis is based on an assumption that Reynolds number effects has similarity that is independent to flight position. Therefore, that the ratio of linear fitting slope of flight spectrum to linear fitting slope of wind tunnel data at overhead position is the same as that at other positions. Then the flight data at all the other locations can be formulated as

$$SPL_{\alpha@F}^{\bar{C}} = SPL_{\alpha@F}^{C} + \Delta SPL_{\alpha@F}^{\bar{C}-C} \tag{1}$$

Fig. 3 A-weighted level comparisons between flight and wind tunnel data for A320
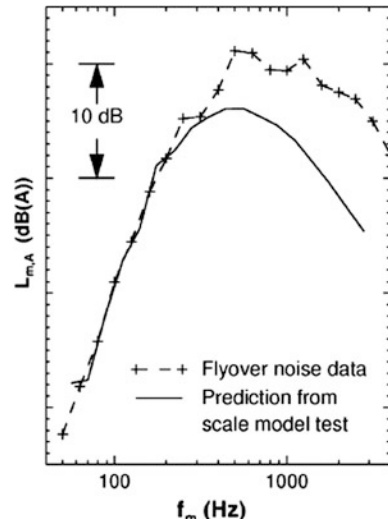
Table 1 Frequency extrapolation results at different locations

Locations	SPL @ 6300Hz		SPL @ 8000Hz		SPL @ 10000Hz	
	With LG	Without LG	With LG	Without LG	With LG	Without LG
MF1	61.56	58.39	59.48	56.32	57.54	54.38
MF7	61.39	60.84	59.31	58.76	57.37	56.83
MF13	57.60	57.05	55.53	54.97	53.59	53.04

Table 1 gives the extrapolation results from wind tunnel to flight data at high frequencies.

4 Directivity Extrapolation

Overall Sound Pressure Level (OASPL) is used to present noise level at each emission position. Figure 4 is acoustic directivity of the model measured in the wind tunnel. The plot shows that the test only can measure directivity in polar angle from 55 to 123°, that can not cover all the emission angles included in the flight test path. In this section, an auto regressive model is developed to explore the data for a wide range directivity. In this model, all the data recorded at each polar angle locations are treated as samples. The auto regressive model is one of the best linear predictions for minimizing fitting variances. $x(n-p), \ldots, x(n-1)$ are the known samples then the next data can be predicted by a linear equation.

$$\hat{x}(n) = - \sum_{k=1}^{p} \alpha_k x(n-k) \qquad (2)$$

Different order AR models are developed, which are 15 order and 10 order. The variances for each model are about 1.4640832E-02 and 9.9888425E-03 respectively. Figure 4 shows the extrapolation results for the OASPL directivity and the prediction results between angles of 55 and 123° can quite match the test data.

Fig. 4 Extrapolation of OASPL directivity with different order AR models
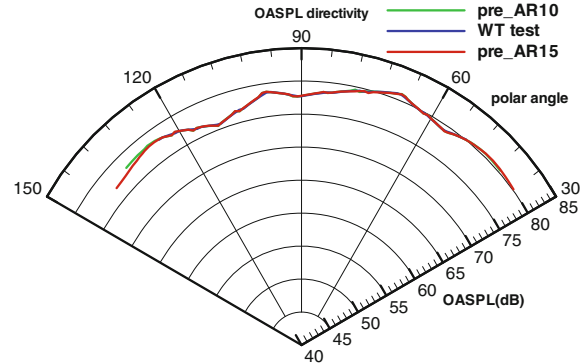
5 Conclusions

In this paper a spectrum and directivity extrapolation method of an acoustic wind tunnel test for a scaled airframe noise is presented. According to the flight data of A320, the whole spectrum is enveloped by two linear segment. The high frequency component can be linearly fitted. In order to acquire the information at two sides polar angle, different AR models are developed and the predictions results by the models can match the test result quit well.

References

Guo YP, Yamamoto K (2003) Component-based empirical model for high-lift system noise prediction. J Aircr 40(5)

Dobrzynski W, Pott-Pollenske M (2001) Slat noise source studies for farfield noise prediction. AIAA p 2158

Test report of an acoustic measurement campaign on the unpowered C919 Model in the DNW-LLF open jet. LLF-2012-32

航空器型号和适航合格审定噪声规定.CCAR-36-R1

Equivalent Acoustic Parameters
in a Periodical Waveguide Structure

C.Y. Jiang, X.L. He and L.X. Huang

Abstract As one of the basic acoustic parameters, the speed of sound is of great importance when considering acoustic effect. This paper explores the equivalent speed of sound, when the structure is modelled as a homogeneous fluid, for a periodic arrangement of a waveguide with alternating channel height similar to a honeycomb structure with open cells. Numerical simulation shows that the equivalent speed of sound is lower than that of pure air and the most important parameter is the height ratio of the waveguide. The lower speed of sound is caused by the increased inertial effect. This inertial effect can be precisely interpreted by the classic concept of tortuosity, which depicts the effect of tortuous fluid path.

1 Introduction

Acoustic interference is the basis for most wave manipulation and control mechanisms. Central to the interference is the phase difference, which can occur either when there is a path difference or speed of sound variation. The latter may be achieved by substituting other gases for air, or changing the temperature, but neither is convenient or easy to apply. One alternative is to use specially designed structures, like a series of resonators (Santillán and Bozhevolnyi 2014), corrugated metawire (Christensen et al. 2008), phononic crystals (Krokhin et al. 2003) and so on. In this paper, a waveguide similar to open-cell honeycomb structure is presented to change the equivalent density and speed of sound, which is simple and easily manufactured. In the following text, the periodic impedance boundary condition

C.Y. Jiang (✉) · X.L. He · L.X. Huang
Lab of Aerodynamics and Acoustics, Zhejiang Institute of Research and Innovation,
Shenzhen Institute of Research and Innovation, Department of Mechanical Engineering,
The University of Hong Kong, Hong Kong, China
e-mail: jiangchangyong1991@connect.hku.hk

(PIBC) is firstly introduced, then the calculation result based on PIBC is compared with direct simulation of a finite structure. Finally, the calculation result is interpreted by the classic concept of tortuosity.

2 Periodic Impedance Boundary Condition (PIBC)

The calculation setting and half of the unit cell is shown in Fig. 1, and a plane wave incidence from the far left inlet is assumed. As the waveguide structure is periodic and symmetric, half of one unit cell of the periodic structure is modeled with the so-called periodic impedance boundary condition (PIBC), instead of modeling a very long geometry approximating an infinite array of periodic structure. The PIBC means that the acoustic impedance (ratio of pressure over volume velocity) on boundary AB is exactly the same as that on boundary CD because of periodicity.

To achieve this PIBC, linearity of acoustic wave equation (or Helmholtz Equation for harmonic problems) is utilized. The general solution of a given problem can be expressed as the linear combination of independent solutions. The half unit cell is illustrated in the upper part of Fig. 1, while the periodic structure is shown in the lower part of the figure. Helmholtz equation, is used for the unit cell,

$$\nabla^2 p + k^2 p = 0. \tag{1}$$

As shown in Fig. 1, the interior thick lines are the hard walls, on which the normal particle velocity vanishes. Boundaries AD and BC are also acoustically hard. Two independent solutions are obtained by using two different sets of boundary conditions on AB and CD. In the first, the pressure of boundary AB is set to be 1, and the pressure of boundary CD is set to be 0, and the entire solution is denoted by S_1. A second solution, S_2, is obtained by swapping the boundary conditions between AB and CD. Note that S represents all solution parameters, such as sound pressure and particle velocity in this problem. The linear combination with any coefficient x,

$$S = S_1 + x \cdot S_2 \tag{2}$$

Fig. 1 The geometry of the calculation domain
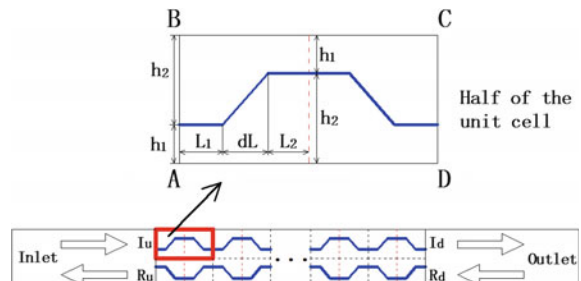
Table 1 The details of the solutions

	Pressure at AB	Pressure at CD	Volume velocity through AB	Volume velocity through CD
S_1	$p_{L1} = 1$	$p_{R1} = 0$	U_{L1}	U_{R1}
S_2	$p_{L2} = 0$	$p_{R2} = 1$	U_{L2}	U_{R2}
S	$p_L = p_{L1} + xp_{L2}$	$p_R = p_{R1} + xp_{R2}$	$U_{L1} + xU_{L2}$	$U_{R1} + xU_{R2}$

satisfies the Helmholtz equation, and the choice of x can be determined by PIBC. The detailed components of each solution are shown in Table 1. In this table, volume velocity, such as U_{L1}, is in fact the integration of axial velocity along the boundary. As required by PIBC, the acoustic impedance Z_a at boundary AB and CD should be exactly the same, which means

$$Z_a = \frac{p}{U} = \frac{p_{L1} + xp_{L2}}{U_{L1} + xU_{L2}} = \frac{p_{R1} + xp_{R2}}{U_{R1} + xU_{R2}}. \tag{3}$$

This is a quadratic equation for coefficient x, and there are two solutions, one for the right-travelling wave and the other for the left-travelling wave. When the frequency of interest is low, the waveguide structure is treated as a uniform channel of height $h_1 + h_2$, without internal wall partitions. In the homogenization point of view, the channel is filled with another fluid, called equivalent fluid whose speed of sound is called equivalent speed of sound. The phase difference between AB and CD, $\Delta\varphi = angle(p_{R3}/p_{L3})$, in solution S is made to be equal to the phase difference of the uniform channel filled with the equivalent fluid. The equivalent speed of sound c_c is thus calculated through this phase difference, that $c_c = \omega D/\Delta\varphi$, where $D = 2(L1 + dL + L2)$, is the total length of the unit cell and ω is the angular frequency. The impedance on the boundaries AB and CD is regarded as the characteristic impedance z_c of the equivalent fluid, is calculated by $z_c = Z_a(h_1 + h_2)$. Hence, the equivalent density ρ_c is calculated by z_c/c_c.

3 Results and Discussion

The interior dimensions of the unit cell are shown in Fig. 1, and the main control parameter is the height ratio h_2/h_1. The detailed result is shown in Fig. 2. When $h_2/h_1 = 1$, the interior wall becomes a straight line, and the honeycomb structure becomes a regular duct. Therefore, the equivalent density and speed of sound are exactly the same as that of pure air. As is shown below, the increase of h_2/h_1 leads to the increase of equivalent density and the decrease of the equivalent speed of sound.

The equivalent parameters calculated by PIBC method is compared with a direct simulation of a finite structure. The latter consists of five unit cells placed in an

Fig. 2 Equivalent density
and speed of sound as a
function of height ratio h_2/h_1
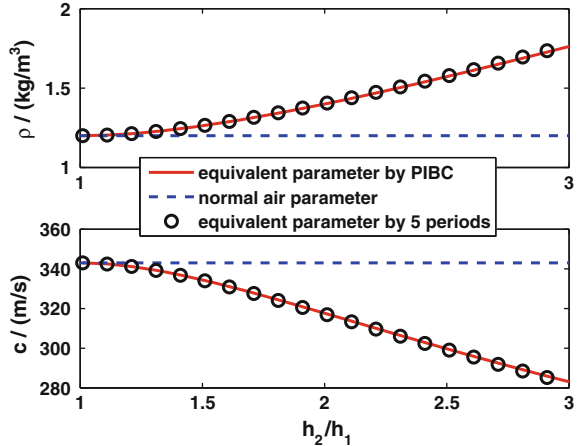
infinite channel of uniform height $2(h_1 + h_2)$, as shown in the lower part of Fig. 1.
A plane incident wave is specified at the far left boundary. The reflected wave to
reach the far left boundary and the transmitted wave at the far right boundary both
satisfy the out-going wave boundary condition. There is no approximation in this
model of the finite structure. The result of this simulation is expected to approach
the periodical solution S in Eq. (2) when the number of unit cells increases from 5
to infinity. A structure of five units is normally sufficient to approximate the true
infinite array of cells for practical purpose. The comparison of results between the
PIBC solution and the five-cell structure is shown in Fig. 2. The proximity of the
two results is in support of the PIBC method.

When the elastic constant $\kappa = \rho_c c_c^2$ is examined as a function of the height ratio,
which is not shown due to page limit, κ is found to be a constant. Therefore, the
decrease of speed of sound and the increase of density are not independent.

The increase of equivalent density, which is also called inertial effect (Johnson
and Sen 1981), can be interpreted by the classic concept of tortuosity α_∞ (Johnson
et al. 1982), which is defined as (Allard and Atalla 2009), $\alpha_\infty = \langle |\vec{v}|^2 \rangle / |\langle \vec{v} \rangle|^2$. Here,
$\langle |\vec{v}|^2 \rangle$ represents the kinetic energy averaged over the volume of the unit cell,
whose square-root is usually described as a micro-scale particle velocity; while $\langle \vec{v} \rangle$
is the average velocity usually called the macro-scale velocity. The ratio α_∞
describes the difference between the micro and macro scales of particle velocity in
the unit cell. Note that $\langle \cdot \rangle$ means taking average over the unit cell while $|\cdot|$ means
the norm of the vector. The agreement between the density ratio (solid line in
Fig. 3) and the classic definition of tortuosity (open circles in Fig. 3) implies that the
equivalent fluid inertial is increased by tortuous particle motion in a specially
designed waveguide.

Fig. 3 Comparison of
density ratio ρ_c/ρ_0 (*solid line*)
and tortuosity α_∞ (*open
circle*)
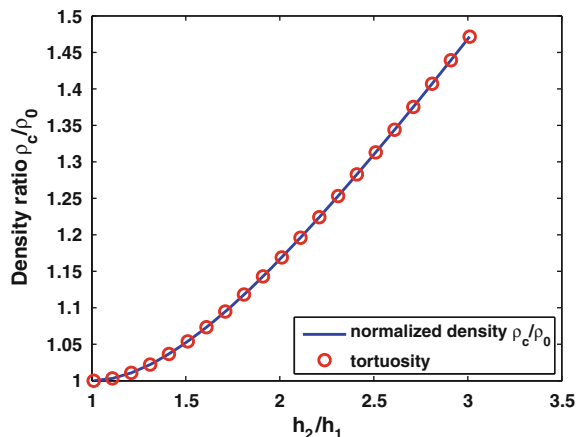
4   Conclusions

In this paper, a new method named as PIBC is proposed, dealing with acoustic
problems with periodic structures. After applying PIBC to the honeycomb-like
waveguide structure, it is found that the equivalent density increases and the speed
of sound decreases. The main control parameter that determines the equivalent
parameters is the ratio of the interior heights ratio (h_2/h_1). In addition, the equivalent
density and speed of sound are not independent. As a simple interpretation, the
decrease of speed of sound is due to the increase of equivalent density, also called
the inertial effect in fluid mechanics (Landau and Lifshitz 1987). This inertial effect
is validated by the classical calculation of tortuosity.

References

Allard J, Atalla N (2009). Propagation of sound in porous media: modelling sound absorbing
    materials, 2nd edn. Wiley, New york
Christensen J, Huidobro PA, Martin-Moreno L, Garcia-Vidal FJ (2008) Confining and slowing
    airborne sound with a corrugated metawire. Appl Phys Lett 93(8):083502
Johnson DL, Plona TJ, Scala C, Pasierb F, Kojima H (1982) Tortuosity and acoustic slow waves.
    Phys Rev Lett 49(25):1840
Johnson DL, Sen PN (1981) Multiple scattering of acoustic waves with application to the index of
    refraction of fourth sound. Phys Rev B 24(5):2486

Krokhin AA, Arriaga J, Gumen LN (2003) Speed of sound in periodic elastic composites. Phys Rev Lett 91(26):264302

Landau LD, Lifshitz EM (1987) Fluid mechanics, vol 6. Course of theoretical physics, pp 26–30

Santillán A, Bozhevolnyi SI (2014) Demonstration of slow sound propagation and acoustic transparency with a series of detuned resonators. Phys Rev B 89(18):184301

Effect of Water Pressure on the Frequency Response of a Thin Rigidly Clamped Plate

Kyle Saltmarsh, David Matthews, Hongmei Sun, Andrew Munyard, Berney Bao and Jie Pan

Abstract A detailed understanding of the vibrational properties of submerged objects such as submarines is essential in order to minimize sound emission and optimise sonar performance. In this work we present some results on the effect of water loading on a simple rigidly clamped plate. Complications arise when hollow structures are submerged in water producing loading on one side. Not only does the water dampen the resonances of the structure but the increase in depth also produces mechanical strain within the structure that also changes the modal frequencies. In this paper some results are presented on the effect of water loading on a simple rigidly clamped plate. The aim of this work is to accurately measure these effects and identify any interesting features that need to be taken into account when modelling.

Keywords Clamped edge thin plate · Modal analysis · Water loading

1 Introduction

The effect of hydrostatic pressure on the modal frequencies of submerged hollow structures is a complex problem and modelling such effects using conventional FEM and BEM is difficult. The accuracy of these models is heavily reliant on user intuition and non systematic methods. Experimental investigation into the sound radiation from a torpedo-shaped structure under axial excitation (Liu et al. 2010) yielded considerable discrepancies between results and predictions. Analysis of

K. Saltmarsh (✉) · H. Sun · B. Bao · J. Pan
School of Mechanical and Chemical Engineering,
University of Western Australia, Perth, Australia
e-mail: Kyle.Saltmarsh@research.uwa.edu.au

D. Matthews · A. Munyard
Defence Science & Technology Organisation, HMAS Stirling,
Perth, Western Australia, Australia

underwater vibration of a torpedo-shaped structure subjected to an axial excitation (Pan and Mathews 2011) showed significant differences between the resonant frequencies and modal shape functions to that of in air. Both theoretical and experimental work in this area is scarce but there are many applications where such effects are very important and need to be understood. One example is submarine design where the hull is subjected to various pressures at different depths. These pressure variations result in changes in the resonant frequencies of the hull that in turn determines many of the design characteristics of the submarine. Despite the complexity of such systems and the lack of experimental data, numerical models are often used to try and predict their performance. This work attempts to address some of these problems by carefully characterising the depth dependent modal frequency response of a simple structure in a small test tank. The results show the significance of this effect and even for changes in depths of as small as 40 cm frequency shifts of up to 50 Hz can be observed in some of the modal frequencies. It clearly highlights the need for incorporating the in plane tension into existing models in order to be able to take these depth effects into account.

2 Experimental Setup

Figure 1 shows a photograph of the equipment used for this work. It consists of a thin (1.6 mm) steel disc of diameter 412 mm and mass 3.125 kg. This is rigidly clamped between two heavy (32 kg each) steel flanges with an outer and inner
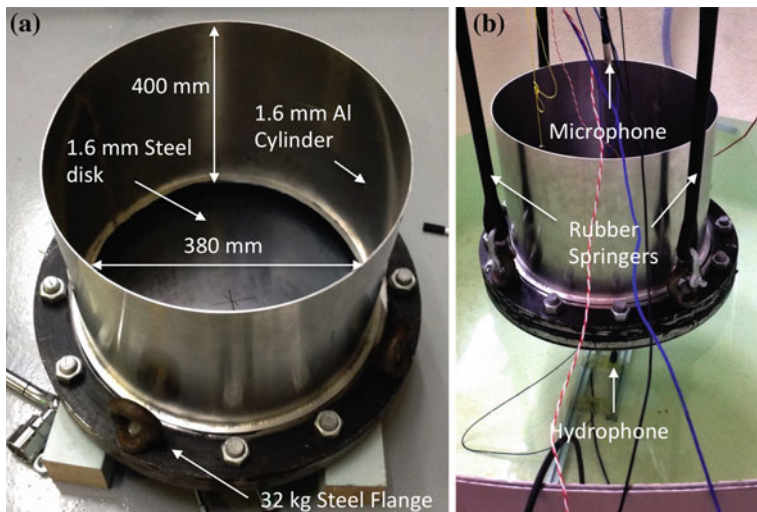
Fig. 1 Photograph of the experimental setup. **a** Dimensions of various parts while **b** entire assembly suspended in a water tank above some water

diameter of 412 and 380 mm respectively. A 400 mm high thin walled (1.6 mm) aluminium cylinder was glued directly onto one of the flanges. This allowed the structure to be submerged in water to a maximum depth of 400 mm while still keeping the upper surface of the disk dry. The entire structure was suspended in a water tank as shown in Fig. 1b. It was initially held above the water to obtain the in air frequency response function. Water was then gradually added to the tank in order to increase the loading on the face of the disc. Measurements were taken every 10 mm.

The depth dependent tension in the plate was measured using nine half bridge strain gauges that were attached to the surface of the plate. Their positions are shown in Fig. 2. Due to sensor failure only sensors #2, 3, 4, 5 and 8 were used for analysis in this paper. Sensors #2–5 measured the radial variation of the tension while sensors #3 and 8 monitored the angular variation.

The frequency response function (FRF) of the disc was measured for the first 1000 Hz using white noise. A B&K 4810 mini-shaker was attached to the disc using a magnetic stud and positioned 145 mm from the centre of the disc as shown in Fig. 2. Mass loading effects were minimized using a pulley system. Data acquisition was done using a B&K Pulse system with a frequency resolution of 1 Hz. A PCB 352C67 test accelerometer was place at a distance of 125 mm from the centre and at an angle of 52° from the horizontal line shown in Fig. 2.

Fig. 2 This shows the positions of the nine strain gauges (#1 to #9) that were attached to the plate to monitor the tension during the experiment. Numbers 2–5 monitored the radial variation and 6–9 the angular
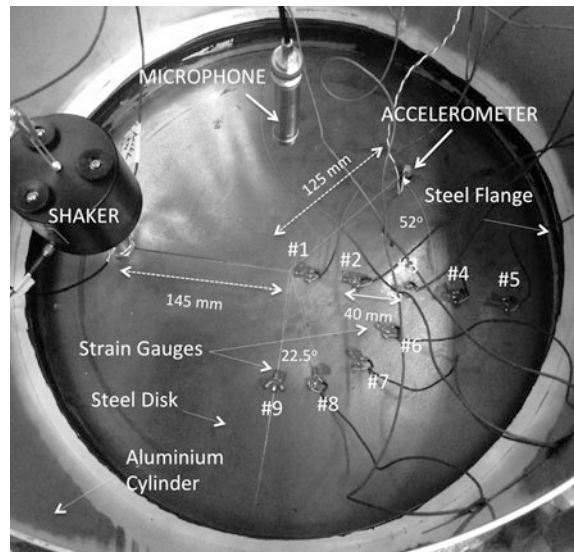
3   Results

Figure 3a, b shows a waterfall plot for the drive point accelerance (DPA) and test point transfer accelerance (TPA) for each depth starting from 0 up to 40 cm in increments of 1 cm. As can be seen there are significant variations with the positions of various modal frequencies over the entire range. In general most modal frequencies increase with increasing depth. This is to be expected since the increase in depth will produce an increase in the pressure on the face of the disc. This in turn will increase the tension in the plate. For example, the fourth mode (#3 in Fig. 3b) showed an increase of 28 % over the 40 cm depth. It should however be noted that some modal frequencies such as numbers 6 and 7 in Fig. 3b decrease with increasing water depth. The mechanism to explain this is unclear. Preliminary calculations have shown that many of these effects can be modeled analytically for a 2D system (Pan 2015) and will be reported elsewhere.

Inspection of the peak heights in both the drive point and test point accelerance show that for the majority the amplitude remains constant with depth. This confirms that once the water makes contact with the surface of the disc it dampens the response after which the tension in the plate has little effect. However, a few peaks (e.g. 4 and 5 in Fig. 3b) are attenuated as the water depth is increased which suggests some other mechanism is also at play.

Another interesting feature observed in the data is modal crossing. This is very evident with the peaks labeled 2 and 3 in Fig. 3b. Similar characteristics are observed with the peaks at 600 Hz.

Previous work on the same disk (Matthews 2014) suggests that these two features are associated with the asymmetric modes. Confirming this is difficult because the water loading produces significant changes in the FRF compared to the in-air results and as a result it is difficult to identify which peak belongs to which mode. Identification of these modes in water is beyond the scope of this work.

Figure 4 shows the measured strain by each of the 5 strain gauges discussed above. As can be seen there is an increase in strain with increasing radius with a maximum in strain gauge #5 at the edge of the disc. The strain maginutudes values obtained for gauges 3 and 8 are comparable, suggesting that there is no significant angular variation in the tension. Close inspection of the data from strain gauge #2 shows that the strain starts negative (i.e. compression) and then changes sign after a few cm. This result is confirmed in the FRF data where some of the modal frequencies reduce slightly at shallow depths before increasing. This has been reported in previous work (Saltmrash 2014) and was associated with the change of curvature of the disk from concave to convex.
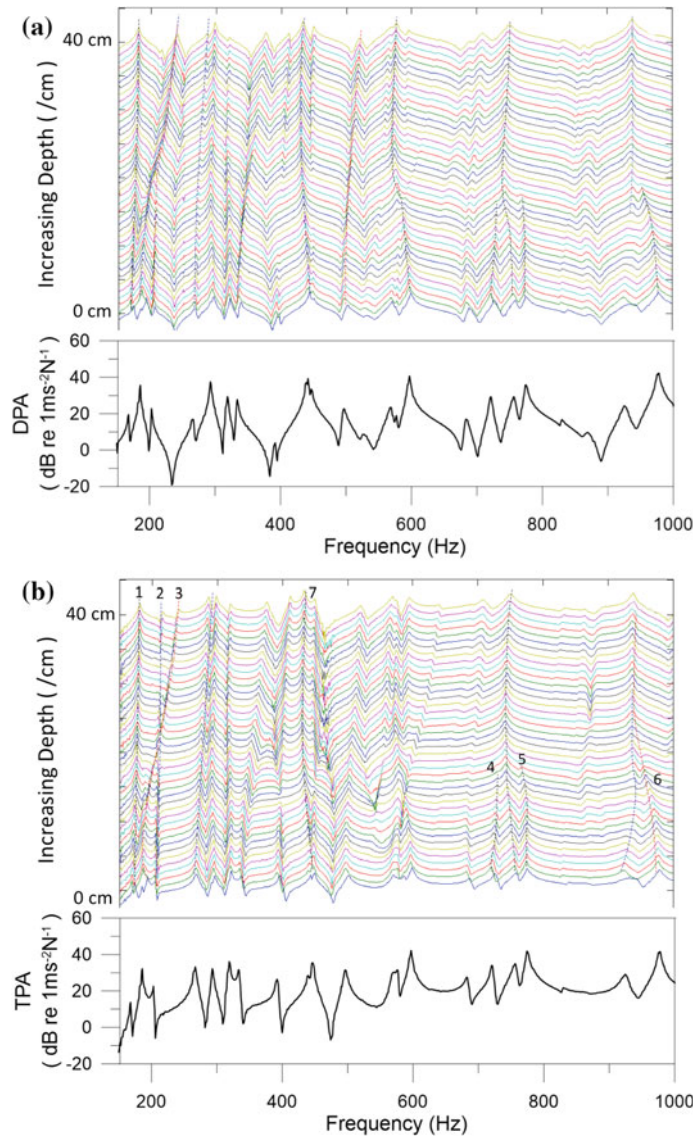
Fig. 3 Depth variation of the drive point (**a**) and test point (**b**) accelerance. The plot shows the frequency response function every 1 cm from 0 to 40 cm. The FRF at 1 cm is shown under each waterfall plot for comparison
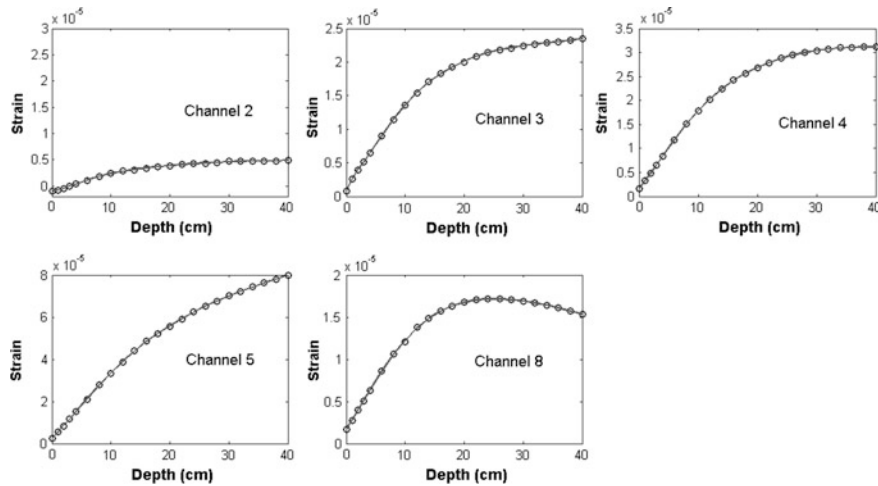
Fig. 4 Strain gauge depth variation for depths 0–40 cm. Maximum tension is observed at the edge of the disk on channel 5

4   Conclusion

It has been shown that increasing the water depth increases the majority of the modal frequencies of a hollow, thin, rigidly clamped disc. Even for the relatively small depths used in this paper (0–40 cm), substantial increases were observed in many of the peaks (27 % maximum increase). These increases have been attributed to the increase in tension in the disc as the depth is gradually changed. This was confirmed by monitoring the radial strain in the disc using strain gauges. It clearly demonstrates the need for these effects to be incorporated into existing models in order to make accurate predictions. Investigation with water on both sides of the plate may allow discernment between mass loading of the water and it's pressure.

References

Liu W et al (2010) Measurement of sound radiation from torpedo-shaped structure subject to an axial excitation
Matthews D et al (2014) A detailed experimental modal analysis of a clamped circular plate. In: Inter-noise 2014, Melbourne, Australia
Pan J (2015) Private communication
Pan J, Matthews D (2011) Analysis of underwater vibration of a torpedo-shaped structure subjected to axial excitation
Saltmarsh K (2014) The effects of sound radiation environment on structural vibration. Honours thesis, School of Mechanical and Civil Engineering, The University of Western Australia

Structural and Acoustic Responses of a Fluid Loaded Shell Due to Propeller Forces

P. Croaker, H. Peters, L. Mulcahy, R. Kinns, P. A. Brandner and N. Kessissoglou

Abstract The low frequency structural and acoustic responses of a fluid loaded shell to propeller induced fluid pressures are investigated. The propeller operates in the non-uniform wake field and produces fluctuating pressures on the blades of the propeller. This in turn generates acoustic waves and a near field that excites the surface of the shell. The resulting incident pressure is scattered and diffracted by the shell surface, and also excites structural vibration. A potential flow panel code is coupled with the Ffowcs-Williams and Hawkings acoustic analogy to predict the fluctuating propeller forces, blade pressures and the resulting incident field on the surface of the fluid loaded shell due to operation of the propeller in a non-uniform inflow. The propeller induced incident pressure field is then combined with a coupled three-dimensional finite element/boundary element model of the submerged shell to predict the vibro-acoustic and scattered field responses.

P. Croaker (✉) · H. Peters · L. Mulcahy · R. Kinns · N. Kessissoglou
School of Mechanical & Manufacturing Engineering, UNSW Australia,
Sydney, Australia
e-mail: p.croaker@unsw.edu.au

H. Peters
e-mail: herwig.peters@unsw.edu.au

R. Kinns
e-mail: rogerkinns@aol.com

N. Kessissoglou
e-mail: n.kessissoglou@unsw.edu.au

L. Mulcahy
Pacific Engineering Systems International, Sydney, Australia
e-mail: lexm@esi.com.au

P.A. Brandner
University of Tasmania (AMC), Launceston, Australia
e-mail: p.brandner@utas.edu.au

95

1   Introduction

Kinns et al. (2007) investigated the fluid path excitation on a submerged shell caused
by a propeller rotating through a non-uniform inflow. The propeller was represented
by axial and radial dipoles located at the propeller hub and the submerged shell was
considered to be rigid. They demonstrated that propeller forces transmitted through
the fluid can be significant for realistic geometries. Merz et al. (2009) considered
the vibro-acoustic response of a submerged shell due to propeller thrust forces using
an axisymmetric, fully coupled finite element (FE)/boundary element (BE) model.
The fluid path excitation was achieved using an acoustic dipole. Peters et al. (2014)
developed a three-dimensional fully coupled FE/BE model of a submerged shell and
investigated the fluid loaded radiation modes of the structure. The hydrodynamic
panel code of Brandner (1998), modified by Mulcahy et al. (2014) for hydroacoustic
applications, is used in the present work to calculate the incident pressure field on
a submerged shell caused by the propeller rotating through a spatially non-uniform
inflow. The vibro-acoustic response of the shell is then predicted using the three-
dimensional FE/BE technique of Peters et al. (2014). Three acoustic dipoles derived
from the propeller forces are also applied to the model for comparison purposes.
Only the sound scattered and radiated by the shell is considered in the present work.
Direct radiation of the propeller noise sources to the far-field is not considered.

2   Numerical Procedure

2.1   Coupled FE/BE Model of the Submerged Shell

The FE method is used to represent the structural shell and the BE method is used to
represent the unbounded fluid domain. The fully coupled three-dimensional FE/BE
model is used to predict the structural and acoustic responses of the fluid-loaded
shell. The structural model consists of a cylindrical shell of 45 m length and 6.5 m
diameter and is closed by flat end plates. A truncated cone of 9.079 m length and a
small base diameter of 0.6 m (18°cone angle) is attached to one end of the cylindrical
shell. Internally, there are two bulkheads spaced 15 m apart and 87 ring stiffeners
spaced 0.5 m apart. A cut view of the model is shown in Fig. 1. The thickness of
the cylindrical shell, conical shell, flat end plates and bulkheads is 40 mm. The ring
stiffeners are 150 mm deep and 80 mm thick. Additional mass is distributed evenly
over the entire structure to achieve neutral buoyancy. This results in an effective
material density of 23,879 kg/m^3, approximately three times the density of steel.
The structural Young's modulus is 210 GPa and the Poisson's ratio is 0.3.
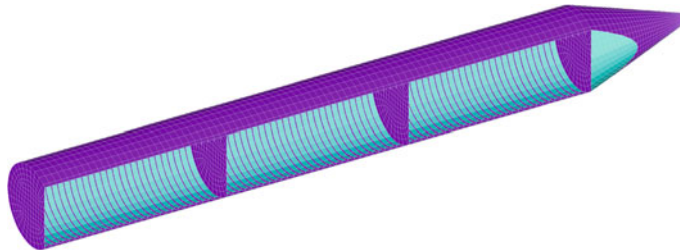
Fig. 1 Cut view of the submerged shell structural model

2.2 Hydrodynamic Panel Code for Propeller Forces and Pressures

The hydrodynamic panel code is a modification of the panel code by Brandner (1998). The flow field around the propeller is assumed to be inviscid, irrotational and incompressible. The coordinate axes translate and rotate with the propeller, so that the solution can be found for a flow problem in which the propeller is at rest in a moving fluid. To demonstrate the proposed technique, a simplified situation has been considered. A five bladed propeller with zero skew and zero rake (propeller 4381 from Boswell (1971)) is used with the non-uniform inflow represented by a four-cycle wake characterised in water tunnel tests by Boswell and Miller (1968). This four-cycle wake inflow field consists of eight sectors with higher than average velocities on four alternate sectors and lower on the others with approximately $+/-$ 25 % maximum variation.

A propeller diameter of 3.5 m, rotation rate of 2.0 revolutions per second and average inflow velocity of 8.9 m/s was used for the present work. This produced an average thrust of 114 kN. The fluctuating propeller forces are used to define the strength of the dipole sound sources located at the propeller hub. Also, propeller blade pressure variations occur as the propeller rotates through the spatially non-uniform inflow. This pressure variation produces acoustic waves and a near-field that excite the surface of the submerged shell. A Hann window is used to enforce periodicity of the propeller forces and FW-H incident pressure time histories created by the panel code. A fast Fourier transform algorithm is used to convert these time histories to frequency spectra, which are applied to the FE/BE model of the shell.

2.3 Incident Pressure Field on the Submerged Shell

The fluctuating blade pressures predicted with the hydrodynamic panel code generate acoustic waves and a near field that excites the surface of the submerged shell. The incident pressure field is calculated at the collocation points of the FE/BE model of the submerged shell. Two approaches are used to predict the incident field:

Fig. 2 Incident pressure on the submerged shell. Pressures in dB (ref. 1×10^{-6} Pa). **a** Idealised dipoles from propeller forces. **b** FW-H acoustic analogy
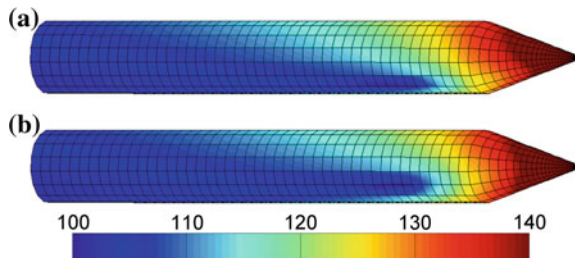
1. Three idealised dipoles at the centre of the propeller hub with the propeller force variations in the x, y and z directions used as the dipole source strengths. This is a similar approach to that used by Kinns et al. (2007) and Merz et al. (2009).
2. The convective Ffowcs Williams-Hawkings (FW-H) equations for moving sources in a uniformly moving medium (Najafi-Yazdi et al. 2011).

Figure 2 shows the pressure incident on the submerged shell at the blade passing frequency due to the combined idealised dipoles (Fig. 2a) and from the FW-H acoustic analogy (Fig. 2b). The incident pressure due to the idealised dipoles closely matches the incident pressure field produced by the FW-H acoustic analogy. The asymmetries in the incident fields arise due to the transverse forces acting on the propeller and rotation of the propeller through the spatially non-uniform wake field.

3 Acoustic Results

The radiated sound power from the submerged shell is presented in Fig. 3 for the idealised dipoles and FW-H incident fields. While the blade passing frequency and its harmonics do not coincide with those of the shell modes, the axisymmetric component of the incident fields predominantly excite the cylinder's breathing modes and the asymmetric component of the incident fields excite the cylinder bending modes. Figure 3 indicates clear tonal peaks at the harmonics of the blade passing frequency. Very similar radiated sound power levels are predicted using both incident field techniques at the blade passing frequency and its first two harmonics. At higher harmonics of the blade passing frequency the sound power level predicted from the idealised dipole incident field is significantly lower than the sound power level predicted from the FW-H incident field. This suggests that at higher frequencies the idealised dipoles are an inadequate representation of the near-field and acoustic pressures produced by a propeller rotating through a non-uniform inflow. Figure 3 shows a significant background level of radiated sound power at all frequencies. This is a numerical artifact resulting from signal processing spectral leakage combining with the radiation modes of the coupled FE/BE model. Peters et al. (2014) have shown that similar submerged shells have over 700 radiation modes up to 140 Hz.
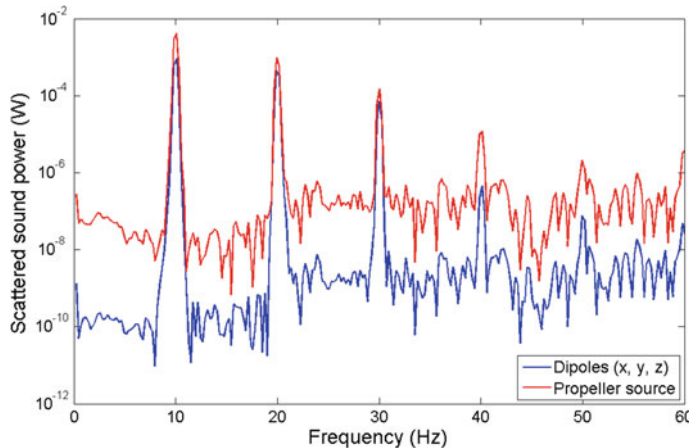
Fig. 3 Comparison of the radiated sound power produced by the dipoles and the FW-H generated incident pressure field

4   Conclusions

The vibro-acoustic response of a submerged shell to propeller fluid loading caused by rotation of the propeller through a non-uniform inflow was presented. A three-dimensional FE/BE model of the submerged shell was combined with the incident pressure field produced by the propeller. The FW-H acoustic analogy and idealised dipoles derived from the fluctuating propeller forces were used to predict the incident pressure on the submerged shell. Although the incident field tends to be underestimated using the simplified dipole model, the radiated sound power predicted with both incident fields are in close agreement at the blade passing frequency and its first two harmonics.

References

Boswell R (1971) Design, cavitation performance and open-water performance of a series of research skewed propellers. Technical Report 3339, DTNSRDC

Boswell R, Miller M (1968) Unsteady propeller loading—measurement, correlation with theory, and parametric study. NSRDC Report 2625

Brandner P (1998) Steady panel method analysis of DTMB 4119 propeller. In: 22nd ITTC propulsion committee propeller RANS/Panel method workshop proceedings, Grenoble, France

Kinns R, Thompson IRM, Kessissoglou NJ, Tso Y (2007) Hull vibratory forces transmitted via the fluid and the shaft from a submarine propeller. Ships Offshore Struct 2:183–189

Merz S, Kinns R, Kessissoglou N (2009) Structural and acoustic responses of a submarine hull due to propeller forces. J Sound Vib 325(1–2):266–286

Mulcahy L, Croaker P, McGuckin DG, Brandner PA, Kessissoglou N (2014) Optimisation applied to composite marine propeller noise. In: Proceedings of the internoise 2014, Melbourne, Australia

Najafi-Yazdi A, Brés GA, Mongeau L (2011) An acoustic analogy formulation for moving sources in uniformly moving media. Proc Roy Soc A 467:144–165

Peters H, Kessissoglou N, Marburg S (2014) Modal decomposition of exterior acoustic-structure interaction problems with model order reduction. J Acoust Soc Am 135:2706–2717

Broadband Noise Control in Ducts via Electro-Mechanical Coupling

Chunqi Wang, Yumin Zhang and Lixi Huang

Abstract Previous studies have shown that a light but stiff plate covering a side-branch rigid cavity may work effectively as a duct noise control device over a wide range of low to medium frequencies. In this study, a passive shunt circuit is introduced to the plate to further enhance the noise reduction performance, which leads to a 'smart plate silencer'. Owing to the electro-mechanical coupling between the electric circuit and the piezo-electro materials, the structural properties of the smart plate vary greatly with frequency. Results show that breakthrough enhancement of the noise control device may be achieved with a proper choice of the shunt circuit.

Keywords Duct noise control · Low frequency noise · Sound reflection · Smart plate silencer · Electro-mechanical coupling

1 Introduction

Duct linings and reactive mufflers are usually used to tackle the noise problem in flow ducts. Lining a duct with porous sound absorbing material is a common technique for duct noise control, but it does not work well at very low frequencies. Reactive mufflers like expansion chambers are usually bulky and the associated back pressure may cause other problems. Recently, the concept of plate silencer was developed by

C. Wang (✉) · Y. Zhang · L. Huang
Lab of Aerodynamics and Acoustics, Zhejiang Institute of Research
and Innovation (HKU), Lin'an, China
e-mail: cqwang@hku.hk; chunqi76@gmail.com

C. Wang · Y. Zhang · L. Huang
Shenzhen Institute of Research and Innovation (HKU), Shenzhen, China

C. Wang · Y. Zhang · L. Huang
Department of Mechanical Engineering, The University of Hong Kong,
Hong Kong, China
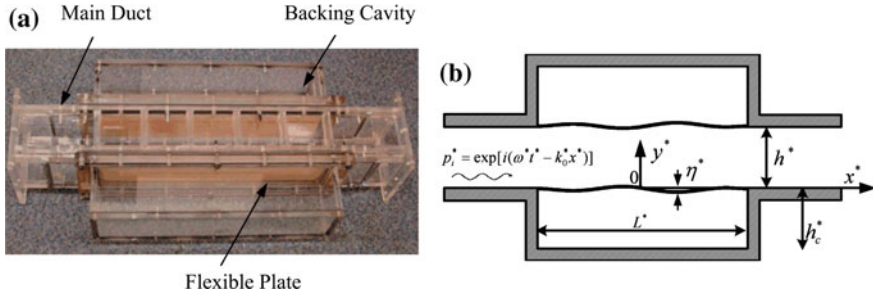
Fig. 1 Configuration of a plate silencer: **a** photo; **b** 2D theoretical model

our group (Huang 2006; Wang et al. 2007, 2008) which works effectively in the low-frequency region with minimum pressure loss. A typical plate silencer consists of an expansion chamber with two side-branch cavities covered by flexible plates, as shown in Fig. 1a. Its effectiveness as broadband low-frequency wave reflector has been demonstrated both theoretically and experimentally. The success of this promising technology is, however, still limited by a number of factors. First, a good plate silencer requires light but stiff plates, however, this requirement cannot be fully met by common materials at this point in technology development. Second, the device exhibits significant noise reduction performance over different frequency regions as the dynamic property varies. It is obvious that both the effective bandwidth and noise reduction levels will be substantially improved if the plate properties are capable of varying with frequency to meet the requirement for optimal silencing at different frequencies. Active control methods may be able to achieve the required frequency-dependent dynamic properties, but a passive approach is preferred for its simplicity and robustness. The purpose of the present study is therefore to investigate the feasibility of achieving frequency-dependent dynamic properties of flexible plate via passive electro-mechanical coupling, which as a result leads to a broadband smart plate silencer.

2 Theory

A two-dimensional (2D) theoretical model of the plate silencer is shown in Fig. 1b. The main duct has a height of h, with two plates (beams) flush-mounted on the duct wall. The leading and trailing edges of the plates can be either simply supported or clamped to the duct. The plates are backed by rigid-walled cavities of depth of h_c. For convenience, all variables are non-dimensionlized by three basic quantities, i.e., air density ρ_0, duct height h and speed of sound c_0 following the scheme in (Wang et al. 2007). Assume a plane incident wave p_i comes from the upstream of the main duct which causes the plate to vibrate, and the structural vibration radiates sound in

both directions. In the plate silencer, the plate vibration is strongly coupled with the sound field, and the vibration motion is governed by

$$m\frac{\partial^2 \eta}{\partial t^2} + B\frac{\partial^4 \eta}{\partial x^4} + (p_i + \Delta p) = 0 \tag{1}$$

where m is the plate-to-air mass ratio, B is the bending stiffness, η is the transverse displacement, Δp is the fluid loading imposed on the upper and lower sides of the plate due to the structural acoustic radiation. Previous studies have shown m and B are the key parameters for the silencer. For given mass ratio m, the transmission loss (TL) spectrum of the plate silencer varies as B increases, referring to Fig. 2. So, the noise reduction bandwidth of the silencer can be substantially extended if B possess some freqeuency-dependent characteristics.

The present study takes advantage of the electro-mechanical coupling property of a specially designed shunted piezoelectric system to change the bending stiffness of a composite plate so that dynamic properties are met in different frequency regions. As shown in Fig. 3, the smart panel consists of a host plate with piezo-electric ceramics (PZT) bonded to both sides. The electro-mechanical coupling property of the composite panel is modeled using a simplified three-layer beam. The thickness of the PZT panel is assumed to be much smaller compared to the panel
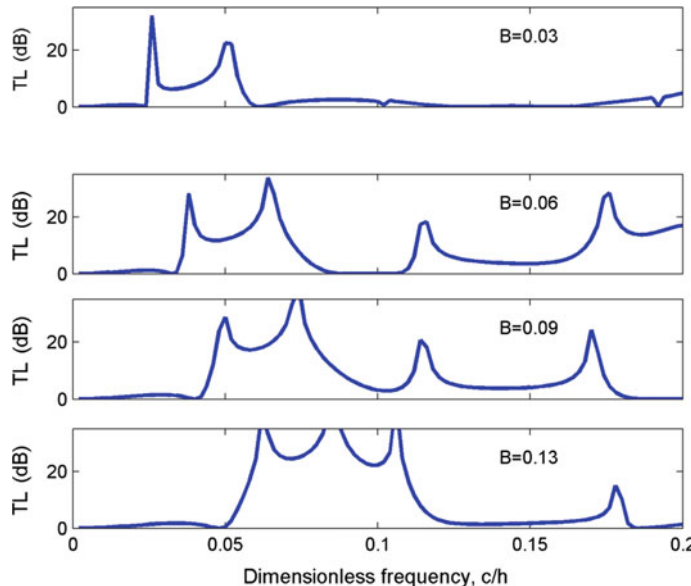
Fig. 2 Variation of the TL spectrum with bending stiffness B ($L = 5$, $h_c = 1$, $m = 1$)
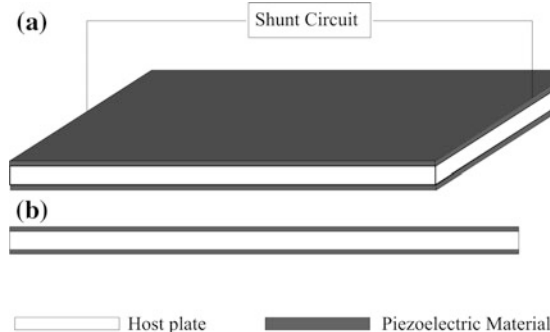
Fig. 3 Schematic of the smart panel with shunted electrical circuit. **a** The host plate and the shunted piezoelectric elements. **b** 2D representation of the composite plate

thickness. The effective bending stiffness per unit width of the three-layer beam is then found as,

$$B = \frac{1}{6} E_p h_p^3 + \frac{1}{2} E_p h_p (h_p + h_h)^2 + \frac{1}{12} E_h h_h^3, \tag{2}$$

where h_p, h_h, E_p and E_h are thickness and elastic modulus of the PZT (subscript 'p') and host plate (subscript 'h') respectively. Since E_p is usually much larger than E_h, B is approximately proportional to E_p. For the PZT, we only consider the x-direction (longitudinal) motion. Therefore, E_p in Eq. (2) refers to elastic modulus in the x-direction. Assume that the piezoelectric material is poled in the x-direction (direction-1), and denote the ratio of the electrical impedances of the piezoelectric element $(i\omega C_s)$-1 and the shunt circuit (Z_{ext}) as $\alpha = 1/(i\omega C_s Z_{\text{ext}})$, where ω is the angular frequency and C_s is the capacitance of the piezoelectric element, the elastic compliance, $S_{11} = 1/E_p$ is found as (Date and Sakai 2000),

$$s_{11} = s_{11}^E \left[1 - k^2 / (1 + \alpha) \right] \tag{3}$$

where s_{11}^E is the elastic compliance under constant electric field; k is the electro-mechanical coupling constant. Note that α is a function of frequency ω except for a pure capacitance shunt circuit, and so are the elastic compliance S_{11} and the bending stiffness of the composite panel defined in Eq. (2).

3 Illustrative Example

We consider a simple RLC circuit shown in Fig. 4a for illustrative purpose. Negative capacitator is used to increase the plate bending stiffness as suggested in (Date and Sakai 2000). The electric impedance of this RLC circuit is
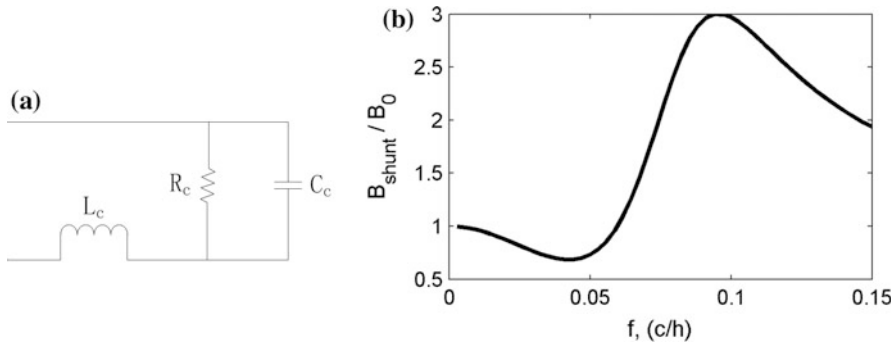
Fig. 4 Design of the shunt circuit. **a** Layout of the electric circuit. **b** Frequency-dependent characteristics of the bending stiffness of the shunted plate

$$Z_{ext} = \frac{R_c / (i\omega C_c)}{R_c + 1/(i\omega C_c)} + i\omega L_c. \tag{4}$$

And the elastic modulus of the piezoelectric material, E_p, can then be calculated based on Eq. (3). Assume that the inherent capacitance of the PZT material is $C_s = 5 \times 10^{-9}$ F. When the parameters of the shunt circuit are chosen as $Rc = 40 \ M\Omega$, $C_c = -4.96 \times 10^{-9}$ F, $L_c = 0.25$ H, the ratio of the bending stiffness with and without the shunt circuit is shown in Fig. 4b. We can observe that the bending stiffness exhibits obvious frequency-dependent characteristics when the shunt circuit is connected.

The noise reduction performance of the smart plate silencer is simulated based on the structural properties of the sandwich construction in (Wang et al. 2008), i.e., $m = 2.75$, $B_0 = 0.061$. Following the non-dimensionlization scheme in (Wang et al. 2007), mass ratio m and bending stiffness B are determined as $m = m^* / \rho_0^* h^*$, $B = B^* / \rho_0^* (c_0^*)^2 (h^*)^3$, with the asterisk representing the corresponding dimensional variables. The bending stiffness of the smart plate is estimated according to Fig. 4b. The details of the simulation procedure can be found in (Wang et al. 2007). Figure 5 compares the predicted TL of the plate silencer with and without the shunt circuit. Owing to the increased bending stiffness, the TL of the plate silencer is greatly enhanced in the frequency range $f \in [0.06, 0.12]$. In the frequency range around $f = 0.04$, however, the TL decreases slightly due to the reduced bending stiffness. This performance degradation in this region can be avoided with a better choice of shunt circuit. A design optimization of the shunt circuit is needed to fulfill this purpose. Moreover, experimental studies will be carried out to verify the theoretical predictions. These tasks are left for future studies.

Fig. 5 Comparison of the predicted TL of the plate silencer with and without the shunt circuit
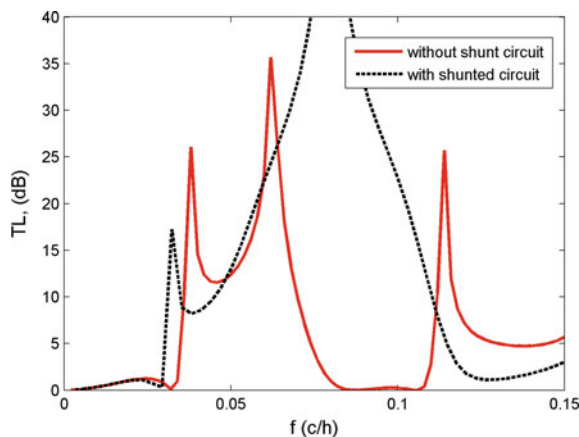
4 Conclusions

A smart plate silencer is proposed to deal with the noise problem in flow ducts. The smart plate consists of a sandwich plate with a specially designed shunted piezoelectric system. The bending stiffness of the smart plate may vary with frequency for certain shunt circuit design. In the illustrative example, the bandwidth of the smart plate silencer is widened by about one octave when the shunt circuit is connected, with the TL being higher than 20 dB at most frequencies.

References

Date MK, Sakai S (2000) Electrically controlled elasticity utilizing piezoelectrtic coupling. J Appl Phys 87:863–868

Huang L (2006) Broadband sound reflection by plates covering side-branch cavities in a duct. J Acoust Soc Am 119:2628–2638

Wang CQ, Han J, Huang L (2007) Optimization of a clamped silencer. J Acoust Soc Am 121:949–960

Wang CQ, Cheng L, Huang L (2008) Realization of a broadband low-frequency plate silencer using sandwich plates. J Sound Vib 318:792–808

Numerical Modelling of Sound Radiation from Marine Pile Driving over Elastic Seabeds

D.R. Wilkes and A. Gavrilov

Abstract This work investigates the underwater sound emission of marine pile driving over elastic seabeds. The finite element method is used to model sound pressure in the near field of an axisymmetric pile and environment model, where the seabed is modelled as both fluid (fluid sand) and elastic (sand, calcarenite) materials. The presented results show that the inclusion of shear in the seabed has a marked effect on the characteristics of the radiated acoustic field in the water column, even for seabed materials which have a low shear speed. In particular, the secondary structural waves reflected from the pile ends in the elastic seabed model emit significantly less acoustic energy compared to the fluid seabed models. Scholte waves also can be observed to propagate along the fluid–solid interface in the elastic seabed models.

Keywords Pile driving · Elastic seabed · Finite element method

1 Introduction

Pile driving in marine environments results in high intensity impulsive underwater noise being radiated from the pile into the surrounding water column and seabed due to the coupled fluid-structure interaction. Typically the numerical formulations employed to investigate the sound radiation mechanisms of marine pile driving approximate the seabed by a fluid medium with a frequency–dependent absorption coefficient (Reinhall and Dahl 2011; Zampolli et al. 2013; Lipper and von Estorff 2014). This approach is justified for materials which have a relatively small shear wave speed (Jensen et al. 2012), such as water–saturated sands and other uncemented seabed materials. The seabed composition in the southern and western Australian

D.R. Wilkes(✉) · A. Gavrilov
Centre for Marine Science and Technology, Curtin University,
GPO Box U1987, Perth, WA 6845, Australia
e-mail: D.Wilkes@curtin.edu.au

continental shelf regions are characterised by a thin layer of unconsolidated sediments, such as sand or silt, over thick layers of more or less cemented sediments, such as calcarenite (Bird 1979). Calcarenite seabeds typically consist of a number of layers which exhibit discontinuously varying acoustoelastic properties between layers and have a much larger shear wave speed (550–1200 m/s; Duncan et al. (2013)) than that in unconsolidated sediments. Thus, for accurate modelling of underwater sound emission by marine pile driving in these environments, the treatment of the seabed as an elastic medium is crucial.

In this work, pile driving over elastic seabeds is modelled to observe the effect of shear waves in the sediment and Scholte waves at the water–seabed interface on the radiated sound. Pile driving over elastic seabeds has previously been modelled via both analytical (Tsouvalas and Metrikine 2014) and numerical (Finite Element Method, FEM) (Milatz et al. 2012; Heitmann 2014) methods, but these papers have mainly focused on the sandy seabeds found in the North Sea.

2   Problem Configuration

The pile driving configuration modelled here is adopted from the COMPILE workshop on predicting noise from offshore pile driving (Lippert and Ruhnau 2014), with pertinent details of the pile dimensions, embedding configuration, material properties and forcing function of the hammer–impact found therein. For the present purpose the fluid seabed for the sand–type seabed specified in the COMPILE documentation is compared with the same type of sediment but with a small shear effect taken into account. Sound radiation from a pile driven over an elastic seabed with the typical material properties of calcarenite is also modelled for comparison. The material properties for all three seabed materials are presented in Table 1.

An axisymmetric FEM model of the near field pile region (i.e. the pile, water column and seabed) was constructed for each of the seabed materials defined in Table 1, using the PAFEC–FE software suite, developed by PACSYS (PACSYS 2014). Numerical results from this software were shown to be in good agreement with those results from the other FEM models tested for a fluid bottom model of the COMPILE benchmark setup. The pile wall is coupled to the fluid in contact with the pile via a fluid–structure interaction, while a full coupling of axial and radial displacements is applied between the pile and contacting seabed material for the

Table 1 Seabed material properties

Material property	Unit	Sand (fluid)	Sand (elastic)	Calcarenite
Density	kg/m^3	2000	2000	1900
Shear speed	m/s	N/A	250	600
Compressional speed	m/s	1800	1800	2100

embedded pile section in the elastic seabed models. In reality the pile–sediment boundary condition is more complex, as the pile will slip relative to the sediment with each hammer impact. This results in a partial decoupling of the axial displacements between the pile and sediment, as well as energy losses due to friction. The full coupling condition employed in this work ignores these effects, to consider only the relative effect of including shear in the sediment on the emitted acoustic field. The effect of material absorption is similarly ignored for this comparison. Finally, the sea surface is modelled as a pressure release boundary and the fluid and solid media limited by the FEM mesh are coupled with the external media via perfectly matched layers.

3   Results and Discussion

Figure 1 presents the FEM time series predicted for the three seabed models at two locations: one mid–depth in the 10 m water column and one on the seabed, both at a range of 1 m from the outer pile wall. The fluid sand model at the mid–depth location (Fig. 1a) shows strong pressure oscillations from the train of downward and upward deformation waves in the pile which emit Mach cones in the water column. The signals emitted over the elastic seabeds more quickly decay due to energy transfer into the shear waves in the sediment. After the initial pulse from the hammer impact the elastic seabed models exhibit a slow periodic oscillation at the seabed location resulting from the Scholte interface wave (Fig. 1b). Another distinguishing feature of the elastic seabed models are the large negative pressure waves excited after the main Mach cone impinges the seabed.
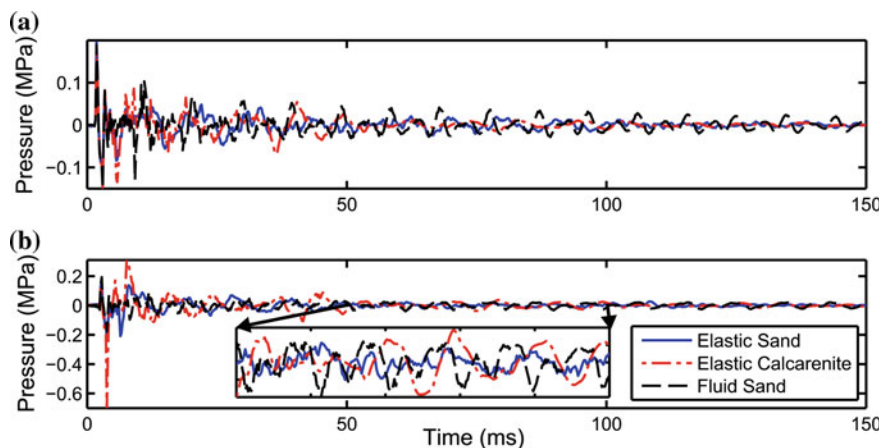
Fig. 1 FEM time series results from the three considered seabed models at two locations: one mid–depth in the water column (**a**) and one on the seabed (**b**) at 1 m range from the pile

Figure 2 shows vertical time slices of the pressure field in the water column for the three seabed models (columns) at times of 4, 8, 12 and 20 ms after the hammer impact (panels (a)–(c), (d)–(f), (g)–(i) and (j)–(l) respectively). The downward propagating Mach cone radiated from the pile is clearly visible for all three models at the 4 ms time step. The large negative pressures observed in the elastic seabed time series (Fig. 1) can be seen to be emanating from the pile–seabed contact point in the 4 ms elastic seabed time slices (Fig. 2b, c). The radial/axial deformation of the pile from the hammer impact displaces the seabed around the ring of the pile–seabed contact (due to the full displacement coupling employed here), which result in the large amplitude spherical wave radiating outward from the contact point. At the later time steps the Scholte waves can be recognised in the two elastic seabed models by
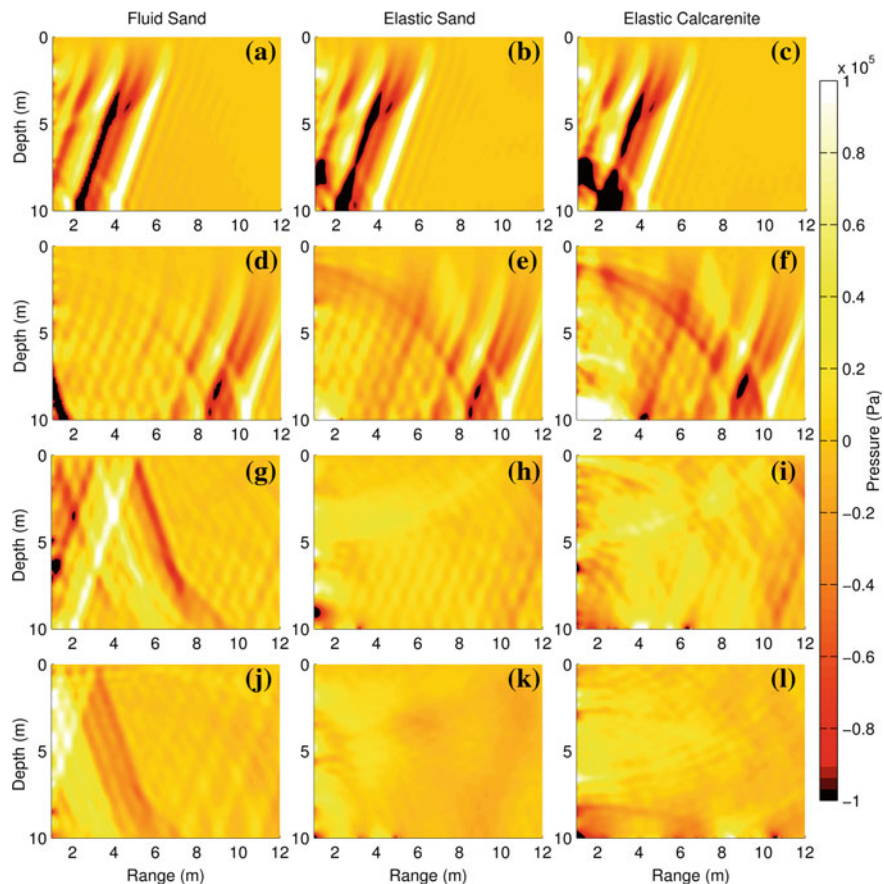
Fig. 2 Pressure fields predicted by FEM for the three seabed models (columns) at times of 4, 8, 12 and 20 ms after the hammer impact (panels (**a**)–(**c**), (**d**)–(**f**), (**g**)–(**i**) and (**j**)–(**l**) respectively)

the pressure waves which slowly propagate along the water–seabed interface. More-over, there are no clearly identifiable Mach cones in the pressure fields for the elastic seabed models at the 12 and 20 ms time steps, whereas the fluid sand model exhibits the downward and upward travelling Mach cone waves.

4 Conclusions

In this work numerical FEM modelling of sound emission from marine pile driving over elastic seabeds has been investigated. The results presented here have shown that the inclusion of shear stiffness in the seabed has a drastic effect on the radiated pressure field in the water column, even for slightly consolidated materials which have a small shear wave speed. In particular, the signals emitted over the elastic seabeds more quickly decayed due to the energy transfer into the shear waves in the seabed, while Scholte waves were observed to propagate along the water–seabed interface. Modelling and analysis of sound emission by pile driving over elastic seabeds with more realistic pile–sediment boundary conditions, such as partial or non-linear coupling conditions, is of future interest. Another objective for the future study is to couple the near–field FEM predictions for elastic seabed models with the under-water sound propagation models to predict the sound pressure in the far–field.

References

Bird ECF (1979) Geomorphology of the sear floor around Australia. In: Prescott JRV (ed) Australia's continental shelf, Nelson, pp 1–21

Duncan AJ, Gavrilov AN, McCauley RD, Parnum IA, Collis JM (2013) Characteristics of sound propagation in shallow water over an elastic seabed with a thin cap-rock layer. J Acoust Soc Am 134(1):207–215

Heitmann K, Lippert T, Ruhnau M, Lippert S (2014) Computational prediction of the underwater sound pressure due to offshore pile driving. In: Proceedings of the 21st international congress on sound and vibration, Beijing, China, 13–17 July 2014

Jensen FB, Kupperman WA, Porter MB, Schmidt H (2012) Computational ocean acoustics. Springer, Heidelberg

Lippert S, Ruhnau M (2014) COMPILE: international benchmark study on the prediction of off-shore pile driving noise. http://bora.mub.tuhh.de/compile/. Accessed 22 Jan 2015

Lippert T, von Estorff O (2014) The significance of parameter uncertainties for the prediction of offshore pile driving noise. J Acoust Soc Am 136(5):2463–2471

Milatz M, Reimann K, Grabe J (2012) Numerical simulations of hydro sound emissions due to offshore pile driving. In: Proceedings of the 7th international conference on offshore site inves-tigation and geotechnics, London, United Kingdom, 12–14 Sept 2012

PAFEC: FEA / BEM solutions (2014) http://www.vibroacoustics.co.uk/. Accessed 23 Jan 2015

Reinhall PG, Dahl PH (2011) Underwater Mach wave radiation from impact pile driving: theory and observation. J Acoust Soc Am 130(3):1209–1216

Tsouvalas A, Metrikine AV (2014) A three-dimensional vibroacoustic model for the prediction of underwater noise from offshore pile driving. J Sound Vib 333:2283–2311

Zampolli M, Nijhof MJJ, de Jong CAF, Ainslie MA, Jansen EHW, Quesson BAJ (2013) Validation of finite element computations for the quantitative prediction of underwater noise from impact pile driving. J Acoust Soc Am 133(1):72–81

An Experimental Study of Bubble Dynamics Induced by the Focused Shock Wave of an Ellipsoidal Mirror

J. Zhang, P. Chen and X.N. Wang

Abstract High speed photography was performed to study the dynamics of a spherical bubble in a cluster around the far focus of an ellipsoidal mirror. Schlieren pictures of bubble evolution history were captured and sound pulses radiated during the primary collapse stage were recorded. The experimental result fundamentally agrees with the numerical calculation based on Gilmore equation, which is a validation of the generation of negative pressure of sound in water proposed by Zhang et al. (2012).

1 Introduction

Hydraulic extracorporeal shock wave lithotripter was invented in 1980s, and it's widely accepted around the world for the treatment of renal stones nowadays (Zhou et al. 2004). During lithotripsy, the electrodes are fixed at the near focus of an ellipsoidal mirror, and the shock wave generated by discharge are focused to the far focus, where the renal stones are located and pulverized. Around the far focus, the peak pressure amplitude of shock wave exceeds the cavitation threshold of water with pre-existing nucleus (Akulichev and Ilchev 2005). As a result, a cluster of bubbles are induced to grow, and bubble generates high speed jets and sound waves when they collapse, which is believed to be important stone pulverizing mechanisms (Averkiou and Cleveland 1999). Therefore, for a better understanding of the physics of shock wave lithotripsy, it's necessary to study the dynamics of cavitation bubbles. In this study, high speed photography was performed to study the dynamics of a spherical bubble around the far focus of an ellipsoidal mirror. Based on Gilmore equation, numerical calculations were performed and compared with the experimental results.

J. Zhang (✉) · P. Chen · X.N. Wang
Key Laboratory of Aerodynamic Noise Control, China Aerodynamics
Research and Development Center, Mianyang 621000, China
e-mail: jzhang@nudt.edu.cn

2 Experiment

Details regarding the experimental arrangement for data acquisition are described below in Fig. 1. The experiment system consists of water tank, ellipsoidal mirror and electrodes, high speed camera, NI-PCB138 pressure sensors and PXI series data acquisition card, oscilloscope, and desk-top computer. The water tank is 3 mm thick and with the dimension of 2 m × 1 m × 1 m. Two circular acrylic glass windows of 0.2 m diameter are installed on the lateral sides of the water tank, which is consistent with the location of the far focus of the ellipsoidal mirror. The half major axis length of the mirror is 0.5 m and the half minor axis length is 0.25 m. The electrodes of the mirror are made of tungsten copper alloy and the discharge gap distance is fixed to be 3 mm in experiment. The discharge voltage is adjustable within the range from 12 to 20 kV.

2.1 High Speed Photography

The dynamics of cavitation bubbles around the far focus of an ellipsoidal mirror was filmed with a FASTCAM SA1.1 digital camera (Photron® Company, Japan). The maximum picture acquiring rate of the camera is 16×10^4 frames/second. The far focal spot of the mirror was backlit with a 100 mW 532 nm laser that generates green light. A rectangular window with 27 mm × 54 mm was selected to capture the growth and collapse of a bubble cluster. To reduce the idle time of the camera, a delay trigger that consists of Transistor-Transistor-Logic (TTL) circuit and an opto-coupler was designed. The trigger signal is provided by the divider resistance (see Fig. 1a) which is made of sealed deionized water. The delay time is determined
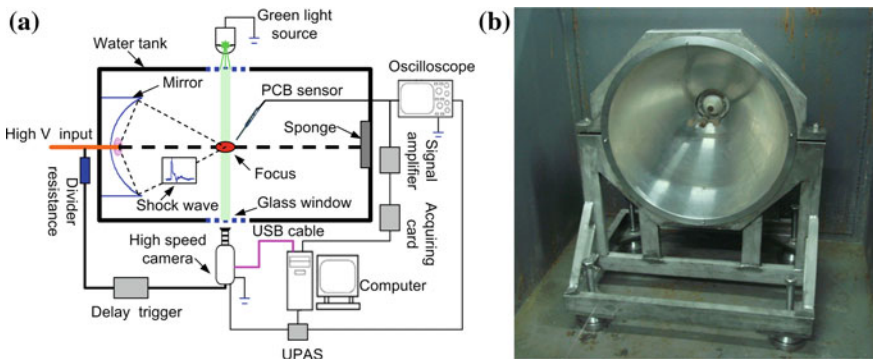
Fig. 1 (Color online) The experimental setup of the current study. **a** The detailed arrangement of the experiment. A shock wave generated by discharge is focused to the far focus of an *ellipsoidal mirror*, where the bubble evolution history is captured and the emitted sound wave is measured; **b** The *ellipsoidal mirror* used to focus shock wave. Its half major axis length is 0.5 m and minor half axis length is 0.25 m

by the distance between the near focus and far focus of the ellipsoidal mirror and the sound speed in water, and it was set to be 0.577 ms.

2.2 Image Processing

A postprocessing code was developed with Matlab® to deal with the measured bubble image. The algorithm includes the following steps: (a) User interactively selects a target bubble for analysis, thereby defining a window with 100×100 pixels. The original photograph was transformed to gray scale image and spatially filtered by Wiener method in order to improve the signal to noise ratio. (b) Utilization of global threshold method to segment bubble images. This step is necessary to reduce the random error caused by the typical frame to frame lighting variation of the multiple-CCD cameras. (c) A "Sobel" operator was applied to the binary image for bubble edge detection. The resulting image contains binary data that outline the bubble edge. However, the actual bubble size needs to be calibrated using a known size object at the same spot. A 10 mm diameter cylinder shape hydrophone (i.e., the PCB pressure sensor) was used to calibrate the bubble image. The final calibrated bubble radius to pixels ratio is 12.4 pixels/mm.

3 Results

A spherical bubble in a cluster near the far focus of the ellipsoidal mirror was pinged, and the expanding and collapse after the passage of the shock wave is shown in Fig. 2. In the following pictures, cavitation bubbles are shown as black dots. The growth and collapse of a spherical bubble can be clearly seen from the
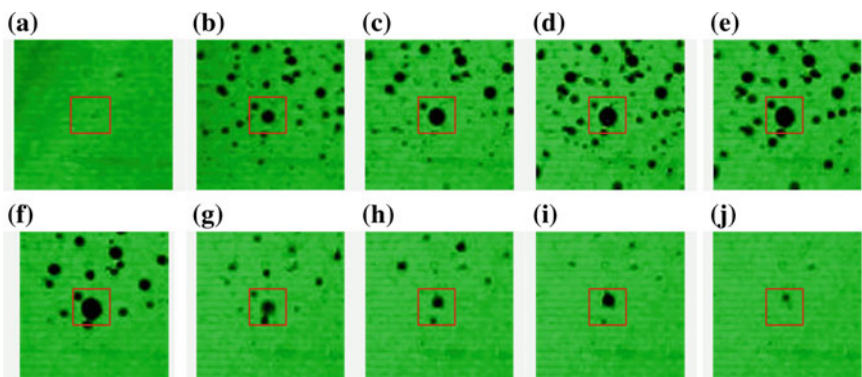
Fig. 2 (Color online) The growth and collapse of a *spherical bubble* in a cluster induced by the focused shock wave of an ellipsoidal mirror. **a** $t = 0$ μs. **b** $t = 13$ μs. **c** $t = 25$ μs. **d** $t = 38$ μs. **e** $t = 50$ μs. **f** $t = 63$ μs. **g** $t = 75$ μs. **h** $t = 82$ μs. **i** $t = 113$ μs. **j** $t = 120$ μs

pictures. The life time of the bubble is several times of that of the duration of the incident shock wave, which implies that the later expanding of the bubble is fueled mostly by the inertia of fluids. A simple estimation with Rayleigh formula tells us that the maximum bubble radius can be as large as 650 μm. As the dynamics of a bubble could basically represents the behavior of the cluster, bubble clusters along the propagation path of shock wave can scatter and absorb the succeeding shock waves. Therefore, to improve the efficiency of shock wave lithotripsy, some method is needed to surpress the growth of bubbles, e.g., adding a succeeding shock wave that consists of only positive pressure (Zhou and Zhong 2006). It should be noticed that between 75 and 82 μs, a larger bubble is influenced by its adjacent smaller bubble, and the released fluid jets drive bubbles move away from each other.

The oscillation of experimental bubble radiuses are compared with numerical calculation with Gilmore equation (Church 1989).

$$R\left(1-\frac{U}{C}\right)\frac{dU}{dt}+\frac{3}{2}\left(1-\frac{U}{3C}\right)U^2=\left(1+\frac{U}{C}\right)H+\frac{1}{C}\left(1-\frac{U}{C}\right)R\frac{dH}{dt} \quad (1)$$

where R is the bubble radius, and $U(=dR/dt)$ is the velocity of the bubble wall, C is the sound speed of water at the bubble wall, and H is the enthalpy difference between the liquid at pressure $P(R)$ and pressure at infinity P_∞. The Gilmore equation was solved using the fifth-order Runge-Kutta method with a step-size control algorithm (Zhu and Zhong 1999).The initial bubble radius is determined by the prediction-correction method (Tanguay and Colonius 2003), here we use $R_0 = 100$ μm, velocity $U_0 = 0$, and the bubble was insonified by an incident shock wave with peak amplitude $P_a = 7.5$ MPa, duration $t_n = 10$ μs.

As can be seen from Fig. 3 that the spherical bubble ($R_0 = 100$ μm) is compressed to shrink ($R < R_0$) when the shock wave pressure is positive or stretched to grow ($R > R_0$) when the shock wave pressure is negative. After the passage of the positive peak of the shock wave, the maximum bubble radius can be several times of its initial
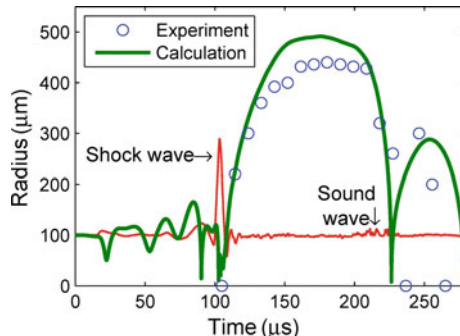
Fig. 3 (Color online) The oscillation of a *spherical bubble* ($R_0 = 100$ μm) after the passage of shock wave with the amplitude $P_a = 7.5$ MPa, the duration $t_n = 10$ μs (*red solid line*); The calculated bubble radius by Gilmore equation (*green solid line*) fundamentally agrees with experimental results (*blue cycles*)

size, which supports the hypothesis proposed by Zhang et al. (2012) that negative pressure is generated in water due to the diffraction of the ellipsoidal mirror. Although the calculated peak bubble radius is a little smaller than that of the experimental result, the latter fundamentally agrees with the former in the primary collapse cycle. It should be aware that Gilmore model doesn't consider attenuation effects of bubble dynamics, such as thermal damping, jet releasing, and non-spherical motion etc., which could be part of the reason of the difference between experiment and calculation. Meanwhile, the shock pulse signal at the far focus of ellipsoidal mirror was recorded using a pressure sensor. It can be seen that about 100 μs after the shock wave, a series of "noise-like" sound wave is generated. According to the delay time between the incident shock wave and the emitted sound wave of bubble, it can be safely concluded that the latter is caused due to the collapse of bubbles in the cluster.

4   Conclusions

During lithotripsy, bubble nucleus along the propagation path of the shock wave focused by an ellipsoidal mirror will be induced to grow. In this study, high speed photography was performed to study the dynamics of a spherical bubble within a bubble cluster. Schlieren pictures of bubble evolution history were captured and sound pulses radiated during the primary collapse cycle were recorded. The experimental oscillation of bubble radius fundamentally agrees with the numerical calculation based on Gilmore equation, which is a validation of the generation of negative pressure in water proposed by Zhang et al. (2012).

References

Akulichev VA, Ilchev IA (2005) Acoustic cavitation thresholds of sea water in different regions of the world ocean. Acoust Phys 51(2):128–138

Averkiou MA, Cleveland RO (1999) Modeling of a shockwave lithotripter with KZK equation. J Acoust Soc Am 106(1):102–112

Church CC (1989) A theoretical study of cavitation generated by an extracorporeal shock wave lithotripter. J Acoust Soc Am 86:215–227

Tanguay M, Colonius T (2003) Progress in modeling and simulation of shock wave lithotripsy. In: Fifth international symposium on cavitation, CAV2003, Osaka, Japan

Zhang J, Zeng XW, Dan C, Zhang ZF (2012) Generation of negative pressure of underwater intensive acoustic pulse and cavitation bubble dynamics. Acta Phys Sin 61(18):184302

Zhou YF, Zhong P (2006) The effect of reflector geometry on the acoustic field and bubble dynamics produced by an electrohydraulic shock wave lithotripter. J Acoust Soc Am 119 (6):3625–3636

Zhou YF, Cocks FH, Preminger GM, Zhong P (2004) Innovations in shock wave lithotripsy technology: updates in experimental studies. J Urol 172:1892–1898

Zhu SL, Zhong P (1999) Shock wave-inertial microbubble interaction: a theoretical study based on the Gilmore formulation for bubble dynamics. J Acoust Soc Am 106:3024–3033

Pre-detachment Acoustic Emission
of a Bubble Emerging from an Orifice

Marcus Fedrizzi and Julio Soria

Abstract The acoustic pulse emitted from a bubble detaching from a submerged orifice begins with a rarefaction before the bubble has detached. By implementing an experimental technique where the acoustic pulse measured from a hydrophone was synchronised with the image acquisition from a high-speed camera the behaviour of the bubble surface can be observed during the initial stage of the acoustic emission. The bubble is found to detach slightly before the local minimum pressure measured in the acoustic signal.

1 Introduction

The formation of an underwater gas bubble is a phenomenon which has long been known to produce an acoustic pulse, commonly heard as the sound of flowing water such as rivers or drop splashes (Minnaert 1933). The frequency of the bubble acoustic emission has been the subject of a number of previous studies (Minnaert 1933; Longuet-Higgins et al. 1991; Plesset and Prosperetti 1977) and is well established but the mechanism that forces the bubbles into acoustic emission is not well understood. Given the acoustic pulse occurs as a bubble pinches off, an understanding of the dynamics of the detachment process is important in understanding the acoustic emission. The bubble detachment involves a bubble forming a neck which rapidly collapses in such a short time that it has been difficult to observe until recent developments in high speed cameras (Thoroddsen et al. 2007). An example of the final neck pinching and detachment of a bubble emerging from an orifice is shown in Fig. 1a.

M. Fedrizzi(✉) · J. Soria
Laboratory for Turbulence Research in Aerospace and Combustion,
Department of Mechanical and Aerospace Engineering, Monash University,
Clayton, VIC, Australia
e-mail: marcus.k.fedrizzi@monash.edu

J. Soria
Department of Aeronautical Engineering, King Abdulaziz University,
Jeddah, Saudi Arabia
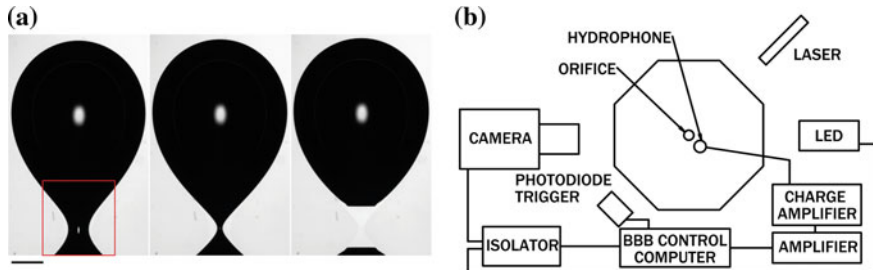
Fig. 1 **a** Image sequence of a bubble detaching from an orifice with 500 μs between images. The *red box* around the neck of the bubble in the first image of (**a**) represents the restricted field of view for the 10 kHz frame rate. The *black horizontal bar* in the bottom left corner of (**a**) represents 1 mm. **b** Experiment schematic including the Beaglebone Black control system

One previous study (Czerski and Deane 2010) has suggested that the acoustic pulse always begins with a rarefaction before the bubble detaches but it does not present any time-resolved data leading to understanding the reason for the acoustic emission. This study presents an experimental technique which can simultaneously obtain time resolved image sequences of the bubble detachment and measure the acoustic emission.

2 Experiment

Experiments were conducted by releasing air from a submerged orifice of 1 mm radius in an octagonal water tank with 130 mm between opposite sides. The orifice exit was 30 mm above the base in the centre of the tank with a sharp edge so that there was a known contact point between the gas and the orifice. Air was injected using a syringe pump to produce bubbles at a very small flow rate of $11.2 \, mm^3 \, s^{-1}$, with one bubble forming every 3.5 s.

Bubbles were imaged using a PCO Dimax camera with a high magnification lens setup to achieve a spatial resolution of 6.6 μm per pixel. A pulsed LED driven at high currents for short pulse times described in (Buchmann et al. 2012) was used as a backlight to illuminate the bubble. In order to image the bubble while it was detaching, a laser and photodiode trigger were used to the start the data acquisition. Images were acquired at 2 kHz for the entire bubble profile shown in Fig. 1a. The field of view was restricted when imaging at a higher frame rate of 10 kHz and this is shown as a red box in Fig. 1a. A Reson TC4013 hydrophone was located approximately 10 mm from the edge of the orifice and as a result there was a 7 μs travel time for sound emitted from the bubble to be detected. The signal out of the hydrophone was passed through a charge amplifier and then further amplified to ensure the output voltage was suitable for the data acquisition system. A schematic of the experiment is shown in Fig. 1b.
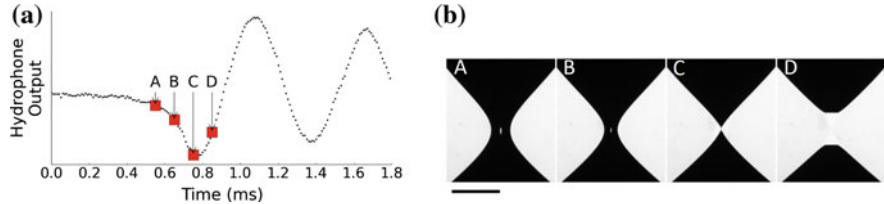
Fig. 2 **a** Acoustic signal acquired by the Hydrophone. **b** Image sequence acquired at 10 kHz showing the neck collapse and bubble detachment in the small field of view shown in Fig. 1a. The *red squares* in (**a**) indicate the acquisition time of the images (A–D) in (**b**)

In order to synchronise the acquisition of the analogue signal from the hydrophone with the imaging a Beaglebone Black (BBB) single-board computer was used. The BBB has two programmable real-time units (PRU), one of which was implemented as a low cost pulse generator as described in (Fedrizzi and Soria 2015) to control the timing of the camera, LED and the analogue data acquisition. The second PRU read from the BBB's inbuilt 12 bit analogue to digital converter (ADC) and passed it to a buffer where it was read and stored by a program running on the main BBB processor. The analogue sample rate was 100 kHz and so the image capture frequency had to be scaled down appropriately, with one image per ten or fifty acoustic samples depending on image magnification. A digital storage oscilloscope was used to verify that the camera exposure and ADC read operation occurred at the same time.

2.1 Results and Discussion

The time-resolved image sequences of the bubble neck region are shown with the hydrophone output in Fig. 2. The hydrophone was uncalibrated and hence, this result is qualitative only. It can be seen from the image sequence that the acoustic pulse begins with a rarefaction during the neck collapse as previous experiments have found (Czerski and Deane 2010). Figure 2 also shows that the instant of detachment occurs approximately 20 µs before the local minimum of the acoustic pulse. In the final image the bubble is detached and the gas surfaces are retreating from each other as the acoustic pulse transitions from a rarefaction to a compression.

The acoustic emission of a surface in a stationary fluid can be described using Lighthill's analogy (Lighthill 1952) which combines the momentum and continuity equations into a wave equation with extra terms, interpreted as acoustic sources. Based on Lighthill's analogy, the density fluctuations, ρ', in a fluid with a sound speed c at a distance r from a source caused by a particular region bounded by a surface S is given by,

$$\rho'(x,t) = \frac{1}{4\pi c^2} \left(\frac{\partial}{\partial t} \int_S \frac{\rho v_j n_j}{r} \, dS - \int_S n_i \frac{\rho v_i v_j + p_{ij}}{r} \, dS \right), \tag{1}$$

where n is the unit surface normal and v_i is the fluid velocity component in the x_i direction (Dowling and Williams 1983). Both terms in Eq. 1 scale linearly with the length scale and by an exponent of the Mach number, M. The first term of Eq. 1 is of order M^2, while the second term is of order M^3. For the small surface velocities of the detaching bubble neck, of order $1\,\mathrm{ms}^{-1}$, $M << 1$ and so $M^3 << M^2$. This suggests that the first term is the dominant term and the second can be neglected. For a compact body, i.e. an acoustically emitting body with wavelength much larger than its characteristic length scale such as a gas bubble, of a uniform density ρ_0, the second term in Eq. 1 can be simplified to yield the following (Dowling and Williams 1983),

$$\rho'(x,t) = \frac{\rho_0}{4\pi c^2} \frac{\partial}{\partial t} \frac{\int_S v_j n_j \, \mathrm{d}S}{r}. \tag{2}$$

The integral in Eq. 2 represents the time rate of change of volume V enclosed by the surface. The density fluctuations in the surrounding fluid are hence proportional to the second time derivative of the instantaneous bubble volume, $\mathrm{d}^2 V/\mathrm{d}t^2$ and this is shown along with the acoustic pulse in Fig. 3. From the image sequences only the reduced field of view was considered in measuring the change in bubble volume, the velocity of the remainder of the surface was small during the neck collapse. The acoustic pulse begins when $\mathrm{d}^2 V/\mathrm{d}t^2 \approx -6 \times 10^{-5}\,\mathrm{m^3\,s^{-2}}$. This result was obtained from a single sequence and the low temporal resolution of the imaging only allowed at most three images during the acoustic rarefaction. Future experiments are planned with a larger temporal resolution to better resolve the bubble detachment behaviour during the initial rarefaction.
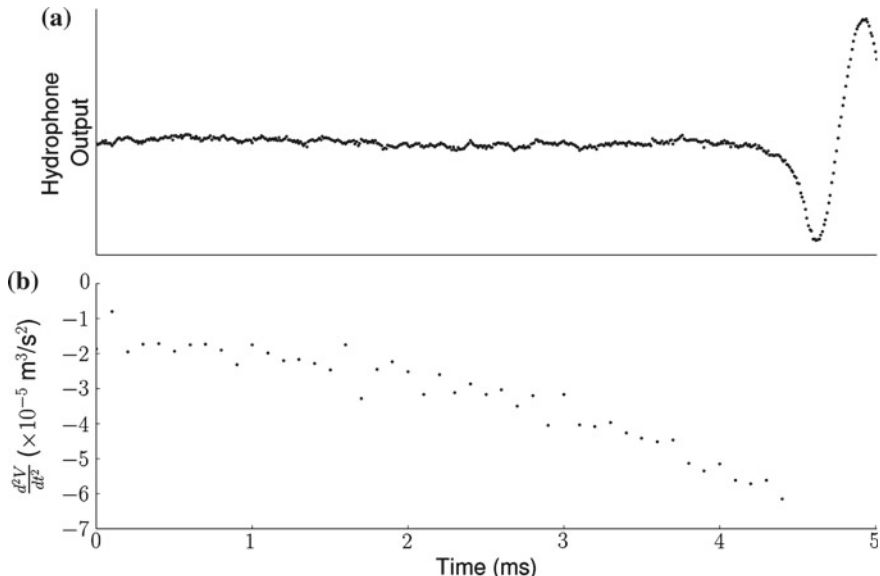
Fig. 3 a Hydrophone output ending with the initial rarefaction and compression of the acoustic pulse and **b** the second time derivative of the neck volume up to the neck pinch off

2.2 Conclusions

A technique to sample analogue acoustic pressure data synchronised with high-speed image acquisition has been implemented to measure the acoustic pulse of a bubble and to investigate the bubble surface behaviour during acoustic emission prior to bubble detachment. It was found that the bubble pinches off approximately $20\,\mu s$ before the local minimum acoustic pressure measured by the hydrophone. The change of volume of the neck region was estimated from the time-resolved image sequences however the temporal resolution only allowed for three instantaneous measurements during the initial rarefaction. The initial rarefaction of the acoustic pulse appeared to begin when $d^2V/dt^2 \approx -6 \times 10^{-5}\ \mathrm{m^3\,s^{-2}}$, however, increased temporal resolution will allow for more confidence in this measurement.

References

Buchmann N, Willert C, Soria J (2012) Pulsed, high-power LED illumination for tomographic particle image velocimetry. Exp Fluids 53:1545–1560

Czerski H, Deane G (2010) Contributions to the acoustic excitation of bubbles released from a nozzle. J Acoust Soc Am 128:2625–2634

Dowling A, Ffowcs Williams J (1983) Sounds and sources of sound. Ellis Horwood Publishers

Fedrizzi M, Soria J (2015) Application of a single-board computer as a low cost pulse generator. Meas Sci Technol 26:095302

Lighthill M (1952) On sound generated aerodynamically I. General theory. Proc R Soc A Math Phys Eng Sci 211:564–587

Longuet-Higgins M, Kerman B, Lunde K (1991) The release of air bubbles from an underwater nozzle. J Fluid Mech 230:365–390

Minnaert M (1933) XVI. On musical air-bubbles and the sounds of running water. Phil Mag 16:235–248

Plesset M, Prosperetti A (1977) Bubble dynamics and cavitation. Ann Rev Fluid Mech 9:145–185

Thoroddsen S, Etoh T, Takehara K (2007) Experiments on bubble pinch-off. Phys Fluids 19:042101

Boundary Effect on Reflected Ultrasound Signals from Adherent Bubbles

N. Godhani, C. Zhang and R. Manasseh

Abstract An experimental apparatus for the analysis of the ultrasonic dynamics of bubbles on a surface is presented, together with preliminary data. Microbubbles offer the potential for targeted imaging and drug delivery utilising ultrasound technology free of ionizing radiation. Despite the development of many theoretical models, few experiments have been reported that differentiate the signals of adherent and non-adherent microbubbles under different boundary conditions. In this study, experiments were designed to capture the fundamental frequency response from freely flowing and adherent bubbles on different boundary conditions. Preliminary data suggested that while bubbles were adhered to an elastic boundary, strong reflections occurred compared to the control; and that while bubbles were adhered to a rigid boundary, weak reflections occurred compared to the control.

1 Introduction

Biomedical applications of bubble acoustics on boundaries include targeted ultrasound contrast agents, for which it is important to distinguish in real time between the ultrasound echoes of bubbles that are freely flowing (unbound) and bubbles that are attached (bound) to target surfaces (Ferrara 2007; Payne 2011). The acoustic scattering from bubbles has been extensively studied theoretically for both unbound and bound bubbles, for bubbles bound to rigid and to elastic surfaces, and for single and multiple numbers of bubble (Illesinghe 2009; Helfield 2014). However, experimental studies are comparatively limited. The experimental apparatus

N. Godhani (✉) · R. Manasseh
Department of Mechanical & Product Design Engineering,
Swinburne University of Technology, Hawthorn, VIC, Australia
e-mail: ngodhani@swin.edu.au

C. Zhang
Department of Telecommunications, Electrical, Robotics and Biomedical Engineering,
Swinburne University of Technology, Hawthorn, VIC, Australia

described in the present paper provides the facility to capture the image and ultrasound echo of bubbles simultaneously in unbound conditions as well as on different boundaries.

2 Experimental Setup

The measurement of ultrasound reflections from bubbles in the unbound condition and in bound conditions when bound to different materials were obtained from the experimental set-up shown in Fig. 1. A single-filament copper wire tip, oriented vertically, was placed at equidistance from the vertical side walls and 20 mm from the base wall of an acrylic box (80 mm × 40 mm × 80 mm) and was connected to a DC voltage supply to generate submicron-sized electrolytic bubbles. The acrylic box was filled with 0.8 g/300 ml NaCl (31434, Sigma-Aldrich Co., LLC, Australia) made up with distilled water. An acrylic frame held an ultrasound transducer and eight LEDs, which were mounted on the periphery of the ultrasound transducer to provide a light source.

The ultrasound transducers were 1 and 2.25 MHz (V314 & V305, Panametrics, Olympus NDT, USA) single-element transducers. The ultrasound transducers were driven by an ultrasound pulser-receiver unit (5077PR, Panametrics, Olympus NDT, USA). The ultrasound pulser-receiver unit and LED light source were triggered by a Mega 2560 microcontroller (Arduino, Italy). Images of bubbles were captured with a long-focus microscope (Nikon SMZ1000, Nikon, Tokyo, Japan) and a digital camera (Canon Kiss X4, Canon Inc., Japan) and processed in ImageJ. Ultrasound echoes in the form of RF data from the ultrasound pulser-receiver unit were captured on an

Fig. 1 Experimental set-up to obtain ultrasound reflection and bubble distribution
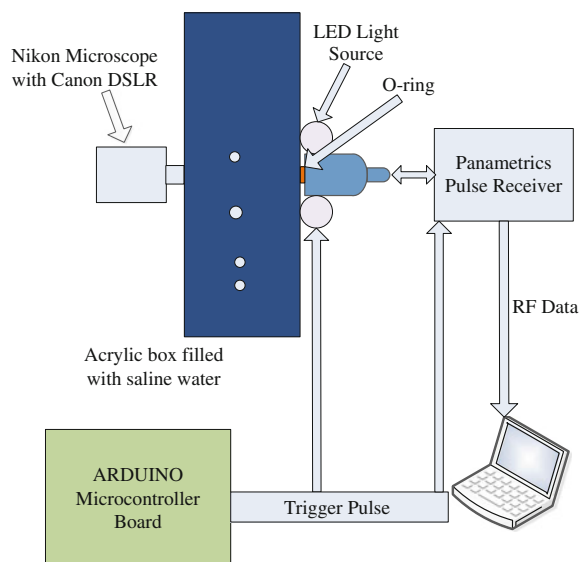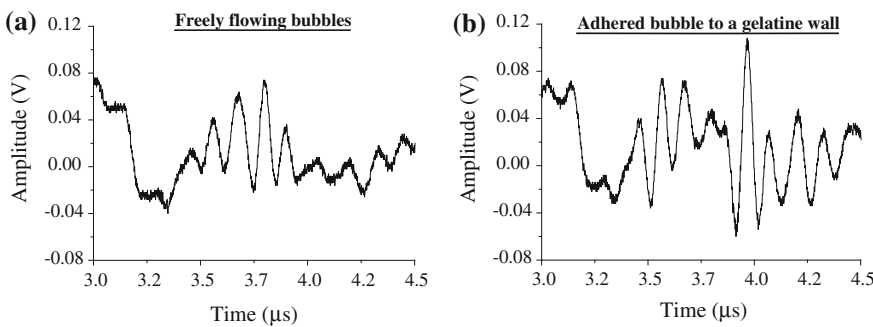
Fig. 2 Ultrasound reflection from bubble under **a** unbound and **b** bound to a gelatine wall conditions detected with 1 MHz transducer

oscilloscope and recorded on a USB flash drive for further processing in MATLAB (The Math Works, Natick, Mass., USA). Statistics were assembled from repeat runs.

While the bubbles were generated electrolitically, they rose owing to buoyancy and thus in an unbound condition. The ultrasound echoes (an example is given in Fig. 2a) with the corresponding images of bubble distributions were recorded simultaneously via the microcontroller which triggered the Panametrics unit and LEDs. For the bound-condition experiments, an acrylic frame that held either gelatine (G250, Sigma-Aldrich Co., LLC, Australia, at 8 g/100 ml distilled water), plastic (transparency film) or glass (a cover slip) was brought near to the electrolitic bubble formation point to facilitate the attachment of the bubbles to the surface. The images of the bubble distribution in the bound condition with gelatin, plastic and glass surfaces are given respectively in Fig. 3a, b, c. The ultrasound echoes (an example is given in Fig. 2b and bubble distribution were recorded as in the unbound condition.
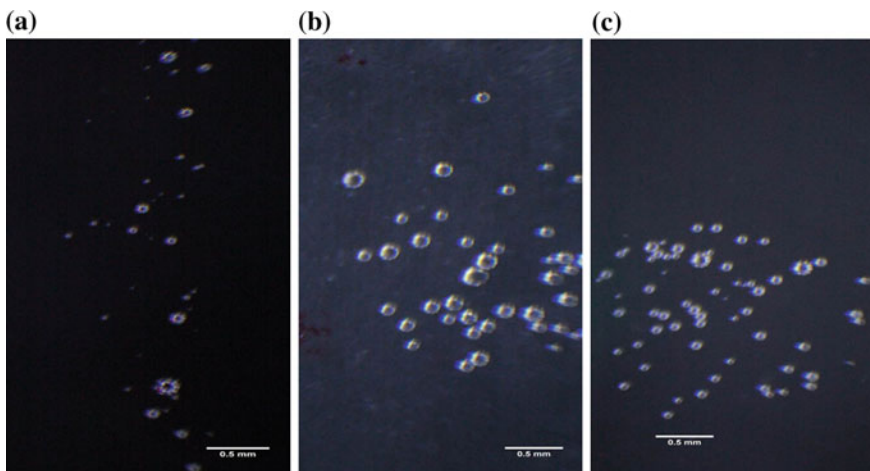
Fig. 3 Images of bubble distribution in the case of bound condition with **a** gelatin, **b** plastic and **c** glass boundary (scale bar represents 0.5 mm)

3   Preliminary Results

Preliminary results (Fig. 4) suggest that the fundamental frequency response from bubbles adhered to an elastic gelatine boundary were greater than those of unbounded bubbles. Moreover, the fundamental frequency response from the bubbles adhered to a plastic boundary was greater than the respective control. However, in the case of bubbles adhered to a glass surface, the fundamental response was lower with respect to its control (Fig. 4). Experiments are required to measure the elasticity of gelatine, plastic and glass boundaries to determine the effect of an elastic boundary on the acoustic scattering from a bubble. More statistically-analysed data are required to further delineate significant differences between bubble reflections in unbound and bound conditions, as well as elastic and rigid boundary conditions (Fig. 5).
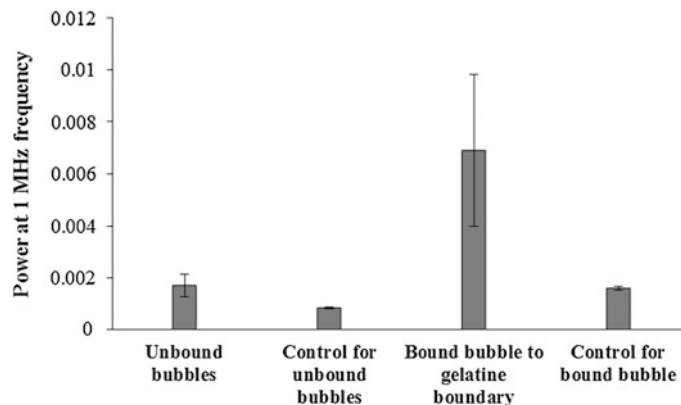
Fig. 4 The fundamental frequency response from bubbles in bound and unbound conditions with their respective controls (error bars are 95 % confidence intervals based on repeated runs)
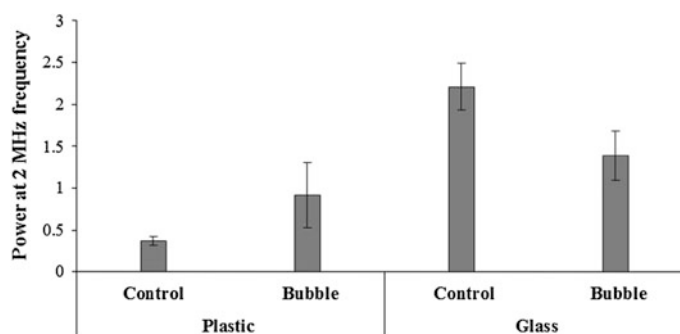
Fig. 5 The fundamental frequency response from bubbles in bound condition with plastic and glass boundary with their respective controls (error bars are 95 % confidence intervals based on repeated runs)

References

Ferrara K, Pollard R, Borden M (2007) Ultrasound microbubble contrast agents: fundamentals and application to gene and drug delivery. Annu Rev Biomed Eng 9:415–447

Helfield BL, Leung BYC, Goertz DE (2014) The effect of boundary proximity on the response of individual ultrasound contrast agent microbubbles. Phys Med Biol 59:1721

Illesinghe S, Ooi A, Manasseh R (2009) Eigenmodal resonances of polydisperse bubble systems on a rigid boundary. J Acoust Soc Am 126:2929–2938

Payne E, Ooi A, Manasseh R (2011) Insonation frequency selection may assist detection and therapeutic delivery of targeted ultrasound contrast agents. Ther Deliv 2:213–222

Part II
Turbulence and Unsteady Fluid Dynamics

New Perspective of Turbulent Skin Friction Reduction by Compliant Coating

Inwon Lee, Andrey V. Boiko and Victor M. Kulik

Abstract Drag reduction capabilities of compliant coatings has long been of a verification issue in experimental fluid mechanics. In this paper, an optimal flow velocity range leading to maximum interaction between coatings and the flow is predicted based on viscoelastic material properties coating. The prediction is performed using a semi-empirical model, which exhibit quite promising results in preliminary tests. Results on turbulent boundary layer in a wind tunnel and a water tunnel and comparison of the experimentally estimated skin friction modifications with the predictions are given.

1 Introduction

Drag reduction capabilities of compliant coatings has long been of a verification issue in experimental fluid mechanics. The remarkable drag reduction claime by Kramer (1957) has not been actually reproduced by other researchers. A review of these trials is given in Gad-el-Hak (1996), who mostly dealt with "soft" coatings (either a sponge or a gel-like substance). In those experiments drag was found to increase with the appearance of λ-shaped surface folds travelling with a velocity much smaller than flow velocity. However, laminar-turbulent transition delay predicted by Carpenter (1990) was confirmed in experiments with the soft compliant coatings.

For turbulent drag reduction which is of more practical importance, a "stiff" compliant coating with relatively large modulus of elasticity (E > 1 MPa) is

I. Lee (✉)
GCRC-SOP, Pusan National University, Busan, Korea
e-mail: inwon@pusan.ac.kr

A.V. Boiko
ITAM, Russian Academy of Sciences, Novosibirsk, Russia

V.M. Kulik
Russian Academy of Sciences, Institute of Thermophysics, Novosibirsk, Russia

133

promising. Kulik et al. (1991) reported the drag reduction about 20 % in a towed model test at velocities 10–20 m/s in a natural basin. An attempt to reproduce these results under well-controlled laboratory conditions was carried out in a cavitation tunnel of Newcastle University (Choi et al. 1997). A drag reduction of about 7 % were measured. The experiments were performed in a different velocity range (1–5 m/s) a long time after the coating manufacture. The aging effect of coating was attributed to be the source of degradation of drag reduction effect (Bandyopadhyay et al. 2005).

The present study is aimed at predicting flow velocity range where an intensive interaction of the coating with the flow is expected. This is based on the measured viscoelastic properties of compliant coating. Experimental drag reduction results taken from turbulent boundary layer flows are then compared with the prediction.

2   Response of Compliant Coating to Turbulent Pressure Fluctuations

The response of the compliant coating to turbulent pressure fluctuations was investigated by Kulik et al. (2005). The stiffness of compliant coating gives rise to deformation amplitude which is less than the thickness of the laminar sublayer (Kulik et al. 2005), thus maintain the coating surface to be hydraulically smooth.

According to the Semenov's interference theory (Semenov 1996), the surface oscillation changes the production of the Reynolds stresses in the near-wall region of the boundary layer

$$\tau = \rho \langle (u_{flow} + u'_{coat})(v_{flow} + v'_{coat}) \rangle \tag{1}$$

where u_{flow}, v_{flow} are undisturbed velocity fluctuations of the flow in the streamwise and transverse directions, respectively; u'_{coat}, v'_{coat} are the disturbance velocities introduced by the compliant coating. The value and the sign of the changes in the Reynolds stresses depend both on the amplitude of the velocity disturbances and the phase shift between them. In order to produce the drag reduction, Semenov (1996) proposed the selection condition for the resonant frequency f_0 of the coating, based on the model of viscous sublayer of Sternberg (1962)

$$6.3 \times 10^{-3} \leq f_0 \nu / u_\tau^2 \leq 1.9 \times 10^{-2}. \tag{2}$$

The interaction intensity becomes the greatest when the frequency of external excitation is equal to the resonant frequency of the coating. In the case of a convecting pressure wave an additional condition of the interaction optimality consisted in equality of the convective velocity of pressure pulsation transport and the propagation speed of disturbances in the compliant coating (Kulik et al. 2005)

$$V = U_C = 0.7 \sim 0.9U. \tag{3}$$

According to the two-dimensional deformation model for viscoelastic coating (Kulik et al. 2008), the resonance frequency is calculated as follows;

$$f_0 = (0.357 + 0.312\sigma)C_t/H \tag{4}$$

where $C_t = \sqrt{E/2\rho(1+\sigma)}$ is the propagation speed of the shear deformations.

Hence, the essential conditions to obtain the drag reduction are the conditions of the maximum interaction of the coating with the flow, namely

- temporal condition: Eq. (2)
- spatial condition: Eq. (3).

These are the necessary conditions, rather than sufficient ones for the drag reduction. In a series of measurements by Amphilokhiev et al. (2000), a significant influence of coating on flow turbulence as well as the drag reduction was indicated.

3 Skin Frictional Reduction Effect in Water Flow

3.1 Viscoelastic Properties of Coating

The experiments were conducted in a water tunnel of Pusan National University. Test section of the facility is 2 m long and has three identical repleaceable windows with area 600×200 mm^2. The bottom of the downstream window was replaced with an insert which had a rectangular opening of 100×50 mm^2 area, where a flating plate is to be placed ionside. The rectangular floating plate is mounted on top of a strain-guage balance to measure the frictional force exerted on the floating plate. Silicone rubbers polymerized with the help of a catalyst at room temperature and pressure were used to manufacture coatings with various thicknesses. The viscoelastic properties of these materials were carefully measured by the method described in detail in Kulik et al. (2009) and Boiko et al. (2010). Then, the dynamic compliance was computed. The computation is based on results of Kulik (2011), where the normal and longitudinal components of deformation of the surface coating affected by a pressure wave were considered.

In the flow velocity ranges considered in this study and the measured frequency ranges for viscoelastic properties, there is found a maximum of the dynamic compliance C_n, which moves towards lower frequencies with increasing thickness of the coating. For example, when $H = 4$ mm, the frequency corresponding to the maximum of C_n is $f_m = 1250$ Hz; when $H = 6$ mm frequency $f_m = 1100$ Hz; when $H = 8$ mm $f_m = 800$ Hz (See Fig. 1; when $H = 12$ mm, $f_m = 550$ Hz. The flow
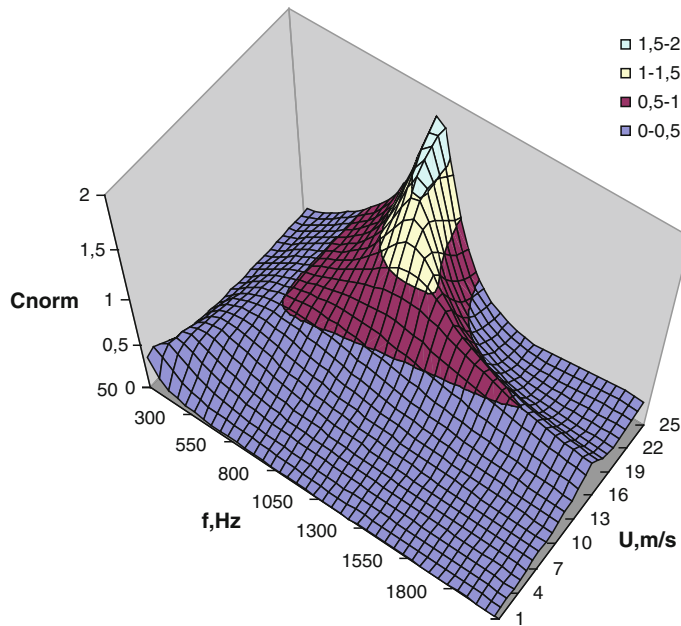
Fig. 1 Magnitude of dynamic compliance of the RTV-3133 coating (H = 8 mm)

velocity corresponding to the edge of the compliance peak depends on the viscoelastic material properties and is independent of the thickness of the coating. For instance, the flow velocity at which $C_n > 1$, is equal to 16–17 m/s and $C_n > 2$ is equal to 20–24 m/c. At $U = 16$–17 m/s, the normal compliance has a crest elongated in the direction of high frequencies.

3.2 Skin Friction Reduction Effect

The primary results of drag measurements of a rigid insert and a series of the compliant coatings of different thicknesses produced of RTV-3133 material are shown in Fig. 2. The 4 and 12 mm thick coatings have an increased drag compared to the rigid wall. The 6 and 10 mm thick coatings show the drag reduction of quite similar value, while maximum effect is reached at 8 mm thickness. The changes of the drag with respect to velocity are monotonous without a dedicated maximum as it might be expected from the computation. The location of the crest of the compliance maximum at high frequencies near $U = 16$–17 m/s which are the maximum possible speeds of the tunnel can be a reason for its absence.
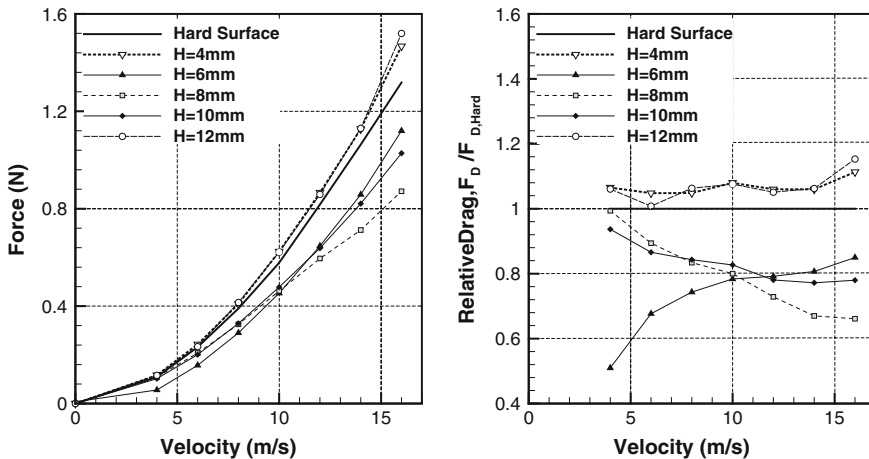
Fig. 2 Measured drag force and drag reduction effect with respect to flow velocity for coatings from material RTV 3133

4 Conclusions

In a measurement campaign carried out in a high-speed water tunnel, the effectiveness of the present estimation of skin frictional reduction efficiency has been again corroborated. Measured skin friction becomes minimum for the thickness which is expected to give the maximum compliance, i.e., the maximum coating deformation under given turbulent pressure fluctuations. The viscoelastic property of the coating material in the prior measurement in wind tunnel has been investigated to give its long-term temporal variations for several years.

References

Amphilokhiev VB, Artyushkov LS, Barbanel BA, Korotkin AI, Mazaev KM, Maltsev LI and Semenov BN (2000) Modern state of the theory of boundary layer control. SUE SPMDB "Malachite", Saint-Petersburg

Bandyopadhyay PR, Henoch C, Hrubes JD, Semenov DN, Amirov AI, Kulik VM, Malyuga AG, Choi K-S, Escudier MP (2005) Experiments on the effects of ageing on compliant coating drag reduction. Phys Fluids 17(085104):1–9

Boiko AV, Kulik VM, Seoudi B, Chun HH, Lee I (2010) Measurement method of complex viscoelastic material properties. Int J Solids Struct 47:374–382

Carpenter PW (1990) Statusof transition delay using compliant walls. In: Bushnell DM, Heffner JN (eds) Viscous drag reduction in boundary layers. Prog Astronaut Aeronaut 123:79–113

Choi K-S, Yang X, Clayton BR, Glover EJ, Atlar M, Semenov BN, Kulik VM (1997) Turbulent drag reduction using compliant surfaces. Proc Roy Soc Lond A 453:2229–2240

Gad-el-Hak M (1996) Compliant coatings: a decade of progress. Appl Mech Rev 49:S147–S157

Kramer MO (1957) Boundary layer stabilization by distributed damping. J Aerosp Sci 24:459

Kulik VM (2011) Peculiarities of deformation of compliant coatings with increased strength. Thermophys Aeromech 18:547–560

Kulik VM, Poguda IS, Semenov BN (1991) Experimental investigation of one-layer viscoelastic coating action on turbulent friction and wall pressure fluctuations. In: Choi KS (ed) Recent Developments in Turbulence Management, Kluwer, pp 263–289

Kulik VM, Rodyakin SV, Suh S-B, Lee I, Chun HH (2005) The response of compliant coating to non-stationary disturbances. Phys Fluids 17(088104):1–4

Kulik VM, Lee I, Chun HH (2008) Wave properties of coating for skin friction reduction. Phys Fluids 20(075109):1–10

Kulik VM, Semenov BN, Boiko AV, Seoudi B, Chun HH, Lee I (2009) Measurement of dynamic properties of viscoelastic materials. Exp Mech 49:417–425

Semenov BN (1996) Analysis of four types of viscoelastic coating for turbulent drag reduction. Emerging Techniques in Drag Reduction, MEP, Edmunds, London, pp 187–206

Sternberg J (1962) A theory for viscous sublayer of a turbulent flow. J Fluid Mech 13:241–271

Skin Friction Drag Reduction Based on Plasma-Induced Streamwise Vortices

C.W. Wong, Y. Zhou, Y.Z. Li and B.F. Zhang

Abstract This work aims to manipulate a fully developed turbulent boundary layer over a flat plate based on plasma-induced streamwise vortices, with a view to reducing the friction drag. Four different plasma actuator configurations for generating streamwise vortices were explored. A surface balance technique is deployed to measure the skin-friction drag. A new calibration method is proposed for this technique to resolve accurately the friction drag change. It is found that the plasma-actuator-generated vortices and their interactions with the boundary layer may lead to a substantial drag reduction. The control efficiency is also estimated. A single hotwire is used to measure the streamwise velocity fluctuation u in the turbulent boundary layer, while flow visualization is performed in the buffer layer, which reveals that the low-speed streaks are pushed by the plasma force toward the centre of the actuator pair, forming a barrier that interferes the turbulence production cycle, and hence allowing substantial drag reduction.

Keywords Turbulent boundary layer · DBD plasma actuator · Streamwise vortices

1 Introduction

Control of turbulent boundary layers (TBL) has received a great attention in the literature due to its practical and fundamental importance. The key of skin-friction drag reduction is to control the quasi-streamwise vortices in the near-wall region. The ejection and sweep events associated with the bursting process occur at 15 wall

C.W. Wong (✉) · Y. Zhou · Y.Z. Li
Harbin Institute of Technology, Shenzhen Graduate School, Shenzhen, China
e-mail: cwwong@hitsz.edu.cn

B.F. Zhang
Department of Mechanical Engineering, The Hong Kong Polytechnic University,
Hong Kong, China

units above the wall (Wallace et al. 1972), and manipulating the near-wall region may directly affect the process of ejection and sweep. Based on computational study, Schoppa and Hussain (1998) achieved a drag reduction of 20 % by using streamwise counter-rotating vortices in a turbulent channel flow, while Cathalifaud et al. (2009) deployed experimentally the jet-generated streamwise co-rotating vortices in TBL, aiming to study the TBL re-organization behind the jet-generated vortices. However, many aspects on plasma-generated drag reduction have yet to be explored. The first objective of this work is to investigate experimentally the drag dependence on the plasma configurations. To this end, four plasma-actuator configurations are deployed for the generation of streamwise vortices and a new calibration method is proposed for the surface balance technique to resolve accurately the friction drag change. The second objective of this work is to provide physical insight on how friction drag is reduced by the plasma-generated vortices.

2 Experimental Details

Experiments were performed in a closed-loop wind tunnel, with a test section of $L \times W \times H = 5.5 \times 0.8 \times 1.0$ m. With its leading-edge tripped, a 4.8-m-long flat plate was placed vertically in the tunnel to generate a fully developed turbulent boundary layer. The boundary layer thickness δ was 85 mm at $x = 3.2$ m (measured from the leading-edge of the flat plate), while the Reynolds number $Re_\theta = 1100$ based on the momentum thickness θ without perturbation. The dielectric barrier discharge DBD plasma actuators consist of two copper electrodes separated by a dielectric panel, which gave an overall thickness of about 1.5 wall unit. The plasma actuators are operated with voltage E ranging from 3.75 to 6.50 kV$_{p-p}$ (subscript p-p deontes the peak-to-peak) at a frequency $f = 11$ kHz. Four different plasma configurations (Fig. 1), i.e., A, B, C and D, are investigated. Note that x, y and z are defined as the streamwise, wall-normal and spanwise directions and they are normalized with the viscous length. A is characterized by colliding counter-rotating vortices, and the streamwise vortex induced by one plasma actuator collides with that by the adjacent one along the entire length of the actuator. B is a counter-rotating vortex generator where the two streamwise vortices do not collide with each other. C is a non-colliding co-rotating vortex generator. D is a sawtooth plasma actuator, which induces streamwise flow and one counter-rotating vortex pair at the tip and between the tips, respectively.

A surface balance is used to measure the averaged skin-friction drag over an area covering 0.2 m × 0.1 m = 0.02 m^2 at $x = 3.2$ m. The skin-friction drag on the flotation surface is resolved using the lever principle. The amplified force is measured by a load cell (Honeywell Model 31-Low, range ±1.50 N). A calibration method is presently proposed for the surface balance. Firstly, measure the velocity profile at the measurement station at $U = 2.4$ and 5 m/s using a hotwire. Secondly, fit the velocity profile to the logarithmic portion of the universal velocity profile.
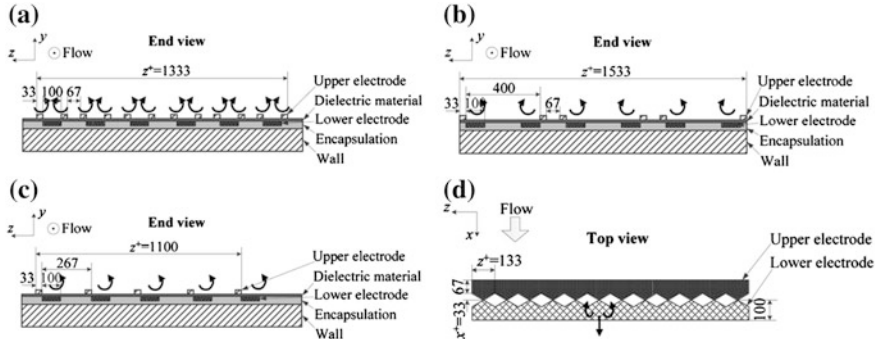
Fig. 1 Four plasma configurations: (*A*); (*B*); (*C*); (*D*), **a** configuration A, **b** configuration B, **c** configuration C, **d** configuration D

The friction velocity u_τ is then determined from Eq. (1) and the skin-friction drag F is estimated from Eq. (2).

$$\frac{\overline{U}}{u_\tau} = 2.44 \ln\left(\frac{u_\tau}{\overline{U}}\right) + 2.44 \ln\left(\frac{\overline{U}y}{\nu}\right) + 4.9 \tag{1}$$

$$F = \rho u_\tau^2 A \tag{2}$$

A single hotwire of 5 μm in diameter and about 1 mm in length is traversed, normally to the wall, across the boundary layer to measure the streamwise mean velocity profile with a resolution of 10 μm. Smoke-wire flow visualization is conducted in the *x-z* plane at $y^+ = 24$ with and without control. The smoke wire is placed at $y^+ = 20$ and 150 mm downstream of the leading-edge of the plasma actuators, parallel to the wall and normal to the free stream. The laser sheet is at $y^+ = 24$, parallel to the wall.

3   Results and Discussion

3.1   Drag Reduction Results

Figure 2 shows the dependence of drag change $\Delta c_f = (F_1 - F_2)/F_2$ on voltage for different plasma configurations, where F_1 and F_2 are the skin-friction drags with and without plasma operated, respectively. Note that, due to the difference in the total "effective" length and electrode geometry of plasma configurations, the comparison in Fig. 2a is based on different power consumption. For configurations A and B, Δc_f increases rapidly with increasing voltage. The Δc_f of A and B is always larger than that of C. The induced vortex pair by A forms an upwash region upon collision, whilst streamwise vortices generated for B and C do not collide with
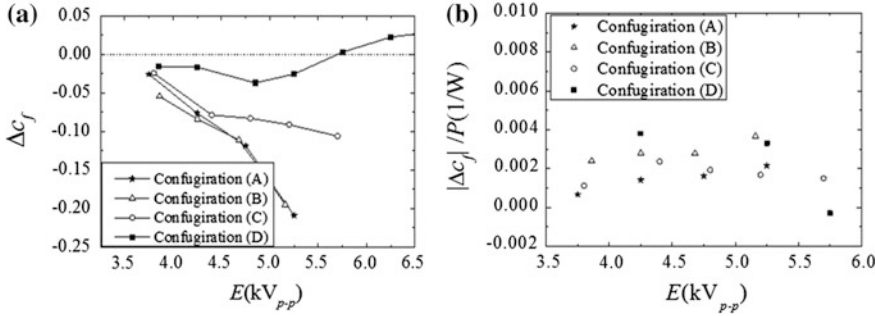
Fig. 2 **a** Dependence of Δc_f on voltage E; **b** dependence of the control efficiency $|\Delta c_f|/P$ on E

each other due to large spanwise spacing between plasma actuators. In contrast, Δc_f of D is significantly lower than others.

The control efficiency, $|\Delta c_f|/P$ was examined (Fig. 2b), where P is the total electrical power consumption of the actuator. Note that Δc_f is negative for the drag reduction. Therefore, $|\Delta c_f|$ is used to calculate the control efficiency. At $E < 5.25$ kV$_{p-p}$, configuration A shows the lowest control efficiency of all, whereas B and C are virtually the same. In general, the $|\Delta c_f|/P$ increases initially for higher voltage in cases of C and D. But beyond a certain level of voltage, the $|\Delta c_f|/P$ drops, because drag reduction diminishes as $E > 4.5$ kV$_{p-p}$ in case of configuration C or the streamwise flow induced at the tip of the sawtooth electrode introduces significant additional drag with increasing E in case of configuration D. At $E = 5.25$ kV$_{p-p}$, configuration B gives the best control efficiency compared with others, the data obtained for this configuration is presented to illustrate the modified flow structure.

3.2 Velocity Measurement and Flow Visualization (Configuration B)

The effect of plasma-induced flow is maintained up to $y^+ \approx 100$, as shown in the distribution of the mean streamwise velocity U^+ (Fig. 3a). The turbulent intensity u_{rms}/U_∞ is reduced at $y^+ < 10$ but increased at $10 < y^+ < 160$ (Fig. 3b), compared with the uncontrolled TBL. The increased u_{rms}/U_∞ is ascribed to the actuator disturbance. On the other hand, the reduced u_{rms}/U_∞ in the near-wall region results from suppressed turbulence activities under manipulation. The typical images of instantaneous flow structure ($y^+ = 24$) show the high- and low-speed streaks without control (Fig. 4a). Note that the slow-moving fluid is pumped away from the wall on the updraught side of the streamwise vortices, resulting in low-speed streaks. Meanwhile, the high-momentum fluid is induced towards the wall on the down-draught side of the streamwise vortices, forming high-speed streaks, which are missed by the laser sheet, thus appearing as dark areas in the photograph. With
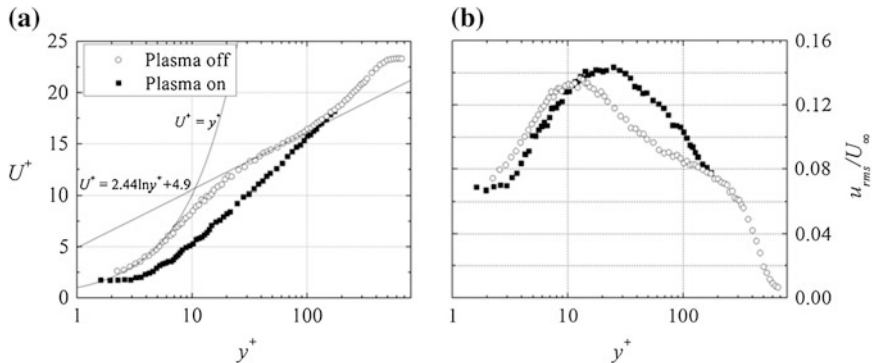
Fig. 3 Distributions of **a** mean streamwise velocity U^+ and **b** turbulent intensity u_{rms}/U_∞ for the natural and controlled cases ($z^+ = 133$)
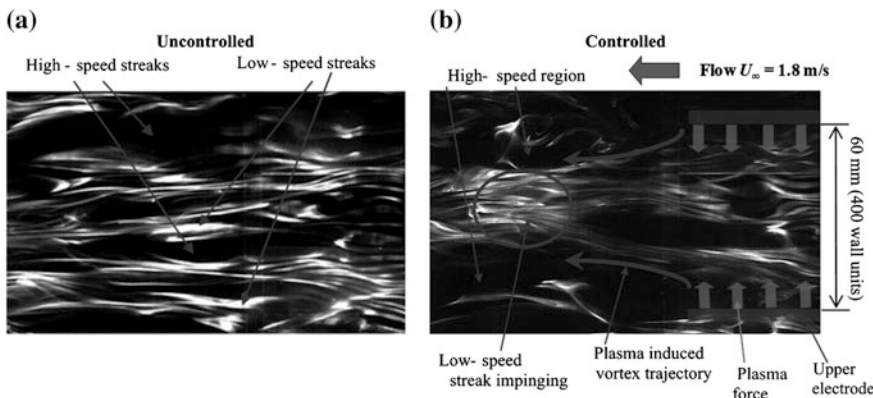
Fig. 4 Smoke-wire flow visualization of instantaneous flow structure at $y^+ = 24$ for **a** natural and **b** manipulated flow with control. The smoke wire and laser sheet are positioned at $y^+ = 20$ and 24, respectively. **a** Uncontrolled, **b** controlled

control, the low speed streaks appear pushed toward the centre of the actuator pair (Fig. 4b), forming a barrier that interferes with the turbulence production cycle, thus allowing the substantially reduced drag. Two high-speed fluid regions occur on each side of the region of low-speed streaks, as a result of the downwash flow due to the plasma-induced rotating vortices (not shown).

4 Conclusions

(1) Preliminary results indicate a maximum drag reduction of about 20 % on the flotation surface under the configurations A and B, about 10 % under C, and about 4 % under D, which have yet to be verified by further experiments.

(2) The low-speed streaks under configuration B are pushed by the plasma force toward the centre of the actuator pair, producing a barrier that interferes the turbulence production cycle, thus attaining the substantially reduced drag.

References

Cathalifaud P, Godard G, Braud C, Stanislas M (2009) The flow structure behind vortex generators embedded in a decelerating turbulent boundary layer. J Turbul 10(42):1–37

Schoppa W, Hussain F (1998) A large-scale control strategy for drag reduction in turbulent boundary layers. Phys Fluids 10(5):1049–1051

Wallace JM, Eckelmann H, Brodkey RS (1972) The wall region in turbulent shear flow. J Fluid Mech 54:39–48

DNS for Turbulent Drag Reduction at $Re_\tau = 1600$

Yongmann M. Chung, Edward Hurst and Qiang Yang

Abstract This study considers the skin friction drag reduction of turbulent flow at high Reynolds numbers. A recent DNS study of flow control found that drag reduction became less effective as the Reynolds number increased from $Re_\tau = 200$ to 1600 (Hurst et al. 2014). To investigate this Reynolds number effect, the drag reduction of the stationary waves is decomposed into laminar and turbulent components, and the turbulent contribution is further decomposed into inner and outer regions. The current analysis based on the Reynolds number up to $Re_\tau = 1600$ appears to suggest that the Reynolds number effect on the drag reduction could be relatively modest than suggested in the previous studies, and this could mean that a significant drag reduction could be achieved at a flight condition.

Keywords Flow control · Drag reduction · Reynolds number effect · Stationary waves · Direct numerical simulation

1 Introduction

Flow control of turbulent flow has attracted a significant interest over the past decade. In particular, a skin friction drag reduction has been investigated for channel, pipe and boundary layer flows both experimentally and numerically (Chung and Hurst 2014; Hurst et al. 2014; Gatti and Quadrio 2013). Recently, an extensive DNS study was performed by Hurst et al. (2014) for a range of Reynolds numbers. They considered wall oscillation, stationary waves, and streamwise travelling waves for $200 \leq Re_\tau \leq 1600$. Their DNS results confirm that drag reduction ($\mathcal{DR}$) becomes less effective as the Reynolds number increases (Chung and Hurst 2014; Hurst et al. 2014). They also observed that $\mathcal{DR}$ becomes less effective at different rates depending on the control parameters.

Y.M. Chung (✉) · E. Hurst · Q. Yang
School of Engineering and CSC, University of Warwick, Coventry CV4 7AL, UK
e-mail: Y.M.Chung@warwick.ac.uk

A particular interest in the drag reduction research is the effect of flow control at high Reynolds number flows. The highest Reynolds number reported in a full DNS study is $Re_\tau = 1600$ by Hurst et al. (2014) while relatively lower Reynolds numbers were used in the majority of previous DNS studies. An extensive review of previous DNS studies of drag reduction is available (Hurst et al. 2014). Although over 2×10^9 grid points were used in their simulation, this Reynolds number is still somewhat smaller than the flight Reynolds number for the cruise condition, and the effectiveness of the current flow control methodologies at such a high Reynolds number would be of critical importance to the aerospace industry. In this study, we conjecture a possible scenario for the drag reduction at high Reynolds numbers. The analysis was based on the stationary waves but the general trend can be applied to other near-wall flow control methodologies.

2 Numerical Method

In this study, we focus on the flow control with stationary waves (Quadrio et al. 2009). The unsteady spanwise wall velocity is applied at both channel walls, $w(x, y = 0, z) = A \sin\left(\kappa_x x\right)$, where A is the maximum wall velocity, κ_x is the streamwise wavenumber. The amplitude is chosen as $A^+ = 12$ from the previous study. The top and bottom walls can move in the same spanwise direction or the opposite direction. Both symmetric and anti-symmetric configurations were tested, and the difference was found to be rather small. The effect of a domain size was tested using preliminary simulations. The DNS results with two domain sizes ($32h \times 2h \times 6h$ and $16h \times 2h \times 12h$) were compared. The grid resolutions and time step size were also carefully chosen based on test simulations. An MPI version of an in-house DNS code was used. Simulation parameters are shown in Table 1 and further details can be found in Hurst et al. (2014).

Table 1 Simulation parameters used. Here, h is the channel half-height. $Re = U_m h / \nu$ and $Re_\tau = u_\tau h / \nu$

Case	Re_τ	Re	$L_x \times L_y \times L_z$	$N_x \times N_y \times N_z$
CH200	200	3,150	$16h \times 2h \times 6h$	$320 \times 140 \times 240$
CH400	400	7,000	$16h \times 2h \times 6h$	$640 \times 240 \times 480$
CH800	800	15,700	$12h \times 2h \times 4h$	$960 \times 384 \times 640$
CH800L	800	15,700	$24h \times 2h \times 8h$	$1920 \times 384 \times 1280$
CH1600	1,600	34,500	$12h \times 2h \times 4h$	$1920 \times 800 \times 1280$

3   Results and Dicussion

At high Reynolds numbers, the large-scale structure plays an important role in the deterioration of drag reduction. In Fig. 1, the footprints of the large-scale structure are clearly evident in the low-speed streaks of the controlled flow shown. To study the Reynolds number effect, C_f is decomposed into laminar and turbulent components (Fukagata et al. 2002), and the turbulent part is again decomposed into two regions: the inner region is defined as $0 < y < y_p$, and the outer region is defined as $y_p < y < 1$. y_p is the location for the maximum Reynolds shear stress, and varies as a function of Reynolds number, $y_p^+ = 2Re_\tau^{1/2}$ (Guala et al. 2006; Sreenivasan and Sahay 1997).

$$C_f = \frac{6}{Re} + 6 \left[\int_0^{y_p} (1 - y)\,(-\overline{uv})\,\mathrm{d}y + \int_{y_p}^1 (1 - y)\,(-\overline{uv})\,\mathrm{d}y \right]. \qquad (1)$$

The first part in Eq. 1 is the laminar flow component. Since the Reynolds number of the control case is the same as the no-control case, this part does not contribute to the drag reduction. Only turbulent parts (the second and third terms in Eq. 1) contribute to the drag reduction. C_f contributions from the inner and outer regions were compared with the no-control flow, and the difference is shown in Fig. 2. Since the constant flow rate condition was imposed in the flow control cases, $\mathscr{DR}$ can be defined as $\mathscr{DR} = \left(1 - \frac{C_f}{C_{f,no}}\right) \times 100(\%)$.
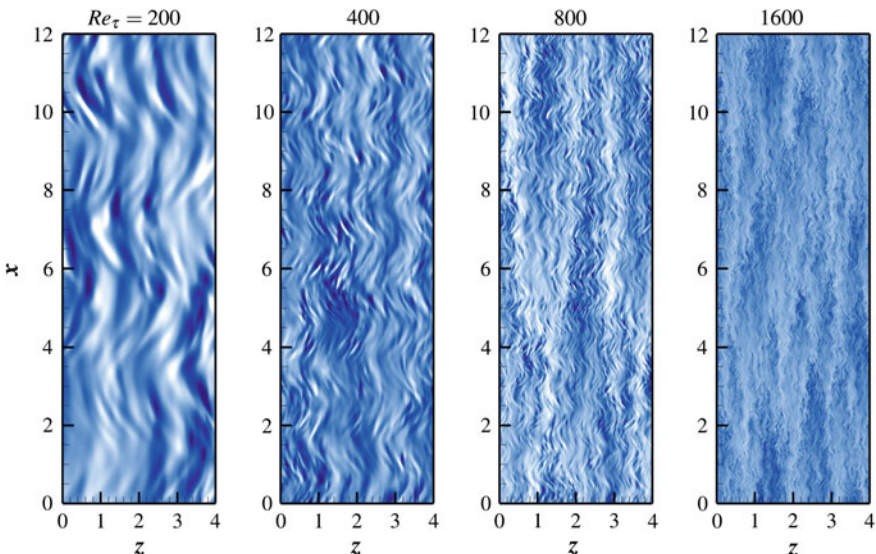
Fig. 1   Low speed streaks at $y^+ = 10$ for stationary wave for four Reynolds numbers

Fig. 2 Contribution from
turbulent parts to $\mathscr{DR}$ from
the inner and outer regions
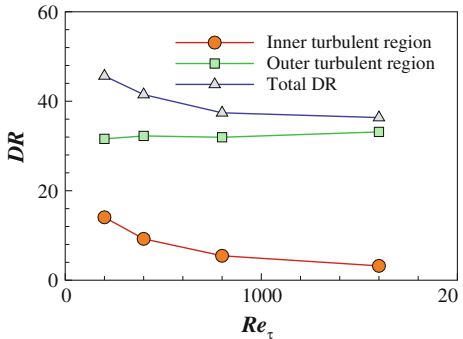
In Fig. 2, it can be seen that the total drag reduction is decreased with the Reynolds number, and $\mathscr{DR} = 33\,\%$ at $Re_\tau = 1600$. The contribution from the inner turbulent region shows a similar decrease with the Reynolds number, and the outer turbulent region appears to have the same amount of $\mathscr{DR}$ for all Reynolds numbers considered. Although the range of Reynolds number used in this study is not very large, the trend is quite clear. Of course, these results should be taken with some caution. In this study, the inner and outer turbulent regions were defined by y_p, and slightly different trends could be observed with the use of different definitions for the inner and outer regions. However, the overall trend would be still similar to this finding.

4   Conclusion

The Reynolds number effect of drag reduction was investigated using DNS in the case of the stationary waves. Based on the Reynolds shear stress decomposition analysis, it is found that the major Reynolds effect is associated with the outer region, while there appears to be little changes in the inner region. This finding could suggest that a finite amount of drag reduction can be attained at very high Reynolds numbers. The flight experiment results with riblets appears to support this conclusion. DNS results from a larger Reynolds number range could provide a more conclusive evidence.

References

Chung YM, Hurst E (2014) Turbulent drag reduction at high Reynolds numbers. In: Zhou Y, Liu Y, Huang L, Hodges DH (eds) Fluid-structure-sound interactions and control. Springer-Verlag, pp 95–99

Fukagata K, Iwamoto K, Kasagi N (2002) Contribution of Reynolds stress distribution to the skin friction in wall-bounded flows. Phys Fluids 14(11):L73–L76

Gatti D, Quadrio M (2013) Performance losses of drag-reducing spanwise forcing at moderate values of the Reynolds number. Phys Fluids 25(12):125109

Guala M, Hommema SE, Adrian RJ (2006) Large-scale and very-large-scale motions in turbulent pipe flow. J Fluid Mech 554:521–542

Hurst E, Yang Q, Chung YM (2014) The effect of Reynolds number on turbulent drag reduction by streamwise travelling waves. J Fluid Mech 759:28–55

Quadrio M, Ricco P, Viotti C (2009) Streamwise-travelling waves of spanwise wall velocity for turbulent drag reduction. J Fluid Mech 627:161–178

Sreenivasan KR, Sahay A (1997) In: Panton R (ed) Self sustaining mechanisms of wall turbulence. vol. 15. WIT Press

Active Skin Friction Drag Reduction Using Different Schemes

Y. Zhou, Z.X. Qiao and Z. Wu

Abstract This work explores experimentally the active control techniques for skin friction drag reduction in a turbulent boundary layer based on wall perturbation generated by piezo-ceramic actuators. Three different schemes, i.e., the open-loop, feed-forward, and combined feed-forward and feedback controls are investigated, achieving the maximum drag reductions of 30, 24 and 29 %, respectively. The corresponding duty cycles are 100, 50, and 60 %, respectively, suggesting a good potential to cut down substantially the input energy under the closed loop control strategy. The flow physics behind is also discussed.

1 Introduction

Active skin-friction drag reduction represents a fascinating challenge to the experimental fluid dynamics community due to its great importance and direct practical significance in many fields of engineering. Bai et al. (2014) recently developed an open-loop control technique for the friction drag reduction in a fully developed turbulent boundary layer over a flat plate, where a spanwise-aligned array of 12–16 piezo-ceramic (PZT) actuators was deployed to generate a local surface oscillation. A maximum drag reduction by 50 % was achieved locally. They found that the surface perturbation is highly dissipative, causing the streaky structures to be stabilized and further suggested the stabilization of the streaks to be a generic feature of any local flow region associated with substantial drag reduction. However, the control efficiency of their technique is very low. One naturally asks

Y. Zhou (✉) · Z.X. Qiao · Z. Wu
Institute for Turbulence-Noise-Vibration Interaction and Control, Harbin Institute
of Technology, Shenzhen Graduate School, Shenzhen, China
e-mail: zhouyu@hitsz.edu.cn

the question whether this efficiency can be increased by deploying a closed-loop control scheme.

This work aims to address the issue raised above and to explore and compare different closed-loop control strategies, with a view to determine the extent to which the control efficiency can be improved.

2 Experimental Details

Experiments were conducted in a closed-circuit wind tunnel with a 5.6-m-long test section of 0.8 m in width and 1.0 m in height. A 4.8-m-long flat plate, rounded at the leading edge, was placed vertically in the test section. The flow was tripped at the leading edge by two arrays of screws to generate a fully developed turbulent boundary layer. As shown schematically in Fig. 1, an array of two piezo-ceramic actuators, each with a dimension of 21.5 mm $\times$ 2 mm $\times$ 0.33 mm, was placed 3.1 m downstream of the leading edge of the plate. The actuators, cantilever-supported on a substrate, are driven by in-phased sinusoidal signals to produce a spanwise flapping motion. Their peak-to-peak oscillating amplitude A_o^+ and frequency f_o^+ were 0.80–2.69 and 0.14–0.71, respectively, where superscript + denotes normalization by wall unit. A fixed hotwire or wall wire was placed downstream of the actuators at $x^+ = 14$, chosen rather arbitrarily, and $y^+ = 3.4$ in the viscous sub-layer. In this paper, the instantaneous velocity U_β, measured by the wall wire, may be decomposed into a time-averaged mean $\bar{U}_\beta$ and a fluctuating component u_β, where subscript β may represent m, d, and p. The output signal U_m of the wall wire, approximately proportional to the wall shear stress τ_w, is used to estimate or monitor τ_w. Another wall wire was placed upstream of actuators and its output signal U_d may act to detect the incoming large events of the wall shear stress. The longitudinal separation L^+ between the wall wires is determined based on two considerations, i.e., larger than the actuator length (144 wall units) and adequately small variation in coherent structures. Averaged time delay $\Delta_{\tau_{max}}$ for streaky structures to be convected from the upstream detecting to the monitoring sensor may be estimated from the maximum correlation function, written as
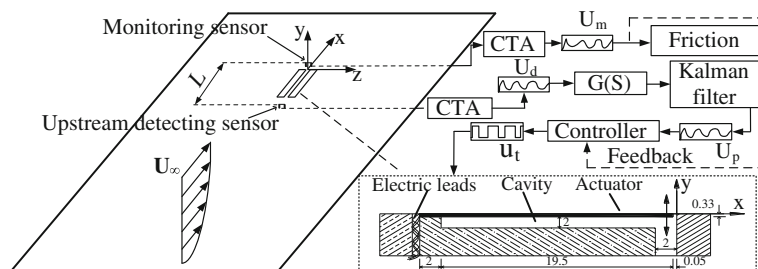
Fig. 1 Experimental arrangement

$\rho_{u_{\mathrm{m}}u_{\mathrm{d}}}(\Delta_{\tau_{\max}}) = \overline{u_{\mathrm{m}}(t)u_{\mathrm{d}}(\bar{t} \pm \Delta_{\tau_{\max}})}/(u_{\mathrm{m,rms}}u_{\mathrm{d,rms}})$. The $\Delta_{\tau_{\max}}$ and L^+ are linearly correlated up to $L^+ = 460$, implying small variation in coherent structures. $L^+ = 250$ is chosen, corresponding to $\rho_{u_{\mathrm{m}}u_{\mathrm{d}}}(\Delta_{\tau_{\max}}) = 0.55$ and $\Delta_{\tau_{\max}} = 30.8$ ms. Measurements were conducted at a wind speed of $U = 2.4$ m/s, corresponding to a momentum-thickness-based Reynolds number $Re_\theta = 1450$. The free-stream turbulence level is 0.4 %.

3 Results and Discussion

The open-loop control was first performed following Bai et al. (2014). The dependence of $\delta_{\tau w} = (\bar{\tau}_w - \bar{\tau}_{wo})/\bar{\tau}_{wo}$ on f_o^+ and A_o^+ may be determined, where $\bar{\tau}_w$ and $\bar{\tau}_{wo}$ are the averaged wall shear stress at $x^+ = 14$ with and without control, respectively. This dependence is qualitatively the same as Bai et al.'s report, though the maximum $\delta_{\tau w}$ and the corresponding f_o^+ and A_o^+ may differ due to different flow conditions and actuation systems. The maximum local drag reduction δ_w is -30 %, achieved at $f_o^+ = 0.56$ and $A_o^+ = 1.61$ (Fig. 2).

The flowchart for the feed-forward control system is given in Fig. 1 and the online signals U_d, U_m, U_p and u_t captured simultaneously are illustrated in Fig. 4, where friction velocity $u_\tau = \sqrt{\tau_w/\rho}$ (ρ is the fluid density). After passing a transfer function $G(s)$, determined offline based on both U_m and U_d, U_d is filtered by a Kalman filter to yield the predicted signal U_p. The actuators are triggered for the duration of a high skin-friction event when U_p exceeds a threshold $Th_1 = \kappa_1 \bar{U}_p$, where $\bar{U}_p$ is calculated from the first 5000 data points of U_p and κ_1 is adjusted to obtain a compromise between the duty cycle and $\delta_{\tau w}$. The actuators are operated at preset f_o^+ and A_o^+, which are presently made the same as the optimum control parameters determined from the open-loop control for the purpose of comparison, especially in terms of the duty cycle d_c and $\delta_{\tau w}$. The cost functional $\emptyset$ for the feed-forward control, given by $d_c/\delta_w = L(d_c)$, provides a measure for the input control energy as per each unit energy saved from drag reduction, and its minimum

Fig. 2 Dependence of $\delta_{\tau w}$ on A_o^+ ($f_o^+ = 0.56$)
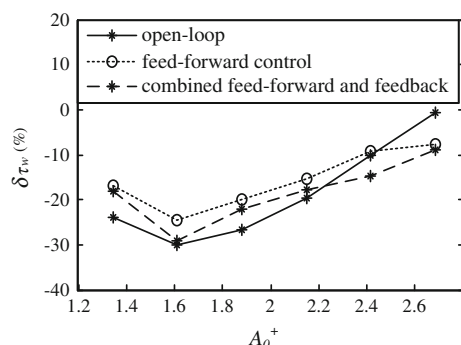
Fig. 3 Dependence of the cost functional $\varnothing$ on the duty cycle d_c for the feed-forward control ($f_o^+ = 0.56$, $A_o^+ = 1.61$)
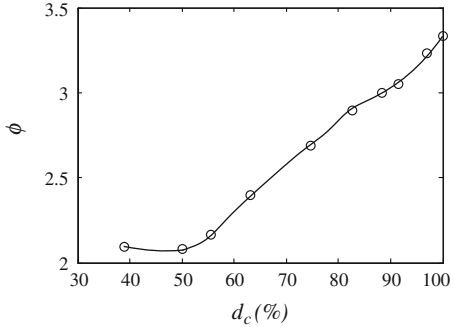
can be experimentally determined by varying d_c, as illustrated in Fig. 3. The minimum $\varnothing$ occurs at $d_c \approx 50$ %, which is used for the feed-forward control. Note that $\delta_{\tau w}$ achieved may depend on A_o^+ and the $\delta_{\tau w} - A_o^+$ relation is qualitatively the same as that in the open-loop control (Fig. 2). However, the drag reduction achieved is up to 6 % less. This is not unexpected. Turbulent structures constantly evolve. As such, the predicted structure from U_d is bound to deviate from the real that is $L^+ = 250$ away. Nevertheless, the duty cycle drops to 50 %, the input energy being substantially reduced.

In order to address the deviation between U_p and the real flow caused by highly nonlinear turbulence evolution, a feedback signal U_m is introduced into the control system to correct this deviation so as to enhance the control performance. The detecting sensor for U_m located at $x^+ = 14$ has been placed as close as possible to actuators to ensure a minimum time lag from the actuators to the downstream sensor as turbulent structures evolve constantly during advection. The actuators will also be triggered if U_m is above a threshold $Th_2 = \kappa_2 \bar{U}_m$. The values of κ_2 and $\bar{U}_m$ are determined similarly to κ_1 and $\bar{U}_p$. Please refer to Fig. 4 for illustration. During the control process, κ_1 for the feed-forward component is firstly adjusted to a value so that d_c is 50 %. Then, κ_2 is adjusted, which leads to an increase in d_c, to achieve

Fig. 4 Simultaneously obtained U_d, U_m and U_p, along with u_t ($t = 4.1$ s is chosen arbitrarily)
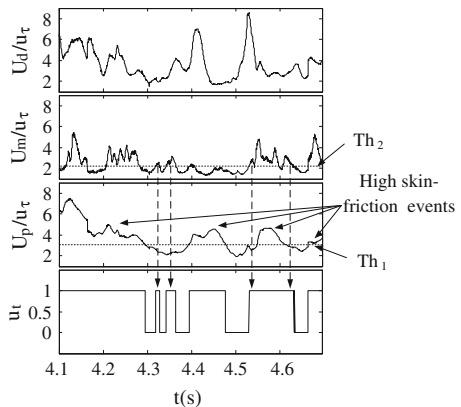
the optimum $\varnothing$. The duty cycle increases slightly to 60 %, compared to the feed-forward control. However, adding this feedback component improves considerably δ_{τ_w} and the maximum drag reduction reaches 29 %, almost the same as that obtained from the open-loop control (Fig. 2). It is interesting to note that the closed-loop control may achieve a drag reduction even considerably larger than the open-loop, e.g., at $A_o^+ > 2.42$. As shown by U_m in Fig. 3, the magnitude of high skin-friction events may be reduced by 2.5 u_τ. So may that of low skin-friction events be, given no constraint on the duty cycle.

The weighted power spectral density function $f^+E_u^+$ (Fig. 5) of u_m measured at $(x^+, y^+, z^+) = (14, 3.4, 0)$ indicates clearly a shift in energy to higher frequencies under control, irrespective of control schemes, indicating an energy transfer from large- to small-scale turbulence. Note that the pronounced peak at the imposed $f^+ = 0.56$ for the open-loop control is 6.2 and 2.3 times that for the feed-forward and the combined feed-forward and feedback controls, respectively, in conformity to the difference between their duty cycles.

The weighted spectrum $f^{+2}E_u^+$ provides a measure for the energy dissipation rate. Evidently, $f^{+2}E_u^+$ (Fig. 6) increases greatly over the range of $f^+ = 0.03$–0.3 under control, albeit with a small variation for different schemes. Note a considerable increase in $f^{+2}E_u^+$ for $f^+ = 0.44$–0.56 for the two closed-loop schemes but not open-loop, suggesting that the closed-loop scheme may enhance the energy dissipation over a broader range of frequencies than the open-loop. Another pronounced

Fig. 5 The u_m spectra E_u at $(x^+, y^+, z^+) = (14, 3.4, 0)$; $f_o^+ = 0.56$ and $A_o^+ = 1.61$ for control
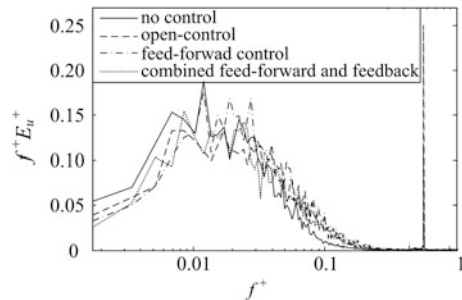
Fig. 6 Dependence of $f^{+2}E_u^+$ on f^+ at $(x^+, y^+, z^+) = (14, 3.4, 0)$; $f_o^+ = 0.56$ and $A_o^+ = 1.61$ for control
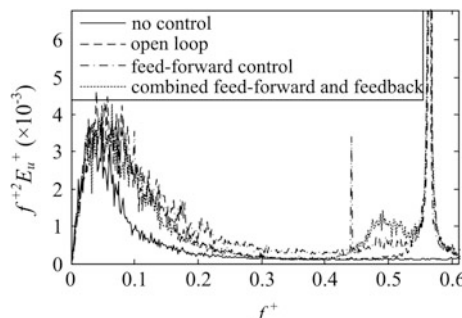
peak occurs at $f_N^+ = 0.44$ for closed-loop controls, not for open-loop. This peak results from the natural frequency of actuators. When u_t changes from 1 to 0 (Fig. 3), the actuators may not stop all of a sudden but, instead, continue oscillating at the natural frequency, thus producing this peak. This peak is more pronounced for the combined feed-forward and feedback control than the feed-forward control as the former is associated with more sudden drops in u_t.

4   Conclusions

(1)   The feed-forward control achieves a maximum drag reduction up to 24, 6 % less than that obtained from the open-loop. However, the duty cycle is only 50 %, suggesting a substantial drop in the input energy. With 29 %, almost the same as that from the open-loop and the duty cycle increases only slightly to 60 %
(2)   The energy dissipation rate grows significantly for higher frequencies, regardless of the control scheme deployed, which is fully consistent with possibly stabilized velocity streaks of smaller scales (Bai et al. 2014) and hence the substantially reduced drag. The closed loop schemes enhance the energy dissipation rate over a broader range of frequencies than the open-loop.

(1) .

Reference

Bai HL, Zhou Y, Zhang WG, Xu SJ, Wang Y, Antonia RA (2014) Active control of turbulent boundary layer based on local surface perturbation. J Fluid Mech 750:316–354

Skin Friction Drag Reduction Based on Unsteady Blowing Through One Array of Streamwise Slits

Y.Z. Li and Y. Zhou

Abstract An experimental study is conducted to reduce the skin friction drag in a turbulent boundary layer using periodic blowing through one array of streamwise slits. The blowing amplitude and frequency have been investigated and found to have great effects on the control performance. A maximum local skin friction reduction of 70 % has been observed at 33 wall unit downstream of the actuators, which is connected to a greatly enhanced mean energy dissipation rate based on the analysis of the hotwire and PIV data.

Keywords Turbulent boundary layer · Drag reduction · Active control

1 Introduction

Active control of a turbulent boundary layer for drag reduction has long been an important research area in fluid mechanics and attracts more attention in recent years due to the strong need to cut down fuel costs and the ever increasing concern of emissions. Bai et al. (2014) deployed one array of 12–16 piezo-ceramic actuators to generate local wall oscillation, forming a transverse wave, in a turbulent boundary layer and observed a local skin friction drag reduction by 50 %. One of their interesting observations is that, when the actuators are oscillated in phase, i.e., producing a flapping motion, the control performance can be as good as that when a transverse wave is generated. However, the drag fully recovered by $x^+ \approx 160$, resulting in a very low control efficiency. They ascribed this rapid recovery to a very short effective streamwise length of the actuators, which were cantilever-mounted. This assertion has yet to be confirmed. Furthermore, they found that the surface perturbation is highly dissipative, causing the streaky

Y.Z. Li · Y. Zhou (✉)
Institute for Turbulence-Noise-Vibration Interaction and Control,
Shenzhen Graduate School, Harbin Institute of Technology, Shenzhen, China
e-mail: zhouyu@hitsz.edu.cn

structures to be stabilized. One naturally asks the question whether the stabilization of the streaks is a generic feature associated with substantial drag reduction. This investigation aims to address the above issues and explores the effectiveness of drag reduction based on unsteady blowing through one array of streamwise slits.

2 Experimental Details

A 4.8-m-long and 0.8-m-wide flat plate, tripped at the leading edge, is placed in a low-speed wind tunnel to generate a turbulent boundary layer (Fig. 1a). An array of 9 streamwise slits is placed 3 m downstream of the leading edge, where the boundary layer disturbance thickness, friction velocity, shape factor and Reynolds number based on the momentum thickness and U_∞ are 0.085 m, 0.105 m/s, 1.45 and 1450, respectively, at an incoming flow velocity of 2.4 m/s. Each slit is 20 mm long, 0.5 mm wide and 3 mm thick, corresponding to $133.3 \times 3.3 \times 20$ in wall units (Fig. 1b). The centre-to-centre spacing between slits is 2 mm or 13.3 in wall units. The idea of the slit size and separation originates from Bai et al.'s arrangement of the piezo-ceramic actuators. Air from a compressor goes through a filter, a pressure relief valve, a throttle valve, a flow meter and an electromagnetic valve before reaching a plate of 30 mm $\times$ 120 mm, with 8 equally distributed holes of 10 mm in diameter, and a contraction with an area ratio of 6, which are mounted to ensure the uniformity of jets through slits. The electromagnetic valve with a 20 % duty-cycle is characterized by a frequency range of $f = 5$–400 Hz. The outlet velocity U_{out} of the jets through slits, its distribution at the different locations of the slit and its frequency are all measured carefully using a Dantec hotwire anemometer at various volume flow rates Q and frequencies f. The time-averaged jet velocity $\overline{U_{out}}$ is 0.5 m/s, corresponding to $A^+ = \overline{U_{out}}/u_\tau = 4.6$, where superscript + denotes normalization by wall units. The f^+ range is 7–560×10^{-3}. The wall shear stress is estimated from the slope of the velocity profile in the viscous layer measured using a single hotwire. The wall shear stress is estimated from the gradient of the hotwire-measured mean streamwise velocity at $x^+ = 33$–460 ($z^+ = 0$) and
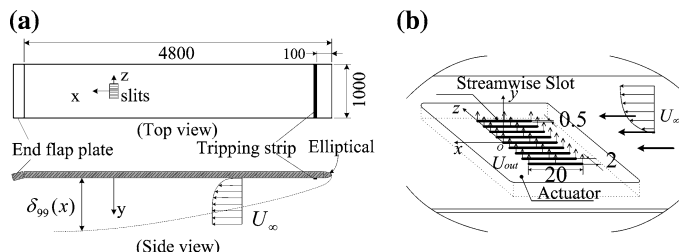
Fig. 1 Experimental setup. **a** Flat plate, **b** actuator and its installation. The length unit is mm

$z^+ = -90$–90 ($x^+ = 33$) over $y^+ = 2.5$–8. The flow field is captured in the xz-plane at $y^+ = 13$ using PIV.

3 Dependence of Drag Reduction on A^+ and F^+

The drag change $\delta_{\tau_w} = (\overline{\tau_w} - \overline{\tau_{w0}})/\overline{\tau_{w0}} \times 100\%$ depends on both A^+ and f^+, where $\overline{\tau_w}$ and $\overline{\tau_{w0}}$ are time-averaged wall shear stresses with and without control, respectively. As A^+ increases, δ_{τ_w} initially drops, irrespective of f^+, and then grows before approaching an asymptotic value at $f^+ = 0.07, 0.14$ (Fig. 2a), indicating the presence of an optimum A^+, which is 1.63, 1.14 corresponding to $f^+ = 0.07, 0.14$, respectively. After an initial drop, δ_{τ_w} begins to approach its asymptotic value at $A^+ \approx 0.66$ for $f^+ = 0.42$. On the other hand, at a given A^+, δ_{τ_w} initially drops rapidly with increasing f^+ and then levels off (Fig. 2b). The dependence of δ_{τ_w} on A^+ and f^+ exhibits similarity to that observed by Bai et al. (2014). Finally, δ_{τ_w} also depends on the streamwise measurement location. The maximum δ_{τ_w} reaches 70 % at $x^+ = 33$ and rises slowly, not fully recovered until at $x^+ = 460$ (Fig. 3), much farther than that ($x^+ = 160$) reported by Bai et al. (2014). Note that the present effective
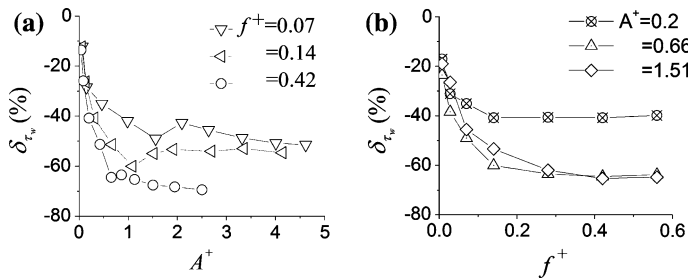
Fig. 2 Dependence of δ_{τ_w} on (a) A^+ at difference f^+ and (b) f^+ at difference A^+
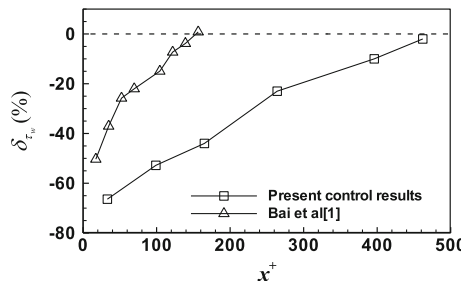
Fig. 3 Dependence of δ_{τ_w} on x^+: $\square$ present data ($A^+ = 0.66$, $f^+ = 0.42$); $\triangle$ **(b)** Bai et al. ($A^+ = 1.94$, $f^+ = 0.39$, and $\lambda_z^+ = 416$)

streamwise length (20 mm) is much larger than theirs. The result suggests that an increase in this length may substantially prolong the downstream distance up to which the friction drag is reduced. It is worth mentioning that A^+ corresponding to 66 % drag reduction is only 0.66 ($f^+ = 0.42$), way below that (2.4) Tardu and Doche (2009) used to achieve 50 % drag reduction ($x^+ = 40$, $f^+ = 0.0134$) with a single spanwise slit.

4 Altered Flow Structure

Figure 4 compares the mean and fluctuating components, $\overline{U}^+$ and u_{rms}^+, of the streamwise velocity with and without control. The control parameters used are $A^+ = 0.66$, $f^+ = 0.42$. The $\overline{U}^+$ distribution follows the universal law reasonably well in the natural boundary layer. Once control is on, the profiles are considerably modified. The linear region of $\overline{U}^+$ is thickened from $y^+ \approx 7$ without control to $y^+ \approx 14$ with control (Fig. 4a). The result agrees with previous reports that substantial drag reduction in a controlled turbulent boundary layer is accompanied by a thickened viscous sublayer. The logarithmic region appears is pushed upwards. The u_{rms}^+ value drops at $y^+ < 8$ but rises at $8 < y^+ < 20$ under control (Fig. 4b). The increased u_{rms}^+ is ascribed to the disturbance of blowing as observed by Itoh et al. (2006). On the other hand, a reduction in u_{rms}^+ in the near-wall region may result from suppressed turbulence activities under control as noted in Bai et al. (2014).

The iso-contours of instantaneous streamwise velocity from PIV measurements in the xz plane are presented in Fig. 5. The large-scale near-wall streaky structures are evident without control (Fig. 5a). However, these structures disappear under control and more and smaller scale longitudinal structures appear. Moreover, Taylor's microscale calculated using the hotwire signals shrinks by more than 50 % (not shown), suggesting a greatly enhanced energy dissipation rate (Tardu 2001). It seems plausible that the control interrupts the turbulence production cycle on one hand and promotes enormously the energy dissipation rate on the other hand, thus promoting relaminarization and resulting in drag reduction.
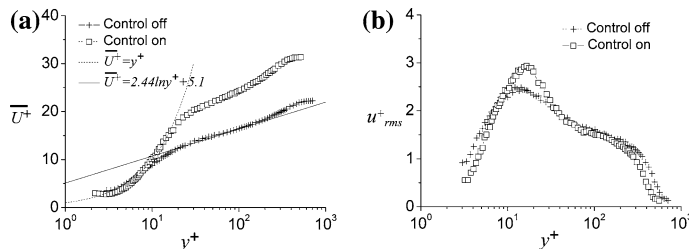
Fig. 4 The profiles of **a** $\overline{U}^+$ and **b** u_{rms}^+ with ($\square$, $A^+ = 0.66$, $f^+ = 0.42$) and without (+) control
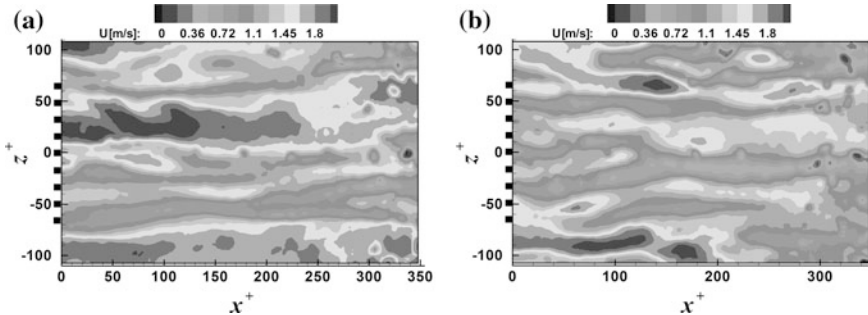
Fig. 5 The iso-contours of instantaneous streamwise velocity in the xz plane (PIV measurement, $Re_\theta = 1450$, $y^+ = 13$): **a** natural boundary layer, **b** perturbed ($A^+ = 0.66$, $f^+ = 420 \times 10^{-3}$). Flow is left to right. Small squares indicate the streamwise slits, whose trailing edge is at $x^+ = 0$

5 Conclusions

1. The drag reduction δ_{τ_w} depends on both jet frequency f^+ and amplitude A^+. A maxim drag reduction of 70 % is achieved.
2. The drag recovery is much slower than that in Bai et al. (2014), suggesting that an increase in the effective streamwise length of the actuator may prolong the downstream drag-reduced distance.
3. There has been a great change in the near wall flow structure, highly dissipative and characterized by the stabilized velocity streaks of smaller scales under control.

References

Bai HL, Zhou Y, Zhang WG, Xu SJ, Wang Y, Antonia RA (2014) Active control of a turbulent boundary layer based on local surface perturbation. J Fluid Mech 750:316–354
Itoh M, Tamano S, Yokota K, Taniguchi (2006) Drag reduction on a turbulent boundary layer on a flexible sheet undergoing a spanwise travelling wave motion. J Turbul 7(27):1–17
Tardu SF (2001) Active control of near-wall turbulence by local oscillating blowing. J Fluid Mech 439:217–253
Tardu SF, Doche O (2009) Active control of the turbulent drag by a localized periodical blowing dissymmetric in time. Exp Fluids 47(1):19–26

Comparison of the Direct Numerical Simulation of Zero and Low Adverse Pressure Gradient Turbulent Boundary Layers

V. Kitsios, C. Atkinson, J.A. Sillero, G. Borrell, A. Gul Gungor, J. Jiménez and J. Soria

Abstract Statistics from the direct numerical simulation (DNS) of an adverse pressure gradient (APG) turbulent boundary layer (TBL) are presented. Flow simulations are performed using a TBL DNS code with the desired APG applied via a tailored farfield boundary condition. The APG TBL has a maximum momentum thickness based Reynolds number (Re_{δ_2}) of 6000, and a near constant ratio of pressure velocity to freestream velocity, over a range of Re_{δ_2} from 3000 to 5000. Streamwise velocity variance profiles are shown to collapse under outer velocity scaling as opposed to friction velocity scaling over this range.

1 Introduction

The separation of turbulent boundary layers (TBL) arise from the application of adverse pressure gradients (APG). Engineering systems operating in such environments include aircraft wings, wind turbine blades, and turbo-machinery. Flow separation in these systems has a significant impact on performance/efficiency, and in some cases may lead to catastrophic consequences. The accurate prediction of TBL separation remains a significant challenge for engineering design. An additional complexity of these aerofoil geometries is that the pressure gradient is constantly

V. Kitsios (✉) · C. Atkinson
Laboratory for Turbulence Research in Aerospace and Combustion,
Department of Mechanical and Aerospace Engineering, Monash University,
Melbourne, Australia
e-mail: vassili.Kitsios@monash.edu

J.A. Sillero · G. Borrell · J. Jiménez
School of Aeronautics, Universidad Politécnica de Madrid, Madrid, Spain

A.G. Gungor
Department of Astronautical Engineering, Istanbul Technical University, Istanbul, Turkey

J. Soria
Department of Aeronautical Engineering, King Abdulaziz University,
Jeddah, Kingdom of Saudi Arabia

changing in the streamwise direction, as in the large eddy simulation of Kitsios et al. (2011).

In order to decouple the effect of the surface curvature from the influence of the local pressure gradient, it is instructive to consider the case of a canonical self-similar APG TBL on a flat surface. A self-similar APG TBL is one in which each of the terms in the Navier-Stokes equations have the same proportionality with streamwise position. The DNS of relatively low Reynolds number self-similar APG TBLs have previously been studied in Lee and Sung (2008). A higher Reynolds number separated non-self-similar APG TBL was simulated and studied in Gungor et al. (2012). In the present study we undertake a DNS of a self-similar APG TBL of maximum momentum thickness based Reynolds number $Re_{\delta_2} \equiv U_e \delta_2 / \nu = 6000$, where δ_2 is the momentum thickness, ν is the kinematic viscosity, and U_e is the velocity at the edge of the boundary layer of height δ. We are particularly interested in the incipient separation case in which the skin friction approaches zero.

2   Direct Numerical Simulation Solver

We adopt the hybrid MPI and openMP parallelised DNS code of Simens et al. (2009) and Borrell et al. (2013), with the farfield boundary condition (BC) modified to achieve the desired APG flow. The code solves the Navier-Stokes equations of constant density (ρ) and constant ν, in a three-dimensional rectangular volume. The flow directions are the streamwise (x), wall-normal (y) and spanwise (z), with associated velocity components U, V and W. A Fourier decomposition is used to represent the flow in the periodic spanwise direction, with the compact finite difference method of Lele (1992) used in the aperiodic streamwise and wall-normal directions. The modified three sub-step Runge-Kutta scheme of Simens et al. (2009) is used to step the equations forward in time.

The boundary conditions of the original ZPG version of the TBL DNS code are as follows. The bottom surface is a flat plate with a no-slip (zero velocity) BC. The spanwise boundaries are periodic. Following Sillero et al. (2013) the flow at the inlet is a zero pressure gradient (ZPG) TBL specified by mapping and rescaling a streamwise wall-normal plane from a downstream station, which in the present simulations is at position $x_r = 60\delta(x_0)$, where $\delta(x_0)$ is the boundary layer thickness at the inlet. At the farfield boundary the spanwise vorticity is zero, and the wall normal velocity is

$$V_{ZPG}(x) = \frac{d\delta_1}{dx} \, U_{ZPG} \,, \qquad (1)$$

where δ_1 is the displacement thickness, and U_{ZPG} is the constant freestream streamwise velocity of the ZPG TBL (Sillero 2014).

In order to generate the desired self-similar APG TBL flow the farfield wall normal velocity BC must be modified. In the APG TBL DNS, to allow the rescaling necessary for the inlet boundary condition an initial ZPG TBL is simulated up until the streamwise position $x_s = 100\delta(x_0)$ (located after the recycling plane) by applying $V_{ZPG}(x)$ at the farfield boundary as defined in (1). Note $\delta(x_0)$ is the boundary layer thickness at the inlet. Downstream of the position $x_f = 140\delta(x_0)$ the APG farfield wall normal velocity, $V_{APG}(x)$, is applied. The wall normal component, $V_{APG}(x)$, is related to the streamwise freestream velocity, $U_{APG}(x)$, via the boundary layer streamfunction solution in the farfield, where $U_{APG}(x) \propto x^{-0.23}$ for the desired incipient separation case (Mellor and Gibson 1966). From x_s to x_f the APG BC is introduced in the streamwise direction via a smoothing function.

The domain extents in the streamwise, wall normal and spanwise directions are $(L_x, L_y, L_z)/\delta(x_0) = (801, 38, 134)$ for the ZPG TBL DNS and $(L_x, L_y, L_z)/\delta(x_0) = (801, 70, 134)$ for the APG case. The associated number of grid points are $N_x \times N_y \times N_z = 8193 \times 315 \times 1362$ for the ZPG and $N_x \times N_y \times N_z = 8193 \times 500 \times 1362$ for the APG. The APG simulation has a larger wall normal domain (L_y) and more points in this direction (N_y) due to the APG TBL expanding more quickly in the streamwise direction than the ZPG TBL. Both simulations have the same grid spacings of $(\Delta x, \Delta y_{wall}, \Delta y_\infty, \Delta z)/\delta(x_0) = (0.1, 0.003, 0.17, 0.1)$, where Δx and Δz are the constant spacing in the streamwise and spanwise directions, with Δy_{wall} and Δy_∞ the wall normal grid spacing at the wall and at the farfield boundary respectively. The cell spacings in viscous units are given by $(\Delta x^+, \Delta y_{wall}^+, \Delta y_\infty^+, \Delta z^+) \equiv (\Delta x, \Delta y_{wall}, \Delta y_\infty, \Delta z)u_\tau/\nu$, where friction velocity $u_\tau = \sqrt{\tau_w/\rho}$, with τ_w the mean shear stress at the wall. Using the friction velocity at the inlet as a worst case scenario $(\Delta x^+, \Delta y_{wall}^+, \Delta y_\infty^+, \Delta z^+) = (14, 0.41, 25, 14)$. In both simulations the Courant number was set to unity, with an average time step size of approximately $0.05U_e(x_0)/\delta(x_0)$. Statistics were accumulated over $22,000$ time steps or equivalently 642 eddy-turnover times, where one eddy-turnover time is defined as $\delta(x_0)/u_\tau(x_0)$.

3 Results

The ZPG and APG boundary layers are first compared on the basis of Re_{δ_2}, and the friction and pressure velocity scales. The streamwise velocity variance profiles from various streamwise positions are then non-dimensionalised on the basis of u_τ and U_e to determine the most appropriate scaling. In all of the following figures the green and red lines represent the ZPG and APG cases respectively.

The momentum thickness based Reynolds number illustrated in Fig. 1a, clearly increases in the APG TBL more rapidly than the ZPG TBL, due to the former expanding more quickly (hence larger δ_2) as it decelerates in the streamwise direction. This deceleration of the flow also has the effect of reducing u_τ. As illustrated in Fig. 1b, u_τ of the significantly decelerated APG case is less than that of the lesser decelerated
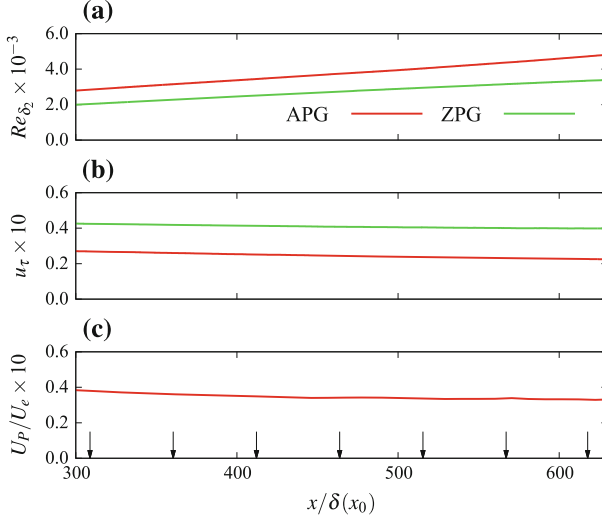
Fig. 1 Boundary layer properties of the APG DNS (*red line*) and the ZPG DNS (*green line*): **a** momentum thickness Reynolds number $Re_{\delta_2} = U_e\delta_2/\nu$; **b** friction velocity $u_\tau = \sqrt{\tau_w/\rho}$; **c** pressure velocity $U_P = \sqrt{(\partial P_e/\partial x)\delta_1/\rho}$ divided by the reference freestream velocity U_e, with arrows indicating the positions of the APG TBL velocity profiles illustrated in Fig. 2

ZPG TBL. However, the APG TBL DNS has not yet attained the desired $u_\tau \rightarrow 0$ condition, representative of incipient separation. Further fine tuning of the BC is required. A TBL is deemed self-similar if the ratio of pressure velocity (U_P) to U_e is constant for a boundary layer growing linearly with streamwise postion (Mellor and Gibson 1966). The pressure velocity, defined by $U_P = \sqrt{(\partial P_e/\partial x)\delta_1/\rho}$, is a velocity scale based on the reference streamwise pressure gradient $\partial P_e/\partial x$. A near constant ratio of U_P/U_e is achieved over the range $300\delta(x_0) < x < 650\delta(x_0)$, see Fig. 1c.

Streamwise velocity variance profiles ($\langle uu \rangle$) are now presented at the streamwise positions indicated by the arrows in Fig. 1c. In Fig. 2a the profiles are nondimensionalised by u_τ and plotted against $y^+ = yu_\tau/\nu$. The blue dots in this figure represent results from the previous ZPG DNS of Jiménez et al. (2010), which agree with the present ZPG simulation. When scaled by u_τ, the non-dimensional velocity variance profiles from each of the various streamwise stations do not collapse, but in fact increase as u_τ decreases in the downstream direction—indicated by the arrow in Fig. 2a. However, the profiles do collapse when scaled by U_e as illustrated in Fig. 2b, with the black line in this figure illustrating the streamwise average. Note the APG case also exhibits an outer peak not observed in the ZPG results.
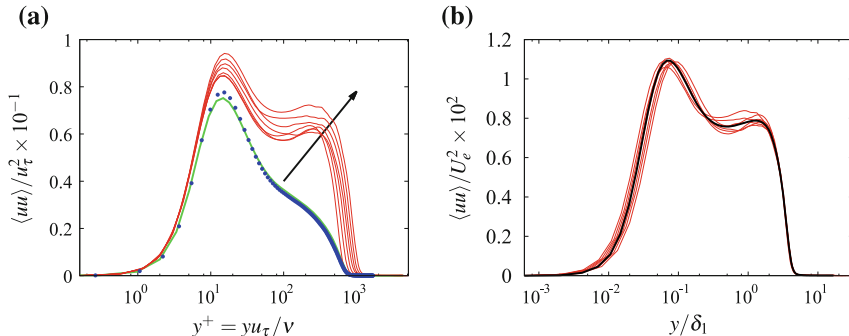
Fig. 2 Profiles of $\langle uu \rangle$ under: **a** friction velocity (u_τ) scaling, arrow indicating increasing streamwise position; and **b** outer velocity (U_e) scaling. ZPG TBL DNS of Jiménez et al. (2010)—*blue dots*. ZPG TBL DNS current simulation—*green line*. APG TBL DNS from current simulation at stream wise locations illustrated in Fig. 1c—*red lines*. Streamwise averaged scaled profiles—*black lines*

4 Concluding Remarks

An adverse pressure gradient turbulent boundary layer was generated via direct numerical simulation with a modified farfield boundary condition. The boundary layer has a near constant ratio of pressure velocity to freestream velocity, over a momentum thickness based Reynolds number range from 3000 to 5000. Within this domain, streamwise velocity variance profiles were shown to collapse under outer velocity scaling as opposed to friction velocity scaling.

References

Borrell G, Sillero JA, Jiménez J (2013) A code for direct numerical simulation of turbulent boundary layers at high reynolds numbers in BG/P supercomputers. Comput Fluids 80:37–43

Gungor AG, Simens MP, Jiménez J (2012) Direct numerical simulation of wake-perturbed separated boundary layers. J Turbomach 134:061024

Jiménez J, Hoyas S, Simens MP, Mizuno Y (2010) Turbulent boundary layers and channels at moderate Reynolds numbers. J Fluid Mech 657(22):335–360

Kitsios V, Cordier L, Bonnet J-P, Ooi A, Soria J (2011) On the coherent structures and stability properties of a leading edge separated airfoil with turbulent recirculation. J Fluid Mech 683:395–416

Lee J-H, Sung J (2008) Effects of an adverse pressure gradient on a turbulent boundary layer. Int J Heat Fluid Flow 29:568–578

Lele SK (1992) Compact finite difference schemes with spectral-like resolution. J Comput Phys 103:16–42

Mellor GL, Gibson DM (1966) Equilibrium turbulent boundary layers. J Fluid Mech 24:225–253

Sillero J (2014) High Reynolds number turbulent boundary layers. PhD thesis, Universidad Politénica de Madrid

Sillero JA, Jiménez J, Moser RD (2013) One-point statistics for turbulent wall-bounded at Reynolds numbers up to $\delta^+ \approx 2000$. Phys Fluids 25:105102

Simens MP, Jiménez J, Hoyas S, Mizuno Y (2009) A high-resolution code for tubulent boundary layers. J Comput Phys 228:4128–4231

Turbulent Kinetic Energy Budget in the Far Field of a Square Cylinder Wake

S.L. Tang, N. Lefeuvre, L. Djenidi, R.A. Antonia and Y. Zhou

Abstract In this paper, the transport equation for the turbulent kinetic energy (TKE) is tested in the far field of a square cylinder wake (hereafter denoted SC). It is found that the physical mechanism for transporting TKE along the axis is different from that in a circular cylinder (hereafter denoted CC) wake. For the SC wake, the $\overline{q^2}$ diffusion term is negligible compared to advection term along the axis and the advection and energy dissipation terms dominate the budget. However, in the CC wake, aside from the advection and energy dissipation terms, the $\overline{q^2}$ diffusion term also contributes significantly to the budget. At the region close to the centreline, the gain of the energy due to the contributions from the advection and diffusion terms is equal to the loss due to the isotropic dissipation, indicating that the isotropic dissipation rate $\bar{\varepsilon}_{iso}$ is a good surrogate of the mean TKE dissipation rate $\bar{\varepsilon}$.

Keywords Far-wake · Turbulent kinetic energy budget

1 Introduction

The transport equation for the average kinetic energy ($\overline{q^2} = \overline{u^2} + \overline{v^2} + \overline{w^2}$, where u, v, and w are the velocity fluctuations in the x, y, and z directions, and overbar denotes time averaging) in the far field of a plane wake can be approximated to (Browne et al. 1987).

S.L. Tang (✉) · Y. Zhou
Shenzhen Graduate School, Institute for Turbulence-Noise-Vibration Interaction and Control, Harbin Institute of Technology,
Shenzhen 518055, People's Republic of China
e-mail: shunlin.tang88@gmail.com

S.L. Tang · N. Lefeuvre · L. Djenidi · R.A. Antonia
School of Engineering, University of Newcastle, Shenzhen, NSW 2308, Australia

$$\underbrace{\frac{1}{2}U\frac{\partial \overline{q^2}}{\partial x}}_{advection} + \underbrace{\overline{uv}\frac{\partial U}{\partial y}}_{production} + \underbrace{\frac{\partial}{\partial y}(\frac{1}{2}\overline{vq^2} + \bar{p})}_{diffusion} + \underbrace{\bar{\varepsilon}}_{dissipation} = 0 \qquad (1)$$

U is the mean velocity in the streamwise direction and p is the pressure; $\bar{\varepsilon}$ is the mean TKE dissipation rate defined as

$$\bar{\varepsilon} = \frac{v}{2}\overline{(\frac{\partial u_i}{\partial x_j} + \frac{\partial u_j}{\partial x_i})^2} \qquad (i,j = 1, 2, 3) \qquad (2)$$

where v is the kinematic viscosity. Several attempts have been made to measure the various terms of Eq. (1) in a CC. For example, Browne et al. (1987), Aronson and Lofdahl (1993), and Lefeuvre et al. (2014) showed that, on the centreline of a CC, the advection, dissipation and $\overline{q^2}$ diffusion terms in Eq. (1) contribute significantly to the budget. In the region away from the centreline, the production term in Eq. (1) arises. It should be noted that there is a strong anisotropy in the far wake of a CC, even on the flow centreline where the mean shear is zero (e.g. Refs. (Browne et al. 1987; Antonia and Browne 1986)). To our knowledge, there is no previous attempt to test the Eq. (1) in the far wake of a SC, although Lefeuvre (DNS data, private communication) recently observed that the advection term is balanced by the dissipation term in the intermediate wake of the SC up to $x/d = 100$. In the present investigation, Eq. (1) is tested, on the basis of X-wire measurements, in the far wake of a SC, with special attention paid to the surrogate of $\bar{\varepsilon}$.

2 Experimental Details

X-wire Measurements were carried out in an open-return low-turbulence wind tunnel with a 2.2 m long working section (0.35 m × 0.35 m). A SC of $d = 6.3$ mm in diameter was installed in the midplane and the measurement stations are at $x/d = 230$ and 270. Experiments were carried out at a free-stream velocity $U_\infty = 9.5$ m/s, corresponding to a Reynolds number $Re = U_\infty d/v = 4000$.

The Wollaston (Pt-10 % Rh) hot wires (diameter $d_w = 2.5$ µm) were etched to an active length of 0.45–0.5 mm. The length to diameter ratio of the wires was typically 200. The hot wires were operated with constant-temperature anemometers at an overheat ratio of 1.5. The output signals from the anemometers were passed through buck and gain circuits and low-pass filtered (the cut-off frequency f_c was set close to the Kolmogorov frequency f_η). The signals were then digitized into a personal computer using a 12 bit A/D converter at a sampling frequency of 20 kHz. The record duration was about 100 s.

3 Results

3.1 Test of Self-preservation

Distributions of $1 - (U_\infty^* - U^*)$, $\overline{u^{*2}}$, $\overline{v^{*2}}$, and $\overline{u^*v^*}$ are shown in Fig. 1. An asterisk denotes normalisation by the maximum velocity deficit U_d and the half-width L. Also shown are the data of Zhou and Antonia (1995) at $x/d = 165$ and 375 for SC wake. There is reasonable collapse of the distributions for $1 - (U_\infty^* - U^*)$. As pointed out by Zhou and Antonia (1995), the distributions for $1 - (U_\infty^* - U^*)$ are approximately independent of the wake generators in the far-wake region of the plane wakes, although discernible differences can be observed in the Reynolds stresses, spectra of v, and vorticities. In the case of $\overline{u^{*2}}$, there is a good collapse for the present data, and those of Zhou and Antonia (1995). The distributions for $\overline{v^{*2}}$ and $\overline{u^*v^*}$ also show a good collapse for the present measurements. The difference in the distributions for $\overline{u^*v^*}$ between the present data and those of Zhou and Antonia (1995) in the range $y^* = 1$–1.5 may due to the different initial conditions between two experiments. Note that the distributions of $\overline{v^{*2}}$ for Zhou and Antonia (1995) are not shown since we suspect that they inadvertently used $\overline{u^{*2}}$ for $\overline{v^{*2}}$ in their Fig. 2c. Nevertheless, Fig. 1 suggests that self-preservation is well satisfied, at least in the context of Reynolds stresses, the far wake of a SC. This of particular interest in the study of far wake because it will allow the development of a theoretical analysis.

3.2 TKE Budget of $\overline{q^2}$

Figure 2 shows all terms of Eq. (1), normalized by L/U_d^3, for SC wake. The mean TKE dissipation rate $\bar{\varepsilon}$ is estimated by assuming isotropy, $\bar{\varepsilon} = \bar{\varepsilon}_{iso} = 15\nu\overline{(\partial u/\partial x)^2}$. The pressure diffusion term is obtained by difference. In the region close to the wake centreline, i.e. $y^* = 0$–0.3, the gain of the energy due to the contributions from the advection is approximately equal to the loss due to dissipation. The $\overline{q^2}$ diffusion term, however, is negligible (the ratio of the $\overline{q^2}$ diffusion term to advection term is about 1/7 on the flow centerline). This is different from that in a CC wake, where, aside from the advection and energy dissipation terms, the diffusion term also contributes significantly to the budget (the ratio of the diffusion term to advection term is about 1 (e.g. Refs. (Browne et al. 1987; Aronson and Lofdahl 1993; Lefeuvre et al. 2014)). As the distance from the axis increases, both the $\overline{q^2}$ diffusion and production terms
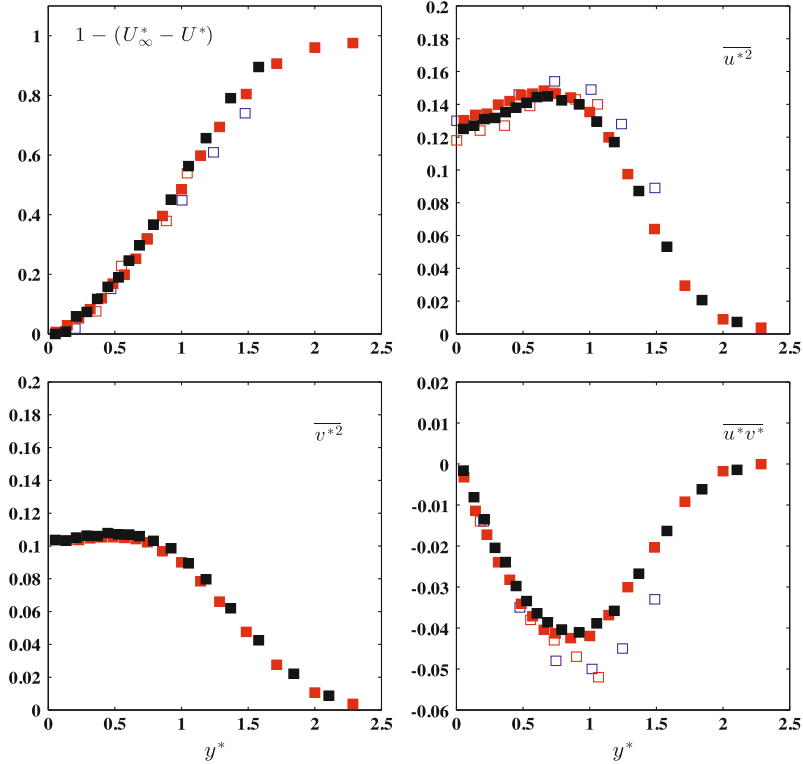
Fig. 1 Normalized mean velocity defect and Reynolds stresses for SC wake; present data: $x/d =$ 230, ■ $x/d = 270$, ■ Zhou and Antonia (1995): $x/d = 165$, ❑ $x/d = 375$, ❑

increase quickly and contribute significantly to the TKE budget. It is interesting to note that, in the region far from the wake centreline $y^* = 1.6$–2.5, both the production and dissipation terms are negligible but the $\overline{q^2}$ diffusion and advection terms contribute to the budget (they are approximately equal and of opposite sign). While the pressure diffusion term is small compared to the $\overline{q^2}$ diffusion term, they both satisfy the integral constraints by assuming symmetry with respect to $y^* = 0$, i.e. $\int_{-\infty}^{\infty} \frac{\partial \overline{vq^2}}{\partial y} dy = 0$ and $\int_{-\infty}^{\infty} \frac{\partial \overline{vp}}{\partial y} dy = 0$, indicating that the isotropic dissipation rate $\bar{\varepsilon}_{iso}$ is a good surrogate of $\bar{\varepsilon}$, as it was also observed in the intermediate wake of SC (Lefeuvre et al. 2014).
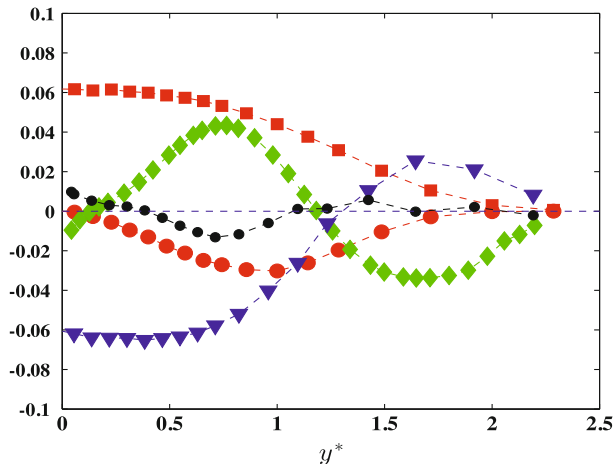
Fig. 2 Measured budget of average turbulent energy at $x/d = 270$ for SC wake. ■, isotropic dissipation; ◆, $\overline{q^2}$ diffusion; ▼, advection; ●, production; ●, pressure diffusion (by difference). Values normalized by L/U_d^3

4 Conclusions

The TKE transport equation (Eq. (1)) is tested in the far field of a SC wake and compared with that in a CC wake. It is found that there are two significant differences between SC and CC wakes associated with the TKE budget:

(1) the physical mechanism for transporting TKE along the axis is different from that in a CC wake. Indeed, for the SC wake, the $\overline{q^2}$ diffusion term is negligible compared to advection term along the axis and the advection and energy dissipation terms dominate the budget. In the CC wake, aside from the advection and energy dissipation terms, the diffusion term also contributes significantly to the budget.

(2) at the centerline of the wake, the gain of the energy due to the contributions from the advection and diffusion terms is equal to the loss due to the isotropic dissipation. This indicates that the isotropic dissipation rate $\bar{\varepsilon}_{iso}$ is a good surrogate of the mean TKE dissipation rate $\bar{\varepsilon}$.

References

Antonia RA, Browne LWB (1986) Anisotropy of the temperature dissipation in a turbulent wake. J Fluid Mech 163:393–403

Aronson D, Lofdahl L (1993) The plane wake of a cylinder: measurements and inferences on turbulence modeling. Phys Fluids 5:1433–1437

Browne LWB, Antonia RA, Shah DA (1987) Turbulent energy dissipation in a wake. J Fluid Mech 79:307–326

Lefeuvre N, Djenidi L, Antonia RA, Zhou T (2014) Turbulent kinetic energy and temperature variance budgets in the far wake generated by a circular cylinder. In: 19th Australasian Fluid Mechanics Conference Melbourne, Australia 8–11 Dec 2014

Lefeuvre N, Thiesset F, Djenidi L, Antonia RA (2014) Statistics of the turbulent kinetic energy dissipation rate and its surrogates in a square cylinder wake flow. Phys Fluids 26:095104

Zhou Y, Antonia RA (1995) Memory effects in a turbulent plane wake. Exp Fluids 19:112–120

Passive Scalar and Velocity Fields in a Turbulent Cylinder Near Wake

J.G. Chen, H.L. Cao, T.M. Zhou, R.A. Antonia and Y. Zhou

Abstract This work aims to provide an exploration of the spectral analogy between the enstrophy and the scalar dissipation rate, as well as between the passive scalar and the velocity vector fluctuations, especially in the context of the highly organized aspects that exist in the near wake. Measurements were taken in the wake of a heated circular cylinder at $x/d = 10$–40, with a Reynolds number of 2540. The resutls indicate that there is a reasonable analogy between the spectra corresponding to enstrophy and passive scalar dissipation rate, the small departures being caused by coherent motions. The spectral analogy between the streamwise velocity fluctuation u and the passive scalar θ is better than that between the velocity fluctuation vector q and θ. This is also closely related to the highly organised lateral velocity fluctuation v in this flow.

Keywords Passive scalar dissipation rate · Enstrophy · Spectral analogy · Turbulent wake

1 Introduction

There is a close analogy both in the spectral and physical space domains between passive scalar variance and turbulent kinetic energy in various flows (Fulachier and Antonia 1984), especially in the presence of mean velocity and temperature gradients. Likewise, an analogy also exists between the enstrophy $\omega_i \omega_i$ and the scalar

J.G. Chen · H.L. Cao · Y. Zhou (✉)
Shenzhen Graduate School, Harbin Institute of Technology, Shenzhen 518055, China
e-mail: zhouyu@hitsz.edu.cn

T.M. Zhou
School of Civil, Environmental and Mining Engineering, The University of Western
Australia, Crawley, WA 6009, Australia

R.A. Antonia
School of Engineering, University of Newcastle, Callaghan, NSW 2308, Australia

dissipation rate $\theta_{,i}\,\theta_{,i}$ (Antonia et al. 2009). In this paper, θ and ω_i denote the temperature and vorticity fluctuations and $\theta_{,i} \equiv \partial\theta/\partial x_i$, where $i = 1, 2$ and 3 represent the streamwise, lateral and spanwise directions, respectively, and are used interchangeably with x, y and z, and the summation rule is applied only to i. Nevertheless, it has yet to be clarified whether there is an analogy between θ and the velocity field in the turbulent near wake of a cylinder, a region which is characterised by distinctly coherent and three dimensional structures. In this work, we will address this issue and compare the spectra of the velocity fluctuation and the passive scalar in the turbulent near wake of a cylinder. The analogy between the passive scalar dissipation rate and enstrophy will also be examined. The physical mechanisms behind the possible analogy will be explored, especially in the context of the highly organized aspects that exist in the near wake.

2 Experimental Details

A probe consisting of 8 hot wires (4 x-wires) and four cold wires (e.g. Zhou et al. 2002a, 2012) were used to measure simultaneously the three components of the velocity and vorticity vectors, along with the fluctuating temperature gradient vector, at nominally the same point in the plane of mean shear at x/d = 10–40 in a heated cylinder wake. This allows the scalar dissipation rate and enstrophy to be calculated without assuming isotropy. The Reynolds number is 2540, based on the cylinder diameter d and free stream velocity U_∞. The wire separation is 2.0 and 2.7 mm for the X-hotwires and 2.5 and 2.2 mm for the cold wires in the lateral and spanwise directions, respectively. The maximum mean temperature excess, relative to the ambient fluid, is about 1.6, 1.5 and 1.3 °C on the centreline of the wake at x/d = 10, 20 and 40, respectively. The hot-wire length and diameter are about 0.5 mm and 2.5 μm, respectively. The cold wire length and diameters are about 0.5 mm and 0.63 μm. The Kolmogorov length scale (η) on the centreline is 0.13, 0.18, and 0.3 mm at x/d = 10, 20 and 40, respectively. The ratios of hot-wire length to the Kolmogorov length scales are therefore 3.85, 2.78, and 1.67 at the three x/d positions, respectively.

3 Results and Discussion

In this paper, the power spectral density functions F_β of β, which denotes either u, q, θ or $\theta_{,\alpha}$ and ω_α, are normalized such that $\int_0^\infty F_\beta\, dk^* = 1$, and k^* is the non-dimensional wavenumber defined by $2\pi f/U_\infty\eta$, where f is frequency. The spectrum of $\boldsymbol{q}$ is defined as $F_q = (\overline{uu}/\overline{qq})F_u + (\overline{vv}/\overline{qq})F_v + (\overline{ww}/\overline{qq})F_w$, where $q^2 \equiv u^2 + v^2 + w^2$. Similarly, the spectra of $\theta_{,i}\theta_{,i}$ and $\omega_i\omega_i$ are defined as $F_x = (\overline{\theta_{,1}\theta_{,1}}/\overline{\theta_{,i}\theta_{,i}})F_{\theta,1} + (\overline{\theta_{,2}\theta_{,2}}/\overline{\theta_{,i}\theta_{,i}})F_{\theta,2} + (\overline{\theta_{,3}\theta_{,3}}/\overline{\theta_{,i}\theta_{,i}})F\theta_{,3}$ and $F_\omega = (\overline{\omega_1\omega_1}/\overline{\omega_i\omega_i})F_{\omega1}\cdot + (\overline{\omega_2\omega_2}/\overline{\omega_i\omega_i})F_{\omega2}\cdot + (\overline{\omega_3\omega_3}/\overline{\omega_i\omega_i})F_{\omega3}$, respectively.

Figure 1 shows the power spectral density functions of $\omega_i\omega_i$ and $\theta_{,i}\theta_{,i}$ measured at y/L = 1 at three x/d positions, where L is the mean velocity half width. There is quite a reasonable analogy between the spectra of $\omega_i\omega_i$ and $\theta_{,i}\theta_{,i}$ at all stations, notwithstanding some small departures, especially at x/d = 10. The spectral analogy at low wavenumbers (say $k^* \leq 0.1$) is not as good as that at high wavenumbers (say $k^* \geq 0.1$). It seems plausible that large-scale coherent motions are responsible for the departure between the spectra of $\theta_{,i}\theta_{,i}$ and $\omega_i\omega_i$, particularly at low wavenumbers. This is verified by phase-averaged results shown in Figs. 2 and 3.

Figure 2 is the phase-averaged coherent enstrophy and scalar dissipation rate, which clearly reveals the markedly different coherent structures between $\theta_{,i}\theta_{,i}$ and $\omega_i\omega_i$ at all three x/d positions (See Zhou et al. (2002b) for details about the phase
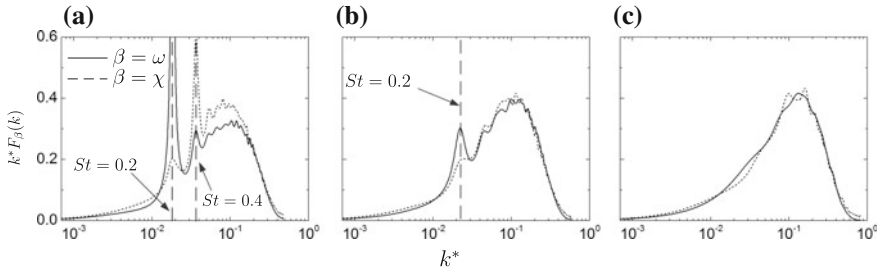
Fig. 1 Pre-multiplied power spectral density functions of ω and χ measured at the y/L = 1 where L is the mean velocity half width. **a** x/d = 10, L = 0.73d; **b** 20, 1.10d; **c** 40, 1.87d
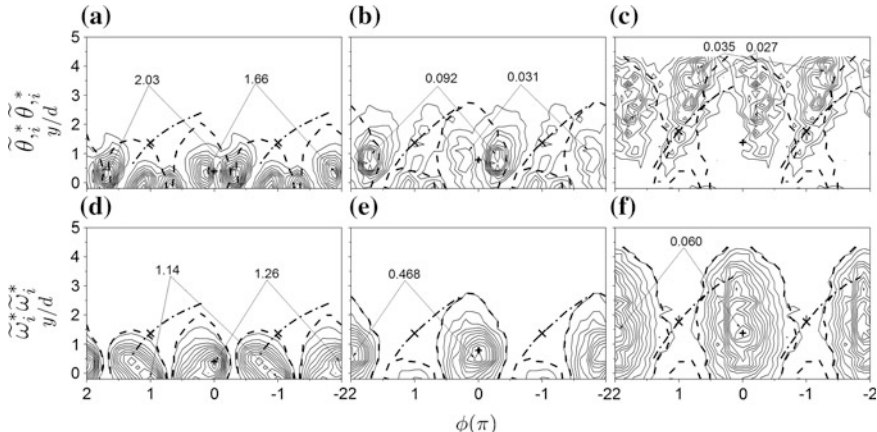
Fig. 2 Phase-averaged coherent scalar dissipation rate and enstrophy at x/d = 10–40. **a–c**: x/d = 10, 20, 40; contour intervals = 0.18, 0.010, 0.004. **d–f**: 10, 20, 40; 0.11, 0.043, 0.005. +, centers of vortices; ×, saddle points. The thicker dashed lines denote the outermost vorticity contours of coherent spanwise vorticity $\widetilde{\omega_z^*}$, and the dash-dot lines denote diverging separatrix. The flow is from *left* to *right*
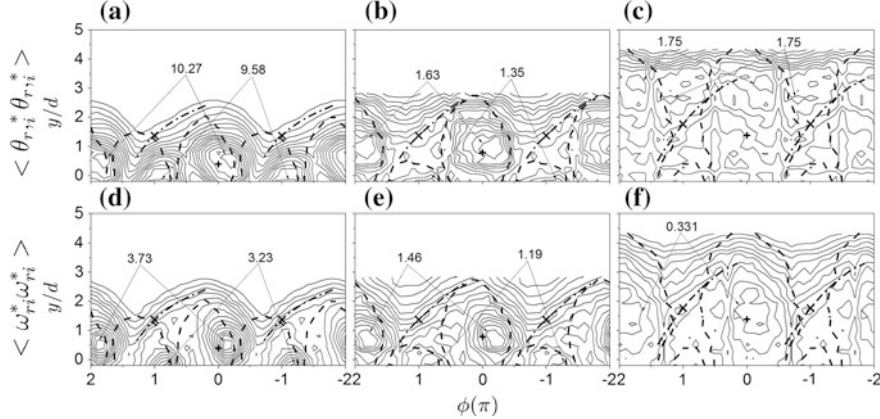
Fig. 3 Remainder of scalar dissipation rate and enstrophy at x/d = 10–40. **a–c**: x/d = 10, 20, 40; contour intervals = 0.68, 0.09, 0.15. **d–f**: 10, 20, 40; 0.25, 0.09, 0.029

averaging technique). Two concentrations can be found in $\theta_{,i}^{*}\theta_{,i}^{*}$ (Fig. 2a–c) immediately downstream and upstream of the vortex centre, while $\widetilde{\omega}_i^{*}\widetilde{\omega}_i^{*}$ display only one concentration at the vortex centre. That is why there is a peak corresponding to St = 0.4 in the spectrum of scalar dissipation rate (especially at x/d = 10 where the fluid motions are highly organized), while the peak of enstrophy occurs at a wavenumber corresponding to St = 0.2, which is largely responsible for the departures between the spectra. The different features of the coherent enstrophy and scalar dissipation rate are attributed to their different generation mechanisms. For $\theta_{,i}^{*}\theta_{,i}^{*}$, the main production is associated with the temperature gradient between cold fluid engulfed by the coherent motion from the freestream and the warm fluid in the wake. Specifically, as is evident in the θ contours (not shown here), the downstream concentration within one vortex structure results from an interaction between the warm fluid in the wake and the cold fluid engulfed from the freestream on the same side of the vortex, while the upstream concentration is due to an interaction between the warm fluid in the wake and the cold fluid from the freestream on the other side of the vortex. The concentration of $\widetilde{\omega}_i^{*}\widetilde{\omega}_i^{*}$ is closely linked with the vortical structures and thus its contours resemble those of the coherent spanwise vorticity (cf. Fig. 11 in Zhou et al. 2003) and the maxima coincide with the vortex centres.

Figure 3 shows the remainder (corresponding to incoherent motions) of enstrophy and scalar dissipation rate. In contrast to the evident difference in their coherent structures, the remainder contours of $\theta_{,i}\theta_{,i}$ and $\omega_i\omega_i$ are quite similar to each other, reflecting the analogous distributions of F_x and F_ω at high wavenumbers (Fig. 1).

Figure 4 presents F_β for $\beta = q$, u and θ at y/L = 1 at all three x/d positions, The distribution of F_θ seems closer to that of F_u than F_q. This is different to what Fulachier and Antonia (1984) observed in the self-preserving wake, at least away
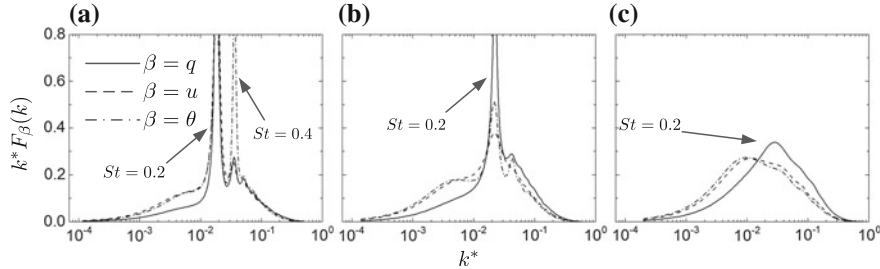
Fig. 4 Pre-multiplied spectral density functions of q, u and θ for $y/L = 1$ at three x/d positions. L stands for the mean velocity half-width. **a** $x/d = 10$, $L = 0.73d$; **b** 20, 1.10d; **c** 40, 1.87d

from the wake centreline. The existence of a local mean shears evidently helped in terms of promoting mixing. In the near wake, the lateral velocity fluctuation v is highly organized. Since v contributes significantly to q in the near wake, q is more organized than u or θ. The contribution due to the coherent motion to $\overline{q^2}$ is 52, 21.1 and 6.8 % at $x/d = 10$, 20 and 40, respectively. In contrast, the contribution to $\overline{u^2}$ is 22.0, 5.7, and 1.3 % and that to $\overline{\theta^2}$ are 24.3, 8.1, and 2.8 %, respectively. Therefore, it is not surprising that F_q in Fig. 4a–c is much larger than F_θ or F_u at about a wavenumber which corresponds to $St = 0.2$ and deviates from F_θ and F_u at other wave numbers. Note that the coherent contributions to $\overline{u^2}$ and $\overline{\theta^2}$ are comparable at the same x/d, which may support at least partially the analogy between F_u and F_θ. The small departure between F_u and F_θ may reflect the different effects of the highly organized v component on u and θ.

4 Conclusions

(1) The spectra of enstrophy and scalar dissipation rate are reasonably analogous in the turbulent near wake. The small departures in Fig. 1 originate from the difference in the highly organized coherent structures.
(2) The spectrum of θ is in closer analogy to that of u than that of q, in distinct contrast to the observations in the self-preserving far wake, at least away from the centreline. This is caused by the large coherent contribution to $\overline{q^2}$, due to the highly organized v component, which exceeds greatly the coherent contributions to $\overline{u^2}$ or to $\overline{\theta^2}$.

References

Antonia RA, Abe H, Kawamura H (2009) Analogy between velocity and scalar fields in a turbulent channel flow. J Fluid Mech 628:241–268

Fulachier L, Antonia RA (1984) Spectral analogy between temperature and velocity fluctuations in several turbulent flows. Int J Heat Mass Trans 27:987–997

Zhou T, Antonia RA, Chua L (2002a) Performance of a probe for measuring turbulent energy and temperature dissipation rates. Exp Fluids 33:334–345

Zhou T, Cao HL, Zhou Y, et al (2012) Phase-average analysis of three-dimensional vorticity and temperature dissipation rate in the near field of a heated circular cylinder wake. In: Proceedings of 18th Australasian fluid mechanics conference. Launceston, Tasmania

Zhou T, Zhou Y, Yiu MW et al (2003) Three-dimensional vorticity in a turbulent cylinder wake. Exp Fluids 35:459–471

Zhou Y, Zhang HJ, Yiu MW (2002b) The turbulent wake of two side-by-side circular cylinders. J Fluid Mech 458:303–332

Visualization of the Flow in the Wake of a Finite-Height Square Prism

R. Chakravarty, N. Moazamigoodarzi, D.J. Bergstrom and D. Sumner

Abstract Flow over a finite-height surface-mounted square prism of aspect ratio AR = 3 (AR = H/D where H is the height and D is the prism width) at a Reynolds number Re = 500 has been investigated using the Snapshot Proper Orthogonal Decomposition (POD) method. In particular, the instantaneous velocity fields in three horizontal spanwise planes at y/D = 1, 2 and 3 generated by Large Eddy Simulation (LES) have been studied to gain insight into the vortical structures in the prism wake. The study tracked the development of the prism wake over a single period using the most energetic POD modes. A scatter plot of the first two POD temporal coefficients successfully extracted the phase information of the flow field, and a reconstruction of the fluctuating velocity field using the first two POD modes was used to approximate the phase-averaged flow structures. Different POD modes can be associated with either anti-symmetric or symmetric vortex shedding characteristics of the wake.

Keywords Square prism · Free end · Wake · Proper orthogonal decomposition

1 Introduction

The turbulent wake of flows over surface-mounted finite-height square prisms exhibit several complex features and are of considerable interest in engineering design and turbulent flow analysis. While time-averaged flow features have been the focus of several studies, the instantaneous topologies of the wake flow field have been studied less frequently. Finite prism wakes have been associated with both anti-symmetric and symmetric vortex shedding motions. Some recent studies have attempted to propose a unifying theory based on the dynamics of the vortical structures shed from the prism (Wang et al. 2009; Bourgeois et al. 2011). Both of

R. Chakravarty · N. Moazamigoodarzi · D.J. Bergstrom (✉) · D. Sumner
Department of Mechanical Engineering, University of Saskatchewan, Saskatoon, Canada
e-mail: don.bergstrom@usask.ca

the studies above considered finite square prisms of larger aspect ratio for relatively high Reynolds numbers. In the present investigation, a shorter prism is considered, i.e. AR = H/D = 3 (where H is the height and D is the prism width), for a much lower Reynolds number, i.e. Re = 500.

2   Computational and Flow Visualization Methodologies

The filtered Navier-Stokes equations with a finite volume discretization were solved using the fractional step method. Time advancement was implemented using the Crank-Nicholson method and an algebraic multigrid method was used to accelerate the solution of the pressure-correction equation. The subgrid-scale (SGS) stress terms were modeled using a localised Dynamic Smagorinsky model. A structured, Cartesian grid with $128 \times 144 \times 96$ control volumes in the x (freestream), y (spanwise) and z (transverse) directions, respectively, was used to discretize the flow domain. The prism was located approximately $3D$ from the inlet plane and the blockage ratio was approximately 7 %.

The POD analysis (Sirovich 1987) of the instantaneous velocity fields in three horizontal planes at $y/D = 1$, 2 and 3 was performed. The POD methodology can be used to extract motions of different scales within the evolving dynamics of a flow. The POD is applied to decompose the time-dependent fluctuating part of the flow field into an orthonormal system of spatial modes or eigenfunctions, $v_m(x)$, and associated temporal coefficients $a_n(t)$, i.e.

$$v(x_i, t) = v_o(x_i) + \sum_{m=1}^{M} a_m(t)v_m(x_i) \tag{1}$$

The coefficients are obtained from the solution of an eigenvalue problem based on the covariance matrix of the velocity field. The relative magnitude of the eigenvalues (λ_m) determines the respective energy contributions in each mode. Finally, the POD modes are computed as

$$v_m(x_i) = \frac{1}{M\lambda_m} \sum_{n=1}^{M} a_m(t_n)v(x_i, t_n) \tag{2}$$

In this case, 100 snapshots of the time-resolved fluctuating velocity field equally distributed in time across approximately one shedding cycle of the flow were used to provide the data base for POD analysis. The temporal coefficients obtained from the POD analysis were also analysed to investigate the periodic features of this flow.

3   Results and Discussion

The POD was successful in capturing the dominant mechanisms of the fluctuating velocity fields with only a few energy modes as shown in Fig. 1. Across the three planes, the first energy mode captured 24–30 % of the total energy with the first 10 modes cumulatively capturing close to 90 % of the total energy. A sharp drop in energy across the first two energy modes was observed for the $y/D = 3$ plane, possibly due to the influence of the downwash from the free end, which creates a strong out-of-plane velocity contribution that is neglected in the two-dimensional (2D) POD analysis. The energy drop was more gradual in the other planes, suggesting that the flow features in these planes were less influenced by the downwash and upwash effects from the free end and the ground plane, respectively.

The variation of the POD temporal coefficients indicated strong periodicity of the flow in all three planes, which was not expected for such a low aspect ratio prism. Analysis of the first four temporal coefficients yields a dominant frequency that corresponds to a Strouhal number of $St = 0.127$, which is in excellent agreement with previous studies (Okajima 1982). Figure 2 shows a scatter plot of the first two normalized temporal coefficients $a_1^* = a_1/(r_1(2\lambda_1))^{1/2}$ versus $a_2^* = a_2/(r_2(2\lambda_2))^{1/2}$ for all three y/D planes. These points are distributed close to a unit circle; each point on the circle corresponds to the phase angle of the vortex shedding, as discussed in Van Oudheusden et al. (2005).

To further assess the wake structure and flow periodicity, two snapshot reconstructions of the fluctuating velocity field separated by approximately half a period were performed to illustrate flow features that are almost similar but opposite in phase. A low-dimensional reconstruction using only the first two energy modes of the velocity fluctuation field for the 10th and 50th snapshots is shown in Fig. 3. Both reconstructions are consistent with anti-symmetric vortex shedding but show

Fig. 1 POD energy distribution percentage for the $y/D = 1$, 2 and 3 planes
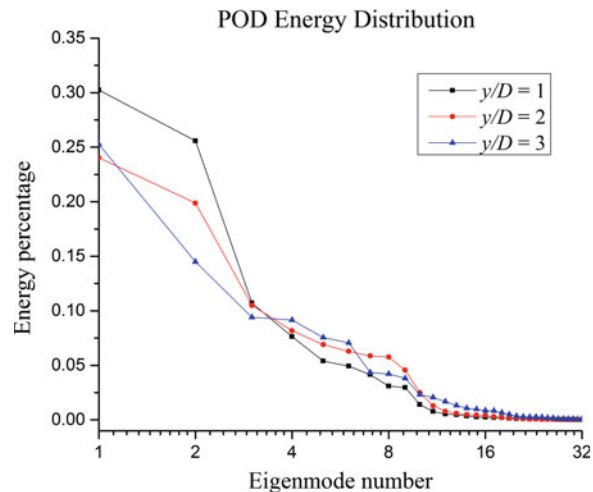
Fig. 2 Scatter plot correlation of first two normalized POD temporal coefficients (a_1*, a_2*) for $y/D = 1$, 2 and 3
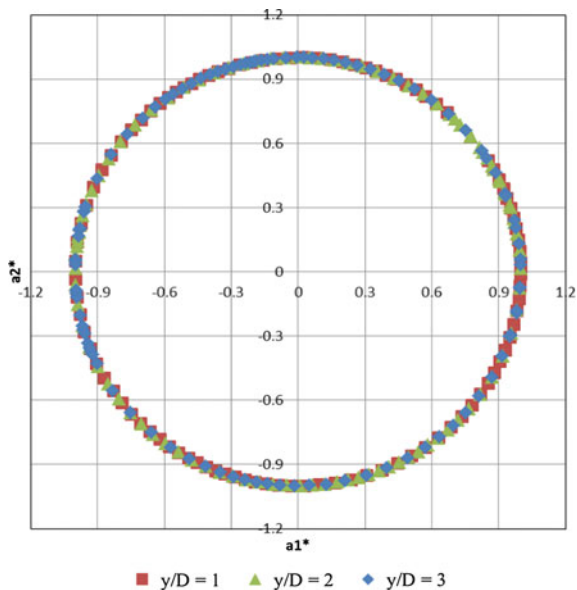
Fig. 3 Transverse (w) velocity contour lines for the POD reconstruction using the first two eigenmodes on the $y/D = 2$ plane of the (**a**) 10th, and (**b**) 50th snapshot
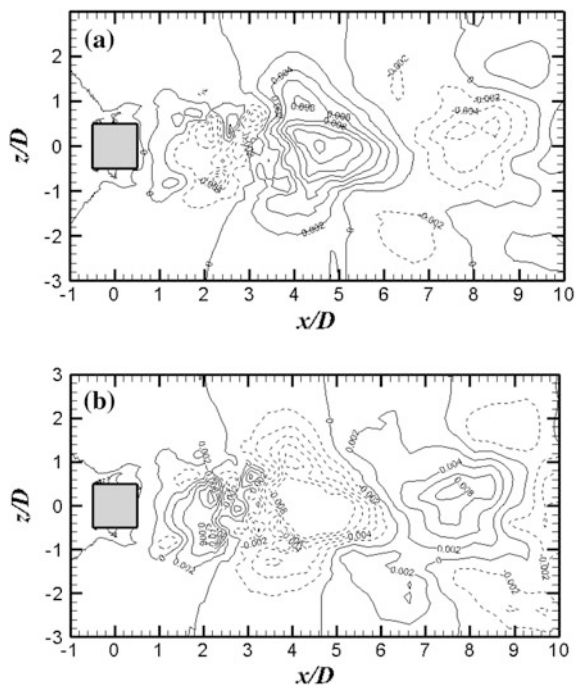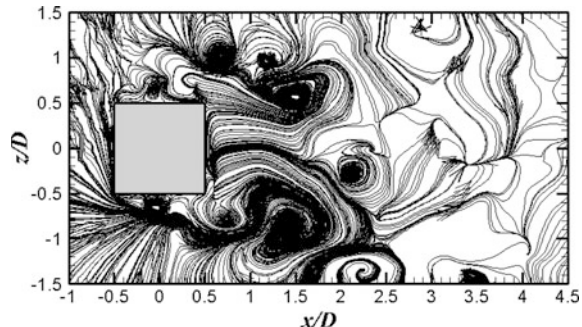
features which are opposite in phase. This indicates that the first two modes are associated with anti-symmetric vortex shedding motions.

Figure 4 shows the plot of streamlines for the 3rd energy mode in the $y/D = 1$ plane. The streamlines reveal some symmetric vortex structures in the near-wake of the prism. This suggests that whereas the first two modes relate to anti-symmetric vortex shedding, the third energy mode may be associated with more symmetric structures of the flow field as seen in Wang et al. (2014).

4   Conclusions

POD analysis based on an LES simulation of a low Reynolds number turbulent flow over a surface-mounted finite-height square prism in three planes at $y/D = 1$, 2 and 3 for an AR = 3 prism was performed. The POD temporal coefficients and a lower order POD reconstruction using the first two modes were used to characterize the periodic and phase characteristics of the wake, even for this low aspect ratio prism. The temporal coefficients show a sinusoidal variation in all three planes reflecting the periodic nature of the wake. Lower order POD reconstructions effectively reveal the phase-averaged realizations of anti-symmetric vortex shedding in the wake of the prism, while the third energy mode gives some indication of the symmetric vortex shedding.

References

Bourgeois JA, Sattari P, Martinuzzi RJ (2011) Alternating half-loop shedding in the turbulent wake of a finite surface-mounted square cylinder with a thin boundary layer. Phys Fluids 23 (9):095101

Okajima A (1982) Strouhal numbers of rectangular cylinders. J Fluid Mech 123:379–398

Sirovich L (1987) Turbulence and the dynamics of coherent structures. Part I: coherent structures. Q Appl Math 45:561–571

Van Oudheusden BW, Scarano F, van Hinsberg NP, Watt DW (2005) Phase-resolved characterization of vortex shedding in the near wake of a square-section cylinder at incidence. Exp Fluids 39:86–98

Wang HF, Zhou Y (2009) The finite-length square cylinder near wake. J Fluid Mech 638:453–490

Wang HF, Cao HL, Zhou Y (2014) POD analysis of a finite-length cylinder near wake. Exp Fluids 55(8):1–15

A Three-Dimensional Heat
and Momentum Transport Model
for a Turbulent Cylinder Wake

H.L. Cao, J.G. Chen, T.M. Zhou, R.A. Antonia and Y. Zhou

Abstract All three components of the velocity and vorticity vectors, along with the fluctuating temperatures, were simultaneously measured, at nominally the same point in the flow, with an eight hotwire vorticity probe and four cold-wire probes. The phase-average data unveils that the spanwise velocity is greatly influenced by the rib-like structures. A 3-D conceptual model is proposed for heat and momentum transport, which complements the previous 2-D model and provides physical insight for the role the rib structures play.

Keywords Heat transport · Rib-like structure · Vorticity vector

1 Introduction

The combined momentum and heat transport characteristics associated with the organization of the intermediate wake have been investigated by Matsumura and Antonia (1993), who addressed only two-dimensional aspects of the flow. Although simultaneously measured previously (Zhou et al. 2003), the three components of the velocity and vorticity vectors have never been connected directly with the three components of the heat flux vector. As a result, the three dimensional (3D) aspects, a crucial facet of turbulence, of the heat and momentum transport are missing in the

H.L. Cao · J.G. Chen · Y. Zhou (✉)
Shenzhen Graduate School, Harbin Institute of Technology, Shenzhen 518055, China
e-mail: zhouyu@hitsz.edu.cn

T.M. Zhou
School of Civil, Environmental and Mining Engineering, The University of Western
Australia, Perth, WA 6009, Australia

R.A. Antonia
School of Engineering, University of Newcastle, Newcastle, Nsw 2308, Australia

literature. This work aims to gain an improved understanding of the three-dimensional aspects of the turbulent structures, passive scalar transport and their streamwise evolution in the turbulent cylinder wake.

2 Exprimental Details

All three components of velocity, vorticity and temperature fluctuations were measured with an eight hotwire vorticity probe and four cold-wire probes (Zhou et al. 2012) in the plane of mean shear at x/d = 10, 20 and 40, where x is the streamwise distance from the cylinder axis. The Reynolds number Re is 2540, based on the cylinder diameter d (= 12.7 mm) and free stream velocity U_∞ (= 3 m/s). The maximum mean temperature excess Θ_0, relative to the ambient, is about 1.6, 1.5 and 1.3°C on the centerline of the wake for x/d = 10, 20 and 40, respectively. The u, v, w and θ measured by this probe may be considered to be obtained at nominally the same point. A phase-averaging method based on Zhou et al.'s work (2002) is modified to capture more accurately the coherent structures. The total number of detections are about 1980, 1700, and 1050 for x/d = 10, 20 and 40, respectively, which have been confirmed to be adequate for the selected data for phase-averaging to be representative to the flow.

3 Results and Discussion

The streamwise and lateral velocity contours are consistent well with Matsumura and Antonia's (1993) data and are therefore not shown here. Figure 1 presents the phase-averaged spanwise velocity component $\widetilde{w}^*$. Asterisk in this paper denotes normalization by d, U and/or Θ_0. The upstanding cross (+) denotes the vortex centre, identified with the maximum vorticity concentration in the phase-averaged spanwise vortcity contours, and the thick broken lines mark the border of the spanwise vortex, corresponding to 25 % of the maximum spanwise vorticity. The broken lines through the saddle points (×) is the diverging separatrix.
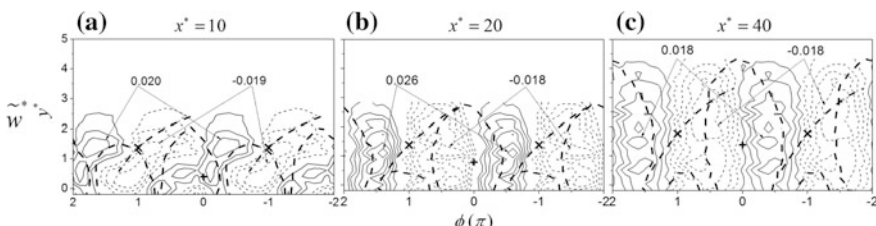
Fig. 1 Phase-averaged spanwise velocity $\widetilde{w}^*$, contour interval, **a–c**: 0.0066, 0.0038, 0.0052

At $x^* = 10$, the oppositely signed concentration of $\widetilde{w}^*$ occurs on the opposite side of the diverging separatrix, but only on the lower side of the separatrix (Fig. 1a). The observation is reasonable since the rib structure is aligned roughly with the diverging separatrix, such a structure would induce the spanwise motions of opposite senses on the either side of the diverging separatrix (e.g. Wu et al. 1996). The $\widetilde{w}^*$ contours evolve into a rather different structure at $x^* = 20$ and 40, being nearly anti-symmetrical with respect to $\phi = 0$ (Fig. 1b, c), which is analogous but opposite in sign to that of the $\widetilde{v}^*$ contours (not shown).

Figure 2 shows the phase-averaged vorticity vectors $\widetilde{\omega}^* \equiv (\widetilde{\omega}_x^*, \widetilde{\omega}_y^*, \widetilde{\omega}_z^*)$, coherent heat flux vectors $\widetilde{q}^* \equiv (\widetilde{u^*\theta}^*, \widetilde{v^*\theta}^*, \widetilde{w^*\theta}^*)$ and incoherent (or remainder) heat flux vectors $\langle q_r^* \rangle \equiv (\langle u_r^*\theta_r^* \rangle, \langle v_r^*\theta_r^* \rangle, \langle w_r^*\theta_r^* \rangle)$. The 3-D vectors are presented in terms of a 2-D vector field (streamwise and lateral components) and the iso-contours of the spanwise component. At $x^* = 10$, the vorticity vectors largely occur within the spanwise vortex roll with the same sign as $\widetilde{\omega}_z^*$ and appears nearly parallel to the wake centerline (Fig. 2a), due to significantly larger magnitude of $\widetilde{\omega}_x^*$ than that of $\widetilde{\omega}_y^*$. Further downstream, the vorticity vectors $(\widetilde{\omega}_x^*, \widetilde{\omega}_y^*)$ tend to point towards the upstream saddle point. At $x^* = 40$, the vectors are almost aligned with the diverging
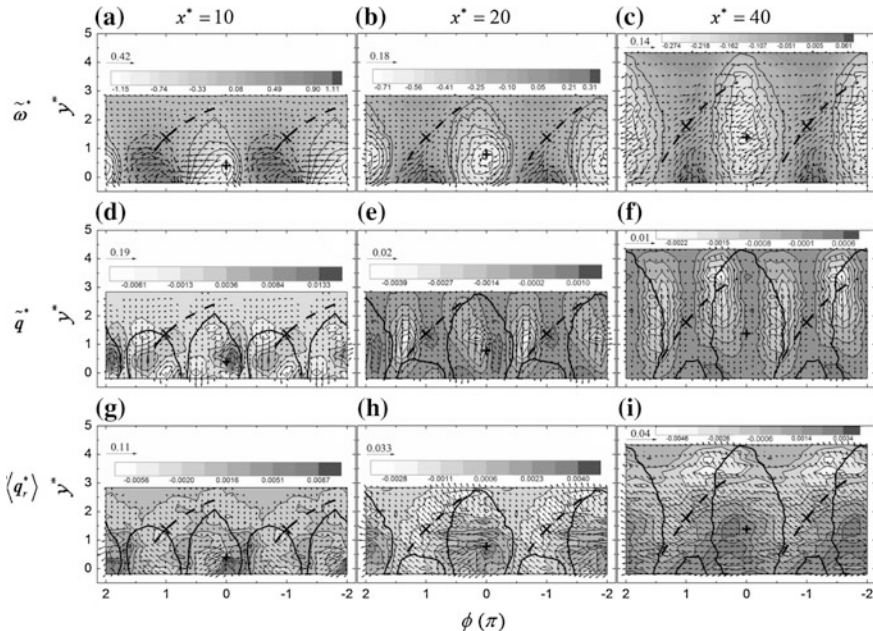
Fig. 2 Phase-averaged vorticity, coherent and incoherent heat flux vectors. **a–c** $\widetilde{\omega}^*$: $(\widetilde{\omega}_x^*, \widetilde{\omega}_y^*)$ is given by vectors and $\widetilde{\omega}_z^*$ is given by the iso-contours. **d–f** $\widetilde{q}^*$: $(\widetilde{u^*\theta}^*, \widetilde{v^*\theta}^*)$ is given by vectors and $\widetilde{w^*\theta}^*$ is given by the iso-contours. **g–i** $\langle q_r^* \rangle$: $(\langle u_r^*\theta_r^* \rangle, \langle v_r^*\theta_r^* \rangle)$ is given by vectors and $\langle w_r^*\theta_r^* \rangle$ is given by the iso-contours

separatrix (Fig. 2c) and are visible only at the border of the spanwise vortex, which reflects the predominant contribution of the longitudinal rib-like structures to $\widetilde{\omega}_x^*$ and $\widetilde{\omega}_y^*$.

Immediately downstream of the vortices, $\widetilde{q}^* = (\widetilde{u^*\theta^*}, \widetilde{v^*\theta^*})$ points either upwards or downwards crossing the wake centerline (Fig. 2d), implying that the coherent motion contributes significantly to the lateral heat flux for $|y^*| < 1.0$. At $x^* = 10$, oppositely signed $\widetilde{w^*\theta^*}$ concentrations occur on the two sides of the diverging separatrix. This is attributed to the induced motion of the rib-like structures along the diverging separatrix, as is confirmed by the coherent spanwise velocity contour $\widetilde{\omega}$ (Fig. 1a). Note that a local maximum of $\widetilde{w^*\theta^*}$ also occurs near the vortex center, suggesting a significant heat transport within the vortex due to the spanwise contortion of the vortex rolls (Hussain and Hayakawa 1987). At $x^* = 20$, the heat flux vector moves upwards and starts to become aligned with the diverging separatrix near the saddle point (Fig. 2e). At $x^* = 40$, the heat flux vector is nearly aligned to the y direction and its magnitude is significant near the vortex border. Negative $\widetilde{w^*\theta^*}$ concentrations are present at both upstream and downstream of each vortex (Fig. 2f).

The incoherent heat flux vector $\langle q_r^* \rangle$ behaves quite differently from $\widetilde{q}^*$. At $x^* = 10$, its streamwise component is comparable to the lateral component, resulting in the vectors $\langle q_r^* \rangle$ pointing upstream within the vortex, almost perpendicular to the diverging separatrix, suggesting the incoherent motion is responsible for heat transport out of the vortices. At $x^* = 20$, a significant amount of $\langle q_r^* \rangle$ point upstream away from the vorticity contour and across the diverging separatrix (Fig. 2h), indicating the incoherent motion contributes to the heat transport significantly for $y^* > 1.0$. At $x^* = 40$, $\langle q_r^* \rangle$ is evenly distributed and directed upstream (Fig. 2i). Clearly, the heat transport by the incoherent motion remains important even near the wake centerline.

A 3D conceptual model (Fig. 3) is proposed based on the present experimental data for the momentum and heat transport in the turbulent near wake. For simplicity, the spanwise rolls are drawn as two-dimensional structures. The rib-like structures are drawn as counter-rotating longitudinal vortices. Part of engulfed cold flow is drawn into the alleyway between Vortices I and II, the remaining flow passes through the saddle point and reaches the braid region. The latter is further bifurcated into two flows and percolate through the rib-structures, as confirmed by the opposite-signed $\widetilde{w}^*$ contour on the two sides of diverging separatrix (Fig. 1a). The 3-D coherent heat flux vector are treated as the predominant heat flux vector $\widetilde{q}_{x,y}$ in the plane of mean shear and a spanwise component $\widetilde{q}_z$. The $\widetilde{q}_{x,y}$ located between the saddle point and the wake centerline is directed upwardly (Fig. 2d), which contributes to the transport of heat away from the centerline to the freestream. While $\widetilde{q}_z$ induced by rib-like structures accounts for transporting heat along the spanwise direction. The incoherent heat flux occurring at the shaded quadrant is
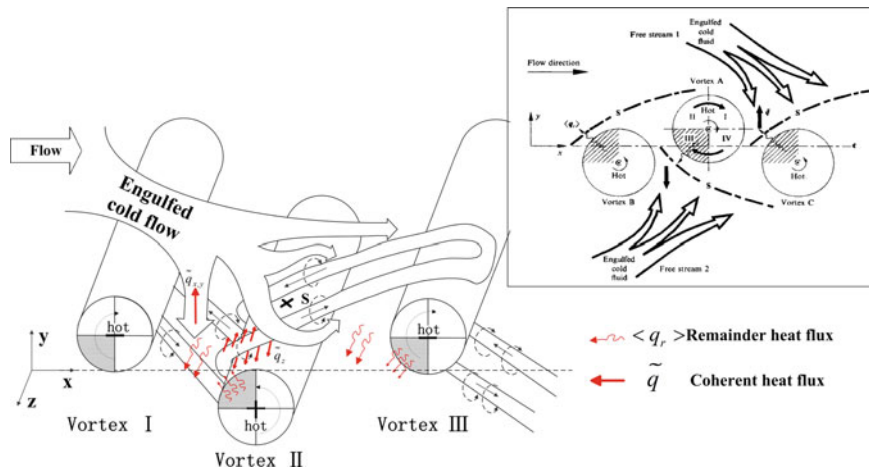
Fig. 3 3D conceptual model of momentum and heat transport at $x/d = 10$, as compared with the 2D model (inset) of Matsumura and Antonia (1993). The thick and thin red arrows denote the coherent and remainder heat fluxes respectively

mainly responsible for the heat transport out of the vortex core region, which can be also observed in the alleyway between two consecutive vortices (Fig. 2g). Compared with Matsumura and Antonia's (1993) 2D model, this model accounts more accurately for the role played by the rib-like structures and the spanwise component of heat flux in transporting heat and momentum. As x^* increases, spanwise roll and rib-like structures gradually decay and break into small-scale three-dimensional vortices, enhancing the incoherent motion and playing a more important role in heat transport between two neighboring vortices at $x^* = 40$ (Fig. 2i).

4   Conclusion

The streamwise evolution of vorticity and heat transport of a slightly heated turbulent wake has been experimentally investigated in terms of three-dimensional aspects. It has been found that the spanwise velocity is greatly influenced by the rib-like structures at $x/d = 10$. A 3-D conceptual model is proposed to account more accurately for the role played by the rib-like structures in transporting heat and momentum.

References

Hussain AKMF, Hayakawa M (1987) Eduction of large-scale organized structures in a turbulent plane wake. J Fluid Mech 180:193–229

Matsumura M, Antonia RA (1993) Momentum and heat transport in the turbulent intermediate wake of a circular cylinder. J Fluid Mech 250:651–668

Wu J, Sheridan J, Welsh MC et al (1996) Three-dimensional vortex structures in a cylinder wake. J Fluid Mech 312:201–222

Zhou T, Cao H, Zhou Y, Hao Z, Cheng L (2012) Phase-average analysis of three-dimensional vorticity and temperature dissipation rate in the near field of a heated circular cylinder wake. In: Proceedings of 18th Australasian Fluid Mechanics Conference, Launceston, Australia

Zhou T, Zhou Y, Yiu MW et al (2003) Three-dimensional vorticity in a turbulent cylinder wake. Exp Fluids 35:459–471

Zhou Y, Zhang HJ, Yiu MW (2002) The turbulent wake of two side-by-side circular cylinders. J Fluid Mech 458:303–332

Visualization of the Flow Above the Free End of a Finite Cylinder

R. Chakravarty, N. Rostamy, D.J. Bergstrom and D. Sumner

Abstract Flow over surface-mounted circular cylinders of finite height, with aspect ratios AR = 3 and 7 (AR = *H/D*, where *H* and *D* are the cylinder's height and diameter, respectively), at a Reynolds number Re = 4.2×10^4, has been investigated using the snapshot proper orthogonal decomposition (POD) method and the swirling strength criterion. The instantaneous velocity fields in two spanwise elevations above the cylinder's free end, at z/D = 0.016 and 0.08, were generated by a two-component particle image velocimetry (PIV) system. Of interest was to identify turbulent flow structures of different scales within the free-end flow field, and investigate how the AR affects these structures.

Keywords Finite cylinder · Free end · Wake · Proper orthogonal decomposition

1 Introduction

Flows over cylinders have been realized in several real-world applications like chimneys, buildings and tanks. Unlike the two-dimensional cylinder, the flow over a finite-height cylinder, one which is oriented normal to a ground plane, is strongly three-dimensional and far more complex due to flow over the free end and the flow near the cylinder-ground plane junction. Studies of the free-end flow field (Fig. 1) have shown varying analyses of the flow topography, e.g., Kawamura et al. (1984), Roh and Park (2003), Hain et al. (2008). In the present study, proper orthogonal decomposition (POD) and the swirling strength criterion are used to study the fluctuating velocity field above a finite cylinder's free end.

R. Chakravarty · N. Rostamy · D.J. Bergstrom (✉) · D. Sumner
Department of Mechanical Engineering, University of Saskatchewan, Saskatoon, Canada
e-mail: don.bergstrom@usask.ca
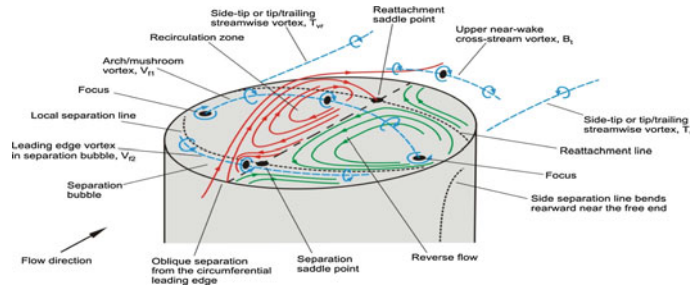
Fig. 1 Flow pattern above the free end of a surface-mounted circular cylinder of finite height

2 Experimental Approach and Numerical Methodology

Low-speed wind tunnel experiments were performed at a Reynolds number of $Re = 4.2 \times 10^4$ based on the cylinder diameter D. Finite cylinders of $AR = H/D = 3$ and 7 (where H is the cylinder height) were placed normal to a ground plane. The boundary layer thickness was $\delta/D = 1.6$. Two-component velocity measurements were made with particle image velocimetry (PIV) in horizontal (x–y) planes at different elevations (z/D) above the free end. In each plane, 528 image pairs were acquired; further details are given in Rostamy et al. (2014).

The POD analysis of the instantaneous velocity fields was performed using the snapshot method (Sirovich 1987), to help identify fluid motions of different scales. The POD is applied to decompose the time-dependent fluctuating part of the flow field into an orthonormal system of spatial modes or eigenfunctions, $v_m(x)$, and associated temporal coefficients $a_n(t)$, i.e.

$$v(x_i, t) = v_0(x_i) + \sum_{m=1}^{M} a_m(t) v_m(x_i) \qquad (1)$$

The swirling strength criterion (Chong et al. 1990) was also used on the highest POD energy mode snapshot to visualize the vortex structures. However, given only two-dimensional (2D) data were available, it was presumed that the regions where the 2D velocity gradient would have complex eigenvalues would be indicative of rotational vorticity.

3 Results and Discussion

The dominant components of the fluctuating velocity field were successfully captured by the POD technique using only a few energy modes. In all the measurement planes, the first mode captured from 13–23 % of the total energy, with the first 10

Fig. 2 POD energy distribution percentage for the $z/D = 1, 2$ and 3 planes
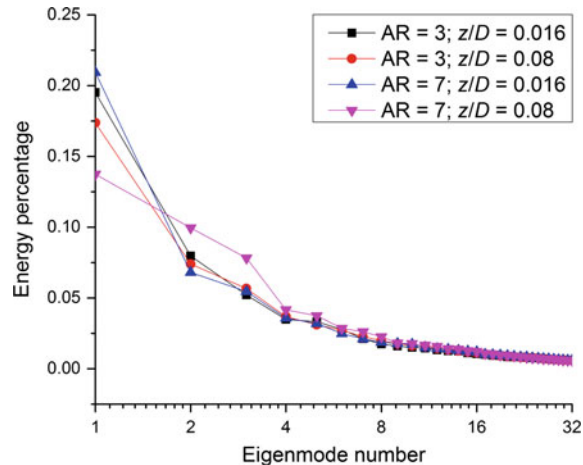
snapshots capturing close to 50 % of the total energy, and around 100–120 snapshots cumulatively capturing 90 % of the total energy. Figure 2 shows the energy distribution for the POD modes in both planes across both cylinder aspect ratios for the first 32 modes. The temporal coefficients of the first few POD modes was analyzed, and no flow periodicity was determined from its investigation; this is consistent with an absence of a strong periodic signal in the upper wake (Sumner 2013).

Figure 3 shows the swirling strength criterion contours and velocity vectors for the first energy mode on the $z/D = 0.016$ plane for the AR = 3 cylinder. Strong vortex structures are noticed near the side-tips of the circular plane, which
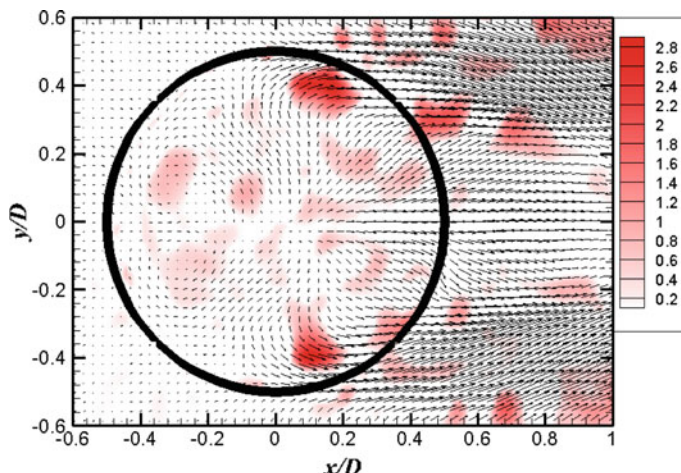
Fig. 3 Swirling strength contour superimposed over the velocity vectors for the first energy mode extracted from the POD bases, in the $z/D = 0.016$ plane for the AR = 3 cylinder
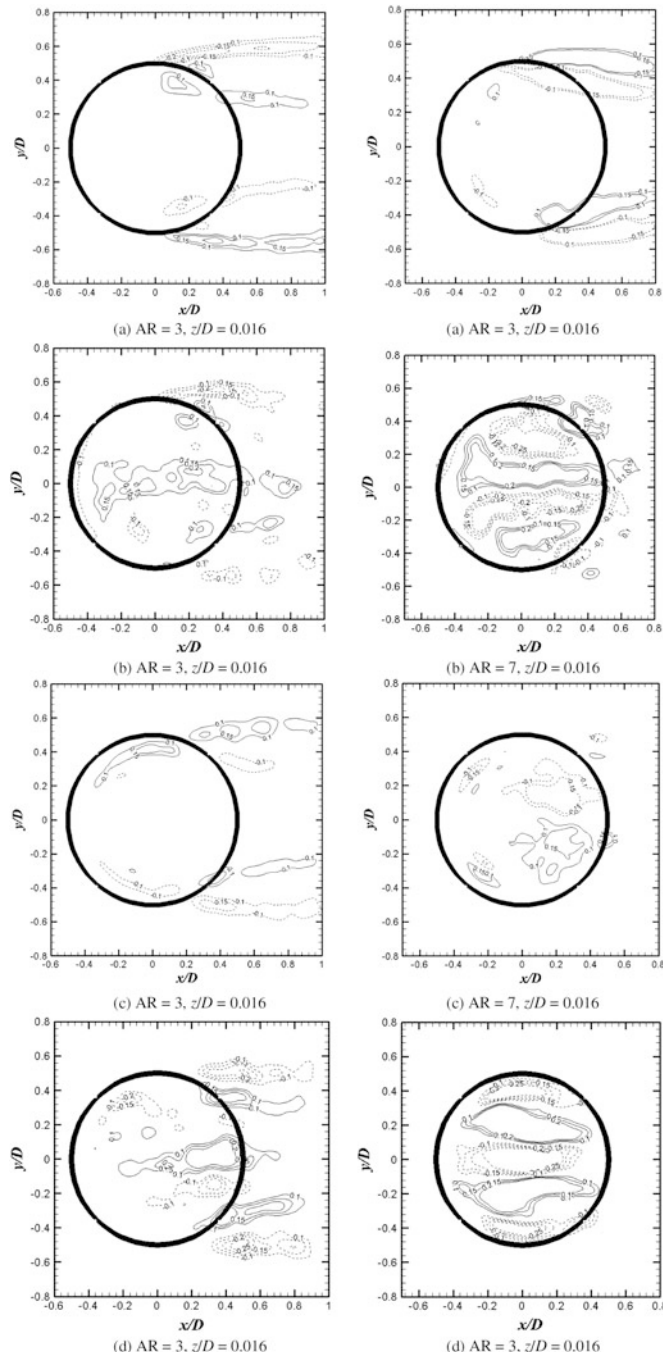
Fig. 4 Vertical vorticity ($\omega_z D/U_\infty$) contour lines (*lines* and *dashes* for positive and negative values, respectively) for the first (**a,c**) and fourth energy (**b,d**) modes extracted from the POD bases, for $z/D = 0.016$ (**a,b**), and 0.08 (**c,d**) planes for the AR = 3 and AR = 7 cylinders

themselves are located near the arch (or "mushroom") vortex termination points (foci) on the free end (Sumner 2013). There also appears to be evidence of two sub-layers of rotational vortices diverging from the foci, as well as some vortex development just after the leading edge showing the leading-edge vortex in the separation bubble.

Figure 4 shows the vertical vorticity ($\omega_z D/U_\infty$, where U_∞ is the freestream velocity) contour lines for the first and fourth energy modes extracted from the POD bases for two planes $z/D = 0.016$ and 0.08, for the AR = 3 and 7 cases. The first energy mode captures vorticity concentrations originating from the sides of the cylinder and extending into the near wake, representing the separated shear layers and the side-tip (trailing) vortices. These structures are seen at most z/D planes but are typically weaker in the fourth energy mode. On either side of the centreline are two additional vorticity concentrations, which are stronger in the fourth mode but move further downstream at $z/D = 0.08$. These resemble some of the secondary trailing vortex structures identified in the flow visualization experiments of Roh and Park (2003) but not seen by other researchers (Sumner 2013). Evidence of the arch vortex (Kawamura et al. 1984) is seen in the first energy mode with two oppositely signed vorticity concentrations on either side of the centreline. In the fourth energy mode, strong reverse-flow on either side of the centreline due to oppositely oriented vortices on either side clearly indicates the region of the vertical recirculation zone. This reverse flow gradually weakens on either side due to the downward arching of the arch vortex.

4 Conclusions

Swirling strength criterion and POD predictions were made on experimental PIV data obtained in the free-end flow field of a finite-height circular cylinder. Data were analyzed within two measurement planes for two cylinder aspect ratios. POD successfully predicted the aperiodic behaviour of the flow and its dominant features with only a few modes. The swirling strength criterion effectively captured the foci with evidence of secondary trailing vortices emerging from them, as well as a faint indication of the reverse flow arch vortex on either side of the centreline. These findings were corroborated in the POD modes. POD additionally revealed the strengthening of these side-tip and arch vortices at higher AR near the free-end surface, but fading rapidly when moving away from the free end for AR = 7.

References

Chong MS, Perry AE, Cantwell BJ (1990) A general classification of three-dimensional flow fields. Phys Fluids A Fluid Dyn (1989–1993) 2:765–777
Hain R, Kahler CJ, Michaelis D (2008) Tomographic and time resolved PIV measurements on a finite cylinder mounted on a flat plate. Exp Fluids 45:715–724

Kawamura T, Hiwada M, Hibino T, Mabuchi I, Kumada M (1984) Flow around a finite circular cylinder on a flat plate: Cylinder height greater than turbulent boundary layer thickness. Bull JSME 27:2142–2150

Roh SC, Park SO (2003) Vortical flow over the free end surface of a finite circular cylinder mounted on a flat plate. Exp Fluids 34:63–67

Rostamy N, Sumner D, Bergstrom DJ, Bugg JD (2014) Effect of aspect ratio on the flow field above the free end of a finite circular cylinder. In: ASME PVP division conference, Anaheim, USA, PVP2014-28218

Sirovich L (1987) Turbulence and the dynamics of coherent structures. Part I: coherent structures. Q Appl Math 45:561–571

Sumner D (2013) Flow above the free end of a surface-mounted finite-height circular cylinder: a review. J Fluids Struct 43:41–63

Slope-Seeking Control for Stall Mitigation of a NACA0015 Airfoil

Z. Wu, C.W. Wong, L. Wang and Y. Zhou

Abstract This paper aims to investigate the response of the slope seeking with extended Kalman filter (EKF) deployed in a closed-loop system for airfoil aerodynamics control. A novel dielectric barrier discharge (DBD) sawtooth plasma actuator is used to manipulate the flow around the NACA 0015 airfoil. The sawtooth plasma actuator leads to a delay in the stall angle by 5° and an increase in the maximum lift coefficient by about 9 %, appreciably better than that with the "traditional" DBD plasma actuator of the same input power. For the closed-loop control, the convergence time t_c of the lift force F_L is investigated for two control algorithms from $Re = 4.4 \times 10^4$ to 7.7×10^4. The t_c is about 70 % less under the slope seeking with EKF than that under the slope seeking with high-pass (HP) and low-pass (LP) filters at $Re = 7.7 \times 10^4$. The slope seeking with EKF shows excellent robustness over a moderate Re range; that is, the voltage amplitude determined by the control algorithm promptly responds to a change in Re, much faster than that of the conventional slope seeking with HP and LP fliters.

Keywords Flow control · Closed-loop control · Slope seeking · Plasma actuator

1 Introduction

Effective control of flow separation is important for aeronautical industry. The use of closed-loop control has been reported in the literature; the controller alters the input autonomously, leading to the desired performance. Benard et al. (2010) studied experimentally the slope seeking with high-pass (HP) and low-pass (LP) filters to control flow separation from an airfoil. However, the convergence

Z. Wu · C.W. Wong (✉) · L. Wang · Y. Zhou
Institute of Turbulence-Noise-Vibration Interactions and Control, Shenzhen Graduate School,
Harbin Institute of Technology, Harbin, China
e-mail: cwwong@hitsz.edu.cn

time t_c of lift coefficient was rather long, over 100 s. Reducing the t_c of the control system is crucial and challenging as it determines the control efficiency. The HP and LP filters of the conventional slope seeking in principle could be replaced by an extended Kalman filter (EKF) (e.g. Wiederhold et al. 2011). On the other hand, the flow control actuator plays a major role in the closed-loop control system. This work aims to find a rapidly settled closed-loop system for airfoil aerodynamics control. To this end, a new DBD plasma actuator is developed and implemented in an open-loop system, with a view to improving the airfoil aerodynamic. For closed-loop control, the t_c of lift force F_L under the slope seeking with EKF is investigated and compared with that associated with the HP and LP filters. The robustness of the developed control system is also examined.

2 Experimental Details

The experiments were performed in a closed circuit wind tunnel with a working section of $L \times W \times H = 5.5 \times 0.8 \times 1.0$ m. A NACA 0015 airfoil, with the span b of 300 mm and the chord length c of 200 mm, was investigated under different chord Reynolds number Re ranged from 4.4×10^4 to 7.7×10^4. The plasma actuators were installed at $0.02c$ downstream from the leading-edge and on the suction side of the airfoil, covering the central $0.6b$. The DBD sawtooth plasma actuator comprised of two sawtooth copper electrodes horizontally separated by a PMMA, and arranged with the opposite sawtooths point at each other, thus altering the gap width periodically between the electrodes in the spanwise direction (Fig. 1a). Two-component PIV was used to obtain the velocity fields in the boundary layer (x-y plane) over the suction side of the airfoil. A dual beam laser system (Litron LDY304-PIV, Nd: YLF) was used to form a thin light sheet of 2 mm thick that allowed PIV measurements. The trigger rate was fixed at 200 Hz for double frame mode. Data were acquired with the high-speed camera (Phantom V641) perpendicular to the light sheet. The viewing area used for the calculations of the vector fields for the airfoil boundary-layer covered $x/c \approx -0.06$–0.44 and
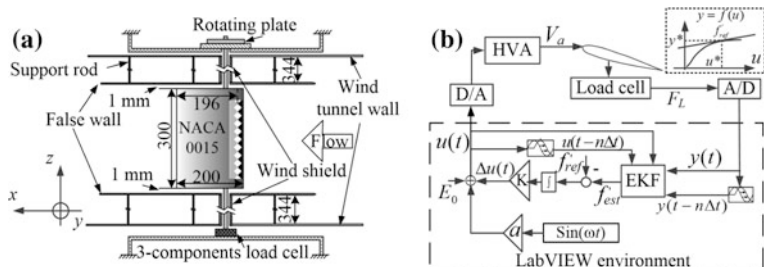
Fig. 1 a Schematic of the airfoil installation in the wind tunnel; **b** block diagram of the closed-loop control system

$y/c \approx -0.09$–0.22. Statistics for the airfoil boundary-layer was calculated from 400 instantaneous velocity fields.

The major components of the closed-loop system consisted of three-component load cell (Kyowa LSM-B10N-SA1), A/D and D/A converter, personal computer, high voltage amplifier (HVA) and the NACA 0015 airfoil with the sawtooth plasma actuator installed (Fig. 1b). In general, the slope seeking with EKF determines the input signal $u(t)$ of the controlled plant, composed of a sinusoidal perturbation signal $a \sin(\omega t)$ (where a and ω are the perturbation amplitude and frequency, respectively) and the quasi-steady signal $[E_0 + \Delta u(t)]$. As such, the $u(t)$ can cause a sinusoidal perturbation in F_L. The instantaneous F_L, measured by the load cell, was fed to the control algorithm to estimate the gradient of the $u(t)$-$y(t)$ curve. The difference between the reference gradient f'_{ref} and the estimated slope f'_{est} ($\Delta f'$) is integrated and amplified with a gain K to get the feedback increment $\Delta u(t)$. The calculated voltage signal $u(t)$ was fed to the HVA. The amplified $u(t)$ led to the discharge between the electrodes, while the iteration of control loop continued to seek for the steady-state response, aiming to suppress flow separation.

3 Results and Discussions

3.1 Open-Loop Control

Figure 2a shows that the sawtooth plasma actuator leads to a delay in the stall angle α_{stall} by 5° and an increase in the maximum lift coefficient C_{Lmax} by about 9 %. On contrary, at the same input power, the traditional "linear" plasma actuator manages a delay in the α_{stall} for 3° only and the increase in C_{Lmax} by about 3 %. It is noteworthy that the voltage amplitude V_a is greater with the sawtooth plasma actuator deployed than with the "traditional" plasma actuator, due to the intermittent discharge in the spanwise direction of the sawtooth plasma actuator. The sawtooth plasma actuator operated in the free-stream velocity of 6 m/s produces two ramifications.
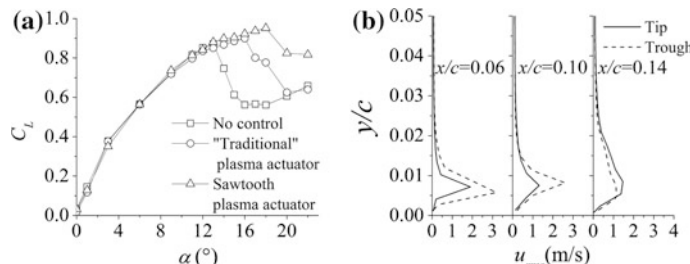
Fig. 2 a Dependence of the lift coefficient C_L on the angle of attack α. The input power of the plasma actuators is 3.3 W/cm. **b** The root-mean-square value u_{rms} of the fluctuating streamwise velocity at the tip and the trough of the sawtooth plasma actuator. $Re = 7.7 \times 10^4$

(i) The induced wall jet at the sawtooth of the actuator adds momentum to the boundary layer, somewhat similar to the DBD plasma actuator of straight edge. (ii) The induced flow between the tips increases the momentum and hence velocity fluctuations near the wall. All of these effects promote the transition of the boundary layer from laminar to turbulence, resulting in postponed flow separation. Note that the sawtooth-plasma-actuator-generated velocity fluctuations is totally different at the electrode tip from that at trough locations along the mean flow direction (Fig. 2b).

3.2 Responses of the Closed-Loop Control System at Different Re

The t_c of F_L by the slope seeking with EKF was investigated and compared with that by the conventional slope seeking at $Re = 7.7 \times 10^4$ (Fig. 3a, b). The choice of the parameters for the two control algorithms were identical; i.e. $a = 1$ kV, $\omega \approx 0.785$, $E_0 = 10.5$ kV and $t = 0.4$ s. The t_c of F_L by the slope seeking with EKF is about 70 % less compared to that by the conventional slope seeking. This is because the K (= 0.04), which was used to amplify the $\Delta f'$ in the conventional slope seeking is much less than that in the slope seeking with EKF. In fact, the conventional slope seeking suffers from the slow gradient detection, which preventing the use of large K. In contrast, the slope seeking with EKF can detect the gradient much faster than the conventional slope seeking, thus allowing a large K (= 0.5). Consequently the increased K leads to a faster convergence speed of the controller. The t_c of the closed-loop systems at different Re ($4.4 \times 10^4 - 7.7 \times 10^4$) is shown in Fig. 3c. In general, the initial V_a in both control algorithms was sufficiently large to allow flow reattachment at low Re (<5.6 × 10^4), hence no tuning was required. However, V_a must be increased in order to enhance the plasma-induced
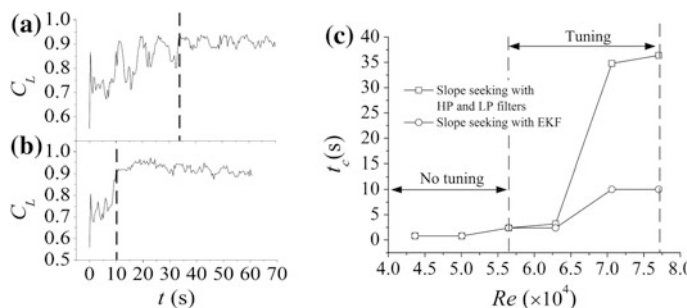
Fig. 3 C_L response of **a** the conventional slope seeking and **b** the slope seeking with EKF; **c** the t_c of the closed-loop systems at different Re

three-dimensional flow for suppressing flow separation at high Re ($\geq 5.6 \times 10^4$), and in view thereof, the slope seeking with EKF reached the steady-state response with less number of control iterations than the conventional slope seeking.

3.3 Robustness of the Closed-Loop Systems

Figure 4 shows the robustness investigation of the two algorithms when the Re changes dynamically, ranged from 5.0×10^4 to 7.7×10^4 at $\alpha = 16°$. Initially, the airfoil is stalled.

Upon actuation and at $U_\infty = 3.9$ m/s, the F_L increases substantially from 0.35 to 0.58 N for both control algorithms (Fig. 4b, d). When the U_∞ increases from 3.9 to 4.9 m/s, the F_L increases to about 1 N, indicating flow reattachment over the airfoil upper surface. The V_a response controlled by the slope seeking with EKF to the velocity change is rapid. On the contrary, the conventional slope seeking has a relatively slow increase in V_a compared to that associated with the EKF, implying that the algorithm takes longer time to reach the steady-state. One remark is due. The fast acceleration rate of estimating f' by the slope seeking with EKF leads to the V_a increment that is more sensitive to the U_∞ change. Upon U_∞ increases from 4.9 to 6.0 m/s, the perturbation of the V_a could cause a negative gradient in the $u(t)$-y (t) curve, resulting a reduction in V_a at t between 55 and 60 s (Fig. 4d). The slope seeking with EKF is able to recover V_a increment in a prompt manner, and so achieving the steady-state in F_L at t just after 60 s. The V_a changes slightly for the conventional slope seeking due to the low convergence speed (Fig. 4b).
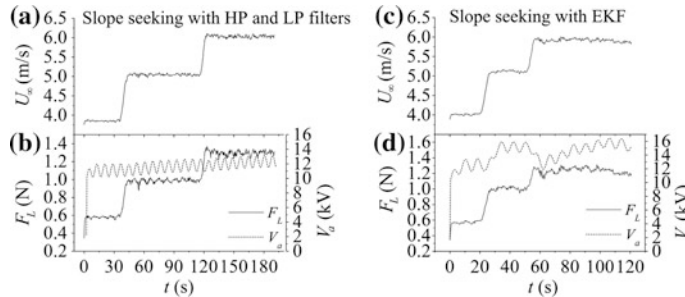
Fig. 4 Response of the slope seeking system: (**a, c**) time history of the free-stream velocity changing; (**b, d**) the corresponding response of F_L and V_a

4 Conclusions

(1) Given the same input power, the sawtooth plasma actuator leads to a post-poned stall by 5° and a 9 % increase in C_{Lmax}, while the traditional straight-edged plasma actuator produces a delay in stall by only 3° and a 3 % rise in C_{Lmax}.

(2) The slope seeking with EKF achieves a large reduction in t_c for $Re > 6.3 \times 10^4$, cutting short t_c by about 70 % at $Re = 7.7 \times 10^4$ compared with the conventional slope seeking. This is due to the fact that the increased K in the slope seeking with EKF enables faster convergence speeds as compared with the conventional slope seeking.

(3) Slope seeking with EKF has excellent robustness over a moderate Re range, that is, the V_a response varies with the velocity increment, reaching the steady-state F_L rapidly.

References

Benard N, Moreau E, Griffin J, Cattafesta LN (2010) Slope seeking for autonomous lift improvement by plasma surface discharge. Exp Fluids 48(5):791–808

Wiederhold O, King R, Noack BR, Neuhaus L, Neise W, Enghard L, Swoboda M (2011) Adaptive control in an axial turbofan: model-free implementation with short response time. AIAA J 49(7):1429–1436

LBM-LES Modelling of Low Reynolds Number Turbulent Flow Over NACA0012 Aerofoil

Nima Nadim, Tilak T. Chandratilleke and Mathias J. Krause

Abstract Contemporary evolution of numerical methods in fluid dynamics includes a growing application of lattice Boltzmann modelling (LBM) for turbulent flows. Large eddy simulation, implemented on LBM framework, is established as a competent alternative for the finite volume turbulence modelling method owing to enhanced feasibility of parallelism and the transient nature of LBM equations. This work utilises a simple Smagorinsky SGS model to investigate fundamental characteristics of a turbulent flow over NACA0012 aerofoil for a range of low Reynolds number in a turbulent flow.

Keywords Lattice boltzmann model · Turbulence · Smagorinsky model · NACA0012 · Openlb

1 Introduction

Recent developments in computational resources and parallel/cloud computing, have shifted boundaries of CFD capacities and made simulation of highly-resolved turbulent structures more feasible. Spatially discretised schemes, such as LES, SAS and DES models, could be classified as extended simulation methods with the ability to capture extensive energy spectrum and instability characteristics. Highly resolved turbulent fields could be essential in applications such as heat transfer and instability analysis (Menter and Egorov 2010) where small turbulent structures could

N. Nadim (✉) · T.T. Chandratilleke
Department of Mechanical Engineering, Curtin University, GPO, Box U1987,
Perth 6845, Western Australia
e-mail: nima.nadim@curtin.edu.au

M.J. Krause
Institutes for Mechanical Process Engineering and Mechanics
and Applied and Numerical Mathematics, Karlsruhe Institute of Technology (KIT),
Karlsruhe, Germany

potentially be significant. Flow over aerofoils has always been an interesting problem owing to its applications in a wide range of engineering fields. Intricate flow pattern and phenomena such as boundary layer transition, flow separation, detachment and vortex shedding, establish it as a common benchmark for evaluation of external turbulent flow models. DNS is known as the extreme modelling choice, providing reliable results, where it demands substantial computational capacity. Such extremely resolved models are still far from being feasible and cost effective simulation choices of industrial and commercial application. Hence, ongoing effort undergoes in the field to achieve a feasible compromise between accuracy and computational demand. More than two decades after its primary introduction, the lattice Boltzmann method (LBM) is becoming a more popular numerical technique, as a result of development in parallel computing and the perfect capability of the LBM algorithm for parallel computer code (especially GPU based hardware). As a developing approach, LBM is currently being applied and evaluated for various complicated flow characteristics including turbulence (Malaspinas and Sagaut 2012).

Using this collision-stream approach in solving the Navier-Stokes (NS) equation excludes the pressure-velocity correction stage and significantly reduces the number of iterations as compared with traditional finite volume methods (FVM). The pressure-velocity de-coupling stage is omitted in the LBM algorithm and this advantage is more prominent for modelling of phenomena such as turbulence fluctuations and vortex instabilities. Current work applies the Smagorinsky model, through LBM framework, to simulate low Reynolds (i.e. $Re < 10^5$) turbulent flow over a NACA0012 aerofoil. The flow field is then visualised and discussed by velocity magnitude, Q-criterion contour (demonstrating three-dimensional vortex structure) and pressure coefficient on the aerofoil.

2 Numerical Model

2.1 Governing Equations

A lattice Boltzmann equation is driven by single-relaxation time approximation though a BGK scheme, to be used in a collision-streaming process (Chen et al. 1992). This formulates the collision operator, for an isothermal flow as:

$$f_\alpha(x + e_\alpha \delta_t, t + \delta_t) = f_\alpha(x, t) - \frac{1}{\tau} \left[f_\alpha - f_\alpha^{eq} \right] + F_\alpha, \tag{1}$$

where Chapman–Enskog analysis reveals how collision relaxation time τ is related to the kinematic viscosity as $\nu_0 = (\tau - 1/2)/3$. As an important highlight of LBM, strain rate is directly obtained from momentum flux, which is basically the second-order moment of the non-equilibrium distribution function (Huidan et al. 2005):

$$S_{ij} = \frac{1}{2\rho_0 c_s^2 \tau} Q_{ij}, \ Q_{ij} = \sum_{\alpha = 0, 18} e_{\alpha i} e_{\alpha j} [f_\alpha - f_\alpha^{eq}]. \tag{2}$$

where by the speed of sound $c_s = 1/\sqrt{3}$ is defined in (5) for the actual chosen lattice. Solely including molecular viscosity in the scheme (relaxation time) represents DNS where all eddies are to be solved and no turbulence viscosity model is included. However, in LES approach, equations are filtered by spatial resolution and the subgrid scale (SGS) characteristics are modelled. In standard LES-LBM, the new relaxation time (τ^*) incorporates SGS turbulence viscosity (ν_T) whilst Eq. 1 is filtered by grid scale of Δ. This will be derived as

$$\nu^* = \nu_0 + \nu_T = \frac{1}{3}(\tau^* - \frac{1}{2}). \tag{3}$$

The standard Smagorinsky model is applied as SGS closure to calculate ν_T:

$$\nu_T = (C_{Sm}\Delta_x)^2 \overline{S}, \tag{4a}$$

$$\overline{S} = \frac{\overline{Q}}{2\rho_0 c_s^2 \tau^*}, \ \overline{Q} = \sqrt{2 \sum_{i,j} \overline{Q_{ij}Q_{ij}}}. \tag{4b}$$

Combining Eqs. 3 and 4a, b the explicit formula for effective relaxation time will be obtained as in (Hou et al. 1994):

$$\tau^* = \frac{1}{2}(\tau_0 + \sqrt{\tau_0^2 + 2\sqrt{2}(C_{Sm}\Delta_x)^2(\rho_0 c_s^4 \delta_t)^{-1}\overline{Q}}) \tag{5}$$

This completes a simple LES-LBM scheme to resolve large (comparable with grid scale) eddies of a turbulent field and model subgrid scale characteristics.

2.2 Boundary Conditions and Solver Setup

The above mentioned numerical scheme is implemented, using the open source LBM code OpenLB (Krause 2015) which has been widely tested for physical validity and parallelism. A three-dimensional geometry of a channel and an aerofoil is imported through a surface mesh (*stl*-file format) and accordingly fluid, solid and interface profiles are indicated using a voxalizing algorithm. BGK dynamic and no-dynamic are assigned for the flow area and the aerofoil (solid) zones, respectively. A halfway version of bounce back boundary is defined for walls including side walls and the interface between BGK and no-dynamic zones (aerofoil wall). To assure convergence and stability of the solver a growing rectangular Poiseuille

velocity profile is applied at the inlet boundary. Standard conversion between physical and lattice units is defined by setting $U_{lattice} = 0.05$, $L_{Lattice} = 0.01/N$ and $\nu = 0.001 \text{ m}^2\text{s}^{-1}$ where N = 1, 2, 3, indicates different uniform spatial resolutions.

3   Results and Discussion

Results are reviewed, in following sections, to evaluate consistency of applied LBM-LES scheme and highlight potential advantages. In achieving that, sensitivity of the developed model is examined against angle of attack (AOA) and Reynolds number within the flow field as well as on the aerofoil.

Figure 1 illustrates the flow field and the three-dimensional structure of vortices by velocity magnitude and Q-criterion iso-volumes. Flow stagnation, separation, reattachment and a vortex street in the wake behind the aerofoil can be visually observed and variation of this pattern is marked as a footprint of change in angle of attack. This result verifies competency of the LBM solver to capture fluid instability originated by the aerofoil, wall and downstream flow. To initiate such instability numerically, a random noise (or periodic boundary for fluctuating velocity component) is usually applied at the inlet boundary in most of the FVM scenarios. Alternatively in the current simulation, numerical residual from the time growing Poiseuille profile and velocity field is solely effective to imitate instability and no extra noise is applied at the inlet boundary.

Vortices originated by the channel walls are more evident in Fig. 1b, where AoA is increased to 15°. Such Q-criterion representation of vortices structure, physically,
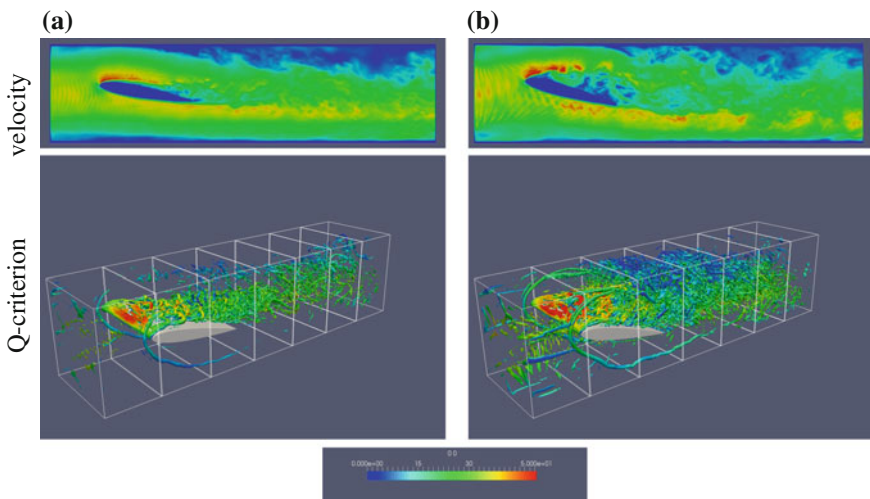
Fig. 1 Flow field and vortices structure ($Q_{range} = [5 \times 10^5, 10^6]$, coloured by velocity), Re = 50,000, **a** AoA = 10°, **b** AoA = 15°
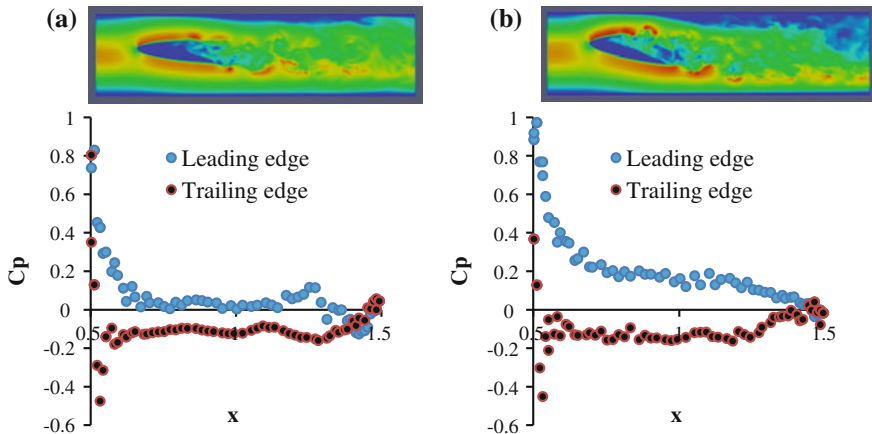
Fig. 2 Velocity contour at the mid-plane of computational zone and pressure coefficient on the aerofoil surface, Re = 15,000, **a** AoA = 10°, **b** AoA = 15°

captures higher intensity of vorticity (from mean flow) against low shear strain rate toward the walls (with low velocity).

Unlike FVM, a voxalized geometry with bounce-back boundary would result in non-zero velocity magnitude on first row nodes on the wall, representing flow velocity at computable y^+. This numerical characteristic is potentially positive and could be used for any boundary layer estimation including modification of velocity profile toward solid boundaries. However, right estimation of pressure, on the solid surface, and accordingly hydrodynamic forces could be a modelling concern.

Pressure coefficient ($C_p = (p - p_{ref})/0.5\rho U_{ref}^2$) is deemed as a common indicator of separation/reattachment pattern in external flows which also lead to estimation of drag/lift coefficients. Figure 2 demonstrates flow pattern and pressure coefficients on the aerofoil surface for two contact angles of 10 and 15°. It is obvious that for both cases, separation occurs at the trailing edge (above side), where C_p is found lower, and therefore higher pressure on the leading edge (below side) would result in upward lift. No reattachment is captured for both cases where by increasing AoA expands the gaps between C_p values of leading and trailing edges and this enhances lift and drag forces.

4   Conclusions

Using the OpenLB LBM code, the standard Smagorinsky model is successfully applied to simulate low Reynolds turbulence flows over NACA0012 aerofoil with AoA variation. LBM-LES is found competent to capture a high-resolution turbulence field with reasonable computational cost, easily distributable over CPU or

GPU parallel schemes. Bounce-back boundary is shown to be applicable for external flows where pressure variation, drag and lift are the parameters of interest. Non-zero velocity at wall adjacent nodes distinguishes LBM flow fields from FVM fields and this could be used for any estimation associated with boundary layer velocity profile.

References

Chen H, Chen S, Matthaeus HW (1992) Recovery of the Navier-Stokes equation using a lattice Boltzmann method. Phys Rev A 45:5339–5342

Hou S, Sterling J, Chen S, Doolen GD (1994) A lattice Boltzmann subgrid model for high Reynolds number flows. http://arXiv:comp-gas/9401004v1

Huidan Y, Sharath SG, Luo LS (2005) DNS and LES of decaying isotropic turbulence with and without frame rotation using lattice Boltzmann method. J Comput Phys 209:599–616

Krause MJ et al (2015) Open source lattice Boltzmann simulation code. http://www.openlb.net

Malaspinas O, Sagaut P (2012) Consistent subgrid scale modelling for lattice Boltzmann methods. J Fluid Mech 700:514542

Menter FR, Egorov Y (2010) The scale-adaptive simulation method for unsteady turbulent flow predictions part 1: theory and model description, flow. Turbul Combust 85–1:113–138

Parabolized Stability Analysis of Jets Issuing from Serrated Nozzles

Aniruddha Sinha, Hao Xia and Tim Colonius

Abstract Jets issuing from serrated nozzles have a correspondingly serrated time-averaged flow field. We solve the mildly non-parallel linear parabolized stability problem for such high speed turbulent jets to model the coherent wavepackets in the flow. The base flow for the analysis is the mean flow field from a large-eddy simulation database of a cold Mach 0.9 fully turbulent jet issuing from a nozzle with six serrations, a benchmark case in the literature. The fluctuation data is also filtered to extract the most-energetic coherent part using proper orthogonal decomposition. Such filtered data is shown to bear an encouraging resemblance with the predicted wavepackets.

1 Introduction

Large-scale coherent structures have been detected in unforced high-speed turbulent jets issuing from round nozzles several decades ago (Mollo-Christensen 1967). Since then, researchers have proposed models for these structures, mostly based on hydrodynamic stability analysis of the turbulent mean flow field (e.g. Tam and Chen 1994). More recent work (e.g. Gudmundsson and Colonius 2011) have presented detailed validation results for such models by suitable filtering of the wealth of flow data that has become available, both from experiments and from large-eddy simulation (LES). These developments have been reviewed in Ref. (Jordan and Colonius 2013).

A. Sinha(✉)
Indian Institute of Technology Bombay, Mumbai 400076, India
e-mail: as@aero.iitb.ac.in

H. Xia
Loughborough University, Leicestershire LE11 3TU, Loughborough, UK
e-mail: H.Xia@lboro.ac.uk

T. Colonius
California Institute of Technology, Pasadena, CA, USA
e-mail: colonius@caltech.edu

Serrations of the nozzle exit (called chevrons) have been demonstrated to grant appreciable acoustic benefit for high-speed jets (Bridges and Brown 2004). The chevrons are designed to impinge on the jet shear layer, so that the flow field assumes a corresponding serrated nature. The time-averaged flow field of the latter configuration, especially the streamwise vorticity therein, has been studied in depth (e.g. Alkislar et al. 2007). The coherent structures existing in such serrated jets have not been analyzed at length, an exception being the work in Ref. (Gudmundsson and Colonius 2007) that modeled them using linear stability theory (LST).

Parabolized stability equations (PSE) are an improvement over LST whereby mildly non-parallel base flows in convectively unstable flows can be addressed at little additional computational cost (Herbert 1994). Linear PSE has been applied successfully to predict the coherent wavepackets extracted from data of round jets (Cavalieri et al. 2013a; Gudmundsson and Colonius 2011; Sinha et al. 2014). In the present work, we extend linear PSE to model the wavepackets in jets issuing from serrated nozzles.

As in classical stability theory, PSE starts by decomposing the instantaneous flow field vector $\boldsymbol{q}$ into a time-invariant base flow (herein the turbulent mean flow) $\overline{\boldsymbol{q}}$ and the residual fluctuations $\boldsymbol{q}'$ that have the wavepacket-like ansatz

$$\boldsymbol{q}'(x,r,\theta,t) = \breve{\boldsymbol{q}}_\omega(x,r,\theta)\,\mathrm{e}^{-\mathrm{i}\omega t} + \text{c.c.}, \quad \breve{\boldsymbol{q}}_\omega = \sum_{m=-\infty}^{\infty} \tilde{\boldsymbol{q}}_{\omega,m}(x,r)\,\mathrm{e}^{\mathrm{i}m\theta + \mathrm{i}\int_{x_0}^{x}\alpha_\omega(\xi)\mathrm{d}\xi}. \quad (1)$$

Here, $\tilde{\boldsymbol{q}}_{\omega,m}$ is a shape function and α_ω is a complex axial wavenumber, both assumed to have mild axial variation, commensurate with the mildly non-parallel base flow. Substution of (1) in the linearized governing equations, and invocation of the slowly-varing wavepacket assumption yields an approximately parabolic system of linear PDE's (in x and r) that may be marched downstream, as detailed in Ref. (Gudmundsson and Colonius 2011; Sinha et al. 2014).

The serrated nozzles typically have L chevrons distributed *uniformly* around the azimuth. Ref. (Gudmundsson and Colonius 2007) presented a method to exploit the corresponding symmetries of the serrated mean flow field to simplify the LST-based analysis. The same procedure is employed herein, but for the PSE model. The analysis shows that Fourier azimuthal modes $m \in \{0, \pm L, \pm 2L, \dots\}$ form a coupled system, which we call 'azimuthal order' $M = 0$. Analogously, the set of coupled modes $m \in 1 + \{0, \pm L, \pm 2L, \dots\}$ constitutes azimuthal order $M = 1$, and so on.

The PSE predictions are validated against an LES database that simulates a Mach 0.9 cold jet issuing from the benchmark chevron nozzle SMC001 having $L = 6$ chevrons. The original simulation (Xia et al. 2009) had 12.5 million grid cells, and demonstrated favorable agreement of the mean velocity and Reynolds stresses with corresponding NASA experimental data (Bridges and Brown 2004). The grid has since been improved with a doubled azimuthal resolution and 20 million grid cells in total.

2 Results

In this section, we will report the circular frequency ω in terms of the corresponding Strouhal number St. Also, all linear dimensions are implicitly normalized by the nozzle exit diameter. The post-processing of the LES data is similar to that described in Ref. (Sinha et al. 2014) for round jet LES data.

Figure 1 shows the nature of the PSE eigensolution for a representative frequency ($St = 0.3$). Although 6-fold azimuthally-symmetric structures are evident near the nozzle, the behavior is low-order downstream; e.g., $m = 1$ is dominant in the $M = 1$ solution by $x = 2$. In fact, the structure of the wavepackets evident in the solution is quite similar to those observed in round jets (Gudmundsson and Colonius 2011).

PSE models the most amplified average wavepacket that is, by definition, coherent over the flow domain of the jet. Proper orthogonal decomposition (POD) is a filtering tool that may be used to extract the energetic coherent structure in turbulence for comparison with the modeled wavepackets (Cavalieri et al. 2013a; Gudmundsson and Colonius 2011; Sinha et al. 2014). The pressure component of the data is favoured in this validation exercise, since it reflects the wavepacket character most clearly (Jordan and Colonius 2013; Mollo-Christensen 1967). The domain of the present POD is chosen to be $x \in [1, 10]$, $r \in [0, 5]$. The first POD mode of pressure captures 17 to 30 % of the fluctuation energy, across a range of $St - M$ Fourier modes. Given the large domain that greatly exceeds the integral length scales of the flow, this attests to very significant coherence in the turbulence.

We present a visual comparison of the PSE eigensolutions with the first POD modes of the LES data in representative $St - M$ pairs in Fig. 2. Since the PSE solutions have arbitrary overall amplitude (the equations being homogeneous), they are scaled to match the LES data. Reasonable resemblance is seen between the model predictions and the data. This is both in regard of the wavelengths (and hence phase speeds) as well as the overall amplitude envelopes. In general, though, the PSE solution appears to decay somewhat earlier than what the data suggests. The comparison appears better for the $M = 1$ mode rather than the $M = 0$. All these observations have also been made regarding PSE solutions for round jets (Cavalieri et al. 2013a; Gudmundsson and Colonius 2011; Sinha et al. 2014).
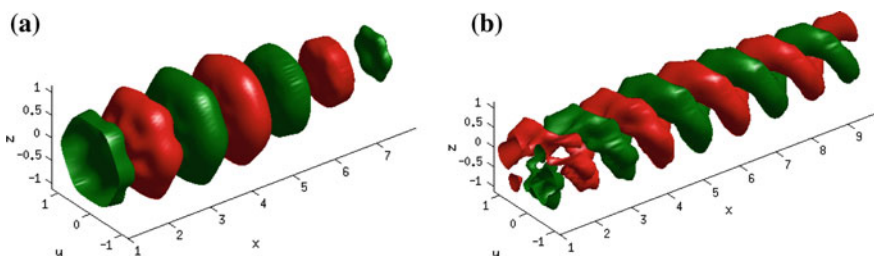
Fig. 1 Representative positive and negative isosurfaces of the real part of pressure in the PSE solution for $St = 0.3$ corresponding to azimuthal orders (**a**) $M = 0$, and (**b**) $M = 1$.

(a)

(b)

(c)

(d)
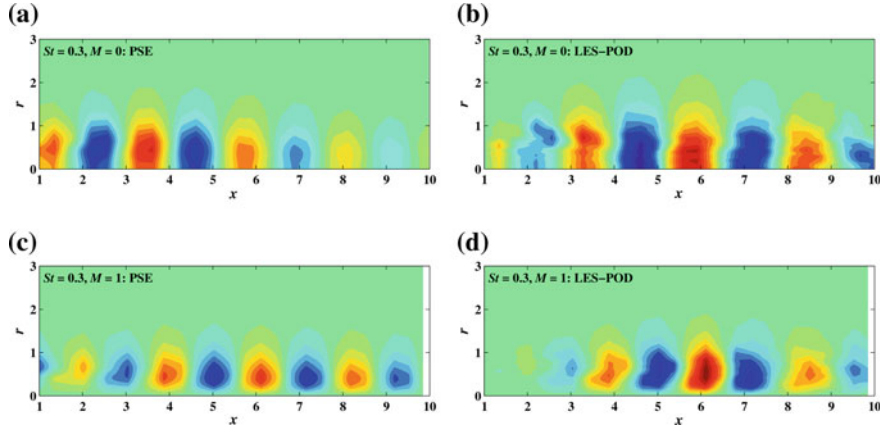
Fig. 2 Least-order azimuthal modes of pressure in PSE solution (*left panels*) compared with corresponding components of first POD mode from LES database (*right panels*) for $St = 0.3$ and azimuthal orders $M = 0$ & 1. Contour levels are identical between each pair of *left* and *right panels*, but not across rows.

A more quantitative comparison is performed using the alignment metric (Sinha et al. 2014)

$$\mathcal{A}_\omega^M := \left| \left\langle \phi_\omega^{M,(1)} , \check{p}_\omega^M \right\rangle \right| \left| \left| \check{p}_\omega^M \right| \right|^{-1} \left| \left| \phi_\omega^{M,(1)} \right| \right|^{-1}. \tag{2}$$

Here, $\check{p}_\omega^M$ represents the pressure component of the PSE solution, and $\phi_\omega^{M,(1)}$ is the first POD mode of pressure. The inner product (and induced norm) represent integration over the spatial domain of interest. The above definition implies that $0 \leq \mathcal{A} \leq 1$. A value close to unity indicates that the PSE solution is structurally equivalent (aligned) to the most coherent wavepacket found in the flow.

The alignment metric is reported for various Fourier mode pairs in Table 1. While the qualitative observations made regarding Fig. 2 are borne out, the degree of similarity between the predicted wavepackets and those found the data is re-emphasized here.

Table 1 Alignment metric for PSE solutions vis-à-vis first POD modes of pressure in LES database.

	$St = 0.2$	$St = 0.3$	$St = 0.4$
$M = 0$	0.78	0.78	0.71
$M = 1$	0.91	0.84	0.86

3 Conclusion

We propose a stability theoretic model of the coherent wavepackets present in the turbulent shear layer of jets issuing from serrated nozzles. We apply the PSE model while making explicit use of the statistical symmetries resulting from the symmetries in the nozzle geometry. The base flow field data for the stability analysis is the time-averaged mean flow taken from a validated LES database that simulated a Mach 0.9 cold jet issuing from the benchmark SMC001 nozzle. The PSE results are validated against the fluctuation data, filtered with POD. Encouraging agreement is observed in qualitative and quantitative terms. We conclude that the PSE-predicted instability waves are indeed detectable in turbulent high speed jets issuing from serrated nozzles.

References

Alkislar MB, Krothapalli A, Butler GW (2007) The effect of streamwise vortices on the aeroacoustics of a Mach 0.9 jet. J Fluid Mech 578:139–169

Bridges JE, Brown CA (2004) Parametric testing of chevrons on single flow hot jets. In: 10th AIAA/CEAS aeroacoustics conference, AIAA Paper 2824

Cavalieri AVG, Rodríguez D, Jordan P, Colonius T, Gervais Y (2013a) Wavepackets in the velocity field of turbulent jets. J Fluid Mech 730:559–592

Gudmundsson K, Colonius T (2007) Spatial stability analysis of chevron jet profiles. In: 13th AIAA/CEAS aeroacoustics conference, AIAA Paper 3599

Gudmundsson K, Colonius T (2011) Instability wave models for the near-field fluctuations of turbulent jets. J Fluid Mech 689:97–128

Herbert T (1994) Parabolized stability equations. In: Special course on progress in transition modelling, AGARD Report No. 793

Jordan P, Colonius T (2013) Wave packets and turbulent jet noise. Annu Rev Fluid Mech 45:173–195

Mollo-Christensen E (1967) Jet noise and shear flow instability seen from an experimenter's point of view. J Appl Mech 34(1):1–7

Sinha A, Rodríguez D, Brès G, Colonius T (2014) Wavepacket models for supersonic jet noise. J Fluid Mech 742:71–95

Tam CKW, Chen P (1994) Turbulent mixing noise from supersonic jets. AIAA J 32(9):1774–1780

Xia H, Tucker PG, Eastwood SJ (2009) Large-eddy simulations of chevron jet flows with noise predictions. Int J Heat Fluid Flow 30:1067–1079

Influence of Blowing Ratio on Flow Structures of an Inclined Jet in Crossflow

L. Jia, C. Dai, J. Zhang and J. Mi

Abstract This study investigates by experiment the influence of the blowing ratio (*BR*) on the flow structures of an inclined turbulent jet in crossflow (JICF). The experiment was conducted in a water tunnel with the jet issuing from a round nozzle inclined at streamwise-oriented 35°, practically relevant to the film cooling configuration. Laser Induced Fluorescence (LIF) and Particle Image Velocimetry (PIV) were adopted. Four cases of *BR* = 0.5, 1.0, 1.5, and 2.0 were considered with Reynolds number based on the jet diameter and crossflow velocity *Re* = 1712. It is shown that the flow patterns change with *BR* drastically. When *BR* = 0.5, the hairpin vortices dominate in the JICF. As *BR* increases, the classic JICF topology recovers and the ubiquitous counter-rotating vortex pair (CRVP) becomes the characteristic feature of the JICF and persists far downstream for *BR* = 2.0.

1 Introduction

The jet in crossflow (JICF) refers to a jet of fluid emanating from a nozzle interacts with the surrounding fluid that flows across the nozzle exit. This phenomenon or the like exists extensively in nature and industrial applications, such as volcanic eruptions, pollutant in plumes and cooling of turbine blades. Consequently, numerous experimental and numerical studies have been focused on it, detailed reviews can be referred to Mahesh (2013) and Karagozian (2014). However, the flow structures of JICF very much depend on *BR* values and the inclined JICF of low *BR* has not been fully researched. Most recently, Bidan and Nikitopoulos (2013)

L. Jia · C. Dai · J. Zhang · J. Mi (✉)
State Key Laboratory for Turbulence and Complex Systems, College of Engineering,
Peking University, Beijing, People's Republic of China
e-mail: jmi@pku.edu.cn

and Cambonie and Aider (2014) considered the normal JICF at low *BR* values. But the flow structures of an inclined JICF are very different, compared to the normal cases, in which the coherent structures developed in the inclined nozzle are not formed. This point of view is illustrated in detail by Dai et al. (2015). As *BR* scales the thermal transport capacity of the coolant, it is arguably the most important parameter for film cooling (Coletti et al. 2013). Thus, this study investigates by experiment the influence of *BR* on the flow structures of an inclined turbulent jet in crossflow. $BR = 0.5, 1.0, 1.5,$ and 2.0 were considered with the density ratio $\rho_j/\rho = 1$ and the jet diameter and free-stream velocity based Reynolds number $Re = 1712$; here $BR = \rho_j U_j/\rho\, U$, where ρ_j and ρ denote the jet and crossflow fluid densities while U_j and U denote the corresponding mean velocities, respectively. In addition, the mean jet trajectory and the unsteady behavior of the shear vortex at the leading edge of the jet/crossflow interface are also analysed.

2   Experimental Procedures

The experiment was conducted in a closed-loop low speed water tunnel with a 6 m long test section by a 0.4 m × 0.4 m cross-section, schematically described in Fig. 1, where the coordinates *X*, *Y* and *Z* were respectively corresponded to the streamwise, spanwise and vertical directions of the flow and the origin was taken at the center of the jet exit. The jet exit center was mounted 13*D* downstream of the test plate leading edge and 26*D* upstream of the trailing edge, with *D* = 23 mm. The test plate served as boundary wall was 0.90 m × 0.36 m in length and width and the plenum supplying the jet was 10*D* of diameter and 6*D* of height. The round honeycomb in the plenum was 6 mm in diameter and 120 mm in length. The flow structures were visualized by LIF before the PIV measurements, for the selected vertical and horizontal planes referred to Jessen et al. (2007).
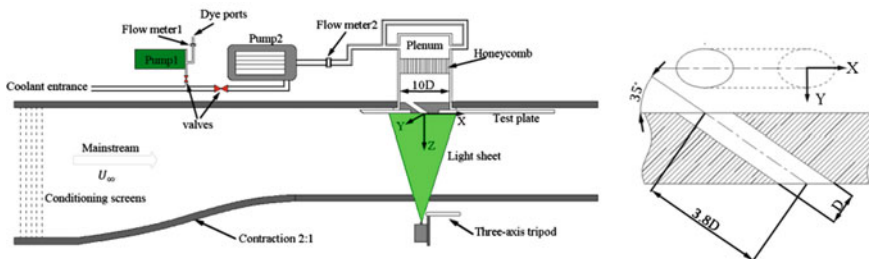
Fig. 1 The schematic experiment configuration: test section (*left*) and the inclined nozzle (*right*)

3 Results and Discussion

3.1 *Flow Structures of Different Blowing Ratios*

The influence of different low *BR* values on the vortical structures in JICF was mainly studied through LIF visualization. Figure 2 shows that the flow patterns change with *BR* significantly. For *BR* = 0.5, the jet momentum is not strong enough to penetrate through the crossflow boundary layer and thus produces less complex vortical structures near the jet exit. Consistent with the observation by Acarlar and Smith (1987), the hairpin vortices, see Fig. $2a_1$, c_1, dominate the JICF, due to the vorticity in the crossflow boundary layer inhibiting roll-up of the nozzle boundary layer at the leading edge. Horseshoe vortices from the crossflow boundary (Fig. $2b_1$, b_2) are formed due to the adverse pressure gradient upstream of the jet. Note that the rhodamine-6G-chloride ejecting through horseshoe vortices visualized the vortex legs. Compared with the case of *BR* = 0.5, the canonical flow topologies of JICF recover as *BR* reaches 2.0, behaving more chaotically. All of the classic large-scale vortical structures documented by Fric and Roshko (1994) are observed for *BR* = 2.0: strong shear-layer vortices on the leading and trailing edges of the jet due to the intense viscous shearing and K-H instability at the jet/crossflow interface; the temporally averaged CRVP shown by Fig. $2c_4$; tornado-like wake vortices just downstream from the recirculation zone, initiated by the entrainment of the CRVP.
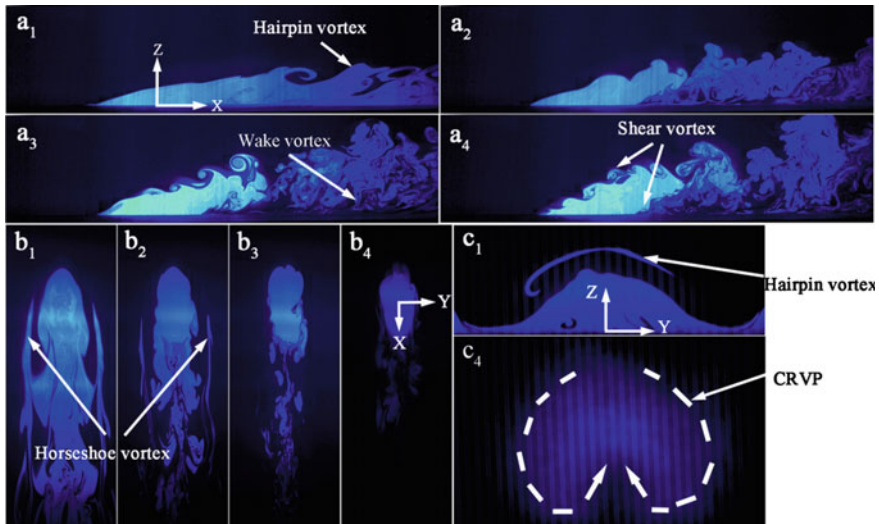
Fig. 2 LIF visualizations in the symmetric (a, *X-Z*), *horizontal* (b, *X-Y*) and *vertical* (c, *Y-Z*) planes. Subscripts 1–4 corresponds to *BR* = 0.5–2.0, respectively. Planes of b_1 to b_4 are all chosen at *Z* = 3 mm. c_1 and c_4 are responsible for the instantaneous and time-averaged vertical sections of the flow structure at *X/D* = 3.0, respectively

The horseshoe vortex is not viewed apparently, because of the low pressure region just behind the jet exit and the CRVP's entrainment, sucking the horseshoe vortices into the wake region together.

3.2 Jet Trajectory

Since the mean jet trajectory reflects the extent to which the jet penetrates into the crossflow, comprehension of the jet trajectory is important for film cooling. The jet trajectory has been studied for a long time and can be defined in many different ways. Here we consider the temporally averaged streamline, based on 900 instants of PIV measured data, emanating from the center of the jet exit as the mean jet trajectory, scaled with $BR \cdot D$. In Fig. 3, the trajectories of $BR = 1.0$, 1.5 and 2.0, except for $BR = 0.5$, collapse onto almost a single curve when the axes X and Z are scaled with $BR \cdot D$. This indicates that the jet trajectory is insensitive to the momentum balance between the jet and the crossflow for BR ranging from 1.0 to 2.0. Since the flow structures of the lowest BR are different from those of the higher BR, as pointed in Sect. 3.1, the similarity of the jet trajectories of $BR = 1.0$–2.0 seen in Fig. 3 could be regarded as another validation for the above conclusion from the time-averaged perspective. Thus, only when $BR < 1.0$, the competition between the momentum of the jet and the crossflow determines the jet trajectory.

3.3 Unsteady Behavior in JICF

Through the discrete fast Fourier transform (FFT), the time series of the instantaneous spanwise vorticity ω_Y, calculated from the PIV velocity field of the symmetric planes, are converted into power spectrum density function. Combined with the analysis of the successive LIF images for the symmetric planes, we found that

Fig. 3 Jet trajectories scaled with $BR \cdot D$
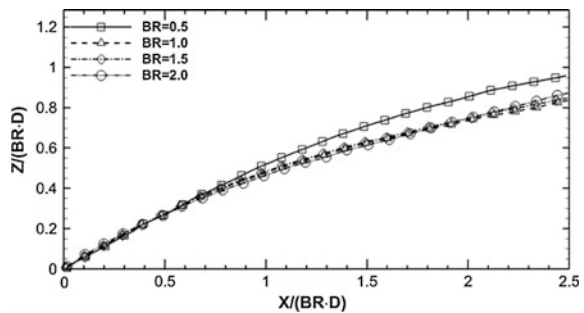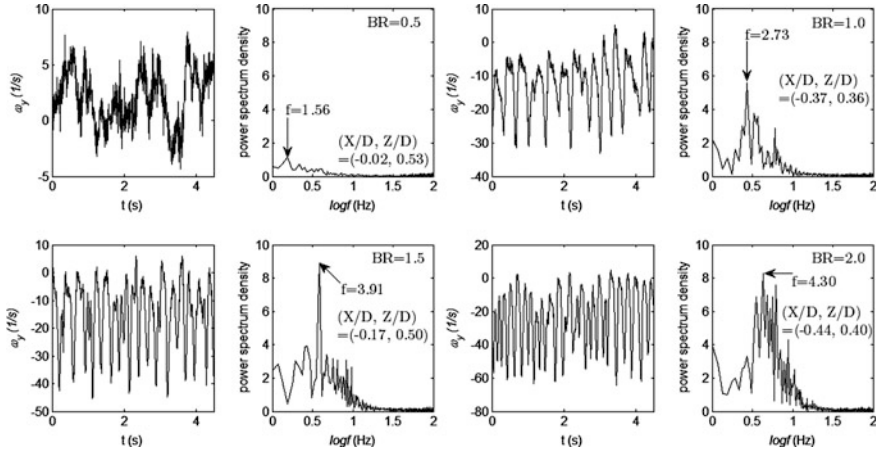
Fig. 4 Time histories of ω_Y and their corresponding power spectra in the windward jet/crossflow shear layer for the symmetric planes ($Y/D = 0$)

the horseshoe vortex occurs and stays steadily at $BR = 0.5$, 1.0, and becomes periodically ejected off for the higher BR values. For the shear vortex on the windward jet/crossflow shear layer, the typical ω_Y and corresponding power spectrum density function at various BR values are shown in Fig. 4. It is inferred that as BR increases from 0.5 to 2.0, the shedding frequency of the shear vortex becomes larger from 1.56 to 4.30 Hz while the corresponding Strouhal Number ($St = fD/U_j$) decreases from 0.96 to 0.66. The frequency of the ejected horseshoe vortex is inferred to be 3.52 Hz at $BR = 2.0$, smaller than that of the shear vortex.

4 Conclusions

Present observations by PIV and LIF have been made to the main large-scale vortical structures of an inclined JICF: i.e., shear layer vortex, horseshoe vortex, wake vortex and CRVP. LIF images and the jet trajectories demonstrated that the flow patterns of the inclined JICF near the jet exit change with BR significantly. The hairpin vortices were found to occur and dominate the JICF only at $BR = 0.5$ whereas the canonical flow topology recovers for the higher BR values. The horseshoe vortices stay steadily for $BR = 0.5$ and 1.0 but become periodically ejected off for the higher BR. For the shear vortex at the leading edge, its shedding frequency becomes larger while the corresponding Strouhal number decreases as BR increases.

References

Acarlar MS, Smith CR (1987) A study of hairpin vortices in a laminar boundary layer. Part 2. Hairpin vortices generated by fluid injection. J Fluid Mech 175:43–83

Bidan G, Nikitopoulos DE (2013) On steady and pulsed low-velocity-ratio transverse jets. J Fluid Mech 714:393–433

Cambonie T, Aider JL (2014) Transition scenario of the round jet in crossflow topology at low velocity ratios. Phys Fluids 26:084101

Dai C, Jia L, Zhang J, Mi J (2015) Formation and evolution of the flow structure of an inclined jet in crossflow. In: 3rd symposium on FSSIC-A061 (accepted)

Coletti F, Elkins CJ, Eaton JK (2013) An inclined jet in crossflow under the effect of streamwise pressure gradients. Exp Fluids 54:1589

Fric TF, Roshko A (1994) Vortical structure in the wake of a transverse jet. J Fluid Mech 279:1–47

Jessen W, Schröder W, Klaas M (2007) Evolution of jets effusing from inclined holes into crossflow. Int J Heat Fluid Flow 28:1312–1326

Karagozian AR (2014) The jet in crossflow. Phys Fluids 26:101303

Mahesh K (2013) The interaction of jets with crossflow. Ann Rev Fluid Mech 45:379–407

Formation and Evolution of the Flow Structure of an Inclined Jet in Crossflow

C. Dai, L. Jia, J. Zhang and J. Mi

Abstract Large-eddy simulation (LES) was used to investigate the formation and evolution of the flow structure of a streamwise-inclined 35° turbulent jet in crossflow (JICF). Predictions by LES agree well with the experimental results of Jia et al. (2015). It is shown that the flow patterns vary with the blowing ratio (*BR*) considerably, based on three-dimensional flow topologies. For *BR* = 0.5, the hairpin-like vortices behave like the classic counter-rotating vortex pair (CRVP) that dominates in the JICF. By comparison, the ubiquitous CRVP becomes the characteristic feature of the JICF and persists far downstream at *BR* = 2.0. Coherent structures developing within the nozzle are incepted by the separation at the jet inlet sharp edge and enhance the formation of the CRVP greatly as *BR* is increased.

1 Introduction

The interaction of a jet with the oncoming crossflow, also known as JICF, exists extensively in nature and engineering applications, such as chimney flow, plume dispersions and dilution jets in combustors. Due to its great importance for industry, a large number of experimental (Fric and Roshko (1994), Coletti et al. (2013), Cambonie and Aider (2014)) and numerical studies (Bidan and Nikitopoulos (2013), Sakai* et al. (2014)) have been performed over the past decades, though the related formation and evolution of large-scale vortical structures are still of much debate. Many fully resolved direct numerical simulations (DNS) of turbulent JICF can be found in the open literature, with detailed rewiews by Karagozian (2014) and Mahesh (2013). However, they are mostly concerned with canonical or simplified configurations using Reynolds-Averaged Navier-Stokes (RANS) solver. Since the consensus is that the RANS models have a poor prediction for the anisotropy JICF

C. Dai · L. Jia · J. Zhang · J. Mi (✉)
State Key Laboratory for Turbulence and Complex Systems, College of Engineering,
Peking University, Beijing, People's Republic of China
e-mail: jmi@pku.edu.cn

223

problem while DNS has the limitation of huge computational costs, the LES model is chosen presently to investigate the formation and evolution of an inclined turbulent JICF at low blowing ratios.

2   Computational Details

LES was implemented with the commercial solver Ansys Fluent using a WALE Subgrid-scale model with second-order accuracy for both spatial and temporal discretization (spectral synthesizer method). The simulated domain, which consists of a crossflow channel, a streamwise-oriented $35°$ film cooling nozzle and a plenum, is presented in Fig. 1, where the diameter of the jet nozzle $D = 10$ mm. The X, Y, Z axes are responsible for the streamwise, spanwise and vertical directions of the flow respectively, with their origin taken at the center of the jet exit. The whole mesh is structured and contained in total 4.2 million cells, of which the dimensionless distance $y^+ < 1.0$. Before the LES, an initial steady RANS was operated to initialize the flow domain and give a maximum viscous dissipation rate (ε) estimate in the domain, used to evaluate the time step of LES according to the Kolmogorov time scale $\tau_K = (\nu/\varepsilon)^{1/2}$ (Bidan and Nikitopoulos 2013). Hence in LES, the time step varied from 1 ms at $BR = 0.5$ to 0.2 ms at $BR = 2.0$. Thousands of time steps were calculated to obtain sufficient data for convergent statistics, based on residuals of less than 10^{-6}. Two typical blowing ratios $BR = 0.5$ and 2.0, as used experimentally by Jia et al. (2015), were researched with the density ratio $\rho_j/\rho_\infty = 1$ and the jet
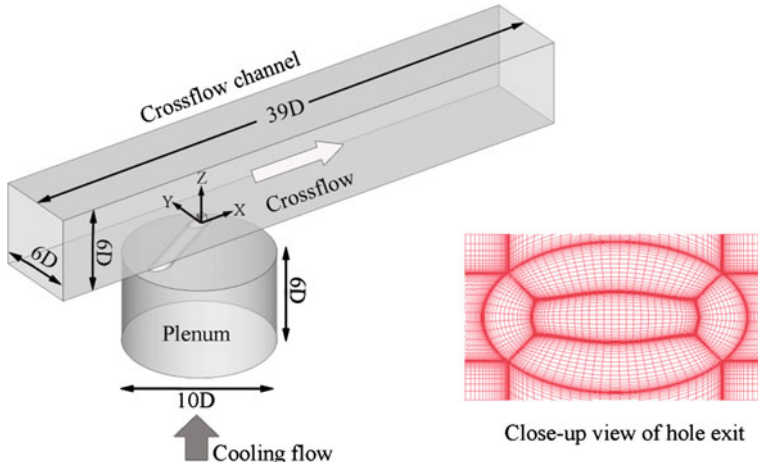
Fig. 1 The computation domain for LES. The coordinates X, Y and Z correspond respectively to the streamwise, spanwise and vertical directions of the flow

diameter and free-stream velocity (constant 0.172 m/s) based Reynolds number $Re = 1712$; here $BR = \rho_j U_j / \rho_\infty U_\infty$, where ρ_j and ρ_∞ denote the jet and crossflow fluid densities while U_j and U_∞ denote the corresponding mean velocities, respectively.

3 Results and Discussion

3.1 Validations

Figure 2 shows lateral profiles of U_x/U_∞, the dimensionless time-averaged streamwise velocity from the present LES prediction and the PIV measurement of Jia et al. (2015), for $BR = 0.5$ and 2.0 at $X/D = 1.5$ and $X/D = 3.0$ in the symmetric plane at $Y/D = 0$ of the JICF. The difference between the two cases of $BR = 0.5$ and 2.0 is obvious (and also expected) from the plot: while the profiles of U_x/U_∞ do not show the existence of the inclined jet at $BR = 0.5$, *i.e.*, the jet issuing at a speed below the cross-flow velocity (U_∞), they clearly display the jet flow when it discharges at a speed of $2U_\infty$. As also demonstrated, overall, the computed velocities at all locations agree well with the experimental data, validating the use of LES for the JICF. More specifically, however, there are some mismatches near the wall at different locations for both blowing ratios. This is not unexpected because the limitation of PIV often occurs in the very near wall region, where the light reflection occurs and the particle tracing characteristic is poor.
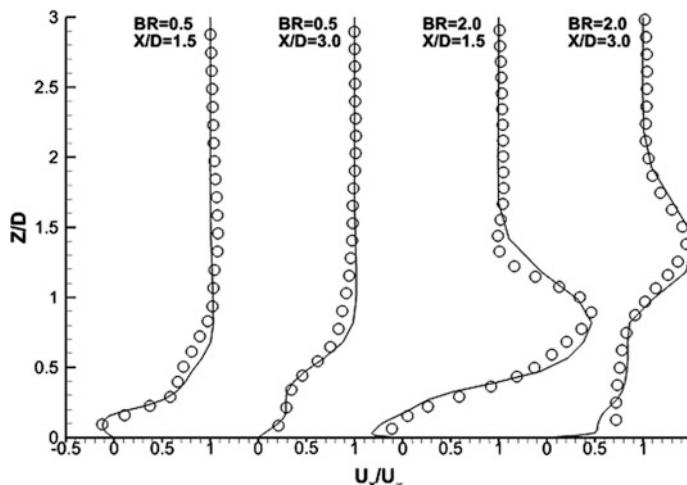
Fig. 2 Simulated (*solid line*) and experimental (Jia et al. (2015), symbols) time-averaged dimensionless streamwise velocity profiles in the symmetry plane at $X/D = 1.5$ and 3.0 for $BR = 0.5$ and 2.0

3.2 Origins of CRVP at Different Blowing Ratios

Figure 3a, b present instantaneous iso-surfaces of different $\Delta P/\rho$, *i.e.* the Δ-criterion, firstly proposed by Dallmann (1983), for $BR = 0.5$ and 2.0. This method is based on the principle that the vortex cores are associated with the minimum local pressure. For this study, the flow is incompressible and $\Delta P/\rho$ is derived to be $\Omega_{ij}\Omega_{ij} - S_{ij}S_{ij}$, where $\Omega_{ij} = (u_{i,j} - u_{j,i})\,/2$ expresses the rotation-rate tensor and $S_{ij} = (u_{i,j} + u_{j,i})\,/2$ the stress tensor. It is obvious that the flow structures change significantly when changing BR from 0.5 to 2.0, which has also been validated experimentally by Jia et al. (2015). At $BR = 0.5$, the hairpin vortices, Fig. 3a, appear to dominate the JICF. For $BR = 2.0$, the canonical flow topology recovers and the CRVP becomes the characteristic feature. Further analysis suggests that the origin of the CRVP is different for the two blowing raitios. For the lower BR, the hairpin vortex, formed from the crossflow boundary layer separation when overwhelming the jet, behaves like the CRVP and is responsible for its generation from the time-averaged perspective, which is consistent with Mahesh (2013). For the higher
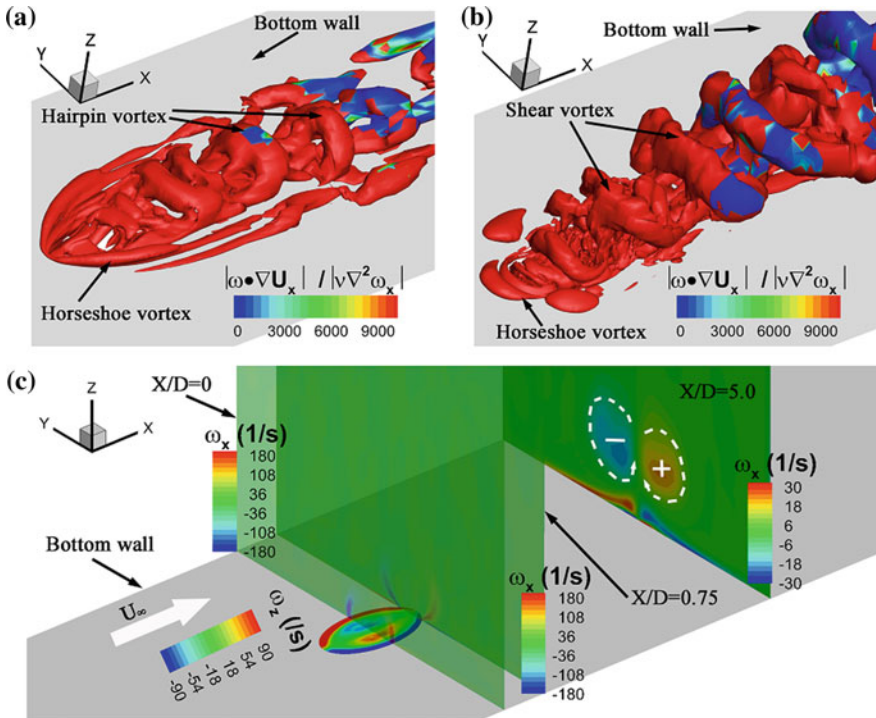
Fig. 3 Instantaneous iso-surface of $\Delta P/\rho$ colored by $|\omega \cdot \nabla U_X|/|\nu\nabla^2 \omega_X|$: **a** for $BR = 0.5$ ($\Delta P/\rho = 25/s^2$); **b** for $BR = 2.0$ ($\Delta P/\rho = 100/s^2$). **c** Time-averaged vorticity contours in the planes of jet exit and the vertical planes of $X/D = 0$, 0.75, 5.0 at $BR = 2.0$

BR, Fig. 3c, the deformation of the vortices within the jet shear layer becomes dominant in forming the CRVP. For this incompressible JICF problem, the transport equation of the instantaneous streamwise vorticity ω_X can be simplified as

$$\frac{d\omega_X}{dt} = \omega_X \frac{\partial U_X}{\partial X} + \omega_Y \frac{\partial U_X}{\partial Y} + \omega_Z \frac{\partial U_X}{\partial Z} + \upsilon(\frac{\partial^2 \omega_X}{\partial X^2} + \frac{\partial^2 \omega_X}{\partial Y^2} + \frac{\partial^2 \omega_X}{\partial Z^2}) \qquad (1)$$

where the first term on the right hand side represents the streamwise stretching; the second and third terms are responsible for the bending of the streamlines; the last term is for the viscous diffusion of streamwise vorticity. Figure 3a, b show the absolute ratio of $\omega \cdot \nabla U_X$ to $\upsilon \nabla^2 \omega_X$, respectively, for $BR = 0.5$ and 2.0. It is demonstrated that, near the jet exit, the viscous term is relatively negligible and thus $\omega \cdot \nabla U_X$ dominates the transport of ω_X. The absolute stretching and bending rates of the vortices near the jet exit are quite large. As seen in Fig. 3c, the CRVP for $BR = 2.0$ mainly originates from the folding and reorientation of the jet shear layer on both sides of the exit and also from the spiral counter-rotating vortex pair (SCRVP, see Fig. 4c) within the nozzle. It is estimated that 25 % of the streamwise vorticity in the plane of $X/D = 0.75$ issues from the SCRVP, through comparing the vorticity magnitude in the plane of the jet exit and $X/D = 0$. Therefore, coherent structures developed within the nozzle are incepted by the separation zone at the nozzle sharp edge and contribute to the formation of the CRVP for the higher *BR*.

3.3 The Sub-Large Coherent Structure in the Jet Nozzle

There is a sub-large coherent structure, which has not been mentioned in the open literature, near the exit in the nozzle boundary layer as shown in Fig. 4. It is marked by the dashed ellipse and we call it the perturbation spiral structure (PSS) which may result from the pressure fluctuation near the leading edge of the jet exit. By comparing the particle pathlines of successive instants, it can be found that the PSS
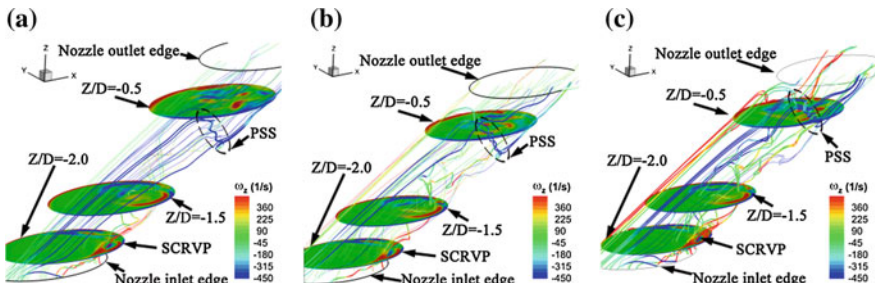
Fig. 4 The pathlines of particles released from the jet *inlet* plane, colored by the instantaneous ω_Z at $BR = 2.0$: **a** t = 1.024 s; **b** t = 1.032 s; **c** t = 1.040 s, with several *horizontal* planes in the nozzle as frames

occurs periodically within the nozzle around the plane of $Z/D = -0.5$. As it approaches the nozzle exit, the PSS becomes more strengthened. However, more study on this interesting finding is needed to understand its formation mechanism and its effects on the flow structure outside the jet nozzle.

4 Conclusions

The present LES calculations have demonstrated that the unsteady large-scale vortical structures change drastically with different blowing ratios. At $BR = 0.5$, the hairpin vortex is observed to dominate the JICF, while the canonical CRVP structure appears to recover and control the evolution of the JICF for $BR = 2.0$. The origin of the CRVP is different for the two values of BR. Moreover, the present study has found perhaps at first that there is a sub-large coherent structure, herein termed as PSS, existing in the nozzle besides the SCRVP. Nevertheless, the PSS character and its effect on the evolution of the JICF needs a detailed investigation.

References

Bidan G, Nikitopoulos DE (2013) On steady and pulsed low-velocity-ratio transverse jets. J Fluid Mech 714:393–433

Cambonie T, Aider JL (2014) Transition scenario of the round jet in crossflow topology at low velocity ratios. Phys Fluids 26:084101

Coletti F, Elkins CJ, Eaton JK (2013) An inclined jet in crossflow under the effect of streamwise pressure gradients. Exp Fluids 54:1589

Dallmann U (1983) Topological structures of three-dimensional vortex flow separation, AIAA-83-1735

Fric TF, Roshko A (1994) Vortical structure in the wake of a transverse jet. J Fluid Mech 279:1–47

Jia L, Dai C, Zhang J, Mi J (2015) Influence of blowing ratio on flow structures of an inclined jet in crossflow, In: 3rd Symposium on FSSIC-A060 (accepted)

Karagozian AR (2014) The jet in crossflow. Phys Fluids 26:101303

Mahesh K (2013) The interaction of jets with crossflow. An Rev Fluid Mech 45:379–407

Sakai E, Takahashi T, Watanabe H (2014) Large-eddy simulation of an inclined round jet issuing into a crossflow. Int J Heat Mass Trans 69:300–311

Visualization Observation of Cavitation Cloud Shedding in a Submerged Water Jet

Guoyi Peng, Yasuyuki Oguma and Seiji Shimizu

Abstract An experiment investigation on the behaviour of cavitation cloud caused in submerged water jets issuing from a sheathed sharp edge orifice nozzle was carried out by high-speed camera visualizing observation. It is demonstrated that cavitation bubble cloud appears when the cavitation number σ decreases to the level of 0.6–0.7. The dominant frequencies of bubble cloud expanding and contracting in the axial direction is closely related to the pressure pulsation of plunger pump, which is often employed in industry application of water jets. However, the dominant frequencies of jet width oscillation in the radial direction mainly depend on the shedding of shear vortexes as well as the collapsing of cavitation bubble clouds.

Keywords Water jet · Cavitation · Bubble cloud · Visualization

1   Introduction

Cavitation is an important phenomenon in submerged water jets and it has an important effect on the working performance of water jets. As a useful technology actively utilizing cavitation impact, high-speed water jet into water, which is usually called submerged water jet, has been developed and widely applied to burry removal and cleaning of complicated mechanical products, cutting and surface improvement of solid materials, etc. in various industry fields (Shimizu and Peng 2009). However, the processing ability of submerged water jet decreases quickly with the increase of standoff distance. In order to ensure the effective standoff of submerged water jet a technology of sheathing nozzle has been proposed by Shimizu et al. (2010) and its effectiveness has been demonstrated experimentally.

G. Peng (✉) · Y. Oguma · S. Shimizu
Department of Mechanical Engineering, College of Engineering, Nihon University,
Koriyama 963-8642, Fukushima, Japan
e-mail: peng@mech.ce.nihon-u.ac.jp

However, the structure of cavitating jet and the behaviour of cavitation bubbles, especially in the sheath, are still unclear (Peng et al. 2013; Sato et al. 2013).

Focused on the behaviour of cavitating water jet issuing from a sheathed sharp edge orifice nozzle an experimental investigation is carried out by means of high-speed camera observation. The area of cavitation bubble cloud and the dominant frequencies of bubble cloud oscillation in both the axial and the radial directions are investigated by image analysis. The relation between the oscillation of cavitating water jet and the pulsation of injection pressure are identified.

2 Experimental Apparatus

Figure 1 shows the schematic diagram of test rig for submerged cavitating jet. The cylindrical pressure chamber is made of acrylic acid resin materials where pressured clear water supplied by a pressure plunger pump is injected to generate a submerged water jet. By the adjusting valves installed at the supplying and the draining pipes the pressure within the chamber can be adjusted to a given level up to 2.0 MPa. The output pressure of the plunger pump can be adjusted according to the requirement of experiments from the chamber pressure to the maximum pump pressure of 21.0 MPa. The throat diameter of orifice nozzle $d = 1.0$ mm and the length of the throat session is $5d$. A sheath to the nozzle is mounted at the exit of the throat and its inner diameter is given to be $3d$. The length of the sheath is $10d$. The cavitation number σ of the water jet device is defined as follows.

$$\sigma = \frac{p_o - p_v(T_\infty)}{P_i - p_o} \tag{1}$$
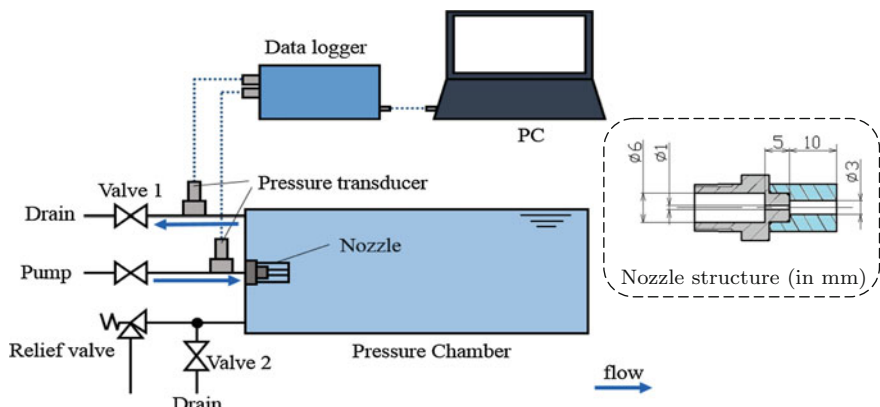
Fig. 1 Scheme of experimental device

where P_i denotes the jet injection pressure, p_o the surrounding static pressure within the chamber and p_v the saturated vapor pressure at the reference temperature T_∞.

For observing the behavior of cavitation cloud in submerged water jet a transparent pressure chamber and a transparent nozzle sheath manufactured by acrylic acid resin were used. A high-speed video camera (Phantom Ver7.2) was applied to record the motion of cavitation bubbles. The error caused by the view angle is estimated to 1.5 % by arranging the distance from the nozzle to the camera. The maximum imaging speed is high as 190,000 fps and the best shutter speed is short as 2.0 μs. A halogen bulb lamp (Yamazen, HSL 500) of 10,500 lm was used as light source. Photographs with resolution of 1.4 megapixel (1.2 k × 1.2 k) were save as picture files and then these file were treated by image analysis software to capture the area of cavitation occurring and the behavior of bubble cloud.

For the convenience of description a cylindrical coordinate system whose origin locates at the center of orifice exit and x axis lays in the direction of jet flow is employed. Experiments were carried out under different cavitation numbers. The pumping pressure P_i was set to 0.6–3.0 MPa and the chamber pressure p_o was adjusted to set the cavitation number to a given level.

3   Experimental Results and Disucussions

Figure 2 shows, as an example, a sequence of pictures taken by high speed video camera under condition that $P_i = 0.6$ MPa and $\sigma = 0.2$. The imaging speed was set to be 27027 fps. Here the light source was set at the opposite side of the camera and the pictures were taken under penetrating light. So, the area full of clear water is observed to be bright but the clouds of cavitation bubbles is observed to be dark areas since the cavitation cloud is almost impermeable to light. As shown in the figure, cavitation cloud at the moment demonstrated by the picture of the left corner contracts to its minimum length in the axial direction and then expands to its maximum and contracts to the minimum again time sequentially. According to images shown in the figure we understand that cavitation clouds accompanying the jet flow expands and contracts periodically both in the axial and radial directions. The approximately elliptical cavitation area is estimated to be about $8.5d$ in the axial length and $2.5d$ in the radial width when $\sigma = 0.2$.
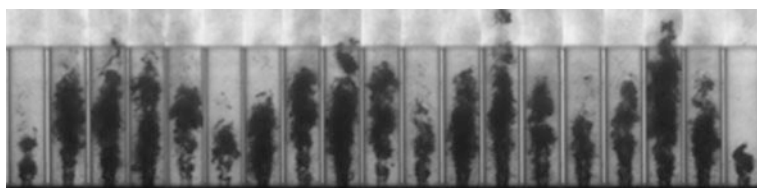
Fig. 2 Periodic variation of cavitation cloud ($P_i = 1.0$ MPa, $\sigma = 0.2$)
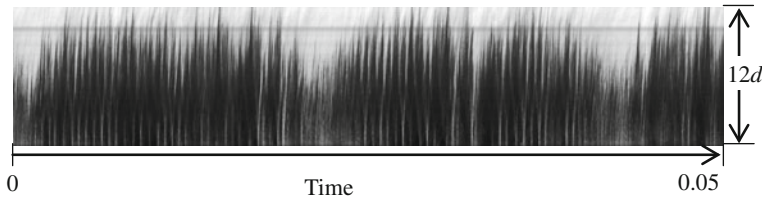
Fig. 3 A sequence of sampling images at the central axis of jet flow

Fig. 4 Dominant frequencies of jet oscillation in the axial direction
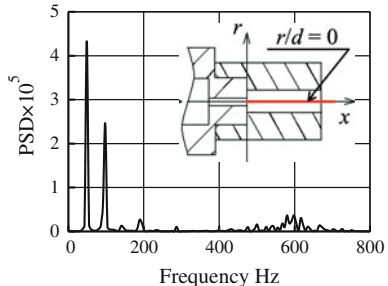
Image analysis of high-speed camera photographs was performed and the variation of grey level was investigated both along the axial and the radial directions. Figure 3 shows, as an example, the stretching and contracting of cavitation cloud in the axial direction, where sampling images of 1 pixel width in the radial direction and 12d length in the axial direction were taken from the center of nozzle exit ($x/d = 0$, $r/d = 0$) and arranged in time sequence. The average grey level of these images was evaluated, and the temporal variation of the average grey level was investigated. The waveform of grey level variation was further treated by FFT (Fast Fourier Transform) analysis. Figure 4 shows the PSD (power spectral density) distribution of the grey level oscillation frequency, where two dominant frequency components, $f_1 = 48$ Hz and $f_2 = 96$ Hz, are demonstrated. In other words, cavitation clouds caused by water jet stretches and contracts mainly at these two frequencies in the axial direction. In order to specify the source causing the oscillation

Fig. 5 Pulsation of jet injection pressure
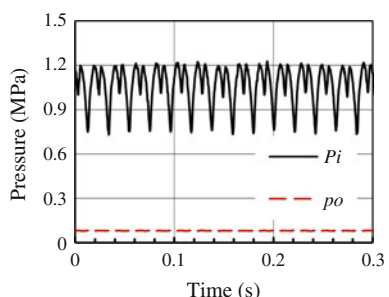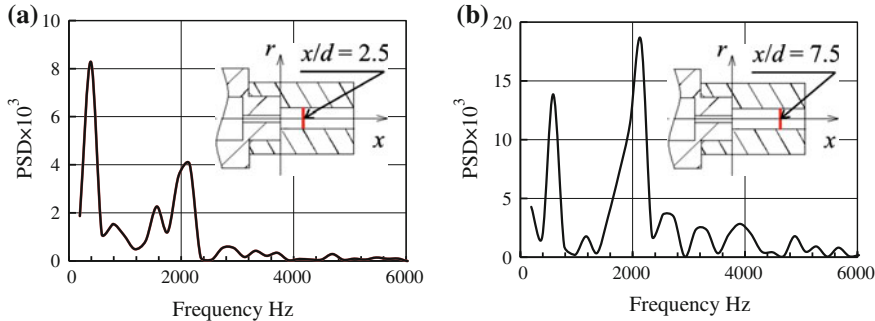
Fig. 6 Dominant frequencies of jet oscillation in the radial direction, **a** $x/d = 2.5$, **b** $x/d = 7.5$

the pulsation of jet injection pressure was monitored. Figure 5 shows the temporal variation of injection pressure P_i, where the pressure p_o of the pressure chamber is denoted by dashed line for reference. FFT analysis of the injection pressure reveals that the dominant frequency components of the pressure pulsation are quite the same as above ones. It means that the frequency of bubble cloud shedding is strongly influenced by the pressure pulsation of plunger pump, which is widely applied in industry practice.

Concerning the oscillation of jet width in the radial direction, similar image analysis was performed. Sampling images of 1 pixel width in the axial direction and $1.0d$ length in the radial direction were taken from positions of standoff $x/d = 2.5$ and 7.5 ($r/d = 0$), and the temporal variation of the grey level was analysed. Figure 6 shows the PSD distributions of the grey level oscillation frequency at different standoffs. The components of dominant frequency are estimated to be 390 and 2150 Hz at $x/d = 2.5$, and 580 and 2150 Hz at $x/d = 7.5$. The frequency component of 2150 Hz is close to that of bubble oscillation, and the components of 390 Hz and 580 Hz are in the order of shear vortex shedding (Nanduri et al. 1996). The results demonstrate that the dominant frequencies of jet width oscillation mainly depends on shear vortex shedding and bubble cloud collapsing along the shear layer around the jet.

4 Conclusions

The behavior of cavitation cloud in submerged water jet issuing from a sheathed sharp edge orifice nozzle is investigated by high-speed camera visualization observation. Image analysis demonstrates that: (1) Cavitation cloud appears while the cavitation number decreases to the level of 0.6–07 and expands and contracts periodically. (2) The dominant frequencies of bubble cloud shedding in the axial direction strongly depend upon the pulsation of jet injection pressure. (3) But the oscillation of jet width in the radial direction is mainly dependent on the shedding of shear vortexes as well as the collapsing of cavitation bubble clouds.

References

Nanduri M, Taggart DG, Kim TJ (1996) High-speed observation of ultrahigh-speed submerged water jets. Exp Thermal Fluid Sci 12(4):411–416

Peng G, Masuda K, Shimizu S (2013) Characteristics of cavitating water jet issuing from a sheathed orifice nozzle. In: Proc. FLUCOME 2013, No OS7-01-3, pp 1–8

Sato K, Taguchi Y, Hayashi S (2013) High speed observation of periodic cavity behavior in a convergent-divergent nozzle for cavitating water jet. J Flow Control Meas Vis 1:102–107

Shimizu S, Peng G (2009) Water jetting technology for LOHAS. International Academic Printing Co., Ltd., Tokyo

Shimizu S, Sakuma M, Hitomi K, Peng G (2010) Submerged cutting by abrasive suspension jet issuing from sheathed nozzle with ventilation. In: Proceedings of the 20th International conference on water jetting, BHR Group, pp 435–441

Influence of Nozzle Exit Velocity Distribution on Flame Stability Using a Coaxial DBD Plasma Actuator

M. Kimura and K. Okuyama

Abstract In this study, a coaxial dielectric barrier discharge plasma actuator (DBD-PA) is applied to control the flame shape, the control to maintain excellent flame stability is attempted. DBD-PA consists of an exposed electrode, an insulated electrode, and a dielectric layer. In a convergent round nozzle having an exit inner diameter of $d = 6$ mm, the electrode set was arranged coaxially with the nozzle. DBD-PA is applied to the control of the flame stability on condition equivalence ratio: $\phi = 0.85$, 1.00. Premixed gas of air and propane was used for fuel. The applied voltage is 5–8 kV and OFF, and frequency is 8 kHz constant. Flame stability limit is taken with a high speed camera. The center of inner flame assumes a crown shape. It is thought that this is due to a change in velocity distribution in the free boundary layer by the effect of the DBD-PA induced flow.

Keywords Jet · Flow control · DBD plasma actuator · Instability · Flame

1 Introduction

In the control of a current jet flow, various researches on the control that have been used many control methods; sound wave, flap type actuator, controlled coaxial flow, MEMS actuator etc. Recently, dielectric barrier discharge plasma actuator (DBD-PA) (Corke et al. 2010) has been applied to flow control. DBD-PA has been investigated as a device for separation control on wings by many investigators (Post ML and Corke TC 2004). And also it was applied to the jet diffusion control

M. Kimura (✉)
Department of Mechanical Engineering, College of Science & Technology,
Nihon University, 1-8-14 Kanda-Surugadai, Chiyoda-ku, Tokyo, Japan
e-mail: kimura@mech.cst.nihon-u.ac.jp

K. Okuyama
Department of Mechanical Engineering, Graduate School of Industrial Technology,
Nihon University, Tokyo, Japan

(Kimura M et al. 2013). On the other hand, control of the jet is that the performance of controlling the mixing of combustible gas and airs in the burner combustion efficiency, small size can be such, for industrial application range is wide, an important field of research. In this study, coaxial DBD-PA is applied to control the flame shape and flame stability.

2 Experimental Details

Figure 1a shows a cross section of the coaxial DBD-PA set up at the round nozzle exit, the main jet, and the overall view of the induced flow due to DBD-PA. It consists of an exposed electrode, an insulated electrode, and a dielectric layer. The dimensions of the actuator are shown in Fig. 1b. The dielectric was made from a machinable ceramic since it needs to be heat resistant, while the electrodes were fabricated from copper. The inside diameter of the jet exit is $d = 6$ mm, the dielectric layer thickness is 1 mm, and the electrodes are 0.5 mm thick. Figure 2 shows a cross-sectional diagram of the DBD-PA attached to the exit of converging round nozzle, which was also manufactured from a machinable ceramic. Plasma was generated by adding the alternating high voltage from the power supply. DBD-PA is applied to the control of the flame stability on condition equivalence
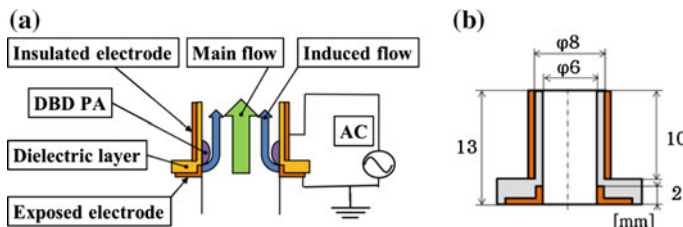
Fig. 1 Coaxial DBD-PA: **a** DBD-PA configuration of electrodes and dielectric layer and induced flow image, **b** DBD-PA dimensions

Fig. 2 Nozzle and coaxial DBD-PA
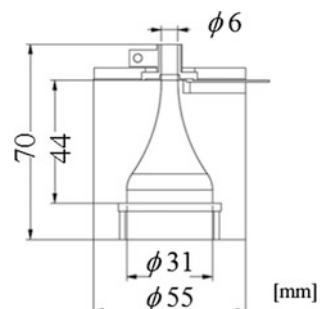
ratio: $\phi = 0.85$, 1.00. Premixed gas of air and propane was used for fuel. Voltage is applied to the coaxial DBD-PA after ignition, to generate an induced flow by plasma. The applied voltage is 5–8 kV and OFF, and frequency is 8 kHz constant. Flame stability limit is taken with a high speed camera. In the case of pure jets, the laser light seat method was used to visualize the jet shape using of Nd:YAG laser (made of Omicron: in the jet flow LA-D40-CW and $\lambda = 532$ nm) and micro oil particles. It took a picture of the jet flow made visible within the range to $x/d = 6$ with a high speed camera. Distance and y from the nozzle exit show the distance in the direction of the diameter from the nozzle center in x. And the visualization picture was PIV (Particle Image Velocimetry) analyzed.

3 Result and Discussion

Figure 3 shows round air jets visualization. Although weak instability ejection when the plasma off, it can be seen that appear remarkably K-H instability. Once the plasma is applied, vortex ring occurs immediately after the jetting, further leading to diffusion. Figure 4 is a velocity distribution immediately after the ejection. If plasma is OFF, the velocity distribution of the central portion is flat. Here, U_0 is the center velocity of $x/d = 1$ when DBD-PA is not generated. If by applying
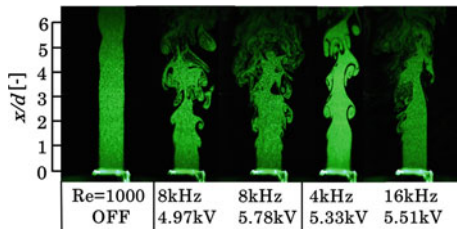
Fig. 3 Round air jet visualization in the case of DBD-PA off and in the case of driving DBD-PA

Fig. 4 Velocity distribution in the cross direction of near the jet exit area ($x/d = 1$)
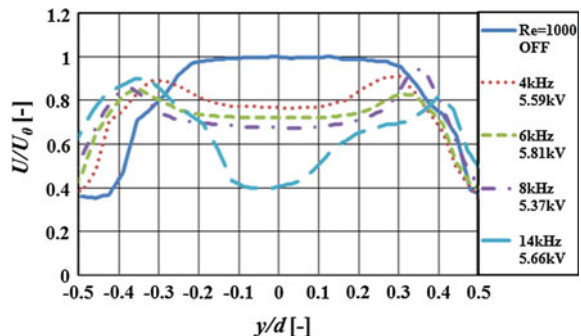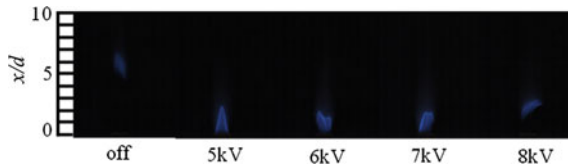
Fig. 5 Images of inner flame shape ($Q = 3.31$ L/min, $\phi = 0.85$, 8 kHz)
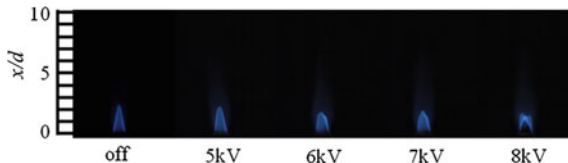
Fig. 6 Images of inner flame shape ($Q = 3.31$ L/min, $f = 1.00$, 8 kHz)

plasma, the velocity distribution in the center portion is decelerating. Blowing flow by DBD-PA accelerate the velocity of the boundary layer by the plasma. Since the jet flow rate is constant, the velocity of the center is to slow down.

Figure 5 is a still photograph of laminar flame taken by high-speed camera. Conditions the volume flow rate $Q = 3.31$ L/min, equivalence ratio is $\phi = 0.85$. Equivalence ratio is a value indicating how many times the fuel of the theoretical amount relative to 1 kg of the air supplied: $\phi = $ (Fuel/Air)/(Fuel/Air: Theoretical air-fuel ratio). For the plasma OFF, so lean condition, the flame blown off without sustained. When the applied voltage is 5 kV, it is stable becomes a cone-shaped flame. If the applied voltage is 6 and 7 kV, although flame shape is deformed, it is stable combustion. Generation of plasma is increased amount of generation of radicals, active species for activating the combustion; flame surface is stable even in dilute state. When the applied voltage is 8 kV, the flame is blown away. When the applied voltage is increased up to 8 kV, blowing force increases. By the velocity of the boundary layer is faster than burning velocity, the flame is blown off.

Figure 6 is a still photograph of laminar flame taken by high-speed camera. Conditions the volume flow rate $Q = 3.31$ L/min, equivalence ratio is $\phi = 1.00$. Even if the plasma OFF, because the equivalent ratio is $\phi = 1.00$, the flame is not blown off. When the applied voltage is 5 kV, it is stable becomes a cone-shaped flame. If the applied voltage is 6 and 7 kV, although flame shape is deformed, it is stable combustion. If the applied voltage is 8 kV, the further flame shape is deformed, the central portion of the flame dent, and the crown-shaped flame configuration.

As indicated in Fig. 4, around velocity by a blowing force of plasma to accelerate, the central portion is slowing down at the same time. Flame front is stabilized at the balance point of burning velocity and gas velocity. Since the velocity of the center part is decelerated, the shape of the flame recessed central portion is formed.

4 Conclusions

In this study, we experimented at controlling laminar flow flames using a coaxial DBD plasma actuator to produce flames that were superior in terms of shape. Two of the action occurs when the plasma is generated. One is blowing force by the plasma, which increases the velocity of the boundary layer, slowing the velocity of the central portion. The other is the generation of active species by the plasma. Active chemical species is intended to activate the combustion reaction; there is action to stabilize the flame even in lean-burn conditions. Plasma both coexist at the time of occurrence, by both the balance with the applied voltage, and a case where the flame front is stabilized, when blown away.

References

Corke TC, Enloe CL, Wilkinson SP (2010) Dielectric barrier discharge plasma actuators for flow control. Ann Rev Fluid Mech 42:505–529

Kimura M, Asakura K, Onishi M, Sayo K, Miyagi N (2013) Jet diffusion control using a coaxial DBD plasma actuator. In: 4th International conference on jets, wakes and separated flows, ICJWSF2013, Nagoya,17–21 Sept 2013

Post ML, Corke TC (2004) Separation control on high angle of attack airfoil using plasma actuators. AIAA J 42:2177–2184

Interaction of Shear Layer Coherent Structures and the Stand-Off Shock of an Under-Expanded Circular Impinging Jet

Paul Stegeman, Julio Soria and Andrew Ooi

Abstract This study looks specifically at the energy transformations that occur during the interaction of strong shear layer coherent structures with the stand off shock. Time resolved data has been produced from high fidelity large-eddy simulations at a nozzle pressure ratio of $NPR = 3.4$ and impingement surface stand-off distance of $z = 5d$. Two dominant instability modes have been analysed using the velocity fluctuation energy density in the shear layer. Stand-off shock position statistics have been found as a function of radial position. Comparison of the shear layer pressure fluctuations and shock position fluctuation through a magnitude squared coherence analysis has been performed. It has been shown that the correlation of the initial shear layer pressure fluctuations and shock position is moderate at the dominant mode Strouhal numbers.

1 Introduction

Under-expanded supersonic impinging (USI) jets characteristically produce large-scale structures at discrete frequencies due to the development of an acoustic forcing mechanism. In this mechanism acoustic waves force an instability at the nozzle lip which grows within the shear layer as it travels downstream. These structures interact with the stand-off shock which produces a disturbance in the wall jet. An acoustic wave is then generated in the wall jet which travels upstream and forces a new jet shear layer instability. This process is often referred to an acoustic feedback loop.

P. Stegeman (✉) · J. Soria
LTRAC, Department of Mechanical and Aerospace Engineering,
Monash University, Clayton, VIC 3800, Australia
e-mail: Paul.Stegeman@Monash.Edu

J. Soria
Department of Aeronautical Engineering, King Abdulaziz University,
Jeddah, Kingdom of Saudi Arabia

A. Ooi
The University of Melbourne, Parkville, VIC, Australia

The most significant parameter for USI jets is the stand-off distance (z) between the nozzle outlet and the impingement surface. Changes in z produces staging behaviour between different forced instability modes and their associated frequencies.

A majority of prior research into USI jets has centred around the analysis of the mean flow field, prediction of the acoustic tone frequencies and coherent structure topology through dynamic mode decomposition (Powell 1988; Donaldson and Snedeker 1971; Henderson et al. 2005). However, the dynamic behaviour of such jets, and specifically, the mechanisms of the forced jet shear layer instabilities and their interaction with the stand-off shock is still an active area of research. This study looks specifically at the energy transformations that occur during the interaction of shear layer coherent vortical structures with the stand off shock. In order to undertake this analysis, time resolved data has been generated at a stand-off distance (z) of 5 nozzle diameters (d), a nozzle pressure ratio of 3.4, exit Mach number of $M_e = 1$, and a jet Reynolds number of $\mathrm{Re}_D = c_e d\rho/\mu = 50,000$.

2   Large-Eddy Simulations

An in house developed three dimensional high fidelity compressible LES solver for non-uniform structured meshes was used to generate the dataset utilized in this study. For spatial differentiation the hybrid solver employs a sixth order central finite difference scheme for the smooth regions and a fifth order weighted essentially non-oscillatory scheme with local Lax-Friedrichs flux splitting in the discontinuous regions. Temporal integration is performed using a fourth order five step Runge-Kutta scheme. The sub-grid scale terms were computed using Germano's dynamic model with the adjustments made by Lilly (1992). The domain consists of approximately 30 million nodes with the spatial extent of $15d$ the radial direction. Locally one-dimensional inviscid compressible boundary conditions defined in (Poinsot 1992) are outflow regions. Sponge regions are employed near the outflow boundary were the flow field is forced to a self similar incompressible wall jet solution that has been determined *a priori*.

3   Results and Discussion

Axisymmetric temporal mean fields of the velocity magnitude and velocity fluctuation magnitude are shown in Fig. 1. For this case the jet exhibits a single shock cell structure with a stand-off shock. Figure 2 shows the fluctuating velocity spectra integrated in the azimuthal direction at $s = 0.05d$. Two dominant modes are present at Strouhal numbers of $St = 0.12$ and $St = 0.54$. For each mode the energy density at their respective Strouhal numbers are plotted in Fig. 3 as a function of distance from the nozzle along the shear layer (s) sampling points shown in Fig. 1. For modes associated with $St = 0.12$ and $St = 0.54$ there is initially a rapid linear growth region
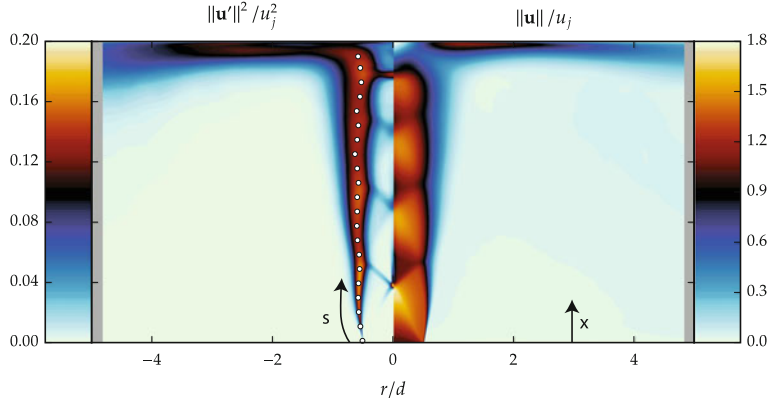
Fig. 1 2D slices of the temporal means of the velocity magnitude (*right* half) and square of the velocity fluctuation magnitude (*left* half). The black dot represents the sound pressure level sampling position and the *white* dots represent every 5th sample position along the shear layer used in the spectral analysis

Fig. 2 Velocity fluctuation spectra integrated in the azimuthal direction. *Vertical coloured lines* represent the dominant modes at $St = 0.12$ and $St = 0.54$
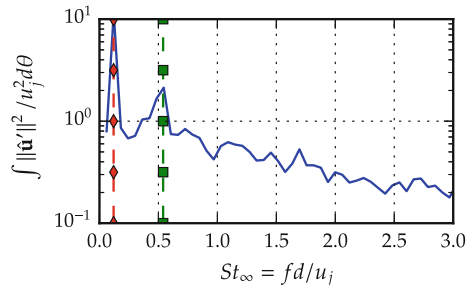
Fig. 3 Energy density of the velocity fluctuations as a function of path length (s) along the shear layer samples. Each colour represents the dominant mode as is given in Fig. 2
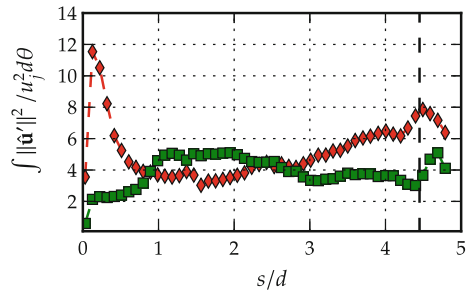
before $0.3d \leq s \leq 0.4d$ after which mode $St = 0.12$ decays and the growth rate of mode $St = 0.54$ declines. The decay of mode $St = 0.12$ is due to the development of the natural broadband shear layer instabilities. The dashed vertical line in Fig. 3 represents the mean stand-off shock position. For the mode associated $St = 0.12$ the velocity fluctuation energy density decays after interaction with the stand-off shock, conversely the mode associated with $St = 0.54$ initially decays. It is unknown at this
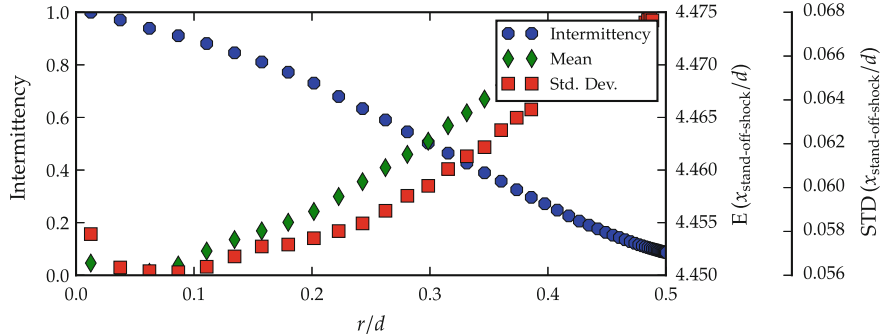
Fig. 4 Intermittency, mean position and standard deviation of the position of the stand-off shock

stage if the cause of this phenomena is due to the coherent interaction with the shock or with the impingement wall.

Figure 4 provides the intermittency, mean position ($x_{\text{stand-off-shock}}$) and fluctuating position ($x'_{\text{stand-off-shock}}$) of the stand-off shock as a function of its radial position. Due to the transient nature of the stand-off shock the intermittency is calculated as the probability in time that the stand-off shock is present at the given radial position. As is expected the variation of the stand-off shock position increases and the intermittency decreases near its edge where the interaction with the coherent structures is likely stronger. There is also a slight increase in the variation near the centreline of the jet which is unexpected and currently under investigation. At various radial positions the shock fluctuations seem to be biased towards the wall as is seen in the longer tail when $x'_{\text{stand-off-shock}} \geq 0$ in the probability density function of Fig. 5.

Finally, to determine the effect of the coherent structures on the stand-off shock position, the magnitude squared coherency of the pressure fluctuations at the first shear layer sample near the nozzle lip with the fluctuations of the stand-off shock position at $r = 0$ is plotted in Fig. 6. At the Strouhal number of each dominant mode there is a moderate correlation between the initial coherent structure and the stand-off shock position. The lower frequency mode $St = 0.12$ exhibits the largest correlation at 0.8. Small correlations are also evident at $St = 0.4$, $St = 0.8$ and $St = 1$ which are evidence of smaller forced modes that have not been resolved in the velocity

Fig. 5 Probability function of the stand-off shock fluctuating position
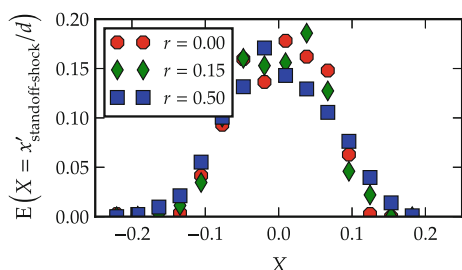
Fig. 6 Magnitude squared coherency of the pressure fluctuation at the first shear layer sample with the fluctuating stand-off shock position
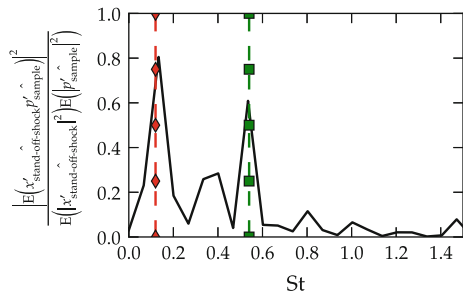
fluctuation energy spectra. While the correlations between the dominant shear layer modes near the nozzle and the stand-off shock position exist, the exact mechanism of interaction is still yet to be determined.

4 Conclusion

Initial results pertaining to the interaction of the coherent shear layer structures with the stand-off shock in an under-expanded impinging jet have been presented. It was found that a moderate to strong linear time based correlation between the initial shear layer perturbations and the axial stand-off shock position exists at the dominant mode frequencies. First and second order statistics of the stand-off shock position as a function of the radial position from the centreline have also been studied. These results will form the basis of further analysis into the energy transfer and dynamics of shock and coherent structure interactions within such jets.

References

Donaldson CD, Snedeker RS (1971) A study of free jet impingement. part 1. mean properties of free and impinging jets. J Fluid Mech 45(2):281–319

Henderson B, Bridges J, Wernet M (2005) An experimental study of the oscillatory flow structure of tone-producing supersonic impinging jets. J Fluid Mech 542:115–137

Lilly D (1992) A proposed modification of the germano subgrid-scale closure method. Phys Fluids 4(3):633–635

Poinsot T (1992) Boundary conditions for direct simulations of compressible viscous flows. J Comput Phys 101(1):104–129

Powell A (1988) The sound-producing oscillations of round underexpanded jets impinging on normal plates. J Acoust Soc Am 83(2):515–533

Interaction of a Supersonic Underexpanded Jet with a Flat Plate

O. Amili, D. Edgington-Mitchell, D. Honnery and J. Soria

Abstract High-spatial resolution measurements of the velocity field of a supersonic jet impinging on a flat surface were conducted. To study the effect of the boundary condition, two nozzle outer geometries were investigated. The experimental results presented here are for a nozzle pressure ratio of NPR = 3.0 and a nozzle to plate spacing of $Z/D = 3.5$. The flow fields of the corresponding cases show that although the general features of the flow are similar, the ambient air entrainment into the shear layer is different. This change in entrainment influences the rest of the jet structure.

1 Introduction

Interaction of a supersonic flow with a solid surface is important in aerospace and industrial applications. When a jet flow exits a nozzle with a pressure higher than the pressure of the surrounding area, an underexpanded jet forms. In this case, the pressure of the jet reaches the ambient pressure through a series of expansion and shock waves. Interaction of this unsteady supersonic flow with an impingement surface creates a high noise level at discrete frequencies. The unsteady flow and production of sound was first described by a feedback loop mechanism (Powell 1988). Powell (1988) hypothesized that the mechanism is initiated by instabilities in the shear layer

O. Amili(✉) · D. Edgington-Mitchell · D. Honnery · J. Soria
Laboratory for Turbulence Research in Aerospace and Combustion,
Department of Mechanical and Aerospace Engineering, Monash University,
Melbourne, Australia
e-mail: omid.amili@monash.edu

D. Edgington-Mitchell
e-mail: daniel.mitchell@monash.edu

D. Honnery
e-mail: damon.honnery@monash.edu

J. Soria
Department of Aeronautical Engineering, King Abdulaziz University,
Jeddah, Kingdom of Saudi Arabia
e-mail: julio.soria@monash.edu

at the nozzle lip. The instability waves grow in size and create large scale structures that travel downstream. When they impact the impingement surface, coherent large pressure fluctuations are generated that travel upstream as acoustic waves. At the nozzle lip, these acoustic waves force the shear layer which completes the feedback loop.

The authors have previously shown the cyclic nature of the impingement process and the closed loop instability mechanisms using two sets of high-spatial and high-temporal resolution schlieren images of an impinging jet (Mitchell et al. 2012) and acoustic measurements (Mason-Smith et al. 2015). In this study, high-spatial resolution two-component two-dimensional (2C-2D) measurements of the velocity fields of this phenomenon are presented. The important parameters that affect the flow structure and noise production are the nozzle pressure ratio (NPR), the nozzle to surface spacing (stand-off distance), the Reynolds number, the nozzle shape, and the impinging plate's size and angle. The flow regime, instabilities, coherent structures, and the acoustic noise generation are sensitive to these parameters especially to the NPR and the stand-off distance. Therefore, it is important to address this fundamental problem at different conditions. In the present study, the measurements are performed along the axial-radial direction at a center plane of the jet. The flow structure for the nozzle pressure ratio of 3.0 and the stand-off distance of 3.5 for two boundary conditions are addressed in this paper.

2 Experimental Methodology

2.1 Jet Rig Facility

The apparatus used in this study was designed and developed based on the performance of an earlier LTRAC Supersonic Jet Facility (Mitchell et al. 2013). Compressed air at a pressure of approximately 7 bar and a temperature of approximately 20 °C is transferred from the supply line into the mixing chamber of the jet facility using a high-pressure hose. The inlet compressed flow is regulated using a Fairchild (0–10 bar) high-flow pressure regulator with the pressure variation of approximately 1 %. The stagnation pressure in the plenum chamber is measured using a RS-461 pressure transducer with an accuracy of approximately 0.25 %. In this experiment, a converging nozzle with an inner exit diameter of 15 mm is mounted on the top of the plenum chamber. The nozzle which was manufactured using CNC machining of a single stainless steel block has a sharp lip with a thickness of 1.5 mm. A square piece of glass with a size of $15D \times 15D$ is used as the impinging surface. For seeding, a Vicount 1300 smoke generator is connected to the mixing chamber as shown in Fig. 1. The smoke generator provides a persistent and high seeding density with a nominal particle size of 0.2–0.3 μm. The particle relaxation time of approximately 2.0 μs is calculated experimentally based on the approach described in Mitchell et al. (2013). The corresponding effective particle diameter is approximately 0.6 μm.
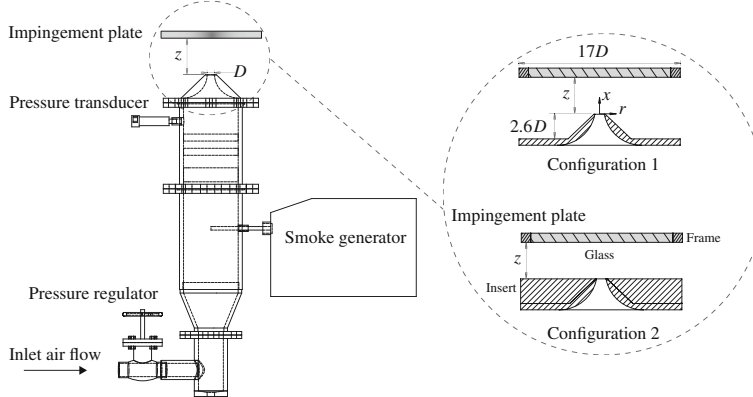
Fig. 1 A schematic diagram of the jet rig facility for two experimental arrangements. **a** Configuration 1 is the nozzle by itself with a lip thickness of 1.5 mm, **b** in configuration 2, a machined insert with a diameter of 17D covers the outer region of the nozzle

To consider the effect of the nozzle lip two configurations as shown in Fig. 1 are investigated.

2.2 Optical Setup-PIV Analysis

The application of particle image velocimetry (PIV) to supersonic flows is accompanied with several challenges as described by Mitchell et al. (2011). However, upon addressing the issues, PIV can be a reliable measuring tool in this type of jet flow. In this study, a 12-bit Imperx B6640 camera with a CCD array of 6,600 px × 4,400 px and a pixel size of 5.5 μm × 5.5 μm is used as the imaging sensor. A two-cavity Nd:YAG pulsed laser (532 nm and 200 mJ per pulse) is used as the illumination source. An appropriate combination of spherical and cylindrical lenses is used to reduce the beam diameter and to produce a collimated laser sheet with a thickness of approximately 1 mm. A 200 mm Micro-Nikkor lens in combination with appropriate extension rings is used to obtain a magnification of approximately 0.65. The mean particle size is approximately 2 pixels using a F-number of 5.6. The depth of field estimation given in Table 1 is based on the diffraction limited image diameter, F-number, and the magnification (Raffel et al. 2007). 10,000 image pairs were recorded at a rate of 1.0 Hz. For the cross correlation of the image pairs, multi-grid cross-correlation digital particle image velocimetry (MCCDPIV) algorithm developed by Soria (1996) was employed. Multi-passing with a small final interrogation window at a high sub-pixel accuracy (using 2D Gaussian peak-fitting function) enables measurements with a high dynamic range. The PIV parameters are shown in Table 1.

Table 1 PIV parameters

Parameter	Physical unit	Non-dimensionalized unit
Imaging resolution	8.65 μm/px	-
Field of view[a]	57 mm × 38 mm	$3.8\,D \times 2.5\,D$
Depth of field	~550 μm	$\sim0.04\,D$
IW_0[a]	128 px × 64 px	$0.074\,D \times 0.037\,D$
IW_1	32 px × 32 px	$0.018\,D \times 0.018\,D$
Grid spacing	16 px × 16 px	$0.009\,D \times 0.009\,D$
Time delay	~880 ns	-

[a]along the axial and radial directions respectively

3 Results and Discussion

Figure 2 shows an instantaneous axial velocity (u) field for each boundary condition at exactly the same operating conditions. The streamlines are shown in order to better visualize the air entrainment into the shear layer and the formation of the wall jet at the impingement surface. The normalization is done using the jet exit velocity (U_e) of approximately 315 m/s.

The flow features of the two cases appear similar, however, there are some evident differences in the entrainment and the flow features initiated at the nozzle exit. A periodic shock cell structure is observed in both the cases. The number of shock cells and position of the shock reflection points at the jet boundaries are similar. The
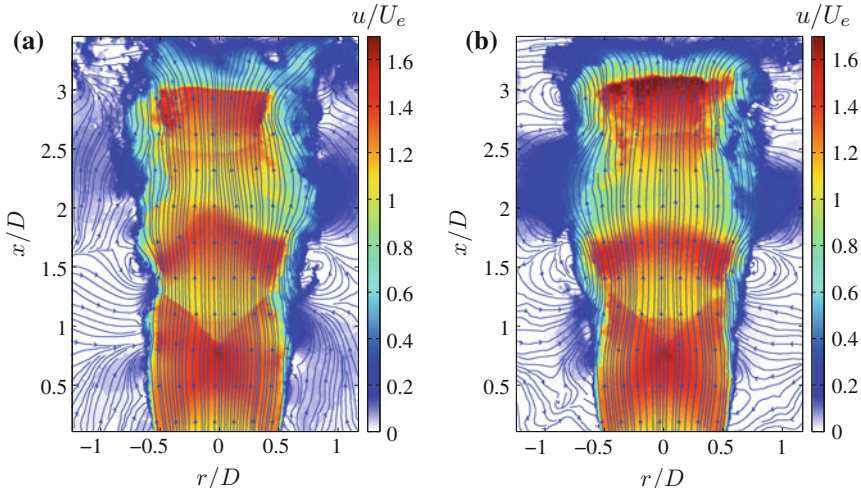
Fig. 2 Instantaneous axial velocity fields at NPR = 3.0 and $Z/D = 3.5$ for **a** the nozzle lip of 1.5 mm (0.1D) (configuration 1), and **b** the orifice geometry (configuration 2)

maxima of the out-of-plane vorticity (not shown here) occur in the shear layer at the jet exit. The vorticity of the opposite sign is observed when the jet hits the wall.

The first- and second-order statistics (not shown here) also show different structures. Although there are similarities in the two jets, there are differences in turbulence intensities. In configuration 1, velocity fluctuation levels near the shock cells appear to be lower than the corresponding regions in configuration 2. This could be explained due to the fact that the ambient air entrainment into the shear layer is easier in Fig. 2a in comparison to Fig. 2b. The enhanced air entrainment resembles the effect of steady flow injection into the shear layer using microjets in order to reduce the flow unsteadiness (Kumar et al. 2013).

4 Concluding Remarks

An ultra high-spatial resolution measurement of an impinging supersonic jet was performed. The complex flow structure that is a resultant of interaction of the jet with the surface and acoustic field was investigated at two nozzle configurations. It has been shown that although the number of shock cells and their spacing are similar, the air entrainment into the shear layer and turbulence intensities are different.

References

Kumar R, Wiley A, Venkatakrishnan L, Alvi F (2013) Role of coherent structures in supersonic impinging jets. Phys Fluids 25(7)

Mason-Smith N, Edgington-Mitchell D, Buchmann N, Honnery D, Soria J (2015) Shock structures and instabilities formed in an underexpanded jet impinging on to cylindrical sections. Shock Waves 25(6):611–622

Mitchell D, Honnery D, Soria J (2011) Particle relaxation and its influence on the particle image velocimetry cross-correlation function. Exp Fluids 51(4):933–947

Mitchell D, Honnery D, Soria J (2012) The visualization of the acoustic feedback loop in impinging underexpanded supersonic jet flows using ultra-high frame rate schlieren. J Visual 15(4):333–341

Mitchell D, Honnery D, Soria J (2013) Near-field structure of underexpanded elliptic jets. Exp Fluids 54(7)

Powell A (1988) The sound-producing oscillations of round underexpanded jets impinging on normal plates. J Acoust Soc Am 83:515–533

Raffel M, Willert C, Wereley S, Kompenhans J (2007) Particle image velocimetry, a practical guide, 2nd edn. Springer, Berlin

Soria J (1996) An investigation of the near wake of a circular cylinder using a video-based digital cross-correlation particle image velocimetry technique. Exp Therm Fluid Sci 12(2):221–233

Near-Wall Anisotropy Under Round and Planar Jet Impingement

Thangam Natarajan, James W. Jewkes, Ramesh Narayanaswamy, Yongmann M. Chung and Anthony D. Lucey

Abstract Anisotropic invariant mapping (AIM) is used to explain the nature of turbulence in the near-wall region of impinging jets. AIM is plotted to gain an understanding of the turbulent stress tensor under round and planar jet impingement. For a fixed jet Reynolds number of 23,000, results of our computational studies (Large Eddy Simulations) show that round jets exhibit isotropic turbulence in the stagnation region that undergoes eddy contraction and stretching as it moves into the wall-jet region. In contrast, planar jets do not exhibit any isotropic turbulence and remain largely dominated by two-component turbulence.

Keywords Anisotropy · Invariants · Impinging jets

1 Introduction

Upon impingement a jet results in various flow fields within the domain and it is important that all elements of the flow field are captured by numerical modelling for a complete understanding. Tracking the expected anisotropy in the resulting flow field presents valuable information about the nature of the turbulence within the flow and its deviation from isotropy. The Reynolds stress anisotropy tensor is used to characterize the flow anisotropy. Anisotropy Invariant Mapping (AIM) proposed by Lumley and Newman (1977) are used to represent the degree of anisotropy in the turbulent flow as these maps present a domain within which all realizable

T. Natarajan (✉) · R. Narayanaswamy · A.D. Lucey
Fluid Dynamics Research Group, Curtin University, Perth, WA 6845, Australia
e-mail: thangam.natarajan@postgrad.curtin.edu.au

J.W. Jewkes
Faculty of Computing, Engineering and Science, University of South Wales,
Pontypridd CF37 1DL, UK

Y.M. Chung
School of Engineering and Centre for Scientific Computing, University of Warwick,
Coventry CV4 7AL, UK
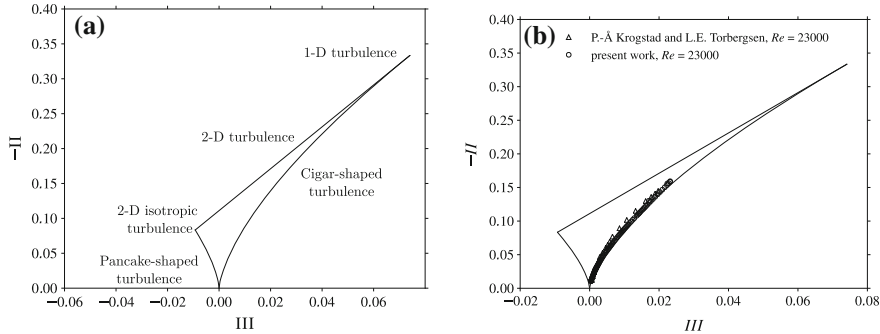
Fig. 1 **a** Anisotropy invariant map and the possible states of turbulence in invariant coordinates $-II$ *vs*. *III* as proposed by Lumley and Newman (1977) and **b** Anisotropy invariant map of Reynolds stress near pipe wall compared to turbulence at round jet nozzle exit of the present work

turbulence must lie. In the present work, the AIM is used to represent the near-wall flow anisotropy under round and planar jet impingement frameworks. The jet Reynolds number in both the cases is 23,000 based on the jet diameter and nozzle width, and a non-dimensional stand-off distance between the nozzle exit and the impingement surface is kept at 4.

The anisotropy tensor b_{ij} is given as, $b_{ij} = \overline{u'_i u'_j}/2k - \delta_{ij}/3$ where u'_i, u'_j are instantaneous velocity fluctuations in directions i & j, while k, is the turbulent kinetic energy and δ_{ij}, the Kronecker delta. The invariants are expressed as, $II = I_2 = -(1/2)b_{ij}b_{ji}$ and $III = I_3 = (1/3)b_{ij}b_{jk}b_{ki}$. Since the flow is incompressible and by the definition of b_{ij}, the first Invariant $I = b_{ii} = 0$. Figure 1a shows an AIM which is a plot of $-II$ versus III along with the definitive bounds within which all realizable turbulence of the flow exists. For further information on the shape of the stress tensor and other terminologies pertaining to AIM plotting theory, the reader may refer Simonsen (2005) and Lumley (1977). AIM was applied to impinging jets by Nishino et al. (1996) and Uddin et al. (2013). However, AIM studies on impinging jets are very limited. Thus, the scope of the work is not to compare the two different configurations, but to understand the nature of turbulence under the two most widely used jet impingement configurations independently for a better understanding of anisotropy in their respective flow fields.

The present work largely adopts the computational methodology used by Natarajan et al. (2014). For further details on numerical schemes, flow initialization, boundary conditions and subgrid scale modelling the reader may refer Natarajan et al. (2014). Deviations from Natarajan et al. (2014) are presented in this study as and when required. The simulation was configured using Cartesian coordinates, $\mathbf{X} = (x, y, z)$; Thus, in the $x - y$ plane, at $z = 0$, x represents the radial direction r and z the azimuthal direction. The jet Reynolds number is given as, $Re = \overline{U}D/\nu$ and is based on the bulk mean velocity $\overline{U}$ and jet diameter D. For the planar jet, nozzle width is used for D.

2 Results and Discussion

Round Jet Impingement Fig. 1b shows the comparison of near-wall anisotropy between the results of pipe flow experiments by Krogstad and Torbergsen (2000) and results obtained at the nozzle exit of the present work. This is carried out as an preliminary validation of the technique used to plot AIM. Good agreement is observed with the experimental data. The near-wall anisotropy at the nozzle exit follows similar turbulent characteristics to that of a pipe flow for the same Reynolds number, and also substantiates the inlet boundary condition used to generate fully-developed flow at the nozzle exit.

AIMs at four different locations on the impingement surface, starting from stagnation zone and extending radially outwards into the wall-jet are examined. Figure 2a shows the AIM plot of invariants at the stagnation zone of the flow domain. The nature of turbulence is partly axisymmetric contraction and a three-component isotropic state. This is due to turbulent fluctuations being similar in magnitude, resulting in similar magnitude of anisotropy tensors ($b_{11} = b_{22} = b_{33}$). This result is in good agreement with the experimental findings by Nishino et al. (1996) and the numerical work by Uddin et al. (2013). At $x/D = 1$ (Fig. 2b), there is considerable
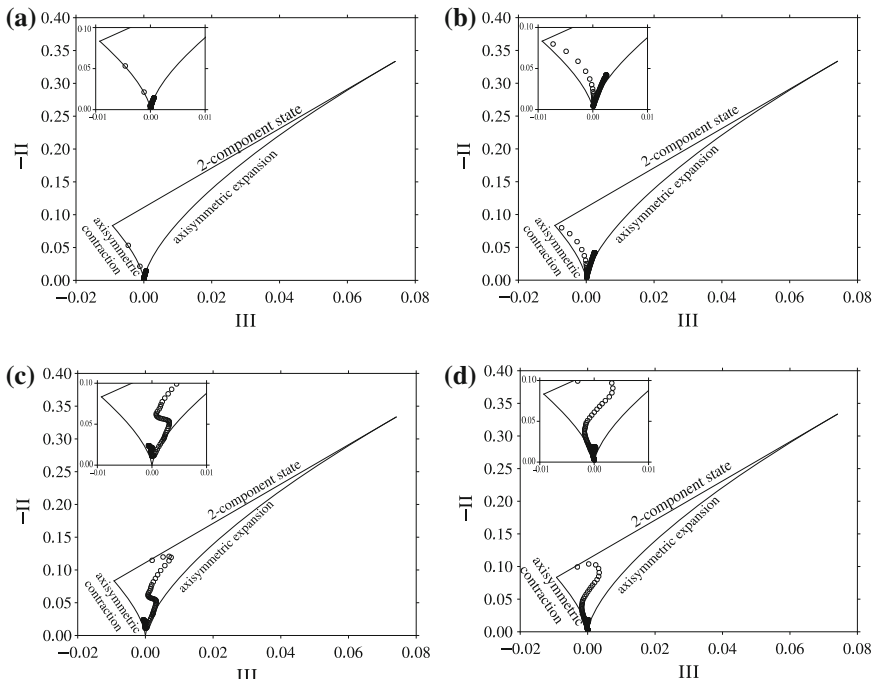
Fig. 2 Anisotropic invariant maps for round jet impingement configuration at **a** $x/D = 0$; **b** $x/D = 1$; **c** $x/D = 2$; **d** $x/D = 3$

deviation from isotropy. At this point, the near-wall eddies undergo an axisymmetric contraction and after $y/D = 0.9$, they undergo axisymmetric expansion due to the change in flow direction. At $x/D = 2$ (Fig. 2c), the near-wall turbulence follows a two-component anisotropic state and also the flow is in an axisymmetric expansion state up to about $y/D = 0.35$.

However, at about $y/D \simeq 0.5$, the anisotropy shows axisymmetric contraction. This could be due to the possible formation of secondary vortices causing flow structures to contract and stretch resulting in a mixed state of anisotropy. After $x/D = 3$ (Fig. 2d), when the flow has developed into the wall-jet region and further, the nature of turbulence straddles an axisymmetric expansion state and a two-component state. This is expected as the flow moves radially outward losing its momentum and kinetic energy; there is no further formation of vortices and turbulent structures and the flow is essentially dominated by two-components alone. The anisotropy remains the same until the flow completely exits the computational domain.

Planar Jet Impingement The AIMs for the planar jet configuration are presented in Fig. 3. Figure 3a shows the AIM at the stagnation zone of the jet where the near-wall anisotropy is largely between a two-component state and axisymmetric
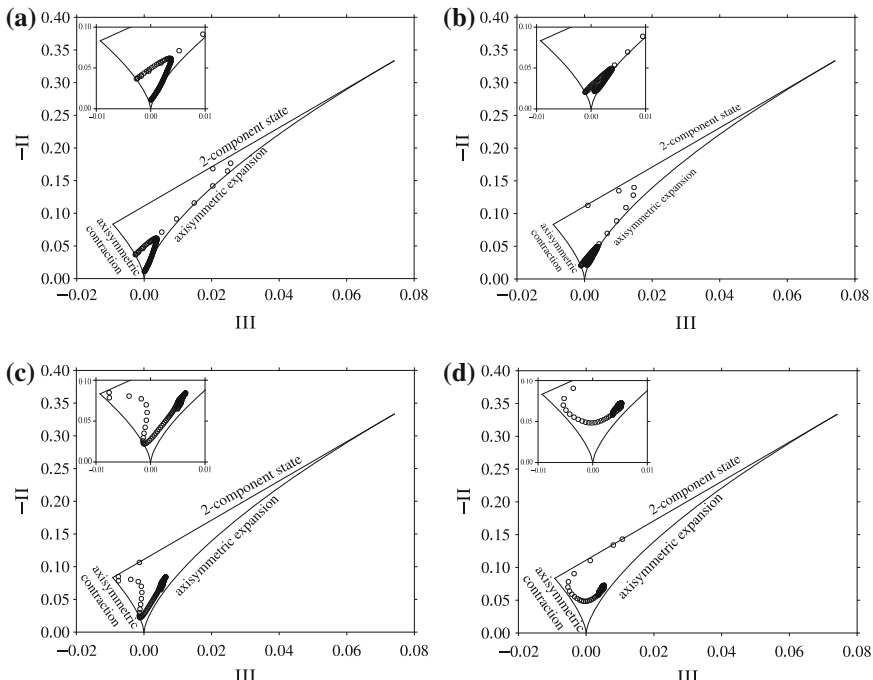
Fig. 3 Anisotropic invariant maps for planar jet configuration at **a** $x/B = 0$; **b** $x/B = 1$; **c** $x/B = 2$; **d** $x/B = 3$

expansion. The flow is not isotropic as in the case of a round jet impingement. The contribution from the third component of the flow is negligible even in the stagnation region of the flow. At $x/B = 1$ (Fig. 3b), it largely remains as a two-component dominated flow and far from three-component isotropic turbulence. At $x/B = 2$ (Fig. 3c), the nature of turbulence undergoes both axisymmetric expansion and contraction due to changes in flow direction and formation of secondary vortices. After $x/B = 3$ (Fig. 3d), the nature of the flow essentially remains the same and largely at a two-component state. The contribution from the third component of the anisotropic tensor is negligible compared to the other tensors.

3 Conclusions

Turbulence and near-wall anisotropy has been studied using AIM for round and planar impinging jets. In round jets, near-wall anisotropy exhibits contraction and isotropy at the stagnation zone and on moving away, the flow undergoes axisymmetric expansion and contraction. In planar jets, the flow does not exhibit any isotropy and remains largely dominated by two-component turbulence. However, similar expansion and contraction of eddies are observed at regions where flow reversal and secondary vortex formation occurs.

References

Krogstad PÅ, Torbergsen LE (2000) Invariant analysis of turbulent pipe flow. Flow Turbul Combust 64(3):161–181

Lumley JL, Newman GR (1977) The return to isotropy of homogeneous turbulence. J Fluid Mech 82(01):161–178

Natarajan T, Jewkes JW, Narayanaswamy R, Chung YM, Lucey AD (2014) Reynolds averaged and large Eddy computations of flow and heat transfer under round jet impingement. ASME Paper FEDSM2014-21435

Nishino K, Samada M, Kasuya K, Torii K (1996) Turbulence statistics in the stagnation region of an axisymmetric impinging jet flow. Int J Heat Fluid Flow 17(3):193–201

Simonsen AJ, Krogstad PÅ (2005) Turbulent stress invariant analysis: clarification of existing terminology. Phys Fluids 17(8):088103

Uddin N, Neumann SO, Weigand B (2013) LES simulations of an impinging jet: on the origin of the second peak in the Nusselt number distribution. Int J Heat Mass Transf 57(1):356–368

Flapping Motion of a Turbulent Jet Under the Asymmetric Excitation of Two Unsteady Minijets

H. Yang, Y. Zhou, Y. Zhu and Y. Liu

Abstract The control of a turbulent round jet is experimentally investigated based on the injection of two radial minijets, separated azimuthally by an angle $\theta = 60º$, prior to the issue of the main jet. It has been found that the asymmetric excitation increases the decay rate of the jet centerline mean velocity by 30 % or more than the symmetric ($\theta = 180º$). A flapping motion of the jet column is found to be responsible for the substantially increased jet mixing.

1 Introduction

The study of jet control has been given a great attention in the literature over the past few decades due to a wide range of relevant industrial applications, such as mixing, noise suppression, combustion, cooling and heating. The rate of jet mixing plays a crucial role in most of these applications. Clearly, this rate is very much influenced by the coherent structures and is thus manipulatable either passively or actively. There have been a number of investigations that deployed fluidic means for jet mixing enahncement (e.g. Davis 1982; Raman 1997; Zhou et al. 2012). Zhang (2014) studied in detail the active control of a round jet using two

H. Yang · Y. Zhou (✉)
Institute for Turbulence-Noise-Vibration Interaction and Control,
Shenzhen Graduate School, Harbin Institute of Technology, Shenzhen, China
e-mail: zhouyu@hitsz.edu.cn

H. Yang · Y. Liu
Department of Mechanical Engineering, The Hong Kong Polytechnic University,
Hung Hom, Hong Kong

Y. Zhou · Y. Zhu
CSIRO Manufacturing Flagship, Private Bag 10, Clayton South MDC,
Victoria 3169, Australia

symmetrically arranged unsteady minijets, and found a much more efficient control than using steady minijets. Three types of coherent structures are identified, i.e., the distorted vortex ring, two pairs of azimuthally streamwise vortices and sequentially ejected mushroom-like counter-rotating structures, and jet mixing is dictated by the interactions of the three distinct coherent structures. Nevertheless, many aspects of this control technique remain to be clarified, such as the effects of the minijet number, orientation and geometric arrangement. This work continues to explore this technique and investigates jet mixing and associated control mechanisms under the asymmetric excitation of two unsteady minijets.

2 Experimental Details

The round air jet consists of the main jet and minijet assemblies (Fig. 43.1). The main jet nozzle is issued from a nozzle with an exit diameter of $D = 20$ mm. The minijet assembly includes a stationary and a rotating disk. The stationary disk is made with two orifices of 0.9 mm in diameter, separated azimuthally by 60 degrees and located at 17 mm upstream of the main jet exit. The rotating disk is drilled with 12 orifices of 1 mm in diameter, azimuthally equally spaced, and is driven by a servo motor. Once the orifices on both disks are aligned during rotation, two minijets are injected into the main jet. The jet Reynolds number Re_D based on D is 8000. Two control parameters are examined; the ratio of the minijet frequency f_e to the vortex frequency f_0 near the end of potential core of the uncontrolled jet is $f_e/f_0 = 0.31 \sim 1.24$ and the mass flow ratio C_m of the minijets to the main is 1.1–10.9 %. The origin of the coordinate system is chosen at the center of the main jet exit, with the x axis along the streamwise direction. Measurements were conducted in the symmetry plane, i.e., the (x, y) plane, of the two minijets, the orthogonal plane through the jet geometric centerline, i.e., the (x, z) plane, and a number of cross-sectional (y, z) planes using flow visualization, PIV and hotwire techniques. The decay rate $K = (U_e - U_{5D})/U_e$ is used to evaluate jet mixing, where U_e and U_{5D} denote the jet centerline time-averaged velocities at $x/D = 0$ and 5, respectively.
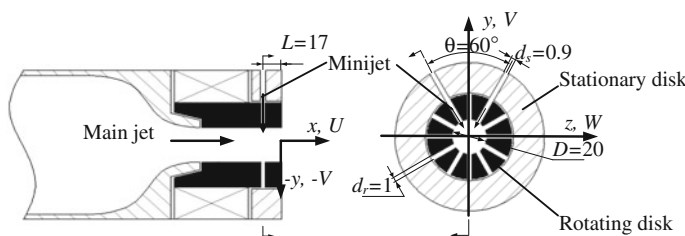
Fig. 43.1 Experimental setup
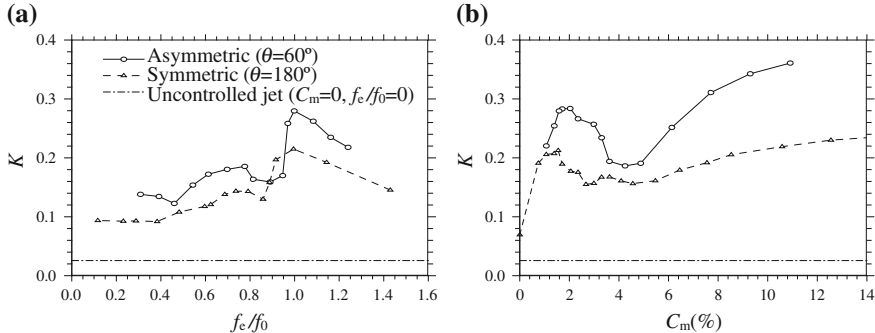
Fig. 43.2 Dependence of K on **a** f_e/f_0 ($C_m = 1.5$ %) and **b** C_m ($f_e/f_0 = 1$), $\theta = 60°$

3 Dependence of Jet Mixing on Mass and Frequency Ratios

Figure 43.2 presents the dependence of the jet decay rate on f_e/f_0 and C_m, which is qualitatively the same as that under symmetric control ($\theta = 180°$). However, the asymmetric control is much more effective than the symmetric. As shown in Fig. 43.2a, the asymmetric control increases K by 30 %, compared with the symmetric, at $C_m = 1.5$ % and $f_e/f_0 = 1$. Figure 43.2b presents the dependence of K on C_m at $f_e/f_0 = 1$. Note that the asymmetric excitation is characterized by a substantially higher K than the symmetric.

4 Evolution of Vortex Rings

The flow physics and control mechanisms are investigated based on flow visualization in the (x, y) and (x, z) planes (Fig. 43.3) as well as in the (y, z) planes (Fig. 43.4). The uncontrolled jet shows the well-known quasi-periodical structure in the (x, y) (Fig. 43.3a) and a 'full moon' enclosed by a ring in the (y, z) plane through the ring vortex (Fig. 43.4a). Once controlled, the flow structure changes greatly. Firstly, the turbulent transition occurs earlier (Fig. 43.3b). Secondly, the upper and lower rollup are not symmetrical about the jet axis but staggered instead (Fig. 43.3c), that is, the vortex ring plane appears turning, forming an angle with respect to the (y, z) plane, and the turning directions of adjacent two ring vortices are opposite to each other. Thirdly, the approaching two ends of two adjacent ring vortices merge together.

A flapping motion of the jet column is identifiable from the sequential photographs (e.g. Fig. 43.3c1–c2) of flow visualization in the (x, y) plane. Insight into the physical process of this motion may be gained by examining flow visualization
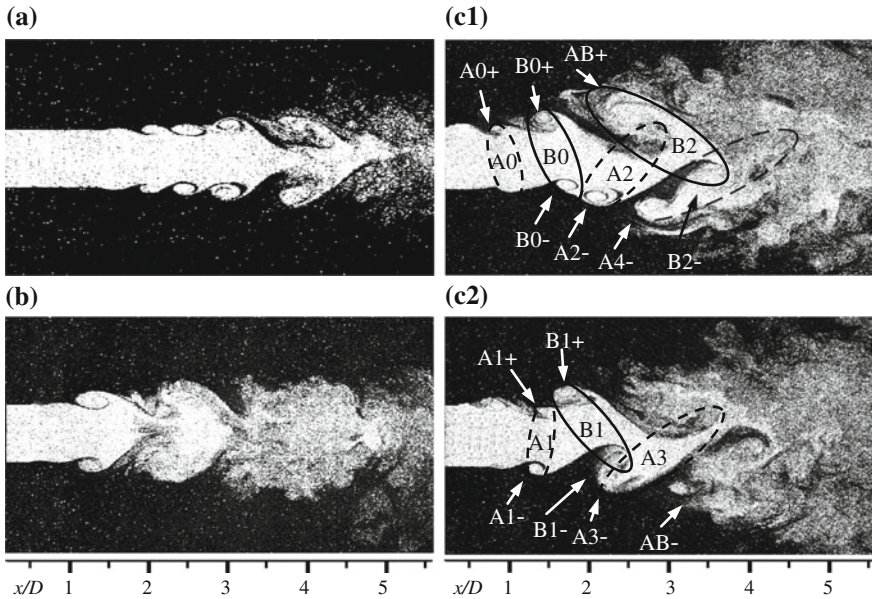
Fig. 43.3 Photographs of typical flow structures from flow visualization. **a** Uncontrolled jet. **b** *x-z* plane and **c1–c2** *x-y* plane of the controlled jet (C_m = 2.0 %, f_e/f_0 = 1)
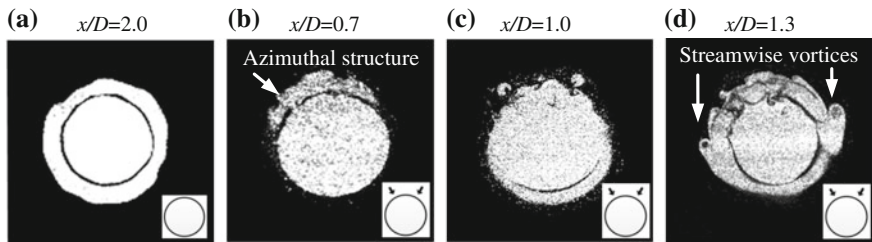
Fig. 43.4 Photographs of flow visualization in the cross-sectional (*y-z*) planes **a** Uncontrolled jet. **b–d** Asymmetric controlled jet (C_m = 2.0 %, f_e/f_0 = 1)

data in the cross-sectional planes (Fig. 43.4). Under excitation, the shear layer on the upper side of the main jet always rolls up first at $x/D = 0.7$ to form an azimuthal structure (Fig. 43.4b). At $x/D = 1.0$, the shear layer on the lower side also starts to roll up (Fig. 43.4c). Meanwhile, a trailing vortex A0 + (Fig. 43.3c1) on the upper side moves inwards to A1 + (Fig. 43.3c2), catching up with the leading vortex B1 + (Fig. 43.3c2), due to their mutual induction. As a result, the vortex ring A0 rotates clockwise to A1 around an axis parallel to the *z* axis. As such, the adjacent vortex rings B0 and A1 are oppositely tilted when reach in $x/D \approx 1.3$, indicated by

the lower and upper ends (B0− and B0 +) and (A1 + and A1−), respectively. Meanwhile, one pair of counter-rotating streamwise vortices is discernible (Fig. 43.4d). Further downstream, two vortices on the upper side undergo pairing, forming AB + (Fig. 43.3c1) and then breaks down at $x/D \approx 3.0$ (Fig. 43.3c2). On the lower side, two vortices, B0− and A2−, upstream of AB + approach each other at $x/D \approx 1.7$ (Fig. 43.3c1). The trailing vortex B0- catches up and pairs with the leading vortex A2-. The merged structure does not break up until $x/D = 3.5$ (AB- in Fig. 43.3c2). Under the effect of the asymmetric vortex induction, the vortex ring undergoes substantial stretching and tilts alteratively (A1-A2-A3 and B0-B1-B2), entraining alternatively the upper and lower ambient fluid into the core region, causing the jet column to flap vigorously.

5 Formation of Flapping Motion

Figure 43.5 presents typical instantaneous lateral velocity $v^* = v/U_e$ contours in the (x, y) plane of the controlled jet, as compared with the uncontrolled jet. Without control, the velocity contours are nearly symmetric about the jet centerline, implying the fluid in the outer region of the jet is induced either outward or inward. The potential core region is unaffected up to $x/D \approx 3$. Once controlled, the velocity contours indicate fluid motions alternately upward and downward. Ambient fluid is entrained upstream of two interacting vortices, evident in the vorticity contours (not shown) and marked by + in Fig. 43.5b, while the jet core fluid is induced outward downstream of the two vortices. Due to the asymmetric vortex interactions discussed above, both entrainment on the lower side and spreading on the upper occur at $x/D \approx 1.8$, producing an upward motion. Similarly, a downward motion occurs at $x/D \approx 2.4$. As such, the flapping motion of the jet column is generated.
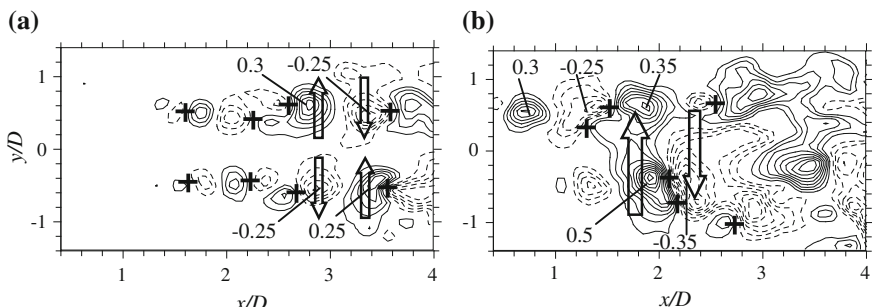
Fig. 43.5 Typical instantaneous lateral velocity $v^* = v/U_e$ contours in the (x, y) plane. **a** Uncontrolled jet. **b** Controlled ($C_m = 2.0$ %, $f_e/f_0 = 1$). Contour interval = 0.05

6   Conclusions

The jet decay rate K exhibits a strong dependence on C_m and f_e/f_0, which is qualitatively the same as that under symmetric control ($\theta = 180°$). However, the asymmetric excitation increases K by 30 % or more than the symmetric, suggesting a considerably more effective control and a possibly different mechanism.

A flapping motion has been observed. Under the asymmetric excitation, the upper-side shear layer rolls up earlier than the lower, and the trailing vortex on the upper side moves inwards to catch up with the leading vortex due to their mutual induction. As a result, the vortex rings are tilted alternately to the opposite directions, creating a 'zigzag' structure and the localized pairing between the ends of adjacent rings. The vigorous interactions of these vortical structures entrain ambient fluid into the jet core alternatively from the upper and lower sides, thus producing the flapping motion, which is responsible for the substantially higher jet mixing.

References

Davis MR (1982) Variable control of jet decay. AIAA J 20(5):606–609

Raman G (1997) Using controlled unsteady fluid mass addition to enhance jet mixing. AIAA J 35 (4):647–656

Zhou Y, Du C, Mi J et al (2012) Turbulent round jet control using two steady minijets. AIAA J 50 (3):736–740

Zhang P (2014) Active control of a turbulent round jet based on unsteady minijets. PhD thesis. The Hong Kong Polytechnic University

Measurements of Prandtl Number
of an Elliptic Jet

Z.K. Zhang and L.P. Chua

Abstract The turbulent Prandtl number, Pr_t, distributions of a heated contoured contraction nozzle elliptic air jet with a 2:1 aspect ratio issuing into stagnant, unconfined surroundings were presented. The measurements were carried out with X-wire and three-wire (a cold wire in front of an X-wire) probes. The normalized RMS velocities in both lateral and span-wise directions were consistently smaller than those in the streamwise direction, indicating the anisotropy of the turbulence in the flow. The Pr_t evaluated based on the self-preserved data of Reynolds shear stress, $\overline{uv}$, and heat flux, $\overline{v\theta}$, at $x = 30D_e$ decrease sharply from the center and only remained at a constant value of about 0.8 within the range of $0.4 \leq y/L_y \leq 1.8$ along the major axis while a gradual increase is observed in the minor axis. A constant Pr_t in both axes should not be granted in the computational modeling and analysis of a heated elliptic jet.

1 Introduction

Noncircular jets offer many performance benefits at a relatively low cost of altering jet nozzle geometry (Zhang and Chua 2012). An application of noncircular heated jets particularly pertinent to the aerospace industry takes advantage of the enhanced mixing of the heated jet fluid with the surroundings, decreasing the likelihood of aircraft detection (Grinstein and DeVore 1996). The lack of a comprehensive study in the literature on heated elliptic jets provide the motivation for the present study, which aims to relate the momentum and heat transfer parameters for the elliptic jet. Measurements of the $\overline{uv}$ in the unheated jet and $\overline{v\theta}$ in the heated jet were carried out.

Z.K. Zhang (✉) · L.P. Chua (✉)
Nanyang Technological University School of Mechanical and Aerospace Engineering,
50 Nanyang Avenue, Singapore 639798, Singapore
e-mail: mlpchua@ntu.edu.sg

These will yield information relating the heat and momentum transfer characteristics in the flow field of the heated elliptic jet. Subsequently, the Pr_t, defined as the ratio of the turbulent eddy diffusivity of momentum to that of heat, can be computed. The Pr_t is an important parameter often assumed to be a constant when carrying out computational analyses. Given the popularity of noncircular jets as a passive flow control device and the numerous heated jet applications, it would be worthwhile to gain a better understanding of the heated elliptic jet so as to enhance its implementation in relevant applications.

2 Experimental Details

The experimental rig is a variable speed centrifugal blower supplies air to the flow system. A transition piece after the 500 mm long settling chamber changes the square cross-sectional duct to a 2:1 aspect ratio ellipse and finally reaches a smooth contracted elliptic jet nozzle exit (50×25 mm^2). The equivalent diameter, De, defined for the present jet as the diameter of a circular jet with the same exit momentum flux, is 35.4 mm. The jet flow is heated by a 1 kW electrical coil element heater attached to the inlet of the centrifugal blower. Figure 1a gives a schematic view of the elliptic jet nozzle and defines the coordinate used. In all experiments, the jet exit velocity, Uj was set at 25 ± 0.5 m/s, which corresponded to a Reynolds number, Re_j ($= U_jD_e/\nu$) of 56,441. For the heated jet measurements, the jet exit temperature, T_j was set to 20 ± 0.5 °C above the ambient. An X-wire probe was used to obtain the $\overline{uv}$ and $\overline{uw}$, in the major and minor axes respectively. For the heated jet experiments, a three-wire probe as shown in Fig. 1b was employed for the simultaneous measurement of the velocity fluctuations and temperature fluctuation, θ to compute the $\overline{v\theta}$ and $\overline{w\theta}$, respectively and subsequently the Pr_t along the major and minor axes.
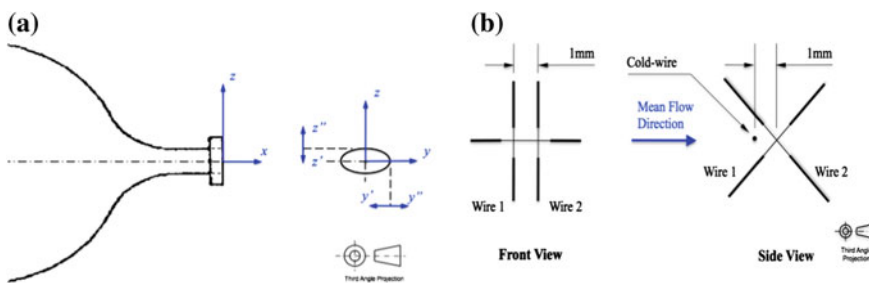
Fig. 1 a Definition sketch of coordinate system at nozzle exit, and b Configuration of three-wire probe

3 Results and Discussion

The mean velocity profile across the boundary layers at the nozzle exit agreed with the Blasius profile, indicating laminar initial conditions. Figure 2a, b show the lateral and span-wise RMS velocity profiles (v'/Uc and w'/Uc) in the major and minor axes respectively. Extending on from the streamwise RMS velocity profiles reproduced in Fig. 2c from (Zhang and Chua 2012), the fluctuating components of velocity in the lateral (y) and span-wise (z) directions are presented. The profiles of v'/Uc and w'/Uc also display two-peak saddle-shaped profiles similar to u'/Uc. In the intermediate-field region immediately after the end of the potential core, both the peak and centerline values of w'/Uc were larger than those of v'/Uc. The evolution of v'/Uc and w'/Uc was more rapid in comparison to u'/Uc (see Fig. 2c) since the saddle-shape is discernible only up to streamwise distances of $x = 8D_e$ for v'/Uc and $x = 10D_e$ for w'/Uc in the major and minor axes respectively. The profiles of v'/Uc and w'/Uc have not attained self-similarity by $x = 38D_e$, an
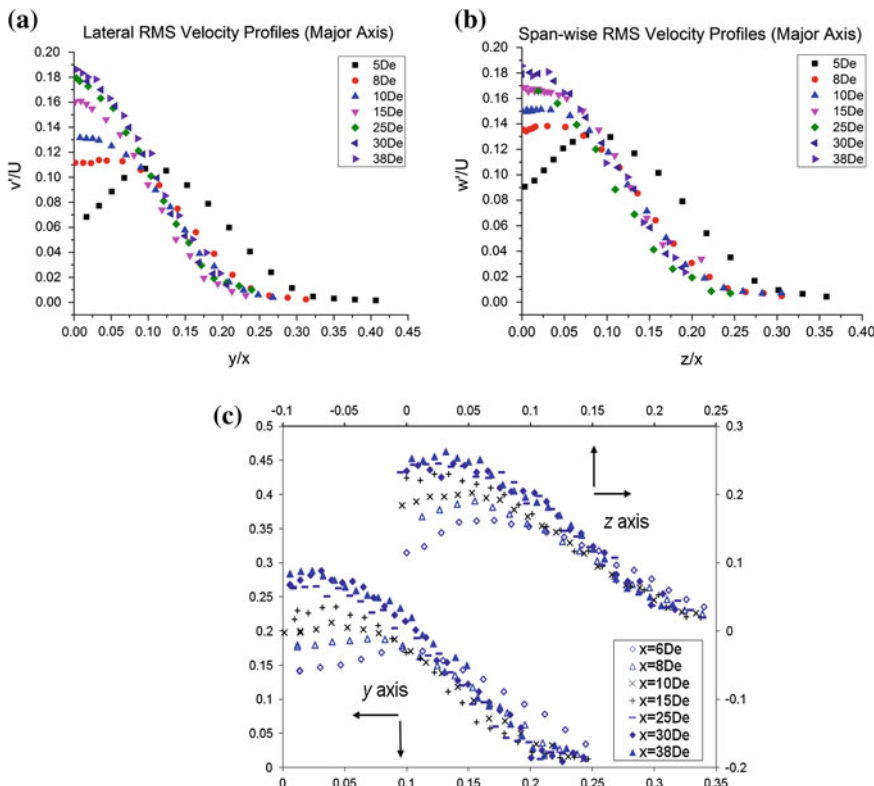
Fig. 2 **a** Lateral, **b** spanwise and **c** streamwise RMS velocity profiles in the intermediate- to far-field of the jet in the major axis (y/x, for a and c) and minor axis (z/x, for b and c)

asymptotic peak value of about 0.18 on the jet centerline was reached by $x = 25D_e$ in both axes. It can be observed that the fluctuating velocities in the lateral (and span-wise) directions acquire their energy from that in the mean flow direction by pressure redistribution, v' (and w') should be smaller than u'. It is of interest to note that the differences between the distributions of u'/Uc and v'/Uc (w'/Uc) indicate a large degree of anisotropy in the turbulent flow field of the elliptic jet, which aids the mixing process through large-scale motion (Xu and Antonia 2002).

The turbulent (or eddy) diffusivities for momentum and heat (V_T and α_T respectively) need to be determined first in order to obtain the Pr_t. For the purpose of evaluating the turbulent diffusivity of momentum V_T, values from the polynomial curve-fit equations for the self-preserved data of $\overline{uv}$ and $\overline{uw}$ (not shown here) respectively were used. The gradients of the streamwise mean velocities, $\partial U_m/\partial y$ and $\partial U_m/\partial z$ were obtained by differentiating the self-preserved profiles in Fig. 8 of (Zhang and Chua 2012) in the major and minor axes respectively. Correspondingly, values from the self-preserved data of $\overline{v\theta}$ and $\overline{w\theta}$ (not shown here), together with the gradients of the mean temperatures, $\partial T_m/\partial y$ and $\partial T_m/\partial z$ obtained by differentiating the self-preserved mean temperature profiles in Fig. 10 of (Zhang and Chua 2012), were used to calculate the turbulent diffusivity of heat, α_T in the major and minor axes respectively. Figure 3a, b present the distributions of the normalized turbulent diffusivities of momentum and heat respectively along both the major and minor axes. In Fig. 3a, the distributions of the turbulent diffusivity of momentum displayed similar trends in both axes although a slightly higher peak value of 0.031 at $y/L_y = 0.46$ in the major axis was observed as compared to 0.029 at $z/L_z = 0.61$ in the minor axis. The turbulent diffusivity of momentum in both axes of the current elliptic jet was found to be larger than those of the circular (Chua and Antonia 1990) and square jets (Chua et al. 2004). In Fig. 3b, the turbulent diffusivity of heat along the major axis was observed to be consistently larger than that in the minor axis throughout the jet column. A pronounced peak of $\alpha_T/(U_c L_y) = 0.055$ was observed at $y/L_y = 0.2$ in the major axis distribution.
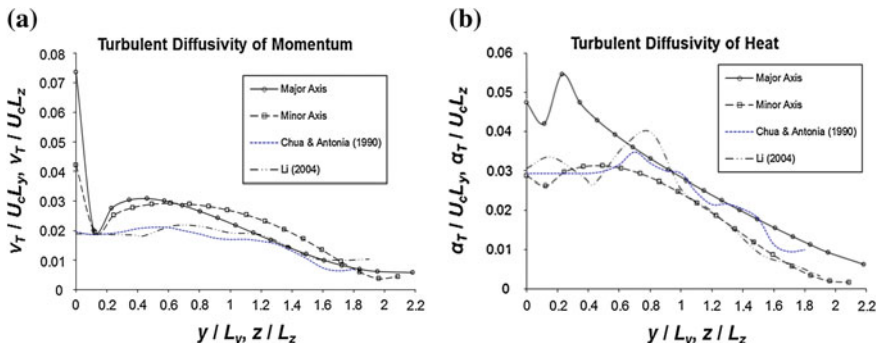
Fig. 3 Distributions of **a** turbulent diffusivity of momentum and **b** turbulent diffusivity of heat along major and minor axes

Fig. 4 Distributions turbulent Prandtl number along major and minor axes
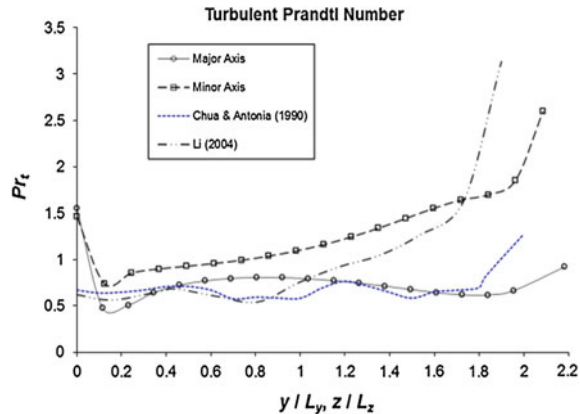
The Pr_t is the ratio of the turbulent diffusivity of momentum, V_T to that of heat, α_T. Figure 4 shows the variations of the Pr_t along both the major and minor axes. On the jet axis, the Pr_t evaluated by applying L'Hôpital's Rule was found to be 1.55 and 1.46, followed by a steep decrease to approximately 0.48 and 0.74 at $y/L_y, z/L_z = 0.1$ in the major and minor axes respectively. This trend is in qualitative agreement with the results of (Browne et al. 1984) at the self-preserved streamwise distance of $x = 40D_e$ for the plane jet, at which the limiting value of Pr_t was found to be 1.43 on the jet centerline followed by a rapid decrease to 0.625 at the lateral distance of 0.5 jet velocity half-widths. Similar to the circular (Chua and Antonia 1990) and square jets (Chua et al. 2004), the Pr_t distributions along both axes showed increasing trends beyond the lateral (and span-wise) distances of 1.8 jet velocity half-widths from the centerline. Within the range of $0.4 \leq y/L_y, z/L_z \leq 1.8$, the Pr_t maintains at about a constant value of 0.8 along the major axis while a gradual increase is seen in the minor axis, demonstrating the unique momentum and heat transfer characteristics in each axis of the elliptic jet. Additionally, this implies that the Pr_t should not be taken to be a common constant value in both axes when analyzing the behaviour of heated elliptic jets, for example, through numerical simulation as this may result in erroneous mean temperature and turbulent heat flux profiles.

4   Conclusions

1. The u'/Uc showed consistently higher peak and centerline values than those of v'/Uc and w'/Uc, showing the anisotropic nature of the turbulence in the flow.
2. After decreasing from its initial peak value on the jet centerline, the Pr_t remained at a constant value of about 0.8 within the range of $0.4 \leq y/L_y \leq 1.8$ along the major axis while a gradual increase is observed in the minor axis. Therefore, a constant Pr_t in both axes should not be assumed in the computational modeling and analysis of a heated elliptic jet.

References

Browne LWB, Antonia RA, Chambers AJ (1984) The interaction region of turbulent plane jet. Fluid Mech J 149:355–373

Chua LP, Antonia RA (1990) Turbulent Prandtl number in a circular jet. Int J Heat Mass Transf 33 (2):331–339

Chua LP, Li YF, Zhou T (2004) Measurements of a heated square jet. AIAA J 42(3):578–588

Grinstein FF, DeVore CR (1996) Dynamics of coherent structures and transition to turbulence in free square jets. Phys Fluids 8(5):1237–1251

Xu G, Antonia RA (2002) Effect of different initial conditions on a turbulent round free jet. Exp Fluids 33:677–683

Zhang ZK, Chua LP (2012) Mixing due to a heated elliptic air jet. Int J Heat Mass Transf 55 (17–18):4566–4579

Simulations of Complex Turbulent Flows with RANS-LES Hybrid Approaches

Zhixiang Xiao and Song Fu

Abstract Two advanced DES (detached eddy simulation) methods, delayed-DES (DDES) and improved-delayed DES (IDDES), are the two wide-used RANS-LES (Reynolds averaged Navier-Stokes and large eddy simulation) hybrid methods. They are applied to accurately simulate the unsteady complex turbulent flows at high Reynolds numbers with a wide Mach number range from low speed to hypersonic. In addition, the dissipation properties of the spatial scheme are also discussed and the adaptive dissipation scheme performs well. After comparing the performance of DDES and IDDES, IDDES is recommended for the following simulations: massive separation flows past tandem cylinders and rudimentary landing gear at low speed, cavity flow at transonic, supersonic and hypersonic conditions. The pressure fluctuations and dynamic loads are accurately captured near the wall.

Keywords DDES and IDDES · Adaptive dissipation · All speed

1 Introduction

In the recent decade, the requirements of the high fidelity simulations for the pressure fluctuations and dynamic loads due to the complex turbulent flows at high Reynolds number are urgent with the fast increase of computational power. They mainly cause complex multi-physics interactions between flows and structures, acoustics, optics, combustions, respectively, or all together.

Limited by computational resources, the combinations of LES with RANS can achieve reasonably consistence in terms of both efficiency and accuracy in simulating the unsteady turbulent flows in industries, always at very high Reynolds number. The modeling strategy of turbulent flows, often referred to as RANS-LES hybrid models (such as DES, detached-eddy simulation, originally proposed by

Z. Xiao · S. Fu (✉)
School of Aerospace Engineering, Tsinghua University, Beijing 100084, China
e-mail: fs-dem@tsinghua.edu.cn

Spalart et al., denoted as DES97 (Spalart et al. 1997)), has recently become much favored in the study of the unsteady and geometry-dependent separated flows. Such hybrid methods combine a high-efficiency turbulence model near the wall, where the flow is dominated by small-scale motions, with a LES-type treatment for the large-scale motions in the separation region far away from the wall. However, some inherent shortcomings are identified for DES97 and some others are demonstrated through further investigation by many researchers. These shortcomings include erroneous activities of the near wall damping terms in LES mode, incursion of LES mode inside boundary layer, gray area and log-layer mismatch. Many of these shortcomings have been successfully solved in the later versions, such as DDES (Menter and Kuntz 2003; Spalart et al. 2006), IDDES (Shur et al. 2008), and some also remain.

In this article, we mainly focus on the applications of advanced DES model, such as DDES and IDDES. In addition, the corresponding spatial schemes with adaptive dissipation are also briefly introduced. For the high-speed flows, the shock detector is introduced to well capture the shock wave and reserve the robustness of the high-order scheme. Some complex turbulent flows at high Reynolds number around such geometries, tandem cylinders (Xiao et al. 2012), rudimentary landing gear (Xiao et al. 2013) cavities are simulated using these advanced DES models.

2 Advanced DES-Type Models and Numerics

Differing from the original DES97, the fundamental turbulence model is taken as two-equation shear stress transport (SST) model (Menter 1994), but not the one-equation Spalart-Allmaras model. Two DDES, versions 2003 (Menter and Kuntz 2003) and 2006 (Spalart et al. 2006), and IDDES (Shur et al. 2008) are briefly described here. The general DES formulations could be constructed by modifying the destruction term of the turbulent kinetic energy (TKE) equation and by introducing a length scale, $L_{\text{hybrid,}}$ as following.

$$\frac{\partial(\rho k)}{\partial t} + \frac{\partial(\rho u_j k)}{\partial x_j} - \frac{\partial}{\partial x_j}\left((\mu + \sigma_k \mu_t)\frac{\partial}{\partial x_j}\right) = \tau_{ij}S_{ij} - \frac{\rho k^{3/2}}{L_{\text{hybrid}}} \qquad (1)$$

For the early DDES version, DDES-2003, the L_{hybrid} can be written as

$$L_{\text{hybrid}} = L_{\text{DDES}-2003} = \min[L_{\text{LES}}/(1 - F_{\text{SST}}); L_{\text{RANS}}] \qquad (2)$$

The turbulence scale L_{RANS} is $k^{1/2}/(\beta^* \omega)$ and the LES length scale $L_{\text{LES}} = C_{\text{DES}}\Delta$, where $\Delta = \max(\Delta x, \Delta y, \Delta z)$. Here, F_{SST} is a delayed function, which is taken as function F_2 in the SST model. It can ensure the DES method acts as the RANS mode in the attached flow, without the negative effect of local clustering mesh.

For the later version of DDES, DDES-2006, L_{hybrid} can be written as

$$L_{\text{hybrid}} = L_{\text{DDES}-2006} = L_{\text{RANS}} - f_d \times \max(0; L_{\text{RANS}} - L_{\text{LES}}) \tag{3}$$

The function f_d is another delayed function.

For the IDDES, the length scale of L_{hybrid} can be written as

$$L_{\text{hybrid}} = L_{\text{IDDES}} = \tilde{f}_d(1 + f_e) \times L_{\text{RANS}} + (1 - \tilde{f}_d) \times L_{\text{LES}} \tag{4}$$

These functions can be found in the original reference (Shur et al. 2008).

From the comparisons of Eqs. (2)–(4), the main differences between DDES-2003 and 2006 are the delayed functions F_2 and f_d, which determine the regions of RANS and LES parts. IDDES combines the advantages of both DDES and WMLES (wall-modelled LES).

Another very important issue is the dissipation level of the numerical scheme. The invicid flux of the Roe scheme with adaptive dissipation (Xiao et al. 2012) is given as:

$$\overline{F}_{i+\frac{1}{2}} = \frac{1}{2}[F(q_L) + F(q_R)]_{i+\frac{1}{2}} - \frac{1}{2}\sigma\left[\left|\widetilde{A}_{inv}\right|(q_R - q_L)\right]_{i+\frac{1}{2}} \tag{5}$$

where q^L and q^R are the original variables at the left and right hand sides of the interface reconstructed by high-order interpolation. σ is the adaptive function, which becomes near zero in the separates region where the flow is dominated by turbulence and it acts as in the central mode. Conversely, near the wall and in the irrotational region, the adaptive function σ is close to one and the scheme practically acts as the originally upwind scheme to keep the robustness.

To resolve the small-scale motions and maintain the capability of capturing the shock wave at the same time, the adaptive function should be modified as

$$\sigma = \sigma_1 + \sigma_2 - \sigma_1\sigma_2 \tag{6}$$

where σ_1 is the original one and σ_2 is the shock detector defined as $(\partial u_j / \partial x_j)^2 / [(\partial u_j / \partial x_j)^2 + \Omega^2]$, where Ω is the magnitude of the vorticity. Function σ_2 is close to 1 near the shock wave, where the large dissipation reserves.

The adaptive function of σ_1, shock detector σ_2 and the final adaptive function σ are presented in Fig. 1. At the same time, the pressure distributions are also plotted in it. From this figure, we can find that the final adaptive function σ can satisfy our intended requirements: it approaches to 1 at the wall, near the shock wave and in the irrotational regions; it becomes very small in the cavity and in the boundary layer.
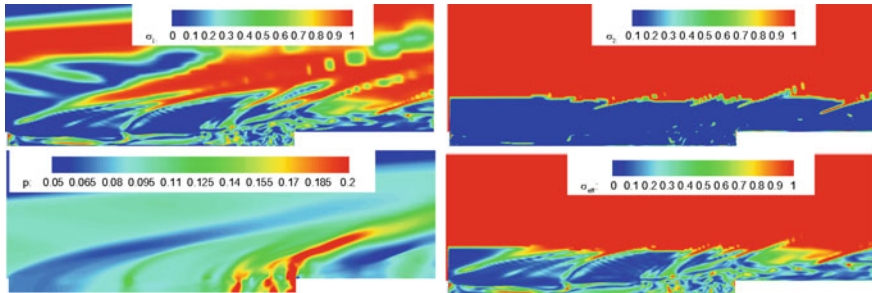
Fig. 1 The distribution of adaptive function past the cavity at Ma 9.575

3 Results and Discussions

In this section, the properties of scheme dissipation are firstly discussed and the adaptive dissipation scheme coupled with the DES-type models was recommended, through simulating the massive separation past the tandem cylinder (TC). Secondly, based on the adaptive dissipation scheme, the performances of DDES- 2003, 2006 and IDDES are briefly discussed through the same TC case by comparing the instantaneous structures and pressure fluctuations. IDDES performs best. Finally, IDDES with the adaptive dissipation scheme is wide applied to predict the high-Reynolds number unsteady flows from low-speed to hypersonic.

3.1 Numerical Dissipation Effects

As we known, large numerical dissipation of the upwind scheme is likely to contaminate and even overshadow the physical viscosity. In that case, only very large-scale unsteady vortices can be captured and most of the small-scale structures are eliminated by the numerical dissipation, even the advanced DES model was applied. To accurately resolve the small-scale structures in the core flow region, the dissipation level is required very small; to keep the robustness of the scheme near the wall and in the irrotational region, the dissipation level should be large enough. In the same computational domain, the numerical dissipations should be varied automatically, from near zero to the original dissipation level of the upwind scheme. The direct dissipation reduction everywhere is too empirical to well predict the flows.

The velocity of freestream past the TC is 44 m/s, the Reynolds number based on D is 1.66×10^5, and the angle of attack is 0 deg. It is a typical low-speed case for the massive separation. This flow is simulated with the original Roe scheme, the fifth-order Roe scheme with a constant σ of 0.12 and fifth-order Roe scheme with adaptive dissipation. The turbulence model is DDES-2003.
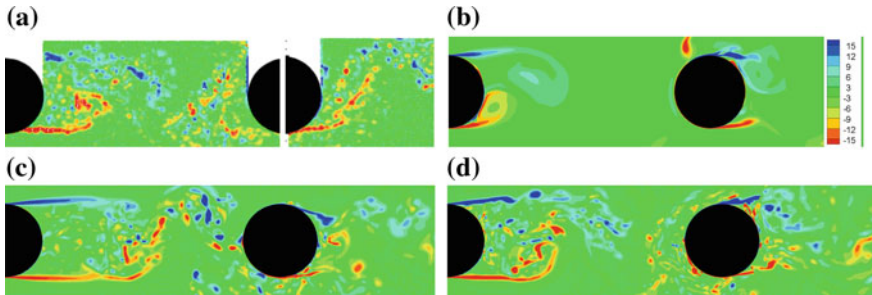
Fig. 2 The shear layer instability. **a** Exp, **b** ORG, **c** σ = 0.12, **d** Adaptive-σ

The instantaneous spanwise vorticity can be used to reflect the dissipation level. If the dissipation level is high, only the large-scale structures can be observed and small-scale structures are eliminated. Reversely, small-scale of structures can be easily distinguished, like the measurements. Figure 2 presents the comparisons of instantaneous spanwise vorticity among the measurements, original Roe, 0.12σ and adaptive σ. Although 0.12σ performs well, it's too empirical. The adaptive σ performs best. The original Roe scheme, whose dissipation is very large, performs worst.

At the same time, the root mean square (RMS) fluctuating pressure can directly reflect the dynamic loads on the surface. The coefficients of $C_{p,\mathrm{rms}}$ on the two cylinders surface are shown in Fig. 3. Unfortunately, the original Roe scheme presents about 5 times larger on the front cylinder surface. The 0.12σ and adaptive σ schemes perform much better on both the front and rear cylinder surfaces.

Therefore, the adaptive dissipation scheme is recommended, and it is applied in the following cases.
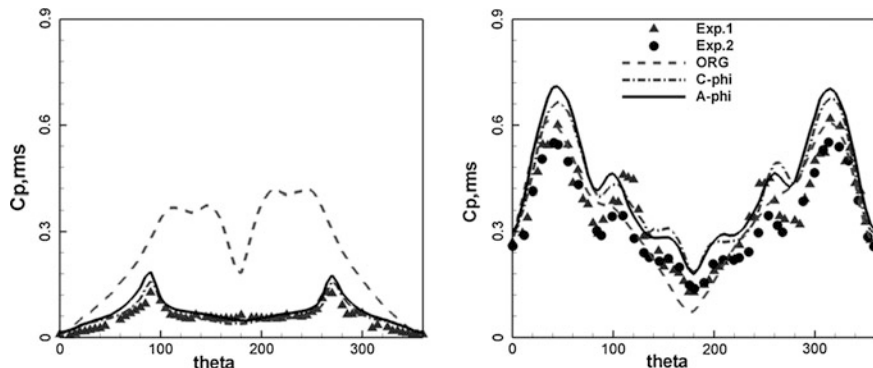
Fig. 3 The pressure fluctuation on the cylinder surfaces

3.2   Comparisons of DDES and IDDES

From the birth of DES to now, several DES revisions are proposed to overcome its original version's limitations. In our previous work, three models (DDES-2003, DDES-2006 and IDDES) are compared through simulating the former TC case. Of course, the adaptive dissipation is applied.

As described in the above subsection, the spanwise vorticity and pressure fluctuations can be applied to explore the advantages and disadvantages of them. All of them can capture the small-scale structures. The most distinct difference among them is the location of shear layer instability. From the comparisons of pressure fluctuations on the front and rear cylinder surface, DDES-2006 overpredicts and IDDES matches the measurement quite well, shown in Fig. 4.

Due to its excellent performance, the IDDES coupled with the adaptive dissipation scheme is the rational choice to predict the unsteady turbulent flows at high Reynolds number.
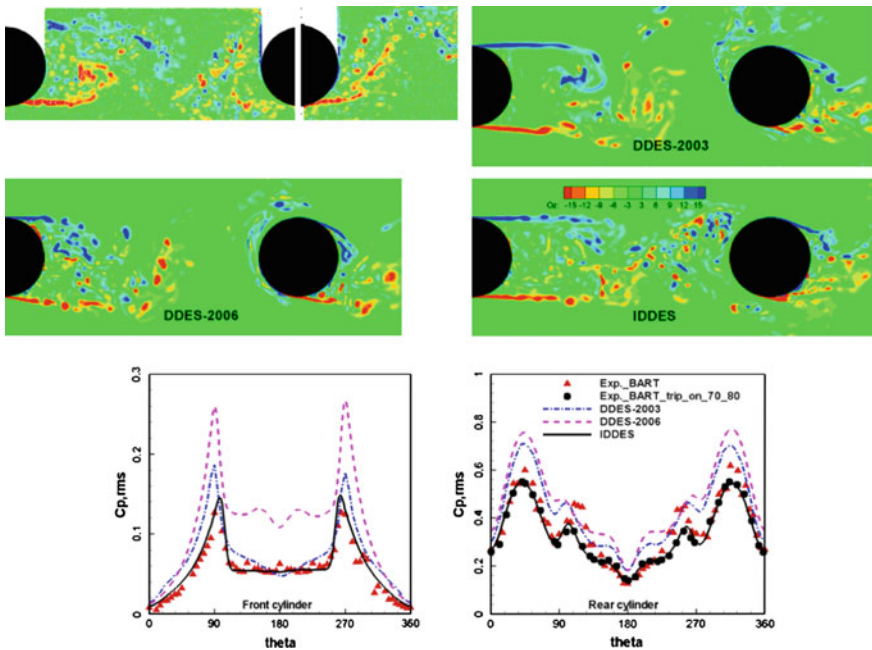
Fig. 4 The effects of three advanced DES models for vorticity and pressure fluctuations

3.3 Applications of IDDES Coupled with Adaptive Dissipation

In this subsection, the wide speed flows, ranging from Ma 0.15 to 10, were simulated by IDDES and adaptive dissipation schemes. For the low-speed case, some typical results of the rudimentary landing gear (RLG) is presented. For the transonic and supersonic case, cavity of M219 at Ma 0.85 and 1.5 is simulated. For the hypersonic case, another shallow cavity at Ma 10 is calculated.

3.3.1 Massive Separations Past the RLG at Low-Speed

The velocity of the freestream is 40 m/s; the Reynolds number based on the diameter of the wheel is 1×10^6 and the angle of attack is zero. Normalized uniform time step is taken as 0.005.

The typical flow features include the massive separation, impingement of vortices and the wall, interactions among different components, and so on.

Figure 5 presents some numerical results comparing with the measurements. In Fig. 5a, the time-averaged surface flows at the rear view are presented. IDDES can present reasonable agreements with the measurements, such as focus of separation
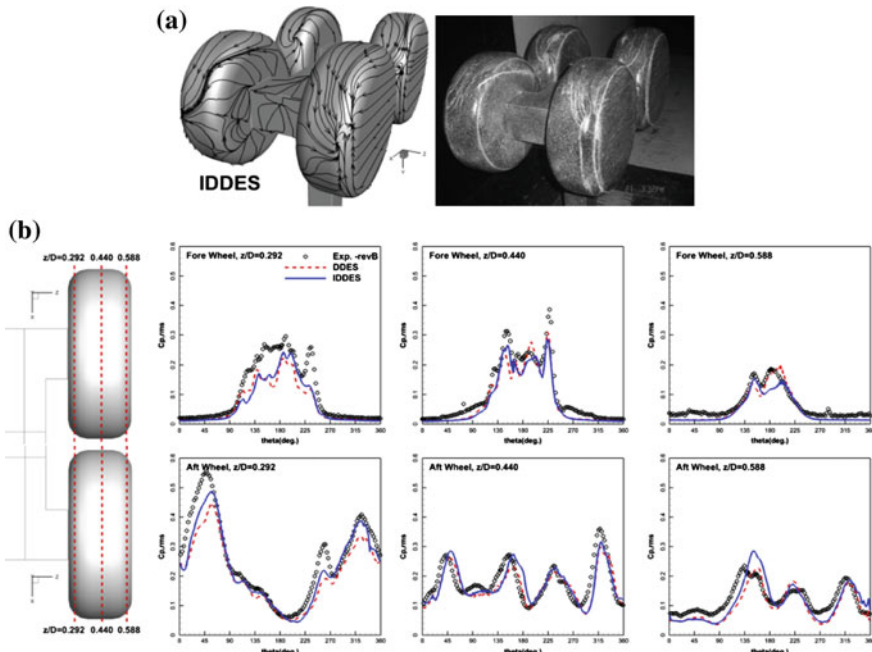
Fig. 5 RLG by IDDES. **a** Surface streamlines, **b** Cp,rms on the fore and aft wheels

on the rearward surface of the both wheels, the horseshoe vortex on the inboard surface of both fore and aft wheels, secondary separation on the rearward surface of both wheels, and so on. On the outer board of the wheel, the flows are attached and no separation can be observed.

For this case, both DDES-2003 and IDDES are applied to predict the flows and their performances are also compared. Here, only the comparisons about the $C_{p,rms}$ on the wheel surface are presented, as shown in Fig. 5b. In fact, for this massive separation, both DDES-2003 and IDDES can well match the measurements and they can capture the similar flow phenomena. IDDES shows a little better $C_{p,rms}$ than DDES-2003 on the aft wheel due to its WMLES mode. On inner side of the front wheel, the difference is a little distinct in the separation region.

3.3.2 Transonic and Supersonic Flows Past the M219 Cavity

Transonic flows past the M219 cavity were studied using IDDES on a high-quality structured mesh. Comparisons with available experimental and LES data corresponding to the same configuration demonstrate a high level of accuracy at Ma = 0.85. The time-averaged turbulent kinetic energy profiles demonstrate very good agreements with those by the LES, shown in Fig. 6a. Rossiter modes are well captured, where the frequencies and amplitudes are well matched with the measurements, shown in Fig. 6b. From the comparisons of overall sound pressure level, the present methods almost fully match with the measurements, shown in Fig. 6c. At the same time, the OASPLs for supersonic case are larger about 5 dB than those of transonic case. In Fig. 6d, the instantaneous Q criterion is presented for both transonic and supersonic case. The shear layer instability, impingements of the aft wall, and some complex flow phenomena can be observed.

3.3.3 Hypersonic Transition Induced by a Shallow Cavity

Hypersonic flow transition from laminar to turbulent due to the surface irregularities, such as the local shallow cavities, can greatly affect the surface heating and skin friction. In this article, the hypersonic flows over a three-dimensional (3-D) rectangular shallow cavity with length-to-width-to-depth ratio, L:W:D, of 19.9:3.57:1 at two angles of attack (AoA) were studied with IDDES method to highlight the mechanism of transition induced by the cavity. Because the flow is laminar in the upstream region of the cavity, the IDDES is switched off. After the leading edge of the cavity, IDDES is enable.

The Mach number is about 9.6. In the hypersonic case, the cavity can be thought as "open" at AoA of −10° but "closed" at AoA of −15°. It is different from the conventional 2-D cavity with length-to-depth ratio L/D larger than 14, where the flows are thought as the 'closed' cavity flow (Fig. 7)
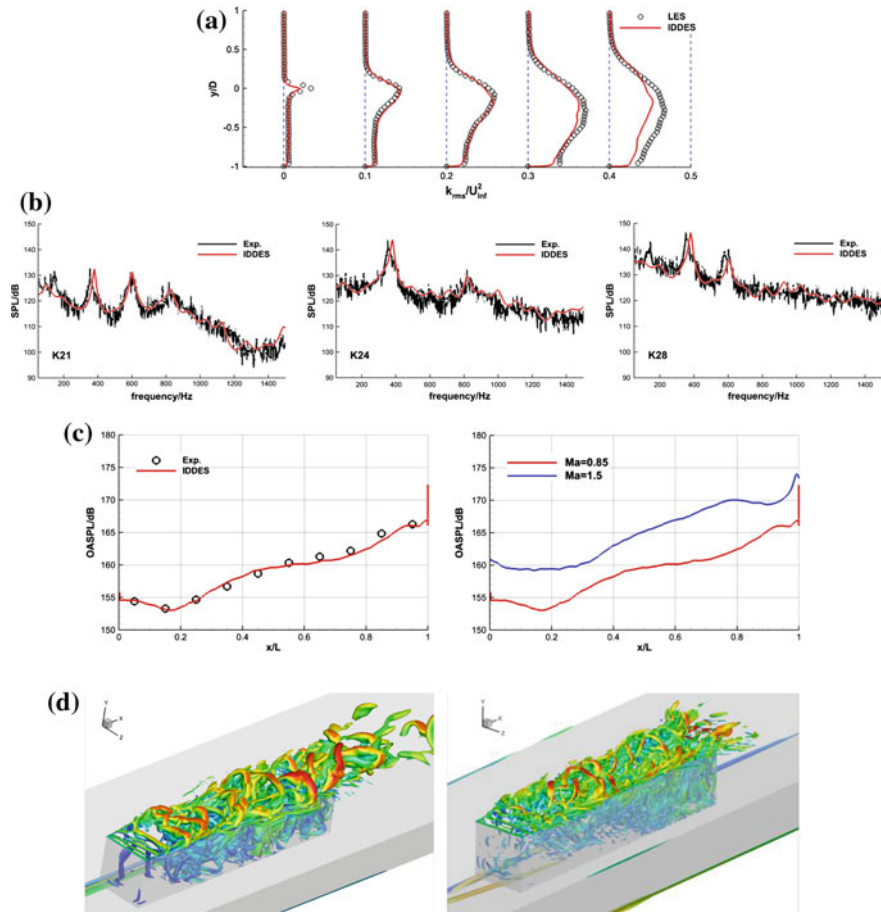
Fig. 6 The turbulent flow past M-219. **a** The turbulent kinetic energy (TKE) at x/D=0.5,1.5,2.5,3.5 and 4.5 (Ma=0.85), **b** SPL at three samples (Transonic), **c** The comparisons of overall SPL between the measurements and different Mach numbers, **d** Q criterion at transonic and supersonic

For the 'open' cavity flow case, where the AoA is −10°, the shear layer is basically steady and the flow maintains laminar. The heating ratio is very low, and the relatively high heat region can be observed only on the aft wall.

For the 'closed' cavity case, where the AoA is −15°, the external flow goes into the cavity and impinges on the bottom floor. High intensity streamwise vortices, impingement shock and exit shock are observed causing breakdown of these vortices triggering rapid flow transition. The high heating region can be observed in the downstream region of the cavity. At the same time, the small-scale of structures can also be easily distinguished. Then, the transition procedure is explored by many relative flow features.
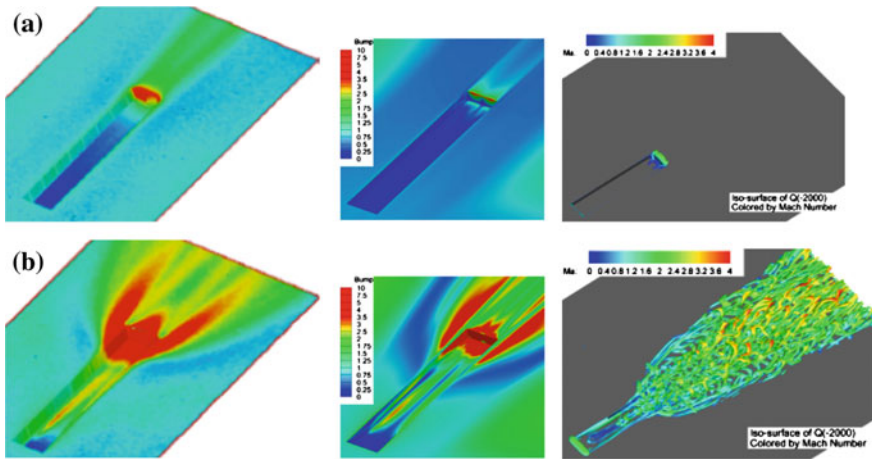
Fig. 7 The structures and heat flux near the cavity at hypersonic (Ma = 9.575, Re = 3.37×10^6/ m). **a** −10deg, **b** −15deg

4 Conclusions

In this article, some issues about model and numerics are discussed.

- Firstly, three levels of numerical dissipation with DDES-2003 are applied to the TC case. The adaptive dissipation is recommended.
- Then, the flows past TC and RLG are predicted by DDES-2003 and IDDES with the adaptive dissipation. IDDES performs better.
- Finally, IDDES coupled with adaptive dissipation is applied to predict the transonic, supersonic and hypersonic flows past cavities. Through comparing with the available measurements, the model and computational method can well resolve the unsteady turbulence flows at high Reynolds number, with the wide velocity ranges.

The dynamic loads, noise and oscillations related to the unsteady turbulent flows can be hoped to well predict by introducing the near-field pressure fluctuations from the turbulence model and numeric in this article.

References

Menter FR (1994) Two-equation eddy-viscosity turbulence models for engineering applications. AIAA J. 32(8):1598–1605

Menter FR, Kuntz M (2003) A zonal SST-DES formulation. DES-WORKSHOP, St. Petersburg, July 2003. (http://cfd.me.umist.ac.uk/flomania/index2.html)

Shur M, Spalart PR, Strelets M, Travin A (2008) A hybrid RANS/LES approach with delayed DES and wall-modelled LES capabilities. Int J Heat Fluid Flow 29:1638–1649

Spalart PR, Jou WH, Strelets M et al (1997) Comments on the feasibility of LES for wings, and on a hybrid RANS/LES approach. In: Liu c, Liu Z (eds) First AFOSR international conference on DNS/LES, LA Ruston. Advanced in DNS/LES, Greyden Press, Columbus, OH

Spalart PR, Deck S, Shur M et al (2006) A new version of detached eddy simulation, Resistant to Ambiguous Grid Densities. Theor Comp Fluid Dyn 20:181–195

Xiao ZX, Liu J, Huang JB, Fu S (2012) Numerical dissipation effects on the massive separation around tandem cylinders. AIAA J 55(5):1119–1136

Xiao ZX, Liu J, Luo KY, Huang JB, Fu S (2013) Numerical investigation of massively separated flows past rudimentary landing gear using advanced DES approaches. AIAA J 51:107–125

Xiao LH, Xiao ZX, Duan ZW, Fu S (2015) Improved-delayed-detached-eddy simulation of cavity-induced transition in hypersonic boundary layer. Int J Heat Fluid Flow 51:138–150

Turbulent Sheared Mixing Layer Generated with a Composite Grid

Md. Kamruzzaman, Lyazid Djenidi and R.A. Antonia

Abstract This paper reports hot-wire measurements in a turbulent sheared mixing layer (SML) generated using a composite grid, with the aim to investigate the downstream development of turbulence in the presence of a mean shear. The Reynolds number based on the mixing layer thickness $\delta (= y_{0.95} - y_{0.10})$ is in the range of $6560 \leq Re_\delta (= U_s \delta/\nu) \leq 12540$, where U_s is the velocity difference between the high and low speeds. The measurements show that the mixing layer thickness δ grows linearly with x. The mean velocity profiles (U) collapse relatively well at all stations when the distance y is normalised by the variable $\eta (= (y - y_{0.50})/\delta)$. Further, the Reynolds stress profiles at $x/M_1 = 60$ and 65 collapse well suggesting that the decaying turbulent in the SML has reached self-preservation.

Keywords Composite grid · Mixing layer · Self-preservation

1 Introduction

A turbulent mixing layer (ML) arises due to the interaction of two uniform and parallel flows, but with different velocities. When the two streams come in contact, large scale coherent vortices are formed via the Kelvin-Helmholtz instability and subsequently play an important role in transporting momentum and heat. Over the past 60 years, the structure of the turbulent mixing layer has been studied extensively by many investigators (e.g. Bell and Metha 1990; Bradshaw 1966; Brown and Rpshko 1974; Gho et al. 2009; Hussain and Husain 1980; Townsend 1976; Oster and Wygnanski 1982; Wygnanski and Fiedler 1970).

Md. Kamruzzaman (✉) · L. Djenidi · R.A. Antonia
School of Engineering, The University of Newcastle, University drive,
Callaghan, NSW 2308, Australia
e-mail: md.kamruzzaman@uon.edu.au
L. Djenidi
e-mail: lyazid.djenidi@newcastle.edu.au
R.A. Antonia
e-mail: robert.antonia@newcastle.edu.au

The novelty of the present work resides in the use of side by side grids with different mesh sizes ($M_1 \neq M_2$) and different solidity ($\sigma_1 \neq \sigma_2$) to generate a turbulent sheared mixing layer (SML). To our knowledge, this is the first time such a SML is generated and investigated. The long term objective of this study is to compare the characteristics of this SML with a shearless ML, generated by a similar type of composite grid with ($M_1 \neq M_2$), but the same solidity ($\sigma_1 = \sigma_2$); the use of the same solidity for the two grid ensures zero mean shear. In this paper, we investigate the self-preservation requirements for a turbulent SML and whether they are achievable.

2 Experimental Set-Up and Measurement Technique

The measurements are carried out in a wind tunnel with a 2.4 m long square (0.3 m $\times$ 0.3 m) working section. The grid is made of a perforated composite grid (Fig. 1) with $M_1 = 19.9$ mm, $M_2 = 10.2$ mm, $\sigma_1 = 43\%$ and $\sigma_2 = 36\%$. The ratio of mesh size to spacing between two square holes is $M_1/D_1 = 4$ and $M_2/D_2 = 5$, respectively. The grid generates two approximately homogeneous and isotropic turbulent flows, which come in contact with each other and create a turbulent SML. Single hot wire and X-wire probes are used to obtain the streamwise (x-direction) and lateral (y-direction perpendicular to the separation line between the two grids) velocity fluctuations u and v, respectively. The hot wire (diameter $d \approx 2.5$ μm and length $l = 200d$) is etched from a coil of Wollaston (platinum) and was operated with an ambient constant temperature anemometer (CTA); with an overheat ratio of 1.5. The velocity ratio of high speed to low freestream speeds (U_1/U_2) is about 1.4. Measurements were carried out at 10 downstream locations from the composite grid and, for each

Fig. 1 Geometrical configuration of the composite grid
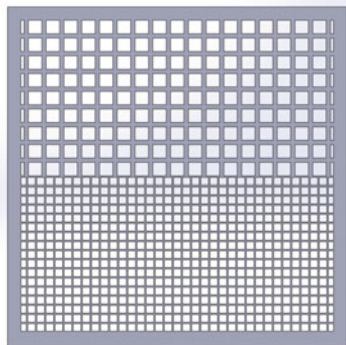
x position, 29 locations along y. It was verified that the single wire and X-wire data yields comparable profiles of the mean velocity (U) and the u' (the prime represents the *rms* of the velocity fluctuation).

3 Theoretical Consideration of Self Preserving in Two Dimensional Mixing Layer

We begin by applying the self-preservation (SP) analysis to a two dimensional plane mixing layer whose mean momentum and continuity equations are

$$U\frac{\partial U}{\partial x} + V\frac{\partial U}{\partial y} + \frac{\partial(\bar{u^2} - \bar{v^2})}{\partial x} + \frac{\partial \bar{u}\bar{v}}{\partial y} = U_1\frac{dU_1}{dx} \tag{1}$$

$$\frac{dU}{dx} + \frac{dV}{dy} = 0 \tag{2}$$

where U, V, u and v are the mean and fluctuating velocity components in the x and y directions, respectively; the overbar denotes the average with respect to time. Following Townsend (1975), we assume:

$$U = U_1 + u_o f(y/l_o); \quad \bar{u}\bar{v} = u^{*2}g_{uv}(y/l_o); \quad \bar{u^2} = u^{*2}g_u(y/l_o); \quad \bar{v^2} = u^{*2}g_v(y/l_o); \tag{3}$$

U_1 is the free stream velocity corresponding to the larger mesh grid ($M_1 = 19.9$ mm). u_o, u^* (not necessary equal to u_o) are the velocity scales and l_o is the length scale, which are independent of x. Substituting (3) into (1) and after some trivial manipulations one obtains the following SP conditions:

$$\frac{u_o l_o}{u^{*2}}\frac{dU_1}{dx} = C_1; \frac{U_1 l_o}{u^{*2}}\frac{du_o}{dx} = C_2; \frac{U_1 u_o}{u^{*2}}\frac{dl_o}{dx} = C_3; \frac{u_o l_o}{u^{*2}}\frac{du_o}{dx} = C_4; \tag{4}$$

$$\frac{u_o}{u^{*2}}\frac{d(u_o l_o)}{dx} = C_5; \frac{l_o}{u^{*2}}\frac{du^{*2}}{dx} = C_7; \frac{dl_o}{dx} = C_8 \tag{5}$$

Note that since U_1 is constant then $C_1 = 0$. Solving the last expression in (5) yields

$$l_o = C_8(x - x_o) \tag{6}$$

where $l_o = 0$ when $x = x_o$; x_o is the virtual origin. Now combining the expressions of C_2 and C_4 we obtain:

$$u_0 \sim U_1 = constant. \tag{7}$$

Then, since U_1 is constant, u_o has to be a constant. Further, C_3 leads to

$$u^{*2} \sim u_0 U_1 \qquad (8)$$

or, using (7),

$$u^* \sim u_0 \qquad (9)$$

Thus, the SP conditions for the present flow impose that the scaling velocity u_0 is constant and the scaling length l_0 increases linearly with x.

4 Results and Discussion

Figure 2 shows the streamwise variation of the SML thickness $\delta = (y_{0.1} - y_{0.1})$ where $y_{0.95}$ corresponds to the location y at which $U = U_1 + 0.1U_s$ and $y_{0.95}$ the location where $U = U_1 + 0.95U_s$ (e.g. Leipmann and Laufer 1947); U_s is defined as the velocity difference between the two freestream velocities U_1 and U_2. The figure shows that δ increases linearly with x, thus satisfying the SP condition (6). Accordingly, one can use δ as a scaling length. Since the SP condition on the scaling velocity u_0 is that the velocity is constant, any (constant) velocity can be used as a scaling velocity. In Fig. 3, we used $u_0 = U_s$. It is evident that the mean velocity profiles collapse very well, when normalised with the scales U_s and δ. It is quite remarkable that SP is verified relatively early behind the grid. To test whether the SP condition (9) is valid, we plotted the Reynolds shear stress profiles in Fig. 4, normalised by U_s and δ. The profiles present a clear collapse for $x/M_1 \geq 60$, while they show an approximative collapse before this position range, indicating that SP for the turbulence takes a longer distance to establish. Indeed, the $\overline{uv}$ collapse only when $x/M \geq 60$. This also shows that both the mean flow and the turbulent flow scale with the same velocity scale.

Fig. 2 Mixing layer thickness linearly grows with downstream distance
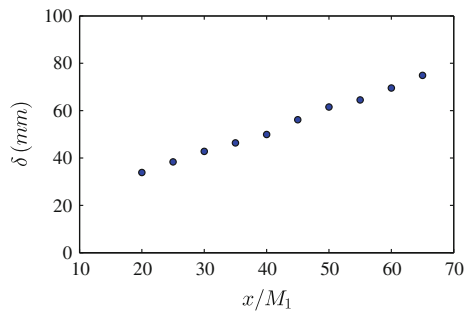
Fig. 3 Normalized mean velocity profile in two dimensional mixing layer
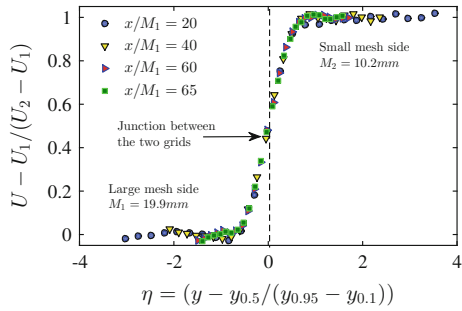
Fig. 4 Reynolds shear stress at different downstream locations. Symbols are the same as in Fig. 3
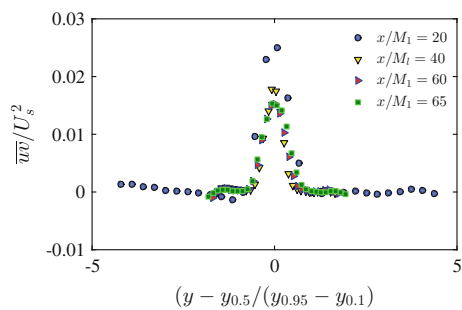
5 Conclusion

Hot-wire measurements are made in a turbulent sheared mixing layer behind a composite grid with two different solidities with the view to test whether the flow satisfies self-preservation or not. The mixing layer thickness δ grows linearly with x, while the mean velocity profiles collapse well rapidly behind a grid when normalised by U_s and δ. The profiles of the Reynolds stresses also exhibited very good collapse but at distances further downstream. These results are in conformity with the analysis the self-preservation applied to the mean momentum and mass equations.

References

Bell JH, Metha RD (1990) Development of a two-stream mixing layer with tripped and untripped boundary layer. AIAA J 28:2034–2042

Bradshaw P (1966) The effect of initial conditions on the development of free shear layer. J Fluid Mech 2(6):771–781

Brown GL, Rpshko A (1974) On density effects and large scale structure in turbulent mixing layers. J Fluid Mech 64(04):775–816

Gho F, Chen B, Guo L, Zhang X (2009) Effects of velocity ratio on turbulent mixing layer at high Reynolds number. J Phys Conf Ser a47:1–6

Hussain AKMF, Husain ZD (1980) Turbulence structure in the axisymmetric free mixing layer. AIAA J 18:1462–1469

Oster D, Wygnanski IJ (1982) The forced mixing layer between parallel streams. J Fluid Mech 10:91–130

Leipmann HW, Laufer J (1947) Investigations of the free turbulent mixing layers. NACA TN-1257

Townsend AA (1976) The structure of turbulent shear flow. Cambridge University Press, Cambridge

Wygnanski I, Fiedler HE (1970) The two dimensional mixing region. J Fliuid Mech 41:327

Convective Heat Transfer from a Vertically-Mounted Vibrating Heated Plate

A.K. Pilli, R. Narayanaswamy, J. Jewkes and A.D. Lucey

Abstract A computational study is conducted to study the effect of vibrational parameters on the heat transfer from a vertically-mounted heated plate. The introduction of vibrations to a heated plate can induce turbulence in the flow field adjacent to the plate under certain combinations of amplitudes and frequencies thus presenting an opportunity to enhance heat transfer rates. The study is performed using Large Eddy Simulations. The variation of the time-and-space-averaged Nusselt number with vibrational Reynolds numbers is presented for the range of parameters considered for the present study. It is observed that the heat transfer rates are strongly dependent on the vibrational Reynolds number; in the present work, increases of up to 107 % in Nusselt number values have been observed.

Keywords Heat transfer enhancement · Vibrating surfaces · Convection

1 Introduction

The introduction of vibrations on a heated surface can increase or decrease the overall rate of convective heat transfer from the surface to the surroundings. For a given fluid, the modification of the heat transfer rate is dependent on the geometry and orientation of the heated surface with respect to gravitational forces, and the characteristics of applied surface vibrations, due to the formation and transport of the associated flow structures in the dynamic boundary layer adjacent to the heated surface. A review of literature on this topic reveals notable numerical studies by

A.K. Pilli (✉) · R. Narayanaswamy · A.D. Lucey
Fluid Dynamics Research Group, Department of Mechanical Engineering,
Curtin University, Perth, WA 6845, Australia
e-mail: a.pilli@postgrad.curtin.edu.au

J. Jewkes
Faculty of Computing, Engineering and Science, University of South Wales,
Pontypridd CF37 1DL, UK

Zhang et al. (2004), Dey and Chakrborty (2009), experimental work by Prasad and Ramanathan (1972), analytical work by Gomaa and Al Taweel (2005), indicating a potential for heat transfer enhancement as compared to a non-oscillating heated surface. Devices that incorporate fluid oscillation have been proven to enhance the performance of heat transfer devices and possess the potential to intensify mixing in thermo-chemical processes. In the present study, a series of numerical simulations are carried out to ascertain the effectiveness of applied transverse (perpendicular to the heated plate) vibrations on a vertically-mounted heated plate on the transient and time averaged heat transfer characteristics, under different operating conditions. The controlling parameters encapsulate heating levels, frequency and amplitude of vibration.

2   Problem Formulation and Computational Models

The geometry and the computational domain considered in this study is shown in Fig. 1. A flat plate of length *l*, positioned between two stationary plates each of length *b*, is set to vibrate at a known frequency *f*, and amplitude *a* in ambient surroundings at 298.16 K. The stationary and vibrating plates have the no-slip boundary condition applied on them. Rest of the boundaries of the domain are set to be as pressure-outlets with ambient conditions of air at 298.16 K. For simulations involving heat transfer, a constant heat flux boundary condition is applied on the vibrating plate, and an adiabatic condition on stationary plates. The properties of air are kept constant because the heat flux considered is not high enough to cause any

Fig. 1 Physical geometry (aspect ratio not to scale) and front face of computational domain
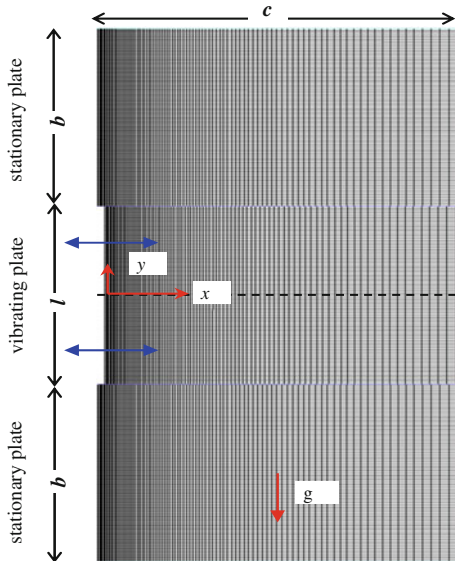
significant change except for the density, when the vibrating plate is heated. Thus buoyancy plays a role in driving the flow and the Boussinesq approximation is used. The length scale of the geometry in the direction perpendicular to the plane of Fig. 1 is much larger than the other length scales in the domain, and hence the problem is assumed to be two-dimensional. To facilitate this in the LES modelling, a periodic boundary condition is applied between the front and rear faces of the domain rendering the modelling quasi two-dimensional.

The three-dimensional mesh used for LES is a fully structured, spatially varying non-uniform mesh with hexahedral elements, as shown in Fig. 1. The mesh has finer cells close to the moving boundary (vibrating plate) to capture sufficiently the near-wall effects. The equations for mass conservation, momentum and energy are solved simultaneously using the finite-volume solver ANSYS-FLUENT. The pressure-velocity coupling is achieved using the SIMPLE method. A second-order upwind differencing scheme is used for solving the pressure, momentum and energy equations. The time step for each case is dependent on the frequency of vibration prescribed. The mesh involves a moving boundary (vibrating plate); therefore, run-time modification of the mesh is essential. In order to study the effects of vibration, the computational domain needs to be dynamically modified based on the frequency and amplitude of vibration. As the region in the close vicinity of the moving boundary is of high importance to obtain physically plausible results, dynamic meshing is achieved in such a way that the mesh close to the moving boundary remains undisturbed.

3 Results and Discussion

Three vibrational frequencies were investigated: 5, 50 and 100 Hz, for different values of amplitude (0.5–2 mm) of the surface vibration.

Figure 2a–d shows the averaged static temperature contours for four cases. It can be observed that for lower frequency vibrations (5 Hz), the thermal boundary layer appears similar to that of the stationary plate regardless of the amplitude of vibration. As the frequency of vibrating plate is increased to 50 Hz it can be observed that thermal boundary layer deviates from that of a stationary vertical plate thermal boundary layer subjected to natural convection. For a further increase in frequency of vibrations to 100 Hz, the thermal boundary layer is seen to be completely different. It almost resembles the boundary layer of a uniformly heated vibrating horizontal plate, as shown in Pilli et al. (2014). This can be attributed to the dominance of vibration-induced heat transfer as opposed to the buoyancy-induced heat transfer seen in natural convection of a vertical plate.

Figure 3a shows the variation in the predicted magnitude of time and space averaged Nusselt number obtained from the simulations with variation in the frequency of vibration, for different values of the amplitude of surface vibration. The Nusselt number for a vertically-mounted stationary plate is also shown in the figure. From Fig. 3a, it is clear that for any given amplitude, a moderate increase in the
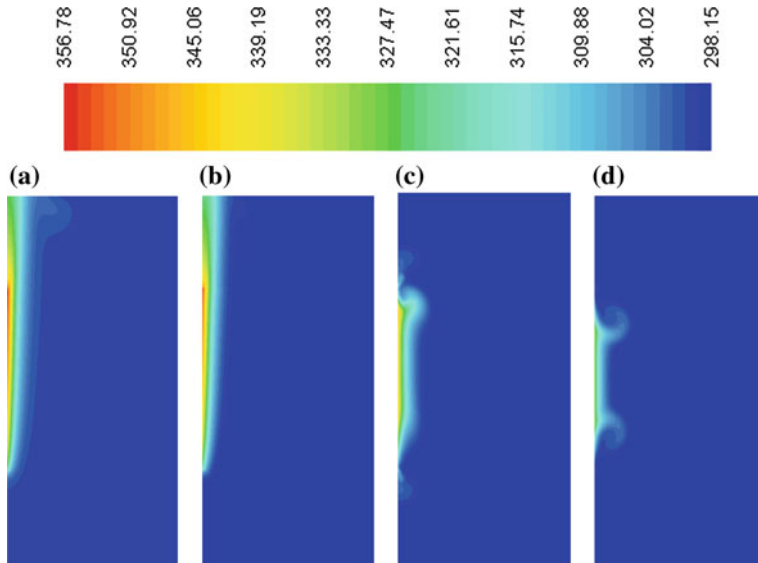
Fig. 2 Contours of averaged static temperature (K) for **a** stationary plate; **b** $f = 5$ Hz, $a = 1$ mm, $\mathrm{Re_v} = 0.27$; **c** $f = 50$ Hz, $a = 2$ mm, $\mathrm{Re_v} = 10.83$; **d** $f = 100$ Hz, $a = 2$ mm, $\mathrm{Re_v} = 21.67$
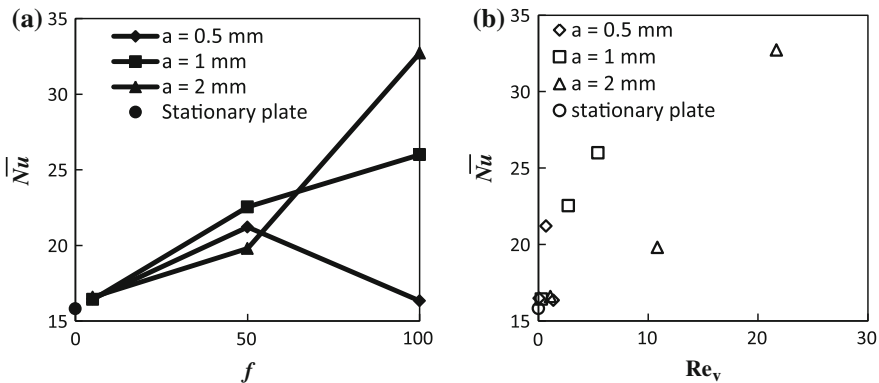
Fig. 3 **a** Variation of time and space averaged Nusselt number with frequency and amplitude of vibration; **b** Variation of time and space averaged Nusselt number with vibrational Reynolds number for all cases considered in the study

frequency of vibration results in higher Nusselt numbers as compared to a stationary plate. For the range of frequencies considered, it can be seen that there is an increase in the Nusselt number with an increase in the frequency of vibration except for the case with amplitude $a = 0.5$ mm. For the operating parameters considered, based on present results, it is also found that there is up to 107 % increase in the Nusselt number due to induced surface vibrations as compared with a stationary

plate subjected to the same heat flux, and exchanging heat to the ambient by natural convection.

The combined effect of frequency and amplitude of vibrations on the fluid dynamic characteristics can be expressed using the vibrational Reynolds number, as defined by $Re_v = a^2 f/\nu$. Figure 3b shows the variation of the Nusselt number with the vibrational Reynolds number for all the cases considered. The general trend shows that there is an increase in the Nusselt number with increase in the vibrational Reynolds number. The exceptions to the increasing trend of the Nusselt number as seen from Fig. 3a is likely due to the effects of fluid viscosity, and the transport of momentum and heat that affects the airflow in and out of the domain. Besides, the time evolution characteristics of the vortices generated by the frequency and amplitude combinations within the boundary layer on the heated plate, and its effect on mixing within the boundary layer to enhance the convective heat transfer rate is also responsible for the observed characteristics. Further work to understand these effects, and the effect of the length of the heated plate is currently underway.

4 Conclusions

A numerical simulation is conducted using LES to study the effect of vibrational parameters on the convective heat transfer rate from a vertically-mounted heated plate, subjected to constant heat flux boundary condition. Three vibrational frequencies were investigated: 5, 50 and 100 Hz, for different values of amplitude (0.5–2 mm) of the surface vibration. The heated plate is maintained at a constant surface heat flux of 400 W/m^2. It is observed that the thermal boundary layer changes significantly with frequency and amplitude of vibrations. For some cases, time and space averaged Nusselt number increases with increase in amplitude and frequency of the vibrating plate. A 107 % increase in heat transfer rate has been found for the case with $f = 100$ Hz, $a = 2$ mm. The Nusselt number representing the convective heat transfer rates appear to have some correlation with the vibrational Reynolds number, for the cases considered.

References

Dey S, Chakrborty D (2009) Enhancement of convective cooling using oscillating fins. Int Commun Heat Mass Transfer 36(5):508–512

Gomaa H, Al Taweel AM (2005) Effect of oscillatory motion on heat transfer at vertical flat surfaces. Int J Heat Mass Transf 48(8):1494–1504

Pilli AK, Abishek S, Narayanaswamy R, Jewkes J, Lucey AD, Narayanan V (2014) Computational analysis of fluid dynamics and heat transfer characteristics of a vibrating heated plate. In: The proceedings of 19th Australasian fluid mechanics conference

Prasad KK, Ramanathan V (1972) Heat transfer by free convection from a longitudinally vibrating vertical plate. Int J Heat Mass Transf 15(6):1213–1223

Zhang XR, Maruyama S, Sakai S (2004) Numerical investigation of laminar natural convection on a heated vertical plate subjected to a periodic oscillation. Int J Heat Mass Transf 47 (19–20):4439–4448

Effect of Vasomotion on Blood Flow Distribution in Microvessels

J.C. Shao, Y. Liu and Z.D. Su

Abstract The control of flow in the microcirculation is crucial to ensure blood supply to the tissues. The spontaneous time-dependent contraction and relaxation of small arteries and arterioles was observed 160 years ago and is termed as vasomotion. Vasomotion is an intrinsic phenomenon unrelated to cardiac rhythm or neural and hormonal regulation; and it works as a local control mechanism to regulate the microvascular blood flow. In spite of tremendous studies on vasomotion, the physiological role of vasomotion is not clear. Vasomotion results in the flow oscillation which is termed as flowmotion. The flowmotion is crucial for optimal blood flow and nutrient delivery in micro vasculature. Blood vessels in tumors are highly irregular and dense compared to those in normal tissue which may affect the flowmotion. As the first attempt, in this study we investigated the effect of irregular microvascular structure on flow delivery in microvascular bed with composite flow oscillating frequencies. The results showed that the irregular micro vasculature would decrease the flowmotion and lead to reduction of nutrient and drug delivery which is consistent with the experimental observation.

1 Introduction

Vasomotion is a rhythmic and spontaneous change in microvascular diameter that is independent of heartbeat, respiration, or neuronal input. In spite of the relative long history, the physiological consequence of vasomotion is still not completely understood. Much of our understanding is based upon direct observations of intramuscular arterioles in response to experimental stimuli through the use of

J.C. Shao · Y. Liu (✉)
Department of Mechanical Engineering, The Hong Kong Polytechnic University,
Hong Kong, China
e-mail: mmyliu@polyu.edu.hk

J.C. Shao · Z.D. Su
College of Metrological and Measurement Engineering, China Jiliang University,
Hangzhou, China

intravital microscopy (Segal 2000). Vasomotion appears as an oscillation of the vessel lumen which modifies blood flow to produce periodic flow fluctuation known as flowmotion. Flowmotion is crucial for optimal blood flow and nutrient delivery in local microvascular bed to ensure adequate material exchanges between the blood circulation and the surrounding tissues. Tumor blood flow controls tumor growth by delivering nutrients and oxygen to tumors and carrying metabolic waste away from tumors. Insufficient delivery of oxygen leads to hypoxic and acidic regions in solid tumors. It also affects the efficacy of treatment by delivering blood-borne therapeutic agents to tumors. Inability of delivering a sufficient amount of drugs to all tumor cells results in residual tumor cells leading to tumor regrowth and development of resistant cells (Vaupel et al. 1989). Hence, investigation of the blood flow in tumor vasculature may lead to a better understanding of tumor pathology and development of new treatment methods (Guo and Fu 2012).

Blood vessels in tumors are highly irregular compared to those in normal tissue. They are more dilated, denser, more tortuous and leakier. The irregular microvascular bed would change the flowmotion, consequently affect the nutrient and drug delivery. There are two major questions in understanding the effect of irregular vessels on tumor blood flow, one is how the blood is redistributed, and the other is its effects on flowmotion. Experimental analysis of the effect of vasomotion on blood flow in vivo is difficult owing to problems with suppressing the relevant mechanisms for a prolonged time while monitoring the changes in vascular network structure and function. Mathematical simulations offer a useful alternative, as the effects of parameters and mechanisms implemented in the model can be analyzed individually. Numerical simulation can help identify some valuable mechanical characteristics of vasomotion, which cannot be easily obtained by experimental methods. In this study, we used the CFD technique to investigate the effect of vasomotion and irregular microvascular structure on flow delivery in microvascular bed.

2 Numerical Details

The structures of real microvessels are very complex, but a microvascular bed can be approximated by a lumped model which consists of viscous resistance R, inductor L and capacitance C. Since the vessel wall has viscoelastic property, the viscoelastic capacitance C is simulated by a purely elastic capacitance and a resistance in series which is appropriately placed in parallel with the viscous resistance R, and the inductance L is appropriately placed in series with R, as shown in Fig. 1. Since oscillation would be important in microvascular bed, for a composite pressure wave consisting of the following harmonics (Zamir 2005):

$$p_n(t) = M_n e^{i(\omega_n t - \phi_n)} \quad n = 1, 2, \ldots, N \tag{1}$$
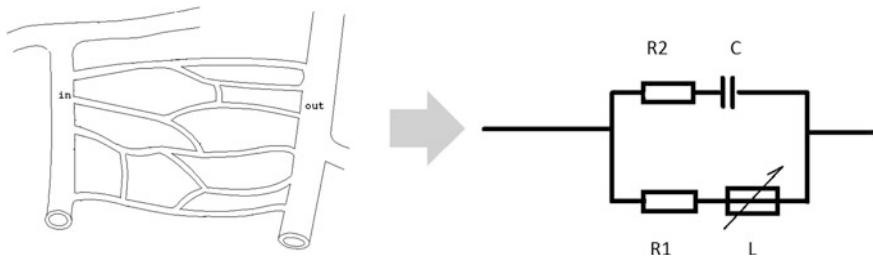
Fig. 1 Schematic view of microvessels

Table 1 Spectral parameters based on measurement

ω_n	ω_1	ω_2	ω_3	ω_4	ω_5
	2π	0.6π	0.2π	0.06π	0.02π
M_n	M_1	M_2	M_3	M_4	M_5
	0.1	0.1	0.3	0.4	0.6
ϕ_n	ϕ_1	ϕ_2	ϕ_3	ϕ_4	ϕ_5
	0	0	0	0	0
R_2/R_1	0.5				

the R-scaled flow waves is (Zamir 2005)

$$R_1 \times q_{nr}(t) = \frac{\left(1 + \omega_n^2 t_C^2 \lambda^2\right)\left[M_n \cos(\omega_n t - \phi_n) + \omega_n t_L M_n \sin(\omega_n t - \phi_n)\right]}{\left(1 + \omega_n^2 t_L^2\right)\left(1 + \omega_n^2 t_C^2 \lambda^2\right)}$$
$$+ \frac{\left(1 + \omega_n^2 t_L^2\right)\left[\omega_n^2 t_C^2 \lambda M_n \cos(\omega_n t - \phi_n) - \omega_n t_C M_n \sin(\omega_n t - \phi_n)\right]}{\left(1 + \omega_n^2 t_L^2\right)\left(1 + \omega_n^2 t_C^2 \lambda^2\right)} \quad (2)$$

Where $T_L = \frac{L}{R}$, $T_L = RC$, M_n and ϕ_n are real constants associated with the Fourier series representation of the composite wave. Power spectral analysis of human skin LDF signals has detected five frequency components of vasomotion (Rossi and Carpi 2004): the band 0.6–1.8 Hz due to heart activity, the band 0.2–0.6 Hz related to the respiratory activity, the band 0.06–0.2 Hz related to myogenic activity of the vessel walls, the band 0.02–0.06 Hz associated to sympathetic activity, and the band 0.007–0.02 Hz related to the activity of vascular endothelium. Table 1 tabulated the spectral parameters based on measurements.

3 Results and Discussion

In order to achieve a better understanding of the biomechanical characteristics of vasomotion, 3-D models of the micro vessel networks are developed in this work. Three models are created with progressively increased capillary density as shown in
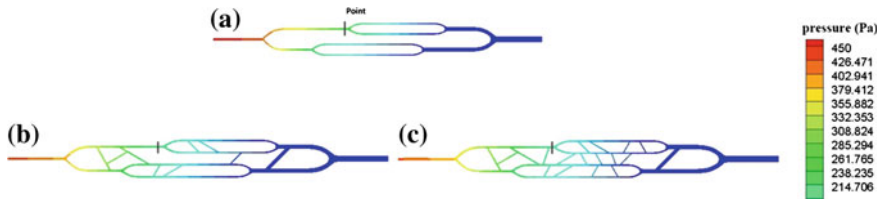
Fig. 2 Pressure distribute of vascular networks

Fig. 2. The constructed vascular network geometry resemble quite close to a structured tree model. There are three kinds of networks in this group. Model A is the simple regular vascular network in which one vessel is divided into two main branches after certain length from the inlet. Then each main branch bifurcates into two sub-branches, and all the four sub-branches merge back into two main branches and one at last. Model B is similar to normal vascular network but has more cross vessel linking among the major branches. Model C simulates the vascular structure in tumor in which the microvessels are irregular and the cross links are not in a plane. Figure 2 shows the pressure distribution in the three vascular models. With increasing the vascular density as B and C models, the pressure drop across the microvascular bed decreases significantly, and the pressure decreases greatly at the sub-bifurcations. It is not surprising because the denser cross-links mean larger volume to accommodate blood and larger effective cross-sectional area. The distribution of pressure is different for different models. Due to the asymmetry of the microvessel distribution, the pressure also exhibits asymmetric distribution.

The static pressure determines only the flow resistance, and it is the flowmotion that affects the nutrient delivery and the efficacy of treatment by delivering blood-borne therapeutic agents to tumors. In real micro arterioles, the vasomotion may exhibit different oscillating frequency and amplitude due to different mechanisms as indicated in Eq. (2). Figure 3 shows the time series of pressure variation at

Fig. 3 Time series of pressure at certain position
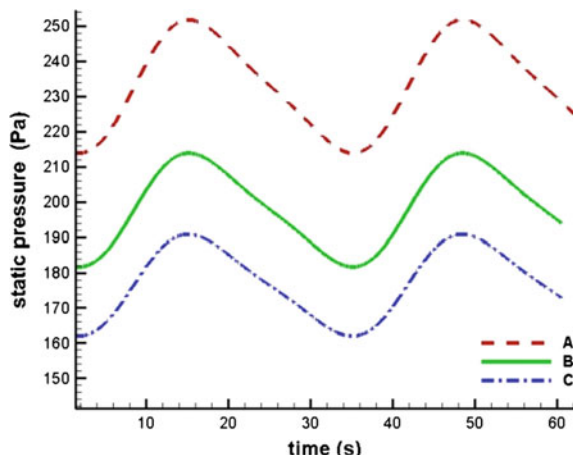
the point indicated in Fig. 2. The amplitude and value of pressure of Model A is much higher than those that of Models B and C, indicating that the rarefaction of microvascular bed would result in stronger flow oscillation. For irregular vascular structure such as in tumor, the pressure value may decrease leading to a lower flow resistance, but the flow oscillation decreses as well which may result in the reduction of drug delivery, nutrients, oxygen and metabolic wastes exchange in microvascular beds. Experimental studies have shown that normalization of tumor vasculature can improve tumor microcirculation and enhance the delivery of therapeutic agents to tumors (Pries et al. 2010). However, this observation is based upon direct observations of blood redistribution through the use of intravital microscopy. Our numerical result can explain clearly the mechanism, i.e., the normalization of irregular tumor vasculature can enhance the flowmotion, consequently improve the drug delivery.

4 Conclusions

The preliminary numerical study indicates that the microvascular structure would affect the pressure distribution and flowmotion significantly. The rarefaction of microvascular bed would result in stronger flowmotion which would enhance the drug and nutrient delivery which is consistent with the experimental observation.

References

Guo P, Fu BM (2012) Effect of wall compliance and permeability on blood-flow rate in counter-current microvessels formed from anastomosis during tumor-induced angiogenesis. J Biomech Eng 134(4):041003

Pries AR, Hopfner M, le Nobel F, Dewhirst MW, Secomb TW (2010) The shunt problem: control of functional shunting in normal and tumor vasculature. Nat Rev Cancer 10:587–593

Rossi M, Carpi A (2004) Skin microcirculation in peripheral arterial obliterative disease. Biomed Pharmacother 58:427–431

Segal SS (2000) Integration of blood flow control to skeletal muscle: key role of feed arteries. Acta Physiol Scand 168:511–518

Vaupel P, Kallinowski F, Okunieff P (1989) Blood flow, oxygen and nutrient supply, and metabolic microenvironment of human tumors: a review. Cancer Res 49(23):6449–6465

Zamir M (2005) The physics of coronary blood flow. Springer, New York

Actuation-Locating in Flow Control

Xiao Ming

Abstract The importance of the location of actuation in flow control is discussed. Several cases of flow control demonstrate the strategy for successful control. To locate the evacuation, analysis of flow fields is necessary to identify some key points where the flow is most sensitive to the disturbances that result from actuators. Instability of shear layer is always utilized for successful and efficient control. To delay the boundary layer transition from laminar to turbulent flow, wave cancellation is possible, depending on where the actuation is located. As there exists absolute instability in wake of bluff body, the effective control of wake flow could be achieved by changing the absolute instability. Some tips or corners in geometry are also sensitive to disturbances and could be taken into account for successful flow control.

Keywords Flow control · Actuation-locating · Transition · Wake · High angle of attack

1 Introduction

The topic of flow control has attracted research interests of scientists and engineers all over the world and much progress has been achieved. Gad-el H M (1998, 2000) reviewed the progress in flow control. As flow control is multi-disciplinary, many experts of automation control and MEMS are also active in this field, in addition to the experts of fluid mechanics (Cattafesta and Sheplak 2011; Collis et al. 2004). However, flow control is within the category of fluid mechanics after all. The automation theory may not be applied to flow control as a transfer function may not be deduced because the control objective is actually the whole flow field when

X. Ming (✉)

Nanjing University of Aeronautics and Astronautics, Nanjing 210016, China
e-mail: mingam@nuaa.edu.cn

actuators in action and the effects are determined eventually by N-S equations which are nonlinear.

Actuation-locating is vital for success in flow control, as a force has three factors: magnitude, direction and origin. The second and the third are concerning actuator-locating in flow control, which means how and where the actuators should be located for best control.

Instability of shear layer is always utilized for successful and efficient control (Schlichting 1979). To delay the boundary layer transition from laminar to turbulent flow, wave cancellation is possible, depending on where the actuation is located. As there exists absolute instability in wake of bluff body, the effective control of wake flow could be achieved by inserting disturbances at certain location to change the absolute instability.

The locations where flow parameters change rapidly (with high gradients) are usually sensitive to actuation. Leading edge, for example, is a sensitive place for high lift devices (Ming 2010). Some tips or corners in geometry should be also taken into account for successful flow control (Ming et al. 1989, 2005, 2013).

2   Control of Boundary Layer Transition

When active control of boundary layer transition by wave cancellation is applied, the locations of the excitation slots are key factor. Figure 1 (left) shows schematically the experimental set-up. The artificial disturbance, that trigs T-S wave, is emitted from the first slot and travelling downstream. From the slots downstream waves, which are out of phase with the coming wave, are emitted to cancel the T-S wave, so that the transition could be delayed.

According the linear stability theory, the Reynolds number and the exciting frequency must be in the unstable region, that is the region ② in the Fig. 1 (right). If the actuation takes place in the region ①, the disturbances will decay, or the action takes places in non-linear region ③ or ④ downstream, the wave-cancellation will fail.

The successful control is shown in the Fig. 2. The left side is signals from hot wire. The magnitudes of fluctuation are much reduced when active control is in
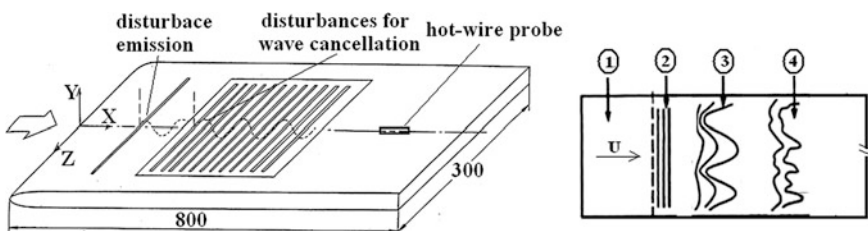
Fig. 1 Experimental set-up for boundary layer transition control
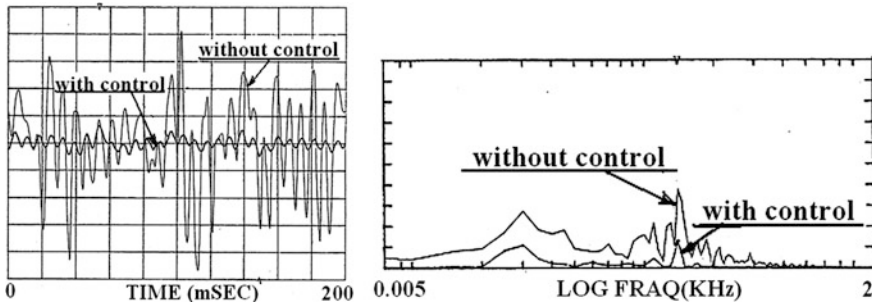
Fig. 2 Experimental results, *left* signals of hot wire; *right* spectrum

actuation, comparing to the case without control. Right side is comparison of the power spectrums with and without control. The peak value of the instability frequency is much less after active control.

3 Wake Flow Control

Figure 3 shows two different techniques for wake flows control. The first one (left side) is split plate, inserted in the wake. Unlike the traditional method, where a split plate in length of more than 5 diameters of the cylinder is used (Fig. 3, left upper), a much shortened split plate with length of 1.1 diameter of the cylinder is carefully located (left lower) where absolute instability occurs. As a result, the vortex street disappears as traditional method. This is because the absolute instability is modified by the short split plate. It is interesting that the short plate is not touched to the cylinder. The successful control relies on understanding of the fluid mechanics.

For the second technique (right), the vortex street at supercritical condition could be resumed and controlled by separation trip wires that change the separation
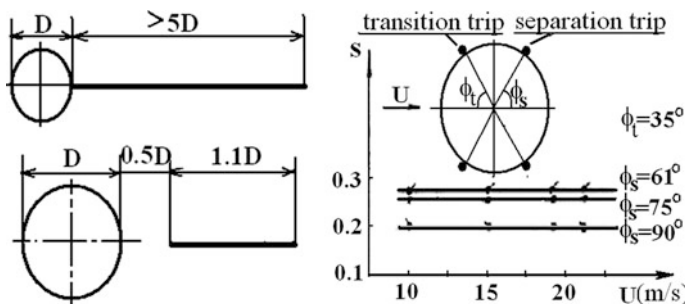
Fig. 3 Control of wake of cylinder (*left* by split plates; *right* by tripping wires)

position and hence the width of the wake, because the absolute instability of wake flow depends on the width of the wake. Transition trip wires are used to emulate supercritical condition at high Reynolds number. Experimental results show that the frequency (Strouhal number) of the vortex street depends on the locations of the separation trip wires. In Fig. 3, **S** stands for Strouhal number, ϕ_t and ϕ_s for locations of transition trip wire and separation trip wire respectively.

4 Flow Control Over Backward Facing Step (BFS) by Suction

Flow over the backward facing step is a typical separation flow. The turbulent boundary layer upstream separates from the corner of the step and becomes free shear layer. The area between free shear layer and wall is "dead water" (recirculation), see Fig. 4. The separation characteristics depend on the ratio of boundary layer thickness over the height of the step.

Flow control over BFS has been studied extensively. Among other active techniques, suction is one of most used methods for flow separation control. The already published research work for flow control of BFS by suction is simply to remove the mass within the recirculating area to improve the mass transfer and heat transfer. In this paper, however, the suction is disposed on the upper surface of the step and close to the upper corner. The purpose is to change the shear layer just before separation.

The results reveal that the location of suction has very strong influence on the flow control, as indicated in Fig. 4. Comparing with the base line (without control, green line), the suction, located close to the corner (L = 1 mm), can change the reattachment and skin friction τ downstream dramatically (red line). As contrasted, when the suction located upstream by only a small distance (8 mm), the control becomes very weak.

Again, the actuation locating is vital for efficient flow control.
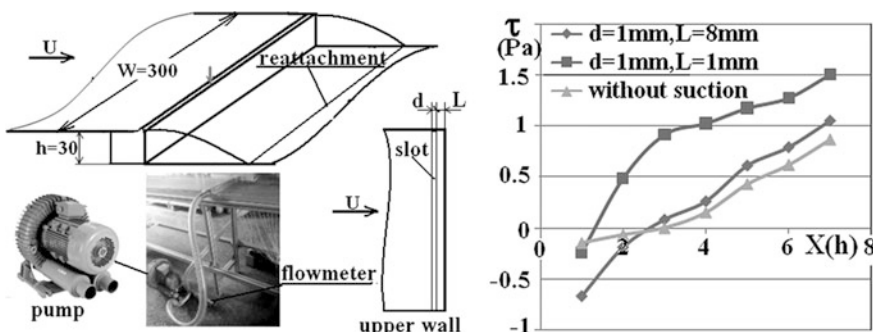
Fig. 4 Experimental set-up of BFS (*left*) and results (*right* τ: skin friction)

5 Asymmetry Control of Flow Around Slender Body at High Angle of Attack

Asymmetry control of flow around slender body at high angle of attack also indicates the importance of actuation-locating. A very tiny strake can control the overall flow field, but only when this strake is located at nose tip and swinging at certain frequency. Instantaneous symmetrical flow fields could be obtained, as shown in Fig. 5 (right), and the side force could be diminished to zero.

It is also possible to control the side force proportionally, depending the location of the average position of the swinging strake, as shown in Fig. 6, where C_z is side force and ϕ_s is the averaged circumferential position of the swinging strake from meridian. In this case the actuation is located dynamically.
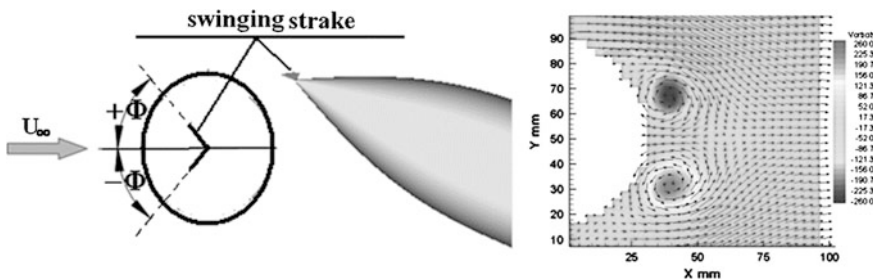
Fig. 5 Flow pattern control of slender body at high angle of attack
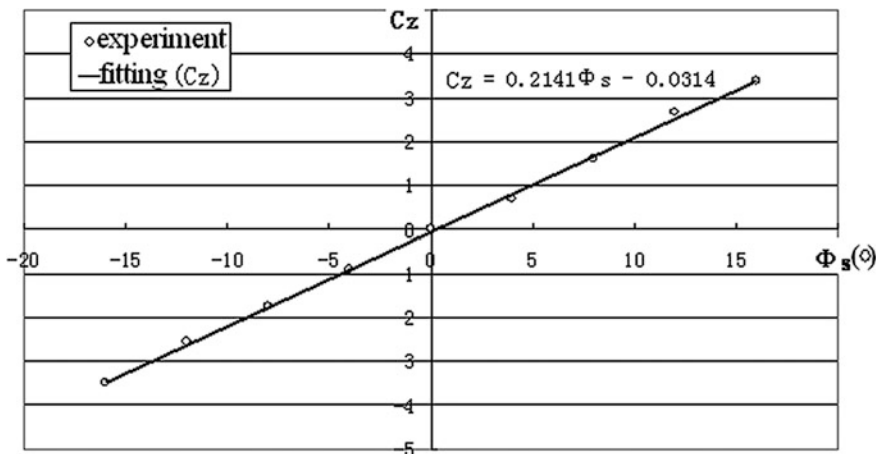
Fig. 6 Proportional control of side force

6   Conclusion

- Actuation-locating is vital for successful and efficient flow control
- Analysis of flow field is necessary to find where the flow is unstable
- Locations where flow parameters change rapidly are sensitive to actuation
- Tips or cornes in geometry should be considered for successful flow control.

References

Cattafesta LN, Sheplak M (2011) Actuators for active flow control. Annu Rev Fluid Mech 2011 (43):247–272

Collis SS et al (2004) Issues in active flow control: theory, control, simulation, and experiment. www.cds.caltech.edu/~murray/courses/cds101/fa04/caltech

Gad-el HM et al (1998) Flow control: fundamentals and practices. Springer lecture notes in physics. New Series Monographs, M53. Springer, Berlin

Gad-el HM (2000) Flow control: passive, active, and reactive flow management. Cambridge University Press, Cambridge

Schlichting H (1979) Boundary layer theory, 7th edn. Mcgraw-Hill Book Company, New York

X. Ming et al (1989) The characteristics and control of separated flow around circular cylinders. In: Proceedings of 4th Asia congress of fluid mechanics, Singapore

X. Ming (2005) Flow control and mechanism for slender body at high angle of attack. Int J Modern Phys Lett B 19(28):2005

X. Ming (2010) An innovative technique for flow separation control. In: Proceedings of 27th international congress of the aeronautical sciences, Marseilles, France

X. Ming (2013) Flow control over backward facing step by synthetic jet. In: The 12th international symposium on fluid control, measurement and visualization, Nara, Japan, 18–23 Nov 2013

Control of Corner Separation in a Linear Highly Loaded Compressor Cascade by Boundary Layer Suction

Yangwei Liu, Jinjing Sun and Lipeng Lu

Abstract Corner separation (CS) which can lead to deleterious consequences is an inherent flow structure in compressor. Two new suction slot configurations (SSCs) were proposed to investigate effects of boundary layer suction (BLS) on CS in a linear highly loaded compressor cascade. Five SSCs, under the same suction mass flows of 0.7 % of the inlet mass flows, were numerically studied over a range of operation incidence angles. The results were compared for different SSCs. Then the flow details were systematically analyzed to reveal the flow mechanisms.

Keywords Corner separation · Boundary layer suction · Compressor cascade

1 Introduction

Three-dimensional corner separation (CS) has been identified as an inherent flow feature of the corner formed by the blade suction surface and endwall of axial compressors. The CS may lead to deleterious consequences, such as increasing passage blockage, total pressure loss and noise, and decreasing static pressure rise and compressor efficiency, and even inducing stall and surge. Hence, controlling and eliminating CS is a key method to enhance compressor performance in routine design (Gbadebo et al. 2008).

Boundary layer suction (BLS) was applied to the theoretical and experimental research on the axial compressor and other turbomachinery in order to improve the performance in the middle of 20th century. The effect of suction slot located on the suction surface of the blade and endwall were compared by numerical and experimental research on a linear low-speed highly loaded compressor cascade of

Y. Liu (✉) · J. Sun · L. Lu
School of Energy and Power Engineering, Beihang University, Beijing, China
e-mail: liuyangwei@126.com

Y. Liu · J. Sun · L. Lu
Collaborative Innovation Center of Advanced Aero-Engine, Beijing, China

modern prescribed velocity distribution (PVD) stators (Gbadebo et al. 2008). The location effect of BLS on the endwall on high Mach number compressor cascade and with experimental validation was investigated (Chen et al. 2014).

In this paper, two new suction slot configurations (SSCs) were proposed, including one pitchwise suction slot on the endwall, and a compound slot configuration with one spanwise slot on the blade suction surface and one pitchwise slot on the endwall. The three suction slots investigated by Gbadebo et al. (2008) were also studied. Thus five SSCs to control CS were numerically investigated in the PVD cascade. The results were compared and the flow details were systematically analyzed to reveal the flow mechanisms.

2   Computational Procedure

A linear highly loaded axial compressor cascade (Gbadebo et al. 2008) with and without BLS was numerically studied using software FLUENT. The grid independence was checked (not shown here due to space limitation) and a gird with total number of 944800 cells was employed in the study. The first cell width from the blade and the endwall was set to $y^+ \approx 1$. Turbulence model is a weakness in CFD for engineering (Liu et al. 2008) and the Reynolds stress model (RSM) gives the best results compared with experiments (Liu et al. 2011) and was employed in this paper. Velocity profiles and absolute flow angles were used to specify inlet boundary and static pressure was given at the outlet boundary.

As shown in Fig. 1, five SSCs were numerically studied and compared. Case1 centers at about 70 % axial chord for the whole span and Case2 runs from 15 to 90 % axial chord paralleling to the suction surface on the endwall. Case4 is the combination of Case1 and Case2. Two new BLS slot configurations are explored, Case3 centers at 25 % axial chord on the endwall paralleling to the picthwise and Case5 is the combination of Case1 and Case3. Mass flow rate for the five SSCs is the same which is set as 0.7 % of the inlet mass flow rate.

Fig. 1 Suction slot configurations
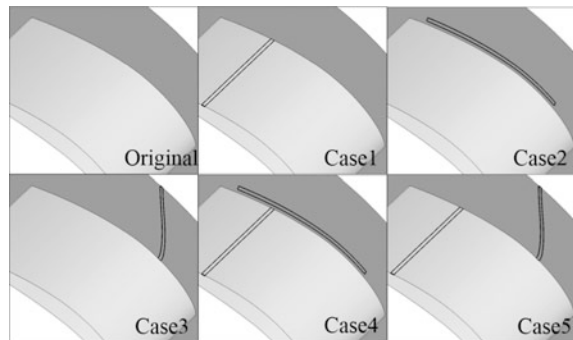
3   Results and Discussion

3.1   Cascade Performance

The results, including static pressure rise (Fig. 2a), total pressure loss (Fig. 2b), passage blockage and flow turning angle (not shown here), were compared systematically for different SSCs. The results show that all suction slots can significantly improve the performance, especially at above 2° incidence because of corner stall. The comparisons indicate that the pitchwise suction slot on the endwall, which is proposed in this paper, shows the best control effects for CS over the whole operation incidence among single SSCs. Also the proposed compound slot configuration, with one spanwise slot on the blade suction surface and one pitchwise slot on the endwall, shows the best control effects for CS over the whole operation incidence among compound slot configurations.

3.2   Static Pressure Coefficient Distribution

In this part, flow details are compared. Figure 3 shows the static pressure coefficient in the cascade passage at 97 % span (near the endwall), which is much smaller than that at 54 % span (not shown here) because of CS. It can be seen that the static pressure coefficient at 97 % span for Case2 and Case3 has been improved compared to the original case, which means the CS and its effect are weakened. And the downstream static pressure for Case3 is higher than Case2, which means that the new control method is better. Also the proposed compound slot configuration shows the best control effects (not shown here) for CS.
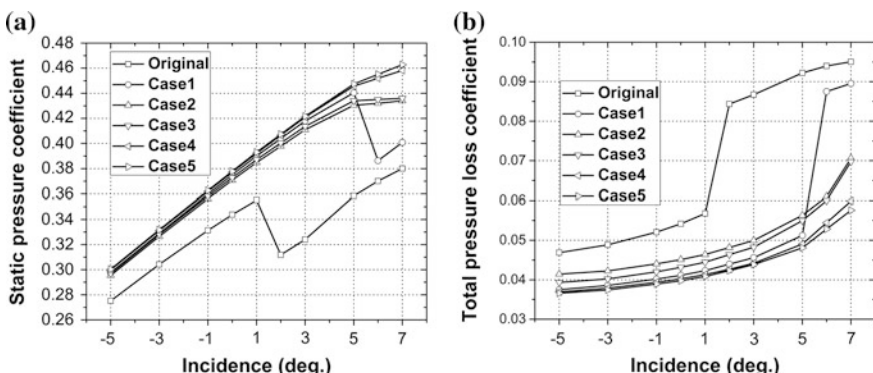
Fig. 2 Cascade performance of different suction slot configurations: **a** static pressure coefficient, **b** total pressure loss coefficient
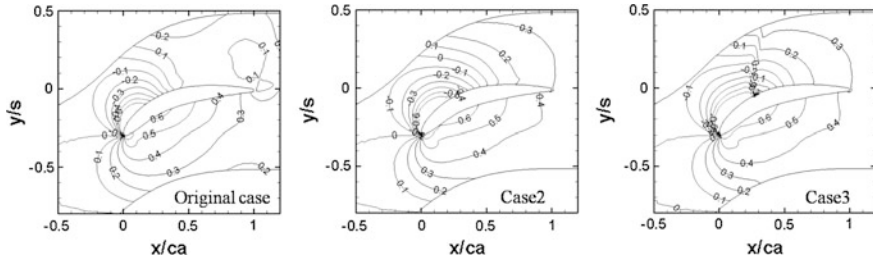
Fig. 3 Static pressure coefficient in cascade passage at 97 % span ($i = 7°$)

3.3 Velocity Profiles in the Passage

According to Lakshminarayana (1996), the endwall boundary layer has a lower velocity than the freestream but has the same pressure gradient normal to the side wall as the freestream if the boundary layer approximation is invoked. Thus an imbalance between the normal pressure gradient and the centripetal acceleration generate the secondary flow, which plays an important role in the CS. To reveal the flow mechanisms, the evolutions of mean velocity profiles in the blade passage are analyzed here. Us indicates the velocity component tangent to the blade suction surface, while Un is normal to the blade suction surface. The velocity Us in the CS for original case (not shown here) shows a decline of the velocity along the blade surface towards to the trailing edge. Considering the profile at 50 % chord, flow starts to separate and back flow exists (Us < 0). And a secondary deficiency region was observed in the simulation at wall distance y ≈ 0.01 m.

Much improvement of the velocity in the cascade passage near the endwall is obtained by the five SSCs, as shown in Fig. 4. It can be seen that all control cases have larger velocity Us (Fig. 4a) near the endwall, resulting in less secondary flow and less CS. Figure 4b shows Un decreases a lot for the slotted cases compared with the original case. Because the slot configuration on the endwall for Case2 and
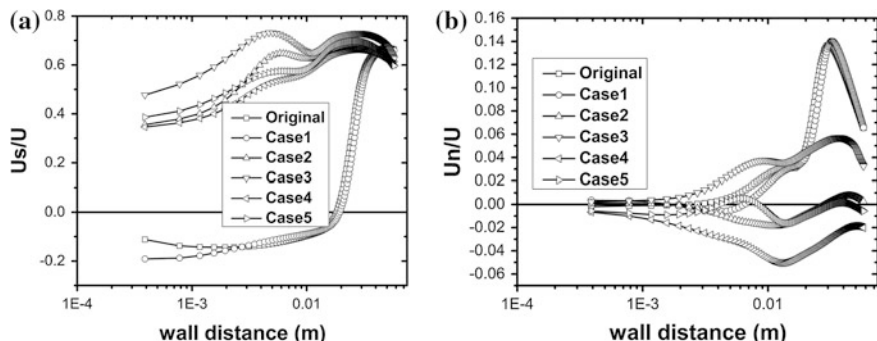
Fig. 4 Velocity profiles at 97 % span at S* = 0.6 (i = 7°): **a** Us, **b** Un

Case4 runs parallel to the suction surface, the flow near the suction slot would be absorbed into the slot. The magnitude of velocity Un is negative and decreases for those cases. Form comparisons, the control effect of Case3 is the best among single SSCs. And the control effect of Case5 is better than the compound slot configuration Case4.

4 Conclusion

The effects of boundary layer suction (BLS) on corner separation (CS) were numerically studied in a linear highly loaded PVD cascade. Five suction slot configurations were investigated. The flow details were systematically analyzed to reveal the flow mechanisms. The results are summarized as follows:

(1) BLS can effectively control CS and then significantly improve the cascade performance. The proposed pitchwise suction slot on the endwall shows the best control effects for CS among single SSCs. And the proposed compound slot configuration, with one spanwise slot on the blade suction surface and one pitchwise slot on the endwall, shows the best control effects for CS.

(2) The proposed control methods can increase larger steamwise velocity in the endwall boundary layer compared with other methods, resulting in less secondary flow and then less CS.

References

Chen PP, Qiao WY, Liesner K, Meyer R (2014) Location effect of boundary layer suction on compressor hub-corner separation. ASME paper GT2014-25043

Gbadebo SA, Cumpsty NA, Hynes TP (2008) Control of three-dimensional separations in axial compressors by tailored boundary layer suction. J Turbomach 130(1):011004

Lakshminarayana B (1996) Fluid dynamic and heat transfer of turbomachinery. Wiley, New York, pp 322–327

Liu Y, Yu X, Liu B (2008) Turbulence models assessment for large-scale tip vortices in an axial compressor rotor. J Propul Power 24(1):15–25

Liu Y, Lu L, Fang L, Gao F (2011) Modification of Spalart-Allmaras model with consideration of turbulence energy backscatter using velocity helicity. Phys Lett A 375(24):2377–2381

Modifications on the Reattachment Region of a Turbulent Step Flow Using a Dielectric Barrier Discharge Actuator

P. Sujar-Garrido, N. Benard, E. Moreau and J.P. Bonnet

Abstract This paper seeks to find an optimal actuation for controlling the reattachment region found downstream of a backward-facing step. The configuration has a 30-mm-height step. The external velocity is fixed at 15 m/s, based on that, the Reynolds number corresponds to 3×10^4. The control is performed via a single dielectric barrier discharge. Several actuation locations along the step model are tested and the best result regarding the modification of the mean reattachment point is observed with the actuator located at the hinge of the step. In terms of unsteady actuation, an optimal frequency is also observed for this position. For these optimal conditions, the paper introduces a brief analysis about the time-dependent modifications of the oscillations around the reattachment region.

Keywords Flow control · Separated shear layer · Backward-facing step · Dielectric barrier discharge · Plasma actuator

1 Introduction

Geometrical irregularities induce drawbacks in aerodynamics configurations and engineering applications such as undesirable noise and vibrations (Blake 1986). The flow over these irregularities separates and produces uncontrolled turbulent phenomena or important problems from an aerodynamic point of view. A simplified representation of a geometrical irregularity is a backward or forward facing step (Simpson 1989). The backward-facing step (BFS) is a typical test case to study all

P. Sujar-Garrido (✉)
Institute for Turbulence-Noise-Vibration Interaction and Control,
Harbin Institute of Technology, Shenzhen, China
e-mail: patricia@hitsz.edu.cn

N. Benard · E. Moreau · J.P. Bonnet
Institut PPRIME (CNRS UPR3346, Université de Poitiers, ISAE-ENSMA),
Bd Marie and Pierre Curie, BP 30279, 86962 Futuroscope, Poitiers, France

the complexity of massively separated turbulent flows. Different passive and active devices have been used to modify this flow. In this paper, the investigations are focused on the reattachment modifications obtained via a single Dielectric Barrier Discharge (DBD). This actuator has had a special attention during the last decades due to the very short time response inducing a high frequency bandwidth and its capability to imposed 2D periodic perturbations (Moreau 2007).

2 Experimental System

The step model configuration is installed in a closed-loop wind tunnel (turbulence intensity level of 1 %) with a 300 mm × 300 mm test section. The boundary layer is forced by a tripping device installed 10 h upstream of the separation point, with h being the height of the step equal to 30 mm. This assures a turbulent boundary layer upstream of the separation. An example of the electrode arrangement for the single DBD device is presented in Fig. 1a. The actuator is composed of two conductive electrodes mounted on each side of a 3-mm-thick dielectric material (PMMA). This arrangement produces an electric field that generates a surface discharge between both electrodes due to air ionization. The produced ElectroHydroDynamic (EHD) force results in a wall jet, developing tangentially to the dielectric wall, and blowing in the positive x direction (Benard and Moreau 2014). The plasma device is supplied by a sinusoidal wave of some kV of amplitude (here 20kV or 24 kV) driven at a frequency f_{AC} of 1 kHz. For the unsteady actuation (Fig. 1b), the reference input signal is modulated using a gate to switch on/off the discharge (with 50 % duty-cycle) producing a deep modulation of the applied signal (this modulation is called burst modulation).
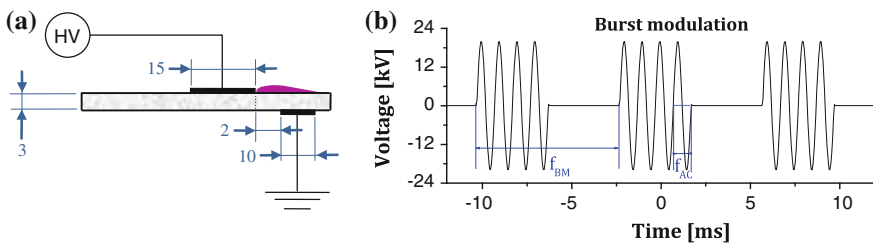
Fig. 1 **a** Sketch of the DBD actuator with the main dimensions. **b** Input signal waveform for the unsteady actuation, burst modulation

3   Results

Measurements are performed for a freestream velocity of 15 m/s ($Re_h = 3 \times 10^4$). The DBD device is installed at several positions, one upstream and three downstream of the separation (Fig. 2), in order to define an optimal device location regarding the modification of the reattachment point (X_R). Firstly, classic PIV gives us the opportunity to look at the time-averaged quantities. Then, high-speed PIV data is analyzed to study the changes at the instantaneous X_R point.

3.1   *Mean Reattachment Modification*

Figure 3 shows the modification of the X_R at each of the four studied positions (Fig. 2) for different forced frequency, f_{BM} (Fig. 1b). By using burst modulation, the produced flow presents periodic fluctuations at frequencies similar to the frequencies of the natural flow that are significantly lower than f_{AC}. The f_{BM} studied here varies from 25 to 500 Hz while the input voltage is maintained at 20 kV. Among all, an optimal frequency is observed ($f_{BM} = 125$ Hz, $St_\theta = 0.011$) for which the location of the mean reattachment is reduced by 17 %. A higher reduction can be achieved (20 %) by increasing the input voltage at 24 kV. This result is observed for an actuator inducing a periodic fluctuation at the step corner, position (1), within the formation region of the shear layer. This change is correlated with an increase of the Reynolds stresses. Also, it is inferred that the 2D forcing has a strong influence on the large-scale structures (Sujar-Garrido et al. 2015).

These results are in agreement with the literature where a minimization of the recirculating region is usually observed for a periodic forcing within a certain range. In particular, Chung and Sung (1996) summarized from their results and others authors, that in all cases the most effective frequency was found for $St_\theta \approx 0.01$.
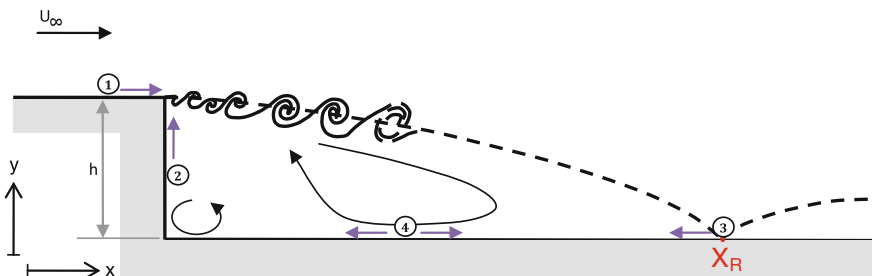
Fig. 2 Sketch of the four different positions of the actuator along the step model

Fig. 3 Mean reattachment position for each DBD location versus the frequency of modulation f_{BM}
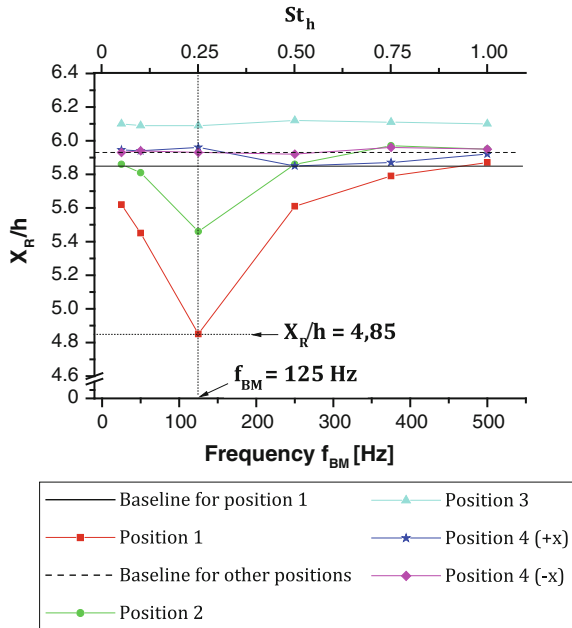
3.2 Time Resolved Information

The time-averaged reattachment point has been reduced by a significant amount. But the unsteadiness of this point plays an important role in noise generation due to its oscillations over a defined region (Jacob et al. 2001). For that reason, a high-speed PIV is used to look in detail the behaviour of the instantaneous reattachment point and the changes introduced by the plasma actuator.

The temporal evolution regarding the reattachment point is introduced in Fig. 4. This graph confirms the unsteady character of the reattachment location in both cases, uncontrolled and controlled flow. But, it seems that there is no significant modification produced by the actuation in its unsteadiness. To clarify this point, the temporal evolution of velocity component U in the reattachment region was analyzed. Packets of negative and positive velocities were observed in some sequences. Supposing that these packets correspond with the reattachment oscillations, a spectral analysis was carried out to precisely access to the repetitive value of this oscillation. The power spectral density (PSD), computed at a fixed point (x, y) near the reattachment, versus the frequency is plotted in Fig. 5. This graph shows a trace at very low frequencies, 9 Hz for the baseline case and 11 Hz for the actuation case. This trace is supposed to be related to the oscillations in the reattachment region. Thus, the results suggest that the frequency of oscillations in the reattachment region are slightly increased by the actuation. This could be the result of the time-averaged modification. The reduction in the reattachment length produces
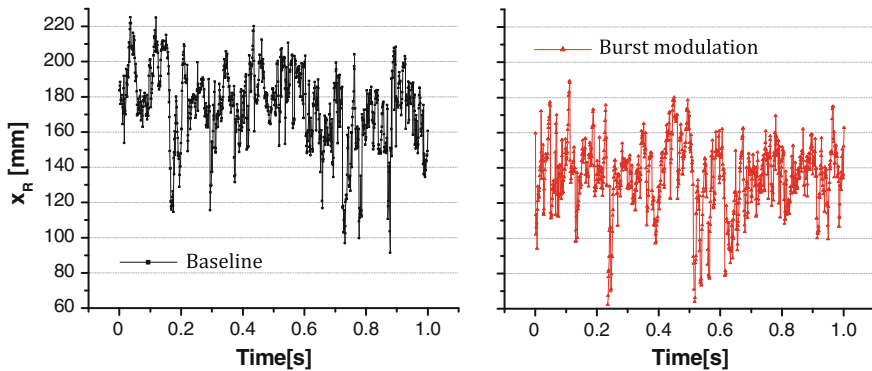
Fig. 4 Instantaneous reattachment positions for baseline and burst modulation

Fig. 5 PSD of the horizontal velocity component at $y/h = -0.96$ and $x/h = X_R$
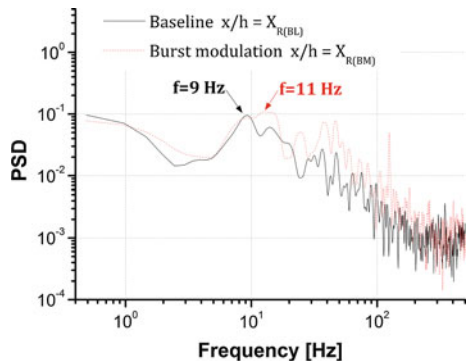
more curvature in the impinged shear layer and it could influence the reattachment oscillations in time and space.

4   Conclusions

The paper focuses on the control of the reattachment region of a turbulent backward-facing step flow using a DBD plasma actuator. The results obtained by a parametric study show the authority of the unsteady plasma to modify the reattachment point by reducing it up to 20 %. However, there is an unsteadiness motion in this reattachment region which is slightly modified in the controlled case. These oscillations are the main source of noise in this flow configuration and it deserves further investigations.

References

Benard N, Moreau E (2014) Electrical and mechanical characteristics of surface AC dielectric barrier discharge plasma actuators applied to airflow control. Exp Fluids 55:1846

Blake WK (1986) Mechanics of flow induced sound and vibrations. Applied mathematics and mechanics. Academic Press Inc, Orlando

Chun KB, Sung HJ (1996) Control of turbulent separated flow over a backward facing step by local forcing. Exp Fluids 21:417–426

Jacob MC, Louisot A, Juve D, Guerrand S (2001) Experimental study of sound generated by backward-facing steps under wall jet. AIAA J 39:1254–1260

Moreau E (2007) Airflow control by non-thermal plasma actuators. JoP D 40:605–636

Simpson RL (1989) Turbulent boundary-layer separation. Annu Rev Fluid Mech 21:205–234

Sujar-Garrido P, Benard N, Moreau E, Bonnet JP (2015) Active control by surface dielectric barrier discharge actuator of a reattached shear layer. Instability and control of massively separated flows. Fluid Mech Appl 107:189–194

Part III
Fluid–Structure Interaction

Power Output of Spring-Mounted Lifting Plates in Axial Flow

R.M. Howell and A.D. Lucey

Abstract In this paper, two different spring-mounting systems of lifting flexible plates in ideal flow are compared for their suitability in energy harvesting of induced flutter instability via the reciprocating motion of the spring system. In previous work, it was found that compared to a fixed cantilever the introduction of the dynamic support in both systems yields lower flutter-onset flow speeds which is desirable for energy harvesting applications. The first system is a cantilevered thin flexible plate aligned with a uniform flow with the upstream end of the plate attached to a spring-mass system. We compare this system to one where the upstream end is hinged with a rotational spring at the mount. We map out the linear stability and power output characteristics of both systems with the introduction of dashpot damping at the mount. As expected the introduction of damping stabilises both systems and the order of magnitude of this stabilisation varies non-linearly for different levels of damping; this results in optimal points for energy harvesting for each system.

1 Introduction

In the recent study of the flutter of plates in uniform axial flow a popular idea has been that of using the flutter instability to generate useful electrical energy; see for example (Tang et al. 2009). This energy could be harvested by various means. This has led us to investigate a fundamental system where a cantilever can move freely in the vertical axis. Its leading edge is attached to a rigid base by mounting it upon a linear spring, this system being depicted in Fig. 1a. This system is compared to a rotational spring, hinged-free system shown in Fig. 1b that was first studied in (Chadd Gibbs et al. 2012). Herein we extend our preliminary study (Howell and Lucey 2014) where we presented the stability space in the absence of damping that charted how the dynamics and the critical velocity $\bar{U}_c$ at a mass ratio of $\bar{L} = 1$ depend

R.M. Howell (✉) · A.D. Lucey
Fluid Dynamics Research Group, Department of Mechanical Engineering,
Curtin University of Technology, Box U1987, Perth, WA 6845, Australia
e-mail: richard.howell@curtin.edu.au

Fig. 1 The fluid-structure
systems under consideration:
a spring-mounted cantilever;
b hinged-free plate with
rotational spring at the
leading edge
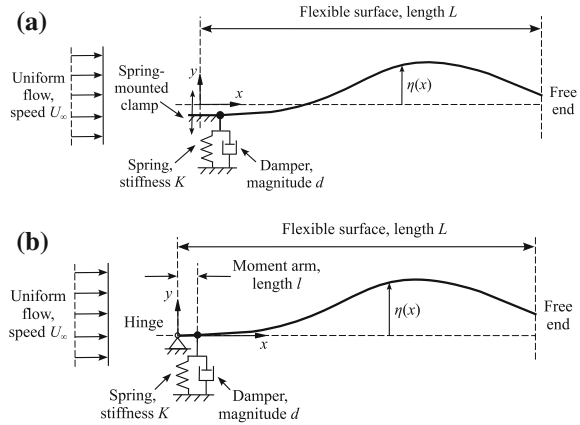
upon the variation in natural frequency of the support of the spring-mass systems
that are $\bar{\omega}_s$ or $\bar{\Omega}_s$ for the clamped-free and hinged-free systems respectively. We now
introduce damping into the spring-mass system and examine the power-extraction
characteristics.

2   Method

The fundamentals of the current method that mixes numerical simulation with eigen-
value analysis is fully detailed in (Howell et al. 2009) for a fixed cantilever. An ideal
two-dimensional flow is assumed wherein the rotationality of the boundary-layers
is modelled by vortex elements on the solid-fluid interface and the imposition of
the Kutta condition at the plate's trailing edge. The Euler-Bernoulli beam model is
used for the structural dynamics. Simply supported free plates where the support can
move vertically and actuate the system have been analysed in, for example, studies
of base-excited, fluid-conveying flexible tubes, see (Chang and Modarres-Sadeghi
2014), and constrain that the leading edge must follow the actuating force. In our
study, as well as applying an actuating force due to the reaction of the spring, we
allow that the motion of the leading edge can also be actuated by the motion of the
flexible plate; these constraints are applied through the inclusion of a shear-force bal-
ance condition at the leading edge, as detailed in (Rao 2011), that transmits the shear
force that drives the vertical motion of the mounting system whilst also enforcing that
neither free nor controlled rotation of the plate about its leading edge is permitted.
This means that the support mechanism can provide, without deformation, any level
of moment reaction to the flexible plate at its upstream end. For the hinged-free plate,
a standard hinge condition of zero bending moment is applied at the leading edge.

3   Results

We first introduce the system parameters and the values used to plot the results. To non-dimensionalise properties we use reference time and length scale $t_r = (\rho h)^{5/2}/(\rho_f^2 B^{1/2})$ and $L_r = \rho h/\rho_f$ respectively where ρ_f is the fluid density and ρ, h and B are respectively the flexible plate density, thickness and flexural rigidity. The merit of our scheme is that for given plate and fluid properties, the non-dimensional length and flow speed become independent control parameters. The mass ratio $\bar{L}$ is equal to L/L_r where L is the plate length: this is set equal to one in the results herein. The non-dimensional forms of the free stream velocity U_∞ and the real and imaginary parts of eigenvalues are $\bar{U} = U_\infty t_r/L_r$, $\bar{\omega}_R = \omega_R t_r$ and $\bar{\omega}_I = \omega_I t_r$ respectively. The sum of fluid pressure work done W (the product of the fluid pressure and wall velocity) and mount energy dissipation D (the product of damping and wall velocity squared) up to time t are converted into their non-dimensional forms $\bar{W}$ and $\bar{D}$ by dividing by the initial strain energy in the plate.

To non-dimensionalise the spring-mount system, spring-mount properties must be applied in their 'per-width' form; for example, the per-width value of the spring stiffness K is $K^* = \int K \mathrm{d}x$. The natural frequencies $\bar{\omega}_s$ or $\bar{\Omega}_s$ are equal to $t_r\sqrt{K^*/M_T^*}$ and $t_r\sqrt{\kappa/I_T}$ respectively where $M_T = \rho h L$ is the total plate mass, I_T is the total moment of inertia of the plate about the hinge and $\kappa = K^* l^2$ is the rotational spring stiffness, where l is the moment arm shown in Fig. 1b. Damping is included at the mount in multiples of critical damping $d_c = 2\sqrt{K^* M_T^*}$ and $C_c = 2\sqrt{\kappa I_T}$ so that $d^+ = d/d_c$ and $C^+ = C/C_c$ where $C = d^* l^2$. In summary, we find that the critical velocity and frequency of the system $\bar{U}_c$ and $\bar{\omega}_c$ take the functional dependence on the system's control parameters $f(\bar{L}, \bar{\omega}_s \text{ or } \bar{\Omega}_s, d^+ \text{ or } C^+)$. Finally, non-dimensional values of time, horizontal distance along the flexible plate and plate vertical displacement are $\bar{t} = t/t_r$, $\bar{x} = x/L$ and $\bar{\eta} = \eta/\eta_0$ respectively, where η_0 is the maximum displacement of the flexible plate at $t = 0$.

In Fig. 2a, d we show the variation of system eigenvalues with flow speed for the clamped-free and hinged-free devices respectively: both plates become unstable through a single-mode flutter of mode 2 (thick red line). The remaining sub-figures were obtained via numerical simulation. In Fig. 2b, e the deflection of the plate at various time steps at instability onset is shown and the mode 2 content in the critical mode shape can be seen. In Fig. 2c, f the area of highest energy transfer from fluid to plate is shown to be along the third quarter of the plate. The power output through the the action of the damper is seen in Fig. 2c, f as the gradient of the dashed energy-dissipation line after transience has died away—the value of this gradient is denoted $\bar{P}$.

Figure 3 shows the variation of $\bar{P}$ for other values of damping. Both Fig. 3a, b demonstrate that, in each system, there exists an optimal level of damping that should be applied (via a load) in the design of these types of energy-harvesting systems: these peak values of $\bar{P}$ occur in both systems around a value of $d^+ = C^+ = 0.5$. Contrasting the two systems for higher levels of damping, although the critical velocities
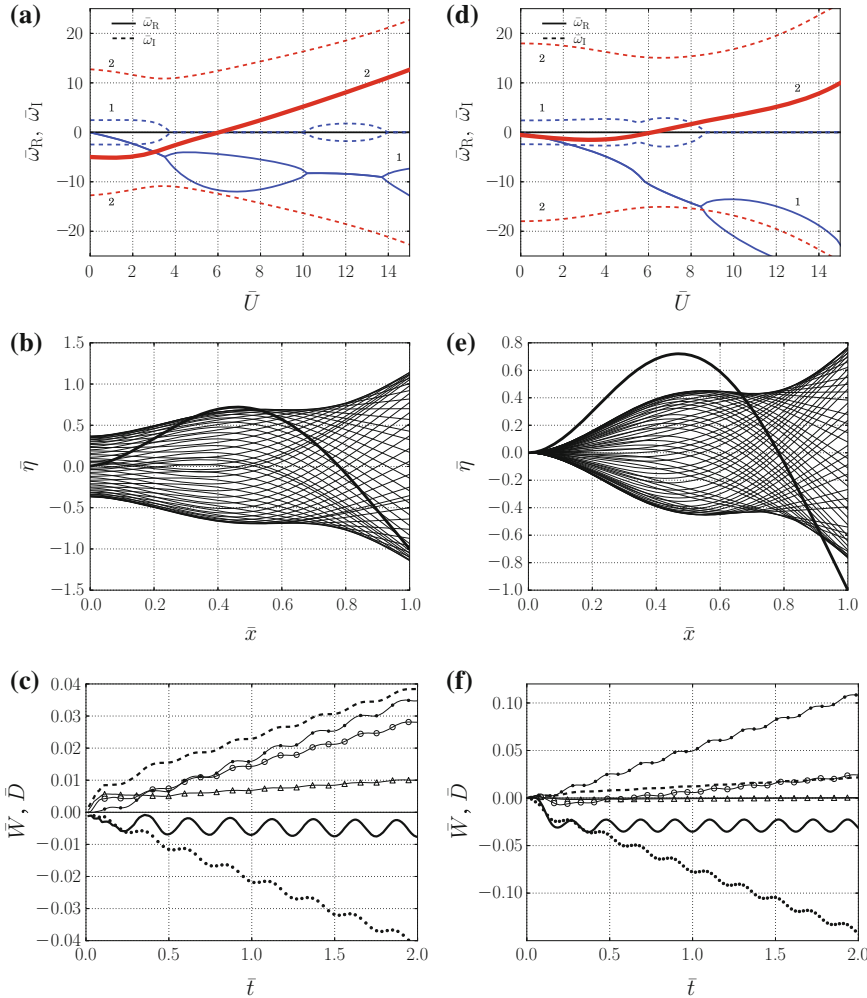
Fig. 2 System dynamics of the spring-mounted systems for $\bar{L} = 1$ with $\bar{\omega}_s = \bar{\Omega}_s = 10$ and mounting-system damping ratios $d^+ = C^+ = 0.5$: Spring-mounted cantilever: **a** Variation of numbered eigenvalues with flow speed (oscillatory and growth/decay parts represented by *broken* and *full lines* respectively) with the real part of Mode 2 that becomes unstable highlighted through a *thicker line* type, and, at the critical speed found as $\bar{U}_c = 6.05$, **b** time-sequence of instantaneous plate position (the *thick line* being the initial deflection with early oscillations removed), **c** time series of cumulative energy transferred from flow to plate in ▵ first, –○– second, –•– third, and ⋯ fourth quarters of the plate while −− is the energy-dissipation by the damper, $\bar{D}$, and —— (*thick*) is ($\bar{W} - \bar{D}$) where $\bar{W}$ is the total energy transferred between fluid and structure. **d**–**f** are the corresponding results for the hinged-free system that has $\bar{U}_c = 6.2$ seen in (**d**)

are of similar magnitude for both systems, more of the free-stream energy is captured by the clamped-free system. This effect is a result of the more favourable mechanics for this application of the spring-mounted clamp over the rotational-spring-hinged
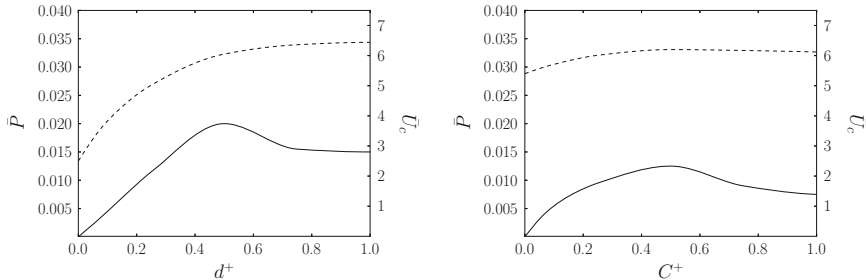
Fig. 3 Variation of power output, $\bar{P}$ (−), and critical speed, $\bar{U}_c$ (−−), with applied critical damping at the spring support when $\bar{\omega}_s = \bar{\Omega}_s = 10$: **a** translational, and **b** rotational systems

mount: as shown in Fig. 2e as the hinge is pinned, the maximum plate deflection close to the leading edge is small, whereas for the spring-mounted clamp shown in Fig. 2b it is of the magnitude of the trailing edge. Furthermore, for lower levels of damping the clamped-free device is able to produce similar levels of power output as compared to the hinged-free device but at a far lower U_c. This is advantageous for energy harvesting applications in a low flow speed regime.

4 Conclusions

We have developed a model for predicting the linear stability and power-output characteristics of two different 2-D linear spring-mounted systems in a uniform ideal flow, one comprising a spring-mounted cantilevered plate and the other a hinged-free plate, with the inclusion of damping at the spring mount. This has allowed a comparison of the efficacy of the two systems for converting flutter motion into reciprocating motion of the mount for power generation. Our simple analysis has shown that there are similar optimum points for power generation in each system. However, the clamped-free set-up has a significant advantage at both high and low levels of damping in terms of power output at the flutter-onset flow speed.

References

Chadd Gibbs S, Wang I, Dowell EH (2012) Theory and experiment for flutter of a rectangular plate with a fixed leading edge in three-dimensional axial flow. J Fluids Struct 34:68–83

Chang GH, Modarres-Sadeghi Y (2014) Flow-induced oscillations of a cantilevered pipe conveying fluid with base excitation. J Sound Vib 333:4265–4280

Howell RM, Lucey AD (2014) Stability of a spring-mounted cantilevered-free flexible plate in a uniform flow. In: 19th Australasian fluid mechanics conference, 8 Dec 2014, Melbourne, Australia

Howell RM, Lucey AD, Carpenter PW, Pitman MW (2009) Interaction between a cantilevered-free
    flexible plate and ideal flow. J Fluids Struct 25:544–566
Rao SS (2011) Mechanical vibrations, 5th edn. Pearson, Upper Saddle River
Tang L, Paidoussis MP, Jiang J (2009) Cantilevered flexible plates in axial flow: energy transfer
    and the concept of flutter mill. J Sound Vib 326:529–542

Effect of Viscous Flow on the Flutter Threshold of a Cantilever Plate

Chao Zhang, Yong Li and Lixi Huang

Abstract The flutter of a flexible plate cantilevered vertically at its leading edge has been investigated experimentally in a wind tunnel. As the wind speed exceeds a critical speed (flutter threshold), the cantilever plate would lose its stability and start to flutter. The motivation of this paper is to study the effects of different configurations of the flexible plate on the flutter threshold. The configurations include changing the thickness of airfoil-shape clamp at the plate leading edge to vary the boundary layer thickness of the plate, and inhibiting the plate wake extension by installing a downstream rigid splitter-plate. Test results show that the flutter threshold increases, but not monotonically, with the increase of boundary layer thickness, while decreasing with the downstream extension of the plate wake, indicating that both the boundary layer and the wake suppression can benefit stabilizing the fluid-structure vibration system.

Keywords Flutter · Cantilever plate · Boundary layer effect · Wake effect

1 Introduction

The instability of a cantilever flexible plate in axial flow is a common phenomenon of flow-induced vibration. When the flow speed exceeds a critical value, any small disturbance in the flow will serve as a trigger to excite the plate to vibrate. This phenomenon is called flutter and the critical speed is called the flutter threshold. In previous studies surveyed by Watanabe et al. (2002), numerical simulation results provided by various methods, such as potential flow theory with Kutta condition (Huang and Zhang 2013), discrete vortex lattice method (Eloy et al. 2007) and

C. Zhang (✉) · Y. Li · L. Huang
Lab for Aerodynamics and Acoustics, HKU Zhejiang Institute of Research and Innovation, and Department of Mechanical Engineering, The University of Hong Kong, Hong Kong, China
e-mail: zchku@hku.hk

Navier-Stokes simulation (Balint and Lucey 2005) for the plate flutter in two-dimensional flow, were consistent. However, the predicted flutter threshold was underestimated to a large extent. It is argued that these consistent results were a coincidence, since the three methods made distinguishing assumptions to the viscous flow effect. Even for Navier-Stokes simulation, the flow was assumed to be laminar in spite of fact that the Reynolds number referred to the plate chord length at the flutter threshold is so large that the laminar-turbulence transition may have already occurred. In addition, the influence of the clamp to cantilever the plate at its leading edge had not been taken into consideration. Therefore, to the author's knowledge, there is not convincing numerical study on the viscous flow effect on the plate flutter so far. In this paper, the effects of two viscous flow characteristics on the flutter threshold, including boundary layer thickness and wake extending from the trailing edge of the plate, are investigated experimentally in a wind tunnel.

2 Experimental Methodology

Experiments are conducted in an open-loop, low-speed wind tunnel with a test section of 0.2 m (width) × 0.2 m (height) × 0.8 m (length). The top view sketch of the experimental setup is illustrated in Fig. 1. A flexible plate with chord length of $L = 100$ mm and spanwise length of $S = 100$ mm is cantilevered vertically by airfoil-shape steel clamps at its leading edge and is in alignment with the axial flow direction. The clamps are rigid enough to keep the leading edge cantilevered boundary condition of the plate during the flutter. To get details of the boundary layer effects, the thickness of the airfoil-shape clamp is increased gradually by adding successive tape-layers on both sides of the clamp. To investigate the wake effect on the flutter threshold, a downstream rigid splitter plate in axial direction with the chord length of $L_s = 100$ mm and thickness 0.5 mm is mounted in the downstream of the flexible plate at a separation gap C.

There are two critical flutter speeds: U_c in the case of bursting into flutter and U_d when the plate returns to the immobile state from the flutter. U_d is usually less than U_c, which leads to a hysteresis loop. U_c and U_d are called ascending and descending critical flutter speeds, respectively. The flow speeds are measured by a pitot tube located at the entrance of the wind tunnel working section. The structures of the
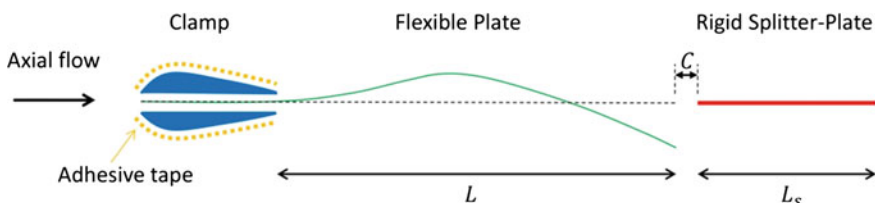
Fig. 1 *Top view* sketch of experimental setup

boundary layer and the plate wake are illustrated using a wire smoke located upstream the model assembly. The beginning and end of flutter process is determined simply through observation. The experimental uncertainty mainly comes from the flow speed measurement which is ± 0.1 m/s in this study.

The flexible plate is made of Polyester sheet with thickness of $h = 0.25$ mm, plate density of $\rho_p = 1400$ kg/m^3 and Young's modulus of $E = 5.22$ GPa. The Young's modulus is calculated from the free decaying signal by the standard first mode oscillation experiment in still air. A dimensionless flow speed $\tilde{U} = UL\sqrt{\rho_p h/D}$ (where U is the mean flow speed and $D = Eh^3/12$ is the bending stiffness) is defined. $\tilde{U}_c$ and $\tilde{U}_d$ are normalized ascending and descending critical flutter speed corresponding U_c and U_d respectively.

3 Results and Discussions

3.1 Flow Visualization

Figure 2 shows the smoke flow visualization of the flow field behind the clamp with and without a flexible plate. The airfoil clamp used is NACA0020 with thickness of 4 mm. The wind speed is 10.5 m/s, which is far less than critical flutter speed $U_c = 15.0$ m/s for this particular configuration. Therefore, the flexible plate is stable and motionless. It can be seen from Fig. 2a that the plate is immersed in a thick boundary layer and the thickness at the trailing edge of the plate is about 12 mm. Downstream the trailing edge, the plate wake develops. The boundary layer structure is obviously disordered and thus the flow is already turbulent. Therefore, in practical application, the boundary layer effect cannot be ignored or simply assumed to be laminar as done in theory studies. Figure 2b presents the wake flow behind the leading edge clamp without the flexible plate. The wake width at the same position is about 13 mm, which is almost identical with the boundary layer thickness in Fig. 2a. From this observation, it is suggested that the boundary layer thickness is mainly determined by the upstream clamp thickness.
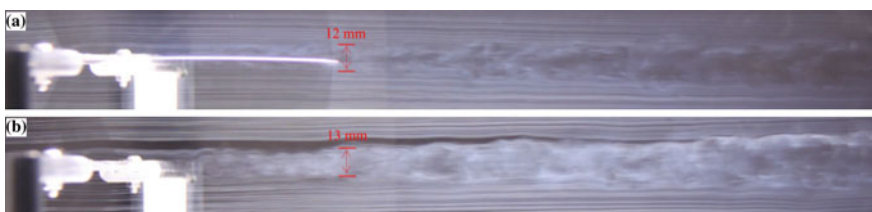
Fig. 2 Photographs of boundary layer and wake **a** with plate, **b** without plate

3.2   Effect of Boundary Layer Thickness

The purpose of this part is to investigate the effect of boundary layer thickness on the flutter threshold by changing the upstream clamp thickness. NACA0010 clamp with thickness of 2 mm is applied and the initial thickness of the assembly including the flexible plate is 2.4 mm. This thickness is increased to 9.6 mm at an interval of 0.8 mm. Figure 3 presents the critical flutter speed against the clamp thickness which is assumed to be the same order as the boundary layer thickness. With the increase of clamp thickness from 2.4 to 4.0 mm, both $\tilde{U}_c$ and $\tilde{U}_d$ increase, as shown in Fig. 3. At the clamp thickness between 4.0 and 6.4 mm, $\tilde{U}_c$ and $\tilde{U}_d$ almost keep constant. When the clamp thickness exceeds a critical value of 7.2 mm, $\tilde{U}_c$ is equal to $\tilde{U}_d$ and both decrease dramatically, indicating that there is no hysteresis anymore. This disappear of hysteresis has not been reported in the literature, and may serve as a benchmark to verify the N-S simulation. The behaviors of the two flutter speeds can be explained as follows. As the clamp thickness is relatively small ($\leq$4.0 mm), the boundary layer thickness increases smoothly. The plate becomes more stable due to the reduction of the fluid loading acting on the plate with a thicker boundary layer. In this range, the increment ratio of $\tilde{U}_c$ is $(10.4 - 9.8)/9.8 = 6.1$ %. With further increase of the clamp thickness, the boundary layer thickens with larger vortices shed from the clamp. Thus, the disturbance in the boundary layer increases. The total effect on the flutter instability is a competition between the reduction of fluid loading to suppress the flutter and the finite disturbance to promote the flutter. Neutralizing the two factors, there is no obvious change for $\tilde{U}_c$ and $\tilde{U}_d$. When the clamp thickness exceeds 7.2 mm, the disturbance is large enough to trigger the flutter leading to the vanishing of hysteresis.

Fig. 3 Evolution of normalized critical flutter speed $\tilde{U}_c$ and $\tilde{U}_d$ as a function of dimensional total clamp thickness
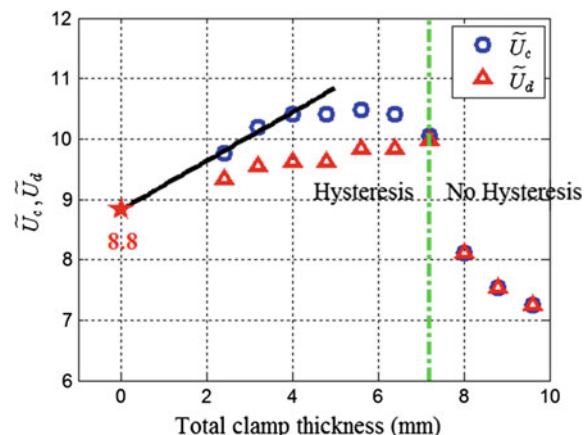
The limit of $\tilde{U}_c$, when the clamp thickness approaches zero, is the most important which can never be realized experimentally. By linear extrapolation using the leftmost three points of $\tilde{U}_c$ in Fig. 3, we can obtain the critical flutter speed limit of 8.8 for $\tilde{U}_c$ shown as a pentagram. The use of linear method is to give a rough estimation. The corresponding increment ratio of $\tilde{U}_c$ due to the presence of NACA0010 clamp is calculated as $(9.8 - 8.8)/9.8 = 10.2$ %. By the way, the discrepancy between the experiment and 2D simulation [2] is $(9.8 - 6.0)/9.8 = 38.8$ %. Therefore, the boundary layer effect is not the only origin for this discrepancy.

3.3 Effect of Plate Wake

Figure 4 presents the effect of the separation gap C on the critical flutter speed. NACA0020 clamp with thickness of 4 mm is applied. A rigid splitter-plate approaching to the trailing edge can suppress the plate wake extension. It can be seen that the wake suppression increases critical flutter speeds $\tilde{U}_c$ and $\tilde{U}_d$. When the gap is big enough, e.g. 35 mm in this case, the influence of the splitter-wall will vanish. The decrease of $\tilde{U}_c$ and $\tilde{U}_d$ with the enlargement of gap C indicates that the plate wake is more likely to destabilize the fluid-structure vibration system due to the increase of fluid loading. The leftmost two measured points reveal slightly irregular drop for $C = 0.5, 1.0$ mm. This is because the alignment of flexible plate and rigid splitter-plate in axial direction cannot sustain when gap is less than 1.0 mm. As a result, the vanishment of vortex shedding or the pressure difference between the two sides of the plate at the trailing edge cannot be achieved by this method. The maximum increment ratio due to the suppression of vortex shedding referred to $\tilde{U}_c$ with infinite gap is $(11.1 - 10.1)/10.1 = 9.9$ %.
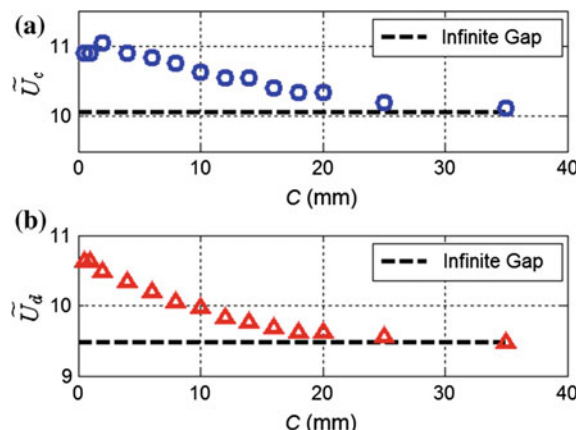
Fig. 4 Evolutions of critical flutter speed $\tilde{U}_c$ and $\tilde{U}_d$ as a function of separation gap C

4 Conclusions

It is proved by experiments that the boundary layer of a flexible plate stabilize the vibration system, while the existence of the plate wake may destabilize it. As a result, the flutter threshold increases with the increase of boundary layer thickness, while decreasing with the downstream extension of the plate wake. It is demonstrated that increasing the thickness of the leading edge clamp and applying a splitter-plate in the downstream can benefit stabilizing the fluid-structure vibration system. The neglect of the effect of boundary layer is proved to be a reason for the discrepancy of the flutter threshold between two-dimensional theoretical predictions and experimental measurements. A total of about 10 % of discrepancy may be attributed to the clamp thickness effect.

References

Balint T, Lucey AD (2005) Instability of a cantilevered flexible plate in viscous channel flow. J Fluids Struct 20:893–912

Eloy C, Souilliez C, Schouveiler L (2007) Flutter of a rectangular plate. J Fluids Struct 23:904–919

Huang L, Zhang C (2013) Modal analysis of cantilever plate flutter. J Fluids Struct 38:273–289

Watanabe Y, Isogal K, Suzuki S et al (2002) Theoretical study of paper flutter. J Fluids Struct 16:543–560

Stability of a Cantilevered Flexible Plate with Non-uniform Thickness in Viscous Channel Flow

Julien Cisonni, Anthony D. Lucey and Novak S. J. Elliott

Abstract Most studies analysing the instability of a cantilevered flexible plate in an axial flow are based on models assuming an inviscid flow and uniform properties for the plate. However, for some applications, such as biomechanical fluid-structure interaction (FSI) systems, these simplifications may not be valid due the scale of the problems and the non-uniform geometric and mechanical properties of the soft tissue. In this study, a parametric investigation is conducted to determine the conditions leading to flutter instability of a cantilevered flexible plate with a non-uniform thickness immersed in a two-dimensional viscous channel flow. It is shown that, depending on the mass ratio, the thinning and thickening of the plate free-end can stabilise or destabilise the FSI system and change the critical mode at instability onset.

1 Introduction

The stability of a cantilevered flexible plate in an axial flow is a fundamental fluid-structure interaction (FSI) problem with applications in many fields of engineering, both long-established and emerging, such as energy harvesting (Tang et al. 2009) and biomechanics. When immersed in a two-dimensional channel flow, a cantilevered flexible plate can constitute a model analogue of the soft-palate in the upper airway, of which the flutter instability represents the occurrence of snoring (Elliott et al. 2011; Cisonni et al. 2014). While the mechanisms and the conditions leading to flutter remain unclear, recent investigations have shown that the critical velocity

J. Cisonni(✉) · A.D. Lucey · N.S.J. Elliott
Fluid Dynamics Research Group, Department of Mechanical Engineering,
Curtin University, Perth, WA 6845, Australia
e-mail: julien.cisonni@curtin.edu.au

N.S.J. Elliott
Grupo de Investigación de la Dinámica de Fluidos, Xe' Lajuj No'j,
Quetzaltenango, Guatemala

333

at which a single-mode instability is triggered is mainly determined by the fluid-to-plate mass and time-scale ratios (Eloy et al. 2008). Further, investigations taking into account the fluid viscosity in the FSI model have provided a better understanding of the energy exchange between the fluid and the flexible structure, particularly for a cantilevered plate in a confined flow (Balint and Lucey 2005). Hitherto, in the vast majority of studies, the properties of the plate have been assumed to be uniform. However, anatomical structures, such as soft tissue, in biomechanical systems can have non-uniform geometric and mechanical properties. Therefore, in this study, a parametric investigation is conducted to determine the conditions leading to flutter instability of a cantilevered flexible plate with a non-uniform thickness immersed in a two-dimensional viscous channel flow.

2   Method

The FSI system is composed of a cantilevered flexible plate immersed in a viscous channel flow, as depicted in Fig. 1. The flow with mean inlet velocity U^* in a two-dimensional channel of height H^* and length L^* is governed by the non-dimensional Navier–Stokes and continuity equations. Using the principle of virtual displacements, the deformation of the flexible plate of length L_P^* and thickness h^* is governed by the one-dimensional Kirchhoff–Love beam equation allowing for geometric non-linearity. The problem is formulated using the open-source finite-element library oomph-lib (Heil and Hazel 2006). The flexible plate is spatially discretised using two-node Hermite beam elements and the fluid domain using nine-node quadrilateral Taylor-Hood elements with adaptive mesh refinement capabilities. Time stepping is done with a Newmark scheme for the solid and a BDF2 scheme for the fluid. The FSI problem is discretised monolithically and the Newton-Raphson method is used to solve the non-linear system of equations, employing the SuperLU direct linear solver within the Newton iteration.

The numerical experiments are carried out at constant Reynolds number $\mathrm{Re} = \rho_f^* U^* H^* / \mu^* = 100$ and plate-to-channel aspect ratio $L_P/H = L_P^*/H^* = 2$. The analysis of the stability/instability of the FSI system is conducted for variations of

Fig. 1 Description of the FSI system modelling a cantilevered flexible plate immersed in a viscous channel flow, and the physical quantities of the problem
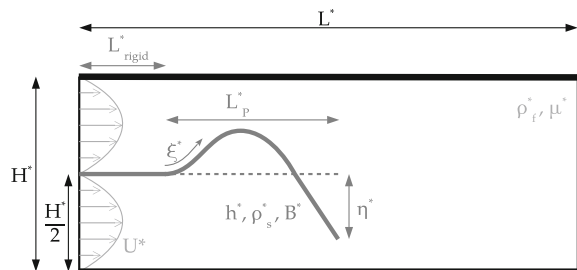
Fig. 2 Flexible plate
thickness profiles showing
the two distinct sections for
the three cases considered:
uniform thickness (*black
solid line*), thinner free-end
(*dark gray dotted line*) and
thicker free-end (*light gray
dashed line*)
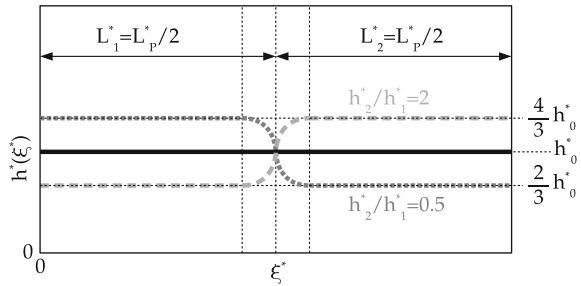
mass ratio $M = (\rho_f^* L_P^*)/(\rho_s^* h^*)$ and reduced flow velocity $U = U^*/(L_P^* f_P^*)$, where
ρ_f^* is the fluid density, μ^* the fluid dynamic viscosity, ρ_s^* the plate density, $f_P^* = \sqrt{B^*/(\rho_s^* h^*)}/L_P^{*2}$ the plate characteristic frequency, and B^* the plate flexural rigidity. The non-uniform flexural rigidity and mass are varied locally through a plate thickness function (see Fig. 2) dividing the plate into two sections (1 and 2 denoting the fixed-end and the free-end, respectively) of equal length ($L_1^* = L_2^* = L_P^*/2$) and keeping the total plate mass, and hence the mass ratio M, constant. Three cases are considered is this study, namely: (i) the reference system including a flexible plate of uniform thickness ($h_2/h_1 = 1$), (ii) a system including a flexible plate with a thinner free-end ($h_2/h_1 = 0.5$) and (iii) a system including a flexible plate with a thicker free-end ($h_2/h_1 = 2$).

3 Results and Discussion

The amplitude decay/amplification of the plate motion for the three cases is determined through the analysis of the exponential growth rate in time of the span-wise deflection η^* of the oscillating plate tip. Figure 3 shows the exponential growth rate normalized by the oscillation frequency as a function of the mass ratio M and reduced flow velocity U for the uniform thickness plate ($h_2/h_1 = 1$). This growth rate "map" illustrates the complex influence of the interactions of the flow with the different structural modes on the stability of the system. The neutral stability curve corresponding to a zero growth rate, as shown in Fig. 3, is characterized by different branches corresponding to different flutter modes. For low mass ratios ($M < 1$), Mode 2 dominates the FSI system behaviour and the growth rate consistently increases as the reduced flow velocity increases. For higher mass ratios ($M > 1$), higher mode ($n > 2$) instabilities start to predominate successively the FSI system behaviour as the mass ratio increases. Moreover, it can be observed that the variation of the pre-critical growth rate as a function of the reduced flow velocity becomes non-monotonic, denoting the changes between predominant flutter modes.

The introduction of a non-uniform thickness produces a shift of the neutral stability curve along both the mass ratio and the reduced flow velocity axes, as can
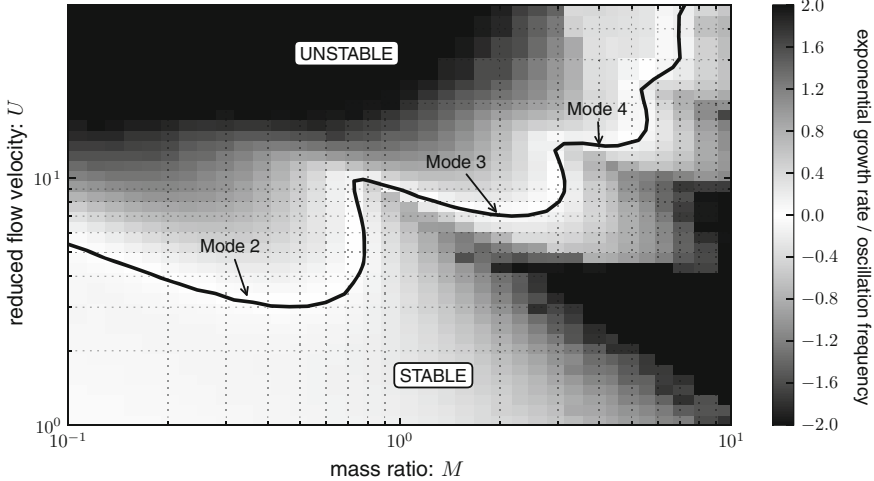
Fig. 3 Exponential growth rate of the tip displacement amplitude during the flexible cantilevered plate oscillation as a function of the mass ratio M and reduced flow velocity U for the uniform thickness plate ($h_2/h_1 = 1$). A higher growth rate (normalized by the oscillation frequency) indicates a more unstable system and a negative growth rate indicates a stabilisation of the FSI system. Neutral stability of the system is indicated with the *black solid line*
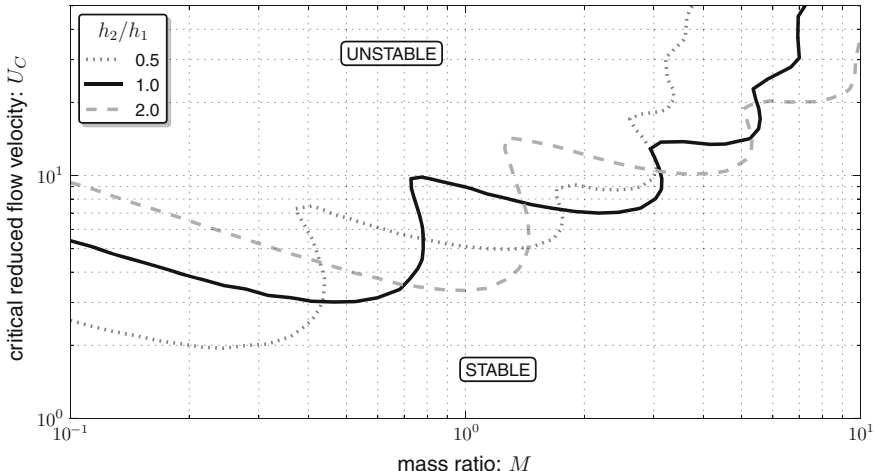
Fig. 4 Critical reduced flow velocity as a function of the mass ratio for the three cases considered: uniform thickness (*black solid line*), thinner free-end (*dark gray dotted line*) and thicker free-end (*light gray dashed line*)

be seen in Fig. 4. For the flexible plate with a thinner free-end, the predominance of the higher mode instabilities is triggered for lower mass ratios, in comparison to the uniform thickness plate. In addition, all the different modal branches of the

neutral stability curve are characterized by lower critical reduced flow velocities, in comparison to the uniform thickness plate. Conversely, for the flexible plate with a thicker free-end, the predominance of the higher mode instabilities is triggered for higher mass ratios and all the different modal branches of the neutral stability curve are characterized by higher critical reduced flow velocities. Despite the similar shapes of the neutral stability curves corresponding to the three cases, the thinning and thickening of the plate free-end greatly influence the motion of the cantilevered flexible plate. The altered plate dynamics result in drastically contrasting effects on the flutter instability thresholds and induce non-linear modifications of the pre- and post-critical behaviours. Thus, depending on the mass ratio, the thinning and thickening of the plate free-end can stabilise or destabilise the FSI system and change the critical mode in which the system first becomes unstable.

References

Balint TS, Lucey AD (2005) Instability of a cantilevered flexible plate in viscous channel flows. J Fluids Struct 20:893–912

Cisonni J, Elliott NSJ, Lucey AD, Heil M (2014) A compound cantilevered plate model of the palate-uvula system during snoring. In: Chowdhury H, Alam F (eds) 19th Australasian fluid mechanics conference, 8 Dec 2014. RMIT University, Melbourne, Australia

Elliott NSJ, Lucey AD, Heil M, Eastwood PR, Hillman DR (2011) Modelling and simulation of fluid-structure interactions in human snoring. In: Chan F, Marinova D, Anderssen RS (eds) 19th International congress on modelling and simulation (MODSIM 2011), 12 Dec 2011, Perth, Australia. Modelling and Simulation Society of Australia and New Zealand Inc, pp 530–536

Eloy C, Lagrange R, Souilliez C, Schouveiler L (2008) Aeroelastic instability of cantilevered flexible plates in uniform flow. J Fluid Mech 611:97–106

Heil M, Hazel AL (2006) oomph-lib—an object-oriented multi-physics finite-element library. In: Schäfer M, Bungartz H-J (eds) Fluid-structure interaction. Springer, pp 19–49

Tang L, Païdoussis MP, Jiang J (2009) Cantilevered flexible plates in axial flow: energy transfer and the concept of flutter-mill. J Sound Vibr 326:236–276

Modelling of a Cantilevered Flexible Plate Undergoing Large-Amplitude Oscillations Due to a High Reynolds-Number Axial Flow

R.O.G. Evetts, R.M. Howell and A.D. Lucey

Abstract We present a new model of the nonlinear fluid-structure interaction of a cantilevered flexible plate with an ideal flow that can account for the effect of boundary-layer separation from the plate surface upstream of its trailing edge. Short plates are studied herein for which the behaviour is dominated by low-order structural modes. When the wake is forced to form from the trailing edge the typical sequence of amplitude growth to nonlinearly saturated oscillations at flow speeds above that of the onset of linear instability is found. However, if separation is included the system evidences the same sequence at a flow speed for which the system is neutrally stable to linear disturbances. This suggests that flow separation may be the cause of the sub-critical instability found in experimental studies of the system.

Keywords Fluid-structure interaction · Flutter · Wake · Cantilever · Separation

1 Introduction

A new model is developed of the nonlinear fluid-structure interaction (FSI) of a cantilevered flexible plate of length L in uniform axial flow of velocity U_∞ as depicted in Fig. 1. Inviscid flow is assumed and therefore the FSI model approximates the very high Reynolds number flows that predominate in engineering applications. However, viscous effects are implicitly incorporated either through the imposition of the Kutta condition at the plate's trailing edge or through boundary-layer separation (as drawn in Fig. 1) that can occur in an adverse pressure gradient upstream of the trailing edge. Previous approaches have modelled this FSI system using the former whereby the wake forms from the trailing edge and in Tang and Païdoussis (2007, 2008) is assumed to follow a sinusoidal path following the spatio-temporal characteristics of the plate motion. Therefore, the main purpose of this paper is to determine the

R.O.G. Evetts (✉) · R.M. Howell · A.D. Lucey
Fluid Dynamics Research Group, Department of Mechanical Engineering,
Curtin University of Technology, GPO Box U1987, Perth, WA 6845, Australia
e-mail: r.evetts@postgrad.curtin.edu.au
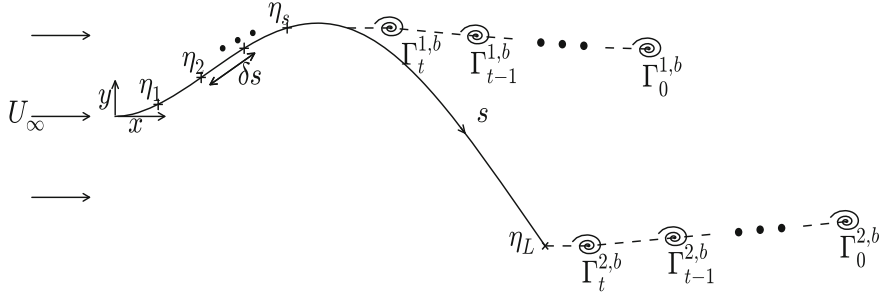
Fig. 1 Schematic of the fluid-structure system studied and the approach taken to model separation

effect of flow separation on the nonlinear stability of the FSI system by comparing its results with those in which the boundary-layer vorticity is assumed to remain attached on both sides for the full length of the flexible plate.

2 Method

The present solution of the Laplace equation utilises a non-linear boundary-element flow solution similar to that developed in Lucey et al. (1997) and is an extension of the second-order linear boundary-element method detailed in Howell et al. (2009) so as to capture finite-amplitude effects. The flexible plate is discretised into N panels each of length $\delta s = L/N$ and the vector of nonlinear vortex strengths, γ, for the N panels is found by imposing the no-flux condition giving

$$\{\gamma\} = [\mathbf{I^N}]^{-1}\{U_\infty \sin\theta + \dot{\eta}\cos\theta - \dot{x}\sin\theta + u^{T_b}\sin\theta - u^{N_b}\cos\theta\}, \quad (1)$$

where θ is the panel angle relative to $y = 0$ and $\dot{x}$ and $\dot{\eta}$ are respectively the velocities of each panel control point in the x- and y-directions. u^{N_b} and u^{Tb} are respectively the normal and tangential velocities induced at the panel control points by the discrete vortices of the wake. $[\mathbf{I^N}]$ comprises the normal influence coefficients. The nonlinear version of the Euler-Bernoulli beam equation, presented in Tang and Dowell (2002), is

$$\begin{aligned}
\delta p = {} & \rho h \ddot{\eta}_s - \rho h \frac{\partial \eta}{\partial s} \int_0^s \left(\left(\frac{\partial^2 \eta}{\partial t \partial s}\right)^2 + \frac{\partial \eta}{\partial s}\frac{\partial^3 \eta}{\partial t^2 \partial s} \right) \mathrm{d}s \\
& - \rho h \frac{\partial^2 \eta}{\partial s^2} \int_s^L \int_0^s \left(\left(\frac{\partial^2 \eta}{\partial t \partial s}\right)^2 + \frac{\partial \eta}{\partial s}\frac{\partial^3 \eta}{\partial t^2 \partial s} \right) \mathrm{d}s \mathrm{d}s \\
& + B \left[\frac{\partial^4 \eta}{\partial s^4} + \frac{\partial^4 \eta}{\partial s^4}\left(\frac{\partial \eta}{\partial s}\right)^2 + 4\frac{\partial \eta}{\partial s}\frac{\partial^2 \eta}{\partial s^2}\frac{\partial^3 \eta}{\partial s^3} + \left(\frac{\partial^2 \eta}{\partial s^2}\right)^3 \right],
\end{aligned} \quad (2)$$

where ρ, h, and B are the plate density, thickness, and stiffness respectively. This model is based upon the assumption that the plate is inextensible; thus, L and therefore δs are constant. To determine the pressure difference across the plate, δp, the vortex-singularity strengths found from Eq. (1) are used to determine the flow perturbations (from the mean flow) and the velocity potential. These are then used in the unsteady Bernoulli equation (see Howell et al. 2009) applied along the upper and lower surfaces of the flexible plate. When separation occurs, the surface pressure downstream of the separation point is taken to be that at the point of separation.

We decompose the transmural pressure using $\delta p = \delta p' + \rho_{\mathrm{f}}[\mathbf{B}]\ddot{\eta}$ to separate out the fluid inertia; herein ρ_{f} is the fluid density and $[\mathbf{B}]$ is a matrix that contains the influence coefficients of the velocity potential. Combining this equation with Eq. (2) gives an equation for the coupled fluid-structure system. This equation is rearranged for plate acceleration and is solved using a semi-implicit Crank-Nicholson-type method of solution, detailed in Lucey and Carpenter (1992), that solves first for the plate acceleration at the next time step followed by integration to determine velocities and displacements. The wake formed by the separation of vorticity from the plate is modelled using a nonlinear version of the discrete-vortex method described in Howell et al. (2009) by Gaussian blobs of strength Γ shown in Fig. 1. Separation from the plate surface is adjudged to occur downstream of the point at which an adverse pressure gradient first occurs and where it exceeds a threshold value of 5 % of the dynamic pressure; this value has been determined by using the present flow solution to model the known separation characteristics of oscillating aerofoils.

3　Results

Results are presented in terms of non-dimensional time $\bar{T} = T\rho_{\mathrm{f}}^2 B^{1/2}/(\rho h)^{5/2}$, flow speed $\bar{U} = U_\infty (\rho h)^{3/2}/(\rho_{\mathrm{f}} B^{1/2})$ and fluid-to-plate mass ratio $\bar{L} = \rho_{\mathrm{f}} L/(\rho h)$ following the scheme presented in Howell et al. (2009). Herein, we use $\bar{L} = 1$ throughout that broadly corresponds to the short plates for which the FSI dynamics are dominated by low-order flexible-plate modes (Tang and Dowell 2002; Tang and Païdoussis 2008; Howell et al. 2009).

Initial results—not shown here—studied the behaviour of the coupled system at a flow speed approximately 40 % higher than the critical flow speed for linear instability determined in Howell et al. (2009) in the absence of a wake. When separation was forced to occur at the trailing edge, the results evidenced excellent agreement with the equivalent models of Tang and Païdoussis (2007, 2008); this served to validate our model and its implementation. When the effect of separation upstream of the trailing edge was included, it was found that the effect on system behaviour was negligible.

However, at lower flow speeds wake-separation effects are found to be very significant. Figure 2 shows the behaviour of the FSI system described for $\bar{U} = 5.96$, the critical flow speed for linear instability. The top row of figures pertains to the wake
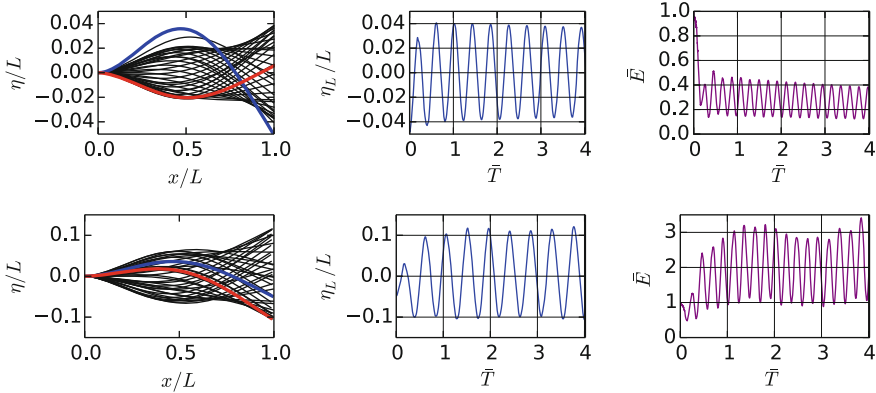
Fig. 2 Oscillation of a cantilevered plate in axial flow at $\bar{L} = 1$ and $\bar{U} = 5.96$: the *top row* of sub-figures for wake formation from the plate trailing edge, and the *bottom row* when separation is included. The *first column* of sub-figures are snapshots in time of plate displacement; *blue* and *red* profiles are respectively the initial (imposed) deflection and the deflection at $\bar{T} = 4$. *Second* and *third columns* respectively show time series of plate-tip defection and plate energy, the latter normalised by the strain energy of the plate in its initial deflection

forced to form from the trailing edge while the bottom row are the corresponding results when flow separation is modelled. The simulations were initiated by releasing the flexible plate from an imposed deformation in the shape of *in vacuo* Mode 2. In both cases the FSI mode principally comprises components of *in vacuo* Modes 1 and 2. In the absence of separation, the top figure shows that after applying the initiating finite-amplitude deflection the plate motion settles quickly into low-amplitude neutrally-stable oscillations as predicted by linear studies. In contrast, the bottom figure shows amplitude growth followed by non-linear saturation at approximately $\bar{T} = 1$ when the plate settles in to limit-cycle oscillations with the steady mode shape of the red line in the plate-deflection history captured at $\bar{T} = 4$; these phenomena are also seen in the time series of both tip deflection (second column of sub-figures) and plate-energy (third column of sub-figures). The results of Fig. 2 demonstrate that flow separation can cause nonlinear instability at a flow speed for which the system is linearly stable. This type of nonlinear sub-critical instability, that causes hysteresis as flow speed is changed, is well known in experimental studies of cantilevered flexible-plate/flag flutter.

To understand the effect of separation on nonlinear motions and stability of the flexible plate, Fig. 3 shows the wake structures at the flow speed used to generate Fig. 2 when the flow is (a) forced to remain attached for the full length of the plate and (b) when separation is modelled. First, (a) demonstrates that the assumption, e.g. in the models of Tang and Païdoussis (2007, 2008), that wake vortices follow a sinusoidal path when separation occurs at the trailing edge is valid. Second, the effect of separation on stability, discussed above, can be deduced from the structure of the wake in (b). At high flow speed, it was observed that intense vortical structures

(a)

(b)
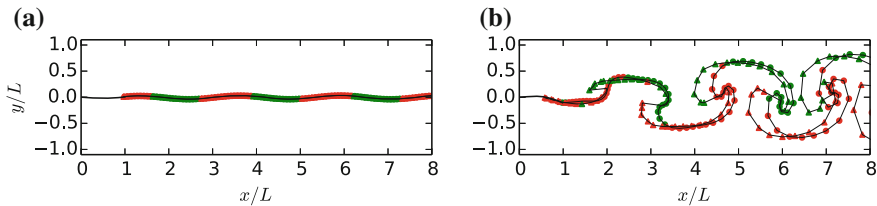
Fig. 3 Wake vorticity generated by a plate undergoing non-linear oscillations for $\bar{L} = 1$ with $\bar{U} = 5.59$: **a** wake vorticity is forced to separate at the trailing edge; **b** separation is modelled. Markers denote a wake vortex shed from either the trailing edge (●), or the separation point (△). Colour denotes vorticity polarity: *green* positive, *red* negative

form but that these convect downstream rapidly and have little effect on the plate behaviour. In contrast, for the lower flow speed that generated Fig. 2, roll-up occurs much closer to the trailing edge of the plate (located at $x/L = 1$ in these figures) and these structures can therefore exercise a significant effect on the flow field that drives the plate motion.

4 Conclusions

It is shown that at flow speeds much higher than the critical speed for linear instability the effects of separation are not significant. Amplification and subsequent nonlinear saturation at finite amplitudes can be adequately modelled by wake formation from the trailing edge of the plate as has been done in previous studies. At the flow speed for which the system is neutrally stable to linear disturbances, separation can lead to nonlinear instability and ensuing limit-cycle flutter. This suggests that flow separation may be a mechanism for the sub-critical instability that is observed in the experimental work of Eloy et al. (2008). Correctly modelling sub-critical instability relies upon choosing a threshold value of pressure gradient for separation that can only be found from experiment. However this does not negate the purpose of the present paper which was to show how separation can cause sub-critical instability.

References

Eloy C, Lagrange R, Souiliez C, Schouveiler L (2008) Aeroelastic instability of cantilevered flexible plates in uniform flow. J Fluid Mech 611:67–106

Howell RM, Lucey AD, Carpenter PW, Pitman MW (2009) Interaction between a cantilevered-free flexible plate and ideal flow. J Fluid Struct 25:544–566

Lucey AD, Carpenter PW (1992) A numerical simulation of the interaction of a compliant wall and inviscid flow. J Fluid Mech 234:121–146

Lucey AD, Cafolla GJ, Carpenter PW, Yang M (1997) The nonlinear hydroelastic behaviour of flexible walls. J Fluid Struct 11:717–744

Tang D, Dowell EH (2002) Limit cycle oscillations of two-dimensional panels in low subsonic flow. Int J Nonlinear Mech 37:1199–1209

Tang L, Païdoussis MP (2007) On the instability and the post-critical behaviour of two-dimensional cantilevered flexible plates in axial flow. J Sound Vib 305:97–115

Tang L, Païdoussis MP (2008) The influence of the wake on the stability of cantilevered flexible plates in axial flow. J Sound Vib 310:512–526

Application of a Multi-objective Genetic Algorithm in a Stabilisation Strategy for Flexible Panels in a Mean Flow

B.H. Tan, A.D. Lucey and R.M. Howell

Abstract The stability-control of a fluid-loaded flexible panel has been studied to determine the effectiveness of adding localized stiffening to control or postpone instability. In our previous work for the 2-D system a stabilisation strategy has been demonstrated by localised stiffening with a spring support. Similarly for the 3-D system, the effectiveness of the stabilisation method has also been shown by adding a transverse or streamwise stiffening strip. The most important goal for such stabilisation methods, for both 2-D and 3-D systems, is to refine the localised stiffening strategy to achieve the best use of multiple springs and stiffeners. In this paper we build upon our previous 2-D and 3-D work to develop and apply multi-objective genetic algorithm tools that are able to optimise the stabilisation strategy of added localised stiffness for different design problems: full solution spaces are presented for these problems from which optimal points are readily located.

1 Introduction

This study considers the application of a multi-objective genetic algorithm in the classical aero/hydro-elastic system comprising a flexible panel with a single-side exposed to incompressible uniform flow; linear studies of this system can be found in (Weaver and Unny 1971; Lucey and Carpenter 1993). The fluid-flow is at a high Reynolds number typical of situations encountered in many engineering problems such as the hydrodynamic loading of the hull panels of fast ferries and the strong wind loading on glass/aluminium panels of curtain walls on modern high-rise buildings. In such applications, a design concern is that the panel loses stability at some critical speed due to divergence that can lead to a buckled non-linearly saturated state (Ellen 1977; Lucey et al. 1997) and to dangerous flutter instability at higher flow speeds. Strategies for instability-free design are usually based upon material

B.H. Tan · A.D. Lucey (✉) · R.M. Howell
Fluid Dynamics Research Group, Department of Mechanical Engineering,
Curtin University of Technology, GPO Box U1987, Perth, WA 6845, Australia
e-mail: a.d.lucey@curtin.edu.au

(a)   **(b)**
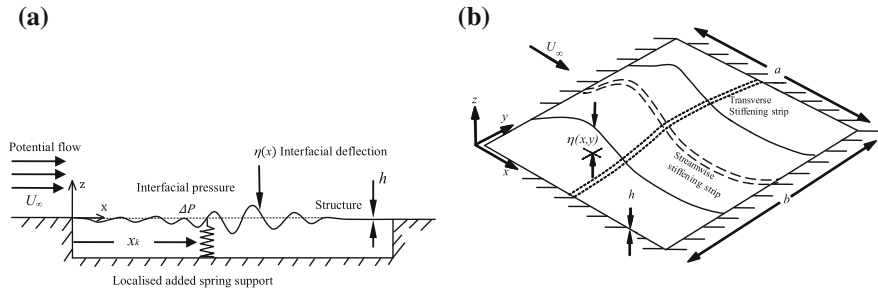
Fig. 1 Schematics of the **a** two-dimensional (*side view*), **b** three-dimensional (isometric view) problems studied wherein a uniform flow interacts with a flexible panel that has localised stiffening; in (**a**) a spring support is added while in (**b**) a stiffening strip, that may be in either the transverse or streamwise direction, is bonded to the underside of the panel

selection or uniform thickening of a panel to achieve a higher critical flow speed. However, this increases cost and dead weight. In contrast, our previous 2-D work represented schematically Fig. 1a Tan et al. (2013b), has demonstrated a stabilisation strategy by localised stiffening with a spring support. For the 3-D system of Fig. 1b we have shown in Tan et al. (2013a) the effectiveness of the stabilisation method by adding a transverse or streamwise stiffening strip. The most important goal for such stabilisation methods, for both 2-D and 3-D systems, is to refine the localised stiffening strategy to achieve the best use of multiple springs and stiffeners in that aero-/hydro-elastic instability can be postponed to higher critical speed with least 'cost' in terms of added material mass. Clearly, combinations of location, orientation (in 3-D) and spring/strip stiffness of either single or multiple additions creates a complicated parametric space over which optimisation must be conducted. In this paper we develop and apply multi-objective genetic algorithm tools that are able to optimise the stabilisation strategy of added localised stiffness.

2 Overview of Methods

The Fluid-Structure interaction (FSI) system is modelled by fully coupling a finite-difference representation of the structural mechanics with a boundary-element solution for the ideal-flow fluid mechanics. An Euler-Bernoulli beam is used for the 2-D model and classical thin-plate mechanics is used for the 3-D model. Our methods extend the hybrid of theoretical and computational approach of Pitman and Lucey (2009) to conduct an eigen-analysis of the governing wall-flow matrix equation for both 2-D and 3-D systems. Instead of solving the resulting second-order matrix differential equation for the temporal evolution of wall displacements in the coupled system, we use the fact that instability first sets in, with increasing flow speed, at divergence onset. We then use this to define the critical speed for instability in the

optimisation process. The merit of this approach is that at divergence onset, the wall velocity and acceleration are zero and therefore the critical speed can be determined directly from the eigenvalues of the steady system matrix.

The 3-D homogeneous fluid-structure system is controlled by three parameters, namely the fluid-to-solid mass and stiffness ratios, respectively defined by $L' = L_1 L_2$ and $\Lambda^{\mathrm{F}} = Ca L_1^3$, where $L_1 = a/h$, $L_2 = \rho/\rho_{\mathrm{m}}$ and $Ca = \rho U_\infty^2/E^*$ is the Cauchy number where $E^* = E/(12(1 - \nu^2))$; the final control parameter is the aspect ratio of the plate, $A = b/a$. For the plate, the properties a, b and h are respectively the length (in the flow direction), width and thickness of the plate that has density, Young's modulus, Poisson's ratio and flexural rigidity ρ_{m}, E, ν and $B = E^* h^3$ respectively; the fluid has density ρ and speed U_∞. In the 2-D case $a = L$ and $A = \infty$. The results presented herein are for water flow over an aluminium panel ($L_2 = 0.4$) typical of that for a thin hull panel of a high-speed ferry, i.e. at high L'. Finally, spring stiffness k is non-dimensionalised as $k'_{\mathrm{s}} = k/E^*$.

The multi-objective genetic algorithm used is a standard function in MATLAB the derivation of which is fully detailed in (Deb 2001). It has a fitness function comprised of two objective functions, *goal*(1) and *goal*(2): *goal*(1) is to search the control parameters to achieve the non-dimensional design critical speed or *design stiffness ratio* Ca_{d}; *goal*(2) minimises the weight of the added stiffening component(s) that is equivalent to minimising stiffness k of the spring or stiffening strip as these are assumed proportional to weight. The aim is to find the minimum of *goal*(1) and *goal*(2): *goal*(1) = 0 when the algorithm has searched for *goal*(2) successfully.

3 Results and Discussion

To demonstrate the integrity and implementation of the genetic algorithm approach, Fig. 2a, b respectively show typical results for the effect on *Ca*—the quantity on the vertical axis—of different stiffening strategies that have been validated against previous known results.

The result in Fig. 2a is for a 2-D case that shows the effect on *Ca* of adding an isolated spring: the horizontal axis on the left-hand side are values of k'_{s} and the right-hand side axis details the location x/L of the spring along the plate. Selecting individual results from this graph at specific values of Ca_{d} allow comparisons with previous results in Tan et al. (2013b): good agreement is found and thus confirms that the multi-objective genetic algorithm correctly minimises *goal*(1) and *goal*(2). As in Tan et al. (2013b), the results herein show that the maximum effectiveness of stiffening occurs at the panels' mid-chord because this location is the anti-node of the fundamental mode that yields the critical mode for divergence-onset of such panels.

The result in Fig. 2b is for a 3-D case that shows the effect on *Ca* of adding a streamwise stiffening strip for $A = 1$: the system is structurally inhomogeneous and the horizontal axis on the left-hand side is the stiffness of the added strip described
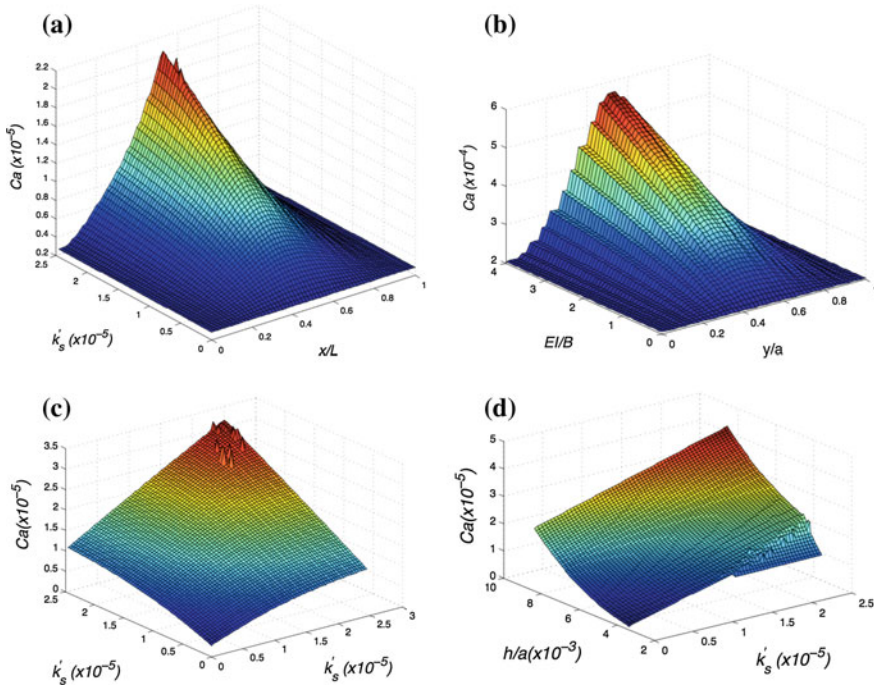
Fig. 2 Variation of a flexible panel's *Ca* value at $L_2 = 0.4$ with the magnitude and location of added localised stiffening for **a** 2-D model with an isolated spring, **b** 3-D model with a streamwise stiffening strip, **c** 2-D model with an upstream spring located at $L/3$ and a downstream spring located at $2L/3$ and **d** 2-D model with an isolated spring and variable panel thickness. The colours on the surface are proportional to the magnitude on the *y*-axis that they relate to, *blue* being the lowest *y* value and *red* the highest

relative to the flexural rigidity of the plate, i.e. *EI/B*; the right-hand side axis is the transverse position *y/a* of the strip. Selecting individual results from this figure at specific values of Ca_d again show good agreement with the values in Tan et al. (2013a), where the maximum effectiveness of stiffening occurs at the panel's mid-width.

We now show how the multi-objective genetic algorithm can be used for two more advanced 2-D problems. First, the optimal weight at fixed locations of two springs for a specified Ca_d is analysed: the control variables are the spring stiffnesses $k(1)$ and $k(2)$ and these are plotted on the horizontal axes in Fig. 2c When individual results are compared to the single-spring support at mid point in Tan et al. (2013b), the two spring supports are not as effective as the single spring support at mid point: for example at Ca_d values of 0.88×10^{-5} and 1.71×10^{-5}, the increase in spring weight is 31 and 25 % respectively to achieve the same effectiveness as a single spring.

Second, the optimal weight of one spring located at the mid-point of a variable thickness panel for a specified Ca_d is analysed. The control variables are the spring

stiffness k'_s and the panel thickness h and these are plotted on the horizontal axes in Fig. 2d. The graph clearly shows that as h and k'_s are increased, the system stabilises. Also, considerable weight savings are found by using a thinner panel with a spring whilst maintaining the same divergence-onset flow speed $Ca_d = 3 \times 10^{-6}$. For example, if a 2.5 mm plate is replaced by a 2.2 mm plate, the spring stiffness required is $k'_s = 0.86 \times 10^{-5}$: this corresponds to an overall (plate plus springs) weight reduction of 11.81 %.

4   Conclusions

A hybrid of computational and theoretical methods has been developed to form a structural function where divergence-onset stiffness ratio is a function of localised stiffening arrangement. Two problems have been analysed for illustration and design criteria are optimised by the application of a multi-objective genetic algorithm. The optimisation yields a configuration such that the divergence-onset stiffness ratio meets the design requirement as well as minimising the total weight of added spring or stiffening strips.

However, the cases presented herein could have been studied without the use of the GA albeit at much greater computational expense. The optimisation methods developed will confer an even greater advantage for complex multi-stiffener configurations.

References

Deb, K. 2001 Multi-Objective Optimization Using Evolutionary Algorithms. (John Wiley & Sons, first edition)

Ellen CH (1977) The non-linear stability of panels in incompressible flow. Journal of Sound and Vibration 54:117–121

Lucey AD, Cafolla GJ, Carpenter PW, Yang M (1997) The nonlinear hydroelastic behaviour of flexible walls. Journal of Fluids and Structures 11:717–744

Lucey AD, Carpenter PW (1993) The hydroelastic stability of three dimensional disturbances of a finite compliant wall. Journal of Sound and Vibration 165:527–552

Pitman MW, Lucey AD (2009) On the direct determination of the eigenmodes of finite flow-structure system. Proceedings of the Royal Society A 465:257–281

Tan BH, Lucey AD, Howell RM (2013a) The effect of localised stiffening on the stability of a flexible panel in uniform flow. 2nd Symposium on Fluid-Structure-Sound Interactions and Control, 20th-23rd May 2013, Hong Kong & Macau, pp. 325–330

Tan BH, Lucey AD, Howell RM (2013b) Aero-/hydro-elastic stability of flexible panels: Prediction and control using localised spring support. Journal of Sound and Vibration 332:7033–7054

Weaver DS, Unny TS (1971) The hydroelastic stability of a flat plate. ASME. Journal of Applied Mechanics 37:823–827

The Nonlinear Oscillations of a Flexible Surface Comprising One Wall of an Inviscid Channel Flow

M.A. Burke and A.D. Lucey

Abstract Numerical simulations are performed to study the large amplitude oscillations of a flexible surface in the divergence range of flow speeds for a potential flow. A finite-difference method for the structural mechanics is coupled with a boundary-element method for the fluid mechanics. For the open flow, a theoretical equation is derived which accurately predicts the amplitude of the plate's mean state about which limit-cycle flutter-type behaviour occurs. For channel flow it is found that reducing the channel height effects an increase in the amplitude of the oscillations. The relationship between the amplitude of the mean state and maximum deflection of oscillations is characterised and found not to depend upon the channel height.

1 Introduction

This study considers the two-dimensional nonlinear deformations of a finite flexible plate inserted in one wall of an inviscid channel flow as depicted in Fig. 1. The dynamics of flexible plates interacting with an open flow are well known; linear investigations include (Weaver and Unny 1970; Carpenter and Garrad 1985; Lucey and Carpenter 1992; Pitman and Lucey 2009) using analytical, eigen-value, numerical-simulations and Galerkin methods respectively. These studies predicted the onset of the divergence instability that is replaced by modal-coalescence flutter at higher applied flow speeds. Nonlinear plate deformations due to an open flow were studied in (Lucey et al. 1997) using numerical simulations and attention was paid to the nonlinear oscillations that occur within the divergence range of flow speeds.

The instabilities of flexible inserts within a channel for small deflections were investigated by (Burke et al. 2014) and the closely related problem of pipe buckling

M.A. Burke · A.D. Lucey(✉)
Fluid Dynamics Research Group, Curtin University, Bentley, WA 6148, Australia
e-mail: m.burke@curtin.edu.au

A.D. Lucey
e-mail: t.lucey@curtin.edu.au
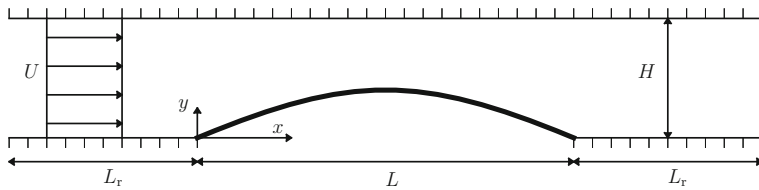
Fig. 1 Schematic of the fluid-structure interaction system studied

in an infinitely long pipe was predicted by (Doaré and de Langre 2002). Experimental studies include the divergence predictions of (Weaver and Païdoussis 1977) and the large-amplitude deformations of (Gavriely et al. 1989). In the present study, potential flow gives an approximate model for flows at very high Reynolds numbers noting that this approximation precludes the effect of boundary-layer separation for high levels of boundary curvature that might occur due to the deformation of the insert. The objective is to develop relatively simple formulae that can be used to evaluate deformation amplitudes. These might find application in engineered systems and over a limited range of bio-mechanical applications wherein the boundary, or a section thereof, of an internal flow is flexible.

2 Method

The linear plate equation, supplemented by a nonlinear term modelling in-plane induced tension, is driven by matching the normal stress due to its deformation with the pressure obtained through the Bernoulli equation applied at the fluid-solid interface. The nonlinear flow solution is found following the method used in (Lucey et al. 1997) whereby source/sink singularities lie upon the discretised interface. The coupled system is then solved using time-stepping numerical simulations. In the present work, the boundary conditions are extended to include an upper channel wall, located at a distance H from the undisturbed surface and include rigid up- and down-stream surfaces; thus, the flexible wall now comprises one wall of a channel.

The present modelling generates results that agree well with (Lucey et al. 1997) for infinitely large channel height. This approach characterises the oscillatory behaviour of the flexible plate within the channel when finite-amplitude deformation is initiated by a small (linear) disturbance. In particular, we focus on the maximum deflection, $\eta_{max}(x)$, reached in the nonlinear oscillations; with the practical relevance that it represents a measure of channel blockage due to flow-induced wall deformation.

To determine the mean state, $\eta_{mean}(x)$, that is the attractor about which the limit-cycle oscillatory behaviour occurs, we can include dissipation (via structural damping) into the forgoing dynamic simulations so that the system spirals into the attractor. However, a more efficient method is used, following the approach of (Knight et al. 2010) for an open flow, whereby we remove time-dependence from

the system and use an iterative steady-state solver. $\eta_{\text{mean}}(x)$ at different applied flow velocities is readily found and these agree excellently (for the open flow) with an approximate theoretical solution of the time-independent system based upon a single Galerkin-type mode.

3 Results and Discussion

Results are presented in terms of a non-dimensional flow speed $\Lambda^F = \rho_f U^2 L^3/B = (\rho_f U^2/E^*)(L/h)^3$ where ρ_f and U are the fluid density and flow speed and L, B and ρ_m are the flexible plate's length, flexural rigidity and density respectively. The first form of Λ^F is well known in system characterisation with respect to divergence-onset for linear disturbances for which the structural forces are dominated by plate flexure. In the second form $E^* = E/12(1 - \nu^2)$ is the effective elastic modulus of the plate material, ν is its Poisson ratio and h is the plate thickness. This can be seen to comprise the product of a Cauchy number and a non-dimensional parameter for the plate dimensions. This demonstrates that Λ^F is also suitable for the characterisation of nonlinear behaviour that is dominated by induced tension with its principal parametric dependence upon E^*, h and L for the structural side of the system.

Time is non-dimensionalised using $t' = \sqrt{B/\rho_m h^3}(t/L) = \sqrt{E^*/\rho_m}(t/L)$ where ρ_m is the density of the plate material; the second form shows that the non-dimensionalisation is based upon the free shear-wave speed in the plate material and the plate length. The system is also dependent on the non-dimensional mass ratio $\mu = \rho_f L/\rho_m h$. The properties used herein give a mass ratio $\mu = 38.5$.

Typical results for an open flow are shown in Fig. 2 in which (a) shows a time-series for the motion of the plate's mid-point and (b) shows plate-deformations over
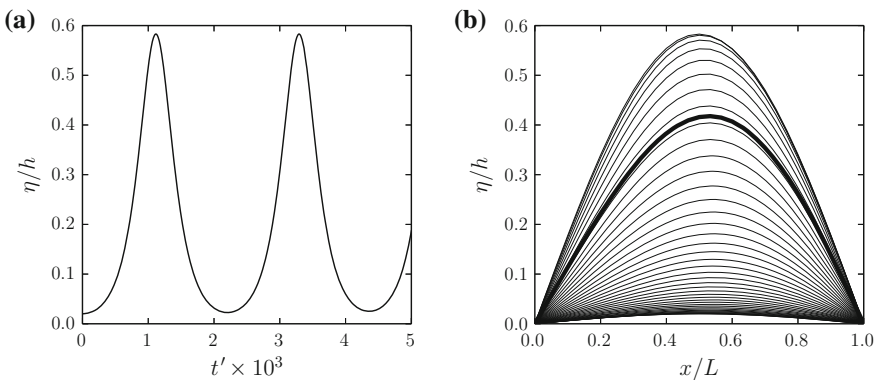

Fig. 2 Open-flow ($H = \infty$) results when $\Lambda^F = 61$: **a** Displacement of the plate mid-point with non-dimensional time, and **b** Plate deformation for a succession of time steps covering the first half of a nonlinear oscillation; the *bold line* represents the plate with the mean state amplitude

one half of the cycle seen in (a). From these and other simulations we can demonstrate that $\eta^o_{\text{max}} = C\eta^o_{\text{mean}}$ for constant $C = 1.435$ that, in particular, is independent of Λ^F and μ, and where η^o_{mean} can be closely predicted by the equation,

$$\frac{\eta^o_{\text{mean}}}{h} = \left[\left(\frac{\pi^2}{6I(\eta'')} \right) \left(\frac{\Lambda^F}{\Lambda_{\text{DO}}} - 1 \right) \right]^{0.5}, \tag{1}$$

where Λ_{DO} is the well-known divergence-onset flow speed of 40.1 (for linear disturbances) and $I(\eta'')$ is the evaluation of an integral that accounts for the flexible-plate shape. In the divergence range of Λ^F, $I(\eta'')$ can be approximated using the fundamental mode to give a constant value. Equation (1) agrees with the results of (Lucey et al. 1997).

We now consider the effect of channel height. Given that nonlinear oscillations only occur at flow speeds higher than the critical flow speed for divergence, the non-dimensional flow speed is normalised by the onset flow speed of divergence for any given channel height, Λ_D, that from (Burke et al. 2014) is given by,

$$\Lambda_D = \Lambda_{\text{DO}}(1 - \exp(-3.3H/L)). \tag{2}$$

Our results show that the ratio, C, of maximum to mean-state amplitudes is not dependent on channel height but is the same for all values of H. However, Fig. 3 shows that η_{max} and η_{mean} are dependent upon channel height and that as H is decreased the amplitudes increase. This could be expected on physical grounds because mass conservation creates higher flow speeds, hence higher flow stiffness ($\rho_f U^2$), in the region where the deformed plate effectively narrows the channel.

To develop a formula for plate-deformations in channel flow requires that $\eta_{\text{mean}} = f(H/L)\eta^o_{\text{mean}}$ where η^o_{mean} is the mean-state amplitude for the open flow given in Eq. (1) and where f is such that $f \to 1$ as $H \to \infty$. By using the η_{mean} predictions from the steady-state solver, f is found and is shown also to apply to the η_{max} data
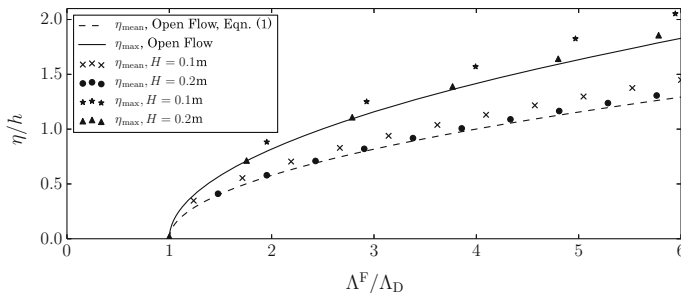
**Fig. 3** Peak values of η_{mean} and η_{max} for an open flow as predicted by theory compared with their values for different channel heights generated respectively by the present iterative solver and full numerical simulations

from numerical simulations. This enables an equation to be developed to predict η_{mean} for all channel heights in terms of the non-dimensional flow speed which is

$$\frac{\eta_{\text{mean}}}{h} = f\left(H/L\right)\left[\left(\frac{\pi^2}{6I\left(\eta''\right)}\right)\left(\frac{\Lambda^{\text{F}}}{\Lambda_{\text{D}}} - 1\right)\right]^{0.5}, \tag{3}$$

in which

$$f(H/L) = 0.52\exp\left(-15H/L\right) + 1, \tag{4}$$

and where Λ_{D} is given by Eq. (2). Using Eq. (3), the maximum deflection for channel flow can then be determined from $\eta_{\text{max}} = C\eta_{\text{mean}}$ where $C = 1.425$. Equation (3) holds within the range of nonlinear divergence flow speeds and for $H/L \geq 0.05$. The first constraint arises from the fact that at higher flow speeds significant levels of Mode-2 content appear in the deformations (Lucey et al. 1997) while the second approximately demarcates the threshold at which viscous effects cannot be neglected (Burke et al. 2014).

4 Conclusions

The flow-induced nonlinear oscillations that evolve from small-amplitude initial perturbations of a flexible plate in open and channel flows have been studied using numerical simulation together with an efficient steady-state solver to determine the nonlinear mean-state amplitude. We have then developed formulae that, for a given mass ratio, can be used to predict both the maximum and mean-state deformation amplitudes, relative to plate thickness, as functions of non-dimensional flow speed and channel height. The main physical finding is that reducing the channel height increases the deformation amplitude. Our potential-flow assumption yields results in the limit of infinite Reynolds number. Flow separation has not been accounted for as plate deformations have very low curvature, $1/R$, that scales with $2\eta_{\text{max}}/L^2$ for the deformations herein; for example, when $\eta_{\text{max}}/h = 2.0$, then $1/R \approx 0.04$. This study serves as a basis for more complete models that would incorporate viscous effects and boundary-layer separation.

References

Burke MA, Lucey AD, Howell RM, Elliot NSJ (2014) Stability of a flexible insert in one wall of an inviscid channel flow. J Fluids Struct 48:435–450

Carpenter PW, Garrad AD (1985) The hydrodynamic stability of flow over Kramer-type compliant surfaces. Part 1. Tollmien-Schichting instabilities. J Fluid Mech 155:465–510

Doaré O, de Langre E (2002) Local and global instability of fluid-conveying pipes on elastic foundations. J Fluids Struct 16:1–14

Gavriely ND, Shee TR, Cugell W, Grotberg JB (1989) Flutter in flow-limited collapsible tubes: a mechanism for generation of wheezes. J Appl Physiol 66:2251–2261

Knight JJ, Lucey AD, Shaw CT (2010) Fluid-structure interaction of a two-dimensional membrane in a flow with a pressure gradient with application to convertible car roofs. J Wind Eng Ind Aerodyn 98:65–72

Lucey AD, Cafolla GJ, Carpenter PW, Yang M (1997) The nonlinear hydroelastic behaviour of flexible walls. J Fluids Struct 11:717–744

Lucey AD, Carpenter PW (1992) A numerical simulation of the interaction of a compliant wall and inviscid flow. J Fluid Mech 234:121–146

Pitman MW, Lucey AD (2009) On the direct determination of the eigenmodes of finite flow-structure systems. Proc R Soc 465:257–281

Weaver DS, Païdoussis MP (1977) On collapse and flutter phenomena in thin tubes conveying fluid. J Sound Vibr 50:117–132

Weaver DS, Unny TE (1970) The hydroelastic stability of a flat plate. ASME J Appl Mech 37:823–827

Global Stability Analysis of Blasius Boundary-Layer Flow over a Compliant Panel Accounting for Axial and Vertical Displacements

K. Tsigklifis and A.D. Lucey

Abstract A state-space method is deployed in order to investigate the global stability of the Blasius base flow over a finite compliant panel embedded between rigid upstream and downstream wall sections accounting both for axial and vertical structural displacements. It is shown that global temporal instability can occur through the resonance between the Travelling-Wave Flutter (TWF) or Tollmien-Schlichting Wave (TSW) instability and the structural modes due to the vertical motion of the compliant section, while the axial structural modes remain stable in time. Local spatial stability of the least stable global temporal TSW mode reveals that a downstream amplified axial structural mode coexists with the downstream amplified TSW mode and it is stabilized by increasing the panel stiffness and destabilized as the Reynolds number decreases.

Keywords Fluid-structure interaction · Boundary-layer stability · Compliant wall/panel · Global stability

1 Introduction

In the design of finite compliant panels for applications such as the control of boundary-layer transition, global/absolute instabilities in the fluid-structure interaction system (FSI) must be avoided if laminar flow is to be maintained (Carpenter et al. 2001). Global stability analysis of the Blasius flow over a finite spring-backed compliant panel, embedded between rigid upstream and downstream wall sections, that accounts only for vertical displacements (Tsigklifis and Lucey 2015), has revealed that global temporal instability occurs when resonance/ coalescence takes place between the flow-based Tollmien-Schlichting Wave (TSW)

K. Tsigklifis(✉) · A. Lucey
Fluid Dynamics Research Group, Department of Mechanical Engineering,
Curtin University of Technology, GPO Box U1987, Perth, WA 6845, Australia
e-mail: k.tsigklifis@curtin.edu.au

or the wall-based Travelling-Wave Flutter (TWF) instability and the structural modes of the one-degree-of-freedom wall.

Local temporal stability and asymptotic analysis of the Couette flow past a flexible surface (Shankar and Kumaran 2002) have shown that if tangential (axial) wall motion is introduced in a spring-backed membrane wall, a new instability associated with the tangential motion appears in the high Reynolds number limit; this is due to energy transfer arising from the interaction of the fluctuating (fluid) shear stress and the axial motion of the wall at the fluid-solid interface. However, less is known about the character of this new instability—whether it is convective or absolute—and its interaction with the structural modes and the TSW or TWF instabilities in a FSI system of finite length. We therefore extend our global stability analysis of the Blasius flow over a finite spring-backed compliant panel (Tsigklifis and Lucey 2015) to account for both vertical and axial displacements of the compliant panel in order to investigate whether axial motion can induce global temporal instability in a finite system through multi-modal interactions.

2   System Modelling

We solve the two-dimensional Navier-Stokes equations written in velocity-vorticity form and linearised for perturbations about the mean Blasius boundary-layer flow. The flow field is characterized by the Reynolds number, $Re_s = \rho_1^* U_\infty^* \delta_s^* / \mu_1^*$, which is defined through the displacement thickness δ_s^* at a distance x_s^* from the origin of the boundary layer, that is the location of the entrance of the flow domain modelled, and the undisturbed-flow velocity, U_∞^* (ρ_1^* and μ_1^* are the fluid density and dynamic viscosity, respectively), Fig. 1. The flow solution is developed using a combination of vortex and source boundary—element sheets on a uniform Chebyshev Gauss-Lobatto computational grid; see (Tsigklifis and Lucey 2015). The dynamics of a plate-spring compliant wall that admits both vertical and horizontal deformations are couched in finite-difference form. Flow and wall dynamics are coupled by the kinematic boundary conditions and matching the fluid and solid shear stresses and pressure at the interface, i.e.,
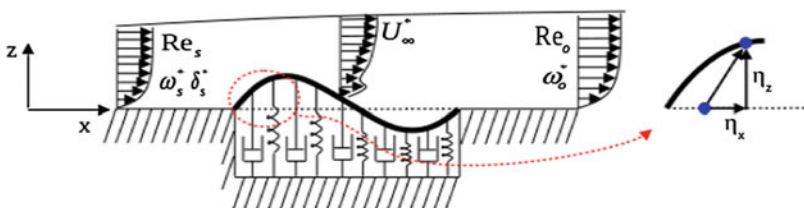

Fig. 1   Schematic of the system studied

$$u_x(x,0,t) + \eta_z \frac{\partial U_x}{\partial z}(x,0) = \frac{\partial \eta_x}{\partial t}, \qquad u_z(x,0,t) = \frac{\partial \eta_z}{\partial t} \tag{1}$$

$$-p(x,0,t) + \frac{2}{Re_s}\frac{\partial u_z}{\partial z}(x,0,t) = M\frac{\partial^2 \eta_z}{\partial t^2} + D_z\frac{\partial \eta_z}{\partial t} +$$

$$+B\frac{\partial^4 \eta_z}{\partial x^4} - T\frac{\partial^2 \eta_z}{\partial x^2} + \frac{2}{Re_s}\left(\frac{\partial U_x}{\partial z}(x,0) + \frac{\partial U_z}{\partial x}(x,0)\right)\frac{\partial \eta_z}{\partial x} + K\eta_z \tag{2}$$

$$\frac{1}{Re_s}\left(\frac{\partial u_x}{\partial z}(x,0,t) + \frac{\partial u_z}{\partial x}(x,0,t)\right) = M\frac{\partial^2 \eta_x}{\partial t^2} + D_x\frac{\partial \eta_x}{\partial t} - A\frac{\partial^2 \eta_x}{\partial x^2} \tag{3}$$

where, $\eta_x(x,t)$, $\eta_z(x,t)$, $u_x(x,z,t)$, $u_z(x,z,t)$, and $p(x,0,t)$ are respectively the non-dimensional plate axial and vertical displacements, disturbance velocities in the directions streamwise and normal to the flow and pressure disturbances at the wall, while $U_x(x,z)$, $U_z(x,z)$ are the streamwise and normal velocity components of the Blasius base flow. In the above expressions, the non-dimensional coefficients of inertia, damping in the streamwise and normal direction, flexural rigidity, spring-foundation stiffness, streamwise tension force per unit span and bending stiffness, are defined by $M = \rho_m^* h_m^*/(\rho_1^* \delta_s^*)$, $D_x = D_x^*/(\rho_1^* U_\infty^*)$, $D_z = D_z^*/(\rho_1^* U_\infty^*)$, $B = B^*/(\rho_1^* U_\infty^{*2}\delta_s^{*3})$, $K = K^*\delta_s^*/(\rho_1^* U_\infty^{*2})$, $T = T^*/(\rho_1^* U_\infty^{*2}\delta_s^*)$ and $A = E^* h_m^*/(\rho_1^* U_\infty^{*2}\delta_s^*)$, respectively, with $B^* = E^* h_m^{*3}/[12(1-v^2)]$ where E^*, ρ_m^*, h_m^* and v are respectively the material elastic modulus, density, thickness of the plate and Poisson ratio. Finally, hinged boundary conditions are applied at the leading and trailing edges of the compliant panel.

The Fluid-Structure Interaction (FSI) system is written (see Tsigklifis and Lucey 2015) as a generalized eigenvalue problem

$$[C_2]\{\hat{X}\} = -i\omega[C_1]\{\hat{X}\}, \quad \{\hat{X}\} = \{\hat{\omega}, \hat{\sigma}, \hat{\eta}_x, \hat{\eta}_z, \hat{\phi}_x, \hat{\phi}_z\}^T, \tag{4}$$

with $\hat{\phi}_x = -i\omega\hat{\eta}_x$ and $\hat{\phi}_z = -i\omega\hat{\eta}_z$. $\hat{\omega}$ and $\hat{\sigma}$ are respectively the strengths of the spanwise vorticity in the domain and of the source-sink on the boundary. If the imaginary part of an extracted eigenvalue $\omega = \omega_R + \omega_I i$ is positive, instability in time occurs, whereas a negative real part indicates that disturbances decay with time. Finally, spatial local stability analysis is also conducted based on the companion matrix method (Bridges and Morris 1984), in order to validate the global numerical scheme but also to reveal the spatial characteristics of the different instability branches.

3 Results and Discussion

Investigations have considered Reynolds numbers at the entrance of the computational domain in the range $700 \leq Re_s \leq 5000$. Figure 2 shows a typical spectrum of eigenmodes from the global-stability analysis with different levels of discretisation

(to show convergence) that also includes corresponding results for a one-degree-of-freedom (vertical) compliant-wall model; ω_R and ω_I are respectively the oscillatory and amplification(+ve)/decay(−ve) parts of the temporal eigenvalue. The additional axial structural mode is seen to be globally stable. Neither does it modify the strong TWF-resonance global instability found in our previous work (Tsigklifis and Lucey 2015), nor generate a globally unstable interaction with the TSW mode branch.

Results of the local spatial stability analysis of the least stable global temporal TSW mode in Fig. 2 are shown in Fig. 3b; α_R and α_I are respectively the wavenumber and spatial amplification(−ve)/decay(+ve) parts of the eigenvalue. This features the expected convectively unstable TSW (that also exists for a one-degree-of-freedom compliant-wall model) and a downstream-directed convectively unstable axial structural mode. The results in Fig. 3c and d respectively show that the latter is stabilised by increasing the elastic modulus of the plate material but is destabilised when the Reynolds number is decreased so as to increase viscous effects. These effects suggest that the instability is due to energy transfer from the mean flow to the wall caused by the interaction of fluid shear stress and axial wall motion and that the instability aligns with the corresponding phenomenon elucidated in (Shankar and Kumaran 2002) for Couette flow. The absence of an upstream directed unstable axial structural mode precludes a resonant interaction with the TSW mode to create global instability. This is in contrast to Fig. 3a wherein resonance takes place between the TWF instability and the upstream-directed unstable vertical structural mode; this mechanism is largely unaffected by the presence of the axial structural modes.
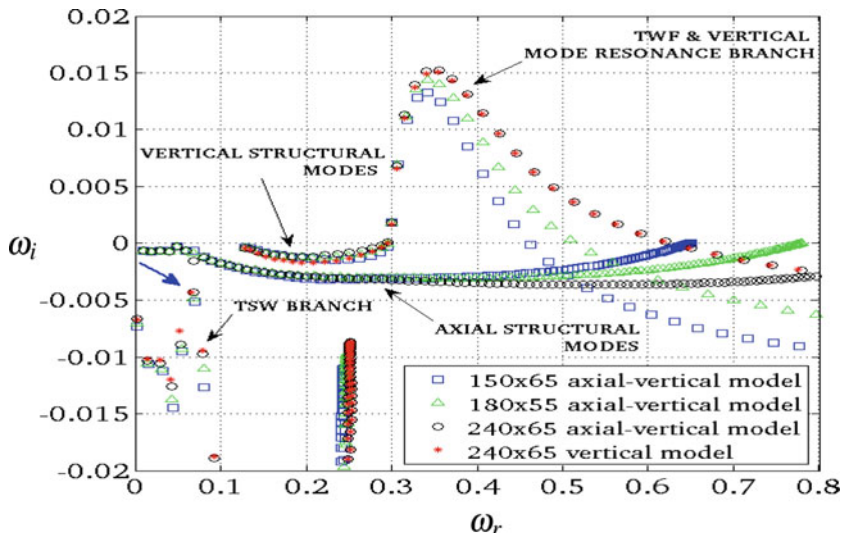

Fig. 2 Eigenvalue spectrum from global temporal stability analysis of the FSI system for $Re_s = 3000$ for different levels of discretisation and comparison with the model accounting only for the *vertical* motion
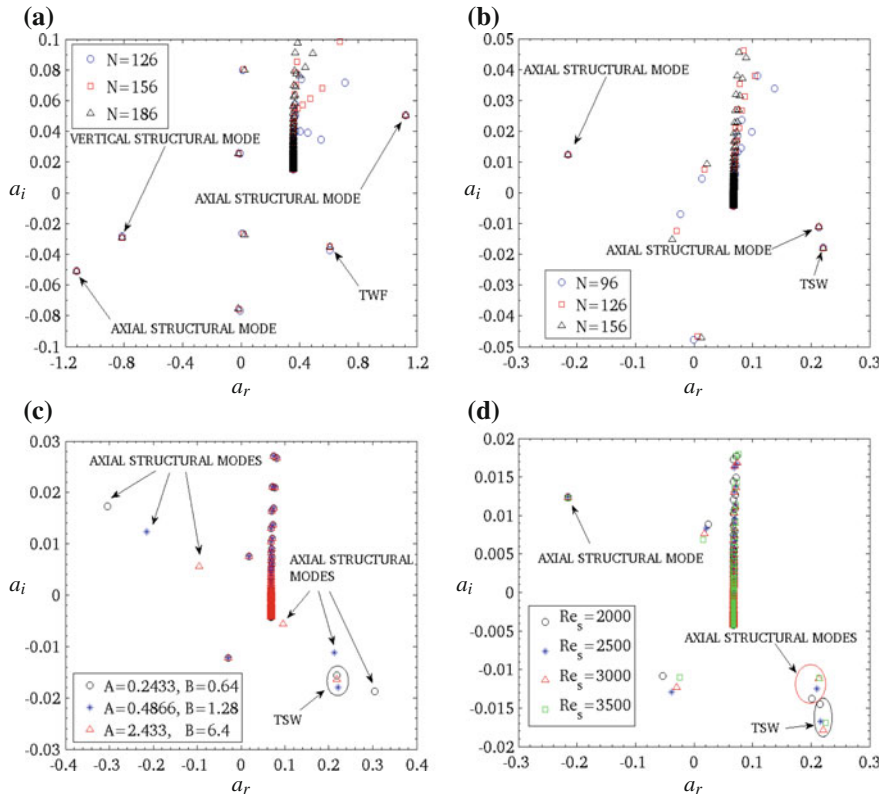
Fig. 3 Results of local spatial stability analysis. **a** The most unstable TWF vertical-mode resonance in Fig. 2 and **b** the least stable TSW mode shown with a *blue arrow* in Fig. 2 for different numbers of Chebyshev Gauss-Lobatto points. Effect of **c** the elastic modulus, E^* and **d** the Reynolds number, Re_s, on the TSW and the axial structural modes, respectively

4 Conclusions

A hybrid of computational and theoretical modelling has been developed to study the global stability of the Blasius base flow over a finite compliant panel embedded between rigid upstream and downstream wall sections, accounting both for axial and vertical structural displacements. It has been demonstrated that global instability of the linear FSI system occurs due to the resonance between the vertical structural and TWF or TSW modes, while the axial structural modes are asymptotically stable in time. However, the local spatial stability of the least stable in time TSW mode shows that, besides the convectively unstable TSW, there exists a downstream-directed convectively unstable axial structural mode which is stabilized by the increase of the structural stiffness and destabilized as the Reynolds number decreases.

References

Bridges TJ, Morris PJ (1984) Differential eigenvalue problems in which the parameter appears nonlinearly. J Comput Phys 55(3):437–460

Carpenter PW, Davies C, Lucey AD (2001) Does the dolphin have a secret? Curr Sci 79(6):758–765

Shankar V, Kumaran V (2002) Stability of wall modes in fluid flow past a flexible surface. Phys Fluids 14(7):2324–2338

Tsigklifis K, Lucey AD (2015) Global instabilities and transient growth in Blasius boundary-layer flow over a compliant panel. Sadhana 40(3):945–960

Turbulent Drag Reduction by Spanwise Traveling Ribbed Surface Waves

W. Li, D. Roggenkamp, W. Jessen, M. Klaas and W. Schröder

Abstract In this paper, the combination of passive and active drag reduction techniques is investigated using Particle-Image Velocimetry (PIV) and Micro Particle-Tracking Velocimetry (μ-PTV). The impact of a riblet-structured surface, which represents the passive control technique, undergoing spanwise transversal wave motion, which defines the active flow control method, on the wall-shear stress distribution of a zero-pressure gradient turbulent boundary layer is analyzed. The PIV and μ-PTV measurements are conducted at two Reynolds numbers based on the momentum thickness of $Re_\theta = 1200$ and 2080, respectively. The results show that the transversal wave motion extends the drag reduction efficiency of the riblets.

1 Introduction

The friction drag is dominated by the near-wall turbulence and constitutes approximately 50 % of the total drag of transportation means, e.g., aircraft. The urgency of developing friction drag reduction techniques has been highlighted by the global warming and the demands of decreasing costs of transportation. Hence, to reduce the friction drag generated by near-wall flow, several strategies have been pursued to control the near-wall flow structures. These approaches can be roughly divided into on the one hand passive methods and on the other hand active methods. Riblets, as a passive flow control technique have been successfully applied to reduce skin friction leading to a drag reduction of up to 10 % (Karniadakis and Choi 2003). However, the drag reduction design range of riblets is narrow. Once beyond the working range, the friction might also be increased instead of being decreased. Besides this passive control method, there is the active control concept based on changing the near-wall

W. Li (✉) · D. Roggenkamp · W. Jessen · M. Klaas · W. Schröder
Institute of Aerodynamics, RWTH Aachen University, Aachen, Germany
e-mail: w.li@aia.rwth-aachen.de

flow by introducing transversal wall motion, which results in a friction drag reduction of up to 45 %. Considering the drag reduction potential of both methods, i.e., passive flow control based on riblets and active flow control based on transversal surface waves, it is natural to link both concepts.

The purpose of this study is to investigate how far the friction drag of a turbulent boundary layer can be reduced by using a riblet surface undergoing spanwise transversal surface waves and to analyze the physical mechanisms underlying this friction drag reduction. Therefore, the wall-shear stress and the near-wall flow field of a turbulent boundary layer are investigated 3 mm downstream of an actuated riblet surface by μ-PTV and PIV.

2 Experimental Setup and Measurement Techniques

The experimental setup consists of a flat plate mounted in the open test section of a low speed Göttingen-type wind tunnel. As shown in Fig. 1 the center of the flat plate is equipped with a flush-mounted aluminum- surface insert which can be
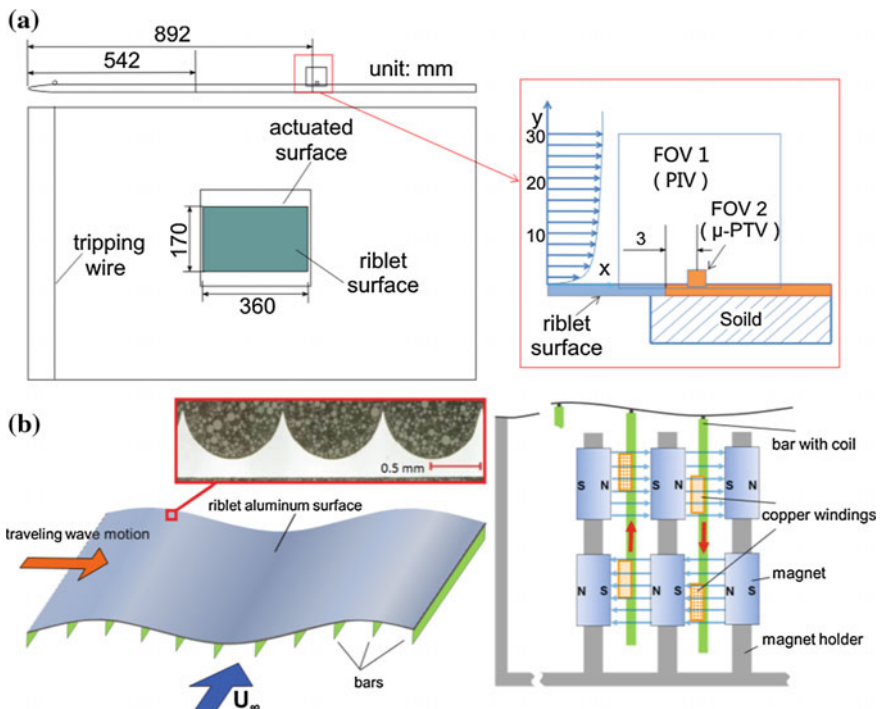

Fig. 1 Experimental setup, sketch of the flat plat and the measurement position (**a**), the actuator system (**b**)

Table 1 Flow parameters, defined in inner wall units by $T^+ = u_\tau^2/(f\,\nu)$, $\lambda^+ = \lambda\,u_\tau/\nu$, $A^+ = A\,u_\tau/\nu$, $s^+ = s\,u_\tau/\nu$, and $h^+ = h\,u_\tau/\nu$, with u_τ of the smooth surface

Test parameters	Normalized	Normalized
Reynolds number	$Re_\theta = 1200$	$Re_\theta = 2080$
Excitation period	$T^+ = 110$	$T^+ = 380$
Wavelength	$\lambda^+ = 3862$	$\lambda^+ = 7170$
Amplitude	$A^+ = 6, 7, 9$	$A^+ = 11, 14, 17$
Riblet spacing	$s^+ = 24$	$s^+ = 45$

actuated by an electromagnetic actuator system that generates a spanwise traveling sinusoidal wave. The riblet structure is produced by cold rolling a 0.5 mm thick aluminum sheet with a structured roll. Details of the manufacturing process are discussed by Pöplau et al. (2014). The transition in the streamwise direction between the flat and riblet structured surface is smoothed to guarantee that recirculation areas downstream of the riblets are avoided. For reference measurements, the insert can be replaced by a smooth surface. The nondimensionalized flow quantities by inner wall units are summarized in Table 1.

To obtain the velocity field, standard 2D-2C PIV and μ-PTV measurements are conducted. A Photron FASTCAM SA3 camera coupled with an Infinity™ K2® model long-distance microscope is used for both methods. The seeded flow is illuminated by a light sheet with a thickness of 0.5 mm. For more details of the PIV and μ-PTV setup, the readers may refer to Roggenkamp et al. (2015).

The wall-shear stress is determined by the velocity profile in the viscous sublayer yielding the wall-shear stress $\tau_w = \mu \partial u/\partial y \approx \mu\,du/dy$. A least-square linear fit is applied to obtain the wall-shear stress resulting in a standard error of less than 1 %. The local drag reduction ratio DR is computed from the variations of the skin-friction coefficients $c_f = \tau_w/(1/2\,\rho\,u_\infty^2)$,

$$\text{DR} = \left(1 - \frac{c_{f,\,\text{riblet/riblet}-\text{actuated}}}{c_{f,\,\text{smooth non}-\text{actuated}}}\right) \times 100\,\%$$

3 Results and Discussion

To evidence the impact of the riblet structure and the wave motion on the near-wall flow field, the mean velocity profiles are illustrated in Fig. 2. The enlargement of the viscous sublayer clearly shows lower gradients for the non-actuated and actuated riblet surface compared to the smooth surface configuration which indicate reduction of the local friction drag.

The local friction drag reduction DR caused by the wave motion over a smooth and a riblet surface is shown in Table 2. At $Re_\theta = 1200$, the drag reduction caused by the non-actuated riblet structure is 4.7 %. The additional drag reduction generated by the wave motion of the riblet surface dependent on the amplitude is in the range of −0.6 to 4.7 %. Considering the measurement uncertainties, the two lower
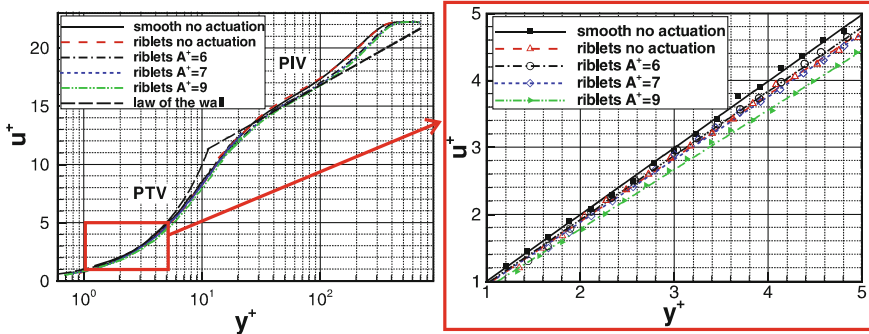
Fig. 2 Mean streamwise velocity for the non-actuated and actuated riblet-structured surface at $Re_\theta = 1200$, inner wall units are defined by the u_τ of the smooth surface

Table 2 Drag reduction by spanwise traveling wave motion

$Re_\theta = 1200$ (Roggenkamp et al. 2015)	Smooth	$A^+ = 6$	$A^+ = 7$	$A^+ = 9$
DR (%)	–	2.0	2.7	3.4
$Re_\theta = 1200$	Riblet	$A^+ = 6$	$A^+ = 7$	$A^+ = 9$
DR (%)	4.7	4.1	5.8	9.4
Additional DR (%)	–	-0.6	1.1	4.7
$Re_\theta = 2080$	Riblet	$A^+ = 11$	$A^+ = 14$	$A^+ = 17$
DR (%)	0.7	0.9	2.2	2.7
Additional DR (%)	–	0.2	1.5	2

amplitude configurations hardly change the drag reduction efficiency of the riblet surface. At the highest amplitude $A^+ = 9$, the wave motion generates an additional local DR of 4.7 %. When the Reynolds number is increased, i.e., at $Re_\theta = 2080$, the efficiency of the passive and the active control methods decreases. The local DR of the non-actuated riblet surface is only 0.7 %. It is increased by the wave motion to 2.7 % at the highest amplitude.

Figure 3 shows the comparisons of the streamwise and wall-normal velocity fluctuations and the Reynolds shear stress at the Reynolds number of $Re_\theta = 1200$. The peak values of the streamwise velocity fluctuations decrease in the near-wall region for all actuated and non-actuated riblet configurations compared to the non-actuated smooth configuration. This reduction of the streamwise fluctuations due to the riblet structure and the actuation is evident in the boundary layer up to $y^+ \leq 250$. In the outer boundary layer ($250 \leq y^+ \leq 500$), only the fluctuations for the moving riblet configurations are clearly increased which shows that the wave motion leads to a shift of the mixing region further off the wall. A similar tendency is also shown by the distributions of the wall-normal velocity fluctuations and the Reynolds shear stress. A decrease of the velocity fluctuations and Reynolds shear stress is an indication of drag reduction which was shown by Klumpp et al. (2011), Ricco and Wu (2004). While at $Re_\theta = 2080$ the optimum range ($15 \leq s^+ \leq 25$) of
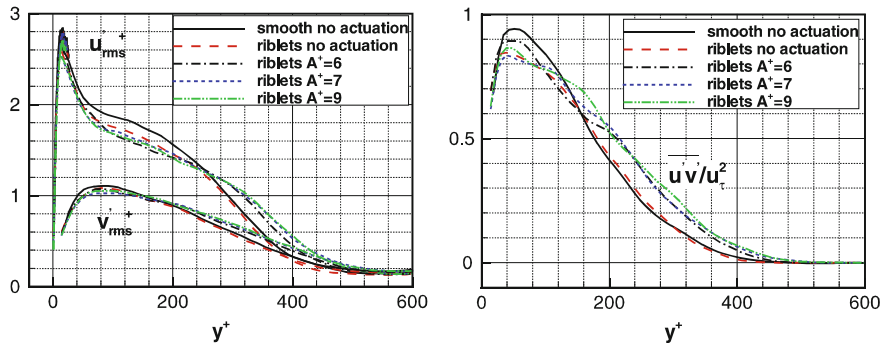
Fig. 3 Comparison of the velocity fluctuations (*left*) and the Reynolds shear stress (*right*) at $Re_\theta = 1200$, inner wall units are defined by the u_τ of the smooth surface

riblet is not valid anymore, the efficiency of the passive drag reduction drops. Since the normal momentum input via the actuated surface at $Re_\theta = 2080$ is smaller compared to that at $Re_\theta = 1200$, the drag reduction efficiency is decreased yielding DR = 2.7 % at $Re_\theta = 2080$ instead of DR = 9.4 % at $Re_\theta = 1200$.

4 Conclusions

The combination of riblet and transversal surface waves has been investigated by PIV and μ-PTV in a turbulent boundary layer. The results clearly show that the passive and active control methods complement each other with respect to drag reduction. In comparison to the non-actuated smooth surface the non-actuated riblet surface yields a local drag reduction of 4.7 %. Due to the wave motion the local drag reduction is increased up to 9.4 %. The findings of ribbed wall motion on the one hand confirm the findings of smooth wavy surfaces by Roggenkamp et al. (2015) that the drag reduction impact is enhanced by increasing the amplitude of the wave motion, and on the other hand show that the drag reduction effect is not only a simple sum up of the benefits of the active and passive methods.

References

Karniadakis G, Choi K-S (2003) Mechanisms on transverse motions in turbulent wall flows. Annu Rev Fluid Mech 35:45–62
Klumpp S, Meinke M, Schröder W (2011) Friction drag variation via spanwise transversal surface waves. Flow Turbul Combust 87:33–53

Pöplau J, Stille S, Romans T, Singheiser L, Hirt G (2014) The influence of process parameters on forming of riblets during riblet rolling. Key Eng Mater 5:1–18

Ricco P, Wu S (2004) On the effects of lateral wall oscillations on a turbulent boundary layer. Exp Therm Fluid Sci 29:41–52

Roggenkamp D, Jessen W, Li W, Klaas M, Schröder W (2015) Experimental investigation of turbulent boundary layers over transversal moving surfaces. CEAS Aeronaut J 1–14. doi:10.1007/s13272-015-0155-2

An Experimental Study on Transitional Boundary Layer Excitation on a Bulbous Bow of a Fast Ship

F. Magionesi

Abstract The present paper deals with the results of an experimental campaign aimed at characterizing the wall pressure fluctuations (WPF) beneath transitional boundary layer acting along the bulbous bow of a fast ship. The measurements were performed for three different velocities, corresponding to a variation of Reynolds numbers between 9.1×10^5 and 6×10^5. The acquired pressure signals are characterized by the presence of both turbulent bursts, with high frequency fluctuations, and low frequency fluctuations due to instability waves (Tollmien-Schlichting waves) in the laminar portion. The study focuses on three aspects: implementation of a new algorithm to detect turbulent bursts from wall pressure signals, identification of scaling laws for the auto spectral density of WPF in the transition process and characterization of the time-evolution of the their spectral distribution based on Pseudo Wigner Ville distribution.

Keyword Flow induced vibrations · Transitional boundary layer

1 Introduction

Transition from laminar to turbulent boundary layer plays a relevant role in many fields: in aeronautical applications transition controls important aerodynamic quantities as drag, while in turbomachinery is responsible for strong variation of heat transfer. In marine applications transition is a prominent contributor to self-noise in sonar systems. WPF generated in transitional zones are stochastic inhomogeneous fields, which have spectral characteristics rich in both frequency and wavenumber contents, that can couple efficiently to the structural modes of the loaded structures, causing strong vibrations and noise emission. The numerical

F. Magionesi (✉)
CNR-INSEAN, Via di Vallerano 139, 00128 Rome, Italy
e-mail: francesca.magionesi@cnr.it

369

evaluation of WPF would require the solution of the Poisson equations using direct numerical simulations, which are unfeasible for realistic structures due to the high computational cost. Therefore, WPF model continues to be developed using a combination of analytical, numerical and experimental techniques aimed at identifying scaling laws for pressure spectra and a spatial characterization of its evolution in frequency or wavenumber domain. While a number of studies have been performed aimed at modelling the WPF for fully developed turbulent boundary layer, giving rise to mature models in the frequency and wavenumber domains (Bull 1996), for transitional boundary layer only few data regarding WPF statistics and modelling have been presented (Park and Lauchle 2009) and mostly for flat plate geometry with zero pressure gradients. The flow over a bulbous bow, where usually sonar sensors are located, is a complex boundary layer characterized by pressure gradients and curvature effects instead. Previous studies have indicated that the transition region can be modelled as a superimposition of a laminar flow with turbulent spots, which statistical characteristics have similarities with those of a fully turbulent region. Therefore, the flow can be thought as a mixture of turbulent and laminar flow zones, with concentration of the turbulent part determined by the intermittency function $\gamma(x)$. The purpose of the present work is to provide experimental information on the fundamental process involved on boundary layer transition from the analysis of WPF. The study focuses on three aspects: development of an algorithm able to detect turbulent bursts and obtain $\gamma(x)$, identification of scaling laws for the auto spectral density of WPF in the transition process and characterization of the evolution of their spectral distribution.

2   Wall Pressure Fluctuations Measurements and Data Analysis

The experimental campaign was performed at Insean towing tank n°1, which is 470 m long, 13.5 m wide and 6.5 m deep. The object of study is a 1:16 scale model of a bulbous bow of a fast ship (Fig. 1). The analyzed section is located above 30 cm from the stagnation point, corresponding to a value of $x/L = 0.2$ (Fig. 1), in a region of mild longitudinal and transversal curvatures and mild adverse pressure gradient (Fig. 2). Pressure measurements were performed using an array of piezoelectric transducers Kulite XCL-072, characterized by a sensitivity of 20 mV/psi and an external diameter equal to 1.8 mm, with a sampling rate of 12,250 Hz (for more details see Magionesi and Ciappi 2010).

Typical pressure signals acquired in a transitional regime are characterized by the presence of both turbulent bursts, with high frequency fluctuations, and low frequency fluctuations due to instability waves in the laminar portion of the signal trace (Fig. 3a). The eduction of turbulent spots in transitional boundary layer involves as a first step the definition of a turbulent detector function (usually the streamwise velocity and its derivatives, while in this paper WPF have been used

**Fig. 1** 1:16 scale model of bulbous bow
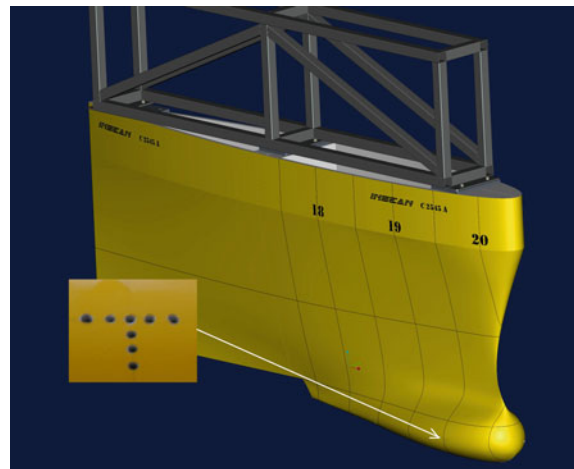
Fig. 2 Mean wall pressure coefficient
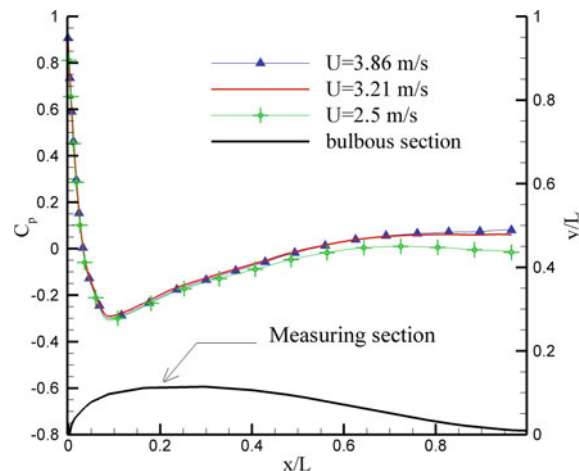
instead), which reflects the nature of the intermittent flow. When a threshold level for this parameter is defined, it is possible to distinguish the time interval over which the flow can be regarded as turbulent from those laminar and to evaluate γ.

To improve the discrimination between the laminar and the turbulent part of the pressure signal a suitable high pass filter is employed, identified as $U/2\pi\delta$ Hz, which corresponds approximately to the frequency of the largest vortices contained within the boundary layer, where δ is the boundary layer thickness. The parameter used as detector function is $p'\partial p'/\partial t$, which is a sensitive indicator of the change of amplitude in p'. The developed algorithm of identification refers to TERA (turbulent eddy recognition algorithm) method (Zhang et al. 1996), where the criteria to discern a turbulent event is identified by $\left| p'\partial p'/\partial t \right| > C(p'\partial p'/\partial t)_{RMS}$, where C is a
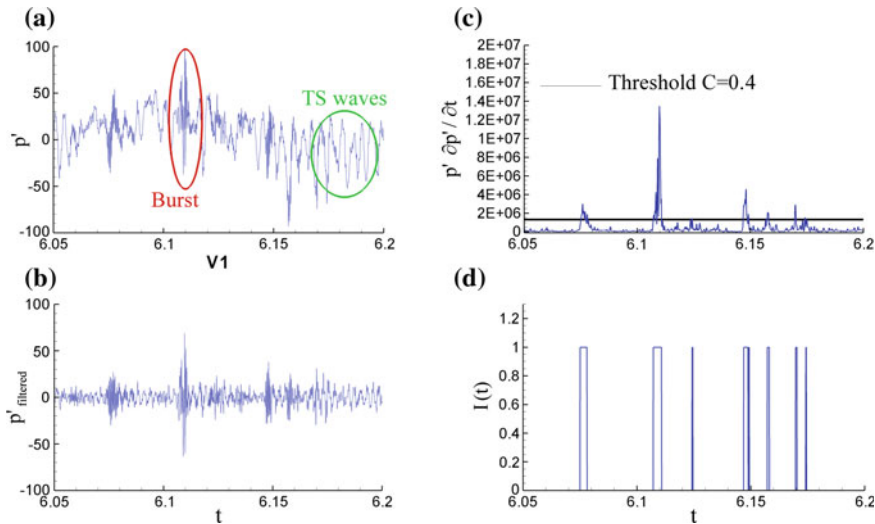
Fig. 3 a WPF signal. **b** High pass filtered signal. **c** Detector function and threshold level. **d** Indicator function $I(t)$ of turbulence

Table 1 Properties of dominating TS waves frequency and boundary layer parameters

U	Re_x	δ	δ^*	γ	U_c	f_{TS}	λ_{TS}
3.86	9.1×10^5	2.98×10^{-3}	5.06×10^{-4}	0.45	1.93	220	8.77E-3
3.21	7.5×10^5	3.21×10^{-3}	5.44×10^{-4}	0.31	1.60	170	9.4E-3
2.57	6.0×10^5	3.26×10^{-3}	5.60×10^{-4}	0.10	1.28	125	1.02E-2

constant chosen accordingly to the experiments. The results of this analysis are shown in Fig. 3 and presented in Table 1.

Boundary layer mean flow parameters (Table 1) were obtained using a finite volume code solving the Reynolds Averaged Navier Stokes Equations that use a Level Set technique to capture the free surface (Magionesi and Ciappi 2010).

The auto spectral densities of wall pressure signals are depicted in Fig. 4 for velocities 3.86, 3.21 and 2.57 m/s corresponding to 30, 20 and 15 knots. This figure provides interesting information about the frequency and energy content of the Tollmien-Schlichting (TS) waves. In fact, among the different type of possible instability mechanisms that may occur in a 3D boundary layer, the attribution of the TS waves to non-turbulent component in WPF has been obtained taking into account the particular location of measurement (convex curvature) and flow condition (mild negative pressure gradient) and also by comparing actual scaled pressure spectra (Fig. 5) with those of other experiments performed in transitional regime on a flat plate (Magionesi et al. 2012) and axisymmetric body (Hong et al. 2008). TS waves have the form of a multi frequency wave train with a spread of energy over a large frequency range. This instability persists for a significant

Fig. 4 ASD of wall pressure fluctuation
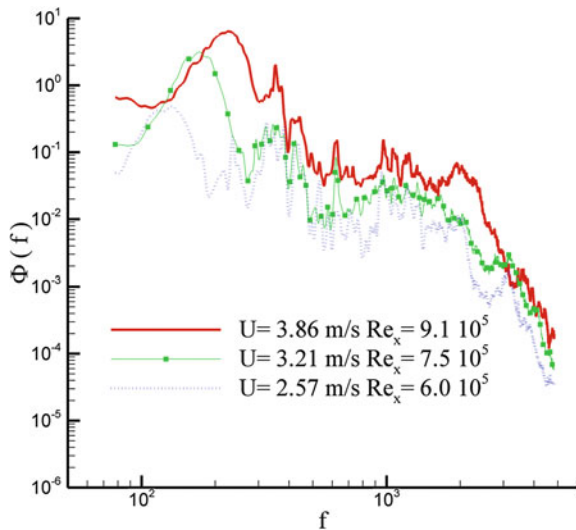
Fig. 5 Scaled ASD of wall pressure fluctuations
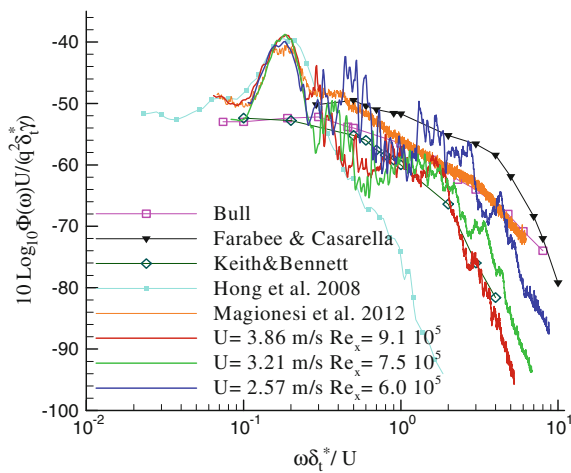
variation of Reynolds number. Moreover, with the increasing of the velocity the instable domain shifts to higher frequencies, being the dominant TS waves (corresponding to the peak of the PSD) moved from 125, 170 to 220 Hz and its amplitude is magnified. Their wavelengths can be calculated as $\lambda_{TS} = U_C/f_{TS}$ where U_C is the convection velocity of the TS waves, assumed equal to 0.5 of the free stream velocity U (Dovgal et al. 1989). In Fig. 5, the pressure spectra scaled using a combination of outer flow parameters and the obtained intermittency are depicted, showing a good collapse of the low frequency range and in particular of the TS bump; measured spectra are also compared with experimental data in turbulent regimes (Farabee and Casarella 1991; Bull 1996).

The characterization of the transitional WPF in the time-frequency domain have been obtained using the Wigner-Ville distribution (WVD) (Cohen 1989), which is defined as

$$W_s(t,\omega) = \frac{1}{2\pi} \int s(t+\tau/2)s^*(t-\tau/2)e^{-i\omega\tau}d\tau \tag{2.1}$$

where * denotes the complex coniugate of signal $s(t)$. To reduce the effect of cross-term interference in WVD, the Pseudo Wigner Ville distribution has been implemented, which introduces a filtering window $H(\omega)$ whereby the result is filtered in the frequency plane:

$$PW_s(t,\omega) = \frac{1}{2\pi} \int H(\omega-\theta)W_s(t,\theta)d\theta \tag{2.2}$$

In Fig. 6, the evolution of a turbulent burst in the WPF spectra is depicted. The energetic contribution of a small pulse in WPF, which is related with a turbulent
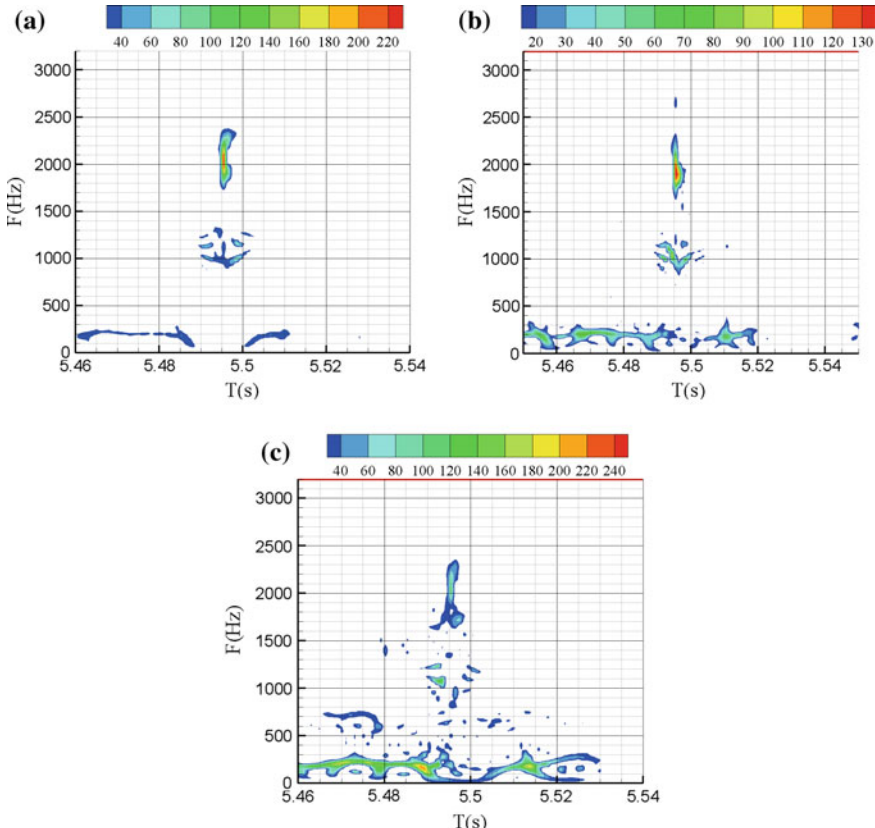

Fig. 6 Spatial evolution of the Pseudo Wigner-Ville distribution of WPF

burst passing over the sensor, gives a distinct contribution at a center frequency equal to 2050 Hz (Fig. 6a). As the fluid flows downstream the bulbous, a decrease of center frequency of pressure pulses arises, reaching 1900 Hz, 12 cm far from the first sensor (Fig. 6b). This is related with the size of the turbulent eddy that increases as the fluid flows downstream, due to the different velocities of the leading and trailing edges of the eddy. In the third position (Fig. 6c) the energy of the eddy is highly reduced, while at frequency around 200 Hz, the TS waves becomes energetically significant.

3   Conclusion

The results of an experimental campaign aimed at characterizing the WPF beneath transitional boundary layer acting on a sonar dome are here presented. The WPF spectra show a large "hump" of energy related with the magnified TS wave instability frequency. A scaling law for WPF spectra in transition has been obtained using a combination of outer flow parameters and intermittency, which in general could be applied to different geometry, as long as pressure gradient are mild. The analysis of the time-frequency spectra of WPF, obtained using Pseudo Wigner Ville distribution, shows a decrease of center frequency of turbulent burst and a slow amplification of the TS wave instability as the fluid downstream the bulbous.

References

Bull MK (1996) Wall-pressure fluctuations beneath turbulent boundary layers: some reflections on forty years of research. J Sound Vib 190(3):299–315

Cohen L (1989) Time-frequency distributions—a review. Proc IEEE 77:941–981

Dovgal A, Kozlov V, Michalke A (1989) Laminar boundary layer separation: instability and associated phenomena. Prog Aerosp Sci 30:61–94

Farabee TM, Casarella MJ (1991) Spectral features of wall pressure fluctuations beneath turbulent boundary layers. Phys Fluids A(3):2410–2420

Hong C, Shin K, Jeon J, Kim S (2008) Transitional wall pressure fluctuations on axisymmetri bodies. J Acoust Soc Am 124(5):2767–2773

Magionesi F et al (2012) Measurement and modeling of turbulent boundary excitation for. In: NOVEM2012, Sorrento, Italy, Keynote lecture

Magionesi F, Ciappi E (2010) Experimental investigation of turbulent boundary layer excitation acting on the sonar dome. In: INTERNOISE2010, Lisbon, Portugal

Park S, Lauchle GC (2009) Wall pressure fluctuation spectra due to boundary layer transition. J Sound Vib 319(3):1067–1082

Zhang DH, Chew YT, Winoto SH (1996) Investigation of intermittency measurement methods for transitional boundary layer. Exp Therm Fluid Sci 12:433–443

Aerodynamic Performance of Flexible Tandem Wings in Hovering Flight

Yingying Zheng and Yanhua Wu

Abstract The aerodynamic performance of flexible tandem wings, including force generations, deformations and flow fields were investigated. With appropriate flexibility, the tandem Wing III models showed advantages over the other wing models in both lift and efficiency. Focusing on the Wing III model, the comparison between the single case and tandem cases with phase differences of 0°, 90° and 180° showed that the 0° phase difference contributed to the highest lift. PIV measurements were also performed to offer the flow fields around the Wing III models in both single and tandem cases. In 0°-phased situation, the existence of forewing resulted in a more attached LEV on the hindwing, which contributed greatly to the lift generation.

1 Introduction

Dragonflies, as representing one kind of four-wing insects, were found to have significant advantages in aerodynamic performance. Previous studies have proven that their ability of controlling the phase difference between fore- and hindwings contributes to the great advantage in maneuverability (Alexander 1984; Somps and Luttges 1985; Azuma and Watanabe 1988). What's more, the flexibility of insect wings was also found to show significantly beneficial effect on the aerodynamic performance of insects (Young et al. 2009; Mountcastle and Daniel 2009; Walker et al. 2009). So far, the combine effect of tandem configuration and flexibility was only investigated in the study of Warkentin and Delaurier (2007). However, their study only investigated one flexibility. Various flexibilities are required to be studied to

Y. Zheng · Y. Wu (✉)
School of Mechanical and Aerospace Engineering,
Nanyang Technological University, Singapore 639798, Singapore
e-mail: yanhuawu@ntu.edu.sg

Y. Zheng
e-mail: zhen0088@e.ntu.edu.sg

explore the effect of flexibility on the aerodynamic performance of flexible tandem wings. The present effort aims to offer a more comprehensive investigation of the flexible tandem wings by studying the aerodynamic forces, deformation and flow fields together.

2 Experimental Setup

The dragonfly-like flexible wing models were fabricated at three levels of flexibilities by rapid prototyping. The wings with different flexibilities were realized by varying the thickness, i.e. 0.5, 0.75 and 1 mm, which were identified as Wing I, Wing II and Wing III, respectively. The dimensions for the fore- and hindwings were 125 mm × 26 mm and 120 mm × 35 mm (span length × mean chord length), respectively. A set of rigid wing models were also fabricated as the reference.

As shown in Fig. 1a, two linear motors and two rotary motors were employed to realize the combined pitching and plunging motions of the tandem wings: $h_F = h_0 cos(2\pi ft)$, $\alpha_F = \alpha_0 cos(2\pi ft + \Phi)$, $h_H = h_0 cos(2\pi ft + \Psi)$ and $\alpha_H = \alpha_0 cos(2\pi ft + \Phi + \Psi)$, where Ψ is the phase difference between tandem wings, f is the motion frequency, and Φ is the phase difference between the plunging and pitching motions. Previous studies (Jones et al. 2001; Ramamurti and Sandberg 2001) have shown that $\Phi = 90°$ is the optimum angle. The pivot axis on the wing for the pitching motion is at 1/4 mean aerodynamic chord. Based on the average flapping stroke amplitude of real dragonflies at 90° and the wing span length of the forewing model at 125 mm, the plunging amplitude is chosen as $h_0 = 0.5L_{fore}sin45° = 44$ mm. The pitching amplitude is set at $\alpha_0 = 30°$ as the real dragonflies'. With oscillating frequency at $f = 1Hz$, the Reynolds number is $Re_{\overline{U}_P} = \overline{U}_P\overline{C}_F/\nu = 4544$, which is close to the Reynolds number of real dragonflies. The separation between fore- and hindwings is 1.5 chord length of forewing.

The experiments were performed in a 120 cm (L) × 50 cm (W) × 60 cm (H) water tank. The forces and moments recorded by a six-axis force/torque sensor consisted of aerodynamic, inertial and gravitational forces. To extract the net aerodynamic force, the same experiment was repeated in air to measure the inertial and gravitational forces since the aerodynamic forces in air have been observed negligible (Zheng et al. 2015). With 0° stroke plane, the lift and thrust are normal to and along the plunging direction, respectively. It should be noted that the stroke plane employed in current study was different from that of real dragonflies, which made our model only cover a limited aspect of tandem-wing flight. However, the present study is still expected to contribute to the further understanding of tandem wings. The lift, thrust, and power coefficients are defined as $C_L = 2F_L/\rho\overline{U}_P^2 S$, $C_T = 2F_T/\rho\overline{U}_P^2 S$ and $C_P = 2P/\rho\overline{U}_P^3 S$ respectively, where $\overline{U}_P$ is the mean plunging velocity, ρ is the density of water, S is the wing area, and $P = \int(F_L\dot{h} + M\dot{\alpha})dt/T$ is the power consumption over a given period T with M as 1/4-chord pitching moment, $\dot{h}$ as the
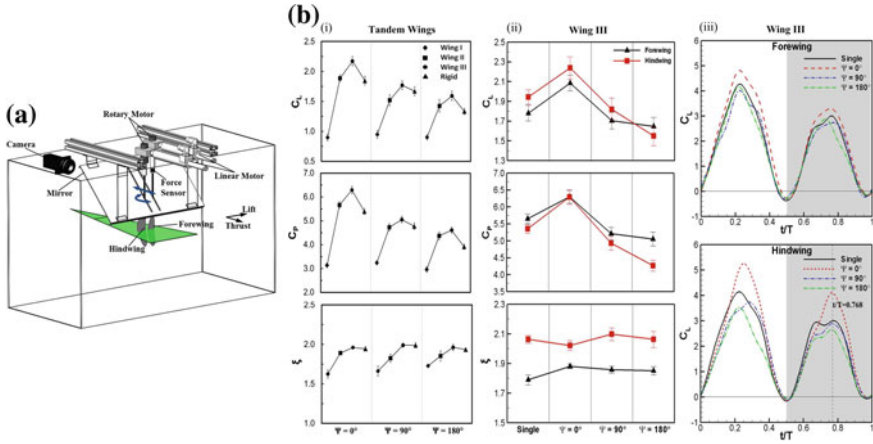
Fig. 1 **a** Experiment setup for the force and PIV measurements. **b** The results of force measurements: (i) Average lift coefficient C_L, power coefficient C_P, and lift efficiency ε for different tandem wing models; (ii) Average lift coefficient C_H, power coefficient C_P, and lift efficiency ε of Wing III *fore-* and *hindwings* in different situations; (iii) Time histories of lift coefficients obtained by Wing III *fore-* and *hindwings* respectively in different situations. The *up-* and *down*-strokes are first and second half of the period which are marked with *white* and *grey* background, respectively

plunging velocity, and $\dot{\alpha}$ as the pitching velocity. $\xi = \overline{F}_L/P$ is used to quantify the lift efficiency.

To investigate the mechanism of how the flexibility affected the flow field, thus the aerodynamic forces, the deformations of flexible wing models were measured using direct linear transformation (DLT) technique (Abdel-Aziz and Karara 1971). The fore- and hindwings were marked with 160 and 192 black dots at diameter of 1.6 mm evenly, respectively. The image locations of the markers were recorded by two high speed cameras (Photron FASTCAM SA3: 1024×1024 pixel, 12-bit) during the motion at frame rate of 125 Hz. Through a calibration procedure, the actual locations of the markers were then reconstructed. The accuracy are 0.05 mm in x and z directions, while 0.3 mm in y direction. Furthermore, 2D phase-locked PIV measurements were performed to obtained the flow fields at $0.5L_{fore}$ spanwise location. A Nd:YAG laser (140 mJ/pulse) used to produce a laser sheet with thickness less than 1 mm. The light reflected off 20 μm particles into the high speed camera. The setup of PIV measurements is shown in Fig. 1a. A 45°-inclined mirror with two slots (width: 6 mm) on it, was employed to get rid of the large blockage of the wing deformations in the capturing of images. The average velocity field was obtained by averaging 250 results. The details of the experimental setup can be found in Zheng et al. (Zheng et al. 2015).

3   Results and Discussions

Figure 1b(i) shows the average lift coefficient C_L, power coefficient C_P, and lift efficiency ε of all tandem wing models at different phase differences. The symmetric motion led to average thrust within a cycle close to zero. Therefore, here we only discuss the lift coefficients, C_L. First, comparing the average lift coefficients of different wing models at the same phase difference, it can be found that the tandem Wing III models always performed best with much higher C_L. However, the Wing III models didn't show significant advantages in the lift efficiency as in the lift coefficients, due to the largest power consumptions at all phase differences. Excluding Wing I models, 0° was the most favourable phase difference for the other wing models.

   Figure 1b(ii) further presents the comparisons between single and tandem cases for the fore- and hindwings of Wing III respectively. Both fore- and hindwings of Wing III showed the highest lift in 0°. However, not all the tandem configurations showed advantages over the single-wing configuration. In 90° and 180°-phased situations, both fore- and hindwings obtained much lower C_H than the single wing. As the efficiency, the forewing at $\Psi = 0°$, and hindwing at $\Psi = 90°$ obtain the highest values. From the lift coefficients within a cycle in Fig. 1b(iii), the differences in peak values should mainly account for the differences in lift generation of different models. For both fore- and hindwings, 0°-phased situation generated much higher peaks than the other situations.

   Figure 2(i) shows the deformation of tandem Wing III with the rigid wings as reference at 0° phase difference during upstroke and downstroke. Taking the rigid wing models as references, the Wing III models deformed significantly with large bending deformations. However, the twisting deformation could be neglected since the change in angle of attack was less than 0.5°. Therefore, the main effect of the deformation was causing a lag in plunging direction between the Wing III and rigid models. This lag made the LEVs closer to the wings which contributed to the lift generation (Zheng et al. 2015).

   To investigate the forewing-hindwing interactions of the flexible tandem wings at different phase differences, time position $(t/T)_H = 0.768$ (mark in Fig. 1b(iii)), where significant differences in C_L happened among various cases, was chosen for the PIV measurements. As shown in Fig. 2(ii), significant interaction between the fore- and hindwings in tandem configurations can be seen. Large leading-edge (LEV) and training-edge (TEV) vortices can be found on both fore- and hindwings in all situations. In tandem-wing flight at $\Psi = 0°$, due to the exist of forewing's TEV, the LEV of hindwing was induced to attach more to the wing model compared with that in the single-wing case. The LEV lay on almost half of the hindwing which leads to the highest lift of 0°-phased case at $(t/T)_H = 0.768$. At $\Psi = 90°$, the effect of forewing was relatively weak. Therefore, the hindwing at $\Psi = 90°$ obtained
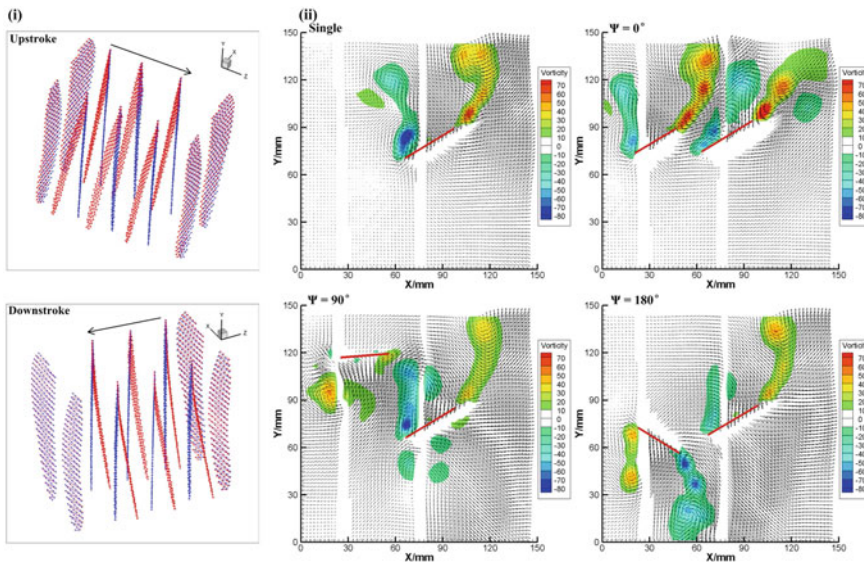
Fig. 2 (i) The deformation of tandem Wing III (*red*) with rigid wings (*blue*) as reference at 0° phase difference during *upstroke* and *downstroke*. (ii) Average velocity and vorticity fields for the single, and tandem Wing III models at $\Psi = 0°$, 90° and 180° at $(t/T)_H = 0.768$

similar lift as that in single-wing case. At 180° phase difference, the forewing had detrimental effect on the hindwing's lift, since the flow induced by the forewing reduced the strength of LEV on hindwing.

References

Abdel-Aziz YI, Karara HM (1971) Direct linear transformation from comparator coordinates in close-range photogrammetry. In: Proceedings of the Symposium on Close-Range Photogrammetry. American Society of Photogrammetry

Alexander DE (1984) Unusual phase-relationships between the forewings and hindwings in flying dragonflies. J Exp Biol 109:379–383

Azuma A, Watanabe T (1988) Flight performance of a dragonfly. J Exp Biol 137:221–252

Jones K, Lund T, Platzer M (2001) Experimental and computational investigation of flapping wing propulsion for micro air vehicles. Prog Astronaut Aeronaut 195:307–339

Mountcastle AM, Daniel TL (2009) Aerodynamic and functional consequences of wing compliance. Exp Fluids 46(5):873–882

Ramamurti R, Sandberg W (2001) Simulation of flow about flapping airfoils using finite element incompressible flow solver. AIAA J 39(2):253–260

Somps C, Luttges M (1985) Dragonfly flight - novel uses of unsteady separated flows. Science 228(4705):1326–1329

Walker SM, Thomas ALR, Taylor GK (2009) Deformable wing kinematics in free-flying hoverflies. J Royal Soc Interface 7(42):131–142

Warkentin J, DeLaurier J (2007) Experimental aerodynamic study of tandem flapping membrane wings. J Aircr 44(5):1653–1661

Young J, Walker SM, Bomphrey RJ, Taylor GK, Thomas AL (2009) Details of insect wing design and deformation enhance aerodynamic function and flight efficiency. Science 325(5947):1549–1552

Zheng Y, Wu Y, Tang H (2015) Force measurements of flexible tandem wings in hovering and forward flights. Bioinspiration Biomimetics 10(1):016021

Effect of Nose Shape on Separation Bubble and Surface Pressure on a Cylinder in Axial Flow

Q. Sun, Md. Mahbub Alam, C.W. Wong and Y. Zhou

Abstract The flow characteristics is experimentally studied over the leading edge of a circular cylinder with blunt, conical, and hemispherical nose shapes, for a range of Reynolds number $Re_D = 2.5 \times 10^3 - 4.2 \times 10^4$. While mean and fluctuating pressure (C_p, C_p') around the leading edge are measured with a pressure transducer, PIV and flow-visualization experiments are performed to assimilate how an increase in Re_D influences the shear layer reattachment length x_R, shear layer transition length x_{Tr}, and bubble width W. The results reveal that x_R, x_{Tr}, and W all shrinking significantly with Re_D up to $Re_D = 10^4$. Their shrinkage is however inconsequential for $Re_D > 10^4$. At a given Re_D, when the nose changes as blunt, conical and hemispherical, x_R and W shorten, but x_{Tr} enlarges. Following the separation bubble size, C_p and C_p' in the bubble are highly sensitive to Re_D for $Re_D < 10^4$, but less for $Re_D > 10^4$.

Keywords Axial flow · Cylinder · Fluctuating pressure · Separation bubble

1 Introduction

Axial flow over a circular cylinder with a blunt leading edge is very complex, particularly around the leading edge, comprising separation bubble/cavitation, shear-layer reattachment, etc. Pressure fluctuations in the separation region may induce structural vibrations and generate noise. The behavior of the separated flow

Q. Sun · Md.M. Alam (✉) · C.W. Wong · Y. Zhou
Shenzhen Graduate School, Institute for Turbulence-Noise-Vibration Interaction and Control, Harbin Institute of Technology, Shenzhen, China
e-mail: alamm28@yahoo.com; alam@hitsz.edu.cn

Md.M. Alam
Key Lab of Advanced Manufacturing Technology, School of Mechanical Engineering and Automation, Shenzhen Graduate School, Harbin Institute of Technology, Shenzhen, China

is thus crucial for a thorough understanding of the flow and has received considerable attention in the literature. x_R (streamwise bubble size) is one of the main characteristic parameters of the flow at the leading edge. It for a blunt cylinder has been well studied (e.g., Ota 1975; Kiya et al. 1991; Dong et al. 1997). Shear layer transition length x_{Tr} and lateral bubble size W are also noteworthy characteristic parameters influencing time-mean and fluctuating pressure (C_p and C_p') in the separation bubble, while they have attracted little attention. Therefore, the first objective of this work is to experimentally investigate the three parameters over a wide range of Reynolds number Re_D (based on cylinder diameter D). The forebody (nose) geometry has a considerable effect on the leading edge flow behavior. Blunt, conical and hemispherical noses are of interest to be studied in the present work, due to fact that they are common in engineering fields. Therefore, the second objective is to study the effect of nose shape on the features of flow around the leading edge of a cylinder.

2   Experimental Details

Experiments were performed in a closed-circuit wind tunnel with a test section of 5.5 m × 0.8 m × 1.0 m. The free-stream velocity, U_∞, was varied from 3.0 to 46.8 m/s. Four models were used. Three of them had the same diameter of $D = 16$ mm, with blunt, conical, and hemispherical noses, respectively. Another of $D = 7.5$ mm with blunt nose was adopted so that the investigated Re_D could be reduced to 2.5×10^3. We are interested to know the difference in pressure fluctuations (i) immediately behind the separation, (ii) around the center of the separation bubble, and (iii) behind the reattachment. Therefore, three pressure taps on the cylinder of $D = 7.5$ mm at $x/D = 0.15$, 1.0 and 2.5, respectively, were made (Fig. 1). The cylinders of $D = 16$ mm were, however, furnished with two pressure taps only at $x/D = 0.15$ and 1.0, respectively. In order to further study the flow separation features, flow visualization and PIV measurements on the leading edge was performed by means of a PIV system.
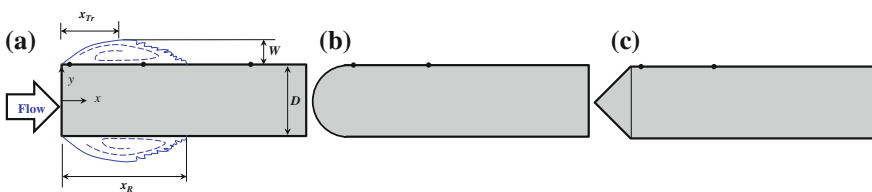

Fig. 1 Sketches of models. **a** blunt cylinder and definations of x_R, W and x_{Tr}, **b** hemispherical, **c** conical. Small *solid circles* denote the pressure tap positions

3 Results and Discussion

3.1 Effects of Nose and Re on Bubble

Figure 2a–h presents flow visualization results obtained for the three nose shapes at two representative $Re_D = 3.0 \times 10^3$ and 1.0×10^4. While Fig. 2a–f are given in the same scale, Fig. 2g, h are the zoomed-in views of Fig. 2e, f, respectively. What is conspicuous in the figures is that as the nose changes as blunt, conical and hemispherical at $Re_D = 1.0 \times 10^4$ (Fig. 2b, d, f), the reattachment position moves forward, the bubble width shrinks, and the shear-layer transition delays. The same observation is made at $Re_D = 3.0 \times 10^3$ (Fig. 2b, d). When Re_D is increased from 3.0×10^3 to 1.0×10^4, the reattachment and transition shift toward the leading edge and the bubble width diminishes for blunt and conical noses. For hemispherical nose, separation was not observed at $Re_D = 3.0 \times 10^3$, but it occurs at $Re_D = 1.0 \times 10^4$, followed by a reattachment. Figure 2i shows PIV-measured mean velocity field corresponding to Fig. 2a. The mean characteristic parameters x_R, x_{Tr}, and W are estimated from both flow visualization (FV) images and PIV-measured flow field. x_R is estimated by measuring the distance between the leading edge and the reattachment point where the mean flow near the wall changes from reversed flow to forward flow. x_{Tr} is estimated as is the horizontal distance between the leading edge and the point where maximum RMS velocity in the shear layer or where the stream of smoke in FV image gets crumbled suddenly.

Shown in Fig. 3 are the variations in x_R/D, x_{Tr}/D, and W/D with Re_D for the three noses. Previous experimental results associated with x_R/D available in the literature for blunt nose are incorporated in Fig. 3a for comparison and validation purposes.
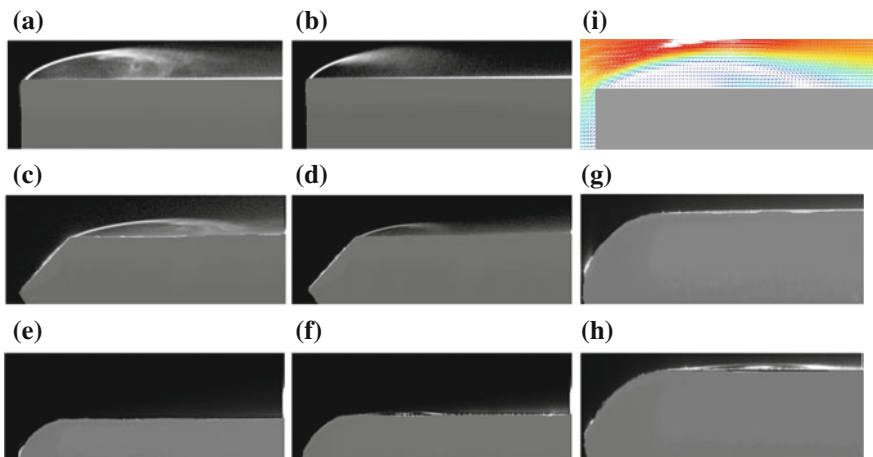

Fig. 2 Flow visualization results for the three noses. **a**, **b** blunt; **c**, **d** conical; **e**, **f** hemispherical; at $Re_D = (3.0 \times 10^3, 1.0 \times 10^4)$, respectively. **g**, **h** are the zoomed-in views of **e**, **f**, respectively. **i** PIV-measured velocity field for blunt at $Re_D = 3.0 \times 10^3$, corresponding to **a**
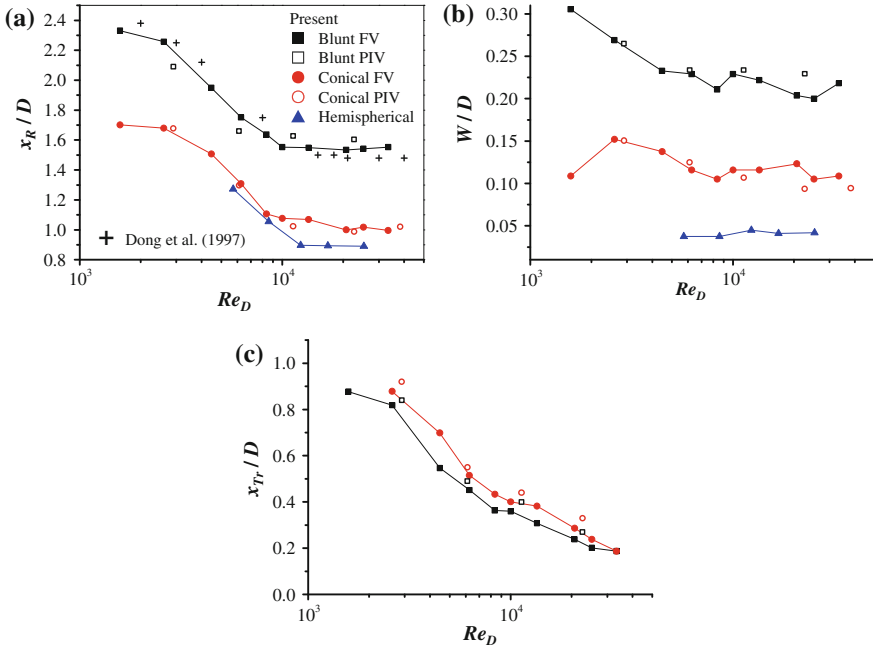
Fig. 3 Effects of Re_D on **a** x_R/D, **b** W/D, **c** x_{Tr}/D

Present results obtained from PIV and FV being close to each other accord well with the results (FV) by Dong et al. (1997). For blunt-nose, x_R/D decreases with increase in Re_D until $Re_D = 10^4$, beyond which x_R/D tends to be a constant of 1.55. The transition moving upstream with increase in Re_D (Fig. 3c) causes a significant decrease in x_R/D. As the transition gets further closer to the separation, the entertainment rate tends to be unchanged, leading to a nearly constant x_R/D. x_R/D for conical becomes smaller than that for blunt while larger than that for hemispherical, having similar trends for all the noses. W/D generically wanes with Re_D for both blunt and conical, particularly for $Re_D < 10^4$ (Fig. 3b). The transition in shear layer was not observed for hemispherical in the Re_D regime examined, hence no x_{Tr}/D data are given for hemispherical.

3.2 Time-Mean and Fluctuating (rms) Pressures

Figure 4a, b shows the dependence of C_p and C_p' on Re_D for blunt cylinder, including data from the literature. The present data accord well with those in the literature. At $x/D = 1.0$, with the increase in Re_D, C_p becomes more negative and C_p' rockets until $Re_D = 6 \times 10^3$. The cause of these changes is two-fold. Firstly, a decrease in W/D with Re_D (Fig. 3b) begets the radius of mean-streamline curvature
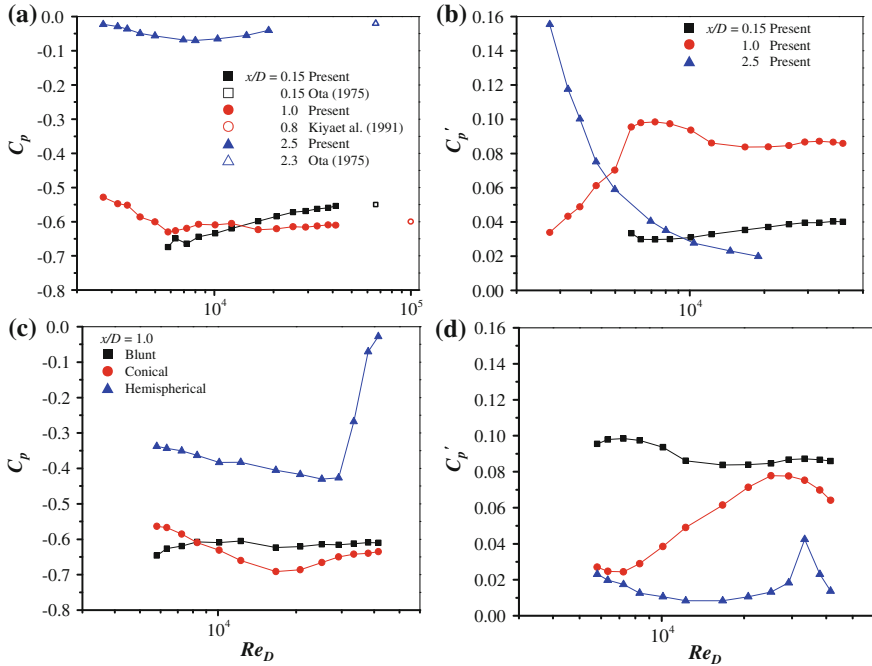
Fig. 4 Dependences on Re_D of **a** C_p, **b** C_p' for blunt, and **c** C_p, **d** C_p' for the three nose shapes

smaller, the shear layer getting closer to the surface in other words. The smaller radius of curvature maintains a higher radial pressure gradient, consequently, C_p is reduced. At the same time, since the shear layer gets closer to the surface, C_p' is more influenced. Secondly, x_R/D moving forward also contributes to the decrease and increase in C_p and C_p', respectively. At $Re_D > 1 \times 10^4$, both x_R/D and W/D being almost insensitive to Re_D keep the bubble unchanged, resulting in hardly change in C_p and C_p'. C_p increases slightly with Re_D, at $x/D = 0.15$ can be attributed to the fact that x_{Tr} approaching the leading edge (Fig. 3c) thickens the shear layer, which maintains a smaller radial pressure gradient. For the same reason, C_p' has the same trend. C_p' decreases with Re_D at $x/D = 2.5$ owing to reattachment moving upstream and away from the pressure tap. Indeed, this x/D is beyond the reattachment, with $x_R/D = 2.35$ at the lowest Re_D examined (Fig. 3a).

Figure 4c, d compares C_p and C_p' at $x/D = 1.0$ among the three noses. The magnitude of C_p is smaller for hemispherical and larger for conical except at $Re_D < 10^4$, compared to that for blunt one. For conical one, C_p reduces at $Re_D < 1.7 \times 10^4$ resulting from x_R/D, i.e. the bubble size, decreasing with Re_D which leads to higher radial pressure gradient, while at $Re_D > 1.7 \times 10^4$, C_p tends to be constant with Re_D due to nearly unchanged x_R/D. Furthermore, both C_p and C_p' are highly sensitive to Re_D for hemispherical, owing to x_R/D varying between 1.3 and 0.9 with Re_D, nestling around the pressure tap (i.e., $x/D = 1.0$). As blunt and

hemispherical corresponding to largest and smallest bubble sizes, respectively, present highest and lowest $C_p{}'$. For hemispherical, a sharp peak in $C_p{}'$ variation at $Re_D = 3.3 \times 10^4$ is observed and C_p around the same Re_D recovers drastically. Both observations indicate that the reattachment occurs downstream and upstream of $x/D = 1.0$ for $Re_D < 3.3 \times 10^4$ and $Re_D > 3.3 \times 10^4$, respectively, and around $x/D = 1.0$ at $Re_D = 3.3 \times 10^4$. The flow visualization results indicate that $x_R/D \approx 0.90$ at $Re_D = 3.3 \times 10^4$. Furthermore, it was observed that separation position occurs shortly downstream of $x/D = 0.1$. All the observations insinuate that the peak in $C_p{}'$ at $Re_D = 3.3 \times 10^4$ is caused by the shear layer reattachment around $x/D = 1.0$. Due to the separation bubble size decreasing with increasing Re_D, the centre of the bubble moving upstream and far away from $x/D = 1.0$ with Re_D results in the maximum magnitude C_p (at $Re_D = 3.0 \times 10^4$) is not at the same Re_D as that in $C_p{}'$ (at $Re_D = 3.3 \times 10^4$). On the other hand, for blunt and conical noses, absences of recovery in C_p and sharp peak in $C_p{}'$ suggest that the reattachment nestles beyond $x/D = 1.0$. An increase in $C_p{}'$ with Re_D prevails for conical nose because the reattachment position proceeds and approaches $x/D = 1.0$.

4   Conclusions

x_R, x_{Tr}, and W all shrink with Re_D. The shrink is however significant for $Re_D < 10^4$, but inconsequential for $Re_D > 10^4$. At a given Re_D, when the nose changes as blunt, conical and hemispherical, x_R and W shorten, but x_{Tr} enlarges. Following the separation bubble size, C_p and $C_p{}'$ in the bubble are highly sensitive to Re_D for $Re_D < 10^4$, but less for $Re_D > 10^4$. The magnitude of C_p is smaller for hemispherical and larger for conical, compared to that for blunt. Blunt and hemispherical correspond to the highest and lowest $C_p{}'$, respectively. Magnitude of C_p is larger in the bubble and much smaller around and behind the reattachment, while $C_p{}'$ is smaller near the separation, but much higher around the reattachment.

References

Dong YF, Wei ZL, Xu C, Jiang XQ, Liao YF (1997) On separated shear layer of blunt circular cylinder. Acta Mech Sin 13:313–322

Kiya M, Mochizuki O, Tamura H, Nozawa T, Ishikawa R, Kushioka K (1991) Turbulence properties of an axisymmetric separation-and-reattaching flow. AIAA J 29:936–941

Ota T (1975) An axisymmetric separated and reattached flow on a longitudinal blunt circular cylinder. J Appl Mech 311–315

A Cylinder Vibration Induced by Shear Layers of Another of Smaller Diameter

Md. Mahbub Alam, B. Qin and Y. Zhou

Abstract Flow-induced vibration of a circular cylinder (diameter D) submerged in the wake of a fixed circular cylinder of smaller diameter d is investigated. The cylinder was spring mounted, allowed to vibrate in the transverse direction only. While d is varied from $0.2D$ to $1.0D$, cylinder spacing L systematically is changed from 1.0 to 5.5, where L is the distance between the forward stagnation point of the downstream cylinder to the center of the upstream cylinder. Measurements of vibration amplitude, lift force and flow field are carried out. A map of vibration regime is provided showing how the vibration of the cylinder is dependent on d and L. At a smaller d, vibration occurs for a longer range of L. The vibration is excited by the two shear layers reattaching alternately on the downstream cylinder. An increase in vibration amplitude is accompanied largely by an increase in lift amplitude.

Keywords Flow-induced vibrations · Wake · Different diameters · Lift

1 Introduction

Flow-induced vibration (FIV), due to its large amplitude and frequent occurrence, is a serious problem associated with the cooling/heat-exchanger systems. Kim et al. (2009) examined vibration characteristics of two tandem circular cylinders, both are spring mounted and allowed to vibrate in the transverse direction, for $0.6 < L/d < 3.7$, $1.5 < U_r < 26$ and mass-damping $m^*\zeta = 0.65$ (where U_r is the reduced velocity, $m^* =$ mass ratio, $\zeta =$ damping ratio). When the upstream cylinder is fixed, vibration of the downstream cylinder was investigated by Assi et al. (2013) for $L/d \geq 4.0$ at a low mass-damping ratio of 0.013. Vibrations of two tandem

Md. Mahbub Alam (✉) · B. Qin · Y. Zhou
Shenzhen Graduate School, Institute for Turbulence-Noise-Vibration Interaction
and Control, Harbin Institute of Technology, Shenzhen, China
e-mail: alamm28@yahoo.com; alam@hitsz.edu.cn

cylinders have been done mostly for two identical diameter cylinders at a low value of mass-damping. However, diameters of structures in a group are not always the same, and vibration response of the downstream cylinder might be dependent on the upstream cylinder size (diameter). The objective of this work is to investigate the dependence of cylinder vibration on the diameter of an upstream fixed cylinder.

2 Details of Experiments

The investigation was conducted in a wind tunnel of 5.5 m × 0.8 m × 1.0 m cross-section. A sketch of the cylinder arrangement and definition of symbols is presented in Fig. 1. While d was varied as 40, 32, 24, 16 and 8 mm, D was kept fixed at 40 mm, corresponding to d/D = 1.0, 0.8, 0.6, 0.4 and 0.2, respectively. L/d = 1.0, 1.5, 2.0, 2.5, 3.0, 3.5, 4.0 and 5.5 were considered. The upstream cylinder was fixed at both ends. Each end of the downstream cylinder was supported by two spiral springs (Fig. 1c). A standard laser vibrometer was used to measure the vibration frequency and vibration-amplitude (A) of the cylinder. ζ, $m^*\zeta$, and the cylinder natural frequency were 0.0021, 0.58, and 11.72 Hz, respectively. Free-stream velocity U_∞ was increased step-by-step from 1.8 to 10.3 m/s, corresponding to variation in U_r from 3.8 to 22.0 and in Re (based on D and U_∞) from 4.8×10^3 to 2.7×10^4. Vortex shedding frequencies were estimated from fluctuating velocity measured by two hot wires, one (HT1) located in the gap at $(x'd, y'/d, z'/d)$ = (1, 1, 0), another (HT2) placed behind the downstream cylinder at $(x/D, y/D, z/D)$ = (4, 1, 0). Flow-induced flift force and displacementorces and flow structures were measured using a pressure scanner and a PIV system, respectively.
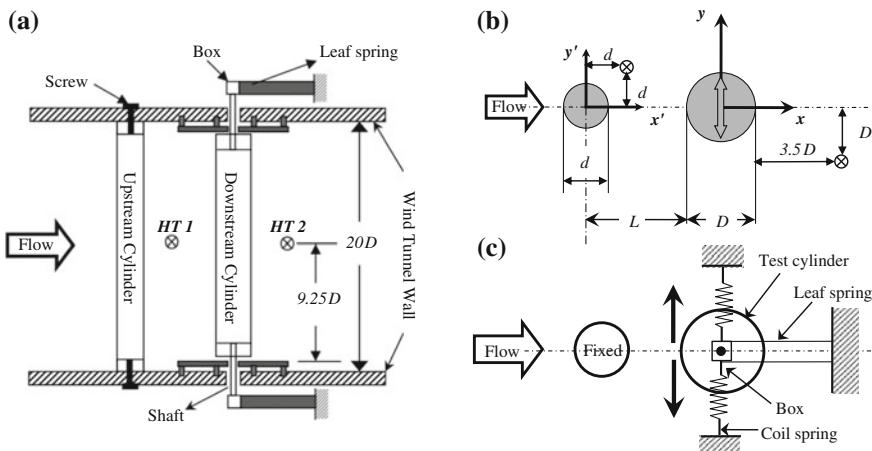

Fig. 1 a Experimental setup, b definition of symbols, c the test cylinder mounting system

3   Results and Discussion

3.1   Vibration Amplitude

Figure 2 illustrates how vibration amplitude ratio (A/D) is contingent on d/D and L/d. Vibration at $L/d = 1.0$ is divergent with increasing U_r for $d/D = 0.2, 0.4, 0.6$, and 0.8. Small humps generated around $U_r = 5$ are the sign of vortex-excitation (VE) (Fig. 2a). At $L/d = 1.5$–2.5 (Fig. 2b–d), $d/D = 0.2, 0.4$ and 0.6 engender large amplitude vibration, but $d/D = 0.8$ and 1.0 do not. With an increase in L/d to 3.0–4.0 (Fig. 2e–g), vibration prevails for $d/D \leq 0.4$ only. When L/d is further increased to 5.5, vibration persists for $d/D = 0.2$ only (Fig. 2h). It thus could be concluded that a cylinder in the downstream of a smaller cylinder may undergo a large amplitude vibration.

3.2   Vibration Regime

A summary of vibration response and flow can be presented in a map on the plane of $d/D - L/d$ (Fig. 3). The regime I enclosed by the solid red line represents the
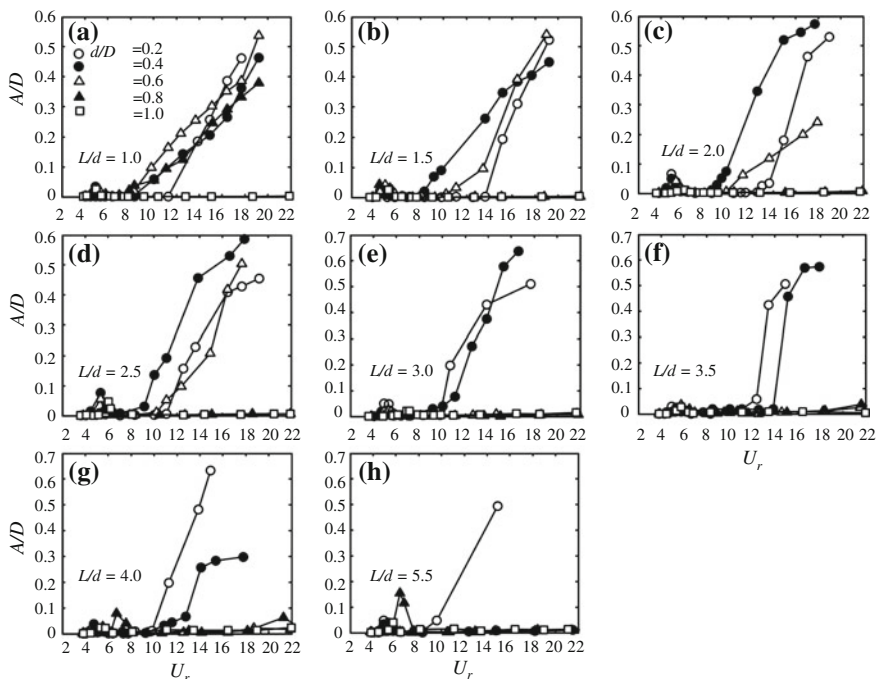

Fig. 2 Vibration responses for different d/D at **a** $L/d = 1.0$, **b** $L/d = 1.5$, **c** $L/d = 2.0$, **d** $L/d = 2.5$, **e** $L/d = 3.0$, **f** $L/d = 3.5$, **g** $L/d = 4.0$, and **h** $L/d = 5.5$
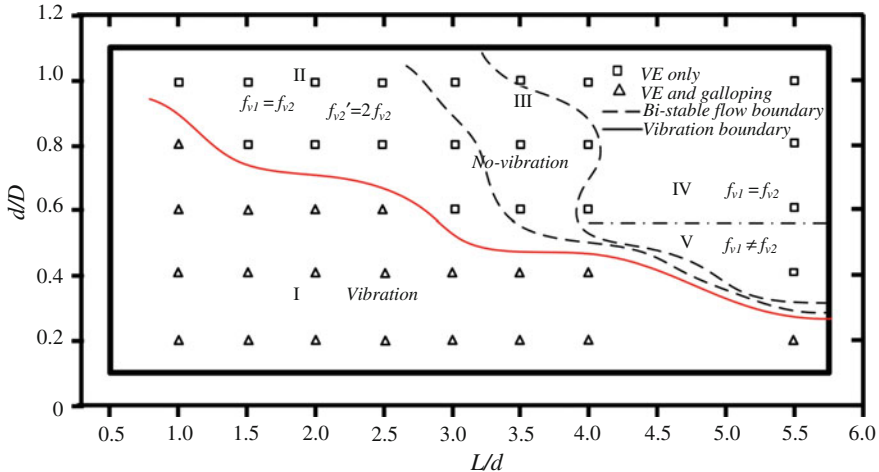
Fig. 3 Vibration regime in $d/D-L/d$ plane

occurrence of violent vibrations. The no-vibration regime can be further divided into four sub-regimes (II–V) depending on the relationship between shedding frequencies (f_{v1}, f_{v2}) in the gap and behind the downstream cylinder, respectively. Regime II corresponds to reattachment flow, where $f_{v1} = f_{v2}$ and a superharmonic frequency ($f_{v2}' = 2f_{v2}$) prevails behind the downstream cylinder. Bistable flow regime (regime III) following the reattachment regime appears at a larger L/d for a smaller d/D. Regimes IV and V belong to coshedding flow, characterized by synchronized ($f_{v1} = f_{v2}$) and non-synchronized ($f_{v1} \neq f_{v2}$) sheddings from the two cylinders.

3.3 Vibration Mechanism

The schematic plot of the cylinder displacement y/D and lift force coefficient C_L in a half cycle of oscillation at $L/d = 2.0$, $d/D = 0.4$ is presented in Fig. 4a, along with the phase-average vorticity and pressure coefficient C_P (positive when the arrow points to the cylinder center) distributions (Fig. 4b–f). When the cylinder moves upward at the centerline ($y/D = 0$), the shear layer emanating from the lower side of the upstream cylinder reattaches on the lower side of the downstream cylinder at $\theta \approx -22.5°$ where $C_P \approx +1$ (Fig. 4b). The part of reattached flow along with the upper shear layer flowing over the upper side of the downstream cylinder causes a highly negative pressure on the upper side, engendering an upward lift force. As the cylinder moves upward, the upper shear layer reattaches, and the lift thus wanes (Fig. 4c). The lift becomes maximum negative when the upper shear flows over the
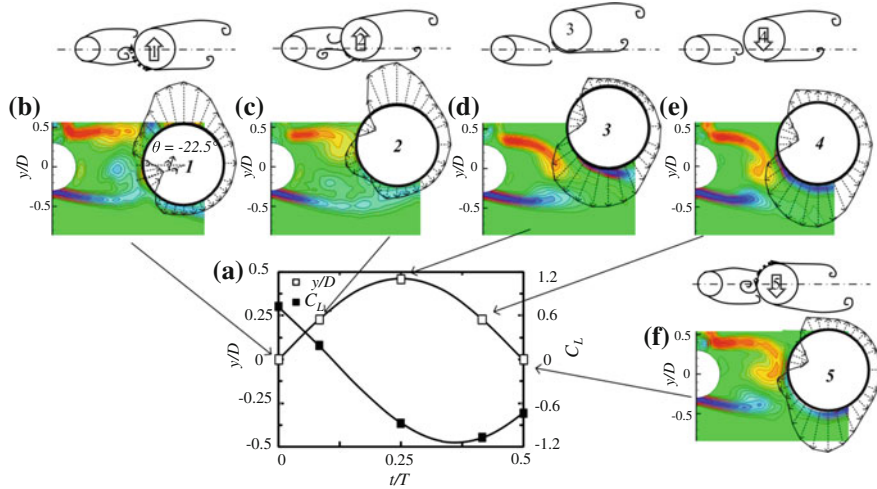
Fig. 4 **a** Cylinder displacement y/D and lift force coefficient C_L in half cycle of the oscillation, **b–f** phase-averaged vorticity and pressure coefficient C_P at $L/d = 2.0$, $d/D = 0.4$, $A/D = 0.48$

lower side and the freestream flow generates stagnation pressure on the upper side (Fig. 4d, e). The cylinder thus accelerates downward.

3.4 Energy Transfer Between Flow and Cylinder

Figure 5 at a representative $d/D = 0.4$, $L/d = 2.0$ shows (i) how fluctuating lift coefficient C_{Lrms} and phase angle ϕ between lift force and displacement are dependent on Ur or A/D, and (ii) information on energy transfer W_f from the flow to the cylinder in one vibration cycle. Interestingly, the escalation in A/D is mainly caused by the increased C_{Lrms}, accompanied by a greater transfer of energy from the flow to the cylinder.

Fig. 5 Variations in ϕ (deg), A/D, C_{Lrms} and energy transfer W_f with U_r
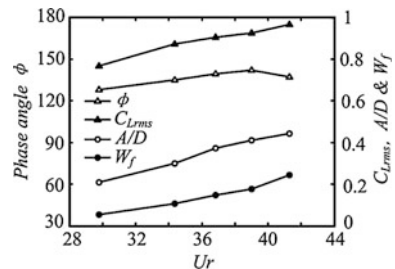
4   Conclusions

How the violent vibration of the cylinder is dependent on d/D and L/d is illustrated on a map in $d/D-L/d$ plane. A decrease in d/D corresponds to vibration for a longer range of L/d. The two shear layers of the upstream cylinder reattaching alternately on the downstream cylinder give rise to a large change in lift, sustaining the vibration. With U_r increasing, an increase in A/D is fed with a greater (additional) W_f. The additional W_f comes mainly from an increased lift amplitude, rather than from the phase lag between the lift and displacement.

References

Alam MM, Moriya M, Takai K, Sakamoto H (2003) Fluctuating fluid forces acting on two circular cylinders in a tandem arrangement at a subcritical reynolds number. J Wind Eng Indust Aerodyn 91:139–154

Assi GRS, Bearman P, Carmo BS, Meneghini JR, Sherwin SJ, Willden HJ (2013) The role of wake stiffness on the wake-induced vibration of the downstream cylinder of a tandem pair. J Fluids Struct 22:819–827

Kim S, Alam MM, Sakamoto H, Zhou Y (2009) Flow-induced vibrations of two circular cylinders in tandem arrangement, part 1: characteristics of vibration. J Wind Eng Ind Aerodyn 97:300–311

Experimental Study of a Spring-Mounted Wide-D-Section Cylinder in a Cross Flow

Qingyang Wang, Kun Song and Shengjin Xu

Abstract Vortex induced vibration (VIV) and galloping of a spring-mounted cylinder with wide-D-section in a cross flow is experimentally investigated. The focus is on the correlation between the vortex structures and the cylinder vibration. It is found that the present wide-D cylinder has a low critical velocity of the occurrence of the galloping, which is lower than that of resonance induced by vortex shedding. A symmetrical vortex structure is found at some time, which results in a slightly drop in lift as well as in vibration amplitude. This finding is useful for developing a mathematical model of flow loadings on the wide-D cylinder.

Keywords Vortex induced vibration · Wide-D-section cylinder · Galloping

1 Introduction

The interaction of fluid and structures has been extensively studied for decades due to its importance in engineering. Those studies mainly concentrated on the vibration, galloping and vortex shedding of the cylinder with simple shape such as circular cylinders (e.g. Feng 1968; Goswami et al. 1993; Govardhan and Williamson 2000; Morse and Williamson 2010, Païdoussis et al. 2011 etc.) or rectangular cylinders (e.g. Bearman and Obasaju ; Amandolèse and Hémon 2010; Mannini et al. 2014, etc.). The advantage of studying the simplest shape is easy to understand physics of flow induced vibration (FIV). Nevertheless, some cylinders with complex shapes are also interesting because there may be potential applications for flow and vibration control. In this paper, the FIV of a wide-D-section cylinder is studied in a wind tunnel. The correlation between the cylinder vibration and vortex structures in the wake is especially concerned. The final aim of the work is to find a precise mathematical model and a control method for the type of cylinders with such shape.

Q. Wang · K. Song · S. Xu (✉)
School of Aerospace Engineering, Tsinghua University, Beijing, China
e-mail: xu_shengjin@tsinghua.edu.cn

2 Experimental Details

The experiment was conducted in a low-speed wind tunnel with a square working section 0.5 m × 0.5 m × 2 m. The testing velocity U_0 range was 1.9–7.0 m/s. The wide-D-section cylinder was horizontally mounted in the middle of the working section with two pairs of springs. The cylinder in the wind vibrates only in the vertical direction (Fig. 1a). The height D of the cylinder is 0.03 m, the width B is 0.045 m and the length L is 0.46 m (width to height ratio $B/D = 1.5$). The flat surface of cylinder was faced to the free flow. The blockage is about 5.5 %. The mass ratio m^*, according to the definition given by Blevins (1990), is 962, the damping ratio ζ is 0.0006 and the structural natural frequency f_n is 11.4 Hz. Both the natural frequency and the damping ratio were measured in the still air. The Strouhal number $St = f_s D/U_0$ (where f_s is the natural vortex shedding frequency for the stationary wide-D cylinder) is 0.087 at the current Reynolds range. The reduced velocity $U_r = U_0/f_n D$ is from 5.56 to 20.47. The Reynolds number Re defined by D is from 3800 to 14,000. The vibration was simultaneously measured using a Laser vibrometer and an accelerator sensor. The vortex shedding frequency and vortex structures were measured using a hot wire and PIV, respectively. For the
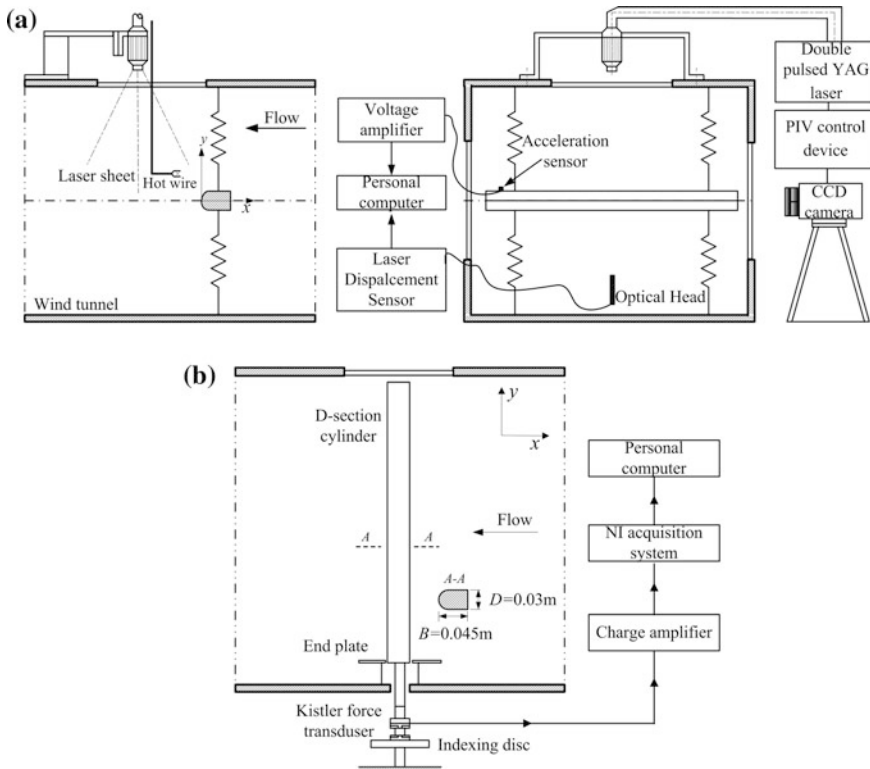

Fig. 1 Experimental setup: **a** PIV and hot wire measurements, **b** lift and drag measurements

stationary case, forces including lift and drag were measured using a Kistler 9317B transducer. Sampling frequency in all measurements was more than 1 kHz and the duration time was more than 20 s.

3 Results and Discussion

The vibration of the wide-D cylinder is presented in Fig. 2a. The data of a circular cylinder and a square cylinder are also included. For the circular cylinder and square cylinder, the resonance induced by vortex shedding occurs at $U_r \approx 5.4$ and 8.6, respectively. For the square cylinder, the galloping occurs at $U_r \approx 25$. Different from the square cylinder, the wide-D cylinder galloping occurs at a very low U_r, i.e., $U_{gr} \approx 3.99$, which is much less than the vortex-resonance of $U_r \approx 11.49$. For $U_r > 11.49$, the amplitude of the vibration increases rapidly, e.g., the amplitude is 8 times as that of the resonance amplitude at $U_r = 20$. Here, the galloping threshold U_{gr} is obtained according to Blevins's book (1990)

$$U_{gr} = 2Sc / \frac{\partial C_y}{\partial \alpha} |_{\alpha=0} \tag{3.1}$$

where $Sc = 4\pi m^* \zeta$, is the Scruton number. C_y is the force coefficient in the transverse direction, can be calculated by $C_y(\alpha) = -C_L(\alpha) \cos \alpha - C_D(\alpha) \sin \alpha$. C_L and C_D are lift and drag coefficient of the wide-D cylinder (Fig. 3). The vortex shedding frequency is locked both on the natural frequency f_n and the harmonic frequency 2 f_n of the wide-D cylinder (Fig. 2b).
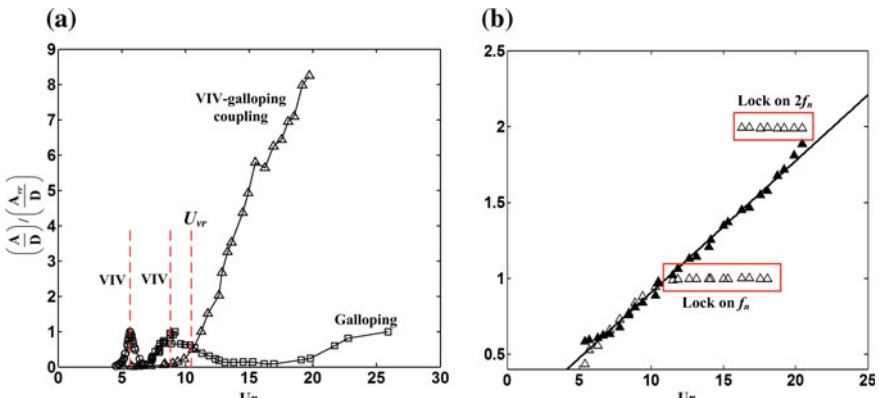

Fig. 2 Vibration of the wide-D cylinder in the flow: **a** The vibration amplitude $((\frac{A}{D})/(\frac{A_{vr}}{D}))$, ○ circular cylinder (Feng 1963), □ square cylinder (Amandolèse and Hémon 2010), △ wide-D-section cylinder, **b** Frequency ratio (f_s/f_n), △ for vibration case, ▲ for fixed case
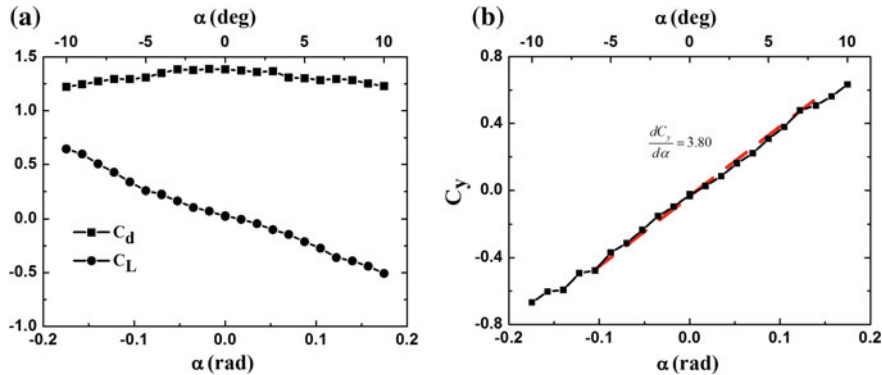
Fig. 3 **a** The mean C_L and the mean C_D; and **b** C_y for different incidence angle ($-10°$ to $+10°$) at $Re = 14000$
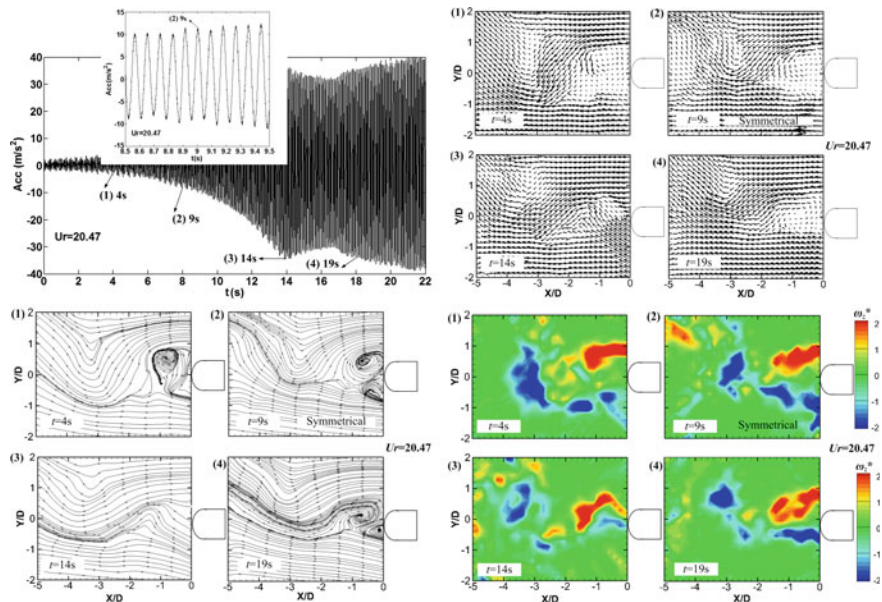

Fig. 4 Cylinder vibration response and instantaneous flow structure at specific time behind the transition vibration cylinder at $U_r = 20.47$

To understand the interaction between vortex shedding and cylinder vibration during the galloping, the time history of vibration is recorded by an accelerator. Meanwhile, the instantaneous vortex structure behind the cylinder is recorded using PIV at specified time interval (Fig. 4). The two kinds of vortex structures, say, alternative mode and symmetrical mode are presented behind the wide-D cylinder. For example, a pair of vortices present symmetrically at the both sides of the cylinder at 9 s but alternately at other time at $U_r = 20.47$. The symmetrical vortex

shedding gives a discount force on the cylinder. At the point of 9 s, the vibration amplitude drops slightly compared with the neighboring points. That illustrates the lift is slightly cut down because of the presence of the symmetrical vortex mode.

4   Conclusions

The present wide-D cylinder has a low critical reduced velocity for galloping, $U_{gr} \approx 3.99$. The resonance induced by vortex shedding occurs after the galloping. The vortex structure behind the cylinder is largely staggered as the Karman Vortex Street. However, the symmetrical vortex structure is also found behind the cylinder. The symmetrical vortex structure causes a drop on the lift, which results in a slight drop on the vibration amplitude. The finding is significant for developing a mathematical model better than the quasi-steady theory for flow loadings on the wide-D cylinder.

References

Amandolèse X, Hémon P (2010) Vortex-induced vibration of a square cylinder in wind tunnel. Comptes Rendus Mécanique 338(1):12–17

Bearman PW, Obasaju ED (1982) An experimental study of pressure fluctuations on fixed and oscillating square-section cylinders. J Fluid Mech 119:297–321

Blevins RD (1990) Flow-induced vibration. Van Nostrand Reinhold Co, New York

Feng CC (1968) The measurement of vortex induced effects in flow past stationary and oscillating circular and d-section cylinders. Master's Thesis, Department of Mechanical Engineering. The University of British Columbia, Canada

Goswami I, Scanlan RH, Jones NP (1993) Vortex-induced vibration of circular cylinders. I: experimental data. J Eng Mech 119(11):2270–2287

Govardhan R, Williamson CHK (2000) Modes of vortex formation and frequency response of a freely vibrating cylinder. J Fluid Mech 420:85–130

Mannini C, Marra AM, Bartoli G (2014) VIV–galloping instability of rectangular cylinders: review and new experiments. J Wind Eng Ind Aerodyn 132:109–124

Morse TL, Williamson CHK (2010) Steady, unsteady and transient vortex-induced vibration predicted using controlled motion data. J Fluid Mech 649:429–451

Païdoussis MP, Price SJ, De Langre E (2011) Fluid-structure interactions: cross-flow-induced Instabilities. Cambridge University Press, Cambridge

Vortex-Induced Vibration Marine Current Energy Harvesting

Brad Stappenbelt, Andrew Dennis Johnstone and Jesse Dylan Lima Anger

Abstract Limited research examining the optimal power take-off conditions for harnessing marine current energy using vortex-induced vibrations (VIV) has been undertaken to date. The studies that have been conducted have focused on translating cylinder VIV. This paper presents the results of an investigation of the effectiveness of energy extraction from pivoted cylinder systems undergoing vortex induced vibrations. The main goal of the present study was to observe the response of cylinders with a single roll rotational degree of freedom under a range of power take-off (PTO) damping values to determine the optimal power extraction rates achievable. At PTO damping values below optimal, there appears to be little change in the lock-in point and lower response branch amplitude response. This has important consequences for low Reynolds number PTO which is one of the primary advantages in utilising vortex-induced vibration for marine current energy harvesting.

Keywords Vortex-induced vibration · Power take-off · Damping · Energy · Marine current · Lock-in

1 Introduction

The use of flow-induced vibration for marine current and tidal flow energy extraction has a number of advantages over the traditional turbine based methods currently employed. As fewer moving parts are required, system complexity and as a consequence reliability are likely to be improved (Johnstone and Stappenbelt 2014).

B. Stappenbelt (✉)
Faculty of Engineering, University of Wollongong, Wollongong, Australia
e-mail: brads@uow.edu.au

A.D. Johnstone · J.D.L. Anger
School of Mechanical, Materials and Mechatronic Engineering, University of Wollongong, Wollongong, Australia

It is also possible to design an axi-symmetric energy harvesting system using the VIV motions of a circular cylindrical device which functions independent of current flow direction. Potentially the greatest advantage of utilising VIV for marine current energy harvesting is the ability to extract energy at very low flow velocities (Johnstone and Stappenbelt 2014). When viewed in light of the ability to design the system to experience an infinite resonance response region (Stappenbelt and Johnstone 2013) by control of the parameters governing the critical point (e.g. the mass or moment ratios for translating and pivoted cylinders respectively), the range of flow velocities over which a VIV dependent device can potentially operate is very large compared to a turbine. The primary drawback, as demonstrated in the translating cylinder VIV power studies by Bernitsas and Raghavan (2008), are the relatively low conversion efficiencies achievable.

There has been very limited experimental research into the amount of energy that can be harnessed from VIV. A dearth in this field is particularly evident for pivoted cylinders. The authors have previously proposed (Stappenbelt and Johnstone 2014) that a pivoted system has significant inherent advantages over a translating system since the force moment and mass moment of inertia parameters may be somewhat independently manipulated to tune the device to the Strouhal frequency whist simultaneously ensuring the system is operating within the infinite resonance regime (i.e. below the critical VIV point). The present work therefore investigates the effectiveness of energy extraction from pivoted cylinder systems undergoing vortex induced vibrations.

2 Experimental Methodology

The experimental study was conducted utilising the University of Wollongong Fluids Laboratory wave tank. The length of the tank is 32.5 m with a 1 m × 1 m cross-section. The tank is fitted with a rail and carriage system that is used to tow models at velocities up to 1.24 m/s. Smooth carbon fibre cylinder test sections were used in the study. These were suspended from a roller bearing pivot attached to the towing carriage. The experimental apparatus restricted all but the roll rotational degree of freedom.

Power take-off damping was introduced by designing the cylinder motions to traverse strong magnets past a thick, fixed aluminium plate. The level of damping the magnet-plate air gap. The natural was controlled by the number of magnets and by varying frequency, force moment and mass moment of inertia ratios were controlled by the placement of springs offset from the pivot point and by the addition of lump masses inside the cylinder. The system response was measured using two laser displacement sensors. The experimental apparatus sketch and key parameter values are included in Fig. 1 and Table 1 respectively. The power take-off was determined using the instantaneous cylinder angular velocity and measured damping torque.
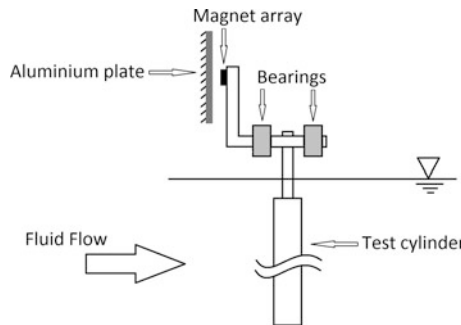
Fig. 1 Elevation sketch of the experimental apparatus

Table 1 Experimental parameter values

Parameter	Symbol	Value	Units
Cylinder diameter	D	0.033	m
Cylinder length	L	0.825	m
Moment ratio	M*	0.810	–
Inertia ratio	I*	1.620	–
System stiffness	k_θ	9.465	Nm/rad
Still water natural frequency	f_{nw1}	0.470	Hz

3 Results

A sample of the amplitude response plots at various PTO damping values is presented in Fig. 2. As expected, the amplitude response of the system showed a consistent decrease with increasing PTO damping. The lock-in region however was relatively unaffected by the level of damping present in the system with the exception of a small shift in lock-in observed at higher damping.

It was also evident that the upper response branch transitioned to the lower response branch at higher reduced velocity with increased damping ratios. The distinction between upper and lower response branches response amplitudes also coalesced with increased PTO damping.

The power take-off results from the present study are presented in Figs. 3 and 4. The power extracted is normalised by the free stream flow power present in the swept frontal projected area of the cylinder. This is of course a measure of the efficiency of the power conversion process. As expected, there exists an optimal PTO damping corresponding to the maximum power take-off and maximum power conversion efficiency. This is clearly evident from the plot of the PTO maxima in Fig. 5.
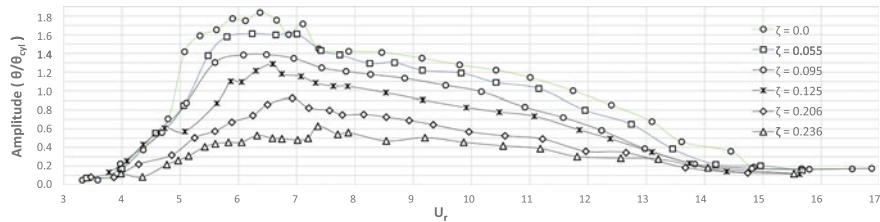
**Fig. 2** Amplitude Response for damping ratios $\zeta = 0.028 - 0.236$
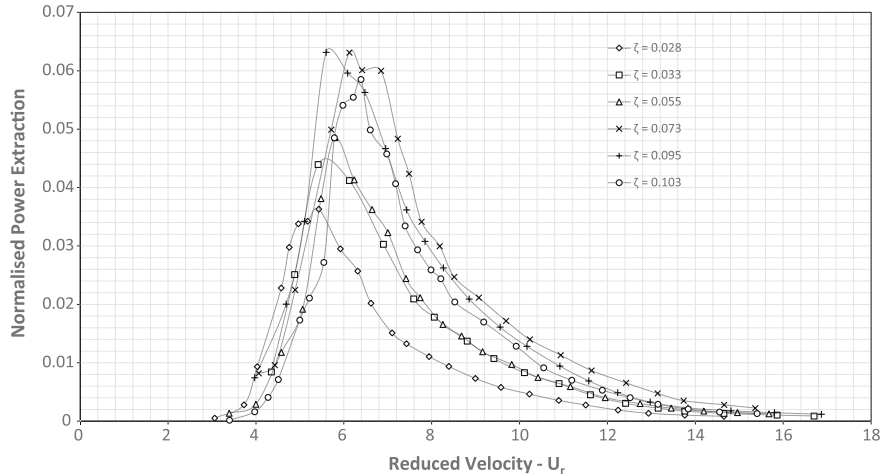
**Fig. 3** Normalised power extraction for PTO damping ratios $\zeta = 0.028 - 0.103$
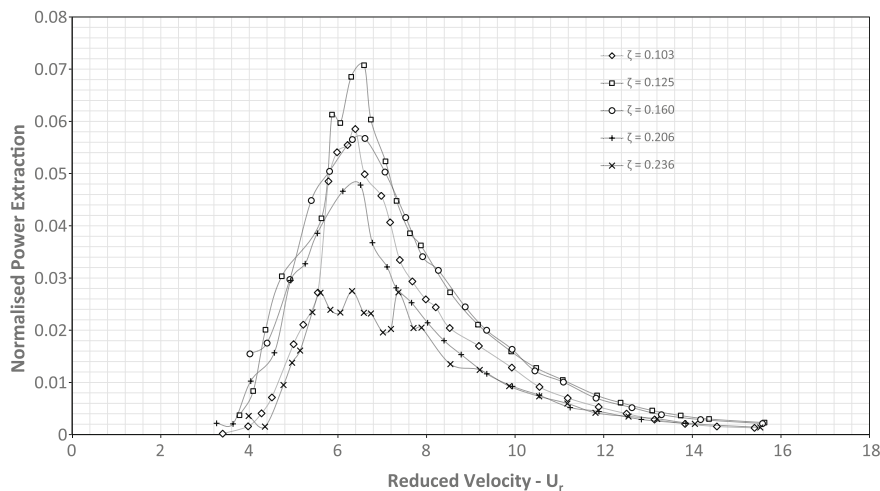
Fig. 4 Normalised power extraction for PTO damping ratios $\zeta = 0.103 - 0.236$

The plotted curve follows $y = 10.235x^3 - 7.2096x^2 + 1.2471x + 0.0027$ with $R^2 = 0.9589$.
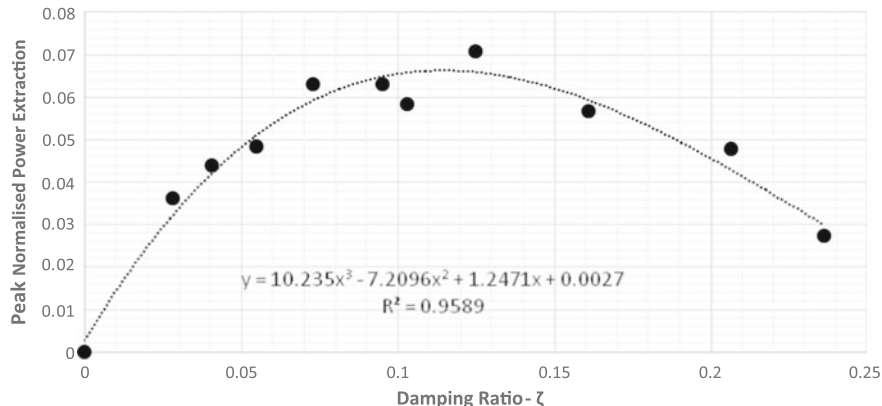
Fig. 5 Peak normalised power vs Damping ratio

4 Conclusions

The results in the present study indicate that the optimal damping for VIV energy extraction using a pivoted circular-cylinder arrangement occurs at approximately 12 % of the critical damping. This agrees remarkably well with study by Lee and Bernitsas (2011) which, despite using translating cylinders, also reported 12 % as the optimal PTO damping ratio.

The maximum power conversion efficiency in the present study is approximately 7 %. It is difficult to compare this value directly with the work by Lee and Bernitsas (2011) since their study was conducted using an array of cylinders. The values do however correspond reasonably well with their reported maximum of 8 %. These values are low relative to non-renewable and other renewable energy conversion processes, even when considered in light of the Betz theoretical limit, and would necessitate a larger device or array of devices for equivalent turbine power production.

The onset reduced velocity of the transverse VIV does not appear to be severely affected by the level of PTO damping present until the system is operating at well above optimal damping. The ability to extract energy from low Reynolds number flow is one of the primary benefits of VIV marine current energy harvesting since energy is available at flow velocities where traditional turbines struggle with low Reynolds number hydrofoil performance issues Bahaj et al. (2007). The observation that there is no significant shift in lock-in therefore has significant implication for the viability of VIV energy extraction.

References

Bahaj AS, Molland AF, Chaplin JR, Batten WMJ (2007) Power and thrust measurements of marine current turbines under various hydrodynamic flow conditions in a cavitation tunnel and a towing tank. Renew Energy 32:407–426

Bernitsas M, Raghavan K (2008) VIVACE (Vortex Induced Vibrations Aquatic Clean Energy): a new concept in generation of clean and renewable energy from fluid flow. J Offshore Mech Arct Eng 130(4)

Johnstone A, Stappenbelt B (2014) Energy capture optimisation of 1-degree-of-freedom pivoted rigid cylinders undergoing flow-induced vibration in cross-flows. In: Proceedings of the 19th Australasian fluid mechanics conference, Melbourne, Australia

Lee JH, Bernitsas MM (2011) High-damping, high-Reynolds VIV tests for energy harnessing using the VIVACE converter. Ocean Eng 38(16):1697

Stappenbelt B, Johnstone A (2013) The critical point in the vortex induced vibration of a pivoted cylinder. Int J Offshore Polar Eng 23(3):205–209

Stappenbelt B, Johnstone A (2014) Reynolds number influence on the vortex-induced vibration critical point of a pivoted cylinder. In: Proceedings of the 19th Australasian fluid mechanics conference, Melbourne, Australia

Simulations of Fluid-Structure Interaction of a Wind Turbine

S. Zheng, L.P. Chua and Y. Zhao

Abstract The numerical simulations of fluid-structure interaction (FSI) of horizontal axis wind turbine in whole flow field are presented. The 5 kW wind turbine 3D model is designed according to blade element momentum (BEM) method. The simulations are carried out in Ansys using one way steady FSI by coupling CFX with Static Structure with total 7×10^6 tetrahedron unstructured meshes. The k-ω SST turbulent model is employed in CFX to precisely capture the flow field variation under different wind speeds. As wind speed increases from 7 to 16 m/s the power coefficient varies from 0.47 to 0.21 and the moment coefficient change from 4.3×10^{-2} to 8.2×10^{-2}. The frequency of 1st flapwise will increase slightly as rpm goes up. The frequency of 1st edgewise is little higher than the 1st flapwise and not affected so much by the increasement of rotor rpm. Potential spots of resonance is near around rpm150.

1 Introduction

There are three main loads applied on wind turbine blade: gravitational, inertial and aerodynamic loads. Each wind turbine blade will experience the integration of all the three loads (Hansen 2008). The FSI of wind turbine blade will affect the power efficiency, stability and life span of wind turbine. Although the FSI effect is very important to wind turbine design and operation, it is very difficult to carry out the analysis for such effect. Wind turbine rotors often operate at large angles of attack,

S. Zheng · L.P. Chua (✉)
School of Mechanical and Aerospace Engineering, Nanyang Technological University, 50 Nanyang Avenue, Singapore 639798, Singapore
e-mail: mlpchua@ntu.edu.sg

Y. Zhao
Mechanical Engineering/College of Engineering, Alfaisal University, Riyadh 11533-50926, Kingdom of Saudi Arabia
e-mail: zyong@alfaisal.edu

which results in strong and large-scale flow separation. Under such conditions, leading-edge vortices grow and subsequently shed into the near wake region. The flow field simultaneously contains laminar, transition and multiple turbulent flow regimes. The flow around wind turbine blades as well as in the wake region include different scale of eddy from the smallest turbulent eddies to the length of the blades. The blades interact nonlinearly with the complex air flow, exhibiting flapwise and edgewise deformation adding complexity to the overall problem. All of these complexities make aerodynamic load and FSI calculations difficult, especially for three dimensional calculations. The crucial point of an accurate simulation of wind turbine FSI by CFD method is to precisely predict the flow separation location and capture different scales of turbulent eddies under high Reynolds number (Anderson 2009) in order to get the accurate steady deformation. The comparison of using k-ω SST turbulent model to predict the flow field based on the NREL phase VI experiment shows a good agreement between the simulation results and the experimental results in a wide range of which the wind turbine is experiencing from low angle of attack to stall working condition (Sørensen et al. 2004). The present study is thus using the k-ω SST turbulent model to carry out a steady CFD simulation to obtain the total deformation which has important impact on the power coefficient and rotor blade natural frequency.

2 Wind Turbine 3D Model

The configuration is a 5 kW horizontal axis wind turbine (HAWT) with tip speed ratio 6. The S-series airfoils are dedicated designed for modern high speed HAWT by the academic institution of NREL which achieves low drag and has a maximized lift coefficient with low sensitiveness to surface roughness. According to the recommendation of (Tangler and Somers 1996), the airfoil S823 deploys from root to the location $r/R = 0.30$ (where r is radial position from the root of wind turbine blade, R is the length of blade) and the S822 from location $r/R = 0.30$ to tip respectively. The chord and twist angle of each wind turbine blade elements are shown in Figs. 1 and 2 respectively according to the results using Wilson and Lissaman design method (Manwell et al. 2002). This is an improved BEM method which not only introduces the axial and rotational factors but also includes the tip and hub loss factors.

3 FSI Simulation Configuration

The k-ω SST turbulent model is a hybrid model using a k-ω model in the near wall region which provide excellent performance for the zero and adverse gradient pressure turbulent boundary layer and then transfers to k-ε model in a fully developed turbulent region far away from the wall (Versteeg and Malalasekera 2007).

Fig. 1 Twist angle
distribution
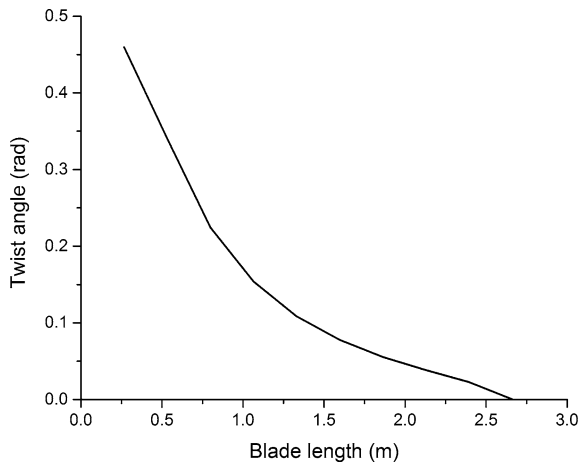
**Fig. 2** Chord length
distribution
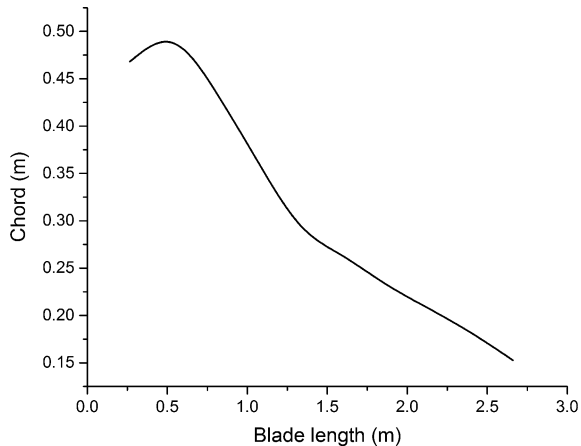
In the near wall region the k-ω model always requires fine mesh to obtain the velocity gradient as the wall treatment is employed. To obtain a comprehensive analysis of the flow in the viscous sub-layer the first grid of the mesh layer is supported to place in the near wall region where $y^+ < 5$. The NASA y^+ calculator is used to get the thickness of the first mesh layer. For structure domain, the refine unstructured mesh near the leading and trailing edges are used due to the high curvature surface. The meshes for flow domain and structure domain are shown in Figs. 3 and 4 respectively.

The shape of the whole flow domain is a cylinder which is 10 time of rotor radius in length and 4 times of rotor radius in radial direction. The wind turbine rotor is placed at the location 3 rotor radii from inlet and the center line of the rotor is concentric with the cylinder domain. The minimum mesh size is 5×10^{-5}m and the total mesh amount is about 7 millions.
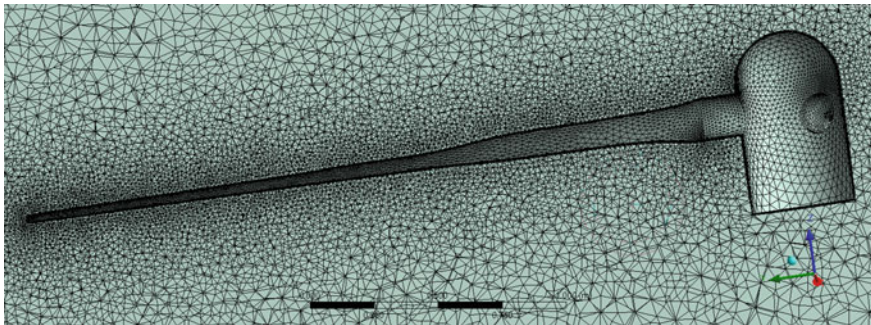
Fig. 3 Flow domain meshes
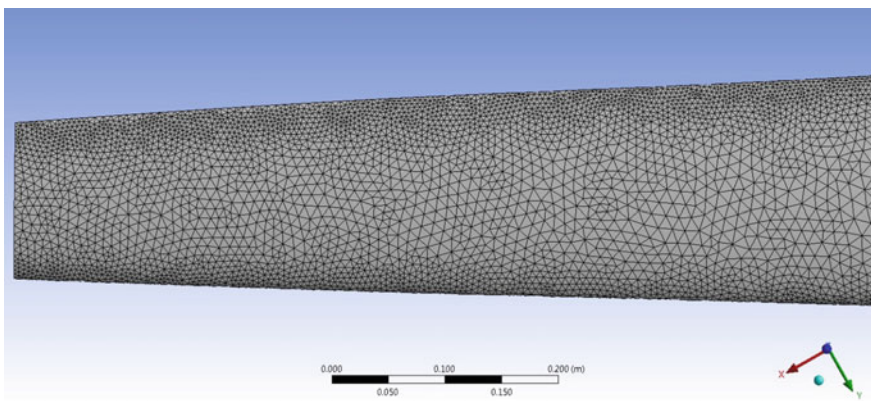
Fig. 4 Structure domain meshes

4 Results and Discussion

Figure 5a, b demonstrates the streamline generated from the suction surface of blade under two different wind speeds of 10 and 13 m/s respectively.

From the comparison of the streamline distributions of wind speeds tested, it is clear that in Fig. 5a most of the flow over the surface remain attached to the blade at wind speed of 10 m/s with the tip speed ratio is 6. However, when the wind speed is increasing from 10 and come to 13 m/s as shown in Fig. 5b, the flow separation begins to emerge. Wind speed increasing changes the relative wind speed direction which leads to large angle of attack. As angle of attack will result in an adverse pressure gradient on the blade surface in the chordwise direction which will cause the flow separation. Due to blade element twist angle distribution the separation should firstly occur near the root region. This expected phenomenon is observed in
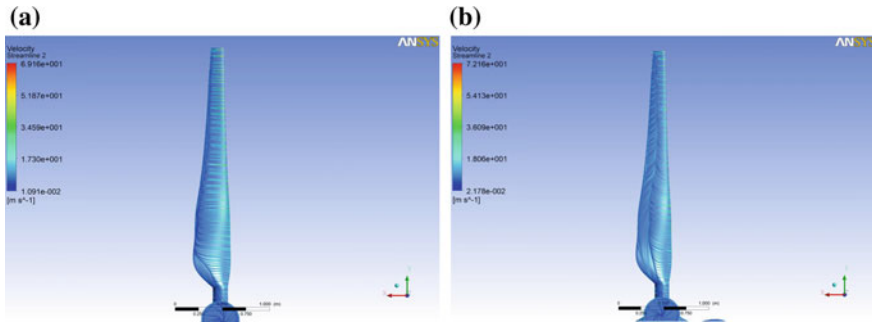
Fig. 5 Suction surface streamline under Wind speed **a** 10 m/s and **b** 13 m/s

the Fig. 5b. A radial direction flow in the flow separation zone emerges near the root region as a result of shedding eddy under the effect of centrifugal force.

The power coefficient and moment coefficient variations with wind are illustrated in Fig. 6a, b respectively. The Fig. 6a demonstrate that the power coefficient will increase to a maximum value of 0.47 as wind speed is reaching 10 m/s and the designed tip speed ratio of 6 is achieved. After the optimal wind speed, the power coefficient begins to drop as wind speed continuously increases to 16 m/s. The precipitous drop in coefficient is happening because the wind turbine has been in a stall condition and the flow separation occurs on the blade surface. Flow separation will dramatically affect the pressure distribution around the blade which will lead to the huge drop in lift force and vast increase in drag force. Figure 6b shows the Moment coefficient will increase to a maximum value of 8.4×10^{-2} as wind speed is reaching 11 m/s, then the moment coefficient begin to slightly drop and keep almost constant as wind speed continus to increase to 16 m/s. This phenomeno is caused by the integrated impact of the wind speed, the position of aerodynamic center and the flow separation. The resonance diagram of rotor blade under flow induced deformation are shown in Fig. 7a, b respectively. The figures show that the frequency of 1st flapwise increase slightly because the increase of the rotor rpm
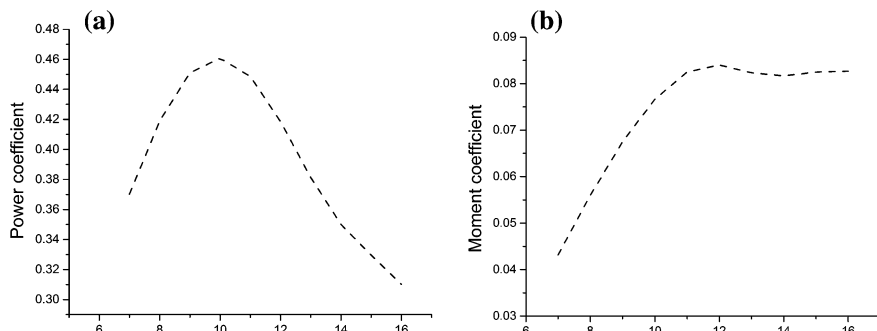

Fig. 6 a Power coefficient, **b** moment coefficient under different wind speed
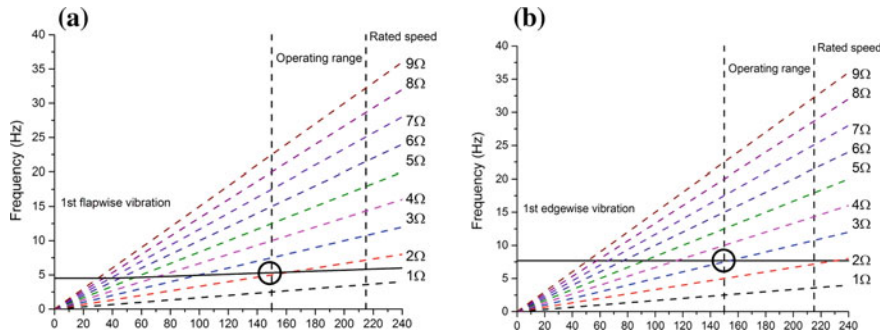
Fig. 7 Resonance diagram of rotor blade under flow induced deformation **a** 1st flapwise vibration **b** 1st edgewise vibration

cause the the increasement of centrifugal force which will influence the effective stiffness of rotor blade. The frequency of 1st edgewise is little higher than the 1st flapwise and not affected so much by the increasement of rotor rpm because the flapwise is the least stiff direction of the blade and the edgewise has higher stiffness compare to flapwise. Potential spots of resonance which are marked with circles shows that the wind turbine blade will experience a resonance near the rpm 150 under 2 and 3Ω excitation These two spots suggest that the long term operating of the wind turbine near this rpm should be avoided.

5　Conclusions

1. The k-ω SST turbulent model is suitable for whole flow field wind turbine FSI analysis and can precisely capture the detailed information in turbulent boundary.
2. The maximum value of power coefficient and moment coefficient is 0.47 and 0.084 respectively.
3. The frequency of 1st flapwise will increase slightly as rpm goes up. Long term operating near rpm 150 should be avoided.

References

Anderson JDJ (2009) Fundamentals of aerodynamics, 5th edn. McGraw, New York

Hansen MOL (2008) Aerodynamics of wind turbines, 2nd edn. Earthscan, London

Manwell JF, McGowan JG, Rogers AL (2002) Wind energy explained: theory, design and application, 1st edn. Wiley, New York

Sørensen NN, Michelsen JA, Schreck S (2004) Navier-stokes prediction of the NREL phase VI rotor in the NASA ames 80-by-120 wind tunnel. Wind Energy 28:275–290

Tangler JL, Somers DM (1996) NREL airfoil families for HAWTs. National Renewable Energy Laboratory, Golden

Versteeg HK, Malalasekera W (2007) An introduction to computational fluid dynamics: the finite volume method, 2nd edn. Prentice Hall, Harlow

Vortex Shedding Intermittency and Its Effects on the Aerodynamics Forces of a Finite-Length Square Cylinder

H.F. Wang, C. Zou and Y.P. Zhang

Abstract The aerodynamic forces on a wall-mounted finite-length square cylinder are experimentally investigated. The width of the tested model $d = 200$ mm, and the aspect ratio $H/d = 5$. The oncoming flow velocity $U_\infty = 13$ m/s, corresponding to a Reynolds number of 1.73×10^5 based on U_∞ and d. It is found that the time-averaged drag coefficient $\overline{C_D}$ and rms value of lift coefficient $C_L^{'}$ of the finite-length cylinder are both smaller than those of 2D square cylinder. Two typical flow modes occur in the flow around the finite-length cylinder: Mode 1 is characterized by alternating spanwise vortex shedding, corresponding to a higher drag and large amplitude fluctuation of lift; Mode 2 is characterized by symmetrical vortex shedding, corresponding to a lower drag and the lift without periodic fluctuation. At the lower part of cylinder, $C_L^{'}$ of Mode 1 is about one times larger than that of Mode 2, this difference reduces gradually with approaching to the free end. The spanwise correlation of aerodynamic force is stronger in Mode 1.

1 Introduction

Finite-length cylinders with one end mounted on a flat wall and the other free are frequently encountered in engineering applications, such as chimneys, cooling towers and high-rise buildings. Under the effects of boundary layer on the wall and cylinder free end, the flow around a finite-length cylinder is highly three dimensional and drastically different from that of a 2D cylinder (Wang and Zhou 2009). In the finite-length cylinder wake, there is a pair of streamwise vortices near the free end, i.e. tip vortices, which induces strong downwash flow. There will be a pair of

H.F. Wang (✉) · C. Zou · Y.P. Zhang
School of Civil Engineering, Central South University, Changsha, Hunan, China
e-mail: wanghf@csu.edu.cn

base vortices, if the thickness on the boundary layer is large enough, which results in an upwash flow in the cylinder near wake (Summer et al. 2004; Wang et al. 2006). Under the effects of both tip vortices and base vortices, the spanwise vortices in the finite-length cylinder wake are weakened relative to those in 2D cylinder wake. Furthermore, the width of the near wake of finite-length cylinder is larger and its vortex shedding frequency is lower relative to that of 2D cylinder (Wang and Zhou 2009).

Both the time-averaged drag coefficient $\overline{C_D}$ and fluctuation lift coefficient C_L' of finite-length cylinder are significantly smaller than those of 2D cylinder (Fox and West 1993). Moreover, the $\overline{C_D}$ reduces gradually with decreasing cylinder aspect ratio, H/d, where H is the cylinder height and d is its characteristic width (Okamoto and Sunabashiri 1992). Since the flow around a finite-length cylinder is high three dimensional, the aerodynamics on it are different at various spanwise positions.

Two typical instantaneous flow modes can be identified in the near wake of a finite-length cylinder based on its near wake experimental results for a finite-length square cylinder with $H/d = 4$ and 7 (Wang and Zhou 2009; Bourgeois et al. 2011). Mode 1 is characterized by alternating larger scale spanwise vortices, similar to that in 2D cylinder wake; on the other hand, Mode 2 is dominated by symmetrical spanwise vortices. The two typical modes occur randomly, which must have significant effects on the aerodyanmics forces on the finite-length cylinder.

2 Experimental Details

Experiments were conducted in a closed-loop wind tunnel in Central South University, with a low speed test section of 12 m (width) × 3.5 m (height) × 18 m (length) and a high speed test section of 3 m (width) × 3 m (height) × 15 m (length), respectively. The present experiments were performed in the high speed section.

A finite-length square cylinder with $d = 200$ mm and $H/d = 5$ was mounted on the wind tunnel bottom wall, as shown in Fig. 1a. The oncoming velocity $U_\infty = 13$ m/s, corresponding to $Re = 1.73 \times 10^5$. Pressure taps were arranged at four spanwise positions, i.e. $z^* = 1$, 2.5, 4 and 4.5. The superscript '*' in the present paper indicates normalization with U_∞ and d. All pressure taps were connected to a pressure scanner. For each tap, 20,000 instantaneous samples were measuremed at a frequency of 625 Hz. Measurements were also conducted for a 2D square cylinder at the same Re for comparison. The boundary layer was documented with a Cobra probe prior to the installation of cylinder. As shown in Fig. 1b, the thickness of boundary layer on the wind tunnel wall is about 200 mm, that is most of the tested cylinder is in uniform oncoming flow, except $z^* < 1$.

The time-averaged pressure coefficient $\overline{C_p} = (\overline{P} - P_\infty)/0.5\rho U_\infty^2$, and the rms value of pressure coefficient $C_{p\_rms} = p_{rms}/0.5\rho U_\infty^2$, respectively. In which, $\overline{P}$ is the time-averaged pressure, p_{rms} is the rms value of fluctuation pressure, p_∞ is the static pressure in the wind tunnel.

(a)

(b)
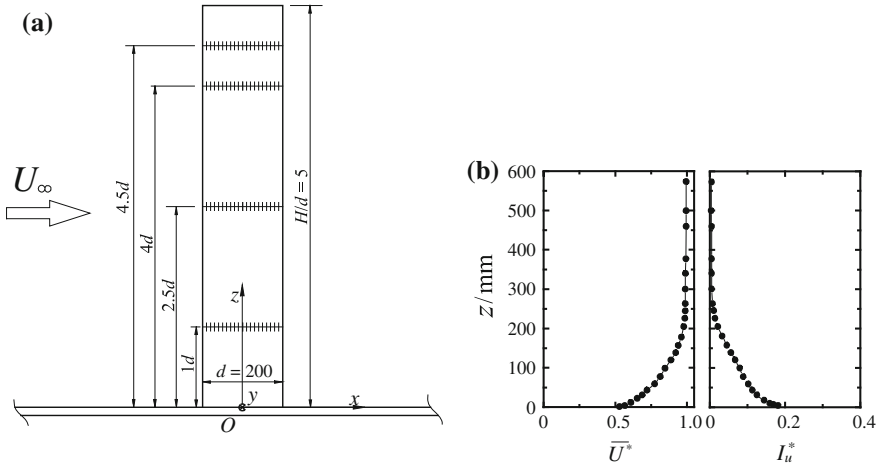
Fig. 1 Experimental setup (**a**) and boundary layer condition (**b**)

3 Results and Discussion

3.1 Time Averaged Results

Figure 2 presents the distribution of $\overline{C_p}$ and C_{p_rms} for both finite length and 2D square cylinder. It can be inferred from Fig. 2 that the $\overline{C_D}$ and C_L' of finite-length cylinder is smaller than those of 2D cylinder. At the windward face (A), $\overline{C_p}$ is quite similar at all spanwise positions, and in line with that of 2D cylinder. On the other hand, the $\overline{C_p}$ on the side faces (B and D) and the leeward face (C) is higher than those of 2D cyinder and quite different at various z^*, i.e., its absolute magnitude is relatively larger near cylinder free end.

For a 2D cylinder, the C_{p_rms} presents the its minimal value at the front stagnation point, and increases quickly with approaching to the side edges. The C_{p_rms} on faces B, D and C is siginificantly larger than that of the cylinder with $H/d = 5$, which may be ascribed to the fact that the spanwise vortex shedding is suppressed in finite-length cylinder wake. The C_{p_rms} at the lower part of the cylinder is relatively larger than that near the cylinder free end, suggesting the suppression of spanwise vortex is more remarkable near cylinder free end under the effects of tip vortices.

3.2 Instantaneous Results

Figure 3 presents the instantaneous C_D and C_L of the finite-length square cylinder and 2D one. The instantaneous pressure coefficients at the centers of both side faces
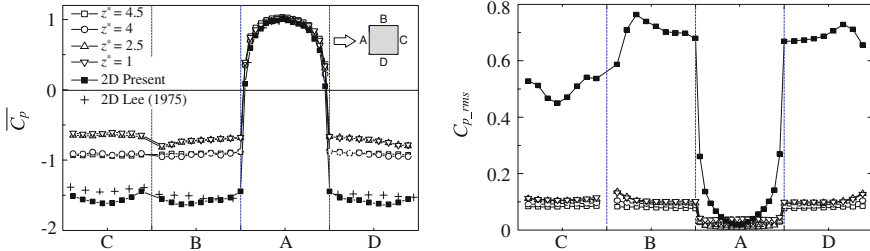
**Fig. 2** Distribution of $\overline{C_p}$ and C_{p_rms}
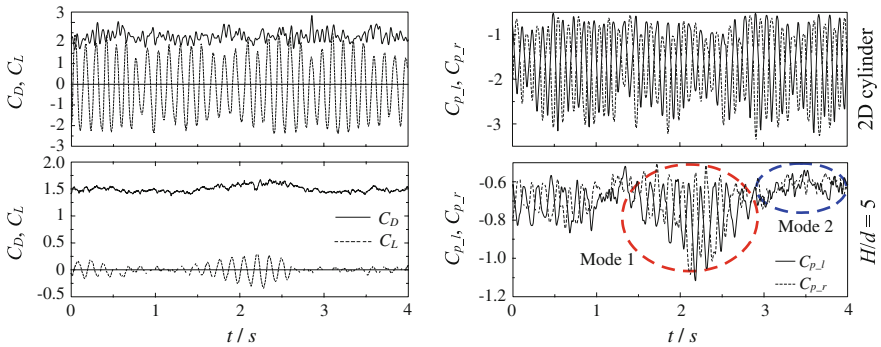
Fig. 3 Instantaneous C_D, C_L and C_p at the center of both side faces

at cylinder midspan, i.e., C_{p_l} and C_{p_r}, are also shown. For the 2D cylinder, C_L presents continues periodic fluctuation, and C_D also fluctuates with a frequency of twice of that of C_L. For the cylinder with $H/d = 5$, the fluctuation of C_L is not continues. This observation should be ascribed to the intermittency of antisymmetrical spanwise vortex shedding, in line with the randomly occurred two typical modes in finite-length cylinder wake (Wang and Zhou 2009; Bourgeois et al. 2011). When antisymmetrical spanwise vortices (Mode 1) occurs, C_L presents periodic fluctuation and the corresponding C_D is relatively larger (1.5–2.5 s); on the other hand, when symmetrical vortices (Mode 2) occurs, C_L has no clear periodicity (2.7–3.5 s). For the 2D cylinder, C_{p_l} and C_{p_r} always are opposite in phase and bear large amplitude fluctuation. For the cylinder with $H/d = 5$, C_{p_l} and C_{p_r} are opposite in phase and fluctuate periodicly when Mode 1 occurs, similar to that for 2D cylinder. On the other hand, C_{p_l} and C_{p_r} do not fluctuate periodicly and have no clear phase relation when Mode 2 occurs, as shown in Fig. 3.
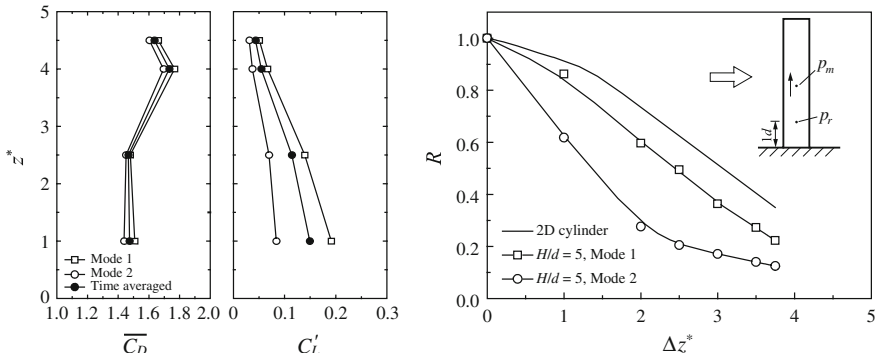
Fig. 4 Conditional averaged $\overline{C_D}$, $C_L^{'}$ and spanwise correlation

3.3 Conditional Averaged Results

In following analysis, we defined the C_L with fluctuation amplitude larger than $1.1\,C_L^{'}$ as Mode 1, otherwise as Mode 2. This criteria was visually chosen so that most large amplitude fluctuation in C_L can be identified as Mode 1. Figure 4 gives the conditional averaged $\overline{C_D}$ and $C_L^{'}$ and also spanwise correlation coefficient R of fluctuation pressure. As shown in Fig. 4, $\overline{C_D}$ of the two typical modes are quite similar, though $\overline{C_D}$ of Mode 1 is slightly larger than that of Mode 2. On the other hand, the difference of $C_L^{'}$ between the two modes is much more significant, especially at the lower part of cylinder. At $z^* = 1$, 2.5, 4 and 4.5, $C_L^{'}$ of Mode 1 is 138, 98, 81 and 65 % larger than that of Mode 2. Under the effects of tip vortices, the difference of $C_L^{'}$ between the two modes reduces gradually with free end approached.

It is also interesting to examine the spanwise correlation of the aerodynamic forces. The reference point is fixed at $z^* = 1$, as shown in Fig. 4. The correlation coefficient R can be determined between the reference point and a moveable point along cylinder span. The spanwise correlation of Mode 1 is also much stronger than that of Mode 2, although both are obviously weaker than that of 2D cylinder.

4 Conclusions

For a finite-length square cylinder in smooth uniform flow, its aerodynamic forces are much smaller than those of 2D cylinder. Two typical modes exist in its near wake. When spanwise vortices are antisymmetrical, i.e. Mode 1, C_L presents large amplitude periodic fluctuation; when symmetrical vortices occur, i.e. Mode 2, C_L has no obvious periodicity and its fluctuation amplitude is limited. The spanwise

correlation of aerodynamic forces in Mode 1 is also significantly stronger than that in Mode 2. Under the effects of tip vortices near cylinder free end, the difference of aerodynamic forces between the two typical modes become less obvious with free end approached.

References

Bourgeois JA, Sattari P, Martinuzzi RJ (2011) Alternating half-loop shedding in the turbulent wake of a finite surface-mounted square cylinder with a thin boundary layer. Phy Fluid 23:095101

Fox TA, West GS (1993) Fluid induced loading of cantilevered circular cylinders in low turbulent uniform flow. Part 2: fluctuating loads with aspect ratios 4 to 25. J Fluid Struct 7:375–386

Okamoto T, Sunabashiri Y (1992) Vortex shedding from a circular cylinder of finite length placed on a ground plane. J Fluid Eng 114:512–521

Summer D, Heseltine JL, Dansereau OJP (2004) Wake structure of a finite circular cylinder of small aspect ratio. Exp Fluids 37:720–730

Wang HF, Zhou Y (2009) The finite-length square cylinder near wake. J Fluid Mech 638:453–490

Wang HF, Zhou Y, Chan CK, Lam KS (2006) Effect of initial conditions on interaction between a boundary layer and a wall-mounted finite-length-cylinder wake. Phy Fluids 18:065106

Wake and Vortex-Sheddings from Different Diameter Cylinders in Tandem

L.J. Wang, Md. Mahbub Alam and Y. Zhou

Abstract The paper associated with two tandem cylinders presents the upstream cylinder size (diameter d) effect on global parameters of the downstream cylinder (diameter D) including time-mean and fluctuating drag (C_D, C_D'), fluctuating lift (C_L'), Strouhal number (St), and flow structures at spacing ratio $L/d = 1.0$–8.0, and diameter ratio $d/D = 0.2$–1.0, where L is the distance between the center of the upstream cylinder and the forward stagnation point of the downstream cylinder. The Reynolds number is kept constant at 4.27×10^4 based on D. C_D, C_D' and C_L' are measured using a sectional load cell, flow structures are obtained using a PIV technique. The critical L/d dividing the reattachment and coshedding flows is larger at smaller d/D. In the coshedding regime, the shedding frequency of the downstream cylinder locks-in with that of the upstream cylinder for $d/D = 1.0$, 0.8 and 0.6, in addition to a subharmonic lock-in for $d/D = 0.6$. The lock-in however does not occur at $d/D = 0.4$ and 0.2. C_D in general increases with d/D. C_D' and C_L' both generally wane and grow as d/D decreases from 1.0 to 0.6 and 0.4 to 0.2, respectively.

Keywords Tandem cylinders · Strouhal number · Fluid forces · Flow structures

L.J. Wang · Md.M. Alam (✉) · Y. Zhou
Institute for Turbulence-Noise-Vibration Interaction and Control,
Shenzhen Graduate School, Harbin Institute of Technology, Shenzhen, China
e-mail: alamm28@yahoo.com; alam@hitsz.edu.cn

Md.M. Alam
Key Lab of Advanced Manufacturing Technology, School of Mechanical
Engineering and Automation, Shenzhen Graduate School,
Harbin Institute of Technology, Shenzhen, China

1   Introduction

Flow around two tandem cylinders of identical diameters is in general classified into three major regimes (Igarashi 1981, Zdravkovich 1987): (i) extended-body regime ($0.5 < L/d < 1.0$); (ii) reattachment regime ($1.0 < L/d < 3.5$); (iii) coshedding regime ($L/d > 3.5$). There is a transition L/d range between the reattachment and coshedding regimes, where both reattachment and coshedding flows appear intermittently, switching from one to the other, known as critical or bistable flow spacing (Xu and Zhou 2004, Sumner 2010). For a given downstream-cylinder cross section, a change in the cross section of the upstream cylinder, with the same characteristic width, results in a different frequency of vortex shedding from the upstream cylinder, and the frequency of vortex shedding from the downstream cylinder modifies accordingly to lock-in, adjusting itself to that of the upstream one (Alam et al. 2005; Alam and Zhou 2008). It was concluded that the hydrodynamic stability of the flow around two tandem cylinders is predominantly controlled by the upstream cylinder, not by the downstream cylinder. Investigations associated with different diameter cylinders are very scarce in the literature. The major objectives of this work are to examine (i) the effect of the upstream cylinder diameter on C_D, C_D', C_L', St and wake of the downstream cylinder at $L/d = 1.0$–8.0, covering all possible flow regimes, and (ii) how the critical L/d corresponding to transition between reattachment and coshedding flows is dependent on d/D.

2   Experimental Details

Experiments were performed in a closed-circuit wind tunnel, with a test section of 0.8 m (width) × 1.0 m (height) × 5.5 m (length). The downstream cylinder diameter D (= 40 mm) was kept fixed, and the upstream cylinder diameter d was changed as $d = 8, 16, 24, 32$ and 40 mm, resulting in diameter ratio $d/D = 0.2, 0.4, 0.6, 0.8$, and 1.0, respectively. The spacing ratio L/d between the cylinders was systematically varied from 1.0 to 8.0. The freestream velocity U was 16 m/s, corresponding to $Re = 4.27 \times 10^4$ based on D. Fluid forces acting on the downstream cylinder are measured using a sectional load cell (65 mm long) installed at the midsection of the cylinder (Fig. 1). Two single tungsten hotwires, placed in the gap between the cylinders and behind the downstream cylinder, respectively, were used to measure longitudinal velocity fluctuations u from which vortex shedding frequencies were extracted using FFT. PIV technique was used to investigate the flow structures in the gap and behind the downstream cylinder.
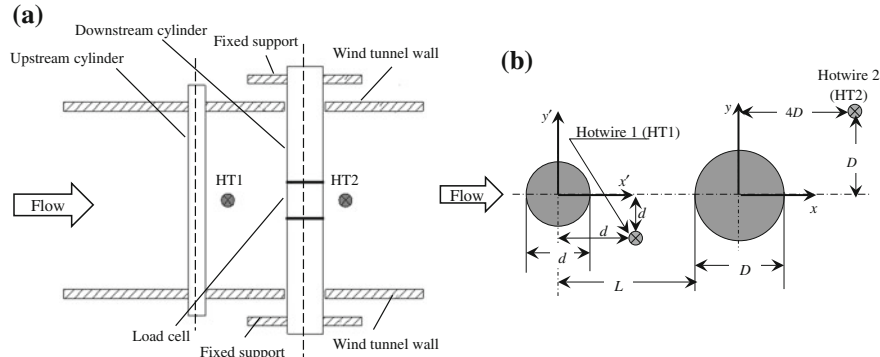
Fig. 1 **a** Experimental set-up, and **b** definitions of symbols

3 Results and Discussion

Figure 2 presents typical power spectral density functions of fluctuating velocities obtained in the gap between the cylinders (HT1) and behind the downstream cylinder (HT2). St ($= f_v D/U\infty$, f_v is the vortex shedding frequency) jumps from 0.141 to 0.172 between $L/d = 2.5$ and 3.0 for $d/D = 1.0$ and from 0.158 to 0.212 between $L/d = 3.0$ and 3.5 for $d/D = 0.8$. Apparently the jump is due to a drastic modification of reattachment flow to coshedding flow when L/d is increased. While the higher St at the former d/D is smaller than the St ($= 0.197$) of an isolated cylinder, that at the latter is higher. In the coshedding flow (i.e., $L/d \geq 3.0$) for $d/D = 1.0$, albeit shedding vortices individually, the two cylinders have an identical St, slightly smaller than the isolated cylinder. This is an established phenomenon for the same diameter tandem cylinders that the convective vortices from the upstream cylinder trigger the shedding from the downstream cylinder, making both St identical. On the other hand, though having different diameters at $d/D = 0.8$, the two cylinders have identical St again due to a lock-in phenomenon. The downstream cylinder displays two St (say, 0.134 and 0.268 at $L/d = 3.5$) at $d/D = 0.6$ in the coshedding regime, where the upstream cylinder $St = 0.268$, suggesting both fundamental and subharmonic locks-in. At $d/D = 0.4$ and 0.2, thought St(s) of two cylinders are identical in the reattachment regime, they are different in the coshedding regime.

C_D, C_D' and C_L' variations with L/d shown in Fig. 3a–c reflect that they are strong functions of L/d and d/D, especially before the critical spacing. For $d/D = 1.0$ and 0.8, as L/d increases from 1.0 to 2.0, C_D, C_D' and C_L' all escalate. At the same L/d range, $d/D = 0.6$ and 0.2 have the opposite behaviors; C_D, C_D' and C_L' all drop. C_D, C_D' and C_L' decrease slightly for $d/D = 1.0$ and 0.8 between $L/d = 2.0$ and 2.5. It is remarkable that at the critical spacing C_D, C_D' and C_L' all jump for $d/D = 1.0$–0.4, but drop for $d/D = 0.2$. C_D in general enhances with a decrease in d/D except at $d/D = 1.0$, $L/d = 2.0$. C_D' and C_L', on the other hand, generally
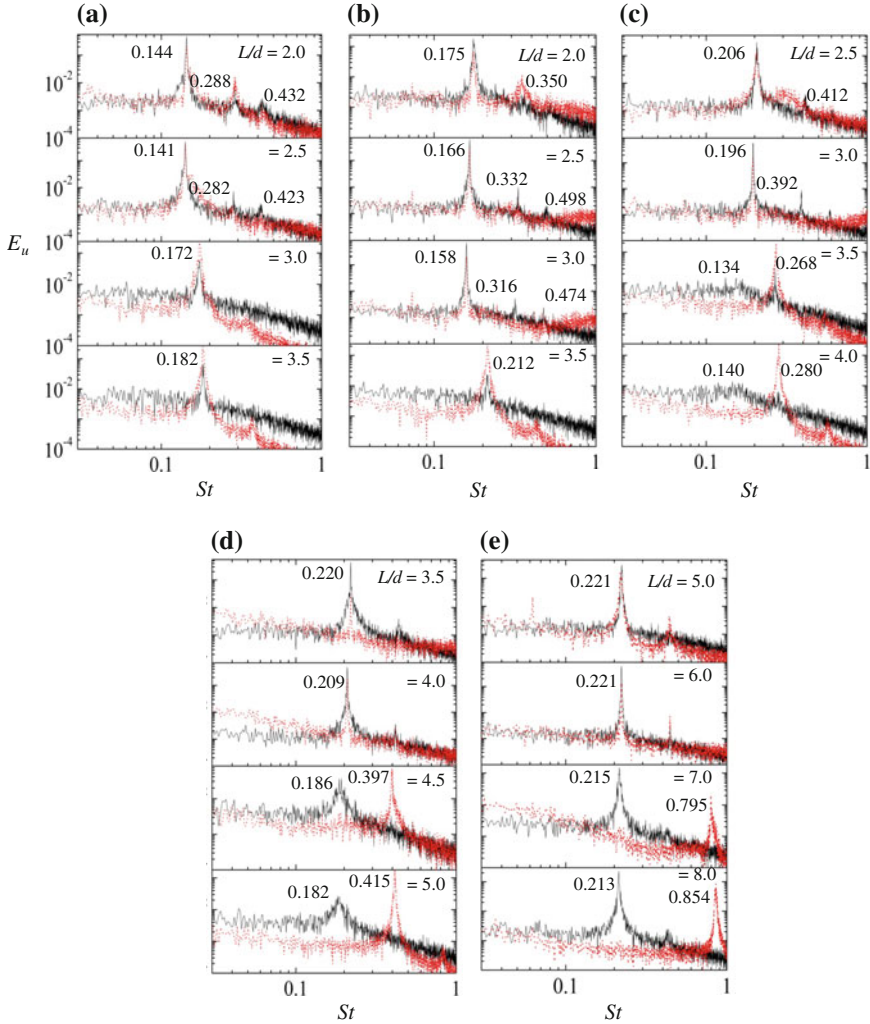
Fig. 2 Power spectra of hotwire (HT1 and HT2) signals: **a** $d/D = 1.0$, **b** $d/D = 0.8$, **c** $d/D = 0.6$, **d** $d/D = 0.4$, and **e** $d/D = 0.2$, at different L/d. *Dotted line* HT1; *solid line* HT2

decrease with d/D decreasing from 1.0 to 0.6 and increase with d/D decreasing from 0.4 to 0.2. While the former behavior is mostly influenced by vortices/shear-layer weakening with the decrease in d/D, the latter by a larger flow velocity in the gap. A flow map showing reattachment, bistable and coshedding flows is given in Fig. 3d. The critical spacing associated with possible bistable flow extends with a decrease in d/D.

Figure 4 presents the contours of the time-mean streamwise velocity, $\overline{U}^{*} = \overline{U}/U_{\infty}$, for $d/D = 0.8$ at $L/d = 3.0$ and 3.5 and for $d/D = 0.2$ at $L/d = 6.0$ and 7.0. The
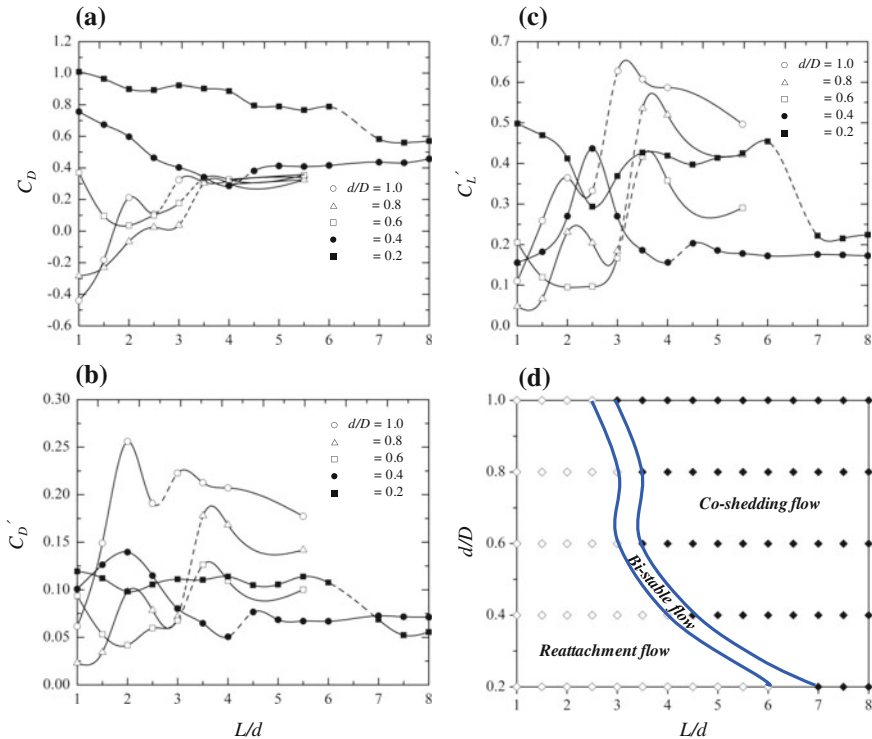
Fig. 3 Dependence of **a** C_D, **b** C_D', **c** C_L' on L/d, and **d** flow regimes on $L/d - d/D$

minimum $\overline{U}^*$ and the recirculation bubble size, enclosed by $\overline{U}^* = 0$, provide a measure for recirculation strength that is highly connected to forces. When the reattachment flow (Fig. 4a1, b1) modifies to coshedding (Fig. 4a1, b1) with increase in L/d, the recirculation bubble size shrinks drastically behind the upstream cylinder, but expands behind the downstream cylinder. In the reattachment flow regime, the shear layers reattaches on the side surfaces of the downstream cylinder at $d/D = 0.8$ (Fig. 4a1) forming a wider bubble in the gap, but on the front surface at $d/D = 0.2$ (Fig. 4b1) forming a narrower bubble. C_D on the downstream cylinder is thus larger at $d/D = 0.2$ than $d/D = 0.8$. On the other hand, the approaching flow momentum on the downstream cylinder ($y^* = -0.5$–0.5) for $d/D = 0.8$ is larger at $L/d = 3.5$ than $L/d = 3.0$, while that for $d/D = 0.2$ is smaller at $L/d = 7.0$ than $L/d = 6.0$, suggesting a jump in forces between reattachment and coshedding flows at $d/D = 0.8$ and a drop at $d/D = 0.2$.
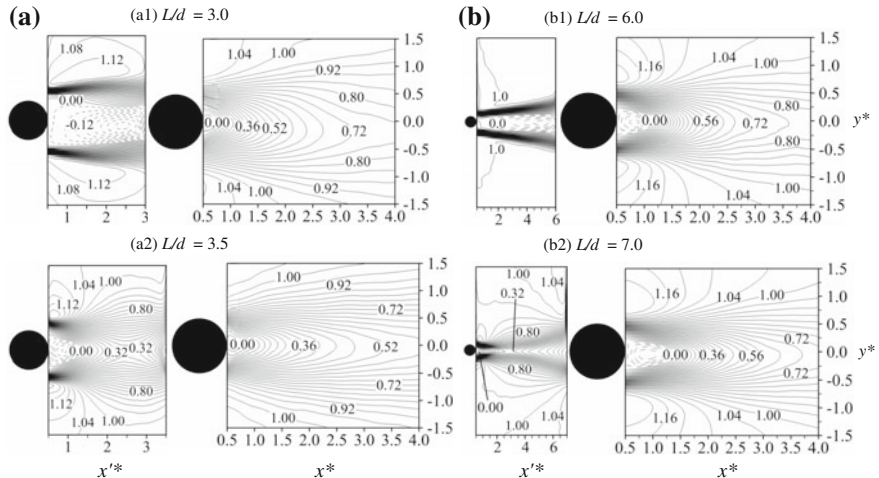
Fig. 4 Contours of time-mean streamwise velocity, $\bar{U}^* = \bar{U}/U_\infty$ at **a** $d/D = 0.8$, **b** $d/D = 0.2$. $x'* = x'/d$, $x^* = x/D$, $y^* = y/D$. Contour increment is 0.04

4 Conclusions

1. *St* is identical for both cylinders in the reattachment regime regardless of *d/D*. In the coshedding regime, the downstream cylinder shedding frequency locks-into the upstream cylinder for *d/D* = 1.0, 0.8 and 0.6. For the other two *d/D*, lock-in is not observed.
2. The critical *L/d* dividing the reattachment and coshedding flows is larger at smaller *d/D*, nestling at 2.5 < *L/d* < 3.0, 3.0 < *L/d* < 3.5, 4.0 < *L/d* < 4.5, and 6.0 < *L/d* < 7.0 for *d/D* = 1.0, 0.8–0.6, 0.4 and 0.2, respectively. While forces jump at the critical spacing for *d/D* = 1.0–0.4, they drops for *d/D* = 0.2. The possible physics behind the two phenomena is unearthed.

References

Alam MM, Zhou Y (2008) Strouhal numbers, forces and flow structures around two tandem cylinders of different diameters. J Fluids Struct 24:505–526

Alam MM, Sakamoto H, Zhou Y (2005) Determination of flow configurations and fluid forces acting on two staggered circular cylinders of equal diameter in cross-flow. J Fluids Struct 21:363–394

Igarashi T (1981) Characteristics of the flow around two cylinders arranged in tandem, 1st Report. Bull JSME B 24:323–331

Sumner D (2010) Two circular cylinders in cross-flow: a review. J Fluids Struct 26:849–899

Xu G, Zhou Y (2004) Strouhal numbers in the wake of two incline cylinders. Exps Fluids 37:248–526

Zdravkovich MM (1987) The effects of interference between circular cylinders in cross flow. J Fluids Struct 1:239–261

Vortex Formation in the Wake of a Streamwisely Oscillating Cylinder in Steady Flow

G. Tang, L. Cheng, L. Lu, M. Zhao, F. Tong and G. Dong

Abstract This study presents the vortex formation in the wake of a cylinder undergoing streamwise oscillations in steady flow. It is found that the global wake structure possesses a spatial-temporal symmetry over N periods of cylinder oscillation when sub-harmonic synchronizations occur. The sub-harmonic synchronization modes are characterized by shedding of M pairs $(1 \leq M < N)$ of vortices in N periods of cylinder oscillation. The wake of M/N modes is comprised of vortex groups of M vortices arranged in a similar way to Kármán vortex street. The lift force shows excellent periodicity when lock-on occurs, and presents multiple peaks in its spectrum. The primary flow mechanism responsible for the sub-harmonic lock-on is identified as the interaction of the small sized shear bands induced by the cylinder oscillation with the shear layers induced by the steady flow.

Keywords Oscillation · Lock-on · Synchronization · Flow structure

1 Introduction

Streamwise oscillations of a cylinder in steady flow have been widely investigated (Ongoren and Rockwell 1988; Zdravkovich 1996; Leontini et al. 2011, 2013). It has been shown that the vortex shedding from the cylinder synchronizes with either the

G. Tang · L. Cheng (✉) · L. Lu · G. Dong
State Key Laboratory of Coastal and Offshore Engineering, Dalian University of Technology, Dalian, China
e-mail: liang.cheng@uwa.edu.au

L. Cheng · F. Tong
School of Civil, Environmental and Mining Engineering,
The University of Western Australia, Crawley, WA, Australia

M. Zhao
School of Computing, Engineering and Mathematics, University of Western Sydney,
Penrith, NSW, Australia

cylinder oscillation frequency or half of it at certain combinations of the oscillation amplitude ($A = A^*/D$) and frequency ($f = f_d/f_{St}$), where A^* is the dimensional amplitude, f_d is the oscillation frequency ($T^* = 1/f_d$), D is the cylinder diameter and f_{St} is the vortex shedding frequency of an identical stationary cylinder. A number of synchronization modes have been identified and were attributed to the competition between modes of vortex formation induced by the steady flow and the cylinder oscillation. The sub-harmonic synchronization modes have also been found (Leontini et al. 2011, 2013; Al-Mdallal et al. 2007). It was shown that synchronization occurs over N periods of cylinder oscillation when the vortex shedding frequency f_s is modulated near $f_d(1 - 1/N)$. An empirical method was proposed (Leontini et al. 2013) to predict f_d and A at which the P_N modes occur.

The aim of this study is to investigate the global wake structure of the P_N modes and the possibility of the existence of other synchronization modes.

2 Numerical Approach

A two-dimensional numerical method, similar to the one employed by Zhao and Cheng (2014), was chosen for the present study. In the simulations, the circular cylinder is placed in a rectangular domain with $145D$ in length ($60D$ upstream and $85D$ downstream) and $90D$ in height, respectively. An oscillation velocity (Tong et al. 2015) with a non-zero mean (U_0) is specified as the boundary conditions, $U(t) = U_0 + 2\pi f_d A \cdot \cos(2\pi f_d t)$. The flow is primarily simulated at Reynolds number (Re) around 200.

3 Result Discussions

The synchronization modes identified are shown in Fig. 1. Apart from the primary synchronization modes which occur either at $0.5f_d$ or f_d, synchronizations at f_d/N with $N = 3$ and 4 are also found. It is seen that the synchronization mode with $M/N = 1/3$ is well outside the region where primary synchronizations occur, while the mode with $M/N = 3/4$ is found near the low f bounds of the primary synchronization region.

The 1/3 synchronization mode is investigated by examining the transient C_L fluctuations in Fig. 2 at (f, A) = (2.80, 0.10). C_L oscillates at a period that is three times of T^* of the cylinder, since the dominant peak is $f_L = f_d/3$ with f_L being the frequency of C_L, rather than f_d or $0.5f_d$ as in the primary lock-in regime. The periodicity of C_D and $X(t)$ oscillations leads to an enclosed Lissajous phase diagram. These characteristics suggest the occurrence of 1/3 synchronization.

The 3/4 synchronization mode is also discovered, where the oscillation of the wake is locked on to $f_d/4$. It is observed in a region where the f_d is close to f_s and A is relatively large, e.g. at points of (A, f) = (0.25, 1.05) and (0.30, 1.00). For the
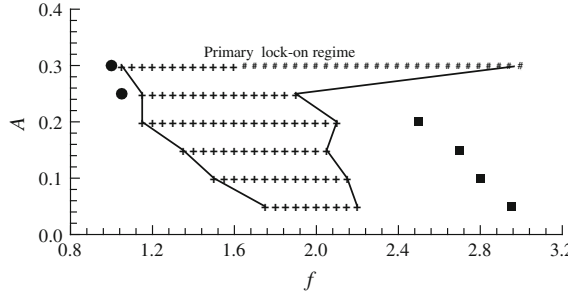
Fig. 1 Occurrence of lock-on for streamwise oscillation of a circular cylinder in uniform flow at $Re = 200$. (+ Primary lock-on with $2.0T^*$; # Primary lock-on with T^*; ■ 1/3 lock-on with $3.0T^*$; ● 3/4 lock-on with $4.0T^*$; T^* is the oscillatory period of the circular cylinder.)
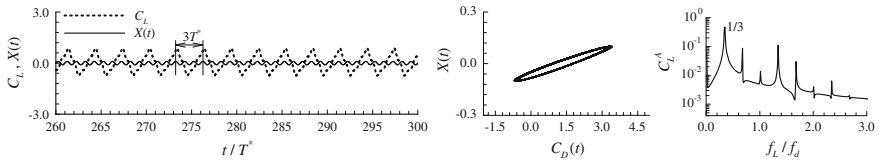

Fig. 2 Transient trace of C_L (*left*), Lissajous phase diagram (*middle*) and spectrum of C_L through FFT analysis (*right*) for a typical 1/3 synchronization case at $A = 0.10$, $f = 2.80$ and $Re = 200$

3/4 synchronization, C_D shows excellent regularity over four T^* (Fig. 3), where the phase diagram is comprised of closed loops and a dominant peak at $f_L/f_d = 1/4$ of the C_L spectra are observed. The wake structure is the most striking flow feature of the 3/4 synchronization and Fig. 4 shows that the wake comprises staggered vortex groups. Each vortex group consists of three vortices and behaves in a similar way to a single vortex in the Kármán vortex street. Compared to the steady flow, the three vortices in each group align along an inclined line relative to the flow direction. The inclination of the vortex groups alternates between two successive groups. Each vortex group in the top row consists of two negative vortices and one positive vortex while the opposite is true for the bottom row. It is also observed that one vortex group is generated within a half of synchronization period or two periods of cylinder oscillation. This is the reason that the frequency of synchronization is $f_d/4$ and that the large spectrum peak of C_L is $f_d/4$. It is observed that the interactions
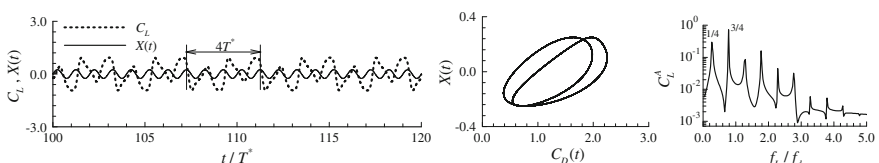

Fig. 3 $M/N = 3/4$ synchronization at $Re = 200$, $A = 0.25$ and $f = 1.05$
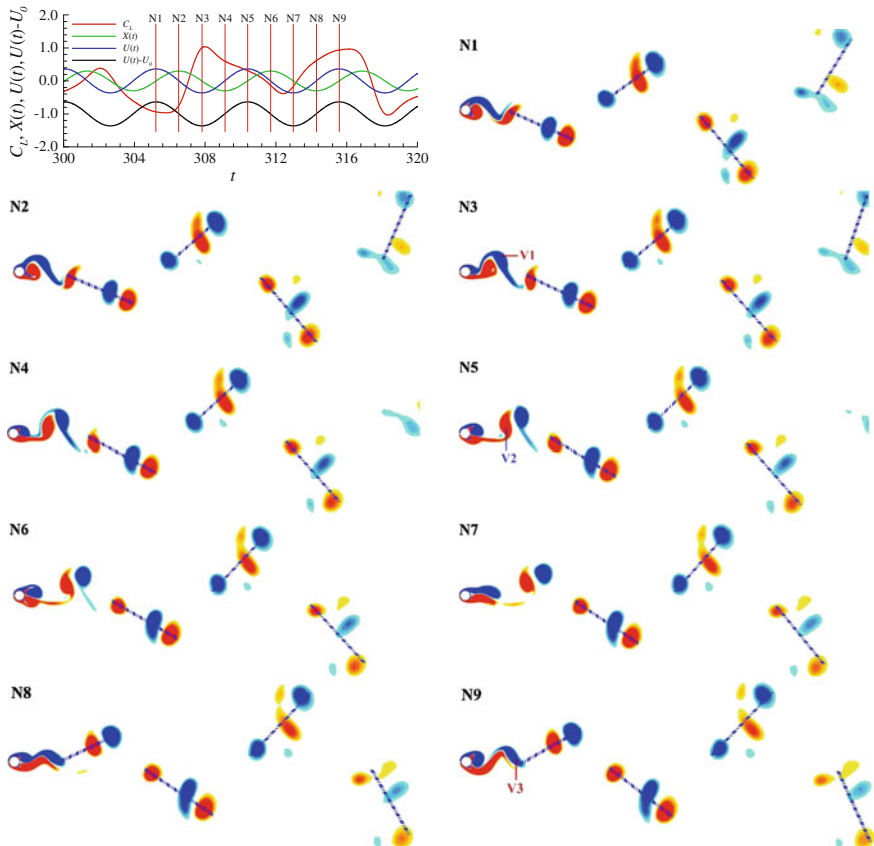
Fig. 4 Instantaneous vorticity contour over half cycle of vortex shedding period at $A = 0.30$, $f = 1.00$, $Re = 200$. Vorticity contours are correlated to the transient traces of $X(t)$, oscillatory velocity $U(t)$, relative velocity of the cylinder oscillation to the flow $U(t) - U_0$ and C_L on the cylinder

between the shear bands generated by the cylinder oscillation and those due to the steady flow around the cylinder delay the vortex shedding from the cylinder and are responsible for the synchronization modes observed in this study.

Multiple peaks are found in the spectrum of the C_L at $f_d/4$, $3f_d/4$, $5f_d/4$, $7f_d/4$ and higher frequencies. Clearly the dominant peak at $3f_d/4$ corresponds to f_s, i.e. three pairs of vortices are shed in four cylinder oscillation periods. The peak at $f_d/4$ corresponds to the synchronization frequency where a pair of vortex groups is generated in four cylinder oscillation periods. These are the fundamental frequencies. The peaks at other frequencies are attributed to the sum frequencies of three fundamental frequencies through nonlinear interactions. A formula to predict the interaction of these frequencies is reported in a separate study (Cheng et al. 2015).
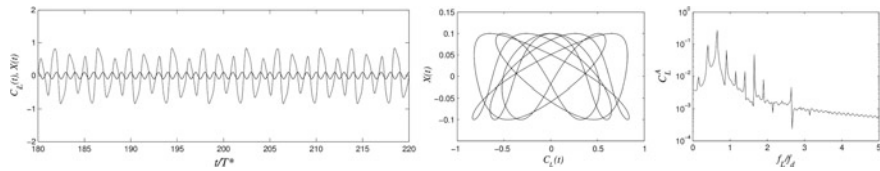
Fig. 5 $M/N = 5/8$ synchronization at $Re = 190$, $A = 0.1$ and $f = 1.405$
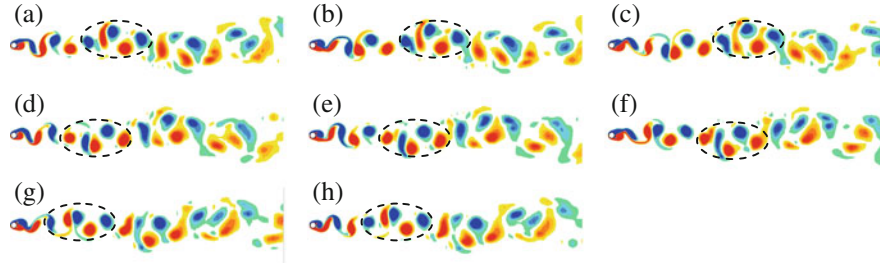

Fig. 6 The wake structures for a sub-harmonic synchronization flow with $M/N = 5/8$ at $(f, A) = (1.405, 0.10)$ and $Re = 190$. Each snapshot represents flow fields at nT^*.

Figures 5 and 6 illustrate the force characteristics of 5/8 synchronization along with eight snapshots of flow structures at $(f, A) = (1.405, 0.10)$. Similar wake structures to those in Fig. 4 are observed, but the difference lies in that two groups of five vortices are shed in eight cylinder oscillation periods, resulting in a synchronization frequency of $f_d/8$ and a vortex shedding frequency of $5f_d/8$. The existence of a general sub-harmonic synchronization mode of M/N, where N is an integer greater than 2 and M is an integer less than N, can be inferred from the occurrence $M/N = 5/8$. The synchronization frequency and vortex shedding frequency are f_d/N and $f_d M/N$ respectively. The M/N synchronization modes found in this study are reported in Cheng et al. (2015).

4 Conclusions

New sub-harmonic synchronization modes for streamwise cylinder oscillations in steady flow, namely M/N synchronization modes, are discovered. These modes are characterized by a spatial-temporal symmetry in the global wake, including flow features of (1) M pairs of shed vortices in N periods of cylinder oscillation ($1 \leq M < N$), resulting in the vortex frequency of M/N, (2) excellent repeatability of transient traces of lift coefficient, and (3) staggered wake groups that behave in a similar way to the single vortex in the Kármán vortex street, which is due to the interaction of the small sized shear bands induced by the cylinder oscillation with the shear layers

induced by the steady flow. These features are classified as sub-harmonic synchronization modes to differentiate them from the conventional primary synchronization modes.

References

Al-Mdallal Q, Lawrence K, Kocabiyik S (2007) Forced streamwise oscillations of a circular cylinder: locked-on modes and resulting fluid forces. J Fluids Struct 23:681–701

Cheng L, Tang G, Lu L et al (2015) Subharmonic synchronizations of streamwise cylinder oscillations in steady flow. J Fluid Mech (Under review)

Leontini JS, Lo Jacono D, Thompson MC (2011) A numerical study of an inline oscillating cylinder in a free stream. J Fluid Mech 688:551–568

Leontini JS, Lo Jacono D, Thompson MC (2013) Wake states and frequency selection of a streamwise oscillating cylinder. J Fluid Mech 730:162–192

Ongoren A, Rockwell D (1988) Flow structure from an oscillating cylinder Part 1. Mechanisms of phase shift and recovery in the near wake. J Fluid Mech 191:197–223

Tong F, Cheng L, Zhao M et al (2015) Oscillatory flow regimes around four cylinders in a square arrangement under small KC and Re conditions. J Fluid Mech 769:298–336

Zdravkovich M (1996) Different modes of vortex shedding: an overview. J Fluids Struct 10:427–437

Zhao M, Cheng L (2014) Two-dimensional numerical study of vortex shedding regimes of oscillatory flow past two circular cylinders in side-by-side and tandem arrangements at low Reynolds numbers. J Fluid Mech 751:1–37

The Wake of Three Square Prisms in Side-by-Side Arrangement

Qinmin Zheng, Md. Mahbub Alam and Yu Zhou

Abstract The wake of three side-by-side square prisms placed normal to the oncoming flow at a Reynolds number $Re = 150$ is examined numerically using finite volume method. The prism center-to-center pitch L is varied from $L/W = 1.1$ to 9.0 where W is the prism width. Five distinct flow structures and their ranges are identified, viz., single-bluff-body flow ($L/W < 1.5$), flip-flopping flow ($1.5 \leq L/W \leq 2.0$), symmetrically-biased interlocked flow ($2.0 < L/W \leq 2.6$), non-biased interlocked flow ($2.6 < L/W \leq 7.0$), and non-biased weakly interlocked flow ($L/W > 7.0$). Physical aspects of each flow regime, such as vortex structures, gap flow deflections, shedding frequencies are discussed in detail. A secondary frequency other than the Strouhal number (primary frequency) is identified in symmetrically-biased and non-biased interlocked flow regimes. The origin and effect of the secondary frequency on lift forces are unearthed.

Keywords Flow-structure interactions · Three side-by-side square prisms · Vortex streets · Secondary frequency

1 Introduction

In spite of its great importance to engineering, the flow around multiple square prisms has received much less attention than that of circular cylinders. Recently, a surge focus has been given on square prisms. Alam et al. (2011) at $Re = 4.7 \times 10^4$ performed systematic measurements of the flow field, Strouhal number (St), and

Q. Zheng · Md.M. Alam (✉) · Y. Zhou
Institute for Turbulence-Noise-Vibration Interaction and Control, Shenzhen Graduate School, Harbin Institute of Technology, Shenzhen, China
e-mail: alamm28@yahoo.com; alam@hitsz.edu.cn

Md.M. Alam
Key Lab of Advanced Manufacturing Technology, School of Mechanical Engineering and Automation, Shenzhen Graduate School, Harbin Institute of Technology, Shenzhen, China

fluid forces on two side-by-side square prisms at $L/W = 1.02 \sim 6.00$. Four distinct flow regimes, namely (i) single-body regime, (ii) two-frequency regime, (iii) transition regime, and (iv) coupled vortex street regime, are identified. At much smaller $Re = 300$, Alam and Zhou (2013) observed qualitatively similar results in flow visualization experiments. Agrawal et al. (2006) using the lattice Boltzmann method (LBM) investigated the laminar wake ($Re = 73$) of two square prisms at $L/W = 1.7$ and 3.5, corresponding to the flip-flop and synchronized regimes respectively. Compared to two side-by-side prisms involving one gap flow, three side-by-side prisms may generate two gap flows. How the two gap flows interact with each other and influence the wake would be much interesting.

The aim of the present work is to examined detailed physics of the flow over three side-by-side square prisms, including the behavior of the gap flows, shedding process and their influences to the wake dynamics. A two-dimensional numerical simulation is conducted at $Re = 150$ for $L/W = 1.1$–9.0 covering all possible flow regimes.

2 Numerical Methods

The dimensionless 2-D N-S equations are discretized using the finite-volume method, which applied on structured meshes. The pressure-velocity coupling is handled with the semi-implicit pressure linked equations (SIMPLE) scheme. Discretizations of the convective terms in the conservation equations are accomplished through a second-order accurate upwind differencing scheme. Second-order implicit forward discretization is adopted for the time derivative term in order to accelerate the convergence process. The length of the computational domain is taken to be $L_x = L_u + L_d$, where $L_u = 13.5 \, W$ and $L_d = 29.5 \, W$ are the upstream and downstream lengths, respectively, from the coordinate origin at the center of the middle prism. The lateral boundaries of the computation domain are located at $L_t/2 = 28.5 \, W$ from the coordinate origin symmetrically, giving a blockage ratio $3 \, W/L_t = 5.26 \, \%$. At the inlet, a uniform velocity profile ($u_1 = U_\infty$, $u_2 = 0$) is imposed, while the stress vector is set to zero at the outlet boundary ($\sigma_{11} = 0$, $\sigma_{21} = 0$). On the upper and lower lateral boundaries, the component of the velocity normal to the surface and the component of the stress vector along the boundaries are prescribed to zero ($u_2 = 0$, $\sigma_{12} = 0$). No-slip boundary condition ($u_1 = u_2 = 0$) is employed on the surfaces of the square prisms. In the computation domain, the initial flow velocities (at $t^* = U_\infty t/W = 0$) are given as $u_1 = U_\infty$, $u_2 = 0$.

3 Flow Structure and Shedding Frequency

Figure 1 shows the contours of non-dimensional instantaneous vorticity patterns at different regimes. The single-bluff-body flow prevails at $L/W < 1.5$, where vortex shedding occurs essentially from the outer shear layers of the outer prisms (Fig. 1a);
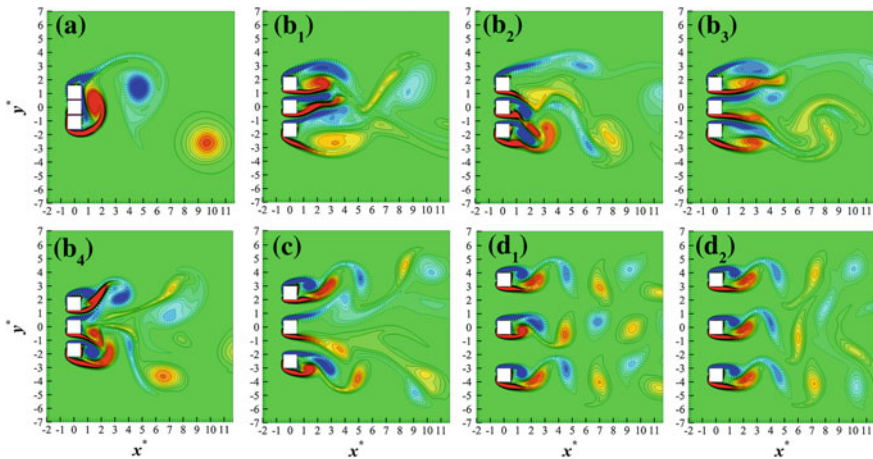
Fig. 1 Contours of instantaneous vorticity for different flow regimes. **a** Single-bluff-body flow (*L/W* < 1.5) *L/W* = 1.1; **b** Flip-flopping flow (1.5 ≤ *L/W* ≤ 2.0) *L/W* = 1.5: the gap flows biased (b$_1$) *upward*, (b$_2$) *downward*, (b$_3$) *straight*, (b$_4$) *outward*; **c** Symmetrically-biased interlocked flow (2.0 ≤ *L/W* ≤ 2.6) *L/W* = 2.5; **d** Non-biased interlocked flow (2.6 < *L/W* ≤ 7.0) *L/W* = 3.5: the middle prism shedding (d$_1$) anti-phase and (d$_2$) in-phase with the others. Non-biased weakly interlocked flow (*L/W* > 7) are not shown here

a single vortex street, thus, forms behind the three prisms, similarly to that of a single bluff body. An identical *St* is observed for the three prisms.

When *L/W* is increased to 1.5 ≤ *L/W* ≤ 2.0, a greater amount of flow can pass through the gaps and can split the wake into three immediately downstream of the prisms. Appreciable vortices from the gap sides form around the prisms, and merge with the outer vortices shed from the freestream sides of the outer prisms. The gap flow now can flip-flop randomly at different fashions to be biased upward (Fig. 1b$_1$), downward (Fig. 1b$_2$), straight (Fig. 1b$_3$), and outward (Fig. 1b$_4$), generating four different flow structures. For the flip-flopping flow, the peaks corresponding to the *St* in the power spectrum are relatively wider than those in the other regimes, because of the random switch of the gap flows. Furthermore, the middle prism's *St* is higher than that of the outer prism, indicating that most of time the middle prism undergoes the narrow wake.

The symmetrically-biased interlocked flow occurring at 2.0 < *L/W* ≤ 2.6 is characterized by the gap flow biased/diverged outward symmetrically (Fig. 1c). A substantial wide wake (associated with the lower *St*) thus accompanies the middle prism and a narrow wake (associated with the higher *St*) complements each outer prism. The vortices shedding from the outer prisms are found to be perfectly coupled with a constant phase lag $\phi = 180°$ (anti-phase).

Non-biased interlocked flow appears at 2.6 < *L/W* ≤ 7.0 where the gap flows are no longer biased. A single vortex street, qualitatively similar to that behind an isolated prism, persists behind each prism. Again the vortex sheddings from the outer prisms occurring at the same frequency are interlocked with a fixed phase lag

ϕ. The vortex shedding frequency of the middle prism is however different, slightly higher than that of the outer prisms. The instantaneous phase relationship between the vortex sheddings from the middle and outer prisms thus changes periodically from anti-phase (Fig. 1d$_1$) to in-phase (Fig. 1d$_2$), and vice versa, which has a great impact on the time histories of lift forces acting on the prisms.

At $L/W > 7.0$, the interlocking between the wakes of three prisms is weak and each prism tends to behave like a single prism with difference in frequencies between the middle and outer prisms getting smaller. This regime, hence, can be regarded as weak-interaction or non-biased weakly interlocked flow.

4 Secondary Frequency and Its Effect on C_L

It has been observed that C_L signals at the symmetrically-biased and non-biased interlocked flows have a short (primary frequency) and long (secondary frequency) periods. Figure 2 shows time histories of lifts of the three prisms at $L/W = 3.5$ and instantaneous phase shift between the vortex sheddings of the middle and outer prisms. In the Fig. 2a, the short period, associated with the shedding, is easily understood, while a beat-like change in C_L amplitude is also obvious, with maximum, minimum and again maximum amplitudes at time $t^* = 1836.3$, 1877.4 and 1923.5, respectively. This beat period is therefore about $T^* = 87.2$, corresponding to $St = 0.0114$, very close to the secondary frequency $St = 0.0112$ obtained in the power spectrum (not shown). It thus proves that the beat phenomenon is associated with the secondary frequency. Indeed the flow structures presented in Fig. 1d$_1$, (d$_2$) correspond to the maximum and minimum amplitude of C_L ($t^* = 1836.3$ and 1877.4, respectively) associated with the secondary frequency, and at the same time both flow structures correspond to a maximum C_L associated with the primary frequency of the outer prism, as indicated by vertical lines. Interestingly, maximum C_L associated with the secondary frequency occurs when an in-phase shedding occurs from the two sides of a gap (Fig. 1d$_1$). On the other hand, an anti-phase shedding from the two sides of a gap results in a minimum C_L associated with the secondary frequency (Fig. 1d$_2$). Fortuitously, both gaps have the in-phase shedding (Fig. 1d$_1$) or anti-phase shedding (Fig. 1d$_2$) synchronously at this L/W, as the shedding phase lag between the outer prisms is a constant of $\approx 0°$. C_L(s) of the three prisms, associated with the secondary frequency, are thus reaching maximum or minimum simultaneously. When the phase lag between the outer prisms is $\neq 0°$, maximum or minimum C_L of the three prisms does not occur simultaneously. So the beat/secondary frequency results from a continuous change in the phase lag between the sheddings from the two sides of a gap, from in-phase to anti-phase, anti-phase to in-phase, and so on, as shown in Fig. 2b.
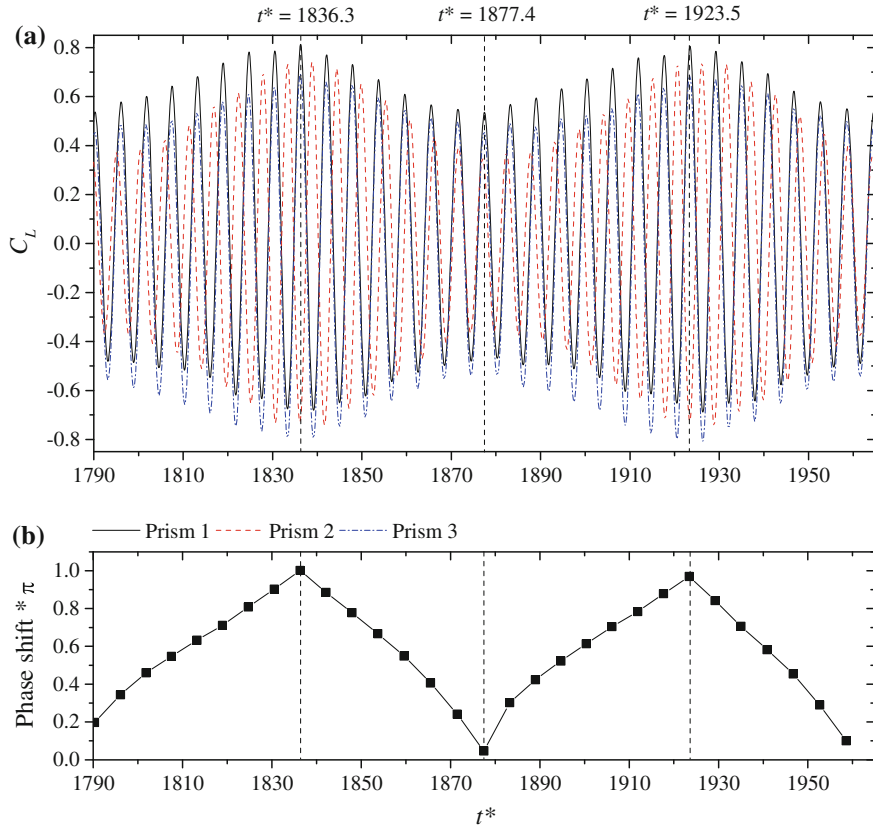
Fig. 2 **a** Signals of lift coefficient acting on the three prisms at $L/W = 3.5$. **b** Instantaneous phase shift between the vortex sheddings of *middle* and *outer* prisms at $L/W = 3.5$, estimated from peak-to-peak phase lag between the *middle* and *outer* prisms' lifts in Fig. (a)

5 Conclusions

Five distinct flow regimes have been identified. (i) Single-bluff-body flow prevailed at $L/W < 1.5$ is characterized by vortex shedding from the freestream sides only, forming a single Karman vortex street with an identical St. (ii) Flip-flopping flow appears at $1.5 \leq L/W \leq 2.0$ where the two gap flows gain adequate strength to split the wake into three immediately downstream, but the three wakes merge into one shortly. The two gap flows flip-flop, both to be biased upward, downward, straight, and outward, and result in the broad banded St, while the St of middle prism is higher than that of the outer prisms. (iii) Symmetrically-biased interlocked flow $(2.0 < L/W \leq 2.6)$ features with the two gap flows deflecting outward symmetrically, forming one wide wake of smaller St behind the middle prism and two narrow wakes of a larger St behind the two outer prisms. (iv) The non-biased interlocked

flow taking place at $2.6 < L/W \leq 7.0$ is exemplified by the fact that the gap flows are not biased anymore; the wake behind each prism is similar to that of an isolated prism. The sheddings from the outer prisms are interlocked with a constant phase lag and identical St, which is smaller than that of the middle prism. (v) In the non-biased weakly interlocked flow ($L/W > 7.0$), the difference in St between the middle and outer prisms is smaller and the interaction between the adjacent wake is weak.

A secondary frequency is observed in the symmetrically-biased and non-biased interlocked flows, equal to the difference in shedding frequencies of the middle and outer prisms. The flow in the gap receives an interaction of the two frequencies, resulting in the secondary frequency. The secondary frequency has a great impact on the time series of the lift force to have a beat-like change, where the lift force of outer prisms associated with the beat is maximum when the sheddings from the two sides of a gap are in-phase, and reaches a minimum when they are anti-phase.

References

Alam MM, Zhou Y (2013) Intrinsic features of flow around two side-by-side square cylinders. Phys Fluids 25(085106):1–21

Alam MM, Zhou Y, Wang XW (2011) The wake of two side-by-side square cylinders. J Fluid Mech 669:432–471

Agrawal A, Djenidi L, Antonia RA (2006) Investigation of flow around a pair of side-by-side square cylinders using the lattice Boltzmann method. Comput Fluids 35:1093–1107

Numerical Simulation Study on a Passive Jet Flow Control Method to Suppress Unsteady Vortex Shedding from a Circular Cylinder

Wenli Chen, Xiangjun Wang, Feng Xu, Hui Li and Hui Hu

Abstract A passive jet flow control method for suppressing unsteady vortex shedding from a circular cylinder via a numerical simulation is presented in this paper. The circular cylinder is wrapped in a hollow pipe. There are a set of the suction/jet holes on the windward side and leeward side of the outer surface of the pipe. The oncoming flow enters into the hollow pipe through the inlet holes and then blows out from the outlet holes. As a result, the vortex shedding alternately in the wake behind the circular cylinder will be suppressed or destroyed. The reliability of the numerical model without control is first verified by comparison with previous research results. Next, the control effectiveness of this method for the pressure distribution, aerodynamic forces and flow characteristics are discussed for a large range of Reynolds number, $Re = 10^3$ to 10^5. The results indicate that the proposed control method has a remarkable effect on the aerodynamic forces on the circular cylinder with high Reynolds number.

Keywords Circular cylinder · Vortex shedding · Jet · Flow control · Numerical simulation

W. Chen (✉) · X. Wang · H. Li
China Key Lab of Structures Dynamic Behavior and Control,
Harbin Institute of Technology, Ministry of Education, Harbin
Heilongjiang 150090, China
e-mail: cwl_80@hit.edu.cn

W. Chen · H. Hu
Department of Aerospace Engineering, Iowa State University,
Ames, IA 50011, USA

F. Xu
School of Civil and Environment Engineering,
Harbin Institute of Technology Shenzhen Graduate School,
Shenzhen 518055, China

441

1   Introduction

In the past several decades, a large number of experiments and numerical simulations have been performed to study the aerodynamic characteristics of a single stationary circular cylinder. Wieselsberger (1921) and Munson (2002) presented the mean drag coefficient of a single stationary circular cylinder in a cross-flow changing with Reynolds number. The relationships between the Strouhal number and Reynolds number for a stationary circular cylinder in a cross-flow was studied by Bearman (1969) and Norberg (1994). As we elucidated the flow around a bluff body, it was revealed that the vortex shedding alternately in the wakes was the main cause of the vortex-induced vibration (VIV). Therefore, a variety of passive and active control methods were proposed to suppress the VIV. An active steady suction flow control was investigated by Chen et al. (2013, 2014)

Compared with the active jet flow control method, which requires external input energy to induce the jet flow, the present passive jet flow control need not consume external energy and is realized as follows: the partial oncoming flow blows into the inlet holes, passes through the ring channels and blows from the jet holes into the near wake for breaking/suppressing the alternating vortex shedding in the wake.

2   System Modelling

Two types of numerical models: baseline and five-hole models are employed in the numerical simulation, as shown in Fig. 1. Each of the models includes five different Reynolds numbers: $Re = 1.0 \times 10^3$, 1.0×10^4, 1.0×10^5, 1.5×10^5 and 2.0×10^5. The baseline case is the flow around a stationary circular cylinder with the diameter, D, of 100 mm. The five-hole model is the cases of the passive jet flow control method. A ring channel with a pipe height of 5 mm covers a stationary circular cylinder. The five-hole model is the case in which five inlet holes are set near the front stagnation point and five outlet holes are close to the rear stagnation point. The interval angle between two neighboring holes is 15°, and the width of each hole accounts for 7.5°. The height of the holes is 0.25*D, which equals half of the cylinder.
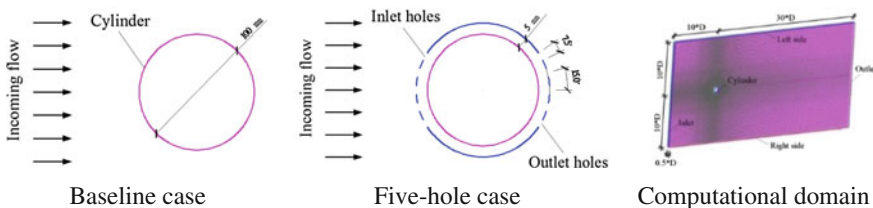

Fig. 1   Information on the numerical model of the passive jet flow control method

The distance between the center of the cylinder and the entrance is 10*D, and the distance to the export is 30*D. The computational domain width is 20*D (the blocking ratio is approximately 5.0 %). The O-shaped grids with 480 uniformly distributed cells around the perimeter of the cylinder are applied. The O-subdivision performed twice makes the grids around the cylinder smoother. The first grid normal to the cylinder surface was enoughly refined which y + ≈1. The cylinder axial is equidistantly divided into 20. The number of grids is approximately two million.

The shear stress transport (SST) $k - \omega$ (2 eqn) ($Re = 1.0 \times 10^3$, 1.0×10^4 and 1.0×10^5 cases) and the transition SST (4 eqn) turbulent ($Re = 1.5 \times 10^4$ and 2.0×10^5 cases) models, based on the Reynolds-averaged Navier-Stokes (RANS) method, are employed to simulate the turbulent behavior of the flow with the CFD software ANSYS FLUENT.

3 Illustrative Results

In advance of the jet flow control method, the validation of the numerical model is performed through the baseline case. The mean drag coefficient, Cd_{mean}, and the Strouhal number, St, are compared with the previous results. The feasibility and reliability of the present numerical method and grids can be accepted.

The numerical simulations of the five-hole case are subsequently performed. Figure 2 shows the distribution of the mean pressure coefficients around the middle plane of the circular cylinder. The results indicate that the distributions of the mean surface pressure in the negative pressure gradient region and the flow separation region of the numerical model were found to change slightly for the five-hole case compared with those of the baseline case when $Re = 1.0 \times 10^3$. The absolute values of the negative surface pressure coefficients on the leeward side of the numerical model were found to decrease greatly when $Re = 1.0 \times 10^4$ to 2.0×10^5 (only $Re = 1.0 \times 10^5$ was shown).
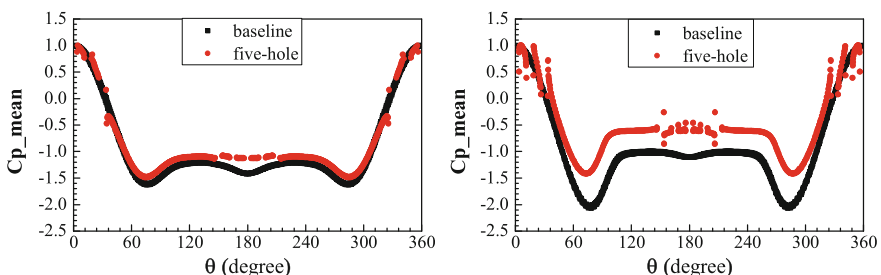

Fig. 2 Mean pressure coefficient on the middle plane of the circular cylinder: on the *left* is $Re = 1.0 \times 10^3$, on the *right* is $Re = 1.0 \times 10^5$
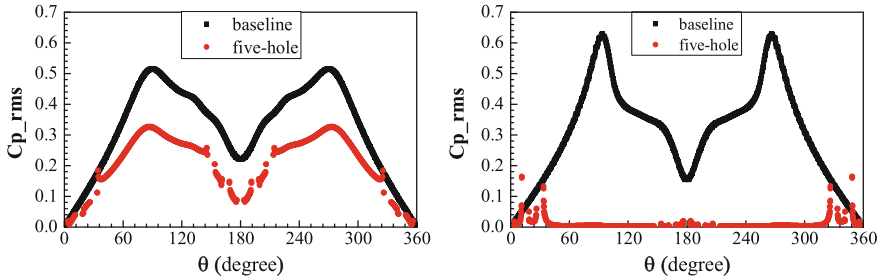
Fig. 3 Fluctuation pressure coefficient on the middle surface of the circular cylinder: on the *left* is $Re = 1.0 \times 10^3$, on the *right* is $Re = 1.0 \times 10^5$

At the same time, Fig. 3 shows the root-mean-square (RMS) values of the instantaneous pressure coefficients around the numerical model of the baseline and five-hole cases. A higher RMS value of the instantaneous surface pressures on the numerical model will result in a larger variation of the dynamic wind loads acting on the numerical model, which may cause a stronger VIV for the numerical model. For the baseline case, the RMS values of instantaneous pressures around the circular cylinder were quite high, particularly in the flow separation region on the leeward side of the numerical model. The RMS values of the instantaneous surface pressures were found to initially decrease when increasing the Reynolds numbers, and they are entirely eliminated when Re is larger than 1.0×10^5, with just a relatively larger variation on the inlet holes.

A comparison of the time histories of the instantaneous aerodynamic coefficients between the baseline case and five-hole case is shown in Fig. 4. Just the aerodynamic coefficients of the cylinder surface were calculated for the baseline case. As for five-hole case, the pipe and the cylinder surfaces were both included. The control effectiveness of the aerodynamic coefficients is initially enhanced with the increase of the Reynolds number and then tends to flatten out when the Reynolds
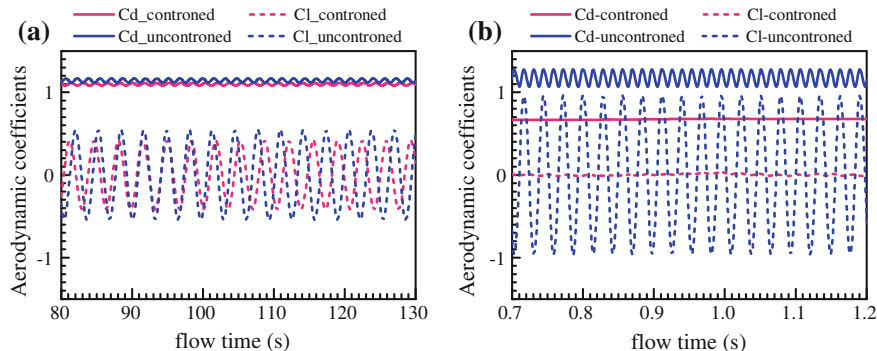

Fig. 4 Time histories of the aerodynamic coefficients: **a** $Re = 1.0 \times 10^3$, **b** $Re = 1.0 \times 10^5$
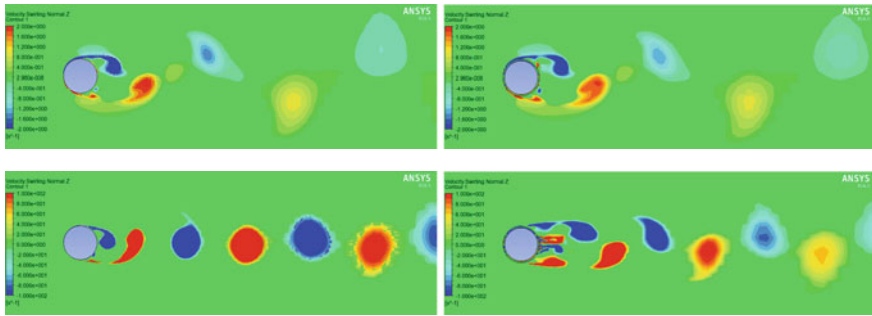
Fig. 5 Z-swirling on the middle surface at the moment of the largest lift: on the *left* are the baseline cases; on the *right* are the five-hole cases; on the *top* is $Re = 1.0 \times 10^3$, at the *bottom* is $Re = 1.0 \times 10^5$

number exceeds 1.0×10^5. Compared with the baseline case, the mean drag coefficients are reduced by 3.79 % and 42.43 % with $Re = 1.0 \times 10^3$ and $Re = 1.0 \times 10^5$ separately. The root-mean-square lift coefficients fell by 23.58 and 98.44 % simultaneously.

The instantaneous z-swirling on the middle surface at the moment of the largest lift with different Reynolds numbers are separately shown in Fig. 5. As the Reynolds number is located in the subcritical region, the wake patterns are in the "2S" mode for the five baseline cases. For the low Reynolds number (i.e., $Re = 1.0 \times 10^3$) case, the jet flow from the outlet holes has nearly no influence on the wake behind the circular cylinder. Therefore, the surface pressure distribution around the cylinder is similar to that of the baseline case. The RMS values of the instantaneous pressure coefficients around the cylinder also do not decrease, basically. The vortices still shed at a major frequency. However, for the high Reynolds numbers (i.e., $Re = 1.0 \times 10^5$), due to the impact of the flow from the outlet holes, the instantaneous z-swirling contours indicate that the vorticity near the outlet holes are in the opposite directions from the main vorticity distribution. This means that the outlet holes can generate small-scale reverse vortices against the main wake vortices. Under the passive jet flow control, the near wake becomes the approximately symmetrical pattern, resulting in a nearly complete elimination of the lift fluctuation compared with the corresponding baseline cases, as shown in Fig. 4b.

4　Conclusions

This paper presented a passive jet flow control method for suppressing unsteady vortex shedding from a circular cylinder based on a numerical simulation. This method not only has good control effectiveness for high Reynolds, but also needs

no additional energy input, as well as the absence of any complicated devices. Compared with the baseline cases, the following conclusions are obtained.

(1) The control effectiveness of this method increases with the increase of the Reynolds number and tends to be steady when $Re > 1.0 \times 10^5$. For low Reynolds numbers (e.g., 1.0×10^3), the drop of the aerodynamic force is small. For high Reynolds numbers, especially when the Reynolds number increases to the magnitude of 1.0×10^5, the reduction of the aerodynamic force is extremely remarkable.

(2) The decrease of the lift coefficient is much larger than that of the drag coefficient, and the fluctuating lift can basically be completely eliminated with a high Reynolds number. The largest reduction was by 98.44 % for Cl_{rms} for the five-hole case; however, the reduction was 42.43 % for Cd_{mean} for the five-hole case.

References

Bearman PW (1969) On vortex shedding from a circular cylinder in the critical Reynolds number regime. J Fluid Mech 37:577–585

Chen WL et al (2013) Suppression of vortex-induced vibration of a circular cylinder using suction-based flow control. J Fluids Struct 42(10):25–39

Chen WL et al (2014) An experimental study on a suction flow control method to reduce the unsteadiness of the wind loads acting on a circular cylinder. Exp Fluids 55(4):1707, 1–20

Munson BR et al (2002) Fundamentals of fluid mechanics, 5th edn. Wiley, New Delhi

Norberg C (1994) An experimental investigation of the flow around a circular cylinder: influence of aspect ratio. J Fluid Mech 258:287–316

Wieselsberger C (1921) Neuere Feststellungen über die Gesetze des Flüssigkeits- und Luftwiderstands. Phys Z 22:8–321